T. K. Datta

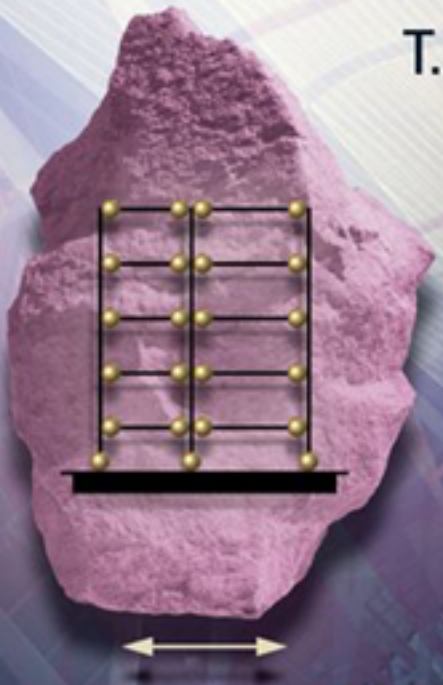

SEISMIC ANALYSIS OF STRUCTURES

Companion Website

WILEY

SEISMIC ANALYSIS OF STRUCTURES

T. K. Datta
Indian Institute of Technology Delhi, India

John Wiley & Sons (Asia) Pte Ltd

SEISMIC ANALYSIS OF STRUCTURES

SEISMIC ANALYSIS OF STRUCTURES

T. K. Datta
Indian Institute of Technology Delhi, India

John Wiley & Sons (Asia) Pte Ltd

Other Wiley Editorial Offices

John Wiley & Sons, Ltd, The Atrium, Southern Gate, Chichester, West Sussex, PO19 8SQ, UK

John Wiley & Sons Inc., 111 River Street, Hoboken, NJ 07030, USA

Jossey-Bass, 989 Market Street, San Francisco, CA 94103-1741, USA

Wiley-VCH Verlag GmbH, Boschstrasse 12, D-69469 Weinheim, Germany

John Wiley & Sons Australia Ltd, 42 McDougall Street, Milton, Queensland 4064, Australia

John Wiley & Sons Canada Ltd, 5353 Dundas Street West, Suite 400, Toronto, ONT, M9B 6H8, Canada

Wiley also publishes its books in a variety of electronic formats. Some content that appears in print may not be available in electronic books.

Library of Congress Cataloging-in-Publication Data

Datta, T. K. (Tushar Kanti), 1944-
Seismic analysis of structures / T.K. Datta.
p. cm.
Includes index.
ISBN 978-0-470-82461-0 (cloth)
1. Earthquake engineering. 2. Structural analysis. I. Title.
TA654.6.D378 2010
624.1′762–dc22

2009044760

ISBN 978-0-470-82461-0 (HB)

Typeset in 9/11pt Times by Thomson Digital, Noida, India.
Printed and bound in Singapore by Markono Print Media Pte Ltd, Singapore.
This book is printed on acid-free paper responsibly manufactured from sustainable forestry in which at least two trees are planted for each one used for paper production.

Dedicated
to
Knowledge

Contents

Preface

For structural engineers, earthquake engineering can be broadly divided into three areas, namely, seismology (including ground effects), seismic analysis, and seismic design. These areas are big subjects in themselves and deserve separate treatment in exclusive books. While there are many excellent books that cover these three areas in varying proportions, none have been written exclusively on the seismic analysis of structures for use in teaching an undergraduate elective or a postgraduate core course. Furthermore, there are virtually no books that contain all aspects of the seismic analysis of structures, combining new concepts with existing ones, which graduate students pursuing research in the area of earthquake engineering would appreciate. Considering these major requirements, the present book has been written despite the fact that a number of masterly textbooks on structural dynamics and earthquake engineering, dynamics of soil structure interaction, and geotechnical earthquake engineering are already available within the earthquake engineering community, and where many of the theoretical concepts presented here have been covered more elaborately. The present book attempts to provide textbook material for the learning and teaching of the seismic analysis of structures in totality. It offers a comprehensive and unique treatment of all aspects of the seismic analysis of structures, starting with seismology and through to the seismic control of structures. The materials in the book are arranged and presented in a manner that is expected to be equally useful to both undergraduate and postgraduate students, researchers, and practicing engineers. Depending on the particular requirements, it is possible to structure courses at various levels on different aspects of seismic analysis based on the contents of this book. It is presumed that the readers have some background of structural dynamics, preferably having undergone a basic course in structural dynamics.

The book is presented in nine chapters. The first chapter, *Seismology*, deals with the fundamentals of seismology that a structural engineer must know. The chapter deals with topics such as the earth and its interior, plate tectonics, causes of earthquakes, seismic waves, earthquake measurement parameters, the measurement of earthquakes, modification of earthquake waves due to the nature of the soil, and seismic hazard analysis. The last topic describes both deterministic and probabilistic seismic hazard analyses, and seismic risk at a site. The concept of microzonation based on hazard analysis is also included.

The second chapter, *Seismic Inputs for Structures*, provides an extensive coverage of the various types of seismic inputs used for different types of seismic analysis. The seismic inputs discussed include time history records and their frequency contents, power spectral density function (PSDF) of ground motion, different types of earthquake spectra, design response spectra, probabilistic response spectra, site specific spectra, and uniform hazard spectra. Generation of the time histories of synthetic ground motion from a response spectrum and the PSDF of ground motion is also briefly discussed. Finally, predictive relationships for different seismic input parameters such as peak ground acceleration (PGA), response spectra, PSDFs, modulating functions, and coherence functions are given.

The third chapter, *Response Analysis for Specified Ground Motions*, deals with different methods of analysis of single and multi-degrees of freedom systems for specified time histories of ground motion. Methods include time domain analysis, frequency domain analysis using fast Fourier transform (FFT), modal time domain, and frequency domain analyses for both single-point and multi-point excitations.

Methods of analysis are described for both second-order and state-space equations. The mode acceleration method is also presented. At the end of the chapter, steps for developing a comprehensive program using MATLAB® are outlined, which can solve single and multi-degrees of freedom systems for a specified time history of ground motion using all of the methods of analysis discussed in the chapter. In addition, use of the SIMULINK toolbox of MATLAB to solve problems is also demonstrated.

The fourth chapter, *Frequency Domain Spectral Analysis*, introduces the concept of spectral analysis of structures, treating the ground motion as a stationary random process and deals with the subject in a manner that does not require an in-depth knowledge of the theory of random vibration. Using FFT, the fundamentals of frequency domain spectral analysis are introduced, and then the required concepts of autocorrelation, cross correlation, power spectral density functions, and so on, are presented. The basic relationship between multi-point input and output PSDFs of a structural system is given using a matrix formulation. Direct and modal spectral analyses are described for single-point and multi-point excitations. Furthermore, a method for the determination of the mean peak response from a spectral analysis is outlined.

The fifth chapter, *Response Spectrum Method of Analysis*, discusses the response spectrum method of analysis for single- and multi-point excitations of multi-degrees of freedom systems. Development of the methods is presented after a brief background of the concept of equivalent lateral load. The necessary explanation for including the effect of spatial correlation for multi-point excitation is duly incorporated in the theory. Other topics discussed in this chapter include modal combination rules, the response spectrum method of analysis for none classically damped systems and secondary systems, the base shear approach, and comparison between the code provisions of a few codes in relation to the base shear and response spectrum methods of analysis.

The sixth chapter, *Inelastic Seismic Response of Structures*, covers the methods of inelastic response analysis of structures and the fundamental aspects of inelastic behavior of structural components for earthquake forces. The topics include the hysteretic behavior of materials, the incremental method of analysis of single- and multi-degrees of freedom systems accounting for the hysteretic effects, the incremental analysis procedure with bidirectional interaction, pushover analysis, ductility demand, inelastic response spectra, and ductility in multi-storey buildings.

The first part of the seventh chapter on *Seismic Soil Structure Interaction*, provides the background to seismic wave propagation through the soil medium and gives the finite element analysis of the wave propagation problem. Next, the dynamic soil–structure interaction is presented by explaining kinematic interaction, inertial interaction, and the direct and multi-step method for bounded problems. Both the finite element method and the substructure technique for solving soil–structure and soil–pile structure interaction problems are described. The topics include time domain and frequency domain analyses using direct, substructure, and modal analysis techniques for single- and multi-point excitations, analyses for soil–pile structure interaction problems, and underground structures.

The eighth chapter, *Seismic Reliability Analysis of Structures*, deals with the seismic reliability analysis of structures in which the basic concept of reliability analysis is introduced first, followed by some popularly used techniques such as the first order second moment (FOSM) method, the Hasofer–Lind method, the second-order method, and a simulation based method for solving the reliability problems. Uncertainties involved in the seismic reliability analysis of structures are then elaborated, and a number of seismic reliability analysis techniques are presented. They include reliability analysis for threshold crossing, the first passage failure of structures, risk assessment using a damage probability matrix, and approximate probabilistic risk assessment of structures.

In the final chapter on *Seismic Control of Structures*, the concepts of passive, active, and semi-active control of structures for earthquake forces are covered. The various topics discussed in the chapter include: the design of base isolators and analysis of base isolated structures (both response spectrum and non-linear time history analyses), different methods of analysis of building frames fitted with viscoelastic dampers and tuned mass dampers, active control of structures with and without an observer using the pole

placement technique, quadratic linear optimal control, and instantaneous optimal control. Finally, an introduction to the semi-active control of structures using semi-active hydraulic dampers is presented.

In each chapter, a number of carefully selected example problems are solved in order to explain the various concepts presented. In addition, many of the problems are solved using MATLAB and standard software such as SAP2000 and ABAQUAS, demonstrating the use of the available software for solving different types of problems in the seismic analysis of structures.

I would like to thank many of my students who directly or indirectly helped me in gaining insight and carrying out research in the area of seismic analysis of structures. Their invaluable contributions are hidden in every page of this book. The textbooks *Dynamics of Structures* by Professor R.W. Clough and Professor J. Penzien, *Dynamics of Structures – Theory and Application to Earthquake Engineering* by Professor A.K. Chopra, *Geotechnical Earthquake Engineering* by Professor S.L. Kramer, and *Structural Dynamics for Structural Engineers* by Garry C. Hart have been valuable references in organizing the many concepts of the book and clarifying many doubts. I am extremely grateful to these authors. I wish to acknowledge my sincere thanks to Mr. Prakash Kedia and Dr. Deepak Kumar who worked untiringly preparing the manuscript of the book. I am also thankful to many of my M.Tech students who helped me solve the example problems. Finally, I thank Dr. (Mrs.) Sabita Karunes for her support and encouragement whilst preparing the book.

The author will be pleased to hear from readers who spot errors and misprints or who find ways of improving the book. All such suggestions will be gratefully acknowledged, and will be used selectively to improve future versions of the book.

1

Seismology

1.1 Introduction

An earthquake is a sudden and transient motion of the earth's surface. According to geologists, the earth has suffered earthquakes for hundreds of millions of years, even before humans came into existence. Because of the randomness, the lack of visible causes, and their power of destructiveness, ancient civilizations believed earthquakes to be supernatural phenomena – the curse of God. In terms of the geological time scale, it is only recently (the middle of seventeenth century) that an earthquake has been viewed as a natural phenomenon driven by the processes of the earth as a planet. Thus subsequent work, especially in nineteenth century, led to tremendous progress on the instrumental side for the measurement of earthquake data. Seismological data from many earthquakes were collected and analyzed to map and understand the phenomena of earthquakes. These data were even used to resolve the earth's internal structure to a remarkable degree, which, in turn, helped towards the development of different theories to explain the causes of earthquakes. While the body of knowledge derived from the study of collected seismological data has helped in the rational design of structures to withstand earthquakes, it has also revealed the uncertain nature of future earthquakes for which such structures are to be designed. Therefore, probabilistic concepts in dealing with earthquakes and earthquake resistant designs have also emerged.

Both seismologists and earthquake engineers use the seismological data for the understanding of an earthquake and its effects, but their aims are different. Seismologists focus their attention on the global issues of earthquakes and are more concerned with the geological aspects, including the prediction of earthquakes. Earthquake engineers, on the other hand, are concerned mainly with the local effects of earthquakes, which are capable of causing significant damage to structures. They transform seismological data into a form which is more appropriate for the prediction of damage to structures or, alternatively, the safe design of structures. However, there are many topics in seismology that are of immediate engineering interest, especially in the better understanding of seismological data and its use for seismic design of structures. Those topics are briefly presented in the following sections.

1.1.1 Earth and its Interiors

During the formation of the earth, large amounts of heat were generated due to the fusion of masses. As the earth cooled down, the masses became integrated together, with the heavier ones going towards the center and the lighter ones rising up. This led to the earth consisting of distinct layers of masses. Geological investigations with seismological data revealed that earth primarily consists of four distinct layers namely:

Seismic Analysis of Structures T.K. Datta

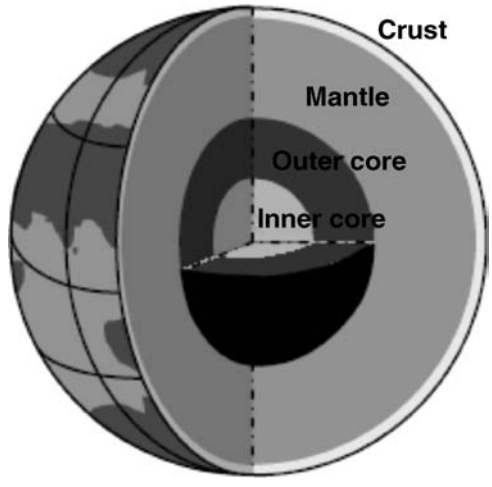

Figure 1.1 Inside the earth (*Source*: Murty, C.V.R. "IITK-BMPTC Earthquake Tips." Public domain, *National Information Centre of Earthquake Engineering*. 2005. http://nicee.org/EQTips.php - accessed April 16, 2009.)

the inner core, the outer core, the mantle, and the crust, as shown in Figure 1.1. The upper-most layer, called the crust, is of varying thickness, from 5 to 40 km. The discontinuity between the crust and the next layer, the mantle, was first discovered by Mohorovičić through observing a sharp change in the velocity of seismic waves passing from the mantle to the crust. This discontinuity is thus known as the Mohorovičić discontinuity ("M discontinuity"). The average seismic wave velocity (P wave) within the crust ranges from 4 to 8 km s^{-1}. The oceanic crust is relatively thin (5–15 km), while the crust beneath mountains is relatively thick. This observation also demonstrates the principle of isostasy, which states that the crust is floating on the mantle. Based on this principle, the mantle is considered to consist of an upper layer that is fairly rigid, as the crust is. The upper layer along with the crust, of thickness ~120 km, is known as the lithosphere. Immediately below this is a zone called the asthenosphere, which extends for another 200 km. This zone is thought to be of molten rock and is highly plastic in character. The asthenosphere is only a small fraction of the total thickness of the mantle (~2900 km), but because of its plastic character it supports the lithosphere floating above it. Towards the bottom of the mantle (1000–2900 km), the variation of the seismic wave velocity is much less, indicating that the mass there is nearly homogeneous. The floating lithosphere does not move as a single unit but as a cluster of a number of plates of various sizes. The movement in the various plates is different both in magnitude and direction. This differential movement of the plates provides the basis of the foundation of the theory of tectonic earthquake.

Below the mantle is the central core. Wichert [1] first suggested the presence of the central core. Later, Oldham [2] confirmed it by seismological evidence. It was observed that only P waves pass through the central core, while both P and S waves can pass through the mantle. The inner core is very dense and is thought to consist of metals such as nickel and iron (thickness ~1290 km). Surrounding that is a layer of similar density (thickness ~2200 km), which is thought to be a liquid as S waves cannot pass through it. At the core, the temperature is about 2500 °C, the pressure is about 4 million atm, and the density is about 14 g cm^{-3}. Near the surface, they are 25 °C, 1 atm and 1.5 g cm^{-3}, respectively.

1.1.2 Plate Tectonics

The basic concept of plate tectonics evolved from the ideas on continental drift. The existence of mid-oceanic ridges, seamounts, island areas, transform faults, and orogenic zones gave credence to the theory

of continental drift. At mid-oceanic ridges, two large land masses (continents) are initially joined together. They drift apart because of the flow of hot mantle upwards to the surface of the earth at the ridges due to convective circulation of the earth's mantle, as shown in Figure 1.2. The energy of the convective flow is derived from the radioactivity inside the earth. As the material reaches the surface and cools, it forms an additional crust on the lithosphere floating on the asthenosphere. Eventually, the newly formed crust spreads outwards because of the continuous upwelling of molten rock. The new crust sinks beneath the surface of the sea as it cools down and the outwards spreading continues. These phenomena gave rise to the concept of sea-floor spreading. The spreading continues until the lithosphere reaches a deep-sea trench where it plunges downwards into the asthenosphere (subduction).

Figure 1.2 Local convective currents in the mantle (*Source*: Murty, C.V.R. "IITK-BMPTC Earthquake Tips." Public domain, *National Information Centre of Earthquake Engineering*. 2005. http://nicee.org/EQTips.php - accessed April 16, 2009.)

The continental motions are associated with a variety of circulation patterns. As a result, the continental motion does not take place as one unit, rather it occurs through the sliding of the lithosphere in pieces, called tectonic plates. There are seven such major tectonic plates, as shown in Figure 1.3, and many smaller ones. They move in different directions and at different speeds. The tectonic plates pass each other

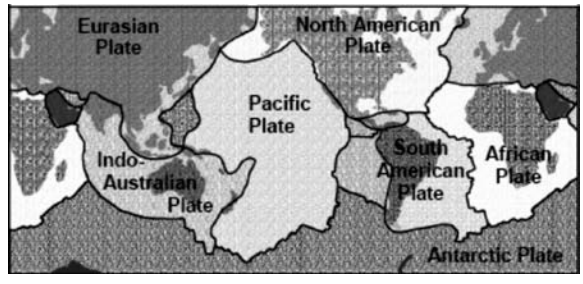

Figure 1.3 Major tectonic plates on the earth's surface (*Source*: Murty, C.V.R. "IITK-BMPTC Earthquake Tips." Public domain, *National Information Centre of Earthquake Engineering*. 2005. http://nicee.org/EQTips.php - accessed April 16, 2009.)

at the transform faults and are absorbed back into the mantle at orogenic zones. In general, there are three types of interplate interactions giving rise to three types of boundaries, namely: convergent, divergent, and transform boundaries. Convergent boundaries exist in orogenic zones, while divergent boundaries exist where a rift between the plates is created, as shown in Figure 1.4.

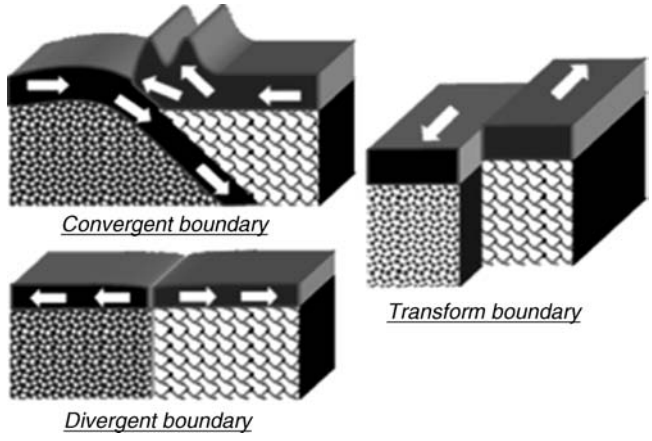

Figure 1.4 Types of interplate boundaries (*Source*: Murty, C.V.R. "IITK-BMPTC Earthquake Tips." Public domain, *National Information Centre of Earthquake Engineering*. 2005. http://nicee.org/EQTips.php - accessed April 16, 2009.)

The faults at the plate boundaries are the most likely locations for earthquakes to occur. These earthquakes are termed interplate earthquakes. A number of earthquakes also occur within the plate away from the faults. These earthquakes are known as intraplate earthquakes, in which a sudden release of energy takes place due to the mutual slip of the rock beds. This slip creates new faults called earthquake faults. However, faults are mainly the causes rather than the results of earthquakes. These faults, which have been undergoing deformation for the past several thousands years and will continue to do so in future, are termed active faults. At the faults (new or old), two different types of slippages are observed, namely: dip slip and strike slip. Dip slip takes place in the vertical direction while strike slip takes place in the horizontal direction, as shown in Figure 1.5.

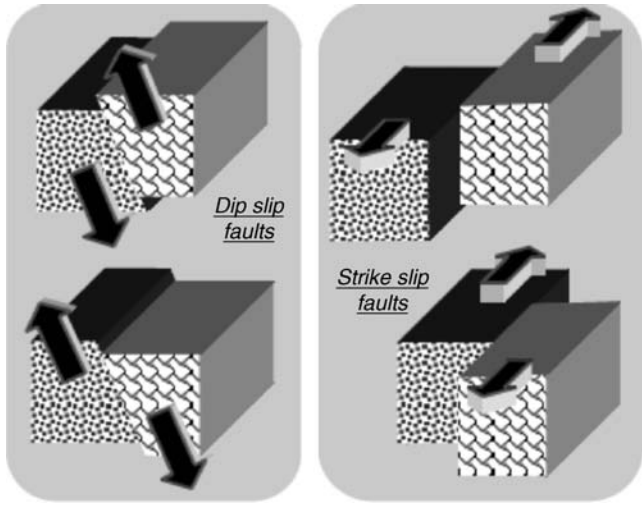

Figure 1.5 Types of fault (*Source*: Murty, C.V.R. "IITK-BMPTC Earthquake Tips." Public domain, *National Information Centre of Earthquake Engineering*. 2005. http://nicee.org/EQTips.php - accessed April 16, 2009.)

Faults created by dip slip are termed normal faults when the upper rock bed moves down and reverse faults when the upper rock bed moves up, as shown in Figure 1.5. Similarly, faults created by strike slip are referred to as left lateral faults and right lateral faults depending on the direction of relative slip. A combination of four types of slippage may take place in the faults. Some examples of earthquake faults are:

a. 300 km long strike slip of 6.4 m at the San Andreas fault;
b. 60 km long right lateral fault at Imperial Valley with a maximum slip of 5 m;
c. 80 km long 6 m vertical and 2–4 m horizontal slip created by the Nobi earthquake in Japan;
d. 200 km long left lateral fault created by the Kansu earthquake in China.

1.1.3 Causes of Earthquakes

Movement of the tectonic plates relative to each other, both in direction and magnitude, leads to an accumulation of strain, both at the plate boundaries and inside the plates. This strain energy is the elastic energy that is stored due to the straining of rocks, as for elastic materials. When the strain reaches its limiting value along a weak region or at existing faults or at plate boundaries, a sudden movement or slip occurs releasing the accumulated strain energy. The action generates elastic waves within the rock mass, which propagate through the elastic medium, and eventually reach the surface of the earth. Most earthquakes are produced due to slips at the faults or at the plate boundaries. However, there are many instances where new faults are created due to earthquakes. Earthquakes that occur along the boundaries of the tectonic plates that is, the interplate earthquakes, are generally recorded as large earthquakes. The intraplate earthquakes occurring away from the plate boundaries can generate new faults. The slip or movement at the faults is along both the vertical and horizontal directions in the form of dip slip or strike slip. The length of the fault over which the slip takes place may run over several hundred kilometers. In major earthquakes, a chain reaction would take place along the entire length of the slip. At any given instant, the earthquake origin would practically be a point and the origin would travel along the fault.

The elastic rebound theory of earthquake generation attempts to explain the earthquakes caused due to a slip along the fault lines. Reid first put into clear focus the elastic rebound theory of earthquake generation from a study of the rupture that occurred along the San Andreas fault during the San Francisco earthquake. The large amplitude shearing displacements that took place over a large length along the fault led him to conclude that the release of energy during an earthquake is the result of a sudden shear type rupture. An earthquake caused by a fault typically proceeds according to the following processes:

a. Owing to various slow processes involved in the tectonic activities of the earth's interior and the crust, strain accumulates in the fault for a long period of time. The large field of strain at a certain point in time reaches its limiting value.
b. A slip occurs at the faults due to crushing of the rock mass. The strain is released and the tearing strained layers of the rock mass bounces back to its unstrained condition, as shown in Figure 1.6.
c. The slip that occurs could be of any type, for example, dip slip or strike slip. In most instances it is a combined slip giving rise to push and pull forces acting at the fault, as shown in Figure 1.7. This situation is equivalent to two pairs of coupled forces suddenly acting.
d. The action causes movement of an irregular rock mass leading to radial wave propagation in all directions.
e. The propagating wave is complex and is responsible for creating displacement and acceleration of the soil/rock particles in the ground. The moment of each couple is referred to as the seismic moment and is defined as the rigidity of rock multiplied by the area of faulting multiplied by the amount of slip. Recently, it has been used as a measure of earthquake size. The average slip velocity at an active fault varies and is of the order of 10–100 mm per year.

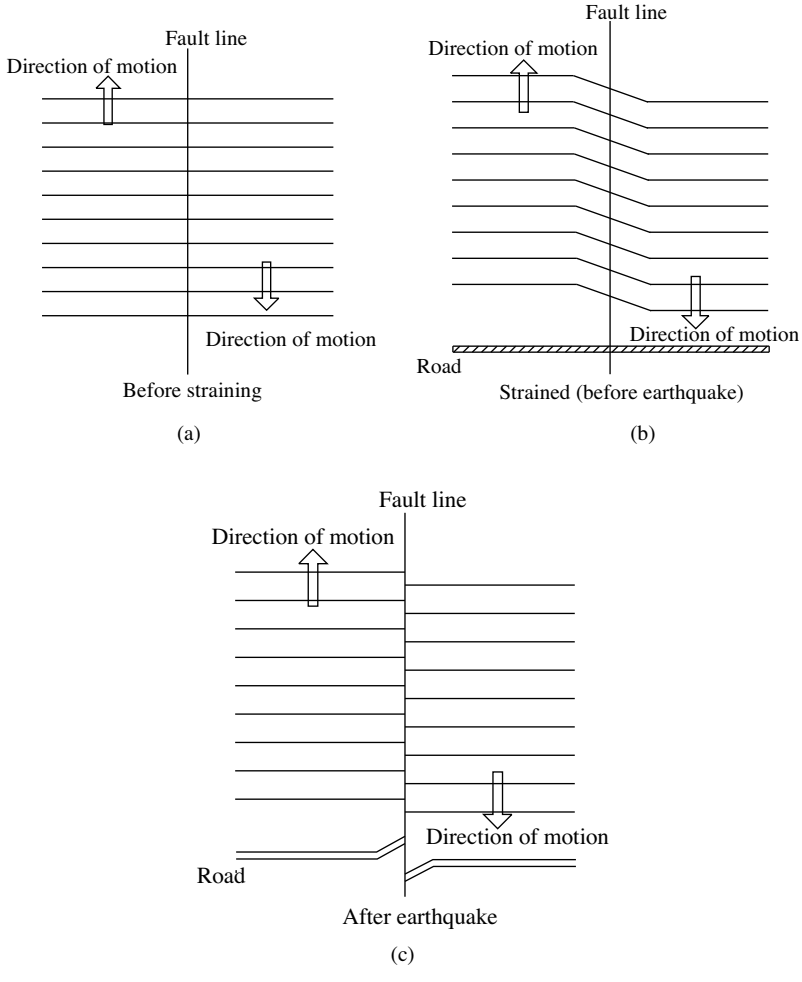

Figure 1.6 Elastic rebound theory

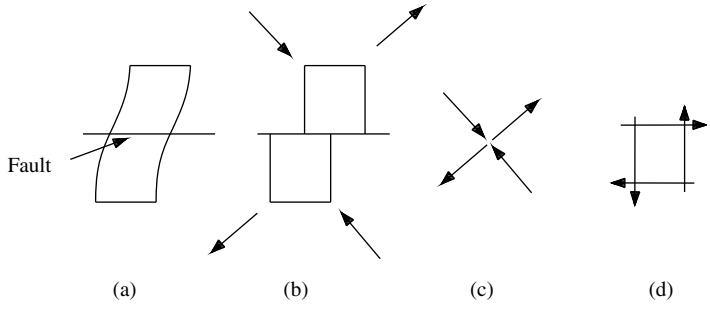

Figure 1.7 Earthquake mechanism: (a) before slip; (b) rebound due to slip; (c) push and pull force; and (d) double couple

Based on the elastic rebound theory, modeling of earthquakes has been a topic of great interest. Two types of modeling have been widely studied, namely, kinematic and dynamic. In kinematic modeling, the time history of the slip on the generating fault is known a priori. Several defining parameters such as shape, duration and amplitude of the source, the velocity of the slip over the fault surface, and so on, are used to characterize the model. In dynamic modeling, the basic model is a shear crack, which is initiated in the pre-existing stress field. The resulting stress concentration causes the crack to grow.

The other theory of tectonic earthquake stipulates that the earthquake originates as a result of phase changes of the rocks, accompanied by volume changes in relatively small volumes of the crust. Those who favor the phase change theory argue that the earthquakes originated at greater depths where faults are likely to be absent because of the high temperature and confining pressure. Therefore, earthquakes are not caused because of a slip along fault lines or a rupture at weak regions.

Apart from tectonic earthquakes, earthquakes could be due to other causes, namely: volcanic activities, the sudden collapse of the roof in a mine/cave, reservoir induced impounding, and so on.

1.2 Seismic Waves

The large strain energy released during an earthquake causes radial propagation of waves within the earth (as it is an elastic mass) in all directions. These elastic waves, called seismic waves, transmit energy from one point of earth to another through different layers and finally carry the energy to the surface, which causes the destruction. Within the earth, the elastic waves propagate through an almost unbounded, isotropic, and homogeneous media, and form what are known as body waves. On the surface, these waves propagate as surface waves. Reflection and refraction of waves take place near the earth's surface and at every layer within the earth. The body waves are of two types, namely, P waves and S waves. P waves, as shown at the top of Figure 1.8, are longitudinal waves in which the direction of particle motion is in the same or opposite direction to that of wave propagation. S waves, also shown in Figure 1.8, are transverse waves in which the direction of particle motion is at right angles to the direction of wave propagation. The propagation velocities of P and S waves are expressed as follows:

$$V_{\mathrm{P}} = \left[\frac{E}{\rho}\frac{1-\upsilon}{(1+\upsilon)(1-2\upsilon)}\right]^{\frac{1}{2}} \tag{1.1}$$

$$V_{\mathrm{S}} = \left[\frac{G}{\rho}\right]^{\frac{1}{2}} = \left[\frac{E}{\rho}\frac{1}{2(1+\upsilon)}\right]^{\frac{1}{2}} \tag{1.2}$$

in which E, G, ρ, and υ are the Young's modulus, the shear modulus, the mass density, and the Poisson ratio of the soil mass, respectively. As the Poisson ratio is always less than a half, P waves arrive ahead of S waves. Near the surface of the earth, $V_{\mathrm{P}} = 5\text{–}7\,\mathrm{km\,s^{-1}}$ and $V_{\mathrm{S}} = 3\text{–}4\,\mathrm{km\,s^{-1}}$.

The time interval between the arrival of the P and S waves at a station is called the duration of primary tremor.

This duration can be obtained by:

$$T_P = \Delta\left(\frac{1}{V_{\mathrm{S}}} - \frac{1}{V_{\mathrm{P}}}\right) \tag{1.3}$$

where Δ is the distance of the station from the focus. During the passage of a transverse wave, if the particle motion becomes confined to a particular plane only, then the wave is called a polarized transverse wave. Polarization may take place in a vertical or a horizontal plane. Accordingly, the transverse waves are termed as SV or SH waves.

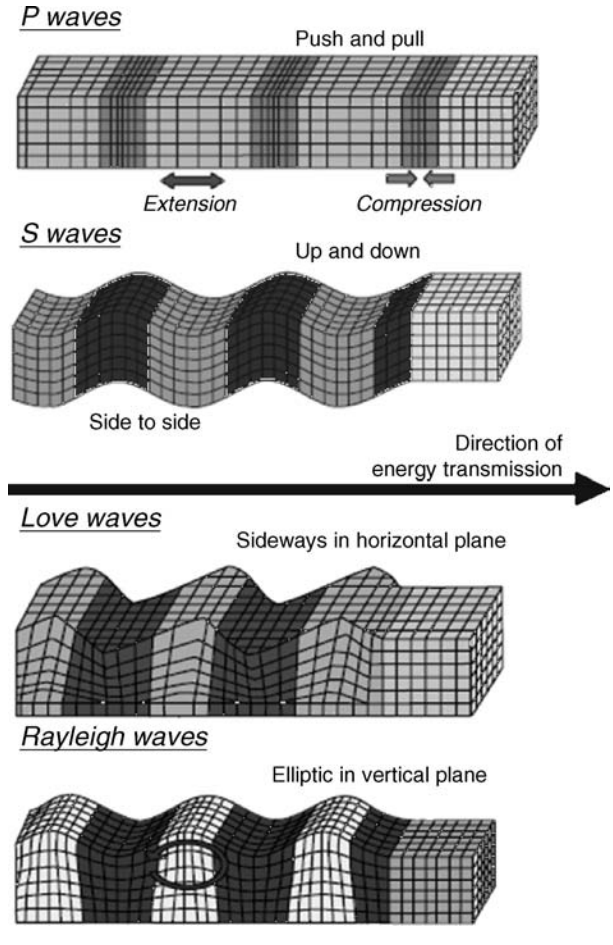

Figure 1.8 Motion caused by body and surface waves (*Source*: Murty, C.V.R. "IITK-BMPTC Earthquake Tips." Public domain, *National Information Centre of Earthquake Engineering*. 2005. http://nicee.org/EQTips.php - accessed April 16, 2009.)

Surface waves propagate on the earth's surface. They are better detected in shallow earthquakes. They are classified as L waves (Love waves) and R waves (Rayleigh waves). In L waves, particle motion takes place in the horizontal plane only and it is transverse to the direction of propagation, as shown in Figure 1.8. The wave velocity depends on the wavelength, the thickness of the upper layer, and the elastic properties of the two mediums of the stratified layers. L waves travel faster than R waves and are the first to appear among the surface wave group. In R waves, the particle motion is always in a vertical plane and traces an elliptical path, which is retrograde to the direction of wave propagation, as shown in Figure 1.8. The R wave velocity is approximately 0.9 times the transverse wave velocity. In stratified layers, R waves become dispersive (wave velocity varying with frequency), as with the L waves.

Waves traveling away from the earthquake source spread in all directions to emerge on the earth's surface. The earthquake energy travels to a station in the form of waves after reflection and refraction at various boundaries within the earth. The P and S waves that arrive at the earth's surface after reflection and refraction at these boundaries, including the earth's surface, are denoted by phases of the wave such as PP,

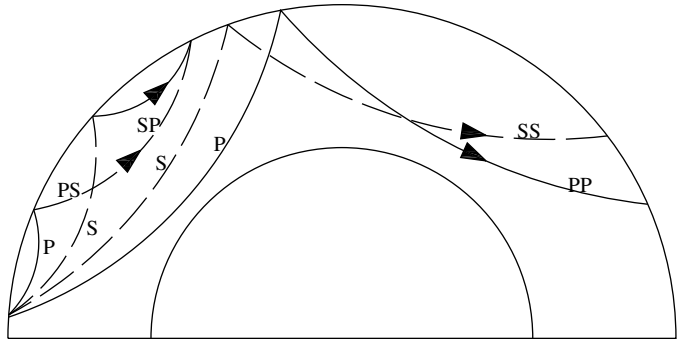

Figure 1.9 Reflections at the earth's surface

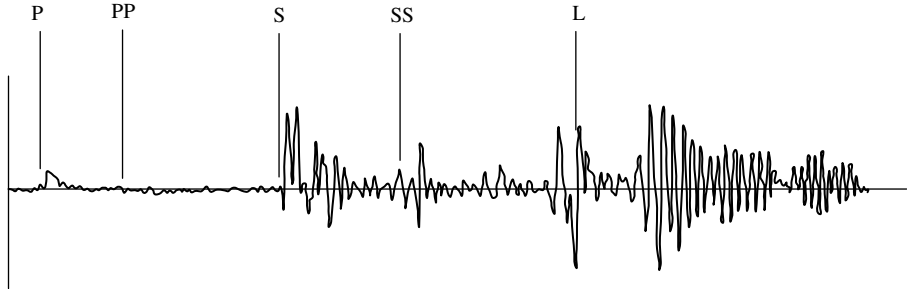

Figure 1.10 Typical strong motion record

PPP, SS, PPS, and so on, as shown in Figure 1.9. PP and PPP are longitudinal waves reflected once and twice, respectively. PS and PPS are phases that have undergone a change in character on reflection.

Earthquake waves that are recorded on the surface of the earth are generally irregular in nature. A record of a fairly strong earthquake shows a trace of the types of waves, as shown in Figure 1.10.

Strong earthquakes can generally be classified into four groups:

a. **Practically a single shock:** Acceleration, velocity, and displacement records for one such motion are shown in Figure 1.11. A motion of this type occurs only at short distances from the epicenter, only on firm ground, and only for shallow earthquakes.
b. **A moderately long, extremely irregular motion:** The record of the earthquake of El Centro, California in 1940, NS component (Figure 1.12) exemplifies this type of motion. It is associated with moderate distances from the focus and occurs only on firm ground. On such ground, almost all the major earthquakes originating along the Circumpacific Belt are of this type.
c. **A long ground motion exhibiting pronounced prevailing periods of vibration:** A portion of the accelerogram obtained during the earthquake of 1989 in Loma Prieta is shown in Figure 1.13 to illustrate this type. Such motions result from the filtering of earthquakes of the preceding types through layers of soft soil within the range of linear or almost linear soil behavior and from the successive wave reflections at the interfaces of these layers.
d. **A ground motion involving large-scale, permanent deformations of the ground:** At the site of interest there may be slides or soil liquefaction. Examples are in Valdivia and Puerto Montt during the Chilean earthquakes of 1960 [3], and in Anchorage during the 1964 Alaskan earthquake [4].

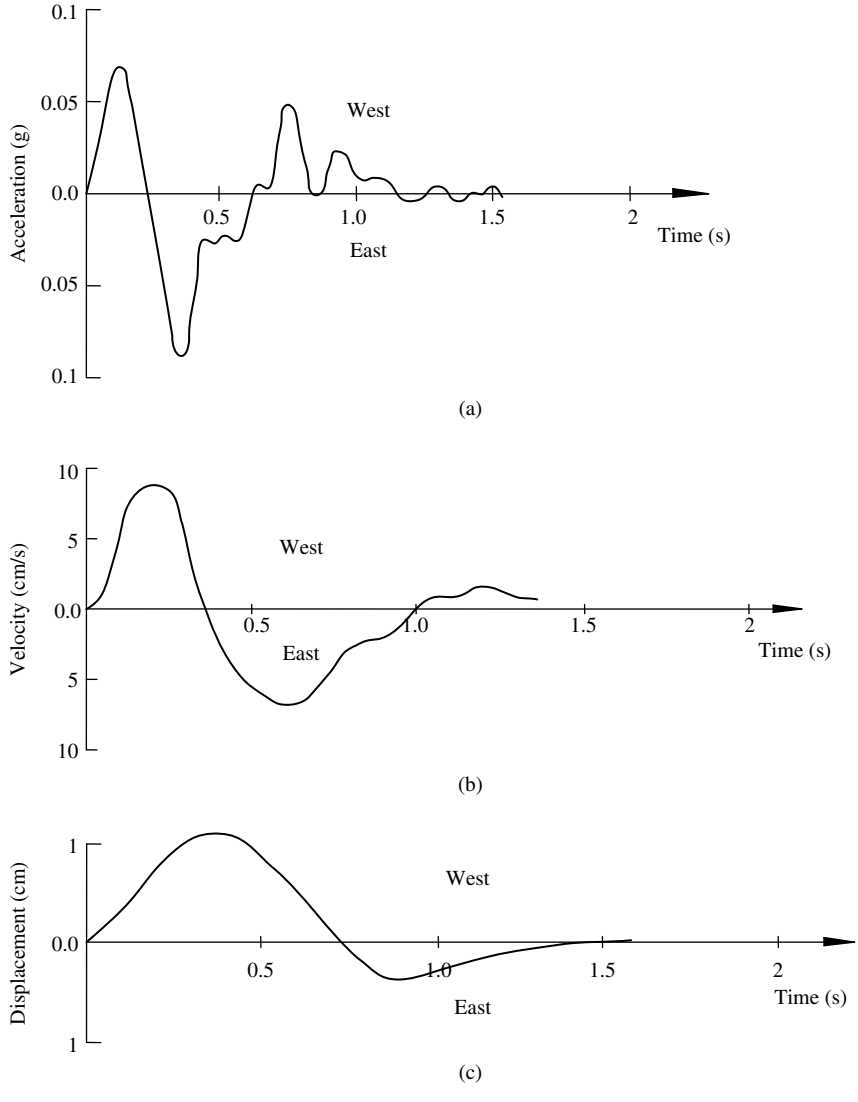

Figure 1.11 Practically single shock: (a) acceleration; (b) velocity; and (c) displacement

There are ground motions with characteristics that are intermediate between those described above. For example, the number of significant, prevailing ground periods, because of complicated stratification, may be so large that a motion of the third group approaches white noise. The nearly white-noise type of earthquake has received the greatest share of attention. This interest in white noise is due to its relatively high incidence, the number of records available, and the facility for simulation in analog and digital computers, or even from the analytical treatment of the responses of simple structures.

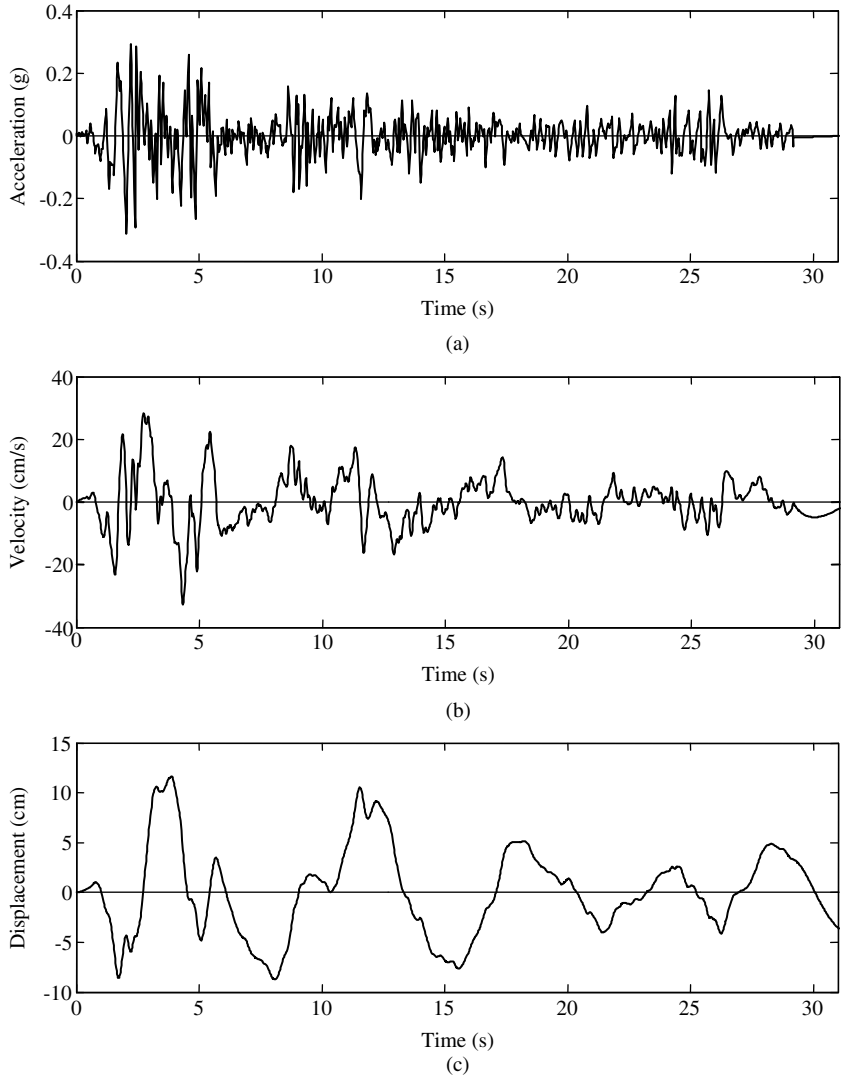

Figure 1.12 Records with mixed frequency: (a) acceleration; (b) velocity; and (c) displacement

1.3 Earthquake Measurement Parameters

Seismic intensity parameters refer to the quantities by which the size of earthquake is described. There is more than one intensity parameter that is used to represent the size and effect of an earthquake. With the help of any or all of these intensity parameters, the size of an earthquake is described. Some of these parameters are measured directly, while others are derived indirectly from the measured ones with the help of empirical relationships. Thus, many empirical relationships have been developed to relate one intensity parameter to another. In the following, intensity parameters along with some of the terminologies associated with earthquake are described.

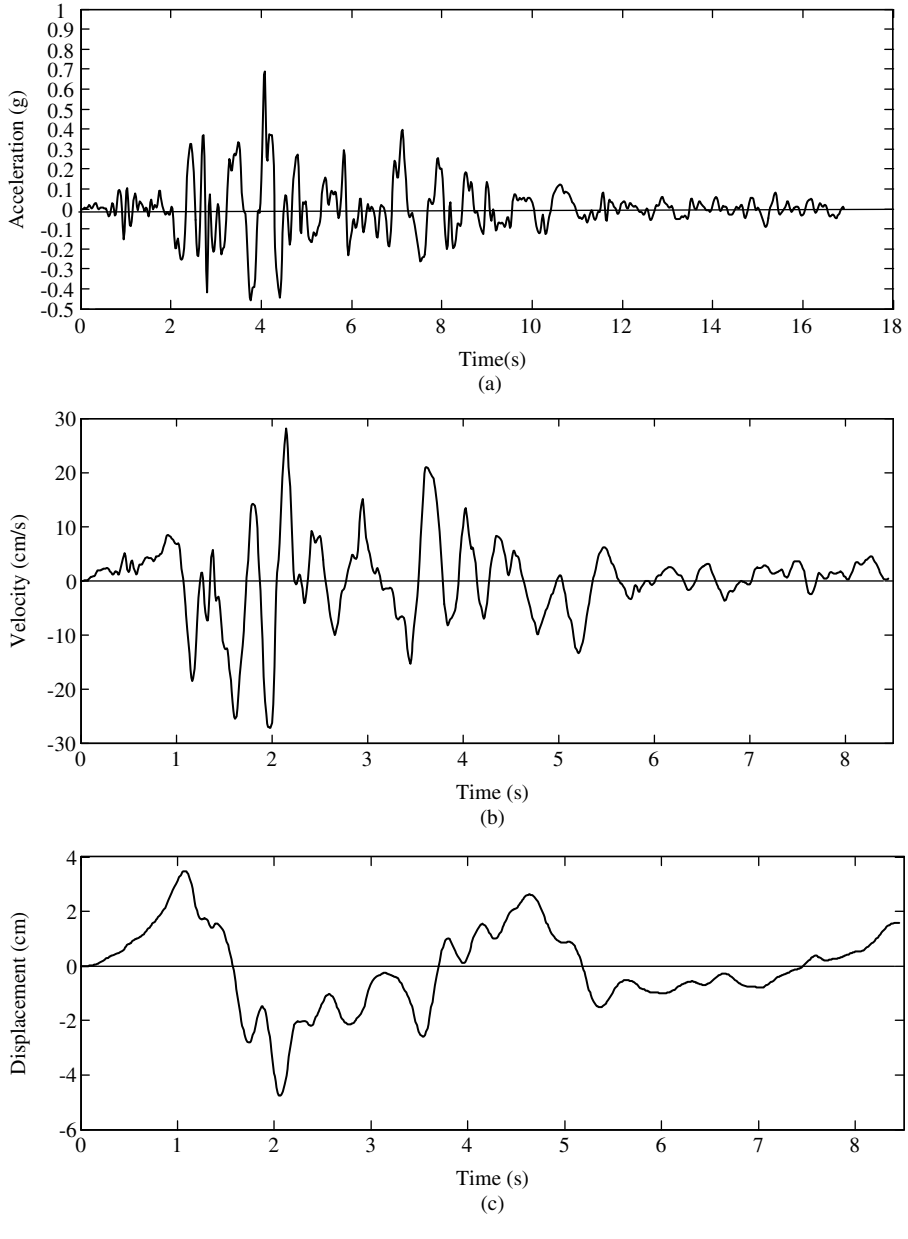

Figure 1.13 Records with a predominant frequency: (a) acceleration; (b) velocity; and (c) displacement

The focus or hypocenter is the point on the fault where the slip starts. The point just vertically above this on the surface of the earth is the epicenter, as shown in Figure 1.14.

The depth of the focus from the epicenter is called focal depth and is an important parameter in determining the damaging potential of an earthquake. Most of the damaging earthquakes have a shallow

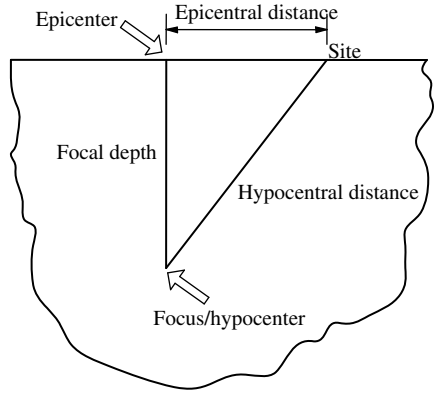

Figure 1.14 Earthquake definitions

focus with a focal depth of less than 70 km. Depths of foci greater than 70 km are classified as intermediate or deep, depending on their distances. Distances from the focus and the epicenter to the point of observed ground motion are called the focal distance and epicentral distance, respectively. The limited region of the earth that is influenced by the focus of earthquake is called the focal region. The larger the earthquake, the greater is the focal region. Foreshocks are defined as those which occur before the earthquake (that is, the main shock). Similarly, aftershocks are those which occur after the main shock.

The magnitude and intensity are the two very common parameters used to represent the size of an earthquake. Magnitude is a measure of the strength of an earthquakes or strain energy released by it, as determined by seismographic observation. It is a function of the amount of energy released at the focus and is independent of the place of observation. The concept was developed by Wadati and Charles Richter in 1935. Richter expressed the magnitude, M, of an earthquake by the following expression:

$$M = \log\left(\frac{A}{T}\right) + f(\Delta, h) + C_{\mathrm{s}} + C_{\mathrm{r}} \tag{1.4}$$

where A is the maximum amplitude in microns; T is the period of the seismic wave in seconds; f is the correction factor for the epicentral distance (Δ) and focal depth (h); C_{s} is the correction factor for the seismological station; and C_{r} is the regional correction factor.

The magnitude value obtained through Equation 1.4 is a unique value for a specific event and there is no beginning or end to this scale. Natural seismic events have a maximum value of $M = 8.5$ or slightly higher. Except in special circumstances, earthquakes below a magnitude of 2.5 are not generally felt by humans. Sometimes, the initial magnitude of an earthquake estimated immediately after the event will be modified slightly when more and more data from other recording stations are incorpotated. Since the first use of Richter's magnitude scale in 1935, several other scales have been proposed that consider various types of waves propagating from the same seismic source. They are described in the following sections.

1.3.1 Local Magnitude (M_L)

The local magnitude M_{L} corresponds to the original formulation proposed by Richter [5] in 1935 for local events in South California. The M_{L} is defined as the logarithm of the maximum amplitude that is obtained from the record of a seismic event using a Wood–Anderson torsional seismograph located 100 km from the epicenter of the earthquake. This seismograph must have a natural period of 0.8 s, a magnification of 2800, and a damping coefficient of 80% of the critical damping. The relative size of the events is calculated

by comparison with a reference event.

$$M_{\mathrm{L}} = \log A - \log A_{\mathrm{o}} \tag{1.5}$$

where A is the maximum trace amplitude in microns recorded on a standard short seismometer, and A_{o} is a standard value as a function of distance where the distance $\leq$100 km. Using this reference event to define a curve, Equation 1.5 is rewritten in the form

$$M_{\mathrm{L}} = \log A - 2.48 + 2.7\log\Delta \tag{1.6}$$

where Δ is the epicentral distance.

The M_{L} in its original form is rarely used today because Wood–Anderson torsional seismographs are not commonly found. To overcome these limitations, the M_{L} for near earthquakes recorded by high frequency systems is now generally determined using the Coda length (T). The Coda length is defined as the total signal duration in seconds from the onset time until the amplitude merges into the background noise level. The suggested nature of the relationship between M_{L} and T is given by:

$$M_{\mathrm{L}} = a + b\log T \tag{1.7}$$

where a and b are constants.

1.3.2 Body Wave Magnitude (M_b)

Although the local magnitude is useful, the limitations imposed by instrument type and distance range make it impractical for the global characterization of earthquake size. Gutenberg and Richter [6] proposed M_{b} based on the amplitude of the compressional body wave, P, with periods in the order of a second. The magnitude is based on the first few cycles of the P-wave arrival and is given by:

$$M_{\mathrm{b}} = \log\left(\frac{A}{T}\right) + Q(h, \Delta) \tag{1.8}$$

where A is the actual ground motion amplitude in microns, T is corresponding period in seconds, and Q is a function of distance (Δ) and depth (h).

Occasionally, long-period instruments are used to determine the body wave magnitude for periods from 5 to 15 s, and these are usually for the largest body waves LP, PP, and so on.

1.3.3 Surface Wave Magnitude (M_S)

The surface wave magnitude, M_{S}, was proposed by Gutenberg and Richter [7] as a result of detailed studies. It is currently the magnitude scale most widely used for great epicentral distances, but it is valid for any epicentral distance and for any type of seismograph. This requires precise knowledge of the wave amplitude as a function of distance. In order to utilize different seismographs, the amplitude of vibration of the soil should be used, not the amplitude recorded. M_{S} can be evaluated for surface waves with periods in the order of 20 s by the following Praga formulation:

$$M_{\mathrm{S}} = \log\left(\frac{A}{T}\right) + 1.66\log\Delta + 2.0 \tag{1.9}$$

where A is spectral amplitude, the horizontal component of the Rayleigh wave, with a period of 20 s, measured on the ground surface in microns, T is the period of the seismic wave in seconds, and Δ is the epicentral distance in km.

1.3.4 Seismic Moment Magnitude (M_W)

A better measure of the size of a large earthquake is the seismic moment, M_o. A rupture along a fault involves equal and opposite forces, which produce a couple. The seismic moment is

$$M_o = GUA \tag{1.10}$$

where A is the fault area (length × depth) in m^2; U is the longitudinal displacement of the fault in m, and G is the modulus of rigidity (approx. $3 \times 10^{10}\,N\,m^{-2}$ for the crust and $7 \times 10^{10}\,N\,m^{-2}$ for the mantle).

The seismic moment is measured from seismographs using very long period waves for which even a fault with a very large rupture area appears as a point source. Because the seismic moment is a measure of the strain energy released from the entire rupture surface, a magnitude scale based on the seismic moment most accurately describes the size of the largest earthquakes. Kanamori [8] designed such a scale, called a moment magnitude, M_W, which is related to a seismic moment as follows:

$$M_W = \frac{2}{3}\log_{10} M_o - 6.0 \tag{1.11}$$

where M_o is in N m.

As shown in Figure 1.15, all the above magnitude scales saturate for large earthquakes. It is apparent that M_b begins to saturate at $M_b = 5.5$ and fully saturates at 6.0. M_S does not saturate until approximately $M_S = 7.25$ and is fully saturated at 8.0. M_L begins to saturate at about 6.5. Because of this saturation, it is difficult to relate one type of magnitude with another at values greater than 6. Up to a value of 6, it may be generally considered that $M_W = M_L = M_b = M_S = M$. Beyond the value of 6, it is better to specify the type of magnitude. However, in earthquake engineering many alternation and empirical relationships are used without specific mention of the type of magnitude. The magnitude is simply denoted by M (or m). In such cases, no specific type should be attached to the magnitude. It is desirable to have a magnitude measure that does not suffer from this saturation.

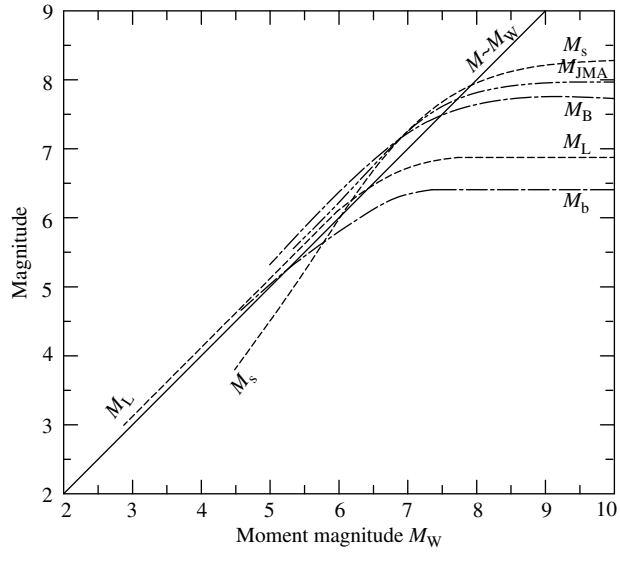

Figure 1.15 Comparison of moment magnitude scale with other magnitude scales

The frequency of occurrence of earthquakes based on recorded observations since 1900 is shown in Table 1.1

Table 1.1 Frequency of occurrence of earthquakes (based on observations since 1900)

Description	Magnitude	Average annually
Great	8 and higher	1
Major	7–7.9	18
Strong	6–6.9	120
Moderate	5–5.9	820
Light	4–4.9	6200 (estimated)
Minor	3–3.9	49 000 (estimated)
Very minor	<3.0	Magnitude 2–3 about 1000 per day Magnitude 1–2 about 8000 per day

1.3.5 Energy Release

The energy, E in joules (J), released by an earthquake can be estimated from the magnitude, M_S as:

$$E = 10^{4.8 + 1.5M_S} \tag{1.12}$$

Newmark and Rosenblueth [9] compared the energy released by an earthquake with that of a nuclear explosion. A nuclear explosion of 1 megaton releases 5×10^{15} J. According to Equation 1.12, an earthquake of magnitude $M_S = 7.3$ would release the equivalent amount of energy as a nuclear explosion of 50 megatons. A simple calculation shows that an earthquake of magnitude 7.2 produces ten times more ground motion than a magnitude 6.2 earthquake, but releases about 32 times more energy. The E of a magnitude 8.0 earthquake will be nearly 1000 times the E of a magnitude 6.0 earthquake. This explains why big earthquakes are so much more devastating than small ones. The amplitude numbers are easier to explain, and are more often used in the literature, but it is the energy that does the damage.

The length of the earthquake fault L in kilometers is related to the magnitude [10] by

$$M = (0.98 \log L) + 5.65 \tag{1.13}$$

The slip in the fault U in meters is related to the magnitude [11] by

$$M = (1.32 \log U) + 4.27 \tag{1.14a}$$

Surface rupture length (L), rupture area (A), and maximum surface displacement (D) are good measurable indices to estimate the energy released and hence, the magnitude M_W of the earthquake. Therefore, several studies have been made to relate M_W to L, A, and D. A few such relationships are given in the reference [12]. From these relationships, the following empirical equations are obtained

$$\text{Log}\, L = 0.69M_W - 3.22 \qquad (\sigma_{\text{Log}\, L} = 0.22) \tag{1.14b}$$

$$\text{Log}\, A = 0.91M_W - 3.49 \qquad (\sigma_{\text{Log}\, A} = 0.24) \tag{1.14c}$$

$$\text{Log}\, D = 0.82M_W - 5.46 \qquad (\sigma_{\text{Log}\, D} = 0.42) \tag{1.14d}$$

in which L is in km, A is in km^2 and D is in m.

1.3.6 Intensity

The intensity of an earthquake is a subjective measure as determined by human feelings and by the effects of ground motion on structures and on living things. It is measured on an intensity scale. Many intensity scales have been proposed and are used in different parts of the world. A few older scales are the Gastaldi scale (1564), the Pignafaro scale (1783), and the Rossi–Forel scale (1883).

The last one, which has ten grades, is still used in some parts of Europe. The Mercalli–Cancani–Sieberg scale, developed from the Mercalli (1902) and Cancani (1904) scales, is still widely used in Western Europe.

A modified Mercalli scale having 12 grades (a modification of the Mercalli–Cancani–Sieberg scale proposed by Neuman, 1931) is now widely used in most parts of the world. The 12-grade Medved–Sponheuer–Karnik (MSK) scale (1964) was an attempt to unify intensity scales internationally and with the 8-grade intensity scale used in Japan. The subjective nature of the modified Mercalli scale is depicted in Table 1.2.

Table 1.2 Modified Mercalli intensity (MMI) scale (abbreviated version)

Intensity	Evaluation	Description	Magnitude (Richter scale)
I	Insignificant	Only detected by instruments	1–1.9
II	Very light	Only felt by sensitive people; oscillation of hanging objects	2–2.9
III	Light	Small vibratory motion	3–3.9
IV	Moderate	Felt inside buildings; noise produced by moving objects	4–4.9
V	Slightly strong	Felt by most people; some panic; minor damage	
VI	Strong	Damage to non-seismic resistant structures	5–5.9
VII	Very strong	People running; some damage in seismic resistant structures and serious damage to un-reinforced masonry structures	
VIII	Destructive	Serious damage to structures in general	
IX	Ruinous	Serious damage to well-built structures; almost total destruction of non-seismic resistant structures	6–6.9
X	Disastrous	Only seismic resistant structures remain standing	7–7.9
XI	Disastrous in extreme	General panic; almost total destruction; the ground cracks and opens	
XII	Catastrophic	Total destruction	8–8.9

Although the subjective measure of earthquake seems undesirable, subjective intensity scales have played important roles in measuring earthquakes throughout history and in areas where no strong motion instruments are installed. There have been attempts to correlate the intensity of earthquakes with instrumentally measured ground motion from observed data and the magnitude of an earthquake. An empirical relationship between the intensity and magnitude of an earthquake, as proposed by Gutenberg and Richter [6], is given as

$$M_S = 1.3 + 0.6I_{max} \tag{1.15}$$

in which M_S is the surface wave magnitude, and I_{max} is the maximum observed intensity. Many relationships have also been developed for relating the intensity, magnitude, and epicentral distance, r. Among them, that of Esteva and Rosenblueth [13] is widely used:

$$I = 8.16 + 1.45M - 2.46l_n r \tag{1.16}$$

in which I is measured in the MM scale and r is in kilometers. Another relationship which provides good correlation between magnitude and intensity is in the form of

$$I = 1.44M + f(R) \tag{1.17}$$

where $f(R)$ is a decreasing function of R and varies slowly with M.

The other important earthquake measurement parameters are the measured ground motion parameters at the rock outcrops. These ground motion parameters are the peak ground acceleration (PGA), peak ground velocity, and ground displacement. Out of these, PGA has become the most popular parameter to denote the measure of an earthquake and has been related to the magnitude through several empirical relationships. The PGA at a site depends not only on the magnitude and epicentral distance of the earthquake, but also on the regional geological characteristics. Therefore, the empirical constants are

derived from the measured earthquake data in the region. As the PGA value decreases with the epicentral distance, these empirical relationships are also called attenuation laws.

1.4 Measurement of an Earthquake

The instrument that measures the ground motion is called a seismograph and has three components, namely, the sensor, the recorder, and the timer. The principle of operation of the instrument is simple. Right from the earliest seismograph to the most modern one, the principle of operation is based on the oscillation of a pendulum subjected to the motion of the support. Figure 1.16 shows a pen attached to the tip of an oscillating pendulum. The support is in firm contact with the ground. Any horizontal motion of the ground will cause the same motion of the support and the drum. Because of the inertia of the bob in which the pen is attached, a relative motion of the bob with respect to the support will take place. The relative motion of the bob can be controlled by providing damping with the aid of a magnet around the string. The trace of this relative motion can be plotted against time if the drum is rotated at a constant speed.

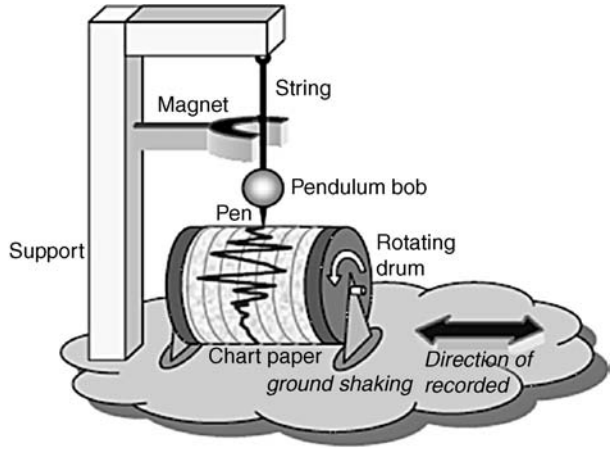

Figure 1.16 Schematic diagram of an early seismograph (*Source*: Murty, C.V.R. "IITK-BMPTC Earthquake Tips." Public domain, *National Information Centre of Earthquake Engineering*. 2005. http://nicee.org/EQTips.php - accessed April 16, 2009.)

If x is the amplified relative displacement of the bob with an amplification of v and u is the ground displacement, then the following equation of motion can be written for the oscillation of the bob:

$$\ddot{x} + 2k\dot{x} + w^2 x = -v\,\ddot{u} \tag{1.18}$$

in which $x = vz$, $2k$ is the damping coefficient, w is the natural frequency of the system, and z is the unamplified displacement. If the frequency of oscillation of the system is very small (that is, the period of the pendulum is very long) and the damping coefficient is appropriately selected, then the equation of motion takes the form:

$$x = -vu \quad \text{or} \quad x \propto u \tag{1.19}$$

Hence, x as read on the recorder becomes directly proportional to the ground displacement. This type of seismograph is called a long period seismograph. If the period of the pendulum is set very short compared

with the predominant period of the ground motion and the damping coefficient is appropriately adjusted, then the equation of motion takes the form:

$$w^2 x = -v\,\ddot{u} \quad \text{or} \quad x \,\alpha\, \ddot{u} \tag{1.20}$$

Thus, x as read on the recorder becomes directly proportional to the ground acceleration. This type of seismograph is called an acceleration seismograph or short period seismograph. If the natural period of the pendulum is set close to that of the ground motion and the damping coefficient is set to a large value, then the equation of motion takes the form:

$$x = -v\dot{u} \quad \text{or} \quad x \,\alpha\, \dot{u} \tag{1.21}$$

Hence, x as read on the recorder becomes directly proportional to the ground velocity.

The pendulum system described above is used to measure the horizontal component of the ground motion.

To measure the vertical component of the ground motion, a pendulum with a weight hanging from spring may be used, as shown in Figure 1.17.

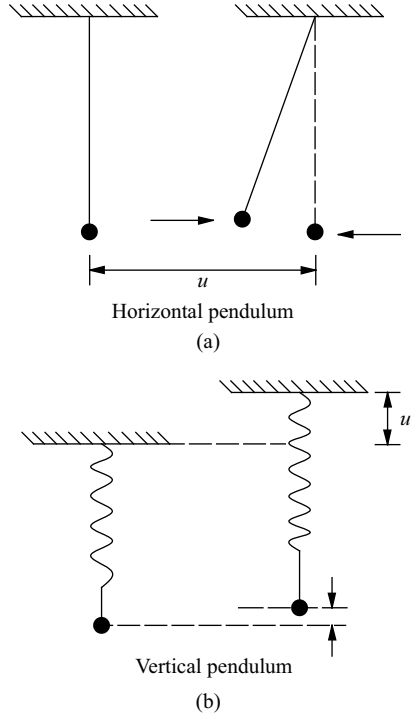

Figure 1.17 Representation of the principle of a seismograph

Amplification of the pendulum displacement can be achieved by mechanical, optical or electromagnetic means. Through optical means, amplifications of several thousand-fold and through electromagnetic means, amplifications of several millionfold are possible. Electromagnetic or fluid dampers may be used to dampen the motion of the system. The pendulum mass, string, magnet, and support together constitute

the sensor. The drum, pen, and chart paper constitute the recorder. The motor that rotates the drum at a constant speed is the timer. All types of seismographs have these three components.

The more commonly used seismographs fall into three groups, namely, direct coupled (mechanical), moving coil, and variable reluctance. The last two use a moving coil galvanometer for greater magnification of the output from the seismographs. In the direct-coupled seismographs, the output is coupled directly to the recorder using a mechanical or optical lever arrangement. The Wood–Anderson seismograph, developed in 1925, belongs to this category. A schematic diagram of the Wood–Anderson seismograph is shown in Figure 1.18. A small copper cylinder of 2 mm diameter and 2.5 cm length having a weight of 0.7g is attached eccentrically to a taut wire. The wire is made of tungsten and is 1/50 mm in diameter. The eccentrically placed mass on the taut wire constitutes a torsion pendulum. A small plane mirror is fixed to the cylinder, which reflects the beam from a light source. By means of double reflection of the light beam from the mirror, magnification of up to 2800 can be achieved. Electromagnetic damping (0.8 of the critical) of the eddy current type is provided by placing the copper mass in a magnetic field of a permanent horseshoe magnet.

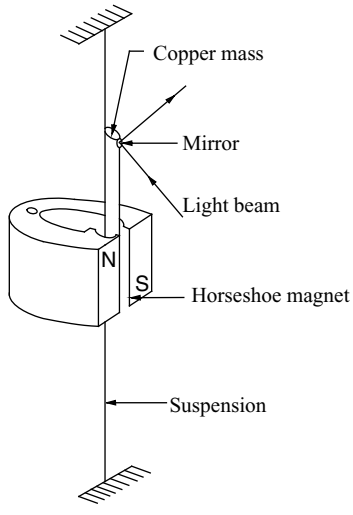

Figure 1.18 Illustration of the torsion pendulum of a Wood–Anderson seismograph

The characteristics of ground motions near and far from the epicentral distances are different. In near earthquakes, waves with a period less than 0.1 s and a very large amplitude are present. For far earthquakes, periods up to 40 s may be commonly encountered with very low amplitude waves. Commonly used seismographs can record earthquake waves within a 0.5–30 s range.

Strong motion seismographs (accelerographs) are used for measuring ground motions for far earthquakes. Such accelerographs are at rest until the ground acceleration exceeds a preset value, and thereby triggering the measurement of any strong earthquake. The earthquake ground motion is recorded in three components of the vibration: two horizontal and one vertical. In general, these accelerographs have:

a. period and damping of the pick up of 0.06–25 cps;
b. preset starting acceleration of about 0.005g;
c. acceleration sensitivity of 0.001–1.0g;
d. average starting time of 0.05–0.1 s.

Micro-earthquake recording instruments also exist, which are able to measure feeble ground vibrations of higher frequencies. These instruments have a low noise to high gain amplifier and operate in the frequency range of 0.1–100 Hz.

1.5 Modification of Earthquakes Due to the Nature of the Soil

Local soil conditions may have a profound influence on the ground motion characteristics, namely, amplitude, frequency contents, and duration. The extent to which this influence is observed depends upon the geological, geographical, and geotechnical conditions. The most influential factors are the properties of the overlying soil layer over the bedrock, topography of the region, the type of rock strata/rock bed, and depth of the overlying soil. The effects of these factors in modifying the free field ground motion have been observed from both theoretical analysis and instrumentally collected earthquake data.

Data from two well recorded earthquakes, the Mexico City earthquake in 1985 and Loma Prieta earthquake in 1989, among many others, revealed some interesting features of the local site effect on free field ground motions. These can be summarized as below:

a. Attenuation of ground motion through rock over a large distance (of the order of 300 km) was significant; a PGA of the order of only 0.03g was observed at a site having an epicentral distance of 350 km for an earthquake of magnitude 8.1.
b. For a soil deposit with $V_s \approx 75\ \mathrm{m\ s^{-1}}$, the magnification factor for the PGA was about 5 for a PGA at the rock bed level, equal to 0.03g. Further, the predominant period was also drastically changed and was close to the fundamental period of the soil deposit.
c. The duration of the shaking was also considerably increased at the site where a soft soil deposit was present.
d. Over a loose, sandy soil layer underlain by San Francisco mud, the PGA amplification was found to be nearly 3 for a PGA level at the rock bed, as 0.035–0.05g.
e. The shape of the response spectrum over soft soil becomes narrow banded compared with that at the rock bed.
f. Spectral amplifications are more for soft soils as compared with stiff soils for longer periods (in the range 0.5–2.0 s).
g. As the PGA at the rock bed increases, the amplification factor for PGA at the soil surface decreases.

Some of the above observations can be substantiated by theoretical analysis, which is usually carried out to obtain the soil amplification factor. It is obtained by one-dimensional wave propagation analysis of S-H waves through the soil layer. For a homogeneous soil medium, closed form expressions may be obtained for the PGA amplification for the harmonic excitation at the rock bed. For an irregular time history of acceleration at the rock bed, free field ground acceleration may be obtained by numerical integration of the equation of motion of the soil mass idealized as the discrete lumped mass shear beam model. The non-linear soil behavior is incorporated into the analysis for a higher level of PGA at the rock bed. The reason for this is that for strong ground shaking, the soil deformation goes into a non-linear range. Because of the hysteretic behavior of soil mass in a non-linear range, the earthquake energy is lost as the wave propagates upward. This loss of energy accounts for the low soil amplification factor for the higher level of PGA at the rock bed.

In addition to the properties of the soil, the effects of the geography/topography of the local site are important. In the San Fernando earthquake ($M_L = 6.4$), the PGA recorded on the Pacoima dam was about 1.25 g, an unusually high value. Subsequent investigations revealed that such a high value of PGA was due to the location of the measuring instrument at the crest of a narrow rocky ridge. Increased amplifications

near the crests of ridges were also measured in five more earthquakes in Japan. Theoretical evaluations show that for vertically propagating S-H waves, apex displacements are amplified by a factor of $2\pi/\varphi$, where φ is the vertex angle of the wedge of the ridge. Topographic effects for the ridge–valley terrain can be treated approximately by using the above factor.

The basin effect is another important issue in local site amplification. The soil amplification factor calculated by one-dimensional wave propagation analysis is valid only for the central region of a basin/valley, where the curvature is almost flat. Near the sides of the valley, where the curvature of the topography is significant, soil deposits can trap body waves and can cause some incident body waves to propagate as surface waves. Thus, free field ground motion obtained by one-dimensional vertical wave propagation analysis does not reflect the true free field ground motion amplitude and duration. Two-dimensional wave propagation analysis is more appropriate to obtain the soil amplification factors near the edges of the valley. Details of one- and two-dimensional analyses are given in Chapter 7.

1.6 Seismic Hazard Analysis

A seismic hazard at a site is defined as a quantitative estimation of the most possible ground shaking at the site. It may be obtained either by a deterministic approach or by a probabilistic approach. The possible ground shaking may be represented by peak ground acceleration, peak ground velocity, or ordinates of the response spectrum. Whatever the approach or the representation of ground shaking are, the seismic hazard analysis requires the knowledge/information about some important factors in the neighborhood of the site. They include geologic evidence of earthquake sources, fault activity, fault rupture length, historical, and instrumental seismicity. Geologic evidence of earthquake sources is characterized by the evidence of ground movement of the two sides of a fault, disruption of ground motion, juxtaposition of dissimilar material, missing or repeated strata, topographic changes, and so on. Fault activity is characterized by movements of ground at the fault region; it is the active fault that leads to future earthquakes. Past earthquake data regarding the relationship between the fault rupture length and the magnitude of earthquake provide valuable information for predicting the magnitude of future earthquakes and, thus, help in seismic hazard analysis. Historical records of earthquakes and instrumentally recorded ground motions at a site also provide valuable information on potential future earthquake sources in the vicinity of the site.

As mentioned above, seismic hazard analysis may be carried out using two approaches, namely, deterministic seismic hazard analysis and probabilistic seismic hazard analysis.

1.6.1 Deterministic Hazard Analysis

Deterministic hazard analysis (DSHA) is a simple procedure which provides a straightforward framework for the computation of ground motions to be used for the worst case design. For specialty or special structures such as nuclear power plants, large dams, and so on, DSHA can be used to provide a safe design. DSHA involves many subjective decisions and does not provide any information on the likelihood of failure of the structure over a given period of time. Because of these reasons, its application is restricted when sufficient information is not available to carry out any probabilistic analysis. DSHA consists of five steps:

a. Identification of all potential earthquake sources surrounding the site, including the source geometry.
b. Evaluation of source to site distance for each earthquake source. The distance is characterized by the shortest epicentral distance or hypocentral distance if the source is a line source.

c. Identification of the maximum (likely) earthquake expressed in terms of magnitude or any other parameter for ground shaking for each source.
d. Selection of the predictive relationship (or attenuation relationship) to find the seismic hazard caused at the site due to an earthquake occurring in any of the sources. For example, the Cornell *et al.* relationship [14] gives:

$$l_n \,\mathrm{PGA(gal)} = 6.74 + 0.859m - 1.80 l_n(r + 25) \tag{1.22}$$

where r is the epicentral distance in kilometers and m is the magnitude of earthquake.
e. Determination of the worst case ground shaking parameter at the site.

The procedure is explained with the help of the following example.

Example 1.1

A site is surrounded by three independent sources of earthquakes, out of which one is a line source, as shown in Figure 1.19. Locations of the sources with respect to the site are also shown in the figure. The maximum magnitudes of earthquakes that have occurred in the past for the sources are recorded as: source 1, 7.5; source 2, 6.8; source 3, 5.0. Using deterministic seismic hazard analysis compute the peak ground acceleration to be experienced at the site.

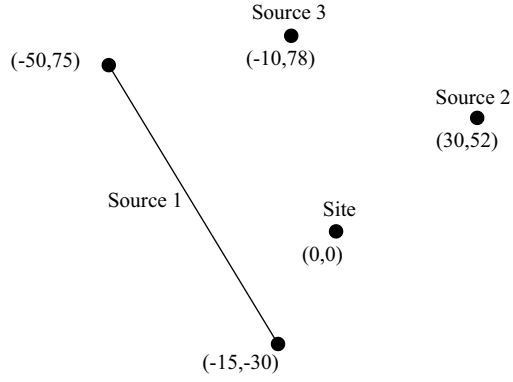

Figure 1.19 Sources of earthquake near the site (DSHA)

Solution: It is assumed that the attenuation relationship given by Cornell *et al.* [14] (Equation 1.22) is valid for the region. The peak ground acceleration to be expected at the site corresponding to the maximum magnitude of an earthquake occurring at the sources is given in Table 1.3:

On the basis of Table 1.3, the hazard would be considered to be resulting from an earthquake of magnitude 7.5 occurring from source 1. This hazard is estimated as producing a PGA of 0.49g at the site.

Table 1.3 PGA at the site for different sources

Source	m	r (km)	PGA (g)
1	7.5	23.70	0.490
2	6.8	60.04	0.10
3	5.0	78.63	0.015

1.6.2 Probabilistic Hazard Analysis

Probabilistic hazard analysis (PSHA) uses probabilistic concepts to predict the probability of occurrence of a certain level of ground shaking at a site by considering uncertainties in the size, location, rate of occurrence of earthquake, and the predictive relationship. The PSHA is carried out using the following steps.

The first step is to identify and characterize the earthquake sources probabilistically. This involves assigning a probability of occurrence of an earthquake at a point within the source zone. Generally, a uniform probability distribution is assumed for each source zone, that is, it is assumed that the earthquake originating from each point within the source zone is equally likely. Secondly, the probability distribution of the source to site distance, considering all points in the source zone to be potential sources of an earthquake, is determined from the source geometry.

The second step is to characterize the seismicity of each source zone. The seismicity is specified by a recurrence relationship indicating the average rate at which an earthquake of a particular size will be exceeded. The standard Gutenberg–Richter recurrence law [7] is used for this purpose, that is,

$$\lambda_m = 10^{a-bm} = \exp(\alpha - \beta m) \tag{1.23a}$$

where

$\alpha = 2.303a$
$\beta = 2.303b$, and
λ_m^{-1} denotes the average return period of the earthquake of magnitude m

If earthquakes lower than a threshold value m_0 are eliminated, then the expression for λ_m is modified [15] as:

$$\lambda_m = \gamma \exp[-\beta(m - m_0)]\, m > m_0 \tag{1.23b}$$

Similarly, if both the upper and lower limits are incorporated, then λ_m is given by:

$$\lambda_m = \gamma \frac{\exp[-\beta(m - m_0)] - \exp[-\beta(m_{\max} - m_0)]}{1 - \exp[-\beta(m_{\max} - m_0)]} \qquad m_0 < m \leq \max \tag{1.24}$$

where

$\gamma = \exp(\alpha - \beta m_0)$

The CDF (cumulative distribution function) and PDF (probability density function) of the magnitude of earthquake for each source zone can be determined from this recurrence relationship as:

$$F_M(m) = P[M < m | m_0 \leq m \leq m_{\max}] = \frac{1 - \exp[-\beta(m - m_0)]}{1 - \exp[-\beta(m_{\max} - m_0)]} \tag{1.25}$$

$$f_M(m) = \frac{\beta \exp[-\beta(m - m_0)]}{1 - \exp[-\beta(m_{\max} - m_0)]} \tag{1.26}$$

In the third step, a predictive relationship is used to obtain a seismic parameter (such as the PGA) at the site for a given magnitude of earthquake and source to site distance for each source zone. The uncertainty inherent in the predictive relationship (attenuation law) is included in the PSHA analysis. Generally, the uncertainty is expressed by a log normal distribution by specifying a standard deviation for the seismic parameter and the predictive relationship is expressed for the mean value of the parameter.

Finally, the uncertainties in earthquake location, earthquake size, and ground motion parameter prediction are combined to obtain the probability that the ground motion parameter will be

exceeded during a particular time period. This combination is accomplished through the following standard equation:

$$\lambda_{\bar{y}} = \sum_{i=1}^{N_S} \gamma_i \iint P[Y > \bar{y}|m, r] f_{Mi}(m) f_{Ri}(r) \mathrm{d}m\mathrm{d}r \tag{1.27}$$

where

$\lambda_{\bar{y}}$ is the average exceedance rate of the seismic parameter Y
N_S is the number of earthquake source zones around the site
γ_i is the average rate of threshold magnitude exceedance for ith source
$P[Y > \bar{y}|m, r]$ is the probability of exceedance of the seismic parameter y greater than $\bar{y}$ for a given pair of magnitude m and source to site distance r
$f_{Mi}(m)$ and $f_{Ri}(r)$ are the probability density functions of the magnitude of the earthquake and source to site distance for the ith source zone

In Equation 1.27, the first term within the integral considers the prediction uncertainty, the second term considers the uncertainty in earthquake size, and the third term considers the uncertainty in location of the earthquake. The above uncertainties for all source zones are considered by way of the double integration/summation. A seismic hazard curve is then constructed by plotting the rate of exceedance of the seismic parameter for different levels of the seismic parameter.

The temporal uncertainty of an earthquake is included in the PSHA by considering the distribution of earthquake occurrences with respect to time. For this purpose, the occurrence of an earthquake in a time interval is modeled as a Poisson process. Note that there are other models that have also been used for the temporal uncertainty of earthquakes. According to the Poisson model, the temporal distribution of earthquake recurrence for the magnitude or PGA is given by:

$$P(N = n) = \frac{(\lambda t)^n e^{-\lambda t}}{n!} \tag{1.28a}$$

where

λ is the average rate of occurrence of the event
t is the time period of interest
n is the number of events

If $n = 1$, then it can easily be shown that the probability of exactly one event $[P(N = n)]$ occurring in a period of t years and the probability of at least one exceedance of the event $[P(N \geq 1)]$ in a period are given by:

$$P(N = 1) = \lambda t \mathrm{e}^{-\lambda t} \tag{1.28b}$$

$$P(N \geq 1) = 1 - \mathrm{e}^{-\lambda t} \tag{1.28c}$$

Thus, the probability of exceedance of the seismic parameter, $\bar{y}$, in a time period, T, is given by:

$$P[y_T > \bar{y}] = 1 - \mathrm{e}^{-\lambda \bar{y} T} \tag{1.28d}$$

Using Equation 1.28d, it is possible to calculate the probability of exceedance of a ground shaking level in a given period of time for a site. Alternatively, the level of ground shaking that has a certain probability of exceedance in a given period can be determined using the above equation and the hazard curve. The PSHA is explained with the help of the following example.

Example 1.2

The site under consideration is shown in Figure 1.20 with three potential earthquake source zones. Seismicity of the source zones and other characteristics are also given. Using the same predictive relationship as that considered for DSHA with $\sigma_{l_n\text{PGA}} = 0.57$, obtain the seismic hazard curve for the site (Table 1.4).

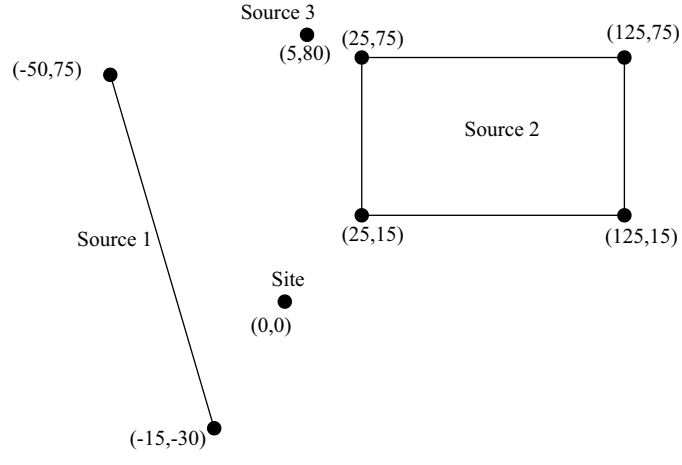

Figure 1.20 Sources of earthquake near the site (PSHA)

Table 1.4 Seismicity of the source zones

Source	Recurrence law	m_0	m_u
Source 1	$\log \lambda_m = 4-m$	4	7.7
Source 2	$\log \lambda_m = 4.5-1.2m$	4	5
Source 3	$\log \lambda_m = 3-0.8m$	4	7.3

Solution: For the first source, the minimum source to site distance (r) is 23.72 km, the maximum distance r is that of point $(-50, 75)$ from the site, that is, $r = 90.12$ km. Dividing $r_{\max} - r_{\min}$ into ten equal divisions and finding the number of points lying within each interval, the histogram as shown in Figure 1.21 is obtained. To obtain this, the line is divided into 1000 equal segments.

For the second source, $r_{\min} = 30.32$ km and $r_{\max} = 145.98$ km. Here the area is divided into 2500 equal rectangular small areas of 2×1.2 km and the center of the small area is considered as the likely point of earthquake origin. The histogram of r for the second source is shown in Figure 1.22. Similarly, the histogram of r for the third source is shown in Figure 1.23.

$$\text{Source zone 1} \qquad \gamma_1 = 10^{4-1\times4} = 1$$

$$\text{Source zone 2} \qquad \gamma_2 = 10^{4.5-1.2\times4} = 0.501$$

$$\text{Source zone 3} \qquad \gamma_3 = 10^{3-0.8\times4} = 0.631$$

in which γ_i is the mean rate of exceedance of magnitude for source zone 1

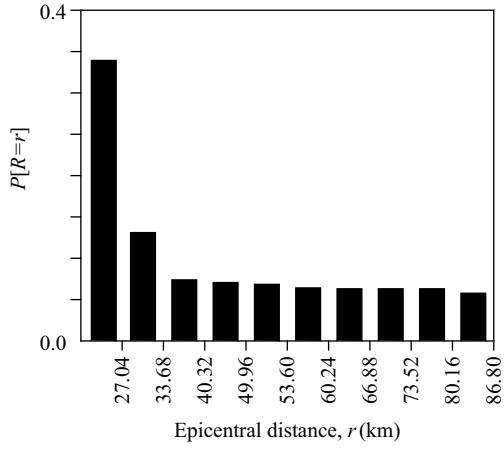

Figure 1.21 Histogram of r for source zone 1

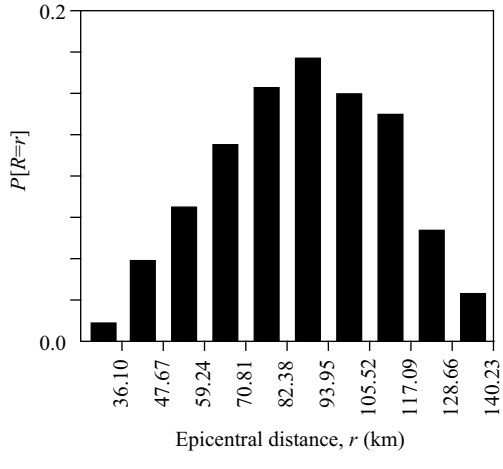

Figure 1.22 Histogram of r for source zone 2

For each source zone,

$$P[m_1 < m < m_2] = \int_{m_1}^{m_2} f_M(m)\mathrm{d}m \simeq f_m\left(\frac{m_1+m_2}{2}\right)(m_2-m_1) \tag{1.29a}$$

say, for source zone 1, the magnitudes of earthquakes m_u and m_0 are divided in ten equal divisions:

$$P[4 < m < 4.37] \approx \frac{2.303\mathrm{e}^{-2.303(4.19-4)}}{1-\mathrm{e}^{-2.303(7.7-4)}}(4.37-4) = 0.551$$

In this manner, the probabilities of the various magnitudes for each source zone can be computed and are shown in the form of histograms in Figures 1.24–1.26.

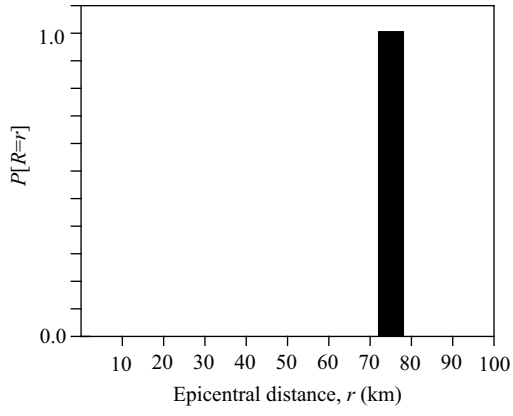

Figure 1.23 Histogram of r for source zone 3

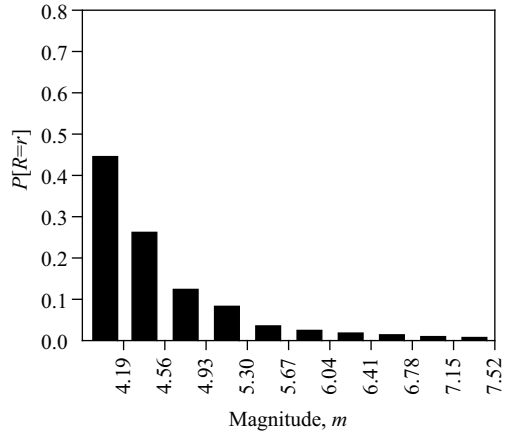

Figure 1.24 Histogram of magnitude for source zone 1

For source zone 1, if the magnitude of an earthquake corresponding to the lowest division and the source to site distance corresponding to the lowest division are considered (Figures 1.21 and 1.24), then

$$P[m = 4.19] = 0.551$$
$$P(r = 27.04) = 0.336$$

For this combination of m and r, the mean value of the PGA is given by Equation 1.22 as L_n PGA = 3.225.

Assuming the uncertainty of predictive law to be log normally distributed, the probability of exceeding the acceleration level of 0.01g for $m = 4.19$ and $r = 27.04$ km is:

$$P[\text{PGA} > 0.01g | m = 4.19, r = 27.04] = 1 - F_Z(Z)$$

where

$$Z = \frac{\ln(9.81) - 3.225}{0.57} = -1.65$$

and $F_Z(Z)$ is the normal distribution function.

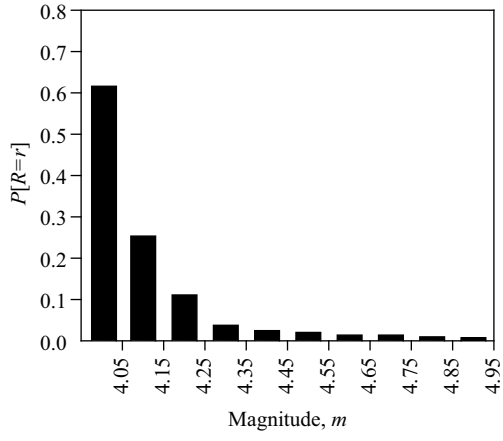

Figure 1.25 Histogram of magnitude for source zone 2

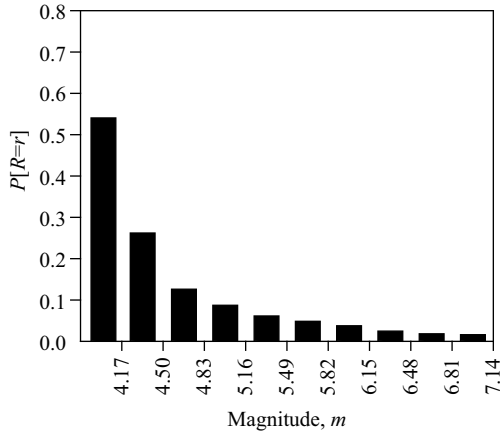

Figure 1.26 Histogram of magnitude for source zone 3

Thus, the above probability is given as

$$1 - F_Z(Z) = 1 - F_Z(-1.65) = 0.951$$

The annual rate of exceedance of a peak acceleration of 0.01g by an earthquake of $m = 4.19$ and $r = 27.04$ for source zone 1 is:

$$\begin{aligned}\lambda_{0.01\text{g}} &= \gamma_1 P[\text{PGA} > 0.01g | m = 4.19, r = 27.04] P[m = 4.19] P[r = 27.04] \\ &= 1 \times 0.9505 \times 0.55 \times 0.336 = 0.176\end{aligned}$$

In this manner, $\lambda_{0.01\text{g}}$ for 99 other combinations of m and r for source 1 can be calculated. The procedure is repeated for sources 2 and 3. Summation of all $\lambda_{0.01\text{g}}$, thus obtained provides the annual rate of

exceedance of PGA = 0.01g at the site. This summation is equivalent to the numerical integration of Equation 1.27 by converting it into

$$\lambda_{\bar{y}} = \sum_{i=1}^{N_S} \sum_{j=1}^{N_M} \sum_{k=1}^{N_R} \gamma_i P[y > \bar{y} | m_j, r_k] P[m = m_j] P[r = r_K] \tag{1.29b}$$

in which N_M and N_R are the number of equal divisions of the ranges of magnitude and source to site distance for each source. For other PGAs, the annual rate of exeedance can be similarly determined. The plot of annual rate of exeedance versus PGA is generally known as the hazard curve.

Example 1.3

The seismic hazard curve for a region shows that the annual rate of exceedance for an acceleration of 0.25g due to earthquakes (event) is 0.02. What is the probability that:

(i) Exactly one such event will take place in 30 years?
(ii) At least one such event will take place in 30 years?

Also, find the annual rate of exceedance of PGA that has a 10% probability of exceedance in 50 years.

Solution:

(i) $P(N = 1) = \lambda t\, e^{-\lambda t} = 0.02 \times 30 e^{-0.02 \times 30} = 33\%$
(ii) $P(N \geq 1) = 1 - e^{-0.02 \times 30} = 45.2\%$

Equation 1.28c may be written as:

$$\lambda = \frac{\ln[1 - P(N \geq 1)]}{t} = \frac{\ln[1 - 0.1]}{50} = 0.0021$$

1.6.3 Seismic Risk at a Site

Seismic risk at a site is similar in concept to that of a probabilistic seismic hazard determined for a site. Seismic risk is defined as the probability that a ground motion X_S that is equal to or greater than a specified value X_1 will occur during a certain period (usually one year) at the site of interest, that is, $P(X_S \geq X_1)$, or it can be defined by the return period T_{X1}, which is the inverse of $P(X_S \geq X_1)$. The study of seismic risk requires:

a. geotectonic information that provides estimates for the source mechanism parameters such as focal depth, orientation of the causative fault rupture, and the earthquake magnitude;
b. historical seismicity presented in the form of a recurrence relationship, which allows the development of the probability distribution of the magnitude of an earthquake and contains information related to the relative seismic activity of the region;
c. a set of attenuation relationships relating the ground motion parameters at any site to the source magnitude and epicentral distance.

Using the above information, the seismic risk can be calculated with the help of either:

a. Cornell's [16] approach, in which the area is divided into zones based on the geotectonic information and observed seismicity, or
b. Milne and Davenport's [17] approach, where the amplitude recurrence distribution for a specified level of shock amplitude is computed using a history of this shock amplitude reconstructed from the records

of earthquake magnitude of observed earthquakes using some empirical relationships; attenuation relationships are then combined with regional seismicity to arrive at seismic risk at a site.

Using the concept above, empirical equations have been derived by researchers to express seismic risk at a site. These empirical equations are obtained using the earthquake data/information of certain regions. Therefore, they are valid strictly for sites in these regions. However, these empirical equations can be used for sites in other regions by choosing appropriate values of the parameters of the equations. A few empirical equations are given below:

a. Milne and Davenport [17] and Atkinson *et al.* [18] proposed an expression for calculating the average annual number of exceedances of a shock amplitude Y_S (Y_S may be a velocity or an acceleration):

$$N(Y_S) = (Y_S/\bar{c})^{-\bar{p}} \tag{1.30}$$

where $\bar{p}$ and $\bar{c}$ are constants established from the observation of $N(Y_S)$ from past earthquake records.

b. Donovan and Bornstein [19] calculated the annual number of earthquakes (γ_1) of magnitude greater than or equal to m_1 as

$$v_1(m_1) = e^{\alpha-\beta m_1}/T_0 \tag{1.31}$$

where
$\alpha = a_s l_n 10$
$\beta = b_s l_n 10$, where β is the seismicity parameter
a_s and b_s = Richter parameters derived for the region from past observations for a period of duration T_0
They also obtained the extreme value probability $\bar{P}$ (which is the probability of maximum-size events occurring every year) as:

$$\bar{P} = \exp[-\exp(\alpha_1 - \beta m_1)] \tag{1.32a}$$

$$\alpha_1 = \alpha l_n T_0 \tag{1.32b}$$

c. Erel *et al.* [20] have provided the following expression to calculate the annual probability of occurrence of an earthquake with intensity I_S exceeding $i_1 P(I_S \geq i_1)$ for the eastern USA:

$$P(I_S \geq i_1) = 47e^{-1.54 i_1} \tag{1.33}$$

Oppenheim [21] presented the following expression for $P(I_S \geq i_1)$ for the same region:

$$P(I_S \geq i_1) = \bar{F}e^{-1.28 i_1} \qquad 6 < i_1 < I_{\max} \tag{1.34}$$

where $\bar{F}$ and $I_{\max}$ depend on the regional expected peak acceleration (EPA).

d. Cornell and Merz [22] developed the following expression to calculate the annual seismic risk $P(I_S \geq i_1)$ in Boston due to nearby earthquakes of intensity exceeding i_1 and distant earthquakes of higher intensity causing site intensity exceeding i_1:

$$P(I_S \geq i_1) \cong \sum_{j=1}^{\bar{S}} \sum_{l=1}^{d_j} \frac{A_{jl}}{A_j} v_{1j} \left[(1-\bar{k}_{i1j})\phi^* \left(\frac{Z_j}{\sigma} \right) + \bar{k}_{i1j} \phi^* \left(\frac{Z_j - 0.44}{\sigma} \right) e^{8.38} r_{1jl}^{-1.43} e^{-1.1 i_1} \right] \tag{1.35a}$$

in which $Z_j = i_1 - (I_{Sj})_u$ and

$$\left.\begin{array}{rl} I_{SJ} = I_{ej} & \\ I_{SJ} = 2.6 + I_{ej} - \ln r_{1j} & \end{array}\right\} \qquad \begin{array}{l} r_{1j} < 10 \text{ mile} \\ r_{1j} \geq 10 \text{ mile} \end{array} \tag{1.35b}$$

where
I_{ej} is the epicentral intensity of source j
I_{Sj} is the site intensity due to source j
$(I_{ej})_u$ and $(I_{sj})_u$ are their upper bound values

$$\bar{k}_{ij} = [1-\exp\{-\beta[(I_{ej})_u-(I_{ej})_0]\}]^{-1} \tag{1.36}$$

where
$(I_{ej})_0$ is the lower bound intensity of the source area j
$\bar{s}$ is the number of geometrical sources
d_j is the number of point sources forming a discretized representation of source j
A_{jl} and r_{1jl} are the area and epicentral distance of the point source l discretized from the source j
A_j is the total area of source j
v_{1j} is the annual occurrence rate of earthquakes exceeding threshold magnitude
ρ is the standard deviation of errors between the expected and observed intensities (they assumed $\sigma = 0.2$)
$\phi^*(x) = 1-\phi(x)$ in which $\phi(x)$ is the Gaussian cumulative distribution function

e. Cornell [16], Talebagha [23], and Kiureghian and Ang [24] presented the following expression for calculating the cumulative distribution function $F_{M_S}(m_1)$ of an earthquake of magnitude m_1:

$$F_{M_S}(m_1) = P[M_S \le m_1 | M_0 \le m_1 \le M_u] = \frac{1-e^{-\beta(m_1-M_0)}}{1-e^{-\beta(M_u-M_0)}} \tag{1.37}$$

M_0 and M_u are the lower and upper bounds of the magnitude m_1. The probability that the earthquake magnitude M_S exceeds or equals a certain value m_1 is:

$$P(M_S \ge m_1) = 1-F_{M_S}(m_1) \tag{1.38}$$

For large values of M_u, $P(M_S \ge m_1)$ can be obtained from Equations 1.37 and 1.38

$$P(M_S \ge m_1) = e^{-\beta(m_1-M_0)} \tag{1.39}$$

f. Talebagha [23] presented the following expression for the probability that the ground acceleration A_S equals or exceeds a certain value a_i,

$$P(A_S \ge a_i) = 1-F_{M_S}(m_i) \tag{1.40a}$$

$$m_i = \frac{1}{b_2}\ln\frac{r_i}{b_1} \tag{1.40b}$$

$$r_i = a_i[f(r_1)]^{b_3} \tag{1.40c}$$

in which b_1, b_2, and $f(r_1)$ are given by $b_1 = 1.83$, $b_2 = 1.15$, $b_3 = 1.0$; $f(r_1) = \max(11.83, r_1)$, and r_1 is the epicentral distance in km.

1.6.4 Concept of Microzonation Based on Hazard Analysis

Microzonation is the delineation of a region or a big city into different parts with respect to the variation of the earthquake hazard potential. Most of the earthquake prone big cities of the world have been microzoned, such as Tokyo and San Francisco. Various parameters are used to microzone a region. Microzonation maps with respect to the variation of each parameter are prepared and then combined to obtain an earthquake hazard index for each microzone by associating a damage weighting to each parameter. Typical parameters used in microzonation include local soil characteristics, earthquake source properties, epicentral distance, topographic structure, ground water and surface drainage, population and construction density, types of construction, importance of the structure, and so on. Each of these parameters contributes to the earthquake hazard potential of a microzone and varies across the region.

Although each parameter has its own importance, the soil characteristics and earthquake source properties, including the epicentral distance, are considered as very important parameters defining the seismic risk or seismic hazard potential of a particular site. Thus, the seismic hazard analysis, described in Sections 1.6.1 and 1.6.2, and modification of an earthquake due to the local nature of the soil, described in Section 1.5, are commonly combined together to obtain a microzonation map of a city. Clearly, the microzonation map thus made is probabilistic or deterministic in nature depending upon whether PSHA or DSHA has been used.

The procedure for constructing a microzonation map consists of the following steps.

1. Divide the region or the city into a number of grids. Grids need not be uniform. They depend upon the variation of the soil characteristics across the region.
2. Considering the centers of the grids as the sites, the PGAs at the sites are obtained by DSHA for the given earthquake source properties surrounding the region.
3. Alternatively, a certain probability of exceedance in a given period is assumed. The PGAs at the sites that have the assumed probability of exceedance are obtained by PSHA for the given uncertainties of the earthquake source properties.
4. For each site, obtain the soil amplification factor by performing one-dimensional wave propagation analysis. For higher values of PGA at the rock bed, the non-linear property of the soil is considered in the analysis.
5. PGA at the free field for each site is obtained by multiplying PGAs obtained in step 2 or step 3 by the corresponding amplification factors.
6. With free field PGAs at the sites, the region is finally divided into a number of microzones, as shown in Figure 1.27.

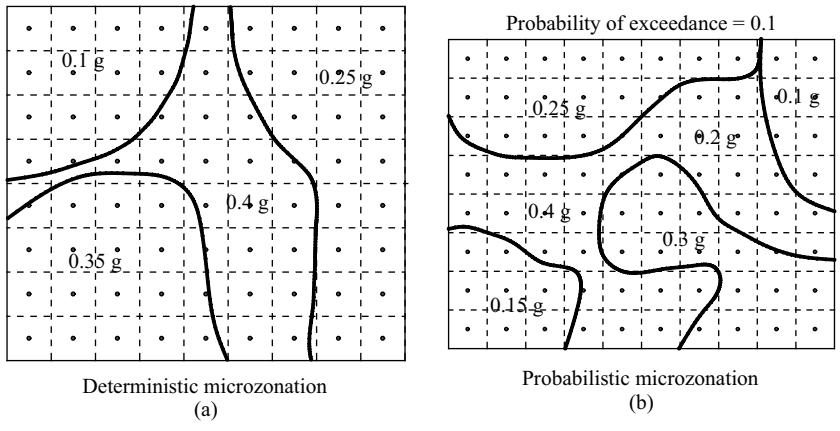

Figure 1.27 Microzonation: (a) deterministic; and (b) probabilistic

Exercise Problems

1.4 Estimate the probabilities of surface rupture length, rupture area, and maximum surface displacement exceeding 90 km, 60 km^2 and 15 m, respectively (use Equations 1.14b–d). Assume the rupture parameters to be log normally distributed.

1.5 A site is surrounded by three line faults as shown in Figure 1.28. Determine the expected mean value of the PGA at the site using the attenuation relationship given by Cornell *et al.* (Equation 1.22).

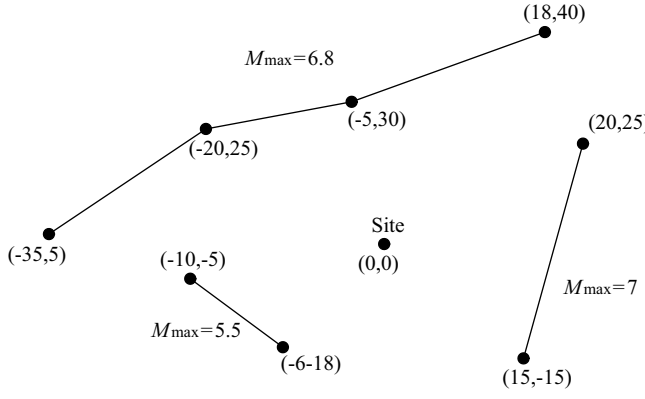

Figure 1.28 A site affected by three line sources of earthquakes

1.6 A site is surrounded by two sources as shown in Figure 1.29. Determine the anticipated mean value of the PGA and the probability of it exceeding the value of 0.2g using the same attenuation law used in problem in Example 1.2.

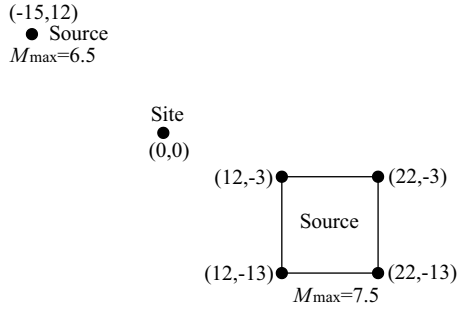

Figure 1.29 A site affected by a point source and an area source of earthquake

1.7 A site has two earthquake sources, a point source (source 1) and segments of line sources (source 2). The distributions of the magnitudes of the earthquake for source 1 and source 2 are shown in Figure 1.30. The distribution of the source to site distance for source 2 is also shown in the same figure. Occurrences of earthquakes for sources 1 and 2 are given by

$$\log \lambda_{m_1} = 4 - 0.7m$$
$$\log \lambda_{m_2} = 3 - 0.75m$$

Develop a seismic hazard curve for peak acceleration at the site using the attenuation relationship given by Equation 1.22. Assume that magnitudes less than 4 do not contribute to the seismic hazard.

1.8 A region, as shown in Figure 1.31 is to be microzoned with respect to the PGA at the ground surface. Use the attenuation relationship given by Equation 1.22 and assume it to be valid for the rock bed. For microzination, the region is divided into 4 sub-areas. Determine the design PGA for the center of each sub-region.

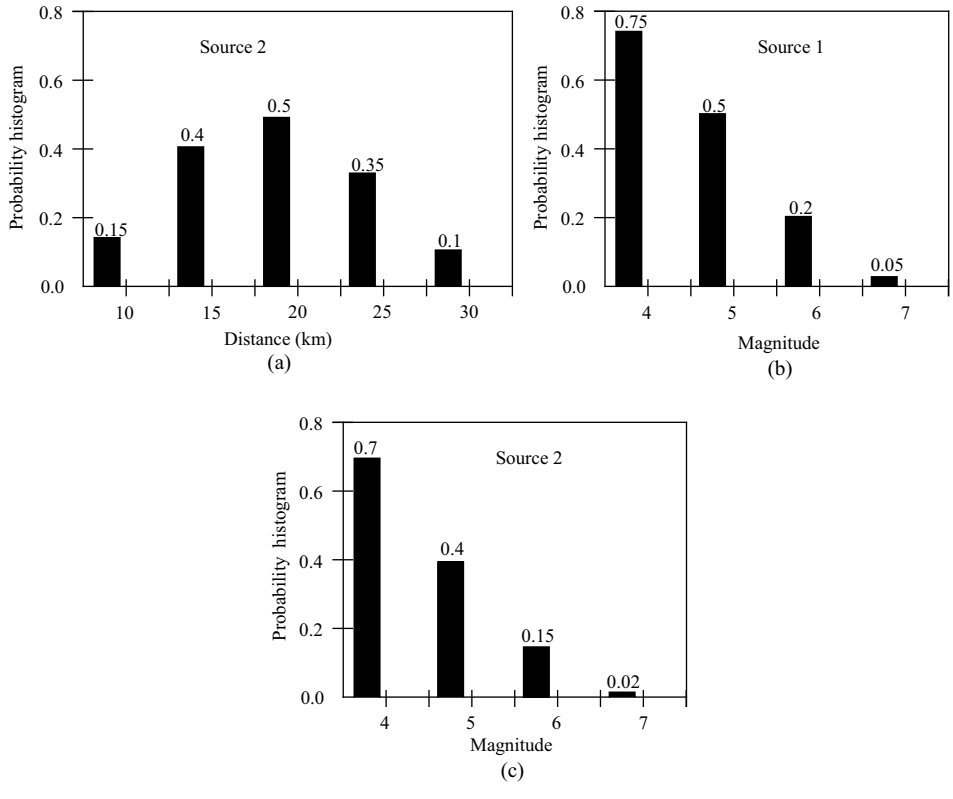

Figure 1.30 Characteristics of the sources: (a) distribution of source to site distance for source 2; (b) distribution of the magnitude of earthquake for source 1; and (c) distribution of the magnitude of earthquake for source 2

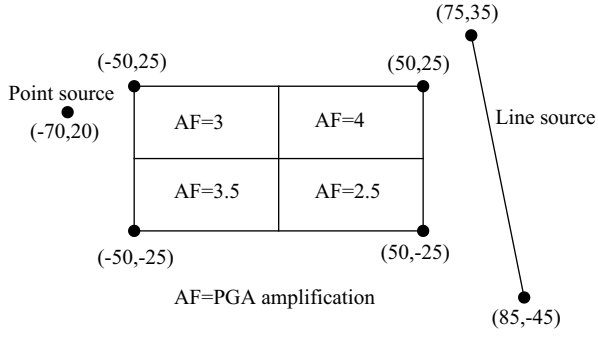

Figure 1.31 Area to be microzoned using both DSHA and PSHA

1.9 A site is 100 km away from a point source of an earthquake. The seismicity of the region is represented by the following recurrence relationship:

$$\log \lambda_m = 3.0 - 0.75M$$

The attenuation relationship for the region is given by:

$$l_n \,\text{PGA} = -4.141 + 0.868M - 1.09\, l_n[R + 0.0606 \exp(0.7M)]$$

a. What are the probabilities that at least one earthquake will produce a PGA greater than 0.2g in 50 and 150 year periods?
b. What is the probability that exactly one earthquake will produce a PGA greater than 0.2g in a 100 year period?
c. Determine the PGA that would have a 10% probability of exceedance in 50 years.

1.10 The site shown in Figure 1.31 is assumed to have only the point source. The histogram for the magnitude of the earthquake is taken to be the same as that shown in Figure 1.30. Using the same attenuation and seismic occurrence (source 1) relationships (for Exercise Problem 1.4), make a probabilistic microzonation of the area in terms of PGA for 10% probability of exceedance. Assume the minimum magnitude of the earthquake as 4.

1.11 Seismic risk of a region with its epicentral distance measured from its center as 100 km is given by Equation 1.40 in which $F_{M_s}(M_i)$ is given by Equation 1.37. Make a microzonation of the region for its 4 sub-regions shown in Figure 1.32 for the probability of exceedance of PGA = 0.3g at the ground surface. Given $M_0 = 4$ and $M_u = 8.5$; $\beta = 1$. Assume the empirical equations to be valid for the rock bed.

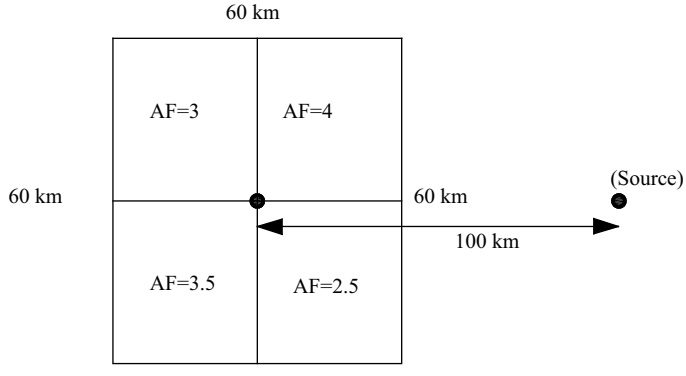

Figure 1.32 Area to be microzoned using PSHA

1.12 State true (T) or false (F) for the following statements:

(i) Earthquake may occur due to–
  (a) interplate movement
  (b) intraplate movement
  (c) rupture of plates at the fault
  (d) underground explosion
  (e) volcanic eruption

(ii) Movement of the plates during earthquake–
  (a) is necessarily a strike slip
  (b) is necessarily a dip slip
  (c) could be a combination of the two

(iii) Fastest wave is–
  (a) love wave
  (b) primary wave
  (c) Rayleigh wave
  (d) S wave

(iv) Movement of soil particles is at right angles to the direction of wave propagation for–
  (a) primary wave
  (b) Rayleigh wave
  (c) polarized wave

(v) Subduction is a process which is responsible for–
  (a) formation of oceans
  (b) formation of mountains
  (c) mid-oceanic ridges

(vi) Moho discontinuity is the name of–
  (a) discontinuity between inner core and outer core of the earth
  (b) discontinuity between the outer core and the mantle
  (c) discontinuity between the crust and the mantle

(vii) Surface waves are–
  (a) largest for shallow focal depth
  (b) increased with depth
  (c) almost periodic at large epicentral distance
  (d) having short period

(viii) Richter magnitude–
  (a) is the same as moment magnitude
  (b) is the same as body magnitude
  (c) can be negative
  (d) is open ended

(ix) Magnitude is–
  (a) exponentially related to the PGA
  (b) linearly related to the PGA
  (c) directly related to the intensity
  (d) directly related to the energy release

(x) Attenuation relationship depends upon–
  (a) local geological conditions
  (b) path of wave travel
  (c) soil conditions
  (d) epicentral distance

(xi) One-dimensional wave propagation through soil from rock bed provides–
  (a) amplified PGA
  (b) amplified ground displacement
  (c) changed frequency contents
  (d) lower value of PGA for strong rock bed motion in soft soil

(xii) One-dimensional wave propagation–
  (a) is valid for ridges
  (b) s valid for boundaries of the valleys

(c) is valid for the center of basins
(d) is valid for highly non-homogenous soil mass with many disjointed layers in different directions

(xiii) Both arrival of an earthquake and the magnitude of an earthquake may be modeled as–
(a) lognormal model
(b) Poisson model
(c) exponentially decaying model

(xiv) Seismic hazard of a site–
(a) primarily depends upon its epicentral distances from sources
(b) primarily depends upon both epicentral distances and magnitudes of earthquakes that occurred at the sources
(c) depends largely on soil amplification
(d) does not depend on attenuation law

(xv) Ground damage in an earthquake can be–
(a) faulting
(b) fissures
(c) liquefaction

(xvi) How many seismograph station are needed to locate the epicenter of an earthquake–
(a) 1
(b) 2
(c) 3
(d) 4

(xvii) M_b is also known as Richter's magnitude.

(xviii) Moment magnitude can be estimated from fault area only.

(xix) Attenuation relationships are developed based on theoretical analysis.

(xx) A seismic hazard curve is used for deterministic seismic hazard assessment.

(xxi) Love waves are slower than Raleigh waves and introduce retrograde elliptical motion.

(xxii) Earthquake intensity is usually higher at the epicenter and in loosely consolidated soil.

References

1. Wiechert, E. (1903) Theorie der automatischen Seismographen. *Abhhandlung der Gesellschaft der Wissenschaften Zu Gottingen, Mathematisch-Physikalische Klasse*, **2**, 1–128.
2. Oldham, R.D. (1906) Constitution of the interior of the Earth as revealed by earthquakes. *Quarterly Journal of the Geological Society*, **62**, 456–475.
3. Rosenblueth, E. (1961) Temblores chienos de mayo 1960: Sus efectos en estructuras civiles. *Ingenieria*, **31** (1), 1–31.
4. Shannon and Wilson, Inc. (1964) Anchorage area soil studies, Alaska, Reports to U.S. Army Engineer District, Anchorage, Alaska.
5. Richter, C.F. (1935) An instrument earthquake magnitude scale. *Bulletin of the Seismological Society of America*, **25**, 1–31.
6. Gutenberg, B. and Richter, C.F. (1956) Earthquake magnitude: intensity, energy, and acceleration. *Bulletin of the Seismological Society of America*, **46**, 104–145.
7. Gutenberg, B. and Richter, C.F. (1944) Frequency of earthquakes in California. *Bulletin of the Seismological Society of America*, **34** (4), 1985–1988.
8. Kanamori, H. (1977) The energy release in great earthquake. *Journal of Geophysical Research*, **82**, 2981–2987.
9. Newmark, N.M. and Rosenblueth, E. (1971) *Fundamentals of Earthquake Engineering*, Prentice-Hall, Englewood Cliffs, NJ.
10. Tocher, D. (1958) Earthquake energy and ground breakage. *Bulletin of the Seismological Society of America*, **48**, 147–152.
11. Chinnery, M.A. (1961) The deformation of the ground around surface faults. *Bulletin of the Seismological Society of America*, **51** (3), 355–372.
12. Kramer, S.L. (1996) *Geotechnical Earthquake Engineering*, Pearson Education Inc., Upper Saddle River, NJ.

13. Esteva, L. and Rosenblueth, E. (1964) Espectros de temblores a distancias moderadas y grandes. *Boletin de la Sociedad Mexicana Ingenieria Sismologia*, **2** (1), 1–18.
14. Cornell, C.A., Banon, H., and Shakal, A.F. (1979) Seismic motion and response prediction alternative. *Earthquake Engineering and Structural Dynamics*, **7** (4), 295–315.
15. McGuire, R.K. and Arabasz, W.J. (1990) An introduction to probabilistic seismic hazard analysis, in *Geotechnical and Environmental Geophysics*., vol **1** (ed. S.H. Ward), Society of Exploration Geophysicists, Tulsa, OK, pp. 333–353.
16. Cornell, C.A. (1968) Engineering seismic risk analysis. *Bulletin of the Seismological Society of America*, **58**, 1583–1606.
17. Milne, W.G. and Davenport, A.G. (1969) Distribution of earthquake risk in Canada. *Bulletin of the Seismological Society of America*, **59**, 729–754.
18. Atkinson, G.M., Davenport, A.G., and Novak, M. (1982) Seismic risk to pipelines with application to Northern Canada. *Canadian Journal of Civil Engineering*, **9**, 248–264.
19. Donovan, N.C. and Bornstein, A.E. (1978) Uncertainties in seismic risk procedures. *Journal of Geotechnical Engineering, ASCE*, **104**, 869–887.
20. Erel, B., Patelunas, G.M., Niece, J.E., and Oppenheim, I.J. (1977) Measuring the earthquake performance of urban water systems, The current State of Knowledge of Lifeline. *Earthquake Engineering, ASCE*, **103**, 183–198.
21. Oppenheim, I.J. (1979) Simulation of water system seismic risk. *Journal of Technological. Councils, ASCE*, **105**, 327–336.
22. Cornell, C.A. and Merz, H.A. (1975) Seismic risk analysis of Boston. *Journal of Structural Engineering, ASCE*, **101**, 2027–2041.
23. Talebagha, G. (1977) Seismic risk analysis of lifeline networks. *Bulletin of the Seismological Society of America*, **67**, 1625–1645.
24. Der Kiureghian, A. and Ang, A.H.S. (1977) A fault-rupture model for seismic risk analysis. *Bulletin of the Seismological Society of America*, **67**, 1173–1194.

2

Seismic Inputs for Structures

2.1 Introduction

Seismic inputs are the earthquake data that are necessary to perform different types of seismic analysis. In the context of seismic analysis and design of structures, various earthquake data may be required depending upon the nature of analysis being carried out. These data are presented in two different ways, namely, in deterministic and probabilistic forms. Seismic inputs in deterministic form are used for deterministic analysis and design of structures, while those in probabilistic form are used for random vibration analysis of structures for earthquake forces, seismic risk analysis of structures, and damage estimation of structures for future earthquakes. Seismic inputs for structural analysis are provided either in the time domain or in the frequency domain, or in both time and frequency domains. In addition, a number of earthquake parameters are also used as seismic inputs for completeness of the information that is required to perform different types of analysis. They include magnitude, intensity, peak ground acceleration/velocity/displacement, duration, predominant ground frequency, and so on. Further, certain types of analysis, such as, seismic risk analysis, damage estimation of structures, and probabilistic seismic analysis, the prediction of seismic input parameters for future earthquakes are essential. Such predictions are provided in the form of empirical equations. In this chapter, different types of seismic input and predictive relationships that are used in practice are described.

2.2 Time History Records

The most common way to describe a ground motion is with a time history record. The motion parameters may be acceleration, velocity, or displacement, or all the three combined together. Generally, the directly measured quantity is the acceleration and the other parameters are the derived quantities. However, displacement and velocity can also be measured directly. The measured time histories of records include errors resulting from many sources, such as noises at high and low frequencies, base line error, and instrumental error. These errors are removed from the data before they are used. Further, measured data are in an analogue form, which are digitized before they are used as seismic inputs. In recent years, digital seismographs are more commonly used but the various errors mentioned above are equally present in the analogue and digital forms. Time histories of ground motions are used directly for the time domain analysis of structures subjected to deterministic seismic inputs. This analysis will be described in Chapter 3.

At any measuring station, ground motions are recorded in three orthogonal directions; two of them are in horizontal directions and the third is in the vertical direction. Thus, three components of ground motions are available from any measuring station. For structural analysis, these three components of ground

Seismic Analysis of Structures T.K. Datta

motions are transformed into those corresponding to the principal directions. It has been observed that the major direction of ground motion lies in the direction of the line joining the measuring station and the epicenter. The other two components of the ground motion are decided accordingly. Stochastically, the components of ground motions in the principal directions are uncorrelated. Based on this concept, three principal components of ground motion are artificially generated in places where representative time histories of the ground motion are not available. Three components of the ground motion for the El Centro earthquake are shown in Figure 2.1. The digitized versions of time histories of many earthquakes are available in web sites such as www.peer.berkeley.edu/sncat.

As discussed in Chapter 1, free field ground motions are the result of a complex phenomenon involving wave reflection, refraction, and surface wave propagation. Furthermore, they are combinations of P, S, and L waves. Therefore, the trains of free field ground motion waves as recorded at different stations vary spatially resulting in both homogeneous and non-homogeneous fields of ground motion. Homogeneous ground motion is idealized as a single train of ground motion moving at a constant speed. As a result, time histories of ground motion at two points, spatially separated, have only a time lag; the peak or rms (root mean square) ground motions remain the same at the two stations. For a non-homogeneous field of ground motion, the peak or rms value of the ground motion varies between two stations in addition to a time lag effect. Because of this spatial variation of ground motions, rotational and torsional (about a vertical axis) components of ground motions are induced. The rotational and torsional components of ground motions are given by:

$$\phi(t) = \frac{\mathrm{d}u}{\mathrm{d}y} + \frac{\mathrm{d}v}{\mathrm{d}x} \tag{2.1}$$

$$\theta(t) = \frac{\mathrm{d}w}{\mathrm{d}x} \tag{2.2}$$

in which u, v, and w are the ground motions in the x, y, and z directions, respectively; x and y are the two horizontal components, with x being the major principal direction. The major principal direction may be at an angle of inclination to the major principal direction of the structure and therefore, an angle of incidence (α) of an earthquake is also defined for the time history. Thus, complete information on time histories of ground motion at a point as seismic input are defined as $u(t)$, $v(t)$, $\omega(t)$, $\phi(t)$, and $\theta(t)$ and their time derivatives. In addition, the angle of incidence α may have to be defined for structures having irregular plans, as shown in Figure 2.2.

2.3 Frequency Contents of Ground Motion

As the response of any structure depends on the ratio between the natural frequency of the structure and the frequency of excitation, it is important to know the frequency contents of the ground motion. In fact, for frequency domain analysis of structures (discussed in Chapter 3), seismic input is required in the form of frequency contents of the ground motion. The most convenient and useful way of providing this information is by way of a Fourier synthesis of the time history of the ground motion. Assuming that the time history of the ground motion repeats itself with a period equal to the duration of the ground motion, it can be represented as a sum of an infinite number of harmonic functions (known as the Fourier series of expansion of a periodic function) by

$$x(t) = a_0 + \sum_{n=1}^{\alpha} a_n \cos \omega_n t + b_n \sin \omega_n t \tag{2.3}$$

where

$x(t)$ is the time history of ground motion (displacement, velocity or acceleration)
ω_n is the nth frequency

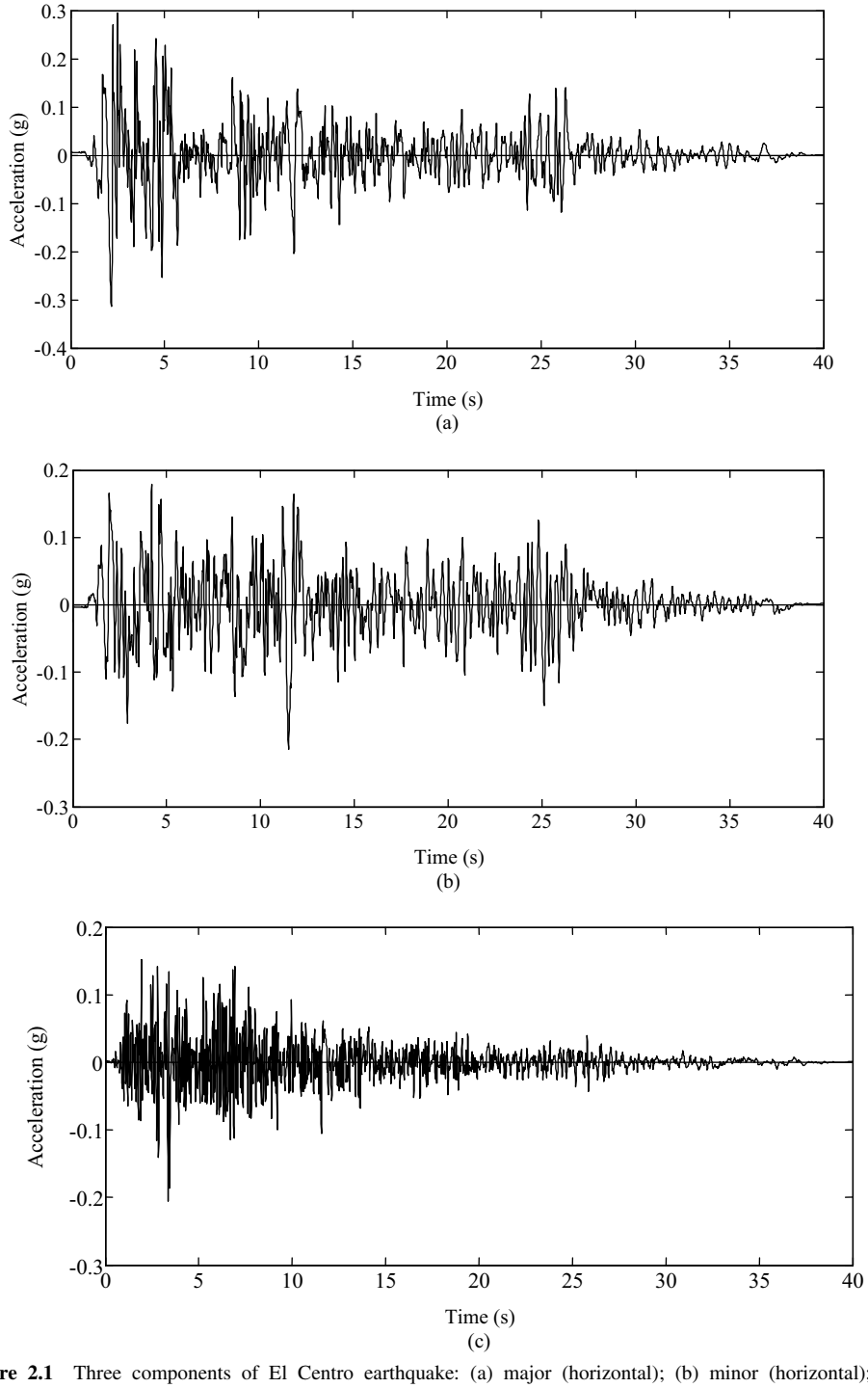

Figure 2.1 Three components of El Centro earthquake: (a) major (horizontal); (b) minor (horizontal); and (c) minor (vertical)

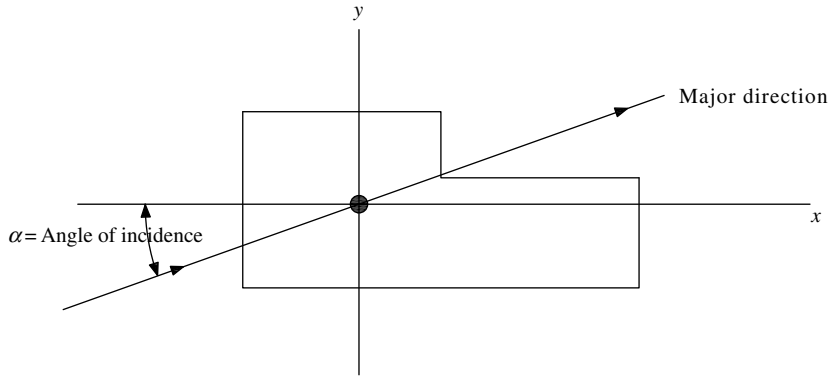

Figure 2.2 Angle of incidence of earthquake

a_n and b_n are the cosine and sine function amplitudes corresponding to the nth frequency
a_0 is the amplitude corresponding to zero frequency, respectively.

The amplitudes a_0, a_n, and b_n are given by:

$$a_0 = \frac{1}{T}\int_{-T/2}^{T/2} x(t)\mathrm{d}t \tag{2.4}$$

$$a_n = \frac{2}{T}\int_{-T/2}^{T/2} x(t)\cos\omega_n t\mathrm{d}t \tag{2.5}$$

$$b_n = \frac{2}{T}\int_{-T/2}^{T/2} x(t)\sin\omega_n t\mathrm{d}t \tag{2.6}$$

$$\omega_n = \frac{2\pi n}{T} \tag{2.7}$$

where

T is the duration of the ground motion.

The Fourier amplitude gives the amplitude of the harmonic at frequency ω_n and is given by:

$$A_n^2 = \left[\frac{2}{T}\int_{-T/2}^{T/2} x(t)\cos\omega_n t\mathrm{d}t\right]^2 + \left[\frac{2}{T}\int_{-T/2}^{T/2} x(t)\sin\omega_n t\mathrm{d}t\right]^2 \tag{2.8}$$

Equation 2.3 can also be represented in the form

$$x(t) = c_0 + \sum_{n=1}^{\alpha} c_n \sin(\omega_n t + \phi_n) \tag{2.9}$$

in which c_n is the same as A_n; $c_0 = a_0$; and ϕ_n is given by:

$$\phi_n = \tan^{-1}\left(\frac{b_n}{a_n}\right) \tag{2.10}$$

The plot of c_n versus frequency ω_n is called the Fourier amplitude spectrum and that of ϕ_n versus ω_n is the Fourier phase spectrum.

To obtain the Fourier amplitude spectrum of a time history of ground motion, integrations given by Equations 2.4–2.6 need to be performed. As $x(t)$ is an irregular function of time, the integration is carried out by a numerical technique. This operation is now performed very efficiently by discrete Fourier transformation (DFT), which is programmed as FFT and available in most mathematical software. In FFT, the Fourier synthesis of a time history record is mathematically treated as a pair of Fourier integrals in the complex domain (that is, with the help of a complex harmonic function) as given below [1].

$$x(i\omega) = \frac{1}{2\pi}\int_{-\alpha}^{\alpha} x(t)\mathrm{e}^{-i\omega t}\mathrm{d}t \tag{2.11}$$

$$x(t) = \int_{-\alpha}^{\alpha} x(i\omega)\mathrm{e}^{i\omega t}\mathrm{d}\omega \tag{2.12}$$

The first integral provides frequency contents of the time history in a complex form, while the second one provides the time history back, given the complex frequency contents. The second one is performed using IFFT (inverse Fourier transform).

The standard input for FFT is the time history of ground motion sampled at a discrete time interval. If N is the number of discrete ordinates of the time history at an interval of time Δt given as the input to FFT, then N numbers of complex quantities are obtained as the output. The first $N/2$ complex quantities provide frequency contents of the time history with amplitude at frequency ω_j as:

$$A_j = (a_j^2 + b_j^2)^{\frac{1}{2}} \qquad j = 0, \ldots, \frac{N}{2} \tag{2.13}$$

where a_j and b_j are the real and imaginary parts of the jth complex quantity, respectively; the phase ϕ_j is given as:

$$\phi_j = \tan^{-1}\left(\frac{b_j}{a_j}\right) \tag{2.14}$$

The frequency is $\omega_j = 2\pi j/T$, where T is the length of the time history. $\omega_n = N\pi/T$, is called the Nyquist frequency, the frequency after which complex conjugates of the first $N/2$ complex quantities are repeated. Using MATLAB®, the FFT and IFFT of a discretized time history record of ground motion may be Fourier synthesized.

A Fourier amplitude spectrum provides a good understanding of the characteristics of the ground motion. Further, as the seismic input, both amplitude and phase spectra are required for the frequency domain analysis of structures. A better input for the frequency domain analysis is the real and imaginary components of frequency contents obtained by the FFT analysis. Fourier amplitude spectra for two earthquake records are shown in Figure 2.3(a and b). It is seen from the figure that the amplitude spectrum could be narrow or broad. The narrow spectrum (Figure 2.3a) shows the predominance of a certain frequency in the ground motion record, which can even produce a smooth, almost sinusoidal time history. A broad spectrum corresponds to a motion that contains a variety of frequencies leading to a very irregular time history. A narrow-band spectrum is typical of free field ground motion for very soft soil, while a broad-band spectrum is generally characteristic of a hard soil. Fourier spectrum for ground motion at the rock bed resembles that of white noise (which has ideally the same frequency contents at all frequencies).

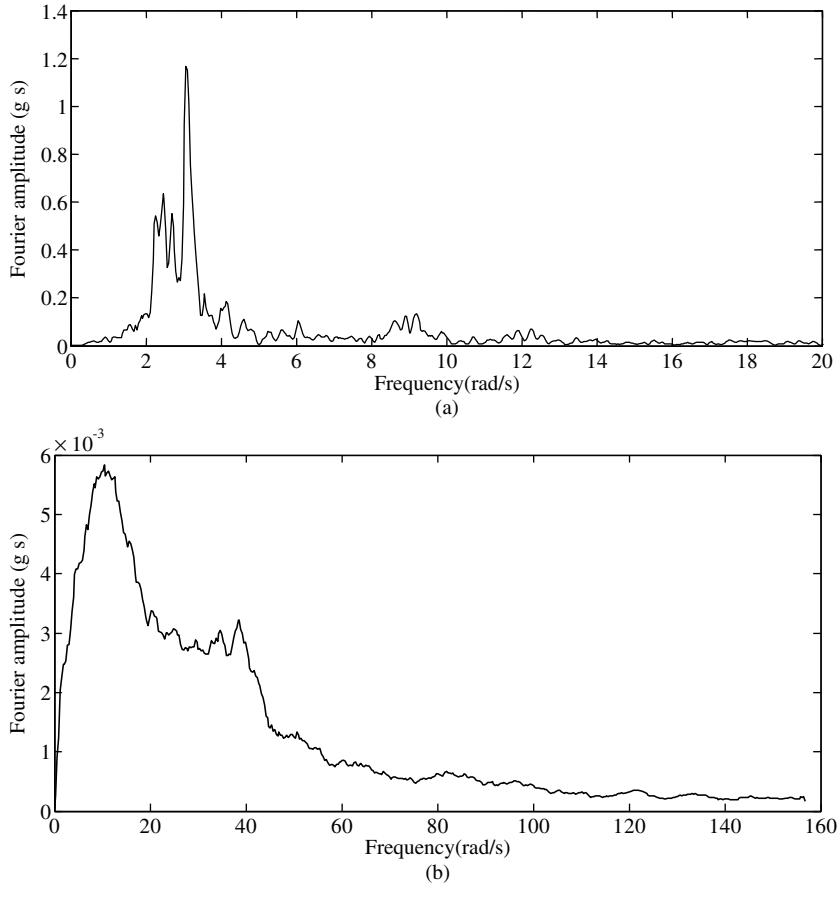

Figure 2.3 Fourier amplitude spectrum: (a) narrow band; and (b) broad band

In order to understand the general nature of the amplitude spectra of ground acceleration, they have been constructed from several earthquake ground motions and smoothed and plotted on a logarithmic scale, as shown in Figure 2.4. It is observed that the Fourier acceleration amplitudes tend to be largest over an intermediate range of frequencies bounded by the corner frequency f_c on the lower side and the cut-off frequency on the higher side. From observations of earthquake data, it is seen that f_c is inversely proportional to the size of the earthquake [2].

Example 2.1

A small segment of the time history of ground acceleration sampled at an interval of $\Delta t = 0.02$ s is given below. With the help of diagrams, represent (i) the set of data for the use in FFT; (ii) the output data from FFT; and (iii) the input data for IFFT. Also, obtain the Nyquist frequency, amplitude spectrum, and phase spectrum. Note that such a small segment of the time history is used only for illustrative purpose.

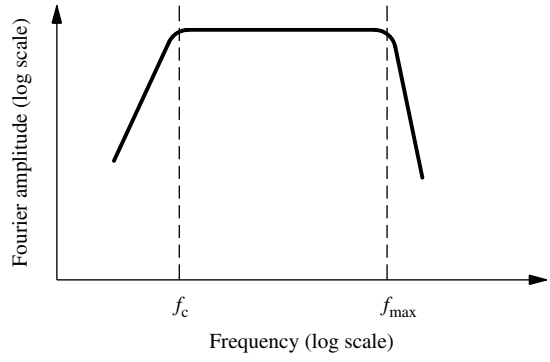

Figure 2.4 Smooth Fourier amplitude spectrum in log scale

Solution:

(i) Figure 2.5 shows the 32 sampled values of the time history of ground acceleration, which are given as input to the FFT program in MATLAB as

$$\mathrm{YY} = \frac{1}{16}\,\mathrm{fft}(\mathrm{y}, 32)$$

in which y is the sampled values of the time history; YY is the output and is of the form $a + ib$ (a real part; b imaginary part).

(ii) Figure 2.6a shows the real parts of the output. Note that it is symmetrical about point A. The last ordinate of the symmetrical half is absent. This is because it is assumed that the sampled values

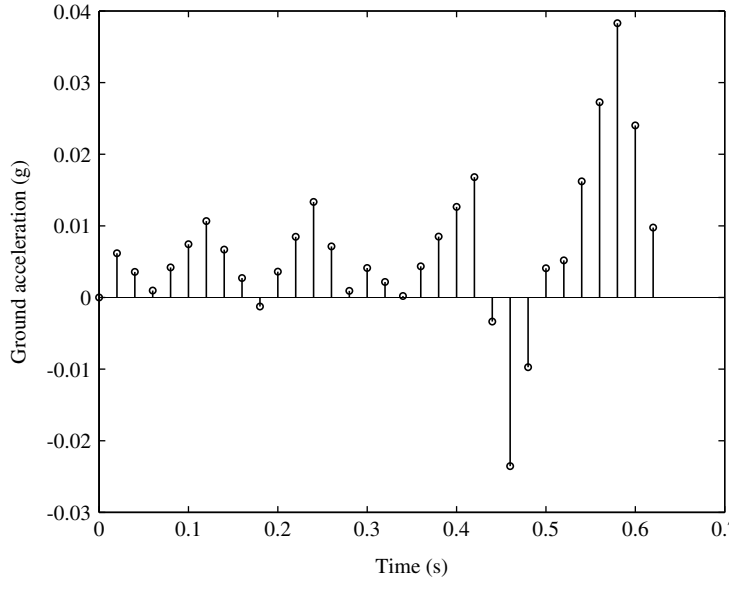

Figure 2.5 Discrete values of time history sampled at 0.02 s

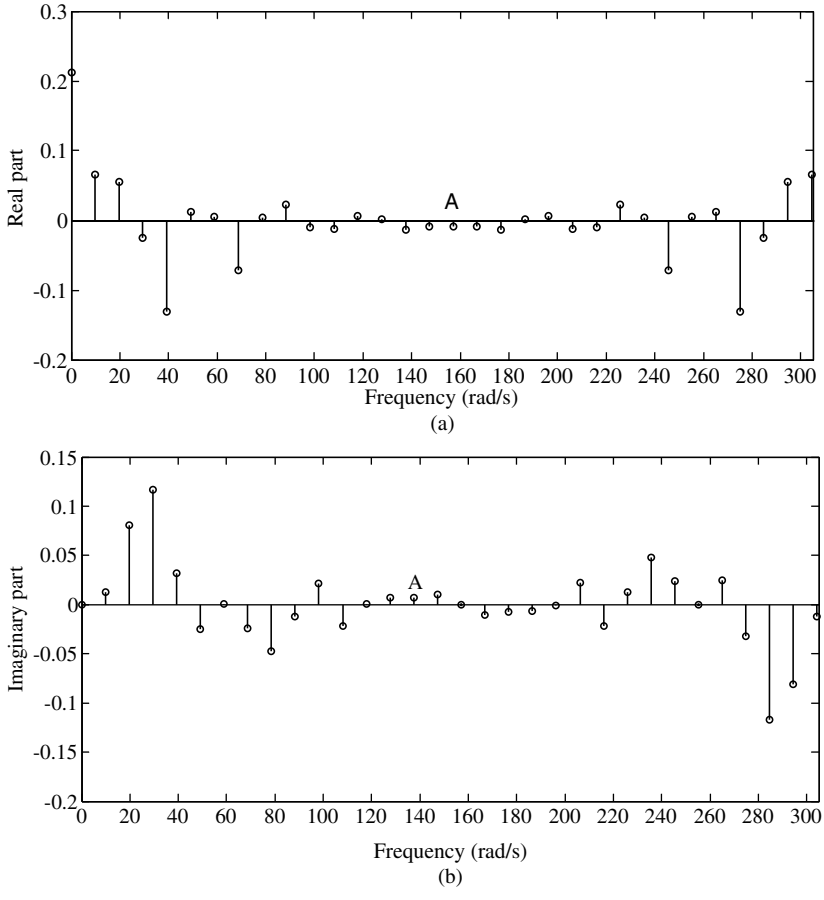

Figure 2.6 Outputs from the FFT: (a) real part; and (b) imaginary part

repeat after N (=32) values. Figure 2.6b shows the imaginary part of the output. Note that it is anti-symmetric about point A. This shows that right half of the FFT of the input data is the complex conjugate of the left half.

(iii) The real and imaginary parts of the output are combined together in the form of complex numbers $a + ib$. There will be 32 such data points. The right half of the data is a complex conjugate of the left half as stated before. These data points constitute the input for IFFT. The output from the IFFT is the same 32 sampled values of the time history shown in Figure 2.5. Note that unless input to IFFT is data which constitutes complex conjugate data pairs as described above, the output from IFFT will not be real numbers. This lesson is important and is used in frequency domain seismic analysis of structures using FFT.

$$\text{Nyquist frequency } (\omega_n) = \frac{N\pi}{T} = \frac{32\pi}{(31 \times 0.02)} = 335.04 \text{ rad s}^{-1}$$

$$\mathrm{d}\omega = \frac{2\pi}{T} = 20.94 \text{ rad s}^{-1}$$

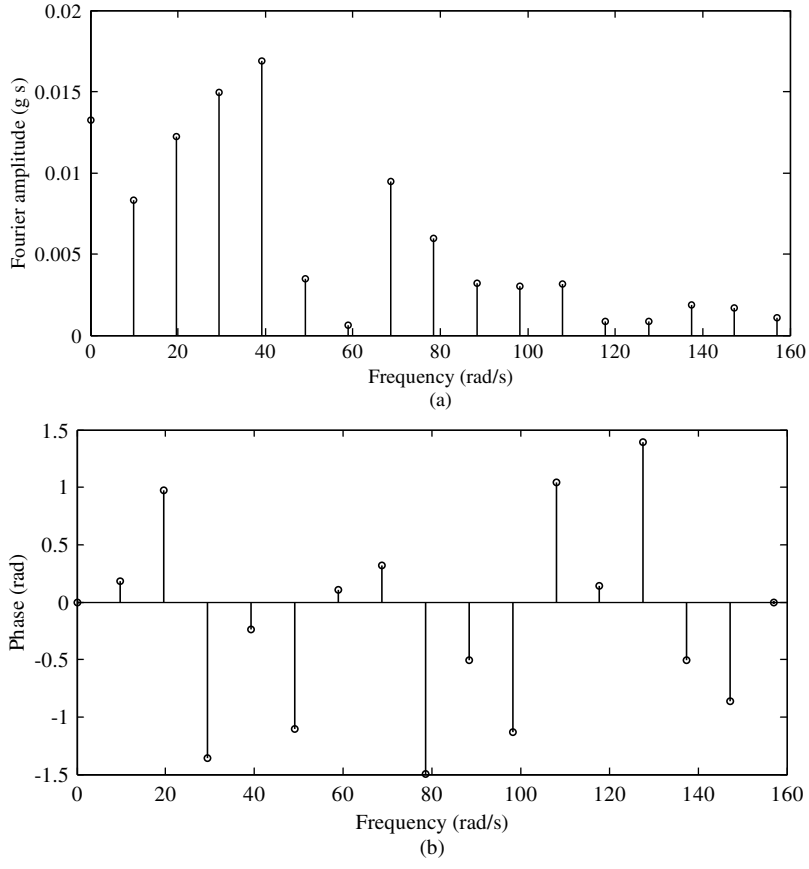

Figure 2.7 Fourier spectra: (a) amplitude spectrum; and (b) phase spectrum

The Fourier amplitude spectrum is the plot of $(a_i^2 + b_i^2)^{1/2}$ $i = 0 \ldots, N/2$ versus $\omega_i (0 - \mathrm{d}\omega - \omega_n)$. In order to get a_i and b_i, the outputs from the FFT of MATLAB are divided by $N/2$. The plot is shown in Figure 2.7a. The phase spectrum is the plot of $\tan^{-1}(b_i/a_i)$ versus ω_i and is shown in Figure 2.7b.

2.4 Power Spectral Density Function of Ground Motion

Frequency contents of ground motion can also be represented by a power spectrum or power spectral density function. The difference between the frequency contents represented by a power spectrum and the Fourier amplitude spectrum is that the former is used to provide a probabilistic estimate of the frequency contents of ground motions at a site, which are unknown. On the other hand, a Fourier amplitude spectrum provides the frequency contents of the actual ground motion at a site (unless any empirical formula is used for predicting the same, where no earthquake data are available).

As future earthquakes are not known, it is reasonable to use a probabilistic model of seismic inputs. The most common way of describing the seismic inputs probabilistically is by means of specifying an expected mean square value or peak value of ground acceleration for future earthquakes at a site. However, for analyzing structures using the methods of probabilistic dynamics, a more popular seismic input is the power spectral density function of ground acceleration, which is defined as the distribution of its mean

square value with frequency. For the purpose of describing the power spectral density function, future earthquakes are assumed as a stationary random process.

How the power spectral density function (PSDF) of a stationary random process is derived requires the knowledge of the theory of stochastic processes or random vibration and is dealt with in a number of textbooks on the subject [1, 3]. Under the assumption of ergodicity, which means that any sample time history of the stochastic process represents the second order statistics of the process, it is possible to derive the PSDF of the process using the concept of Fourier series expansion. For many practical solutions, a stationary stochastic process is also assumed to be ergodic. A brief description of the stationary stochastic process, its PSDF, and other related concepts are given in Chapter 4.

The mean square value of a ground motion time history of duration T is given by:

$$\lambda = \frac{1}{T}\int_0^T [a(t)]^2 \, \mathrm{d}t \tag{2.15}$$

Using Parseval's theorem, λ can also be written as

$$\lambda = \frac{1}{2}\sum_0^{N/2} c_n^2 \tag{2.16}$$

where

c_n is the absolute value of the complex quantity (Equation 2.9) at a frequency ω obtained from the FFT.

The power spectral density function (PSDF) $S(\omega)$ is defined such that

$$\lambda = \int_0^{\omega_{N/2}} S(\omega)\, \mathrm{d}\omega = \sum_{n=0}^{N/2} g_n(\omega) \tag{2.17}$$

Comparing Equations 2.16 and 2.17, it is seen that

$$S(\omega) = \frac{c_n^2}{2\mathrm{d}\omega} \tag{2.18}$$

in which $g(\omega) = S(\omega)\mathrm{d}\omega$ and the integration is converted into a summation of discrete ordinates.

A close relationship between the power spectrum and Fourier amplitude spectrum is evident from Equation 2.18 for an ergodic process. From Equation 2.17, the power spectral density function of a stationary stochastic process can be defined as the distribution of its mean square value (which is unique and time invariant) with frequency. A typical PSDF of ground acceleration is shown in Figure 2.8. Some of the important parameters, which are used to characterize the ground motion, are related to the moments of the PSDF. The nth moment of the PSDF is given by:

$$\lambda_n = \int_0^{\omega_c} \omega^n S(\omega)\, \mathrm{d}\omega \tag{2.19a}$$

in which ω_c is the cut-off frequency of the PSDF, that is, the frequency at which the tail end of the PSDF is truncated. λ_0 is the mean square value of the ground acceleration. A parameter known as the central frequency Ω is given by:

$$\Omega = \sqrt{\frac{\lambda_2}{\lambda_0}} \tag{2.19b}$$

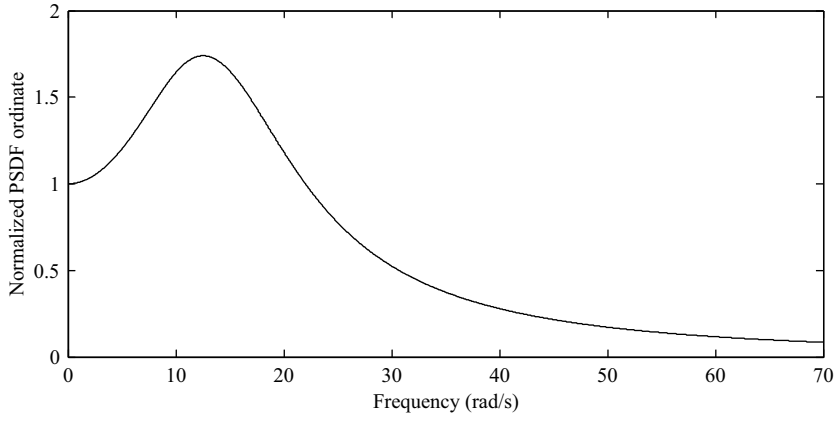

Figure 2.8 Power spectral density function of ground acceleration

in which Ω is a measure of the frequency where the PSDF is concentrated. Using Ω, λ_0, and the duration T_d of the earthquake, the mean peak ground acceleration (PGA) may be obtained as:

$$\ddot{u}_{gmax} = \sqrt{2\lambda_0 \ln\left(\frac{2.8\Omega T_d}{2\pi}\right)} \tag{2.19c}$$

The source of the above expression is discussed in Chapter 5. A related parameter that characterizes the frequency content of ground acceleration is the predominant period or frequency. It is defined as the time period where the Fourier spectrum peaks or the frequency where the PSDF peaks.

To obtain the response of multi-supported structures that have various types of excitations at different supports, the PSDFs of excitations are not sufficient to analyze the structure. An additional input is necessary, which is referred to as the lack of correlation between any two excitations. This lack of correlation is represented by a cross correlation function or cross power spectral density function. The latter is used in frequency domain analysis. The cross power spectral density function for any two excitations x_1 and x_2 (assumed as stationary stochastic processes) is expressed as:

$$S_{x_1x_2} = S_{x_1}^{\frac{1}{2}} S_{x_2}^{\frac{1}{2}} coh(x_1, x_2, \omega) \tag{2.20}$$

where

$S_{x_1}(\omega)$ and $S_{x_2}(\omega)$ are the PSDFs of excitations x_1 and x_2
$coh(x_1, x_2, \omega)$ is the coherence function which denotes the lack of correlation between x_1 and x_2 in the frequency domain.

For a homogeneous field of excitation with a single train of a traveling earthquake wave, the PSDFs of ground acceleration at different supports are the same but there is a lack of correlation between the excitation at any two supports because of the time lag. Under such conditions, the cross power spectral density function between two excitations is given by:

$$S_{x_1x_2} = S_{x_1}^{\frac{1}{2}} S_{x_2}^{\frac{1}{2}} coh(x_1, x_2, \omega) = S_x coh(x_1, x_2, \omega) \tag{2.21}$$

in which $S_x(\omega)$ is the PSDF of the traveling train of ground acceleration. More discussions on cross power spectral density functions are presented in Chapter 4.

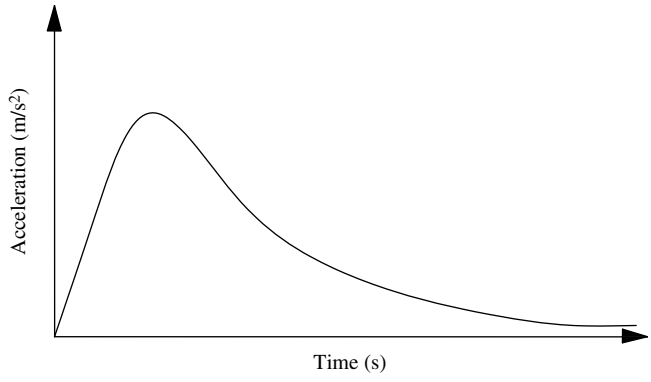

Figure 2.9 Variation of rms value of acceleration with time for uniformly modulated non-stationary process

Records of actual strong motion time history show that modeling of an earthquake process as a stationary random process is not well justified as the ensemble mean square value varies with time. The mean square value gradually increases to a peak value, remains uniform over some time, and then decreases as shown in Figure 2.9. Such type of behavior is often modeled as a uniformly modulated non-stationary process [3]. Such a process is represented by an evolutionary power spectral density function. The evolutionary spectrum is obtained by multiplying a constant spectrum with a modulating function of time t and is given as:

$$S(\omega, t) = \left|q(t)\right|^2 S(\omega) \tag{2.22}$$

From the analysis of collections of earthquake records, various forms of the power spectral density functions, modulating functions, and coherence functions have been presented by different investigators. They are presented in Sections 2.7.5 and 2.7.6.

Example 2.2

Assuming the short segment of the time history for the problem in Example 2.1 to represent an ergodic process, obtain its PSDF.

Solution: Using Equations 2.9, 2.16 and 2.18, c_n^2 is given by

$$c_n^2 = (a_n^2 + b_n^2) \qquad n = 0, \cdots, \frac{N}{2}$$

$$S(\omega)_n = \frac{1}{2\mathrm{d}\omega} c_n^2 \qquad n = 0, \cdots, \frac{N}{2}$$

Values of c_n^2 are obtained by squaring the ordinates of the Fourier spectrum given in Figure 2.7a. The plots of $S(\omega)$ versus ω (PSDF) are shown in Figures 2.10 and 2.11. Note that the width of the bar shown in Figure 2.10 becomes smaller for larger values of T.

The spectrum shown in Figure 2.10 is highly irregular. Generally, such irregular spectrums are smoothed by a spectral smoothing technique. Here, a five-point smoothing procedure is adopted to obtain the spectrum shown in Figure 2.11. For smoothing, the ordinate at a point is taken as the average of five ordinates (average of the ordinate of the point and two ordinates on either side of the point). Ordinates at the beginning and points towards the end are averaged over a fewer number of points. For example, the 1st ordinate is averaged over 1st, 2nd, and 3rd ordinates; the 2nd ordinate is averaged over the 1st, 2nd, 3rd, and 4th ordinates; the 16th ordinate is averaged over the 17th, 16th, 15th, and 14th ordinates, and so on. For

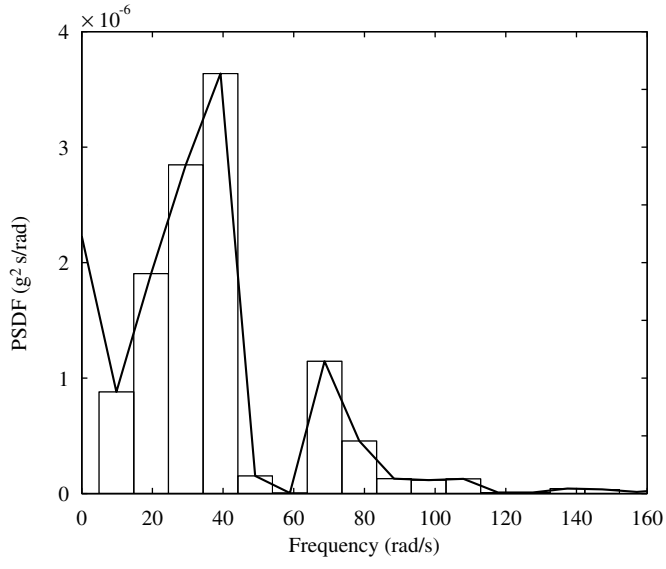

Figure 2.10 Raw PSDF of the time history of acceleration

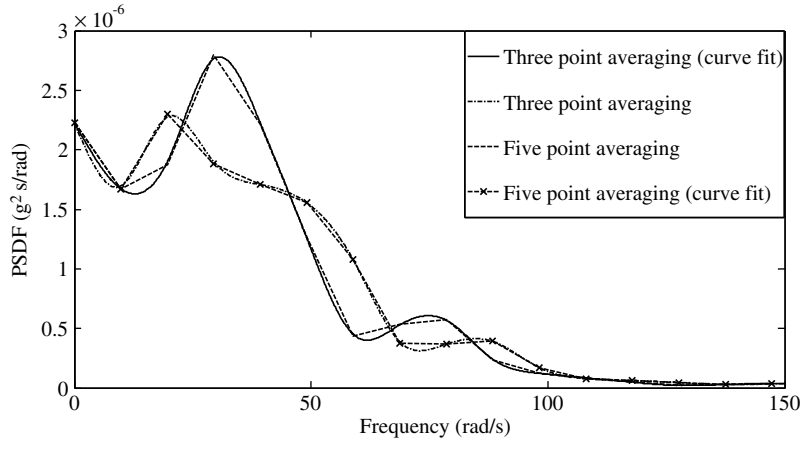

Figure 2.11 Smooth PSDF

a large number of ordinates, higher point averaging is possible. The resulting PSDF becomes smoother. If necessary, a best-fit polynomial can be drawn as shown in Figure 2.11 to obtain a very smooth spectrum. For this problem:

$$\text{Sum of the areas of the bars} = 0.011\ (\text{m s}^{-2})^2$$

$$\text{Area under the smoothed PSDF} = 0.0113\ (\text{m s}^{-2})^2$$

$$\text{Area under the best fit polynomial curves} = 0.0112\ (\text{m s}^{-2})^2$$

$$\text{Mean square value of time history record} = 0.012\ (\text{m s}^{-2})^2$$

2.5 Response Spectrum of Earthquake

A third type of spectrum, which is used as seismic input is the response spectrum of an earthquake. In fact, the response spectrum of an earthquake is the most favored seismic input for earthquake engineers. There are a number of response spectra that are defined for representing the ground motion, such as, displacement response spectrum, pseudo velocity response spectrum, absolute acceleration response spectrum, and energy spectrum. These spectra also show the frequency contents of the ground motion, but not as directly as the Fourier spectrum does. The absolute acceleration response spectrum is commonly used as an input for the response spectrum methods of analysis of structures discussed in Chapter 5.

2.5.1 Displacement, Velocity, and Acceleration Spectra

Derivation of the displacement response spectrum forms the basis for deriving other spectra. By definition, a displacement response spectrum is the plot of maximum displacement of a single degree of freedom system (SDOF) to a particular ground motion as a function of the natural frequency and damping ratio of the SDOF.

The relative displacement of an SDOF system with respect to its base at any instant of time t for a ground acceleration $\ddot{x}_g(t)$ with the initial conditions $x(0) = \dot{x}(0) = 0$ is given by (details are given in the next chapter):

$$x(t) = -\frac{1}{\omega_n}\int_0^t \ddot{x}_g(\tau)e^{-\xi\omega_n(t-\tau)}\sin\omega_d(t-\tau)d\tau \tag{2.23}$$

The maximum value of $x(t)$ may be expressed as:

$$x_m = S_d = \frac{S_v}{\omega_n} \tag{2.24a}$$

in which S_v is given by

$$S_v = \left[\int_0^t \ddot{x}_g(\tau)e^{-\xi\omega_n(t-\tau)}\sin\omega_d(t-\tau)d\tau\right]_{max} \tag{2.24b}$$

At the maximum value of displacement, the kinetic energy $KE = 0$. Thus, the total energy of the system is

$$E = \frac{1}{2}kS_d^2 \tag{2.25a}$$

If this energy were expressed in the form of KE, then the equivalent velocity of the system would be equal to

$$\frac{1}{2}m\dot{x}_{eq}^2 = \frac{1}{2}kS_d^2 \tag{2.25b}$$

which gives

$$\dot{x}_{\text{eq}} = \omega_n S_{\text{d}} \tag{2.25c}$$

Comparing Equations 2.24a and 2.25b, it is seen that $\dot{x}_{\text{eq}} = S_{\text{v}}$. In earthquake literature, this velocity is known as the spectral pseudo velocity and is different from the actual maximum velocity of the system.

For any given earthquake, plots of S_{d} and S_{v} for a full range of SDOF frequencies with a specified damping ratio are called the displacement response spectrum and pseudo velocity response spectrum, respectively. A closely related measure of the SDOF response to ground motion is the spectral acceleration (also called pseudo acceleration) defined as:

$$S_{\text{a}} = \omega_n^2 S_{\text{d}} \tag{2.26}$$

A plot of S_{a} for the full range of SDOF frequencies with a specified damping ratio is called the acceleration response spectrum and is widely used for obtaining the maximum earthquake force induced in structures. For an SDOF system, the maximum force developed in the SDOF spring is given by:

$$(f_{\text{s}})_{\max} = kS_{\text{d}} = m\omega_n^2 S_{\text{d}} = mS_{\text{a}} \tag{2.27}$$

Equation 2.27 shows that spectral acceleration multiplied by the mass of the SDOF gives the maximum earthquake force induced in the system by the earthquake. Because of this reason, spectral acceleration has been defined in a way as shown by Equation 2.26 and is different to the maximum acceleration of the SDOF system. While a displacement response spectrum is a plot of the maximum displacement of the SDOF system as a function of frequency, pseudo acceleration and pseudo velocity spectra are not the plots of maximum acceleration and maximum velocity as a function of the SDOF frequency.

These three spectra, as shown in Figures 2.12(a–c), provide directly some physically meaningful quantities. The displacement spectrum is directly related to the peak deformation of the SDOF system. The pseudo velocity spectrum is directly related to the peak strain energy stored in the system during an earthquake, Equation 2.25a. The pseudo acceleration spectrum is related directly to a peak value of the earthquake force in the system, Equation 2.27.

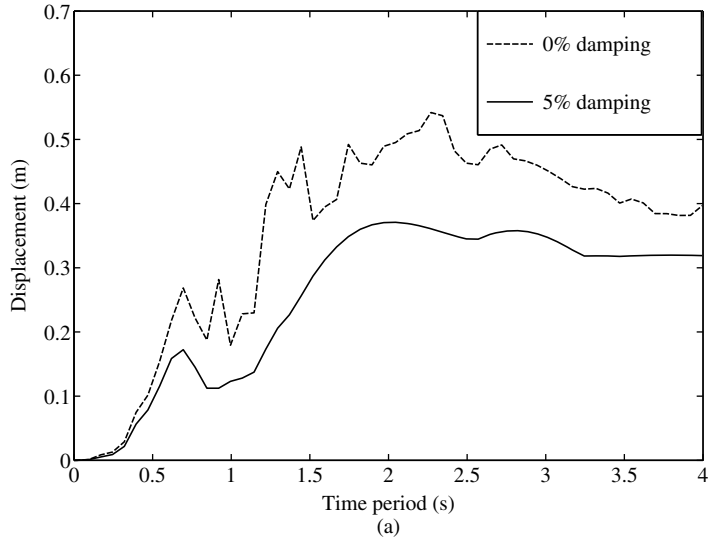

(a)

Figure 2.12 Response spectra of an earthquake: (a) displacement spectrum; (b) pseudo velocity spectrum; and (c) pseudo acceleration spectrum

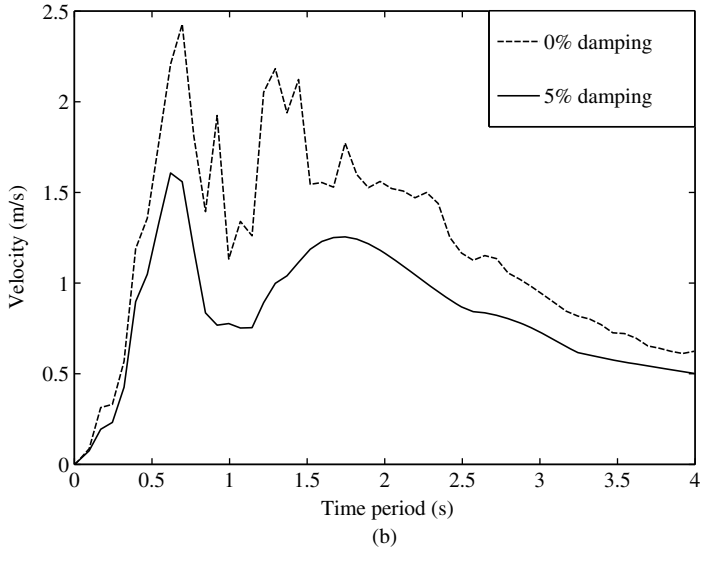

(b)

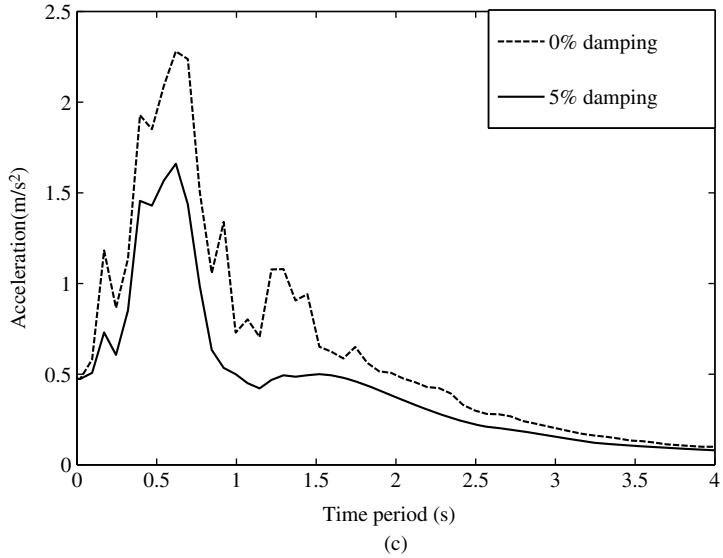

(c)

Figure 2.12 (*Continued*)

2.5.2 *Energy Spectrum and Fourier Spectrum*

Another way of characterizing the ground motion is to obtain the maximum energy response spectrum. The quantity $\left[\sqrt{\frac{2E(t)}{m}}\right]_{\max}$ plotted against a full range of the frequency (or the period) of the SDOF system with a specified value of the damping ratio is called the maximum energy response spectrum. The

energy $E(t)$ at any instant of time t of the SDOF system is given by:

$$E(t) = \frac{1}{2}m\dot{x}(t)^2 + \frac{1}{2}kx(t)^2 \tag{2.28}$$

The quantity $\left[\sqrt{\frac{2E(t)}{m}}\right]$ is then given by;

$$\left[\sqrt{\frac{2E(t)}{m}}\right] = \left\{\dot{x}(t)^2 + [\omega_n x(t)]^2\right\}^{\frac{1}{2}} \tag{2.29}$$

The maximum value of the quantity may be obtained for each frequency (or period) of the SDOF system for a specified damping.

For $\xi = 0$, it may easily be shown from Equations 2.29 and 2.23 that

$$\sqrt{\frac{2E(t)}{m}} = \left\{\left[\int_0^t \ddot{x}_g(\tau)\cos\omega_n\tau \mathrm{d}\tau\right]^2 + \left[\int_0^t \ddot{x}_g(\tau)\sin\omega_\mathrm{d}\tau \mathrm{d}\tau\right]^2\right\}^{\frac{1}{2}} \tag{2.30}$$

Comparing Equations 2.8 and 2.30, the Fourier amplitude spectrum and energy response spectrum have similar forms. Note that $x(t)$ in Equation 2.8 could be any of the ground motion quantities, namely, $x_\mathrm{g}(t)$, $\dot{x}_\mathrm{g}(t)$, and $\ddot{x}_\mathrm{g}(t)$. The Fourier amplitude spectrum may be viewed as a measure of the total energy of an undamped SDOF system at the end of time t (that is, $t = T$). Generally, the maximum energy spectrum is greater than the Fourier amplitude spectrum as the maximum energy is achieved at some time before the end of the earthquake.

Example 2.3

Compare the maximum energy spectrum, smoothed Fourier spectrum, and pseudo acceleration spectrum (for $\boldsymbol{\xi} = 0.05$) for the El Centro ground acceleration record. Also, compare the time periods corresponding to the maximum values of the spectral ordinates of the three spectra.

Solution: The energy spectrum, Fourier spectrum, and pseudo acceleration spectrum for the El Centro earthquake record are shown in Figures 2.13–2.15. These spectra were obtained using Equations 2.20–2.22, 2.29 and 2.13. Using MATLAB, simple programs can be written to obtain these spectra. Alternatively, Seismo signal (www.seismosoft.com) can be used to directly obtain the Fourier spectrum and the pseudo acceleration spectrum. The energy spectrum can be obtained using Equation 2.29 and the results of the seismo signal.

$$T_\mathrm{peak}(\text{energy spectrum})\ \text{ first peak} = 0.55\ \text{s};\ \text{second peak} = 0.95\ \text{s}$$

$$T_\mathrm{peak}(\text{Fourier spectrum}) = 0.58\ \text{s}$$

$$T_\mathrm{peak}(\text{pseudo acceleration spectrum}) = 0.51\ \text{s}$$

It is seen that the peaks of the spectra occur almost at the same period. This shows that the frequency or the time period where the maximum energy of the earthquake is confined can be realized from any of the above spectra.

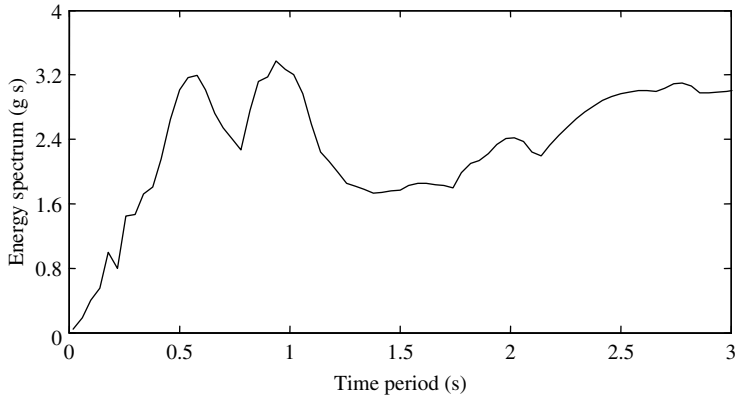

Figure 2.13 Energy spectrum of El Centro earthquake

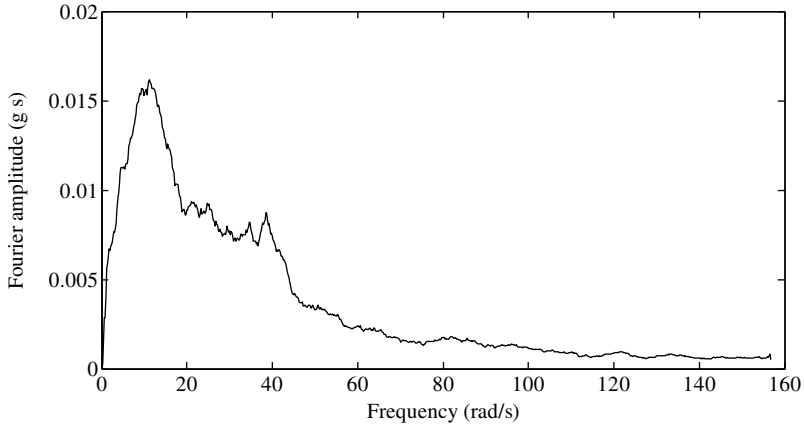

Figure 2.14 Fourier amplitude spectrum of El Centro earthquake

2.5.3 Combined D-V-A Spectrum

Each of the three spectra (displacement, pseudo velocity, and pseudo acceleration) in a way provides the same information on structural response. However, each one of them provides a physically meaningful quantity, as mentioned earlier. Therefore, all three spectra are useful in understanding the nature of an earthquake and earthquake resistant design. More importantly, all three spectra are skillfully used in defining or constructing the design response spectrum, which will be discussed later. Because of this reason, a combined plot showing all three of the spectral quantities is desirable. This integrated presentation is possible because of the relationship that exists between these three quantities.

Taking the log of Equations 2.21 and 2.26:

$$\log S_{\mathrm{d}} = \log\ S_{\mathrm{v}} - \log\ \omega_n \tag{2.31}$$

$$\log S_{\mathrm{a}} = \log S_{\mathrm{v}} + \log \omega_n \tag{2.32}$$

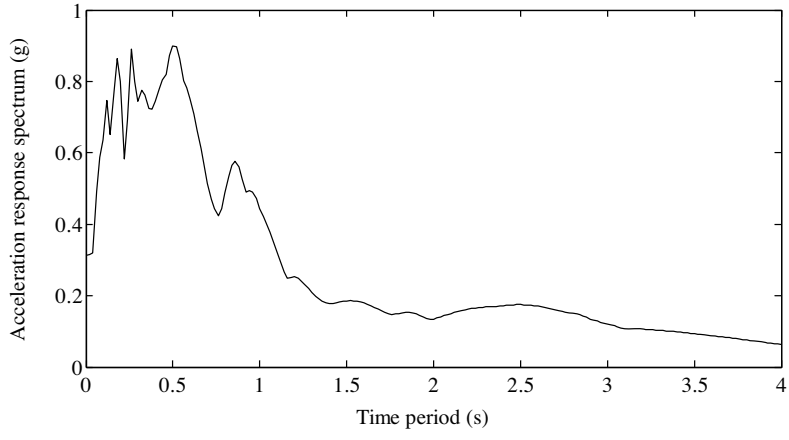

Figure 2.15 Pseudo acceleration spectrum of El Centro earthquake

From Equations 2.31 and 2.32, it is evident that a plot on logarithmic graph paper with $\log S_v$ as ordinate and $\log\omega_n$ as abscissa, the two equations are straight lines with slopes $+45°$ and $-45°$ for constant values of $\log S_d$ and $\log S_a$, respectively.

If log of time period $T(2\pi/\omega_n)$, instead of $\log\omega_n$, is considered, then these orthogonal straight lines are interchanged. Thus, a four way log plot as shown in Figure 2.16 can be used to plot all three spectra

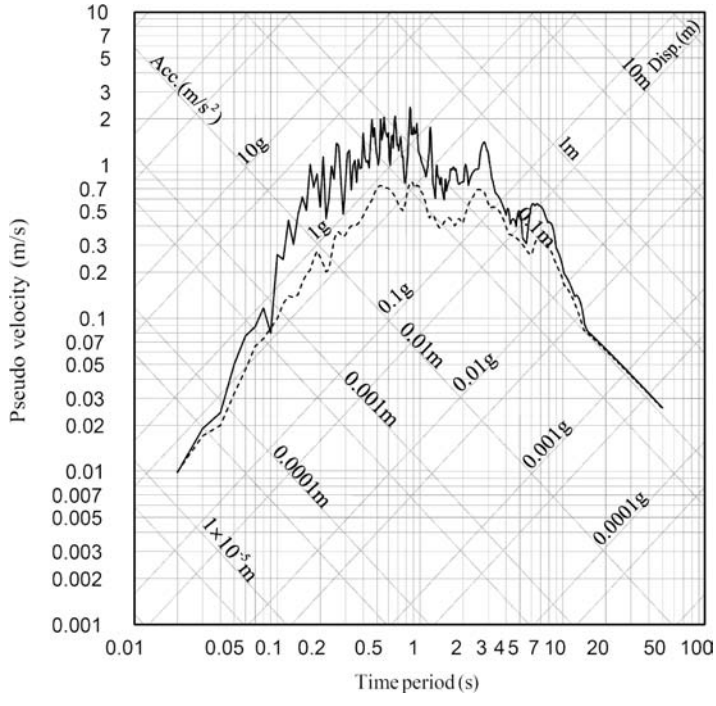

Figure 2.16 Earthquake response spectrum (displacement, pseudo velocity, and pseudo acceleration) in tripartite plot (— for 0% and ---- for 5%)

on one plot. If the data pairs of $\log S_v$ and $\log T$ are used to plot the pseudo velocity spectrum on the graph paper, then values of $\log S_a$ and $\log S_d$ for a particular value of T can be read from the same plot. For plotting the curve, some limiting conditions should be realized as values of $\log T$ as $T \to 0$ and $T \to \infty$ cannot be shown.

The following limiting conditions help in constructing the plot on the graph paper.

$$\lim_{T \to \infty} S_d = u_{g\,max} \tag{2.33}$$

$$\lim_{T \to 0} S_a = \ddot{u}_{g\,max} \tag{2.34}$$

The two limiting conditions can be understood based on physical reasoning. For a very long period system (that is, $T \to \infty$), which means a very flexible system, the mass would be expected to remain stationary while the ground below moves, thus, $u(t) \approx -u_g(t)$ and $S_d = u_{g\,max}$. For a very short period structure, the mass moves rigidly with the support, and its peak acceleration will be the same as that of the support. Thus,

$$\ddot{u}^t \approx \ddot{u}_g;\ \left|\ddot{u}^t_{max}\right| = \left|\ddot{u}_{g\,max}\right|$$

As $\left|\ddot{u}^t_{max}\right| = \omega^2 S_d$ (Chapter 3), $S_a = \ddot{u}_{g\,max}$.

Figure 2.17 shows the response spectrum for 5% damping for the El Centro earthquake. Furthermore, the response spectrum has been idealized by a series of straight lines. It is seen from the figure that straight lines below point "a" and that between points "b" and "c" are parallel to the $S_d/u_{g\,max}$ axis. The line below

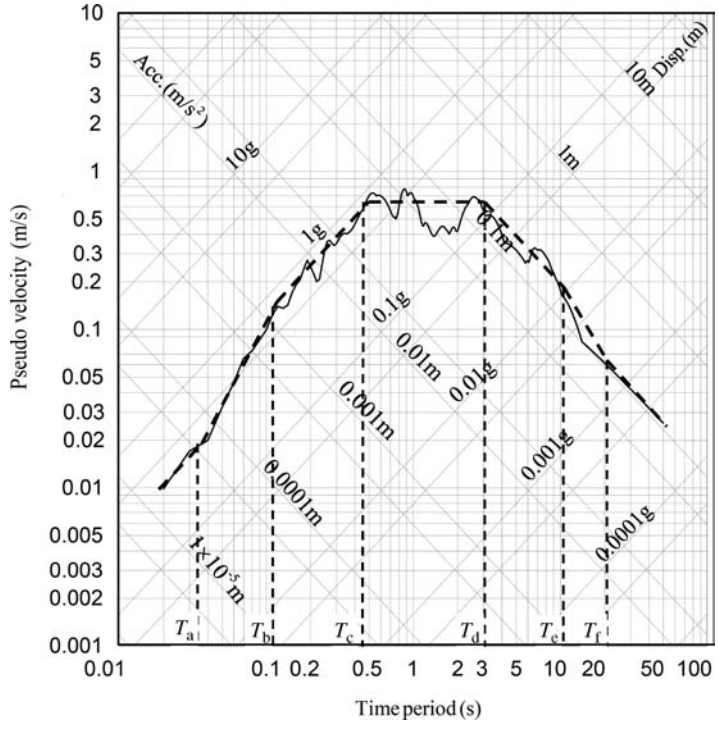

Figure 2.17 Idealized response spectrum by a series of straight lines for El Centro earthquake

point "a" shows constant S_a equal to $\ddot{u}_{gmax}$. Line between points "b" and "c" similarly show constant acceleration, which is equal to a constant factor multiplied by $\ddot{u}_{gmax}$.

Thus, the portion of the response spectrum to the left of point "c" is most directly related to the maximum ground acceleration. Similarly, the portion of response spectrum to the right of "d" is most directly related to the maximum ground displacement. The intermediate portion (c–d) is most related to the maximum velocity of the ground motion. Response spectra drawn for different earthquakes show similar trends of idealization; the points a, b, c, d, e, f and the corresponding periods T_a, T_b, T_c, T_d, T_e, T_f, may vary from earthquake to earthquake and with the damping ratio.

Based on these observations, it is logical to divide the spectrum into three zones, namely, a displacement sensitive region (that is, long period region), an acceleration sensitive region (that is, the short period region), and a velocity sensitive region (that is, the intermediate period region). Earthquakes recorded under similar or dissimilar conditions show the same trend in the response spectrum in these three regions. It should be noted from Figure 2.16 that the effect of the damping on the response spectrum is greatest in the velocity sensitive region, and is least in the acceleration sensitive and displacement sensitive regions.

Idealization of the spectrum by a series of straight lines is not a precise way of defining the spectrum. Such idealization or any smooth curve fitting technique to represent an idealized response spectrum may not appear to be particularly rational in representing the actual spectrum. However, it will be seen in the next section that such techniques are used to evolve the design response spectrum, which is of greater importance in the seismic design of structures than the response spectrum of one particular earthquake.

Example 2.4

Draw the response spectra of ground acceleration for the Parkfield earthquake for $\xi = 5\%$. After idealizing the curve by a series of straight lines, find T_a, T_b, T_c, T_d, T_e, and T_f,and compare them with those of the El Centro earthquake.

Solution: The Parkfield earthquake digitized acceleration record is taken from www.peer.berkley.edu/smcat. The displacement, pseudo velocity and pseudo acceleration spectra were obtained using Equations 2.23–2.26. Alternately, Seismo signal as mentioned in Example 2.3 may be used. The spectra are then drawn in the tripartite plot and idealized by a series of straight lines as shown in Figure 2.18.

The values of T_a, T_b, T_c, T_d, T_e, and T_f as obtained from the plot are compared with those of the El Centro earthquake, as shown in Table 2.1.

2.5.4 Design Response Spectrum and its Construction

The design response spectrum is different to a simple response spectrum of an earthquake. It should satisfy some of the requirements as it is intended to be used for the design of new structures or the risk evaluation of existing structures for future earthquakes, which are not known. These requirements may be stated as below:

a. The spectrum should be as smooth as possible and devoid of high irregularities, as observed in the response spectrum of an earthquake shown in Figure 2.16, for two reasons. Firstly, irregularities in the spectra of two different earthquakes could be significantly different, leading to an erroneous estimate of the spectral ordinates for future earthquakes. Secondly, for a highly irregular spectrum, spectral ordinates may drastically change for a small change in frequency. As there is always a certain amount of uncertainty in the determination of natural frequencies of structural systems, an irregular spectrum can provide a very erroneous estimate of the earthquake forces calculated for the structures. Therefore, a design spectrum in a four way log plot is expected to consist of a series of straight lines, such as that of an idealized spectrum shown in Figure 2.17.

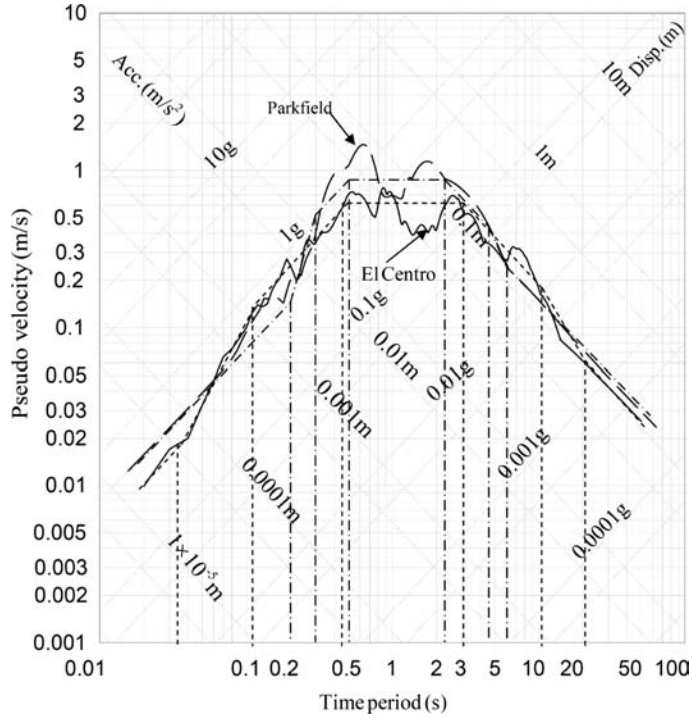

Figure 2.18 Comparison between the response spectra of Parkfield and El Centro earthquakes

Table 2.1 Comparison of periods ($T_a - T_f$) between Parkfield and El Centro earthquakes

Earthquake	T_a (s)	T_b (s)	T_c (s)	T_d (s)	T_e (s)	T_f (s)
Parkfield	0.041	0.134	0.436	4.120	12.0	32.0
El Centro	0.030	0.125	0.349	3.135	10.0	33.0

b. The design spectrum should be representative of spectra for past earthquake ground motions in the region. If there are insufficient or no earthquake records available for the region, then records of other sites under similar conditions may be used. The factors that should be considered for identifying similar conditions include the magnitude of the earthquake, distance of the site from the fault, fault mechanism, geology of the travel path of the seismic waves from the source to the site, and the local soil conditions of the site.
c. A single response spectrum may not be able to represent the variations in the spectra of all past earthquakes in the region. Therefore, two response spectra, one mean spectrum, with the other being the mean plus one standard deviation spectrum, should be considered as design spectra.
d. The design response spectrum should be a normalized response spectrum with respect to the peak ground acceleration (PGA), as the PGA may drastically vary from one place to another. Furthermore, a design response spectrum should be consistent with the specification of the level of the seismic design force, or the deformation of structures experienced during previous earthquakes.
e. Finally, the design response spectrum should be consistent with seismic design philosophy. Currently, a dual design philosophy is adopted (which will be discussed later). This requires specification of two

design spectra, one for designing and the other for safety evaluation for an extreme event. Generally, shapes of both spectra should be considered as being the same.

Following the above requirements and the observations derived from the idealized response spectrum as discussed earlier, a procedure for constructing the design response spectrum has been evolved. The procedure consists of the following steps:

1. Expected PGA values for design and maximum probable earthquakes are derived for the region using the procedure of hazard analysis discussed in the previous chapter.
2. Peak values of the ground velocity and displacement are estimated using empirical relationships valid for the region, which are given in the form of

$$\dot{u}_{\mathrm{g\,max}} = c_1 \frac{\ddot{u}_{\mathrm{g\,max}}}{g};\ u_{\mathrm{g\,max}} = c_2 \frac{\dot{u}^2_{\mathrm{g\,max}}}{\ddot{u}_{\mathrm{g\,max}}}\ [6].$$

The values of c_1 and c_2 are determined from the recorded earthquake data. Typical values of c_1 and c_2 may be taken as $c_1 = 1.22$ to $0.92\ \mathrm{m\,s^{-1}}$ and $c_2 = 6$.

3. On the four way log graph paper, plot the baseline showing $\ddot{u}_{\mathrm{g\,max}}$, $u_{\mathrm{g\,max}}$ and $\dot{u}_{\mathrm{g\,max}}$ as shown in Figure 2.19. Multiply $\ddot{u}_{\mathrm{gmax}}$, u_{gmax}, and $\dot{u}_{\mathrm{gmax}}$ by the amplification factors α_{A}, α_{D}, and α_{V}, respectively, to obtain the lines bc, de, and cd.

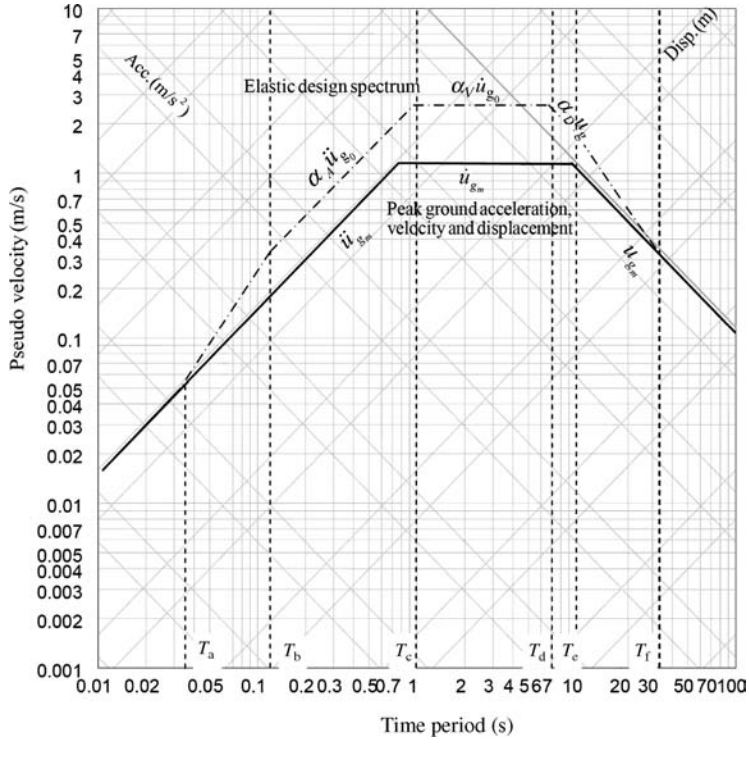

Figure 2.19 Construction of elastic design spectrum

4. Point b corresponds to frequency $f_2(= 1/T_2)$, which may be taken as $f_2 = 4f_1$ where $f_1(= 1/T_1)$, is the frequency corresponding to the intersection point (Figure 2.19). Note that intersection points c and d are fixed by the relative values of α_A, α_D, and α_V. Point a corresponds to the frequency $f_3(= 1/T_3)$, which may be taken as $f_3 = 10f_1$. Points e and f are selected corresponding to very low frequencies (large periods), and could be of the order of (1/10–1/15) and (1/30–1/35) Hz, respectively.
5. Exact values of time periods corresponding to points a, b, e, and f depend upon recorded data in the region. Similarly, values of α_A, α_D, and α_V also depend upon the recorded earthquake data. In reference [4] some representative values of α_A, α_D, and α_V for mean and mean plus one standard deviation spectra obtained from a set of large earthquake data are given. Note that the values of α_A, α_D, and α_V depend upon the damping, as expected.
6. Once the design spectrum is drawn in a four way log plot, the normalized acceleration response spectrum can be obtained in an ordinary plot. A typical plot of the normalized pseudo acceleration spectrum (derived from a log plot) as given in the codes of practice is shown in Figure 2.20. It is seen from the figure that spectral accelerations (Sa) for a soft soil profile are more compared with those of a hard soil profile at periods of more than 0.5 s. This is the case because the amplified factors α_A, α_D, and α_V substantially change with the soil conditions.

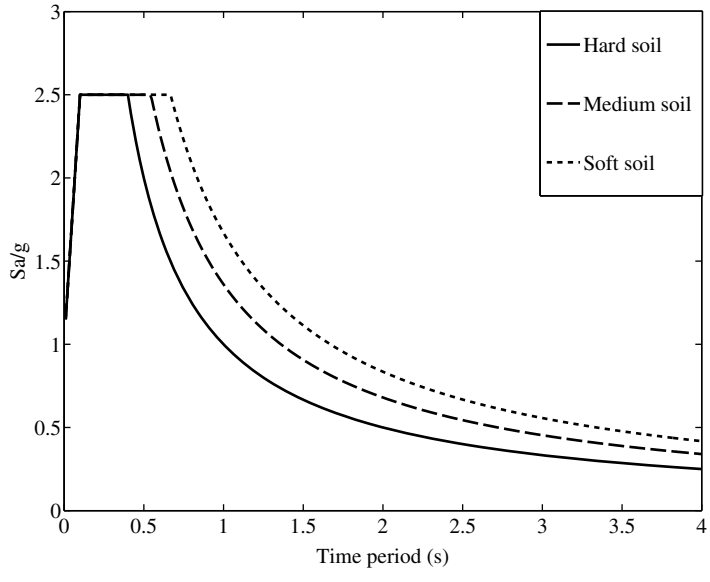

Figure 2.20 Design (pseudo acceleration) spectrum as given in IS Code

For some sites the design spectrum could be the envelope of two or more different spectra. Such sites are affected by more than one active fault. The design spectra obtained by considering the earthquake occurring from the two faults are different. Design response spectra for such a typical site are shown in Figure 2.21. The first spectrum is the one corresponding to the nearby fault producing a small size earthquake. The second spectrum corresponds to that for a far fault producing a large magnitude earthquake. The design spectrum for the site is then defined as the envelope for the two spectra, as shown in Figure 2.21.

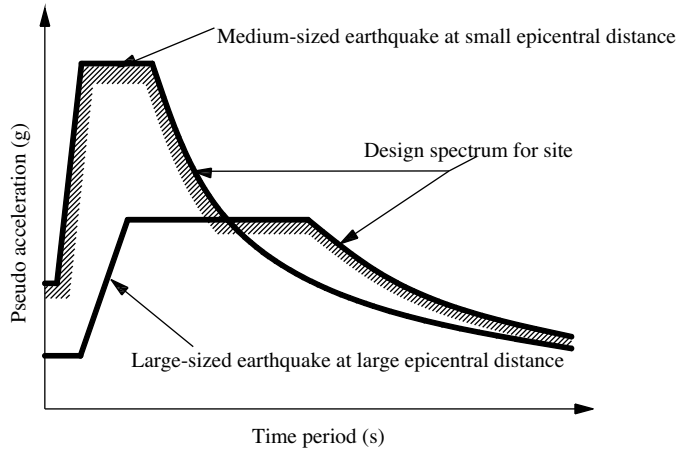

Figure 2.21 Design spectrum defined as an envelope of two design spectra

Example 2.5

Construct design response spectra for the 50th percentile and the 84.1 percentile on four way log graph paper for 5% damping for hard soil. Take $T_a = 1/33$ s, $T_b = 1/8$ s, $T_e = 1/10$ s, and $T_f = 1/33$ s; $\ddot{u}_{g\,max} = 0.6$ g.

Solution:

$$\dot{u}_{g\,max} = \frac{1.22}{g}\ddot{u}_{g\,max} = 0.732\ \text{m s}^{-1}$$

$$u_{g\,max} = \frac{(0.732)^2}{0.6g}6 = 0.546\ \text{m}$$

with these values of $u_{g\,max}$, $\dot{u}_{g\,max}$, and $\ddot{u}_{g\,max}$, and $\alpha_A = 2.12$, $\alpha_v = 1.65$ and $\alpha_D = 1.39$ for 5% damping for hard soil taken from reference [4], the plot of the design response spectrum (median) is shown in a tripartite plot (Figure 2.22). In the same plot, the 84th percentile spectrum is also shown. For the latter, $\alpha_A = 2.71$, $\alpha_v = 2.30$, and $\alpha_D = 2.01$.

2.5.5 Design Earthquakes

While response spectra or PSDF of ground motions are used as inputs for structural analysis, the level of ground shaking is represented by the design earthquake. Generally, design earthquakes are associated with the two level design concept, that is, in one level of motion, the structures remain serviceable (damage is within acceptable limits) and in the other, catastrophic failure (or damage) of the structure without collapse is envisaged. As quantification of the design earthquake requires many considerations, the input response spectrum or the PSDF are provided in the normalized form. This allows different purposes to be incorporated into the analysis.

Many different descriptions of the level of severity defining the design earthquake are available in the literature. Maximum Credible Earthquake (MCE) is usually defined as the largest earthquake that can reasonably be expected from a particular earthquake source. Safe Shutdown Earthquake (SSE) is used in

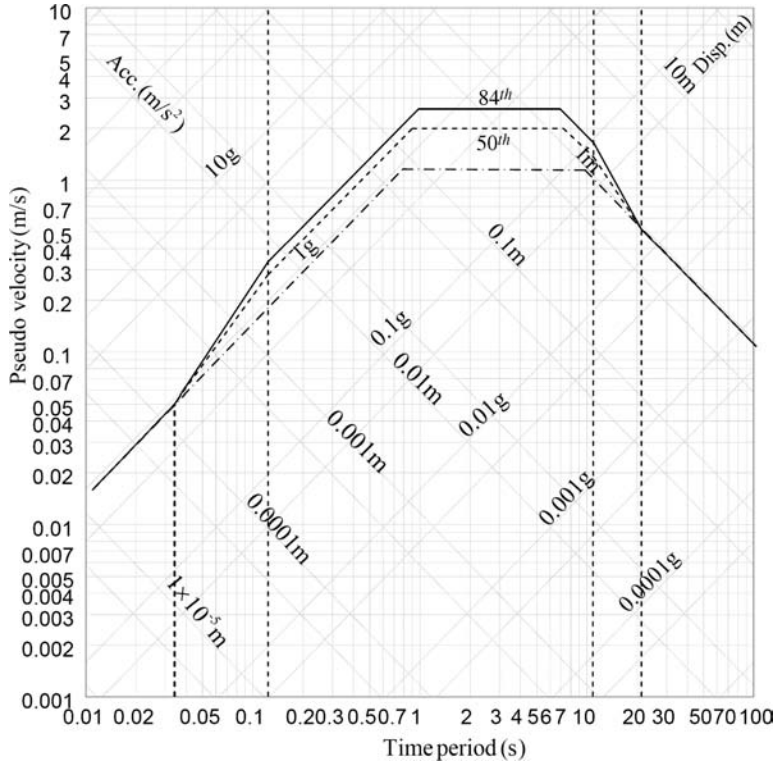

Figure 2.22 Design response spectrums for 50th and 84.1th percentile values

nuclear power plant design and is associated with the peak horizontal ground acceleration specified for the design. Other terms that are used to denote similar levels of earthquakes are Credible Design Earthquake, Safety Level Earthquake, Maximum Design Earthquake, and so on. These levels of earthquake refer to the upper limit of the design earthquake associated with two level design concepts. The lower limit is generally known by Operating Basis Earthquake (OBE), which denotes an earthquake size most expected during the lifetime of the structure. Other terms used for similar level earthquakes are Operating Level Earthquake, Probable Design Earthquake, and Strength Level Earthquake. The OBE is often taken as half of the SSE.

2.5.6 *Probabilistic Response Spectra*

It is evident from the preceding discussions that the design response spectrum for a region depends upon many factors, chief among them are the active faults influencing the region, fault mechanisms, magnitudes of earthquakes, geological characteristics of the region, and local soil conditions. Future earthquakes in the region are indeed uncertain as most of these factors are uncertain. Therefore, a deterministic design response spectrum as described previously is not considered to be sufficient for the safe design of structures for future earthquakes that are essentially not known. As a consequence, a probabilistic model of a response spectrum has been attempted by various investigators. These response spectra are used when probabilistic seismic analysis and design are intended or when probabilistic risk analysis of already designed structures is carried out. These response spectra are derived from statistical analysis of recorded

earthquake data in the region and are generally provided in the form of empirical formulae. Some of the empirical expressions for response spectra are given in Section 2.7.5.

2.5.7 Site Specific Spectra and Uniform Hazard Spectra

2.5.7.1 Site Specific Spectra

Site specific spectra are different from design spectra that are used for the general purpose design of structures and are recommended in the codes of practices. Site specific spectra are those which are exclusively used for the design of structures for that site. These structures are generally specialty structures and require careful consideration of the site conditions at the time of design. Alternatively, special geological, geophysical, and geotechnical conditions may exist at the site, which distinguish the past earthquake records for the site as being distinctly different to other earthquake records of the region. For such sites, site specific spectra are obtained from the family of accelerograms recorded near to the site. If required, they are supplemented by using recorded accelerograms of other sites having similar geological, seismological, and geophysical conditions. All accelerograms are scaled in order to adjust them for single magnitude and single source to site distance of an earthquake. They are also scaled to adjust for the specific site being represented. The scaling is accomplished by Fourier transforming each accelerogram. The real and imaginary parts of the transformed results are multiplied by frequency dependent scaling factors to account for the magnitude and site condition differences. The source to site distance adjustment is done by multiplying the results by a frequency independent scaling factor. This scaling factor is obtained from the attenuation relationships (expressing PGA as a function of magnitude and epicentral distance) valid for the region. After applying three scaling factors, the results are inverse Fourier transformed to obtain the full set of accelerograms compatible for the site. Response spectra obtained from the accelerograms are averaged and then smoothened (using a curve fitting technique) to derive the desired site specific spectrum.

The above procedure may not exactly cater to the actual site effects in terms of soil conditions. The ground motion parameters and the generated time history will correspond to those of the sites in the database for which predictive (attenuation law) relationships were developed. In order to bring the actual soil conditions of the site into the picture, a deconvolution and conventional ground response analysis are performed, as shown in Figure 2.23. Deconvolution is simply the ground motion analysis in the reverse

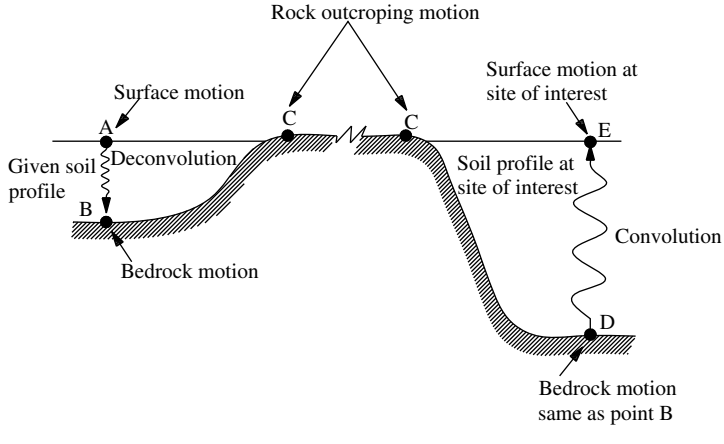

Figure 2.23 Deconvolution and convolution of ground motion to take into account local site conditions

order and provides the time history of ground motion at the rock bed. The same rock bed motion is used at O (Figure 2.23) to obtain the time history of the ground motion at the site of interest at E, which is consistent with the local soil conditions.

Example 2.6

Three time histories of ground acceleration records are available in the vicinity of a site along with their smoothed PSDFs shown in Figures 2.24–2.27. Soil conditions of the sites where earthquake records are available are significantly different than the site for which the site specific response spectrum is to be constructed. It is assumed that the attenuation law given by Toro (Equation 2.46) (Section 2.7.1) is valid for the region at the bed rock level, and vertically propagating earthquake waves from the rock bed predominantly constitute the motion at the ground surface. Construct the site specific response spectrum for $M = 7$ from this limited information. Assume ξ for the soil to be 0.05 and the duration of the earthquake to be 25 s.

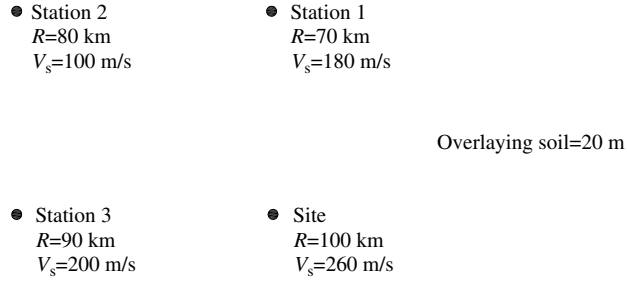

Figure 2.24 Recording stations and the site

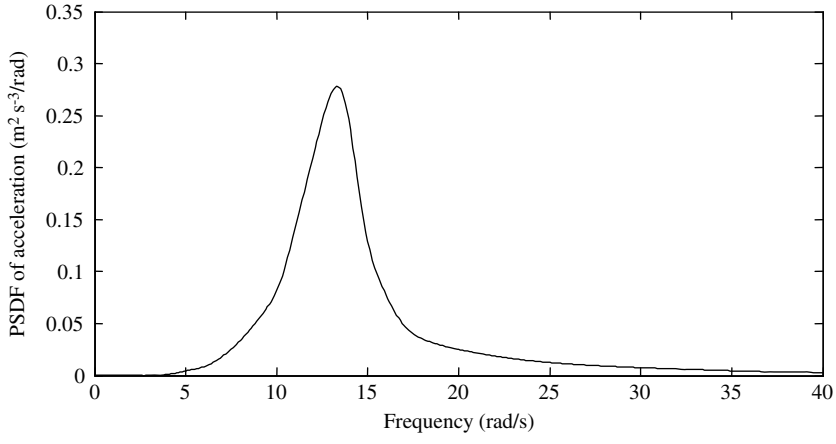

Figure 2.25 Acceleration power spectrum (PSDF) for station 1

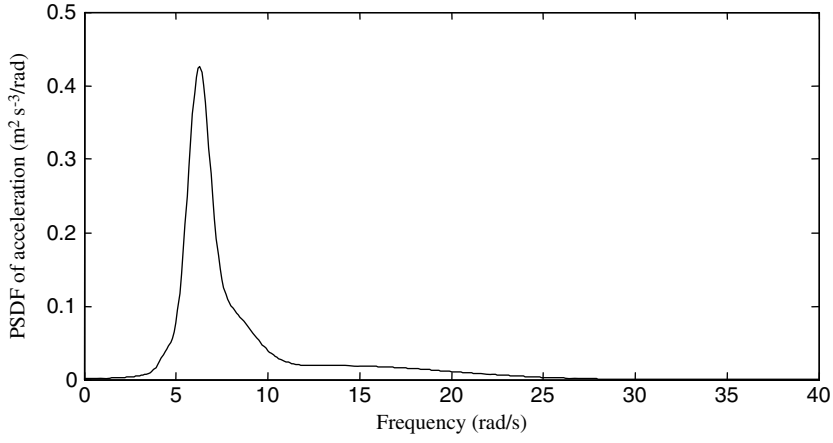

Figure 2.26 Acceleration power spectrum (PSDF) for station 2

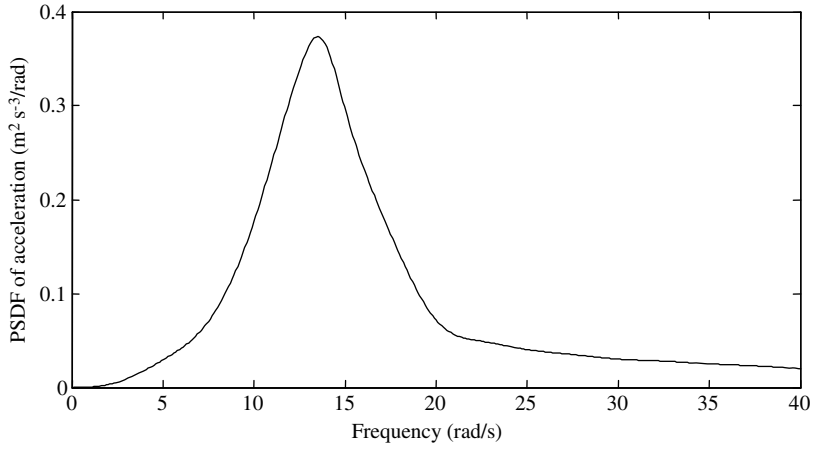

Figure 2.27 Acceleration power spectrum (PSDF) for station 3

Solution: Power spectrums (PSDFs) at the rock bed corresponding to those of the surface stations are shown in Figures 2.28–2.30. They are obtained using the following relationships (Chapter 4):

$$(\text{PSDF})_{\text{surface}} = (\text{PSDF})_{\text{rockbed}}(\text{TF})^2 \tag{2.35a}$$

$$(\text{PSDF})_{\text{rockbed}} = \frac{(\text{PSDF})_{\text{surface}}}{(\text{TF})^2} \tag{2.35b}$$

See the chapter on soil structure interaction, or Chapter 7 (Equation 7.13) of reference [26]:

$$(\text{TF})^2 = \frac{1}{[\cos^2(\omega \text{H}/V_{\text{s}}) + (\xi^2 H^2 \omega^2 / V_{\text{s}}^2)]} \tag{2.36}$$

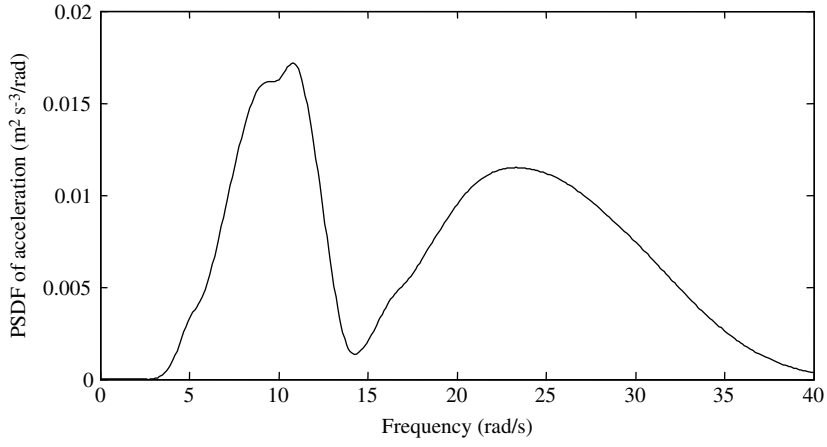

Figure 2.28 PSDF at the rock bed for station 1

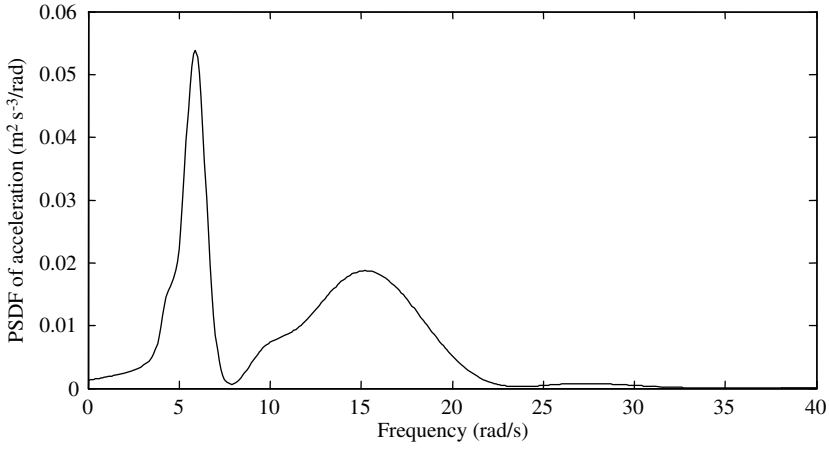

Figure 2.29 PSDF at the rock bed for station 2

where

H = depth of the overlying soil

From the area under the PSDF curves, the standard deviations of the accelerations are obtained as:

$$(\sigma_{\ddot{x}_{g1}})_{\text{rocked}} = 0.12\text{g} \quad \text{p}_1 = 3.2 \quad (\text{PGA}_1)_{\text{rockbed}} = \text{p}_1 \quad \sigma_{\ddot{x}_{g1}} = 0.384\text{g}$$

$$(\sigma_{\ddot{x}_{g2}})_{\text{rocked}} = 0.08\text{g} \quad \text{p}_2 = 2.9 \quad (\text{PGA}_2)_{\text{rockbed}} = \text{p}_2 \quad \sigma_{\ddot{x}_{g2}} = 0.24\text{g}$$

$$(\sigma_{\ddot{x}_{g3}})_{\text{rocked}} = 0.15\text{g} \quad \text{p}_3 = 3.4 \quad (\text{PGA}_3)_{\text{rockbed}} = p_3 \quad \sigma_{\ddot{x}_{g3}} = 0.51\text{g}$$

in which p_1, p_2, and p_3 are the peak factors which can easily be obtained from Equation 2.19a–c.

Using the attenuation law given by Toro, the magnitudes corresponding to the PGAs at the rock bed are:

$$M_1 = 6.2; \qquad M_2 = 5.8; \qquad M_3 = 7.3$$

The PGA at the rock bed below the sites for $M = 7$ and $R = 100$ km is obtained as PGA = 0.38g.

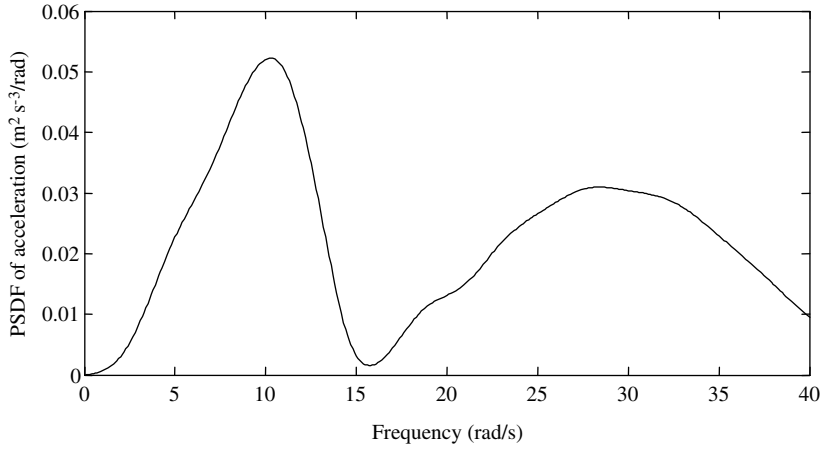

Figure 2.30 PSDF at the rock bed for station 3

The three PSDFs at the rock bed are scaled to have the same PGA of 0.38g by the following relationships:

$$(\text{PSDF})_s = (\text{PGA})_s^2 \frac{(\text{PSDF})_u}{(\text{PGA})_u^2} \tag{2.37}$$

where

$(\text{PSDF})_s$ is the scaled PSDF
$(\text{PSDF})_u$ is the unscaled or original PSDF
$(\text{PGA})_u$ is the PGA for the unscaled PSDF
$(\text{PGA})_s$ is the PGA for the scaled PSDF.

In the above calculation, it is assumed that peak factors are the same for the scaled and unscaled PSDFs. The three scaled PSDFs are shown in Figures 2.31–2.33. The corresponding PSDFs at the ground surface

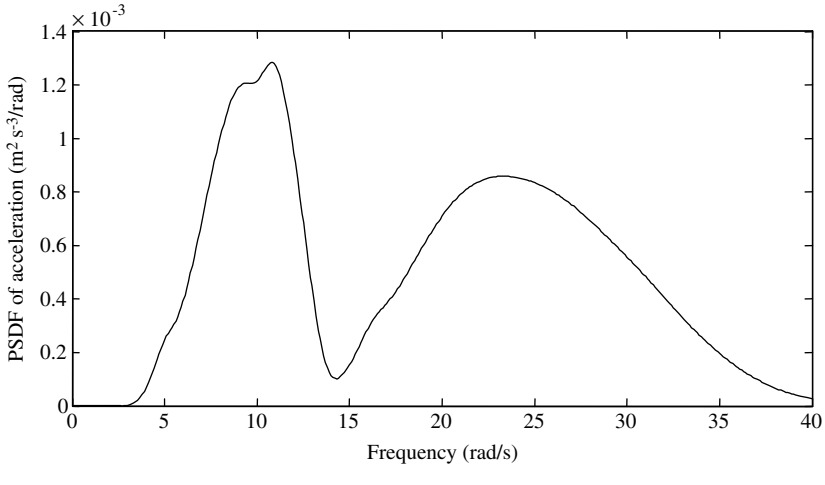

Figure 2.31 Scaled PSDF at the rock bed below the site for station 1

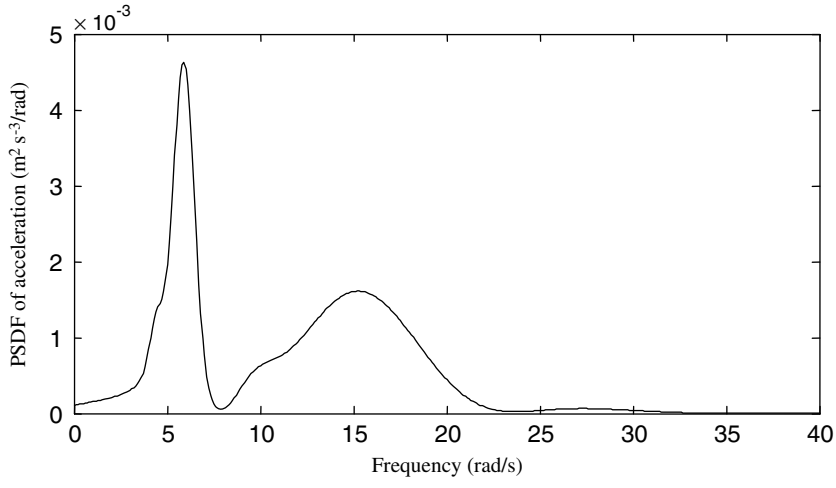

Figure 2.32 Scaled PSDF at the rock bed below the site for station 2

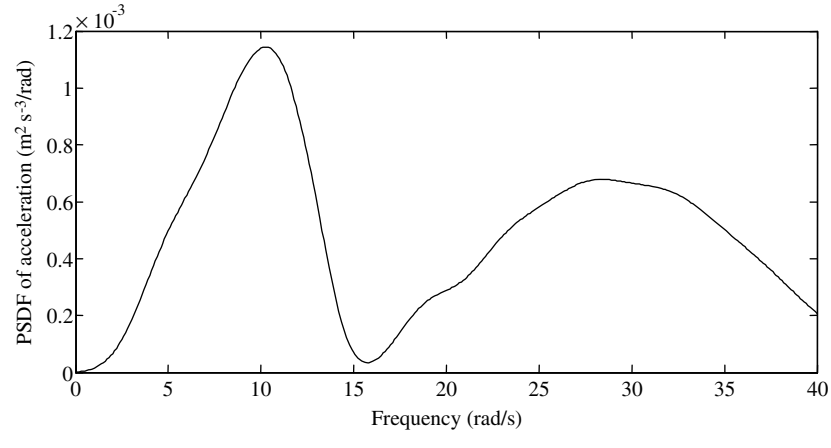

Figure 2.33 Scaled PSDF at the rock bed below the site for station 3

(that is, at the site) are obtained with Equation 2.35a, that is,

$$(\text{PSDF}_1)_{\text{site}} = (\text{PSDF}_1)_s(\text{TF})^2 \tag{2.38}$$

Three PSDFs thus obtained for the site are shown in Figures 2.34–2.36. The above procedure is equivalent to scaling the Fourier components of the three time histories of ground motion near the site to adjust for the site conditions, earthquake magnitude (of 7), and the surface to site distance as described in Section 2.5.7.

From these three PSDFs, three time histories of ground motions are synthetically generated by the procedure given in Section 2.6.2. The response spectra from these three time histories are obtained (Section 2.5.1). These response spectra are shown in Figures 2.37–2.39. The average of the three spectra is the site specific spectrum and is shown in Figure 2.40.

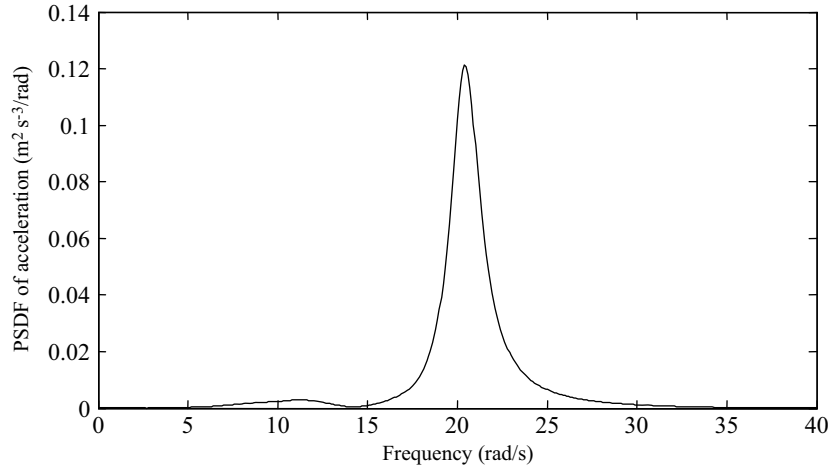

Figure 2.34 PSDF at the site obtained from station 1

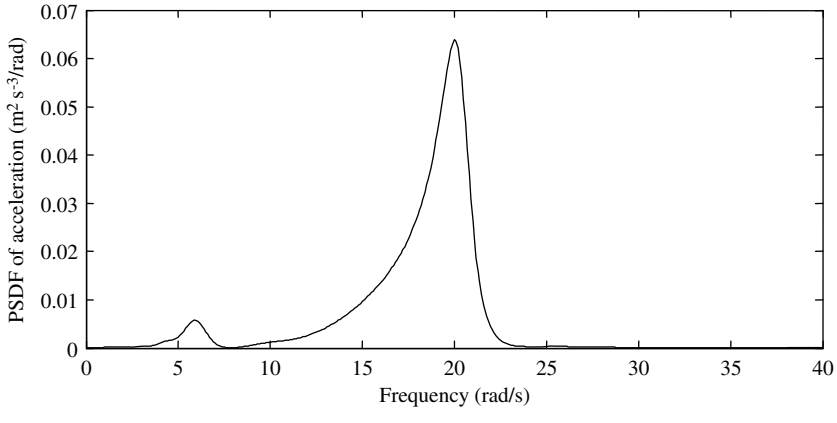

Figure 2.35 PSDF at the site obtained from station 2

2.5.7.2 Uniform Hazard Spectrum

To obtain the uniform hazard spectrum, statistical analyses are carried out on all spectra to obtain the probability distributions of the PGA and spectral ordinates at discrete frequencies over the frequency range of interest. Values of the spectral ordinates denoting the specified probability of exceedance are used to construct the uniform hazard spectrum.

An alternative method to obtaining the uniform hazard spectra is to perform the seismic hazard analysis described in Chapter 1. In place of obtaining the seismic hazard curve for PGA, hazard curves are obtained for spectral ordinates for each time period for a specified damping. From these sets of hazard curves, response spectra for a specified probability of exceedance are determined.

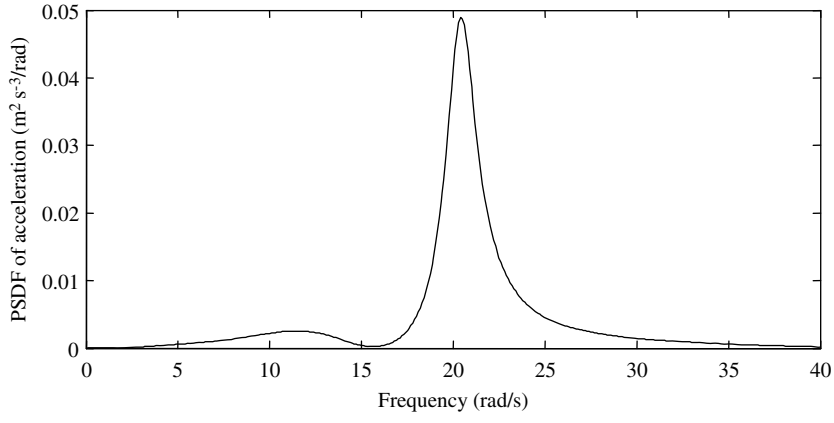

Figure 2.36 PSDF at the site obtained from station 3

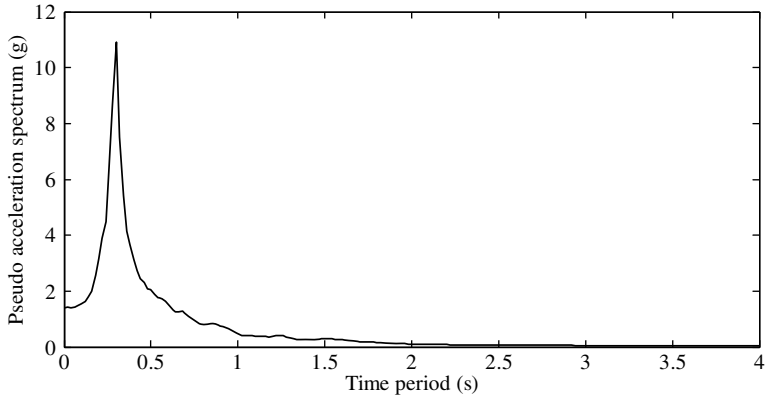

Figure 2.37 Response spectrum ($\xi = 0.05$) at the site obtained from station 1

Example 2.7

Construct a uniform hazard spectrum for acceleration with a probability of exceedance of 0.15 using the following data:

(i) Seismic hazard curve for the region is given in Figure 2.41.
(ii) Normalized response spectrum ordinates to have a probability of exceedance of 0.15 is given by 2 for $0.05 \leq T \leq 0.6$ and $1.2/T$ for $T \geq 0.6$.

Solution: The hazard curve for the region is shown in Figure 2.41. From the figure, it is seen that annual frequency of exceedance of 0.15 corresponds to a PGA = 0.12 g. A normalized response spectrum with a uniform probability of exceedance of 0.15 (for all ordinates) is drawn in Figure 2.42. Normalized ordinates are multiplied by the PGA = 0.12 g to obtain the required uniform hazard spectrum, shown in Figure 2.43.

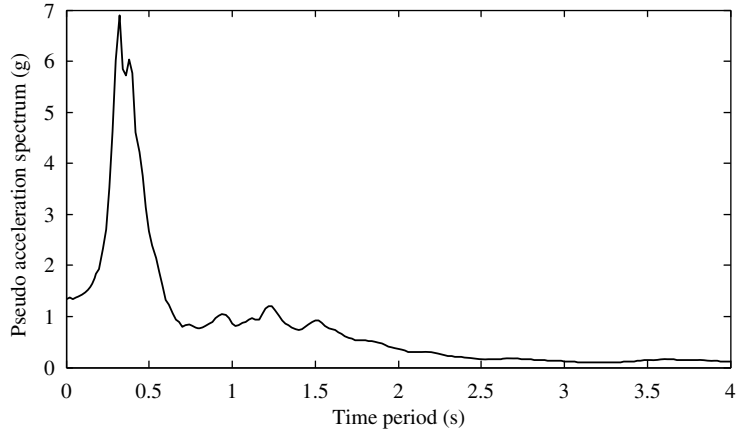

Figure 2.38 Response spectrum ($\xi = 0.05$) at the site obtained from station 2

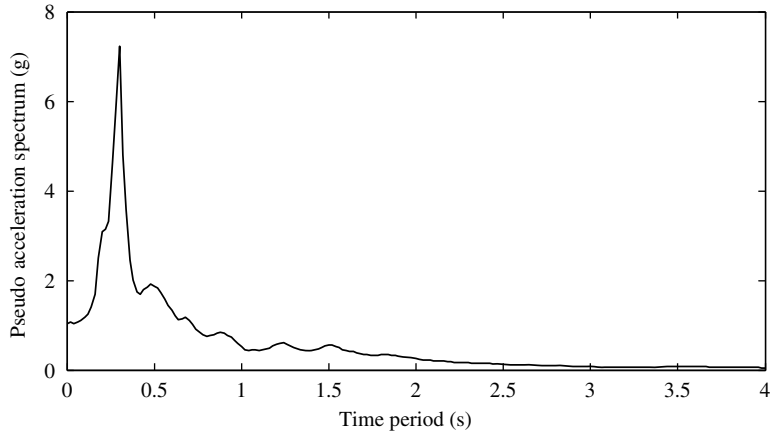

Figure 2.39 Response spectrum ($\xi = 0.05$) at the site obtained from station 3

When seismic design is to be performed for two simultaneous horizontal components of ground motion, the normalized design spectra described earlier can be used for both components. The design and maximum probable intensity level of one component should be reduced by about 15% below the corresponding level of the other component. Components of larger intensity should be directed along the critical axis of the structure.

2.6 Generation of Synthetic Accelerograms

In many instances, the generation of synthetic time histories of the ground motion is desired for seismic design and analysis of structures. Non-linear dynamic analysis of structures under earthquake excitation is one such important case where the required input is the time history of ground motion. This time history should be compatible with a specified response spectrum or a specified PSDF of ground motion. The

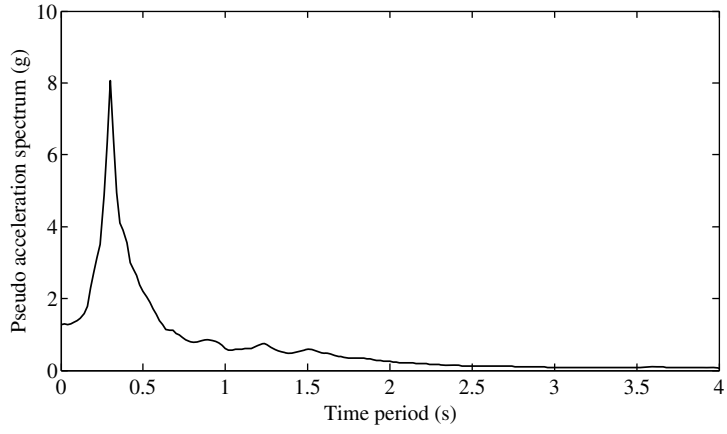

Figure 2.40 Site specific response spectrum (averaged)

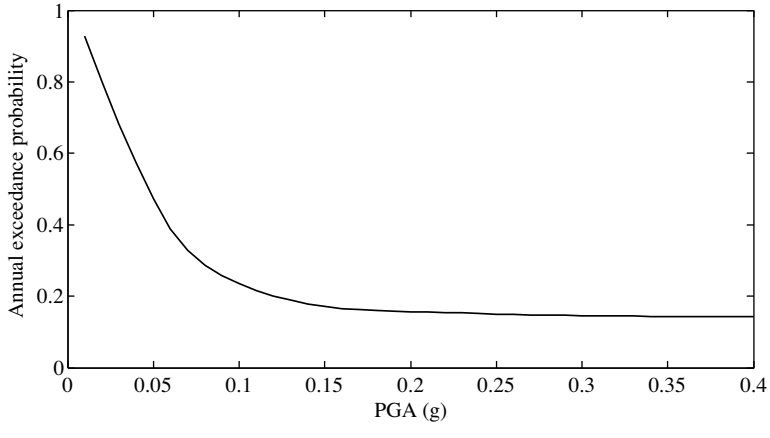

Figure 2.41 Hazard curve for the region

specified response spectrum could be a design spectrum, a site specific response spectrum, or a uniform hazard spectrum. In a similar way, the specified PSDF of ground motion may be site specific, region specific or given by an empirical formula. Many standard programs are now available to generate a response spectrum or PSDF compatible ground motions. Therefore, details of the procedure for generating such ground motions are not included here. The basic principles from which they are developed are only summarized below.

2.6.1 Response Spectrum Compatible Accelerogram

The basic steps involved in the generation of the accelerogram are:

(i) A set of Gaussian numbers are artificially generated having zero mean and unit variance. These numbers are sampled at a time interval of Δt to provide a time history.

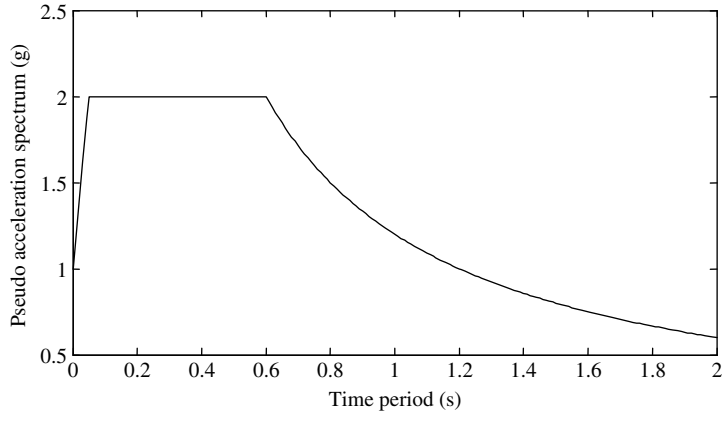

Figure 2.42 Normalized response spectrum

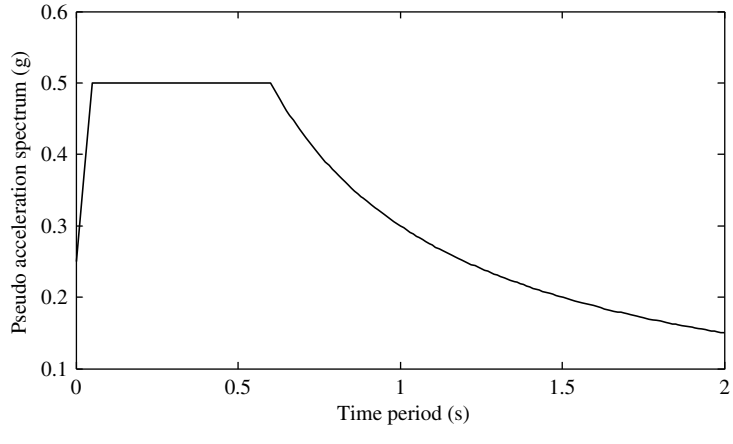

Figure 2.43 Uniform hazard spectrum for acceleration with a probability of exceedance of 0.15

(ii) This time history is then multiplied by a modulating function in order to incorporate the non-stationary nature of the earthquake in the accelerogram. The modulating function is selected such that it is consistent with the expected magnitude of the earthquake and epicentral distance.

(iii) The generated time history $z(t)$ is then modified to take into account the local soil conditions. This is done by Fourier transforming $z(t)$ and multiplying the transformed complex numbers by the double filter frequency response functions discussed in Section 2.7.5.

(iv) The resulting complex numbers are inverse Fourier transformed to obtain a time history $b(t)$ and normalized to a PGA value of 1g.

(v) A pseudo velocity/acceleration response spectrum is generated from the time history for the specified damping ratio and it is compared with the design response spectrum or the target response spectrum.

(vi) The generated response spectrum is iteratively matched with the target one by matching the frequency contents of the two. The iteration is performed by multiplying the $b(i\omega)$ by the average

ratio of the ordinates of the target spectrum and the generated spectrum within a narrow band of frequency centering around ω, and then inverse Fourier transforming $b(i\omega)$ to obtain the new time history. Step (v) is then performed to generate a new spectrum. The process is continued until a reasonable convergence is achieved.

2.6.2 *Power Spectral Density Function Compatible Accelerogram*

Generation of the time history of acceleration for a specified PSDF of ground motion is based on the technique of Monte Carlo simulation [5]. The steps involved in the generation are the following:

(i) Random numbers are generated between 0 and 2π, which are uniformly distributed.
(ii) The time history of acceleration is obtained using

$$a(t) = \sum_i A_i \sin(\omega_i t + \phi_i) \tag{2.39}$$

where

$A_i = \sqrt{2S_i \Delta\omega_i}$
$\omega_i =$ the frequency that is randomly selected between 0 and the cut-off frequency
$\phi_i =$ the randomly generated numbers in step (i)
$\Delta\omega_i =$ the small frequency interval centered around ω_i

The cut-off frequency is the frequency beyond which the PSDF ordinate S_i has negligible value.

(iii) ω_i is a randomly generated number that is uniformly distributed between 0 and ω_c and then arranged in an ascending order.

If time histories of acceleration are to be generated for the same specified design spectrum or PSDF at a number of points that are spatially separated, then the spatial correlation or phase difference between the time histories should be duly considered. Generation of such sets of accelerograms is somewhat involved as it requires consideration of the appropriate correlation function (described in Section 2.7.7) and finding suitable phase differences between different time histories. A procedure is given in reference [6], which may be programmed and added to the program for generating the accelerogram for a single-point excitation.

2.7 Prediction of Seismic Input Parameters

For the design of structures for earthquake forces, it is necessary to estimate the level of ground shaking for which the structures should be designed. These levels of shaking are represented in various ways, described as seismic inputs for structures in Sections 2.1–2.6. While some of these seismic input parameters are directly available from the recorded earthquake data of the region, a number are obtained using different empirical relationships, termed predictive relationships. In fact, predictive relationships are extensively used for the determination of the seismic hazard of a region and for determining the seismic inputs for the regions where available earthquake data are scanty.

Predictive relationships usually express the ground motion parameters and seismic input parameters as functions of magnitude, epicentral distance, and some other variables, if needed. The general form of the predictive relationship expressing the parameter of interest Y is given by:

$$Y = f(M, R, s_i) \tag{2.40}$$

where

$M =$ the magnitude of earthquake
$R =$ the epicentral distance
$s_i =$ some other parameter used in the equation

The predictive relationship is developed based on certain considerations such as: (i) peak values of strong motion parameters are approximately log normally distributed; (ii) decrease in wave amplitude with distance bears an inverse relationship; (iii) energy absorption due to material damping causes ground motion amplitudes to decrease exponentially with epicenteral distance; and (iv) effective epicentral distance is greater than R.

As the peak value of the parameter is log normally distributed, the estimated value of the parameter is represented by a mean and a standard deviation. The mean value is given by the predictive relationship.

The probability that the parameter value will exceed a value Y_1 would be governed by the equation

$$P[Y \geq Y_1] = 1 - F_p(p) \tag{2.41}$$

in which $F_p(p)$ is the cumulative distribution function of p defined by:

$$p = \frac{(\ln Y_1 - \ln \bar{Y})}{\sigma_{\ln Y}} \tag{2.42}$$

where

$\ln \bar{Y}$ = the mean value of the parameter (in ln) given by the predictive relationship
$\sigma_{\ln Y}$ = the standard deviation of the parameter

2.7.1 Predictive Relationships for PGA, PHV, and PHA

The most widely used predictive relationship is that for peak ground acceleration (PGA) as it is one of the most commonly used ground motion parameters. As this parameter decreases with an increase in the epicentral distance, it is also referred to as the attenuation relationship. A large number of attenuation relationships for PGA have been developed over the years. All are best suited for conditions similar to those in the data bases (valid for a particular region) from which they were developed. Attenuation relationships become more refined and modified as more and more strong motion data are available. Generally, the validity of attenuation relationships is dictated by the ranges of epicentral distance, magnitude of earthquakes, and nature of earth medium. A few of the attenuation relationships for peak horizontal ground acceleration (PHA), also known as PGA, peak ground velocity (PGV), and some of the basic relationships between earthquake intensity parameters are given below. Note that in defining the magnitude of earthquakes, $M = M_1 = M_W$ (up to $M = 9$); M_0 is defined as the seismic moment and M_S is defined as the surface magnitude (Chapter 1).

An early attenuation relationship for PHA was proposed by Esteva [7] for ground motion on firm soil as:

$$\text{PHA} = 1230 e^{0.8M} (R + 25)^{-2} \tag{2.43}$$

where

PHA is in cm s^{-1}
M is the local magnitude
R is the epicentral distance measured in km.

Campbell [8] developed an attenuation relationship for PHA based on world-wide data in the form of

$$\ln \text{PHA (g)} = -4.141 + 0.868M - 1.09 \ln(R + 0.0606 e^{0.7M}) \tag{2.44}$$

where

M is the local magnitude
R is the epicentral distance in km.

The relationship is valid for small epicentral distances within 50 km and for magnitudes varying between 5 and 7.7. $\sigma_{\ln PHA}$ is given as a constant value of 0.37.

Cambell and Bozorgnia [9] developed a modified attenuation relationship, again based on the world-wide data, for a greater range of magnitude of earthquake in the form of:

$$\begin{aligned}\ln \text{PHA (g)} = &-3.512 + 0.904M_{\text{W}} - 1.328\ln\sqrt{R^2 + [0.149\exp(0.647M_{\text{W}})]^2} \\ &+ (1.125 - 0.112\ln R - 0.0957M_{\text{W}})F + (0.440 - 0.171\ln R)S_{\text{SR}} \\ &+ (0.405 - 0.222\ln R)S_{\text{HR}}\end{aligned} \tag{2.45a}$$

$$\sigma_{\ln PHA} = \begin{cases} 0.889 - 0.0691M & M \leq 7.4 \\ 0.38 & M > 7.4 \end{cases} \tag{2.45b}$$

where

R = the short epicentral distance (preferably within 60 km)
F = zero for strike slip and normal faulting, and 1 for reverse oblique and thrust faulting
$S_{\text{SR}} = 1$ for soft rocks
$S_{\text{HR}} = 1$ for hard rocks
$S_{\text{SR}} = S_{\text{HR}} = 0$ for alluvium sites

Comparison of Equations 2.44 and 2.45 shows how the attenuation relationship is refined as more data are available.

Toro *et al.* [10] developed an attenuation relationship for PHA based on the data available for eastern North America in the form of:

$$\ln \text{PHA (g)} = 2.20 + 0.81\,(M_{\text{W}} - 6) - 1.27\ln R_{\text{m}} + 0.11\max\left(\ln\frac{R_{\text{m}}}{100}, 0\right) - 0.0021R_{\text{m}} \tag{2.46}$$

where

$R_{\text{m}} = \sqrt{R^2 + 9.3^2}$
R = the closest horizontal distance to the earthquake rupture (in km)
$\sigma_M = 0.36 + 0.07(M_{\text{W}} - 6)$

and

$$\sigma_R = \begin{cases} 0.54 & R < 5\,\text{km} \\ 0.54 - 0.0227(R-5) & 5 \leq R < 20\,\text{km} \\ 0.20 & R > 20\,\text{km} \end{cases} \tag{2.47}$$

$$\sigma_{\ln \text{PHA}} = \sqrt{\sigma_M^2 + \sigma_R^2} \tag{2.48}$$

One of the earliest attenuation relationships for PHV was given by Esteva [7] in the form of:

$$\text{PHV} = 15\text{e}^{M}(R + 0.17\text{e}^{0.59M})^{-1.7} \tag{2.49}$$

in which M is the local magnitude, R is the epicentral distance in km, and PHV is in cm s^{-1}. The attenuation relationship is valid for firm ground.

Another empirical relationship between PHV and earthquake intensity was proposed by Esteva and Rosenblueth [11],

$$I = \frac{\log 14\,\mathrm{PHV}}{\log 2} \tag{2.50}$$

where I is in the MM intensity scale and PHV is in cm s^{-1}.

There are a number of other predictive relationships that relate intensity with various other seismic parameters. The intensity and magnitude of an earthquake were related by Shinozuka [12]:

$$I = 1.667M - 2.167 \tag{2.51}$$

Cornell [13] proposed another relationship between the two:

$$I = 8.16 + 1.45M - 2.46 \ln\left(\sqrt{R^2 + h^2}\right) \tag{2.52}$$

in which h is the depth of the focus.

An important relationship between the energy release (E) and the magnitude of earthquake (M) was proposed by Gutenberg [14] in the form:

$$\log_{10} E = 11.8 + 1.5M \tag{2.53}$$

Using Equations 2.51 and 2.53, the energy released can be related to intensity.

Trifunac and Brady [15] proposed a relationship between intensity and PGA (in cm s^{-1}) as:

$$\log\,(\mathrm{PGA}) = 0.3I - 0.014 \tag{2.54}$$

A relationship between intensity, and peak horizontal ground velocity, PHV (in cm s^{-1}) was given as [16]

$$\mathrm{PHV} = 0.3 \times 10^{0.18I} \tag{2.55}$$

Joyner and Boore [17] used strong motion records from earthquakes of M between 5 and 7.7 to develop an attenuation relationship for PHV as:

$$\log \mathrm{PHV} = j_1 + j_2(M-6) + j_3(M-6)^2 + j_4 \log R + j_5 R + j_6 \tag{2.56}$$

in which PHV (in cm s^{-1}) is selected as randomly oriented or as a larger horizontal component depending upon the coefficients j_1–j_7 as given in Table 2.2. R is taken as $\sqrt{r_0^2 + j_7^2}$; r_0 is the epicentral distance (in km).

McGuire [18] proposed empirical expressions for $V_{\max}/a_{\max}$ (a measure of the equivalent period of an earthquake), which were dependent on magnitude and epicentral distance. The dependences are shown in Table 2.3.

Table 2.2 Coefficients of the attenuation relationship for PHV

Component	j_1	j_2	j_3	j_4	j_5	j_6	j_7	$\sigma_{\log \mathrm{PHV}}$
Random	2.09	0.49	0.0	−1.0	−0.0026	0.17	4.0	0.33
Larger	2.17	0.49	0.0	−1.0	−0.0026	0.17	4.0	0.33

Table 2.3 Magnitude and distance dependence of $V_{\max}/a_{\max}$

Site conditions	Magnitude dependence	Distance dependence
Rock sites	$e^{0.40M}$	$R^{0.12}$
Soil sites	$e^{0.15M}$	$R^{0.23}$

An empirical formula was also proposed by Esteva [7] to obtain the peak ground displacement (in cm) on firm ground as:

$$\text{PHD} = \frac{(\text{PHV})^2}{\text{PHA}}\left(1 + \frac{400}{R^{0.6}}\right) \tag{2.57}$$

Example 2.8

At epicentral distances of 75 and 120 km, find the PHA (PGA) by using the attenuation relationship given by Esteva (Equation 2.43), Campbell (Equation 2.44), Campbell and Bozorgnia (Equation 2.45), and Toro (Equation 2.46) and compare them for $M(= M_W = M_S) = 7$. For the same magnitude of earthquake and epicentral distances, compare between the PHVs obtained by the relationships given by Esteva (Equation 2.49), Joyner and Boore (Equation 2.56 for random) and Esteva and Rosenblueth (Equation 2.50). Use Cornell's equation (Equation 2.52) to obtain I from M. Investigate how the computed I compares with that given by Shinozuka (Equation 2.51) and how the computed PGA given by Trifunac and Brady (Equation 2.54) compares with PHAs obtained by different attenuation relationships.

Solution: It is assumed that the epicentral distance and the hypocentral distance are nearly the same. According to Cornell (Equation 2.52), I values calculated for $R = 75$ and 120 km for $M = 7$ are 7.68 and 6.53, respectively. The distance independent empirical formula given by Shinozuka (Equation 2.51) for calculating I gives a value of 9.5, much higher than those calculated above. Tables 2.4 and 2.5 compare the PHAs and PHVs obtained by different empirical equations.

It is seen from Table 2.4 that PHAs calculated by Equations 2.43 and 2.45 give nearly the same values; those calculated by Equations 2.44 and 2.46 compare reasonably well for the epicentral distance of 120 km, but they provide twice the values given by Equations 2.43 and 2.45. PHAs calculated by Equation 2.54 based on intensity provide much higher values.

It seen from Table 2.5 that PHVs calculated by Equations 2.49, 2.56 and 2.50 vary widely; those calculated by Equation 2.49 give the maximum values, while that calculated by Equation 2.50 gives the least values.

Table 2.4 Comparison of PHAs obtained by different empirical equations for $M = 7$

Empirical relationship	PHA (g)	
	75 km	120 km
Esteva (Equation 2.43)	0.034	0.015
Campbell (Equation 2.44)	0.056	0.035
Bozorgnia (Equation 2.45)	0.030	0.015
Toro (Equation 2.46)	0.072	0.037
Trifunac (Equation 2.54)	0.198	0.088

Table 2.5 Comparison of PHVs obtained by different empirical equations for $M = 7$

Empirical relationship	PHV (cm s^{-1})	
	75 km	120 km
Esteva (Equation 2.49)	8.535	4.161
Joyner (Equation 2.56)	4.785	2.285
Rosenblueth (Equation 2.50)	2.021	1.715

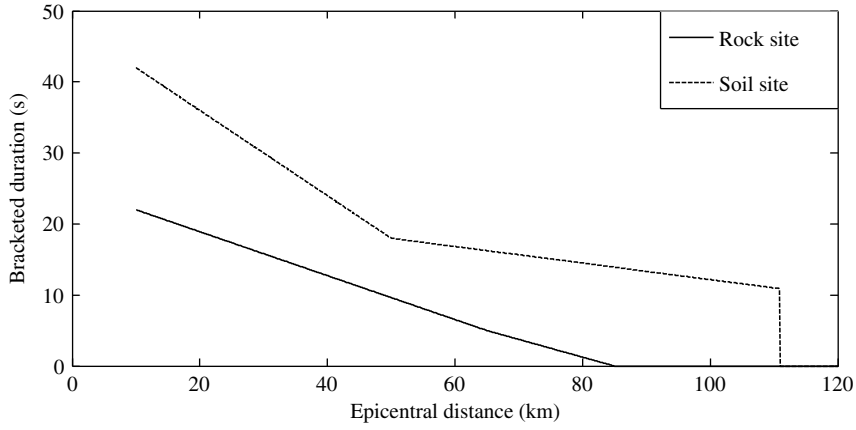

Figure 2.44 Variation of bracketed duration with epicentral distance

2.7.2 Predictive Relationship for Duration

The duration of strong ground motion increases with increasing magnitude. The relationship between epicentral distance and duration of an earthquake depends upon how the duration is defined. Two definitions for the duration of an earthquake are widely used. The first one is bracketed duration, which is defined as the first and last exceedances of a threshold acceleration (usually 0.05 g). The second is significant energy duration, which is defined as the time interval between the points at which 5 and 95% of the total energy has been recorded. Other definitions of the duration of earthquakes also exist. Bracketed duration is expected to decrease with distance, while duration based on the significant energy recorded [15] is expected to increase with increasing distance. An early study by Chang and Krinitzsky [19] is given in Figure 2.44, which shows that bracketed duration decreases with increasing distance. Boore [20] prescribed the duration to be equal to the corner period (inverse of corner frequency).

No good correlation between the duration of earthquake with magnitude and epicentral distance can be obtained from recorded earthquake data. Some studies by Esteva and Rosenblueth [11] showed that the duration of earthquake on firm ground/rock bed could be of the form:

$$T = 0.02\mathrm{e}^{0.74M} + 0.3R \tag{2.58}$$

where T is given in seconds and R is in km.

2.7.3 Predictive Relationships for rms Value of Ground Acceleration (A_{rms})

Hanks and McGuire [21] obtained an attenuation relationship for rms acceleration for M of between 4 and 7 and hypocentral distances of between 10 and 100 km as:

$$A_{\mathrm{rms}} = 0.119\frac{\sqrt{\frac{f_{\max}}{f_{\mathrm{c}}}}}{R} \tag{2.59}$$

where

f_{c} is the corner frequency
$f_{\max}$ is the cut-off frequency
R is in km.

Kavazanjian *et al.* [22] obtained another relationship for A_{rms} for

$$M_{\text{W}} > 5 \text{ and } R < 110 \text{ km}$$

as

$$A_{\text{rms}} = 0.472 + 0.268M_{\text{W}} + 0.129 \log\left(\frac{0.966}{R^2} + \frac{0.255}{R}\right) - 0.1167R \tag{2.60}$$

Campbell and Duke [23] obtained an attenuation relationship for the Arias intensity I_{a} for M_{S} of between 4.5 and 8.5 and for R of between 15 and 110 km as:

$$I_{\text{a}}\,(\text{m s}^{-1}) = 313\frac{e^{M_{\text{S}}(0.33M_{\text{S}}-1.47)}}{R^{3.79}}S \tag{2.61}$$

$$\text{where} \quad S = \begin{cases} 0.57R^{0.46} & \text{for basement rock} \\ 1.02R^{0.51} & \text{for sedimentary rock} \\ 0.37R^{0.81} & \text{for alluvium} \leq 20 \text{ m thick} \\ 0.65R^{0.74} & \text{for alluvium} > 20 \text{ m thick} \end{cases} \tag{2.62}$$

I_a is defined as

$$I_a = \frac{\pi}{2g}\int_0^{\alpha} [a(t)]^2 \text{d}t$$

in which $a(t)$ is the ground acceleration.

2.7.4 Predictive Relationships for Fourier Spectrum and Response Spectrum

Ground motion parameters that reveal the frequency contents of the ground motion are the Fourier amplitude spectra, power spectra, and the response spectra of ground motion. Out of these three, the last two are widely used for seismic analysis of structures as it is not possible to provide any empirical relationship for these parameters without incorporating frequency or period. Therefore, predictive relationships contain the frequency/period as one of the key variables. McGuire and Hanks [24] and Boore [20] provided a predictive relationship for Fourier amplitude spectra for a far field events at distance R as:

$$|A(f)| = \left[CM_0 \frac{f^2}{1-(f/f_{\text{c}})^2} \frac{1}{\sqrt{1+(f/f_{\text{max}})^8}}\right] \frac{e^{-\pi f R/Q(f)V_s}}{R} \tag{2.63}$$

where f_{c} and f_{max} are the corner frequency and cut-off frequencies, respectively; $Q(f)$ is the frequency dependent quality factor; and C is a constant given by:

$$C = \frac{r_0 FV}{4\pi\rho V_{\text{S}}^3} \tag{2.64}$$

where

$r_0 (\approx 0.55)$ accounts for the relation pattern
$F (= 2)$ accounts for free surface effect
$V\left(=\frac{1}{\sqrt{2}}\right)$ accounts for participating the energy into two horizontal components
ρ and V_s (in m s^{-1}) are the density and shear wave velocity of the rock along the surface
M_0 is the seismic moment in dyn cm
f_{max} is assumed constant for a region that may typically vary between 10 and 50 Hz.

M_0 and f_c are related by [2]:

$$f_c = 4.9*10^6 V_S \left(\frac{\Delta\sigma}{M_0}\right)^{\frac{1}{3}} \tag{2.65}$$

in which V_S is in km s^{-1}, M_0 is in dyn cm, and $\Delta\sigma$ is the stress drop, which may vary between 50 and 100 bars.

Example 2.9

Compare between the smoothed normalized Fourier spectrum obtained from the El Centro earthquake records and that obtained by the empirical equation given by McGuire and Hanks, and Boore (Equation 2.63).

Solution: Assuming $f_c = 0.2$ Hz, $f_{max} = 10$ Hz, and $V_S = 1500$ m s^{-1}, the smoothed Fourier spectrum obtained from Equation 2.63 is shown in Figure 2.45. The spectrum is obtained for $M_W = 7$ and the corresponding M_0 is calculated using Equation 1.11 (Chapter 1) as 35.4. In the same figure, a smoothed Fourier spectrum obtained for the El Centro earthquake is compared. It is seen from the figure that the two spectra resemble each other. Note that Equation 2.63 is obtained from the shape of an average spectrum derived from the spectra of a number of earthquakes. Therefore, Equation 2.63 gives a smoother flat portion in the central region.

Prediction of response spectra is generally based on the concept of developing the shape of smoothed spectra for design purposes. The method of arriving at the smooth shapes has been discussed in Section 2.5.4. Scaling the design spectral shapes by the ground motion parameter, for example, PHA (PGA) which is obtained using a predictive relationship makes the response spectra M and R dependent. However, the spectral shape remains invariant with M and R. With more recorded motions becoming available, the magnitude dependence of spectral shapes has been increasingly recognized, particularly in

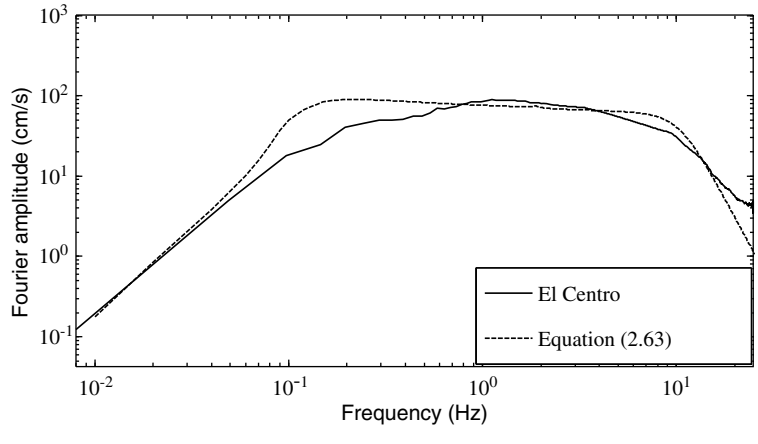

Figure 2.45 Comparison between the smooth Fourier spectrum of El Centro earthquake and that obtained by empirical Equation 2.63

the long period range. Boore *et al.* [25] obtained predictive relationships for spectral ordinates for different periods using regression analysis in the form:

$$\log S_V(T) = b_1 + b_2(M_W - 6) + b_3(M_W - 6)^2 + b_4 R + b_5 \log R + b_6 G_B + b_7 G_C \tag{2.66}$$

in which $R = (d^2 + h^2)^{\frac{1}{2}}$; the epicentral distance is in km and $G_B = 1$ for V_S within 360–750 m s^{-1}; $G_C = 1$ for V_S within 180–360 m s^{-1}; otherwise, $G_B = G_C = 0$. Values of the constants b_1 to b_7, h and $\log S_V$ for each time period T is given in reference [26]. S_{V_0} is obtained in cm s^{-1}. Ishii *et al.* [27] proposed M and R dependent predictive relationships for spectral acceleration using regression analysis of available earthquake motions in the form of:

$$\log \bar{S}_a(T) = a(T) + b(T)M + c(T)\log R \tag{2.67}$$

in which $\bar{S}_a$ is the normalized ordinate of the acceleration response spectrum, normalized with respect to PGA; $a(T)$, $b(T)$, and $c(T)$ are coefficients given in the form of a graph.

Kanai [28] proposed a predictive relationship for the pseudo velocity spectrum at the surface of soil as

$$S_V = 10^{(0.61M_S - 1.73\log r_1 - 0.67)} \times \left(1 + \left\{\left(\frac{1+\bar{\alpha}}{1-\bar{\alpha}}\right)^2 \left[1 - \left(\frac{T}{T_g}\right)^2\right]^2 + \left(\frac{0.3}{\sqrt{T_g}}\right)^2 \left(\frac{T}{T_g}\right)^2\right\}^{-\frac{1}{2}}\right) \tag{2.68}$$

where

M_S is the surface magnitude of the earthquake
R is the epicentral distance in km
T is the period
T_g is the predominant period of the wave
$\bar{\alpha} = \dfrac{\rho_1 v_1}{\rho_2 v_2}$
ρ_1 and ρ_2 are the mass densities
v_1 and v_2 are the wave velocities in the soil layer and the adjacent medium, respectively.

Example 2.10

Construct a design response spectrum using the expression given by Boore *et al.* (Equation 2.66) for $M\ (= M_W) = 7$ and $R = 50$ km. Take $V_S = 400$ m s^{-1}. Normalize the spectrum with respect to PHA (PGA), which is obtained by the attenuation relationship given by Campbell (Equation 2.44) and compare the spectrum with those of IBC, Euro-8, and IS 1893.

Solution: Values of b_1 to b_6 are taken from Table 3.9 of reference [26]; $G_C = 0$. For these values of b_1–b_6 and $M_W = 7$, the pseudo acceleration spectrum (pseudo velocity spectrum multiplied by frequency) is constructed. Using Equation 2.44, the PGA is obtained as 0.35 g. The ordinates of the pseudo acceleration spectrum are divided by 0.35 g to obtain the normalized spectrum and is shown in Figure 2.46. In the same figure, the normalized spectrum is compared with those of IBC, Euro-8, and IS 1893 (Chapter 5). It is seen from the figure that the shape of the normalized spectrum in the initial and end portions are similar to those of the code recommended spectra.

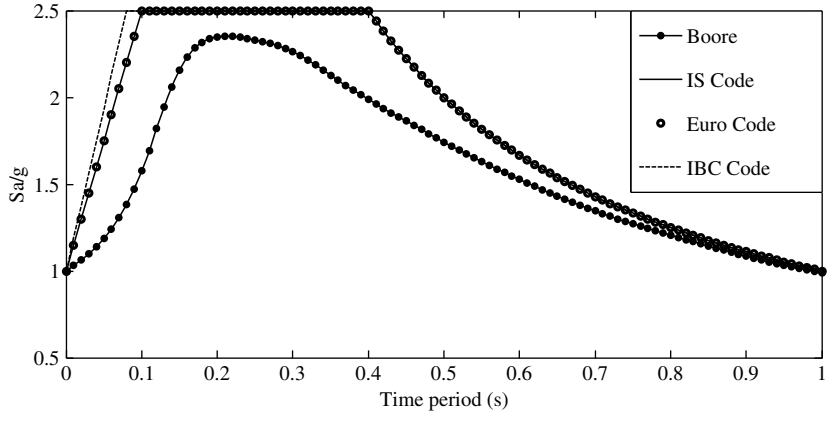

Figure 2.46 Comparison between design response spectrums given by Boore *et al.*, and various codes

2.7.5 Predictive Relationships for PSDF of Ground Motion

Prediction of the power spectral density function of ground motion is again based on the shape of the power spectrum obtained by averaging a number of power spectra from similar ground motions. In predicting the power spectrum, it is tacitly assumed that the ground motion sample record is a typical sample of a stationary ergodic process. However, actual strong motion accelerograms frequently show that the intensity builds up to a maximum value in the early part of the motion, then approximately remains constant for a period of time, and finally decreases near the end of the motion. Such a non-stationary random process is modeled by multiplying a stationary random process by a deterministic modulating function, that is, the non-stationary nature of the random process is represented by an evolutionary power spectrum obtained by multiplying the stationary power spectrum by a modulating function.

Most of the expressions for power spectra are in the form of a power spectrum of filtered white noise. Housner and Jennings [29] provided an expression for PSDF in the form of:

$$S_{\ddot{u}_g}(\omega) = \bar{\beta}\frac{1+\left(2\xi_g\dfrac{\omega}{\omega_g}\right)^2}{\left[1-\left(\dfrac{\omega}{\omega_g}\right)^2\right]^2+\left(2\xi_g\dfrac{\omega}{\omega_g}\right)^2} \tag{2.69}$$

in which $\bar{\beta}$ is a constant, and ξ_g and ω_g are the damping ratio and natural frequency of the filter, respectively. The above expression was adjusted for earthquakes on firm ground as:

$$S_{\ddot{u}_g}(\omega) = \frac{11.5\left(1+\dfrac{\omega^2}{147.8}\right)}{\left[1-\left(\dfrac{\omega^2}{242}\right)\right]^2+\dfrac{\omega^2}{147.8}} \tag{2.70}$$

in which $S_{\ddot{u}_g}(\omega)$ is in $\text{cm}^2\,\text{s}^{-3}$.

Newmark and Rosenblueth [30] proposed an expression for PSDF in a similar form as:

$$S_{\ddot{u}_g}(\omega) = \frac{25\dfrac{\omega^2}{289}}{\left[1-\left(\dfrac{\omega^2}{242}\right)\right]^2+\dfrac{\omega^2}{289}} \tag{2.71}$$

Kanai [28] suggested a PSDF in the form of

$$S_{\ddot{u}_g}(\omega) = \left|H_1(i\omega)\right|^2 S_{\ddot{u}_0}(\omega) \qquad -\infty\omega < \infty \tag{2.72}$$

in which the filter transfer function $\left|H_1(i\omega)\right|^2$ is given by:

$$\left|H_1(i\omega)\right|^2 = \frac{1+\left(2\xi_g\dfrac{\omega}{\omega_g}\right)^2}{\left[1-\left(\dfrac{\omega}{\omega_g}\right)^2\right]^2+\left(2\xi_g\dfrac{\omega}{\omega_g}\right)^2} \tag{2.73}$$

where

$S_{\ddot{u}_0}(\omega)$ is the constant PSDF of white noise
$S_{\ddot{u}_g}$ is the PSDF of the filtered process $\ddot{u}_g$
ω_g and ξ_g are as defined previously.

He suggested $\omega_g = 5\pi$ rad s^{-1}, $\xi_g = 0.6$ as being representative of firm soil conditions.

Clough and Penzien [6] modified the Kanai–Tajimi PSDF by passing white noise bed rock acceleration (with PSDF $S_{\ddot{u}_0}$) through two filters. This modification was made to prevent excessive velocities and displacements at very low frequencies.

$$S_{\ddot{u}_g}(\omega) = \left|H_1(i\omega)\right|^2\left|H_2(i\omega)\right|^2 S_{\ddot{u}_0}(\omega) \tag{2.74}$$

$$\left|H_2(i\omega)\right|^2 = \frac{\left(\dfrac{\omega}{\omega_f}\right)^4}{\left[1-\left(\dfrac{\omega}{\omega_f}\right)^2\right]^2+\left(2\xi_f\dfrac{\omega}{\omega_f}\right)^2} \tag{2.75}$$

where ξ_f and ω_f are the damping ratio and resonant frequency, respectively, of the second filter, and $H_1(\omega)$ remains the same as given by Equation 2.73. ω_f and ξ_f should be set such that correct filtering of the low frequency contents is achieved. Generally, ω_f may be taken as $0.1\omega_g$ and ξ_f as between 0.4 and 0.6.

The above expressions may be made M and R dependent by employing attenuation laws to predict the expected PHA (or PGA). Note that the expected PHA may be derived from Equation 2.44 and, finally, $S_{\ddot{u}_0}$ can be expressed in terms of M and R.

Shinozuka *et al.* [31] provided an expression for PSDF of ground surface acceleration directly in terms of M, R, and the soil condition in the following form:

$$S_{\ddot{u}_{gs}}(\omega, M_S, r_1, SC) = (A_1)^2\hat{S}_{\ddot{u}_{gs}}(\omega, M_S, r_1, SC) \tag{2.76}$$

$$\widehat{S}_{\ddot{u}_{gs}}(\omega, M_S, r_1, SC) = \begin{cases} \hat{\alpha}_{ms}^2\left(\dfrac{\omega}{2\pi}\right) & 0.2 \le \omega \le 28\pi \\ 0 & \text{otherwise} \end{cases} \tag{2.77}$$

$$\hat{\alpha}_{ms}\left(\frac{\omega}{2\pi}\right) = \hat{C}_0\hat{\alpha}_m\left(\frac{\omega}{2\pi}\right) \tag{2.78}$$

$$\log\hat{\alpha}_m\left(\frac{\omega}{2\pi}\right) = B_0\left(\frac{\omega}{2\pi}\right) + B_1\left(\frac{\omega}{2\pi}\right)M_S - B_2\left(\frac{\omega}{2\pi}\right)\log(r_1+30) \tag{2.79}$$

where $\widehat{C}_0$ is a modification factor given as a function of $N(z)$.

$$\log\widehat{C}_0 = 0.215\int_0^{d_1}\exp\left(-0.015N(z)-0.19z\right)\mathrm{d}z - 0.704 \tag{2.80}$$

where

B_0, B_1, and B_2 are listed functions of $(\omega/2\pi)$
$N(z)$ is the N value obtained from a standard penetration test at a depth of z from the ground surface
d_1 is the maximum depth at which the data of $N(z)$ are available
A_1 is a factor representing the statistical uncertainty of $\bar{\alpha}_{ms}$ due to scattering of data
$\log A_1$ is assumed to be frequency independent and normally distributed with zero mean and standard deviation = 0.626.

Example 2.11

Compare the shapes of PSDFs of ground accelerations as obtained by empirical expressions given by Housner and Jennings (Equation 2.70), Newmark and Rosenblueth (Equation 2.71), Kanai and Tajimi (Equation 2.73), Clough and Penzien (Equation 2.75).

Solution: Figure 2.47 shows the shapes of the spectrums given by Equations 2.70, 2.71, 2.73 and 2.76. Note that only the transfer function parts of the equations are compared (that is, all constant multiplication terms are removed). It is seen from the figure that Equations 2.73 and 2.75 provide almost identical shapes except near the zero frequencies. The other two spectra also have almost the same shape.

2.7.6 Predictive Relationships for Modulating Function

Different types of modulating functions have been proposed based on the observations of ground motion records. The commonly used modulating functions are box car type, trapezoidal type, and a modified form of the trapezoidal type in which the beginning and end portions of the trapezoid are non-linear. A box car type modulating function is expressed as:

$$\begin{aligned} A(t) &= A_0 \quad \text{for} \quad 0 \le t \le T_0 \\ &= 0 \quad \text{for} \quad t > T_0 \end{aligned} \tag{2.81}$$

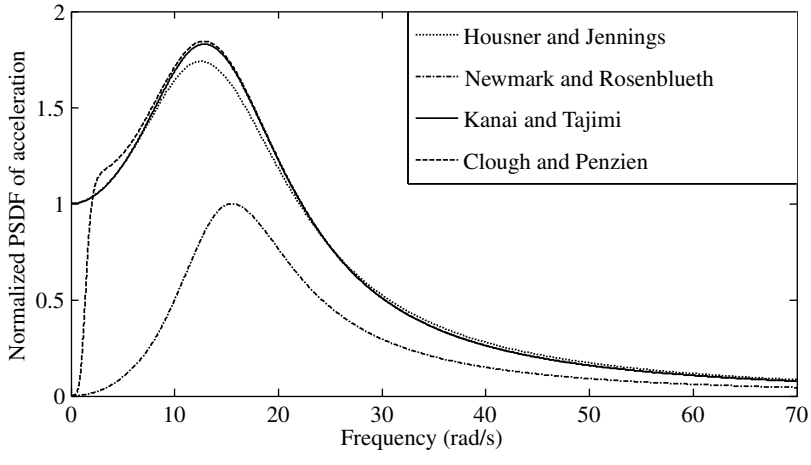

Figure 2.47 Comparison between PSDFs of ground acceleration (obtained by various empirical equations)

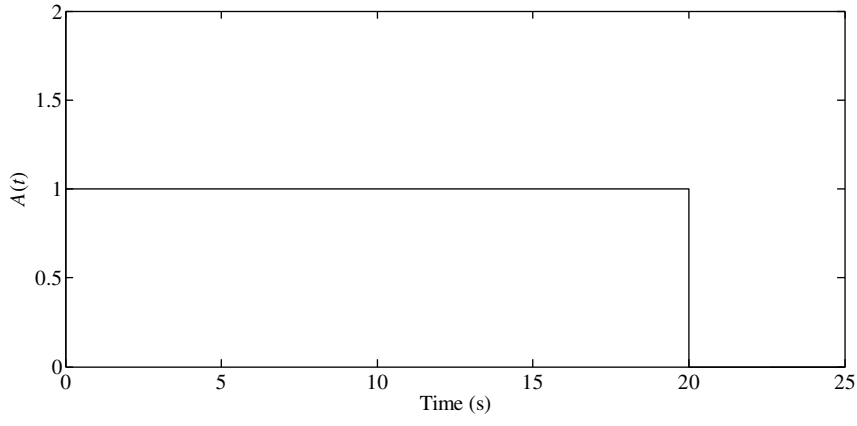

Figure 2.48 Box type modulating function

in which A_0 is the scaling factor and T_0 is the strong motion duration of earthquake. A box car type modulating function is shown in Figure 2.48.

A trapezoidal modulating function is expressed as:

$$\begin{aligned} A(t) &= A_0\left(\frac{t}{t_1}\right) && \text{for} \quad 0 \le t \le t_1 \\ &= A_0 && \text{for} \quad t_1 \le t \le t_2 \\ &= A_0\left(\frac{t-t_3}{t_2-t_3}\right) && \text{for} \quad t_2 \le t \le t_3 \\ &= 0 && \text{for} \quad t \ge t_3 \end{aligned} \tag{2.82}$$

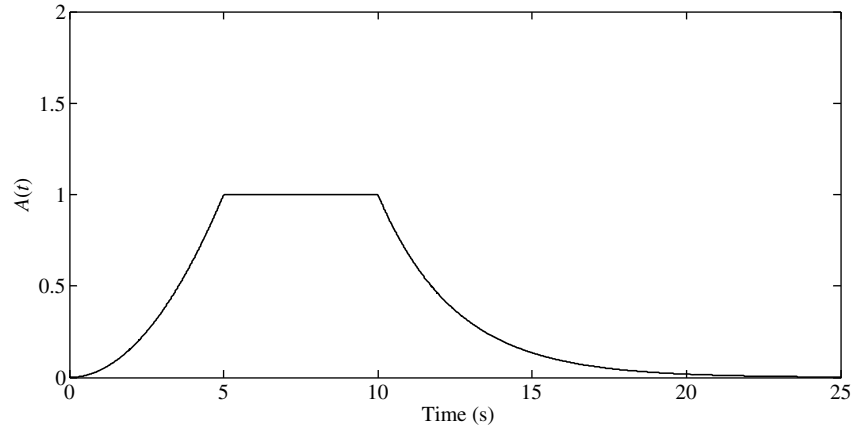

Figure 2.49 Modified trapezoidal type modulating function

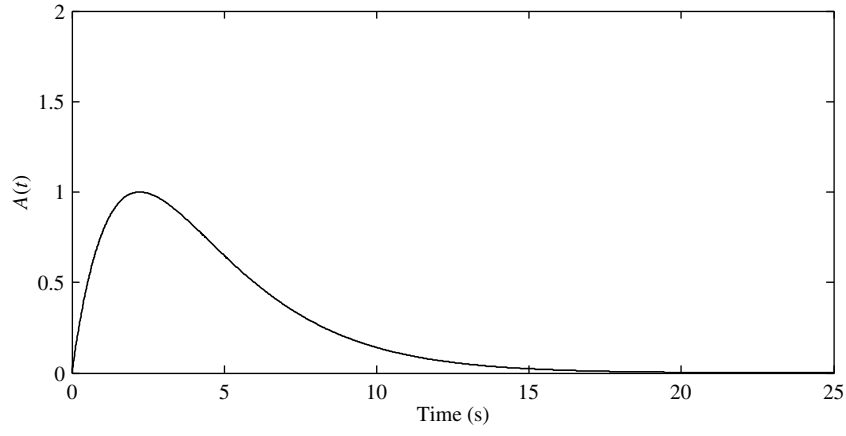

Figure 2.50 Exponential type modulating function

in which A_0 is the scaling factor and t_1, t_2, and t_3 are the transition times of the modulating function. A modified form of the trapezoidal type modulating function [29] is shown in Figure 2.49 and is given by

$$\begin{aligned} A(t) &= A_0\left(\frac{t}{t_1}\right)^2 \quad \text{for} \quad 0 < t \leq t_1 \\ &A_0 \quad \text{for} \quad t_1 \leq t \leq t_2 \\ &A_0 \mathrm{e}^{c(t-t_2)} \quad \text{for} \quad \mathrm{t} \geq \mathrm{t}_2 \end{aligned} \tag{2.83}$$

Other forms of modulating functions have been proposed by various researchers.

An exponential type modulating function (Figure 2.50) is given by:

$$A(t) = A_0(\mathrm{e}^{-b_1 t} - \mathrm{e}^{-b_2 t}) \qquad b_2 > b_1 \tag{2.84}$$

in which b_2 and b_1 control the shape of the modulating function and A_0 is the scaling factor. The parameters b_2 and b_1 are defined with the help of strong motion duration T_0 and ε, the fraction of the rise time. Trifunac and Brady [15] defined the fraction of rise time as:

$$\varepsilon = \frac{t_{\mathrm{m}}}{t_{95}} \tag{2.85}$$

in which t_m is the time at which $A(t)$ attains the maximum value and t_{95} is the time at which the energy content of the modulating function is 95%.

Kubo and Penzien [32] proposed the following modulating function:

$$A = at\mathrm{e}^{-bt} \tag{2.86}$$

in which the values of a and b are given as 0.453 and 1/6, respectively. Nielsen and Kiremidjien [33] gave an expression for modulating function as

$$A(t) = \beta t^{\gamma} \mathrm{e}^{\alpha t} \tag{2.87}$$

in which

$$\alpha = \frac{\mu_{\text{dur}}}{\sigma^2_{\text{dur}}} \quad \text{and} \quad \gamma = \frac{\mu_{\text{dur}}}{\sigma^2_{\text{dur}}} - 1 \quad \text{and} \quad \beta = \left(\frac{\gamma}{\alpha}\right)^{-\gamma} \text{e}^{\gamma} \tag{2.88}$$

where

μ_{dur} = mean duration of earthquake motion
μ^2_{dur} = variance of the duration

Spanos and Vargas Loli [34] defined an envelope function of the form

$$A(t) = t^2 \text{e}^{-\alpha t} \tag{2.89}$$

in which α is the decaying coefficient.

2.7.7 *Predictive Relationships for Coherence Function*

The spatial effect of an earthquake representing the lack of correlation between ground motions at two points that are spatially separated by a long distance has been investigated by various researchers in the context of stochastic modeling of earthquake. The analysis of strong motion data recorded at several stations led to different forms of correlation function to represent the lack of correlation between ground motions at two points. Veletsos and Prasad [35] proposed a correlation function of the form

$$\rho(|r_1 - r_2|, \omega) = \Gamma(|r_1 - r_2|, \omega) \text{e}^{\frac{-i\omega d}{c}} \tag{2.90}$$

where

d is the projected distance between the two points with position vectors r_1 and r_2
c is the apparent horizontal velocity of the form $V_s/\sin\alpha$
α is the angle of incidence of wave and $\Gamma(|r_1 - r_2|, \omega)$ is given by:

$$\Gamma(|r_1 - r_2|, \omega) = \text{e}^{(-\varepsilon\omega|r|/V_S)^2} \tag{2.91}$$

in which V_S is the shear wave velocity and ε is a factor taken between 0 and 0.5.

Harichandran and Vanmarcke [36] developed a correlation function of the form

$$\rho(r, \omega) = A\text{exp}\left[\frac{2r}{\alpha\theta(\omega)}(1 - A + \alpha A)\right] + (1 - A)\text{exp}\left[\frac{2r}{\theta(\omega)}(1 - A + \alpha A)\right] \tag{2.92}$$

in which

$$\theta(\omega) = K\left[1 + \left(\frac{\omega}{\omega_0}\right)^b\right]^{-\frac{1}{2}}$$

and where $A = 0.736$, $\alpha = 0.147$, $K = 5210$, $\omega_0 = 1.09$, $b = 2.278$ are empirical values that can be adjusted.

Hindy and Novak [37] used the following expression for the cross-correlation function between two stations as:

$$\rho(x_1, x_2, \omega) = \exp\left[-c\left(\frac{r\omega}{2\pi V_S}\right)\right] \tag{2.93}$$

where

$r = |x_2 - x_1|$ is the separation between two stations x_2 and x_1
V_S is the shear wave velocity and ω is the frequency of ground motion
c is a constant depending on the epicentral distance and inhomogeneity of the medium.

Typically, the value of c may vary between 0.5 and 4.

Loh [38] proposed expressions for the correlation function from the analysis of a SMART-1 array in the following form:

$$\rho(D_{ij}) = \exp\left(-a|D_{ij}|\right)\cos 2\pi K_0 D_{ij} \tag{2.94}$$

in which D_{ij} is the separation distance; a and K_0 are parameters that control the spatial correlation shape and which depend on the direction of wave propagation, wave type, earthquake location, and magnitude. Some reported values of a and K_0 in the reference [38] are given as $a = 2.756$; $K_0 = 4.769$. The above expression is frequency independent and analysis developed for time domain analysis. For frequency domain analysis, the following was suggested:

$$\rho(\omega, x) = \exp[-(\alpha_1 + \alpha_2 \omega |x|)] \tag{2.95}$$

in which α_1 and α_2 are constants and x is the separation distance. Banerji [39] introduced a spatial coherence function in the form of:

$$\rho(d, \omega) = \exp[-(a\omega^2 d)^{0.75}] \tag{2.96}$$

where d is the separation distance, ω is the frequency, and $a = 5 \times 10^5$. Abrahamson *et al.* [40] proposed a spatial correlation function as:

$$\rho(d, \omega) = \tanh\left[(a_1 + a_2 d)\{\exp[(b_1 + b_2 d)\omega]\} + \frac{1}{3}\omega^c + K\right] \tag{2.97}$$

in which $a_1 = 2.535$, $a_2 = -0.0118$, $b_1 = -0.115$, $b_2 = 0.000837$, $c = -0.878$, and $K = 0.35$.

Clough and Penzien [6] suggested a correlation function of the form:

$$\varsigma_{ij}(i\omega) = \exp\left(-\alpha|d_{ij}|\right)\exp\left[-i\omega\frac{d_{ij}}{V_s(\omega)}\right] \tag{2.98}$$

where

d_{ij} is the distance between two points i and j
α is a parameter reflecting the rate of loss of correlation
$V_s(\omega)$ is the frequency dependent apparent wave velocity
ω is the frequency.

A simpler form of the above equation has also been suggested which considers $V_s(\omega)$ to be frequency independent and the rate of loss of the correlation term is ignored. Thus, $\varsigma_{ij}(i\omega)$ is given by:

$$\varsigma_{ij}(i\omega) = \exp\left[-i\omega\frac{d_{ij}}{V_S}\right] \tag{2.99}$$

Equation 2.99 is a complex (function) form of Equation 2.93 proposed by Hindy and Novak [37].

Exercise Problems

(Use standard programs like MATLAB, SAP2000 and ABAQUAS to solve the problems; you may also use your own program developed using the methods presented in the chapter.)

2.12 Take the Lomaprieta earthquake acceleration record from web site www.pear.berkely.edu/scat and obtain the Fourier amplitude and phase spectra using FFT. Retrieve the time history of acceleration taking IFFT of the Fourier components. Find the values of the following:
(i) Maximum ordinates of Fourier amplitudes and frequencies of their occurrence before and after smoothening.
(ii) Maximum phase angle and Nyquist frequency.
(iii) Rms acceleration obtained from the time history and Fourier components.
(iv) Absolute maximum ordinates of original time history and the retrieved one.

2.13 Assuming the above time history of acceleration to be a sample of an ergodic stationary process, obtain a smoothed PSDF of acceleration. Find the rms and expected peak values of acceleration from the PSDF and compare them with the rms and absolute peak values of the actual time history of acceleration.

2.14 Take the San Fernando earthquake acceleration from web site www.peer.berkley.edu/smcat and obtain the normalized smoothed Fourier spectrum, energy spectrum, and pseudo acceleration spectrum($\xi = 0.05$). Compare between the maximum values of the ordinates and the corresponding time periods of the three spectra.

2.15 Draw the response spectrum of the earthquake given in Exercise problem, 2.14 in the tripartite plot, and then idealize it by a series of straight lines. Compare T_a, T_b, T_c, T_d, T_e, and T_f with those of the El Centro earthquake.

2.16 Construct design response spectra for the 50th and 84th percentiles on a four way log graph paper for 5% damping for the hard soil for a site with $R = 75$ km and $M = 7.5$. Use Equations 2.44, 2.49 and 2.57 for finding PHA, PHV, and PHD. Take $T_a = 1/33$ s; $T_b = 1/8$ s; $T_e = 10$ s, and $T_f = 33$ s.

2.17 For a site, the mean annual rate of exceedances of normalized ordinates of acceleration response spectrum and PGA are given in Table 2.6 and 2.7. Obtain a uniform hazard spectrum that has a 10% probability of exceedance in 50 years:

Table 2.6 Annual rate of exceedance (a_r) of acceleration response spectrum ordinates

T	$\bar{S}$							
	0.05	0.2	0.6	1	1.5	2	2.5	3
0.1	0.4	0.4	0.4	0.3	0.25	0.2	0.15	0.12
0.3	0.3	0.3	0.3	0.26	0.22	0.18	0.11	0.08
0.5	0.22	0.22	0.22	0.19	0.16	0.13	0.09	0.06
0.7	0.1	0.1	0.1	0.07	0.05	0.02	0.008	0.005
0.9	0.05	0.05	0.05	0.03	0.015	0.009	0.007	0.004
1.0	0.01	0.01	0.01	0.007	0.005	0.003	0.001	0.0008
1.2	0.008	0.008	0.008	0.006	0.005	0.004	0.0009	0.0007
1.4	0.005	0.005	0.005	0.004	0.003	0.002	0.0007	0.0005
1.6	0.004	0.004	0.004	0.004	0.003	0.0015	0.0006	0.0004
1.8	0.003	0.003	0.003	0.002	0.002	0.001	0.005	0.0003
2.0	0.0025	0.0025	0.0025	0.0025	0.001	0.0008	0.0004	0.0002

Table 2.7 Annual rate of exceedance (a_r) of PGA

PGA	0.01 g	0.05 g	0.1 g	0.15 g	0.2 g	0.3 g	0.4 g	0.45 g
a_r	0.45	0.2	0.1	0.05	0.02	0.006	0.002	0.001

2.18 A site specific acceleration spectrum is to be constructed for a site that has a layer of soft soil over a rock bed. Past earthquake records on the rock outcrop at some distance away from the site shows that the pseudo velocity spectrum of the expected earthquake can be fairly represented by Equation 2.69. The values of the ordinates of the pseudo acceleration spectrum are given in Figure 2.45. The soft soil deposit has a predominant period of 2 s. The soil condition modifies the shape of the normalized spectrum at rock level in the following manner.

(i) At the predominant period ($T = 2$ s) ordinate of the modified spectrum is three times that of the rock bed spectrum.

(ii) At other periods, the ordinates of the modified spectrum are given by $S_i = S_{oi} \times \lambda$ in which $\lambda \approx 1.5$.

(iii) At $T = 0$, $S_o(0) = S(0) = 1$.

If the PGA amplification is 3.0 due to the soft soil deposit, construct the site specific acceleration response spectrum for $M_W = 7$. Use the attenuation relationship (at the rock bed) proposed by Esteva (Equation 2.43) for finding PGA with a value of R taken as 100 km.

2.19 Assuming $\omega_f = 0.1\omega_g$, $\xi_g = \xi_f$, $\omega_g = 10\pi$, and $\xi_g = 0.4$, obtain an expression for the PSDF of ground acceleration in terms of M, R, and the filter characteristics using double filter PSDF (Equation 2.75) and attenuation relationship given by Campbell (Equation 2.44). From this expression, find the peak values and corresponding frequencies of the PSDF for $M = 7$, $R = 50$ and 100 km. If Equations 2.54 and 2.51 were used in place of Equation 2.44, find the same expression in terms of only M. Also, find the peak value and the corresponding frequency of the PSDF for $M = 7$.

2.20 A traveling train of seismic wave moves with a shear wave velocity of $V_S = 150\ \text{m s}^{-1}$. The direction of wave propagation is at an angle of 20° with the line joining three bridge piers (A, B, C): AB = BC = 400 m. If the ground acceleration produced by the seismic wave is modeled as a stationary random process, then find PSDF matrix of ground accelerations in the major principal direction (assumed as the direction of wave propagation) at the base of the piers (A, B, C) using the following data:

(i) PSDF of ground acceleration is represented by the expression given by Clough and Penzien (Equation 2.75) with a PGA = 0.4 g.

(ii) Coherence functions to be used are

(a) that given by Hindy and Novak (Equation 2.94)

(b) that given by Clough and Penzien (Equation 2.99)

(c) that given by Harichandran and Vanmarcke (Equation 2.93)

(d) that given by Loh (Equation 2.95)

2.21 A time history of ground motion is artificially generated using the following Fourier series coefficients for a duration of 20 s.

$$\ddot{x}(t) = \sum_{n=1}^{16} A_n Cos\,(\omega_n t + \varphi_n);\ \omega_n \text{ is in rad s}^{-1} \text{ and } \varphi_n \text{ is in rad.}$$

$A_1 = 0.25g\ (\omega_1 = 0.85;\quad \phi_1 = 0.1)\quad A_9 = 0.05g\ (\phi_9 = 0.05)$

$A_2 = 0.2g\ (\phi_2 = 0.18)\quad A_{10} = 0.2g\ (\phi_{10} = -0.12)$

$A_3 = 0.1g\ (\phi_3 = 0.3)\quad A_{11} = 0.15g\ (\phi_{11} = -0.05)$

$A_4 = 0.05g\ (\phi_4 = 1.25)\quad A_{12} = 0.1g\ (\phi_{12} = -0.02)$

$A_5 = 0.12g\ (\phi_5 = 2)\quad A_{13} = 0.12g\ (\phi_{13} = 0.12)$

$A_6 = 0.18g\ (\phi_6 = 2.6)\quad A_{14} = 0.08g\ (\phi_{13} = 0.15)$

$$A_7 = 0.2g\ (\phi_7 = -0.2) \quad A_{15} = 0.04g\ (\phi_{14} = 0.4)$$

$$A_8 = 0.1g\ (\phi_8 = -0.4) \quad A_{16} = 0.02g\ (\phi_{16} = 0.25)$$

ω_2–ω_{16} is given by $\omega_n = n\omega_1 n = 2$–16

The generated time history is modulated by modulating functions given by Equations 2.84, 2.85, and 2.87. Find the absolute peak and rms values of acceleration and compare them. Also, make a comparison between the times at which (absolute) peaks occur. Take the maximum value of the modulating function to be unity. Take $c = 0.5$, $t_1 = 5$ s, $t_2 = 10$ s for Equation 2.84 and $b_1 = 0.412$,; $b_2 = 0.8$ for Equation 2.85.

References

1. NewLand, D.E. (1978) *An Introduction to Random Vibrations and Spectral Analysis*, 2nd edn, Longman, London.
2. Brune, J.N. (1970) Tectonic stress and the spectra of seismic shear waves from earthquakes. *Journal of Geophysical Research*, **75**, 4997–5009.
3. Lin, Y.K. (1967) *Probabilistic Theory of Structural Dynamics*, McGraw-Hill International, New York.
4. Chopra, A.K. (2001) *Dynamics of Structures, Theory and Application to Earthquake Engineering*, 2nd edn, Prentice Hall, Englewood Cliffs, NJ.
5. Yang, C.Y. (1967) *Probabilistic Theory of Structural Dynamics*, McGraw-Hill International, New York.
6. Clough, R.W. and Penzien, J. (1993) *Dynamics of Structures*, 2nd edn, McGraw-Hill International, New York.
7. Esteva, L. (1969) Seismic risk and seismic design decisions. Paper presented at the Seminar on Seismic Design of Nuclear Power Plants, Cambridge.
8. Campbell, K.W. (1981) Near source attenuation of peak horizontal acceleration. *Bulletin of Seismological Society of America*, **71**, 2039–2070.
9. Campbell, K.W. and Bozorgnia, Y. (1994) Near-source attenuation of peak horizontal acceleration from worldwide accelerograms recoded from 1957 to 1993. Proceedings, Fifth U.S. National Conference on Earthquake Engineering, Earthquake Engineering Research Institute, Berkeley, California, vol. 1, pp. 283–292.
10. Toro, G.R., Abrahamson, N.A., and Schneider, J.F. (1995) Engineering model of strong ground motions from earthquakes in the central and eastern United States. *Earthquake Spectra*, **10**, 13–30.
11. Esteva, L. and Rosenblueth, E. (1964) Espectros de temblores a distancias moderadas y grandes. *Boletin de la Sociedad Mexicana Ingenieria Sismologia*, **2**(1), 1–18.
12. Shinozuka, M., Takada, S., and Ishikawa, H. (1979) Some aspects of seismic risk analysis of underground lifeline systems. *Journal of Pressure Vessel Technology, Transactions of the ASME*, **101**, 31–43.
13. Cornell, C.A. (1968) Engineering seismic risk analysis. *Bulletin Seismological Society of America*, **58**, 1583–1606.
14. Gutenberg, B. and Richter, C.F. (1956) Earthquake magnitude: intensity, energy, and acceleration. *Bulletin of Seismological Society of America*, **46**, 104–145.
15. Trifunac, M.D. and Brady, A.G. (1975) On the correlation of seismic intensity with peaks of recorded strong ground motion. *Bulletin of Seismological Society of America*, **65**, 139–162.
16. Shinizuka, M., Takada, S., and Ishikawa, H. (1979) Some aspects of seismic risk analysis of under ground infinite systems. *Journal of Pressure Vessel Technology, Transactions of the ASME*, **101**, 31–43.
17. Joyner, W.B. and Boore, D.M. (1988) Measurement, characterization, and prediction of strong ground motion, *Earthquake Engineering and Soil Dynamics II – Recent Advances in Ground Motion Evaluation*, Geotechnical Special Publication 20, ASCE, New York, pp. 43–102.
18. McGuire, R.K. (1978) Seismic ground motion parameter relations. *Journal of the Geotechnical Engineering Division, ASCE*, **104**(GT4), 481–490.
19. Chang, F.K. and Krinitzsky, E.L. (1977) Duration, spectral content, and predominant period of strong motion earthquake records from western United States. Miscellaneous Papers 5-73-1, U.S. Army Corps of Engineers Waterways Experiment Station, Vicksburg, Mississippi.
20. Boore, D.M. (1983) Stochastic simulation of high-frequency ground motions based on seismological models of radiated spectra. *Bulletin of Seismological Society of America*, **73**, 1865–1884.
21. Hanks, T.C. and McGuire, R.K. (1981) The character of high-frequency strong ground motion. *Bulletin of Seismological Society of America*, **71**(4), 2071–2095.
22. Kavazanjian, E., Echezuria, H., and McCann, M.W. (1985) RMS acceleration hazard for San Francisco. *Soil Dynamics and Earthquake Engineering*, **4**(3), 5.

23. Campbell, K.W. and Duke, C.M. (1974) Bedrock intensity, attenuation, and site factors from San Fernando earthquake records. *Bulletin of Seismological Society of America*, **64**(1), 173–185.
24. McGuire, R.M. and Hanks, T.C. (1980) RMS accelerations and spectral amplitudes of strong ground motion during the San Fernando, California earthquake. *Bulletin of Seismological Society of America*, **70**, 1907–1919.
25. Boore, D.M., Joyner, W.B., and Fumal, T.E. (1993) Estimation of response spectra and peak accelerations from western north America earthquakes: An interim report, Open-File-Report 93-509, U.S. Geological Survey, Reston, Virginia, p. 72.
26. Kramer, S.L. (1996) *Geotechnical Earthquake Engineering*, Pearson Education Inc., Upper Saddle River, NJ.
27. Ishii, K., Kumwra, T., and Suzuki, M. Earthquake ground motions consistent with probabilistic hazard analysis. Structural Safety and Realiability, vol. 1, Proceeding of ICOSSAR'89, San Francisco.
28. Kanai, K. (1957) Semi empirical formula for the seismic characteristics of the ground. *Bulletin of Earthquake Resistant Institute, University of Tokyo*, **35**, 309–325.
29. Housner, G.W. and Jennings, P.C. (1964) Generation of artificial earthquakes. *Journal of Engineering Mechanic Division, ASCE*, **90**, 113–150.
30. Newmark, N.M. and Rosenblueth, E. (1971) *Fundamentals of Earthquake Engineering*, Prentice-Hall, Englewood Cliffs, NJ.
31. Shinozuka, M., Kameda, H., and Koike, T. (1983) Ground strain estimation for seismic risk analysis. *Journal of Engineering Mechanic Division, ASCE*, **109**, 175–191.
32. Kubo, T. and Penzien, J. (1979) Simulation of three-dimensional strong ground motions along principal axes, San Fernando Earthquake. *Earthquake Engineering and Structural Dynamics*, **7**, 279–294
33. Nielson, R.J. and Kiremidjien, A.S. (1988) Tall column reliability under non-stationary loads: Model formulation. *Journal of Engineering Mechanic Division, ASCE*, **114**(7), 1107–1120.
34. Spanos, P.D. and Vargas Loli, L.M. (1985) A statistical approach to generation of design spectrum compatible earthquake time histories. *Soil Dynamics and Earthquake Engineering*, **4**(1), 2–8.
35. Veletsos, A.S. and Prasad, A.M. (1989) Seismic interaction of structures and soils: Stochastic approach. *Journal of Engineering Mechanic Division, ASCE*, **115**(4), 935–956.
36. Harichandran, R.S. and Vanmarcke, E.H. (1986) Stochastic vibration of earthquake ground motion in space and time. *Journal of Engineering Mechanic Division, ASCE*, **112**(2), 154–174.
37. Hindy, A. and Novak, M. (1980) Pipeline response to random ground motion. *Journal of Engineering Mechanic Division, ASCE*, **106**, 339–360.
38. Loh, C.H. (1985) Analysis of the spatial variation of seismic waves and ground movements from SMART-1 array data. *Earthquake Engineering and Structural Dynamics*, **13**, 561–581.
39. Banerji, P. (1994) Earthquake ground motion characterization for large or multiply-supported structures. *Current Science*, **67**, 386–394.
40. Abrahamson, N.A., Scheider, J.F., and Stepp, J.C. (1991) Empirical spatial coherency functions for application to soil-structure interaction analysis. *Earthquake Spectra*, **7**, 1–27.

3

Response Analysis for Specified Ground Motions

3.1 Introduction

Different types of ground motion inputs for the seismic response analysis of structures are described in the previous chapter. Depending upon the available input information, methods for seismic response analysis of structures may be classified under: (i) time history analysis; (ii) response spectrum method of analysis; and (iii) frequency domain spectral analysis. While the time history analysis is applicable for both elastic and inelastic ranges of response, the other two methods are essentially valid within the elastic range. However, both methods may be extended for the approximate response analysis in the inelastic range by using suitable techniques. Time history analysis is performed to obtain the response of structures for a specified time history of excitation using different techniques, such as the Duhamel integration, step-by-step numerical integration, and the Fourier transform approach. The response spectrum method of analysis uses response spectra of earthquakes as input and obtains a set of lateral equivalent (static) forces for the structure, which will provide the maximum effect on it caused by the ground motions. The internal forces in the structure are obtained by a static analysis. Frequency domain spectral analysis is performed when the earthquake ground motion is modeled as a stationary random process. Using the principles of random vibration analysis, it provides the power spectral density function (PSDF) of any response quantity of interest for a given PSDF of ground motion as the input. The root mean square response and expected peak response are obtained from the moments of the PSDF of response. In this chapter, the time history analysis of structures for a specified time history of ground motion is presented.

3.2 Equation of Motion for a Single Degree of Freedom (SDOF) System

The equation of motion for the single degree of freedom system can be written in three different forms, namely: (i) with relative motions of the mass with respect to the support as unknown variables; (ii) with absolute motions of the mass as unknown variables; and (iii) with state variables as the unknown. Use of the three different forms of the equation of motion depends upon the available input information, the response quantity of interest, and the type of analysis performed.

Seismic Analysis of Structures T.K. Datta

3.2.1 Equation of Motion in Terms of the Relative Motions of the Mass

The equation of motion of the single degree of freedom system, shown in Figure 3.1, for the support acceleration defined by $\ddot{x}_g$ can be written as:

$$m\ddot{x} + c\dot{x} + kx = -m\ddot{x}_g \tag{3.1}$$

in which m, c, and k are the mass, the damping coefficient of the viscous damper, and the stiffness of the spring, respectively; x, $\dot{x}$, and $\ddot{x}$ are the relative displacement, velocity and acceleration of the mass with respect to the support, respectively. The equation of motion can be derived using D'Alambert's principle and is given in any standard textbook on dynamics. It is evident from Equation 3.1 that only support acceleration is to be specified as input for finding the relative motions. Furthermore, Equation 3.1 shows that $|\ddot{x}^t| = |\omega_n^2 x_{max}|$ in which $\ddot{x}^t = \ddot{x} + \ddot{x}_g$ and $\omega_n^2 = k/m$, as $\dot{x} = 0$ at $x = x_{max}$.

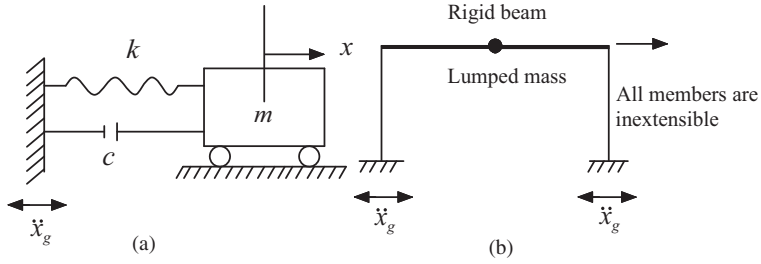

Figure 3.1 Models for a single degree of freedom (SDOF): (a) spring-mass-dashpot system; and (b) idealized single frame

3.2.2 Equation of Motion in Terms of the Absolute Motion of the Mass

The absolute motions can be obtained by adding the support motions to the relative motions, that is,

$$x^t = x + x_g; \qquad \dot{x}^t = \dot{x} + \dot{x}_g; \qquad \ddot{x}^t = \ddot{x} + \ddot{x}_g \tag{3.2}$$

in which x^t, $\dot{x}^t$, and $\ddot{x}^t$ are the total or absolute motions of the mass. Substituting for x, $\dot{x}$, and $\ddot{x}$ in Equation 3.1 and recognizing that the inertia force depends upon the absolute acceleration, Equation 3.1 can be rewritten as:

$$m\ddot{x}^t + c\dot{x}^t + kx^t = c\dot{x}_g + kx_g \tag{3.3}$$

The solution to Equation 3.3 provides the absolute motions of the mass directly. The required inputs for Equation 3.2 are both support displacement and velocity. Note that the expressions for the effective dynamic force acting on the SDOF system due to earthquake excitation are different for the two equations, that is, Equations 3.1 and 3.3. For the equation of motion written in terms of relative motions, the equivalent dynamic force is the inertia force produced by the support acceleration only, while that written in terms of absolute motions, the equivalent dynamic force is the sum of the damping force and spring force (elastic force) produced by the velocity and displacement of the support, respectively.

3.2.3 Equation of Motion in State Space

Equations 3.1 and 3.2 are the second-order differential equations representing the equation of motion of the SDOF system subjected to the support motion. These two equations can also be written in the form of

a set of coupled first-order differential equations, known as the equations of motion in the state-space form. The state-space form of Equation 3.1 is

$$\dot{\boldsymbol{X}} = \boldsymbol{A}\boldsymbol{X} + \boldsymbol{f} \tag{3.4a}$$

in which

$$\boldsymbol{X} = \begin{Bmatrix} x \\ \dot{x} \end{Bmatrix}; \qquad \boldsymbol{A} = \begin{bmatrix} 0 & 1 \\ -\dfrac{k}{m} & -\dfrac{c}{m} \end{bmatrix}; \qquad \boldsymbol{f} = \begin{Bmatrix} 0 \\ -\ddot{x}_g \end{Bmatrix} \tag{3.4b}$$

The state of the system at any instant of time is represented by the vector $\boldsymbol{X}$. Similarly, the state-space form of Equation 3.3 is

$$\dot{\boldsymbol{X}}^{\mathrm{t}} = \boldsymbol{A}\boldsymbol{X}^{\mathrm{t}} + \boldsymbol{F}\bar{\boldsymbol{f}} \tag{3.5a}$$

in which

$$\boldsymbol{X}^{t} = \begin{Bmatrix} x^{t} \\ \dot{x}^{t} \end{Bmatrix}; \qquad \boldsymbol{F} = \begin{bmatrix} 0 & 0 \\ k & c \end{bmatrix}; \qquad \bar{\boldsymbol{f}} = \begin{Bmatrix} x_g \\ \dot{x}_g \end{Bmatrix} \tag{3.5b}$$

The solution of the equation of motion written in state-space form is useful in many applications such as, structural control problems, and is better suited for the use of certain computational schemes for solving the equation of motion. Methods of solution for the three forms of the equations of motion will be described later.

3.3 Equations of Motion for a Multi-Degrees of Freedom (MDOF) System

For the extension of the equation of motion of the SDOF system to the multi-degrees of freedom system (MDOF), the nature of the support motions (excitations) is important. Two types of support excitations namely, single-support excitation and multi-support excitations are possible. In the case of single-support excitation, it is assumed that the ground motion is the same for all supports of the structure so that the support points move as one rigid base, as shown in Figure 3.2. As a consequence, masses attached to dynamic degrees of freedom are excited by the same ground motion (acceleration). Examples of such systems are tall buildings, towers, chimneys, and so on, for which the distances between the supports are not very large compared with the predominant wave length of the ground motion. In the case of multi-support excitations, the ground motions or support excitations are different at different support points, as shown in Figure 3.3. For the same traveling wave of an earthquake, the time histories of ground motion at two supports could be different if the two supports are spatially separated by a large distance. This is the case because the travel time of the wave between any two supports is not sufficiently negligible to make the assumption that the ground motions are the same at the two supports. Examples of such systems are a big network of pipelines, underground pipelines, very long tunnels, trans-country pipelines carrying gas, long dams, and bridges.

3.3.1 Equations of Motion for Single-Support Excitation

For single-support excitation, the same ground acceleration excites all masses. Therefore, the equation of motion of the MDOF system in the matrix form can be written as:

$$\boldsymbol{M}\ddot{\boldsymbol{X}}^{t} + \boldsymbol{C}\dot{\boldsymbol{X}} + \boldsymbol{K}\boldsymbol{X} = 0 \tag{3.6}$$

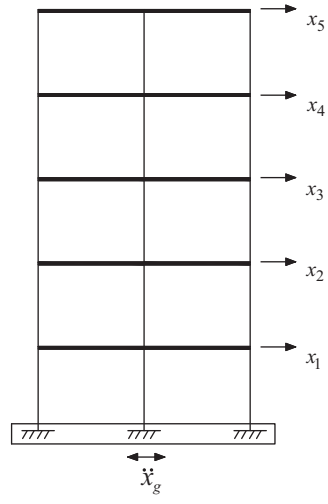

Figure 3.2 Multi-degrees of freedom system with single-support excitation

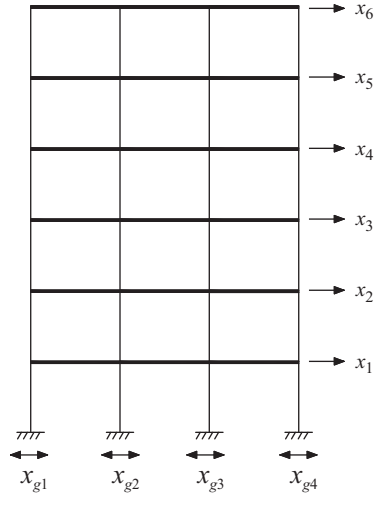

Figure 3.3 Multi-degrees of freedom system with multi-support excitations

in which $\boldsymbol{M}$, $\boldsymbol{C}$, and $\boldsymbol{K}$ are the mass, damping, and stiffness matrices, respectively. If a lumped mass idealization is made, then the mass matrix is a diagonal matrix; $\ddot{\boldsymbol{X}}^t$ is the vector of absolute acceleration; $\dot{\boldsymbol{X}}$ and $\boldsymbol{X}$ are, respectively, the vectors of relative displacement and velocity with respect to the supports. Derivation of the equation of motion is available in any standard textbook on dynamics. For the ith degree of freedom, the mass associated with it and the corresponding acceleration are m_i and $\ddot{x}_i^{\mathrm{t}}$, where $\ddot{x}_i^{\mathrm{t}}$ is given by:

$$\ddot{x}_i^{\mathrm{t}} = \ddot{x}_i + \ddot{x}_{gi} \tag{3.7}$$

in which $\ddot{x}_i$ is the relative acceleration of the mass m_i with respect to the support and $\ddot{x}_{gi}$ is the component of ground acceleration in the direction of the ith degree of freedom. For single-component earthquake excitation, that is, ground motion applied only in one direction, $\ddot{x}_{gi} = \ddot{x}_g$ for degrees of freedom that have the same direction as that of the applied ground motion; and $\ddot{x}_{gi} = 0$ for other degrees of freedom. Then, Equation 3.6 can be written as

$$\boldsymbol{M}\ddot{\boldsymbol{X}} + \boldsymbol{C}\dot{\boldsymbol{X}} + \boldsymbol{K}\boldsymbol{X} = -\boldsymbol{M}\boldsymbol{I}\ddot{\boldsymbol{X}}_{\boldsymbol{g}} \tag{3.8}$$

in which $\ddot{\boldsymbol{X}}$ is the vector of relative acceleration and $\boldsymbol{I}$ is the influence coefficient vector, having 1 for elements corresponding to degrees of freedom in the direction of the applied ground motion and zero for the other degrees of freedom.

For the two-component and the three-component ground motions, $\boldsymbol{I}$ is a matrix of the form, and T stands for transpose:

$$\boldsymbol{I}^T = \begin{bmatrix} 1 & 0 & 1 & 0 & - & - & - & - & - & - \\ 0 & 1 & 0 & 1 & - & - & - & - & - & - \end{bmatrix} \tag{3.9a}$$

for the two-component ground motion and

$$\boldsymbol{I}^T = \begin{bmatrix} 1 & 0 & 0 & 1 & 0 & 0 & - & - & - & - \\ 0 & 1 & 0 & 0 & 1 & 0 & - & - & - & - \\ 0 & 0 & 1 & 0 & 0 & 1 & - & - & - & - \end{bmatrix} \tag{3.9b}$$

for the three-component ground motion, in which 1 corresponds to degrees of freedom in the direction of the component of ground motion. Then, $\ddot{\boldsymbol{X}}_{\boldsymbol{g}}$ in Equation 3.8 is replaced by a vector of the form

$$\ddot{\boldsymbol{X}}_g = \begin{Bmatrix} \ddot{x}_{g1} \\ \ddot{x}_{g2} \end{Bmatrix} \tag{3.10a}$$

for the two-component ground motion and

$$\ddot{\boldsymbol{X}}_g = \begin{Bmatrix} \ddot{x}_{g1} \\ \ddot{x}_{g2} \\ \ddot{x}_{g3} \end{Bmatrix} \tag{3.10b}$$

for the three-component ground motion.

Example 3.1

Determine the influence coefficient vectors or matrices for the following structures subjected to ground excitations as shown in Figure 3.4(a–c). The dynamic degrees of freedom are indicated in the figure.

Solution: For the structures shown in Figure 3.4(a–c), the degrees of freedom and the corresponding influence coefficient vectors or matrices $\boldsymbol{I}$ are:

$$\boldsymbol{I} = \begin{Bmatrix} 1 \\ 0 \\ 1 \\ 1 \end{Bmatrix} \begin{matrix} u_1 \\ v_1 \\ u_2 \\ u_3 \end{matrix}$$

Refer to Figure 3.4a

$$\boldsymbol{I} = \begin{Bmatrix} 1 \\ 1 \\ 1 \end{Bmatrix} \begin{matrix} u_1 \\ u_2 \\ u_3 \end{matrix}$$

Refer to Figure 3.4b

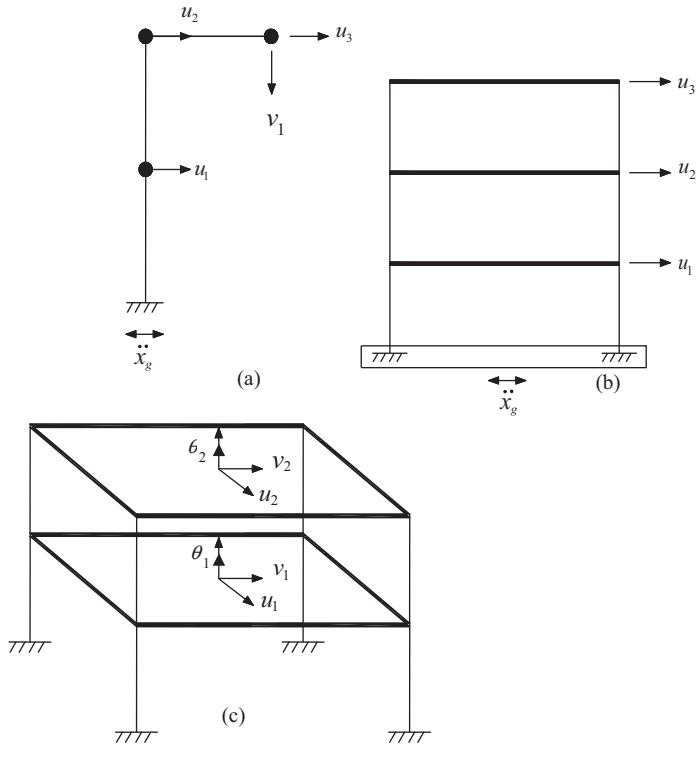

Figure 3.4 Frame structure: (a) bracket frame; (b) shear building frame; and (c) 3D model of a shear building frame

$$\boldsymbol{I} = \begin{Bmatrix} 1 \\ 0 \\ 0 \\ 1 \\ 0 \\ 0 \end{Bmatrix} \begin{matrix} u_1 \\ v_1 \\ \theta_1 \\ u_2 \\ v_2 \\ \theta_2 \end{matrix} \qquad \boldsymbol{I} = \begin{bmatrix} 1 & 0 \\ 0 & 1 \\ 0 & 0 \\ 1 & 0 \\ 0 & 1 \\ 0 & 0 \end{bmatrix} \begin{matrix} u_1 \\ v_1 \\ \theta_1 \\ u_2 \\ v_2 \\ \theta_2 \end{matrix}$$

Case 1; refer to Figure 3.4c Case 2; refer to Figure 3.4c

Case 1 refers to the single component ground motion acting along the direction of u_1
Case 2 refers to the two-component ground motion acting along both u_1 and u_2 directions.

Example 3.2

The framed structure supporting a rigid slab as shown in Figure 3.5(a and b) can be modeled for dynamic degrees of freedom in two different ways. For the first model (Figure 3.5a), three independent degrees of freedom can be selected as u_1, u_2, and u_3. For the second model (Figure 3.5b), three dynamic degrees of

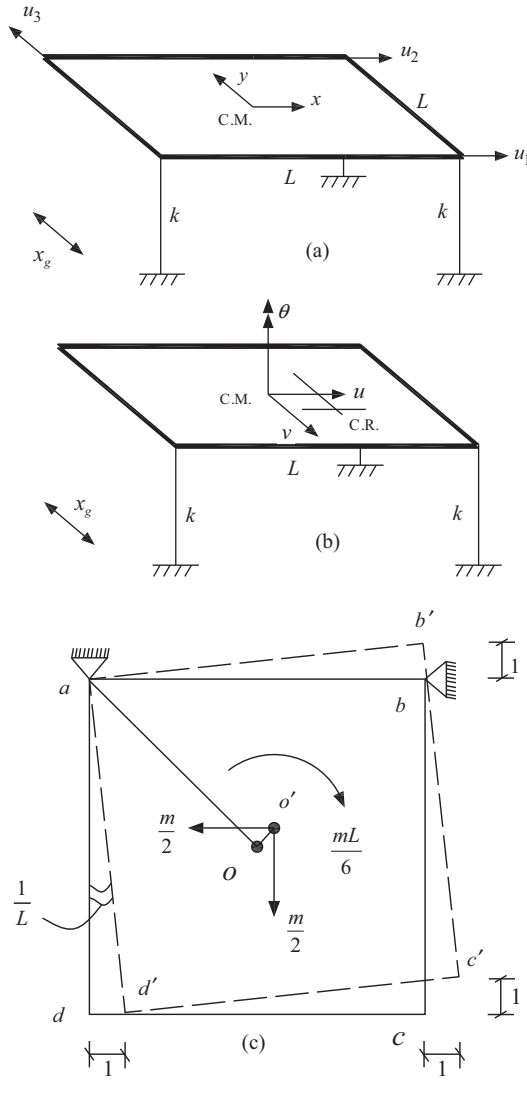

Figure 3.5 A rigid slab supported by three columns: (a) model 1; (b) model 2; and (c) unit acceleration given to u_1

freedom are considered at the center of mass (C.M.) of the rigid slab. In the same figure, the center of resistance (C.R.) is shown. Determine the mass and stiffness matrices for the two models and the corresponding influence coefficient vectors $\boldsymbol{I}$. The lateral resistance provided by each column in both directions are the same and is equal to k. Total mass of the slab is m (uniformly distributed over the area). The masses of the columns are ignored.

Solution: The derivation of stiffness matrices for the two models follows the standard procedure for the direct generation of the stiffness matrix of the structure.

The mass matrix for model 2 is a diagonal matrix and is obtained by lumping the total mass corresponding to the translational degrees of freedom and by finding the mass moment of inertia corresponding to the torsional degree of freedom, θ.

The mass matrix for model 1 is generated by applying a unit acceleration to a particular degree of freedom keeping the other dynamic degrees of freedom locked. The mass inertia coefficients at different degrees of freedom required to equilibrate the resulting inertia forces developed in the masses are arranged in the matrix form to generate the mass matrix. For example, generation of the first column of the mass matrix of model 1 is explained below. Other columns are similarly generated.

The slab *abcd* is given a unit acceleration consistent with the motion of the degree of freedom u_1, keeping u_2 and u_3 locked as shown in Figure 3.5c. Because of the rigid body motion, d will move to d' in a direction perpendicular to *ad. S*imilarly, c and b will move to c' and b' in directions perpendicular to *ac* and *ab*, respectively, and the centre o of the slab will move to o' in a direction perpendicular to *ao*. Note that b undergoes no displacement along the direction u_2. As o moves to o', the center of mass of the slab has a rotational acceleration of $1/L$ and is displaced in the x and y directions such that the respective inertia forces at the center of mass are as shown in the figure. An opposing rotational force is required in the form of a couple of forces $m/6$ and $m/6$ at b and c, respectively, to equilibrate the rotational inertia force at the centre. At b, the force is opposite to the direction of u_2, while at c it is in the same direction as u_1.

Furthermore, a mass inertia coefficient of $m/2$ is to be applied at c to cause the motion in the direction of u_1 and to equilibrate the horizontal inertia force at the center of the slab. Similarly, a mass inertia coefficient of $m/2$ is applied at a to equilibrate the vertical inertia force at the center of the slab. Thus, the total mass inertia coefficient corresponding to u_1 is

$$\frac{m}{6}+\frac{m}{2}=\frac{4m}{6}$$

For u_2, it is $-m/6$ and for u_3, it is $m/2$. Note that the net vertical and horizontal forces form opposing couples to hold the slab in rotational equilibrium. The mass matrix, stiffness matrix, and influence coefficient vectors for the two models are given below.

For model 1

$$\boldsymbol{K}=k\begin{bmatrix}4&-2&2\\-2&3&-2\\2&-2&3\end{bmatrix};\quad \boldsymbol{M}=\frac{m}{6}\begin{bmatrix}4&-1&3\\-1&4&-3\\3&-3&6\end{bmatrix};\quad \boldsymbol{I}=\begin{Bmatrix}0\\0\\1\end{Bmatrix}$$

For model 2

$$\boldsymbol{K}=k\begin{bmatrix}3&0&0.5L\\0&3&0.5L\\0.5L&0.5L&1.5L^2\end{bmatrix};\quad \boldsymbol{M}=m\begin{bmatrix}1&0&0\\0&1&0\\0&0&\frac{L}{6}\end{bmatrix};\quad \boldsymbol{I}=\begin{Bmatrix}0\\1\\0\end{Bmatrix}$$

Note that there is an inertia coupling between the three degrees of freedom for model 1 and therefore, the mass matrix is not diagonal.

Effective force vectors for the two models are:

$$\boldsymbol{P}_{\mathbf{eff}}\ (\text{model 1})=-\frac{m}{6}\begin{Bmatrix}3\\-3\\6\end{Bmatrix}\ddot{x}_g;\quad \boldsymbol{P}_{\mathbf{eff}}\ (\text{model 2})=-m\begin{Bmatrix}0\\1\\0\end{Bmatrix}\ddot{x}_g$$

Thus, the mass matrix, the influence coefficient vector, and the effective force vector may be different for different types of modeling. This is further illustrated by showing another example.

Example 3.3

A pitched roof portal frame has three masses lumped as shown in Figure 3.6(a and b). All members are inextensible. EI_c/L of the columns are K and those of the inclined members are 0.5 K (that is, EI_b/l). Only sway degrees of freedom are considered as the dynamic degrees of freedom. Obtain the mass matrix, the influence coefficient vector, and the effective force vector.

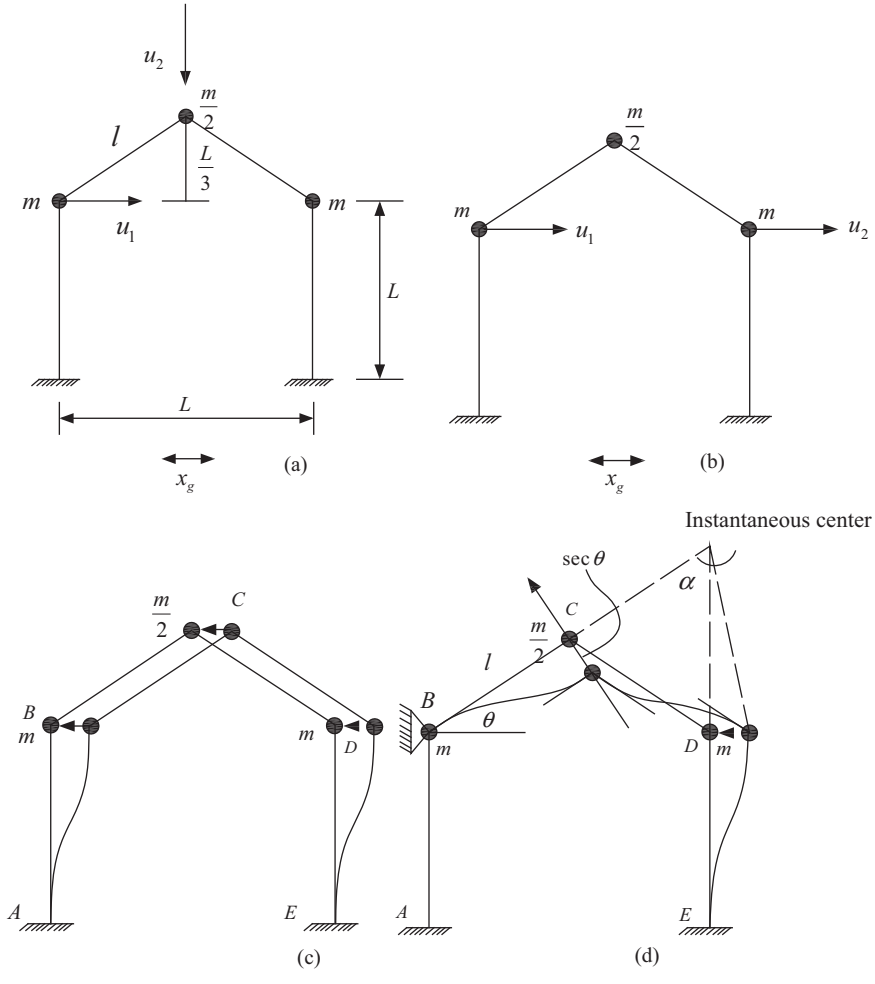

Figure 3.6 Inclined portal frame subjected to the same support excitation: (a) model 1; (b) model 2; (c) unit acceleration given to u_1 (model 1); and (d) unit acceleration given to u_2 (model 2)

Solution: As the members are inextensible, there could be only two independent sway degrees of freedom; the third one is dependent on the other two. Two models for choosing independent sway degrees of freedom are possible, namely, model 1 and model 2. They are shown in Figure 3.6(a and b). The stiffness matrix corresponding to the two independent sway degrees of freedom can be obtained by using the standard procedure of direct generation of stiffness matrix and by condensing out the rotational degrees of freedom at the three joints *B*, *C,* and *D*.

For model 1, the independent sway degrees of freedom (DOF) are shown in Figure 3.6a. The mass matrix is generated by applying unit acceleration to one DOF keeping the other two DOF locked, and finding the inertia forces developed at the two DOF. Generation of the first column of the mass matrix is described below.

For unit acceleration applied at *B*, the inertia forces developed at the masses are shown in Figure 3.6c. The mass inertia coefficients to equilibrate the inertia forces are shown by dotted lines. As the DOF at *D* is not an independent DOF, no mass inertia coefficient can be attached to this DOF and, therefore, it is resolved in two directions, one along *DE* and the other along *DC*. Thus,

$$f_{DE} = -1.20\,m \qquad f_{DC} = -0.67\,m$$

At *C*, the mass inertia coefficient $m/2$ and f_{DE} are resolved in two directions, one along *CB* and the other in the vertical direction corresponding to the DOF, u_2. Thus,

$$f_{CB} = -1.803\,m \qquad f_{u_2} = 1.67\,m$$

Finally at *B*, the inertia coefficient m and f_{CB} are resolved in the two directions, one along *BA* and the other in the horizontal direction corresponding to the DOF, u_1. Thus,

$$f_{BA} = -m \qquad f_{u_1} = 2.5m$$

Hence, the net inertia coefficients $m_{11} = 2.5\,m$ and $m_{21} = 1.67\,m$.

In a similar way, the second column of the mass matrix can be generated by giving unit acceleration to the DOF u_2. To determine the motion of the masses at the DOF, the rigid body rotation of the shaded area about the instantaneous center of rotation may be considered as that shown in Figure 3.6d. The final mass matrix is obtained by arranging the mass inertia coefficients corresponding to the independent DOF The resulting mass matrix is obtained as:

$$\boldsymbol{M} = \begin{bmatrix} 2.5 & 1.67 \\ 1.67 & 2.5 \end{bmatrix} m \quad \mathrm{I} = \begin{Bmatrix} 1 \\ 0 \end{Bmatrix}$$

For model 2, the independent DOF are shown in Figure 3.6b. The mass matrix corresponding to these DOF are obtained as:

$$\boldsymbol{M} = \begin{bmatrix} 1.406 & -0.156 \\ -0.156 & 1.406 \end{bmatrix} m \quad \mathrm{I} = \begin{Bmatrix} 1 \\ 1 \end{Bmatrix}$$

It is seen that the mass matrix provides the effective load vector as:

$$\boldsymbol{P}_{\mathbf{eff}} = -m \begin{Bmatrix} 1.25 \\ 1.25 \end{Bmatrix} \ddot{x}_g$$

When the two supports have the same excitation, the frame will have only one sway displacement because of the inextensibility condition of the members. The effective force will then be $-2.5m\ddot{x}_g$.

Using the method of virtual work, the mass matrices can also be generated for the problems in Examples 3.2 and 3.3. In Appendix 3.A, the method is applied for the problems in Examples 3.2 and 3.3. Also, applying the same method the stiffness matrix for Example 3.3 is derived.

3.3.2 Equations of Motion for Multi-Support Excitation

For multi-support excitation, the excitations at the various supports are different. In matrix form, the equations of motion for the MDOF system with multi-support excitation can be written as:

$$\begin{bmatrix} \boldsymbol{M}_{ss} & \boldsymbol{M}_{sg} \\ \boldsymbol{M}_{gs} & \boldsymbol{M}_{gg} \end{bmatrix} \begin{Bmatrix} \ddot{\boldsymbol{X}}^{\mathrm{t}} \\ \ddot{\boldsymbol{X}}_g \end{Bmatrix} + \begin{bmatrix} \boldsymbol{C}_{ss} & \boldsymbol{C}_{sg} \\ \boldsymbol{C}_{gs} & \boldsymbol{C}_{gg} \end{bmatrix} \begin{Bmatrix} \dot{\boldsymbol{X}}^{\mathrm{t}} \\ \dot{\boldsymbol{X}}_g \end{Bmatrix} + \begin{bmatrix} \boldsymbol{K}_{ss} & \boldsymbol{K}_{sg} \\ \boldsymbol{K}_{gs} & \boldsymbol{K}_{gg} \end{bmatrix} \begin{Bmatrix} \boldsymbol{X}^{\mathrm{t}} \\ \boldsymbol{X}_g \end{Bmatrix} = \begin{Bmatrix} 0 \\ \boldsymbol{P}_g \end{Bmatrix} \tag{3.11}$$

where

$\boldsymbol{M}_{ss}$ is the mass matrix corresponding to non-support degrees of freedom
$\boldsymbol{M}_{gg}$ is the mass matrix corresponding to the support degrees of freedom
$\boldsymbol{M}_{sg}$ and $\boldsymbol{M}_{gs}$ are the coupling mass matrices that express the inertia forces in the non-support degrees of freedom of the structure due to the motions of the supports (inertia coupling)
Terms of damping and stiffness matrices are defined in similar ways
$\boldsymbol{X}^{\mathrm{t}}$ is the vector of total displacements corresponding to non-support degrees of freedom
$\boldsymbol{X}_g$ is the vector of input ground displacements at the supports; a dot denotes the time derivatives
$\boldsymbol{P}_g$ denotes forces generated at the support degrees of freedom.

For an MDOF system with single-support excitation, the total displacement of the non-support degrees of freedom is obtained by simply adding the input support motion to the relative displacements of the structures with respect to the support. For multi-support excitation, the support motions at any instant of time are different for the various supports and, therefore, the total displacements of the non-support degrees of freedom (NSDF) are equal to the sum of the relative displacements of the structure with respect to the supports and the displacements produced at NSDF due to quasi-static motions of the supports. The latter are obtained by a quasi-static analysis of the structure for the support motions.

Therefore, the displacement $\boldsymbol{X}^{\mathrm{t}}$ is given as

$$\boldsymbol{X}^{\mathrm{t}} = X + r\boldsymbol{X}_{\boldsymbol{g}} \tag{3.12}$$

where

r is an influence coefficient matrix of size $n \times m$
n is the number of non-support degrees of freedom
m is the number of input support motions.

As the responses of NSDF are of interest, the first set of equations obtained from Equation 3.11 are considered for the analysis, that is,

$$\boldsymbol{M}_{ss}\ddot{\boldsymbol{X}}^{\mathrm{t}} + \boldsymbol{M}_{sg}\ddot{\boldsymbol{X}}_{\boldsymbol{g}} + \boldsymbol{C}_{ss}\dot{\boldsymbol{X}}^{\mathrm{t}} + \boldsymbol{C}_{sg}\dot{\boldsymbol{X}}_{\boldsymbol{g}} + \boldsymbol{K}_{ss}\boldsymbol{X}^{\mathrm{t}} + \boldsymbol{K}_{sg}\boldsymbol{X}_{\boldsymbol{g}} = 0 \tag{3.13}$$

or

$$\boldsymbol{M}_{ss}\ddot{\boldsymbol{X}}^{\mathrm{t}} + \boldsymbol{C}_{ss}\dot{\boldsymbol{X}}^{\mathrm{t}} + \boldsymbol{K}_{ss}\boldsymbol{X}^{\mathrm{t}} = -\boldsymbol{M}_{sg}\ddot{\boldsymbol{X}}_g - \boldsymbol{C}_{sg}\dot{\boldsymbol{X}}_g - \boldsymbol{K}_{sg}\boldsymbol{X}_g \tag{3.14}$$

Equation 3.14 is in terms of total displacements of NSDF with inputs as the support displacements, velocities, and accelerations. If the effects of mass and damping couplings are ignored, then Equation 3.14 takes the form

$$\boldsymbol{M}_{ss}\ddot{\boldsymbol{X}}^{\mathrm{t}} + \boldsymbol{C}_{ss}\dot{\boldsymbol{X}}^{\mathrm{t}} + \boldsymbol{K}_{ss}\boldsymbol{X}^{\mathrm{t}} = -\boldsymbol{K}_{sg}\boldsymbol{X}_g \tag{3.15}$$

As $\boldsymbol{K}_{sg}$ can be determined, the right-hand side of the equation is known and Equation 3.15 can be solved to obtain the total displacements.

An equation of motion can also be written in terms of relative displacements of the structure by substituting Equation 3.12 into Equation 3.14 leading to:

$$\boldsymbol{M}_{ss}\ddot{\boldsymbol{X}} + \boldsymbol{C}_{ss}\dot{\boldsymbol{X}} + \boldsymbol{K}_{ss}\boldsymbol{X} = -(\boldsymbol{M}_{sg} + r\boldsymbol{M}_{ss})\ddot{\boldsymbol{X}}_{\boldsymbol{g}} - (\boldsymbol{C}_{sg} + r\boldsymbol{C}_{ss})\dot{\boldsymbol{X}}_g - (\boldsymbol{K}_{sg} + r\boldsymbol{K}_{ss})\boldsymbol{X}_g \tag{3.16}$$

To find the quasi-static displacement $\boldsymbol{X}_s$ produced due to the support displacement $\boldsymbol{X}_g$, the quasi-static equation of equilibrium can be written as:

$$\boldsymbol{K}_{ss}\boldsymbol{X}_s + \boldsymbol{K}_{sg}\boldsymbol{X}_g = 0 \tag{3.17}$$

The solution for $\boldsymbol{X}_s$ gives

$$\boldsymbol{X}_s = -\boldsymbol{K}_{ss}^{-1}\boldsymbol{K}_{sg}\boldsymbol{X}_g = \boldsymbol{r}\boldsymbol{X}_g \tag{3.18a}$$

Substituting Equation 3.18a into Equation 3.17, it is seen that

$$\boldsymbol{r}\boldsymbol{K}_{ss} + \boldsymbol{K}_{sg} = 0 \tag{3.18b}$$

From Equation 3.18a, it is seen that the $\boldsymbol{r}$ matrix can be obtained by knowing $\boldsymbol{K}_{ss}$ and $\boldsymbol{K}_{sg}$. It is evident from Equation 3.18b that the last term of Equation 3.16 is zero. Furthermore, $\boldsymbol{M}_{sg}$ denoting the inertia coupling is generally neglected for most structures. The contribution of the damping term $(C_{sg} + rC_{ss})\dot{x}_g$ for any rational damping to the response is found to be small and can be ignored [1]. With these two assumptions, Equation 3.16 takes the form

$$\boldsymbol{M}_{ss}\ddot{\boldsymbol{X}} + C_{ss}\dot{\boldsymbol{X}} + K_{ss}\boldsymbol{X} = -\boldsymbol{r}\boldsymbol{M}_{ss}\ddot{\boldsymbol{X}}_g \tag{3.19}$$

Comparing Equations 3.19 and 3.8, it is seen that the forms of the two equations of motion are the same. The coefficient vector or matrix $\boldsymbol{I}$ in Equation 3.8 can be obtained straight away without performing any analysis of the structure, whereas the coefficient matrix $\boldsymbol{r}$ in Equation 3.19 is obtained from a static analysis of the structure for relative support movements.

To solve Equation 3.19, the inputs are the time histories of ground accelerations to be applied at the supports. The solution of the equation of motion provides the responses of the non-support degrees of freedom relative to the support. In order to obtain the total (absolute) responses at the non-support degrees of freedom, Equation 3.12 is used. The internal forces in the member are obtained using the absolute responses (not the relative responses). Generation of the mass matrix for multi-support excitation remains the same as that for single-support excitation. Some example problems are shown below for the generation of the $\boldsymbol{r}$ matrix.

Example 3.4

Find the $\boldsymbol{r}$ matrices for the two frames shown in Figures 3.7 and 3.8. All members are inextensible. EI (flexural rigidity) values are the same for all the members.

Solution: For the two-bay frame shown in Figure 3.7

$$\boldsymbol{K}_{ss} = \begin{bmatrix} 3 & -3 \\ -3 & 9 \end{bmatrix} k \quad \boldsymbol{K}_{sg} = \begin{bmatrix} 0 & 0 & 0 \\ -2k & -2k & -2k \end{bmatrix} \quad \boldsymbol{K}_{gg} = \begin{bmatrix} 2k & 0 & 0 \\ 0 & 2k & 0 \\ 0 & 0 & 2k \end{bmatrix}$$

$$\boldsymbol{r} = -\boldsymbol{K}_{ss}{}^{-1}\boldsymbol{K}_{sg} = -\frac{1}{k}\begin{bmatrix} \frac{1}{2} & \frac{1}{6} \\ \frac{1}{6} & \frac{1}{6} \end{bmatrix}\begin{bmatrix} 0 & 0 & 0 \\ -2k & -2k & -2k \end{bmatrix} = \frac{1}{3}\begin{bmatrix} 1 & 1 & 1 \\ 1 & 1 & 1 \end{bmatrix}$$

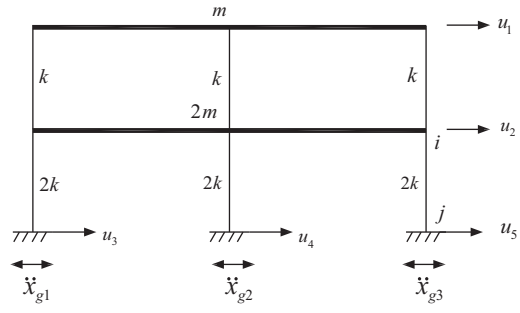

Figure 3.7 Multi-bay portal frame subjected to different support excitations

For the inclined leg portal frame, shown in Figure 3.8, the stiffness matrix is written in the partitioned form with $\boldsymbol{r}$ as rotational degrees of freedom and $\boldsymbol{u}$ as translational degrees of freedom as:

$$\boldsymbol{K}_{rr} = \frac{EI}{3.6}\begin{bmatrix} 38.4 & 12 & 0 \\ 12 & 48 & 12 \\ 0 & 12 & 38.4 \end{bmatrix} \quad \boldsymbol{K}_{ru} = \frac{EI}{L^2}\begin{bmatrix} -6 & -20 & 6 & 0 \\ 0 & 0 & 0 & 0 \\ -6 & 12 & 6 & 6 \end{bmatrix}$$

The derivation of the elements of the matrices $\boldsymbol{K}_{rr}$, $\boldsymbol{K}_{ru}$, and $\boldsymbol{K}_{uu}$ are given in Appendix 3.A

$$\boldsymbol{K}_{uu} = \frac{EI}{L^3}\begin{bmatrix} 24 & 16 & -12 & -12 \\ 16 & 181 & 0 & -16 \\ -12 & 0 & 12 & 0 \\ -12 & -16 & 0 & 12 \end{bmatrix} \quad \boldsymbol{K}_{rr}^{-1} = \frac{L}{EI}\begin{bmatrix} 0.104 & -0.028 & -0.801 \\ -0.028 & 0.266 & -0.028 \\ -0.801 & -0.028 & 9.456 \end{bmatrix}$$

$$\overline{\boldsymbol{K}}_{uu} = [\boldsymbol{K}_{uu} - \boldsymbol{K}_{ur}\boldsymbol{K}_{rr}^{-1}\boldsymbol{K}_{ru}]$$

$$\overline{\boldsymbol{K}}_{uu} = \frac{EI}{L^3}\begin{bmatrix} 24 & 16 & -12 & -12 \\ 16 & 181 & 0 & -16 \\ -12 & 0 & 12 & 0 \\ -12 & -16 & 0 & 12 \end{bmatrix} - \frac{EI}{L^3}\begin{bmatrix} 4.44 & 5.51 & -4.05 & -4 \\ 5.51 & 52 & -11.84 & 6.33 \\ -4.05 & -11.84 & 3.74 & 0.36 \\ -4 & 6.33 & 0.36 & 3.69 \end{bmatrix}$$

$\overline{\boldsymbol{K}}_{uu}$ is partitioned with respect to non-support (s) and support (g) DOF. Thus,

$$\overline{\boldsymbol{K}}_{us} = \frac{EI}{L^3}\begin{bmatrix} 19.56 & 10.49 \\ 10.49 & 129 \end{bmatrix} \quad \overline{\boldsymbol{K}}_{usg} = \frac{EI}{L^3}\begin{bmatrix} -8 & -8 \\ 11.84 & -22.3 \end{bmatrix}$$

$$\boldsymbol{r} = -\overline{\boldsymbol{K}}_{us}^{-1}\overline{\boldsymbol{K}}_{usg} = \begin{bmatrix} 0.0034 & -0.0043 \\ -0.0043 & 0.0081 \end{bmatrix}\begin{bmatrix} -8 & -8 \\ 11.84 & -22.31 \end{bmatrix} = \begin{bmatrix} 0.479 & 0.331 \\ -0.131 & 0.146 \end{bmatrix}$$

Example 3.5

A simplified model of a cable stayed bridge is shown in Figure 3.9. Obtain the $\boldsymbol{r}$ matrix corresponding to the translational DOF 1, 2, and 3. Assume the towers to be inextensible. Properties of the members are

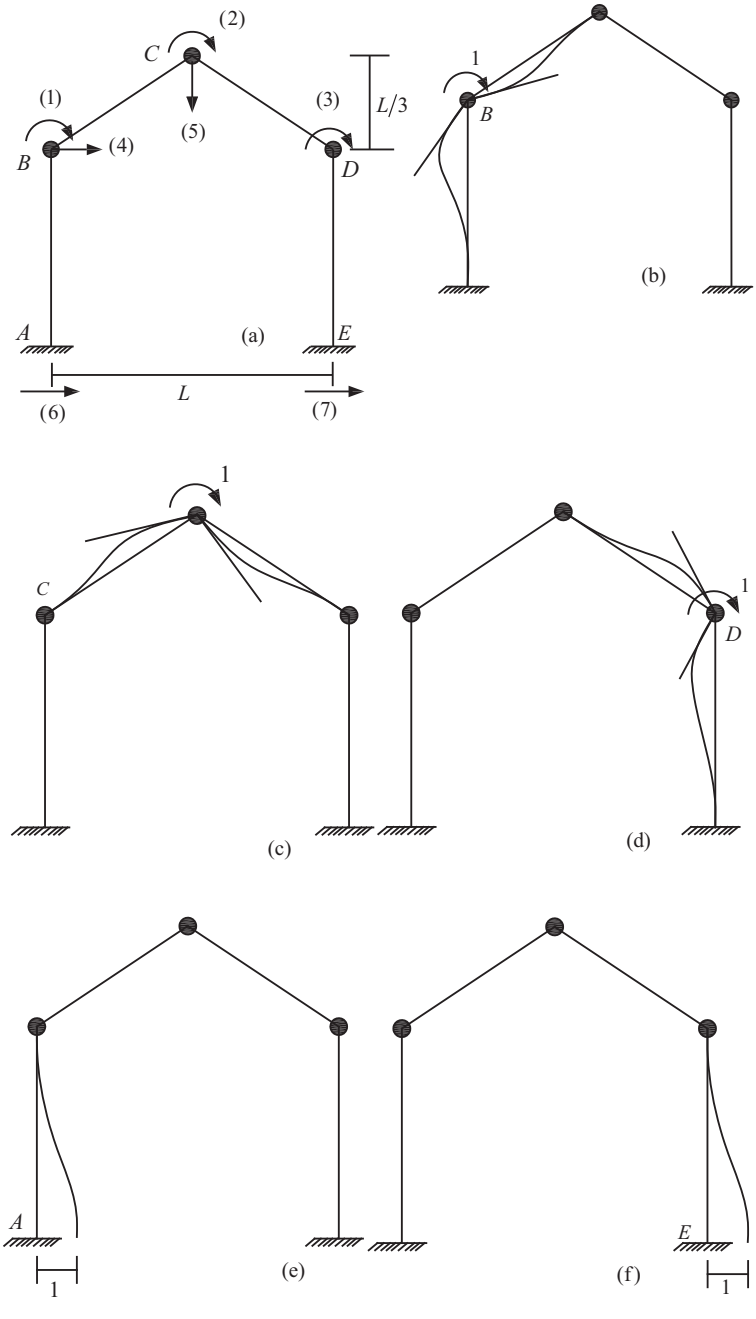

Figure 3.8 Different support excitations: (a) kinematic DOF; (b) unit rotation given at *B*; (c) unit rotation given at *C*; (d) unit rotation given at *D*; (e) unit displacement given at *A*; and (f) unit displacement given at *E*

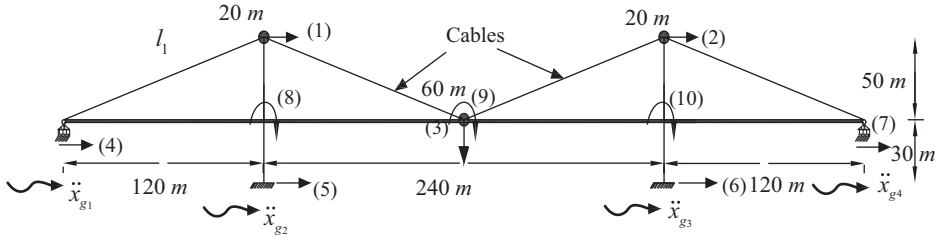

Figure 3.9 Simplified model of a cable stayed bridge

given below. Geometric non-linearity of the pre-tensioned cable members are ignored in obtaining the stiffness matrix. Furthermore, there is no moment transfer between the deck and the pier, but the deck is vertically supported by the towers.

Solution: To solve the problem, the following values are assumed.

$$EI_{\mathrm{t}} = 1.25EI_{\mathrm{d}} = 1.25EI$$

$$\left(\frac{AE}{480}\right)_{\mathrm{deck}} = 0.8\left(\frac{AE}{L_1}\right)_{\mathrm{cable}}$$

$$\cos\theta = \frac{12}{13} \quad \sin\theta = \frac{5}{13} \quad \frac{AE}{l_1} = \frac{12EI}{(120)^3}$$

$$\frac{3EI}{(80)^3} = \frac{120m}{80} \quad \frac{12EI}{(120)^3} = 400m$$

With the above assumed values, the stiffness coefficients are calculated as

$$K_{11} = \frac{3.75EI}{(80)^3} + \frac{2AE}{l_1}\cos^2\theta = 1.875m + 800m\cos^2\theta$$

$$K_{21} = 0; \quad K_{31} = -\frac{AE}{l_1}\cos\theta\sin\theta;$$

$$K_{41} = -\frac{AE}{l_1}\cos^2\theta; \quad K_{51} = -\frac{3.75EI}{(80)^3}$$

$$K_{61} = K_{71} = K_{81} = K_{91} = K_{101} = 0$$

$$K_{22} = K_{11}; \quad K_{32} = -K_{31}; \quad K_{42} = K_{52} = 0;$$

$$K_{62} = K_{51}; \quad K_{72} = K_{41}; \quad K_{82} = K_{92} = K_{102} = 0$$

$$K_{33} = \frac{24EI}{(120)^3} + \frac{2AE}{L_1}\sin^2\theta = 800m(1 + \sin^2\theta);$$

$$K_{43} = K_{53} = K_{63} = K_{73} = 0$$

$$K_{83} = -\frac{6EI}{L^2} = -24\,000m; \quad K_{93} = 0; \quad K_{103} = 24\,000m$$

$$K_{44} = \left(\frac{AE}{480}\right)_{\text{deck}} = 320m; \quad K_{74} = -320m$$

$$K_{54} = K_{64} = K_{84} = K_{94} = K_{104} = 0$$

$$K_{55} = \frac{3.75EI}{(80)^3}; \quad K_{65} = K_{75} = K_{85} = K_{95} = K_{105} = 0$$

$$K_{66} = \frac{3.75EI}{(80)^3}; \quad K_{76} = K_{86} = K_{96} = K_{106} = 0$$

$$K_{77} = 320m; \quad K_{87} = K_{97} = K_{107} = 0$$

$$K_{88} = \frac{7EI}{120} = \frac{7}{12} \times 400m \times (120)^2; \quad K_{98} = \frac{2}{7}K_{88}; \quad K_{108} = 0$$

$$K_{99} = \frac{8EI}{120} = \frac{8}{7}K_{88}; \quad K_{109} = \frac{2}{7}K_{88}; \quad K_{1010} = K_{88}$$

The resulting partitioned matrices for rotational and translational degrees of freedom are:

$$\boldsymbol{K}_{\theta\theta} = m \begin{bmatrix} 336 & 96 & 0 \\ 96 & 384 & 96 \\ 0 & 96 & 336 \end{bmatrix} \times 10^4$$

$$\boldsymbol{K}_{\Delta\Delta} = m \begin{bmatrix} 0.684 & & & & & & \\ 0 & 0.684 & & & \textit{sym} & & \\ -0.149 & 0.149 & 0.918 & & & & \\ -0.342 & 0 & 0 & 0.32 & & & \\ -0.002 & 0 & 0 & 0 & 0.002 & & \\ 0 & -0.002 & 0 & 0 & 0 & 0.002 & \\ 0 & -0.342 & 0 & -0.32 & 0 & 0 & 0.32 \end{bmatrix} \times 10^3$$

$$\boldsymbol{K}_{\theta\Delta} = m \begin{bmatrix} 0 & 0 & -2.4 & 0 & 0 & 0 & 0 \\ 0 & 0 & 0 & 0 & 0 & 0 & 0 \\ 0 & 0 & 2.4 & 0 & 0 & 0 & 0 \end{bmatrix} \times 10^4$$

$$\overline{\boldsymbol{K}}_{\Delta\Delta} = \boldsymbol{K}_{\Delta\Delta} - \boldsymbol{K}_{\Delta\theta}\boldsymbol{K}_{\theta\theta}^{-1}\boldsymbol{K}_{\theta\Delta}$$

$$\overline{\boldsymbol{K}}_{\Delta\Delta} = m \left[\begin{array}{ccc|ccc|c} 684 & 0 & -149 & -342 & -2 & 0 & 0 \\ 0 & 684 & 149 & 0 & 0 & -2 & -342 \\ -149 & 149 & 575 & 0 & 0 & 0 & 0 \\ \hline -342 & 0 & 0 & 320 & 0 & 0 & -320 \\ -2 & 0 & 0 & 0 & 2 & 0 & 0 \\ 0 & -2 & 0 & 0 & 0 & 2 & 0 \\ 0 & -342 & 0 & -320 & 0 & 0 & 320 \end{array}\right]$$

The first 3 × 3 sub-matrix is $\boldsymbol{K}_{ss}$ and corresponds to non-support degrees of freedom. The last 4 × 4 sub-matrix is $\boldsymbol{K}_{gg}$ and corresponds to support degrees of freedom.

$$\mathrm{r} = -\boldsymbol{K}_{ss}^{-1}\boldsymbol{K}_{sg} = \begin{bmatrix} 5.318 & 0.031 & -0.002 & -0.318 \\ -0.318 & -0.002 & 0.031 & 5.318 \\ 1.416 & 0.008 & -0.008 & -1.460 \end{bmatrix} \times 10^{-1}$$

3.3.3 Equations of Motion in State Space

Equations of motion in state space can be written by extending Equations 3.4 and 3.5 for an MDOF system. The state-space forms of Equations 3.19 and 3.15 are given by

$$\dot{\boldsymbol{Z}} = \boldsymbol{A}\boldsymbol{Z} + \boldsymbol{f} \tag{3.20}$$

in which

$$\boldsymbol{Z} = \begin{Bmatrix} \boldsymbol{x} \\ \dot{\boldsymbol{x}} \end{Bmatrix}; \quad \boldsymbol{f} = \begin{Bmatrix} 0 \\ -\boldsymbol{r}\ddot{x}_g \end{Bmatrix}; \quad \boldsymbol{A} = \begin{bmatrix} 0 & \boldsymbol{I} \\ -\boldsymbol{K}_{ss}\boldsymbol{M}_{ss}^{-1} & -\boldsymbol{C}_{ss}\boldsymbol{M}_{ss}^{-1} \end{bmatrix} \tag{3.21}$$

and

$$\dot{\boldsymbol{Z}}^{\mathrm{t}} = \boldsymbol{A}\boldsymbol{Z}^{\mathrm{t}} + \bar{\boldsymbol{f}} \tag{3.22}$$

in which

$$\boldsymbol{Z}^{\mathrm{t}} = \begin{Bmatrix} \boldsymbol{x}^{\mathrm{t}} \\ \dot{\boldsymbol{x}}^{\mathrm{t}} \end{Bmatrix}; \quad \bar{\boldsymbol{f}} = \begin{Bmatrix} 0 \\ -\boldsymbol{M}_{ss}^{-1}\boldsymbol{K}_{sg}\boldsymbol{x}_g \end{Bmatrix} \tag{3.23}$$

Example 3.6

Write the equations of motion for the frame (Figure 3.7) of the problem in Example 3.4 in state space using both relative and absolute motions of the structure.

Relative motions of the structure: The solution of the eigenvalues for the problem in Example 3.4 gives $\omega_1^2 = 1.9\dfrac{k}{m}$; $\omega_2^2 = 19.1\dfrac{k}{m}$.

Assuming 5% damping in each mode, $\alpha = 0.105\sqrt{\dfrac{k}{m}}$; $\beta = 0.017\sqrt{\dfrac{m}{k}}$

$$-\mathrm{K}_{ss}\mathrm{M}_{ss}^{-1} = -\begin{bmatrix} 3 & -3 \\ -3 & 9 \end{bmatrix}\begin{bmatrix} 1 & 0 \\ 0 & 0.5 \end{bmatrix}\frac{k}{m} = -\begin{bmatrix} 3 & -1.5 \\ -3 & 4.5 \end{bmatrix}\frac{k}{m}$$

$$\mathrm{C}_{ss} = \alpha\begin{bmatrix} 1 & 0 \\ 0 & 2 \end{bmatrix}m + \beta\begin{bmatrix} 3 & -3 \\ -3 & 9 \end{bmatrix}k = \begin{bmatrix} 0.156 & -0.051 \\ -0.051 & 0.205 \end{bmatrix}\sqrt{km}$$

$$\boldsymbol{A} = \begin{bmatrix} 0 & 0 & 1 & 0 \\ 0 & 0 & 0 & 1 \\ -3\rho^2 & 1.5\rho^2 & -0.156\rho & 0.026\rho \\ 3\rho^2 & -4.5\rho^2 & 0.051\rho & -0.182\rho \end{bmatrix}$$

$$\rho = \sqrt{\frac{k}{m}}$$

$$\boldsymbol{f} = \begin{Bmatrix} 0 \\ 0 \\ -0.33(\ddot{x}_{g_1} + \ddot{x}_{g_2} + \ddot{x}_{g_3}) \\ -0.33(\ddot{x}_{g_1} + \ddot{x}_{g_2} + \ddot{x}_{g_3}) \end{Bmatrix}$$

For $\ddot{x}_{g_1} = \ddot{x}_{g_2} = \ddot{x}_{g_3} = \ddot{x}_g$

$$\boldsymbol{f} = \begin{Bmatrix} 0 \\ 0 \\ -\ddot{x}_g \\ -\ddot{x}_g \end{Bmatrix}$$

Absolute motion of the structure: Matrix $\boldsymbol{A}$ remains the same. Taking $\boldsymbol{K}_{sg}$ from Example 3.4 and using Equation 3.23:

$$\bar{\boldsymbol{f}} = \begin{Bmatrix} 0 \\ 0 \\ 0 \\ (x_{g_1} + x_{g_2} + x_{g_3})\rho^2 \end{Bmatrix}$$

3.4 Response Analysis for Single Degree of Freedom (SDOF) System

The responses of a single degree of freedom for specified time histories of ground motions can be obtained by:

a. Integration of the equation of motion in the time domain (time history analysis).
b. Fourier synthesis of the time histories of ground motion and the solution of the equation of motion in frequency domain (Fourier method of analysis).

The first method is called the time domain analysis of structures under earthquake excitation. The method of analysis can provide responses for both linear and non-linear structures. In particular, the method is adopted for finding the seismic response of structures in the inelastic range. In this method, numerical techniques (time marching schemes) for the integration of the equation of motion are employed for finding the responses at discrete time intervals. For linear systems, two such schemes are presented here namely, the Duhamel integration and the Newmark integration schemes. Both numerical integration schemes are popular in earthquake engineering. There are many other time marching integration schemes, such as the Wilson θ-method, Houbolt's method, Adam's integration scheme, Alpha method, and Argary's large time step integration schemes [2, 3]. Using the SIMULINK toolbox of MATLAB®, numerical integration of the equation of motion can also be performed (Appendix 3.D).

The second method is called the frequency domain analysis for earthquake excitation. It requires the knowledge of the complex frequency response function of the system. The method is not strictly applicable for short duration excitations such as earthquake induced forces. This is the case because it cannot account for the transient (homogeneous) part of the response produced due to the initial conditions, which may significantly change the rms and peak values of the response. However, under certain conditions, such as the period of the structure being small compared with the predominant period of excitations, the method is found to give good estimates of the rms and peak values of the responses. It may be noted that the time histories of responses obtained by the time domain and frequency domain of analyses are different in time, but the rms and peak responses obtained by the two may compare well. Frequency domain analysis for irregular excitations, such as earthquakes, is also called the Fourier method

of analysis as it uses Fourier series analysis or discrete Fourier transform (DFT). The frequency domain analysis or the Fourier method of analysis is not applicable for non-linear systems.

3.4.1 Time Domain Analysis using the Duhamel Integral

In this method, the excitation force produced by the earthquake is treated as a series of impulses of short duration Δt as shown in Figure 3.10. To derive the method, the homogeneous solutions of a damped single degree of freedom (SDOF) given by Equation 3.1 are considered. The displacement and velocity responses of the SDOF are given in any standard textbook on dynamics and are given by:

$$x(t) = \mathrm{e}^{-\xi\omega_n t}(C_1' \cos \omega_\mathrm{d} t + C_2' \sin \omega_\mathrm{d} t) \tag{3.24}$$

$$\dot{x}(t) = \mathrm{e}^{-\xi\omega_n t}[(-\xi\omega_\mathrm{n} C_1' + C_2'\omega_\mathrm{d}) \cos \omega_\mathrm{d} t + (-\omega_\mathrm{d} C_1' - \xi\omega_\mathrm{n} C_2') \sin\ \omega_\mathrm{d} t] \tag{3.25}$$

where

ξ is the percentage critical damping and is given as $\xi = \dfrac{c}{2m\omega_\mathrm{n}}$
ω_d is the damped natural frequency $\left(\omega_\mathrm{d} = \omega_\mathrm{n}\sqrt{1-\xi^2}\right)$
ω_n is the natural frequency
C_1' and C_2' are integration constants.

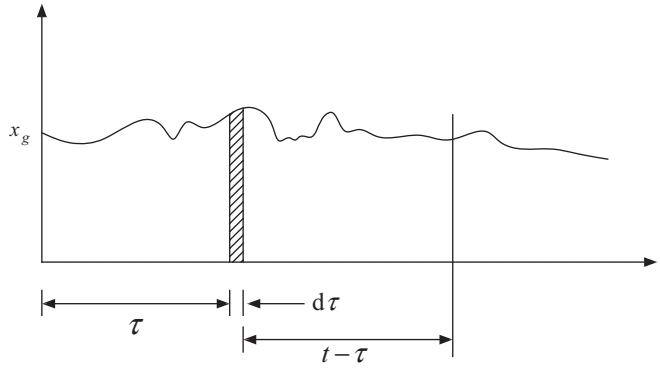

Figure 3.10 Idealization of earthquake excitation as a sum of a series of impulses

For the initial conditions defined as $x(0) = 0$ and $\dot{x}(0) = \dot{x}_0$, C_1' and C_2' are evaluated as:

$$C_1' = x_0; \qquad C_2' = \frac{\xi\omega_\mathrm{n} x_0 + \dot{x}_0}{\omega_\mathrm{d}} \tag{3.26}$$

and $x(t)$ and $\dot{x}(t)$ are given by

$$x(t) = \mathrm{e}^{-\xi\omega_\mathrm{n} t}\left[x_0 \cos \omega_\mathrm{d} t + \left(\frac{\xi\omega_\mathrm{n} x_0 + \dot{x}_0}{\omega_\mathrm{d}}\right) \sin \omega_\mathrm{d} t\right] \tag{3.27}$$

$$\dot{x}(t) = \mathrm{e}^{-\xi\omega_\mathrm{n} t}\left[\dot{x}_0 \cos \omega_\mathrm{d} t - \left(\frac{\omega_\mathrm{n} x_0 + \xi\dot{x}_0}{\sqrt{1-\xi^2}}\right) \sin \omega_\mathrm{d} t\right] \tag{3.28}$$

For initial conditions of zero displacement and finite velocity $\dot{x}_0$, the expressions simplify to

$$x(t) = \mathrm{e}^{-\xi\omega_\mathrm{n}t}\frac{\dot{x}_0}{\omega_\mathrm{d}}\sin\omega_\mathrm{d}t \tag{3.29}$$

$$\dot{x}(t) = \mathrm{e}^{-\xi\omega_\mathrm{n}t}\left[\dot{x}_0\cos\omega_\mathrm{d}t - \frac{\xi}{\sqrt{1-\xi^2}}\dot{x}_0\sin\omega_\mathrm{d}t\right] \tag{3.30}$$

For a very small damping ratio ξ, such as 0.02 for steel and 0.05 for concrete, $\omega_\mathrm{d} \approx \omega_\mathrm{n}$ and $\sqrt{1-\xi^2} \approx 1$, and the expressions could be further simplified to

$$x(t) = \mathrm{e}^{-\xi\omega_\mathrm{n}t}\frac{\dot{x}_0\sin\omega_\mathrm{n}t}{\omega_\mathrm{n}} \tag{3.31}$$

$$\dot{x}(t) = e^{-\xi\omega_\mathrm{n}t}\dot{x}_0[\cos\omega_\mathrm{n}t - \xi\sin\omega_\mathrm{n}t] \tag{3.32}$$

The ratio between velocity and displacement at any instant of time t is nearly equal to

$$r(t) = \frac{\dot{x}(t)}{x(t)} \approx \omega_\mathrm{n}\cot\omega_\mathrm{n}t \tag{3.33}$$

Referring to Figure 3.1, the external force produced due to ground acceleration for an SDOF system represented by Equation 3.1 is $F(t) = -m\ddot{x}_g$. Let the response of the system at time t_k be known, then the intent is to obtain the response at time t_{k+1}. The time increment between t_{k+1} and t_k is

$$\Delta t = t_{k+1} - t_k \tag{3.34}$$

For a time increment τ less than Δt between t_{k+1} and t_k, the excitation is given by:

$$F(\tau) = F_k + \left(\frac{F_{k+1} - F_k}{\Delta t}\right)\tau \tag{3.35}$$

The response at time t_{k+1} is the sum of the following responses:

(i) Responses due to damped free oscillation of the SDOF for initial conditions as $x(0) = x_k$ and $\dot{x}(0) = \dot{x}_k$.
(ii) Responses due to constant excitation F_k between time t_k and t_{k+1}.
(iii) Responses due to the triangular variation part of the excitation given by $F(\tau)$ between t_k and t_{k+1}.

Therefore, the responses at t_{k+1} depend upon x_k, $\dot{x}_k$, F_k, and F_{k+1}. As a result, the responses at t_{k+1} may be written in the following form:

$$x_{k+1} = C_1x_k + C_2\dot{x}_k + C_3F_k + C_4F_{k+1} \tag{3.36}$$

$$\dot{x}_{k+1} = D_1x_k + D_2\dot{x}_k + D_3F_k + D_4F_{k+1} \tag{3.37}$$

$$\ddot{x}_{k+1} = -\ddot{x}_{gk+1} - 2\xi\omega_\mathrm{n}\dot{x}_{k+1} - \omega_\mathrm{n}^2x_{k+1} \tag{3.38}$$

C_1, C_2, D_3, and so on are obtained from the solutions obtained from (i), (ii) and (iii) as stated above. Solutions for (i) are given by Equations 3.27 and 3.28 after replacing x_0 and $\dot{x}_0$ with x_k and $\dot{x}_k$, respectively. Solutions to (ii) and (iii) are given in Appendix 3.B. Adding up these solutions and collecting the terms corresponding to x_k, $\dot{x}_k$, F_k, and F_{k+1} for the expressions of x_{k+1} and $\dot{x}_{k+1}$, the expressions for C_1, C_2 and so on, are given as:

$$C_1 = \mathrm{e}^{-\xi\omega_\mathrm{n}\Delta t}\left[\cos\omega_\mathrm{d}\Delta t + \left(\frac{\xi}{\sqrt{1-\xi^2}}\right)\sin\omega_\mathrm{d}\Delta t\right] \tag{3.39a}$$

$$C_2 = \mathrm{e}^{-\xi\omega_\mathrm{n}\Delta t}\left[\left(\frac{1}{\omega_\mathrm{d}}\right)\sin\omega_\mathrm{d}\Delta t\right] \tag{3.39b}$$

$$C_3 = \frac{1}{k}\left\{\left(\frac{2\xi}{\omega_\mathrm{n}\Delta t}\right) + \mathrm{e}^{-\xi\omega_\mathrm{n}\Delta t}\left[-\left(1+\frac{2\xi}{\omega_\mathrm{n}\Delta t}\right)\cos\omega_\mathrm{d}\Delta t + \left(\frac{1-2\xi^2}{\omega_\mathrm{d}\Delta t} - \frac{\xi}{\sqrt{1-\xi^2}}\right)\sin\omega_\mathrm{d}\Delta t\right]\right\} \tag{3.40}$$

$$C_4 = \frac{1}{k}\left\{1-\left(\frac{2\xi}{\omega_\mathrm{n}\Delta t}\right) + \mathrm{e}^{-\xi\omega_\mathrm{n}\Delta t}\left[\left(\frac{2\xi}{\omega_\mathrm{n}\Delta t}\right)\cos\omega_\mathrm{d}\Delta t + \left(\frac{2\xi^2-1}{\omega_\mathrm{d}\Delta t}\right)\sin\omega_\mathrm{d}\Delta t\right]\right\} \tag{3.41}$$

$$D_1 = \mathrm{e}^{-\xi\omega_\mathrm{n}\Delta t}\left[-\left(\frac{\omega_\mathrm{n}}{\sqrt{1-\xi^2}}\right)\sin\omega_\mathrm{d}\Delta t\right] \tag{3.42}$$

$$D_2 = \mathrm{e}^{-\xi\omega_\mathrm{n}\Delta t}\left[\cos\omega_\mathrm{d}\Delta t - \left(\frac{\xi}{\sqrt{1-\xi^2}}\right)\sin\omega_\mathrm{d}\Delta t\right] \tag{3.43}$$

$$D_3 = \frac{1}{k}\left\{-\left(\frac{1}{\Delta t}\right) + \mathrm{e}^{-\xi\omega_\mathrm{n}\Delta t}\left[\left(\frac{1}{\Delta t}\right)\cos\omega_\mathrm{d}\Delta t + \left(\frac{\omega_\mathrm{n}}{\sqrt{1-\xi^2}} + \frac{\xi}{\Delta t\sqrt{1-\xi^2}}\right)\sin\omega_\mathrm{d}\Delta t\right]\right\} \tag{3.44}$$

$$D_4 = \frac{1}{k\Delta t}\left\{1-\mathrm{e}^{-\xi\omega_\mathrm{n}\Delta t}\left[\cos\omega_\mathrm{d}\Delta t + \left(\frac{\xi}{\sqrt{1-\xi^2}}\right)\sin\omega_\mathrm{d}\Delta t\right]\right\} \tag{3.45}$$

As $F_k = m\ddot{x}_k + c\dot{x}_k + kx_k$, then x_{k+1} and $\dot{x}_{k+1}$ may be written in the form

$$\begin{aligned} x_{k+1} &= C_1x_k + C_2\dot{x}_k + C_3(m\ddot{x}_k + c\dot{x}_k + kx_k) + C_4F_{k+1} \\ &= (C_1 + kC_3)x_k + (C_2 + cC_3)\dot{x}_k + mC_3\ddot{x}_k + C_4F_{k+1} \end{aligned} \tag{3.46}$$

$$\begin{aligned} \dot{x}_{k+1} &= D_1x_k + D_2\dot{x}_k + D_3(m\ddot{x}_k + c\dot{x}_k + kx_k) + D_4F_{k+1} \\ &= (D_1 + kD_3)x_k + (D_2 + cD_3)\dot{x}_k + mD_3\ddot{x}_k + D_4F_{k+1} \end{aligned} \tag{3.47}$$

Substituting the expressions for $\dot{x}_{k+1}$ and x_{k+1} given by Equations 3.46 and 3.47 in Equation 3.38 results in

$$\begin{aligned} \ddot{x}_{k+1} = \frac{F_{k+1}}{m} &- 2\xi\omega_\mathrm{n}[(D_1 + kD_3)x_k + (D_2 + cD_3)\dot{x}_k + mD_3\ddot{x}_k + D_4F_{k+1}] \\ &-\omega_\mathrm{n}^2[(C_1 + kC_3)x_k + (C_2 + cC_3)\dot{x}_k + mC_3\ddot{x}_k + C_4F_{k+1}] \end{aligned} \tag{3.48}$$

Now, arranging Equations 3.46–3.48 in matrix form, the displacement, velocity, and acceleration at time t_{k+1} can be related to those of time t_k by a recursive relationship:

$$\boldsymbol{q_{k+1}} = \boldsymbol{A}\boldsymbol{q_k} + \boldsymbol{H}F_{k+1} \tag{3.49}$$

where

$$\boldsymbol{q}_i = \begin{Bmatrix} x_i \\ \dot{x}_i \\ \ddot{x}_i \end{Bmatrix}; \quad \boldsymbol{H} = \begin{Bmatrix} C_4 \\ D_4 \\ \dfrac{1}{m} - 2\xi\omega_\mathrm{n}D_4 - \omega_\mathrm{n}^2C_4 \end{Bmatrix} \tag{3.50}$$

and

$$\boldsymbol{A} = \begin{bmatrix} \{C_1 + kC_3\} & \{C_2 + cC_3\} & mC_3 \\ \{D_1 + kD_3\} & D_2 + cD_3 & mD_3 \\ \left\{ \begin{array}{c} -\omega_n^2(C_1 + kC_3) \\ -2\xi\omega_n(D_1 + kD_3) \end{array} \right\} & \left\{ \begin{array}{c} -\omega_n^2(C_2 + cC_3) \\ -2\xi\omega_n(D_2 + cD_3) \end{array} \right\} & \left\{ \begin{array}{c} -mC_3 \\ -2\xi\omega_n mD_3 \end{array} \right\} \end{bmatrix} \tag{3.51}$$

3.4.2 Time Domain Analysis using Newmark's β-Method

The second method uses a step-by-step numerical integration scheme using Newmark's β-method. In this method, the equation of motion at the $k+1$th time is solved using the known displacement, velocity, and acceleration at time k and the excitation F_{k+1} at $k+1$th time. For this, the following relationships are used:

$$\dot{x}_{k+1} = \dot{x}_k + (1-\delta)\ddot{x}_k \Delta t + \ddot{x}_{k+1}\delta\Delta t \tag{3.52}$$

$$x_{k+1} = x_k + \dot{x}_k \Delta t + \left(\frac{1}{2} - \beta\right)(\Delta t)^2 \ddot{x}_k + \beta(\Delta t)^2 \ddot{x}_{k+1} \tag{3.53}$$

These two relationships are derived by obtaining a general form of the solutions to

$$\dot{x}(t) = \dot{x}(t_0) + \int_{t_0}^{t} \ddot{x}(s)\mathrm{d}s \tag{3.54}$$

or

$$\dot{x}_{k+1} = \dot{x}_k + \int_{t_k}^{t_{k+1}} \ddot{x}_S(\mathrm{d}s) \tag{3.55}$$

and

$$x(t) = x(t_0) + \int_{t_0}^{t} \dot{x}(s)\mathrm{d}s \tag{3.56}$$

or

$$x_{k+1} = x_k + \int_{t_k}^{t_{k+1}} \dot{x}(s)\mathrm{d}s \tag{3.57}$$

with

$$\Delta t = t_{k+1} - t_k \quad \text{and} \quad \dot{x}(s) = \dot{x}_k + \dddot{\tilde{x}}(s - t_k) \tag{3.58}$$

in which $\dddot{\tilde{x}}(s-t_k)$ could be constant acceleration, average acceleration, linear acceleration or a general form of linear acceleration over the time interval Δt. A linear variation of acceleration means that a cubic variation of displacement over the time interval Δt is assumed. The difference between various types of integration algorithms essentially lies in the assumption of the order of variation of displacement over the time interval.

Substituting Equations 3.52 and 3.53 into the equation of motion

$$\begin{aligned}\dot{x}_{k+1} + 2\xi\omega_{\mathrm{n}}[\dot{x}_k + (1-\delta)\ddot{x}_k\Delta t + \ddot{x}_{k+1}\delta\Delta t] \\ + \omega_{\mathrm{n}}^2\left[x_k + \dot{x}_k\Delta t + \left(\frac{1}{2}-\beta\right)(\Delta t)^2\ddot{x}_k + \beta(\Delta t)^2\ddot{x}_{k+1}\right] = \frac{F_{k+1}}{m}\end{aligned} \tag{3.59}$$

Rearrangement of terms in Equation 3.59 gives

$$\begin{aligned}(1 + 2\xi\omega_{\mathrm{n}}\delta\Delta t + \omega_{\mathrm{n}}^2\beta(\Delta t)^2)\ddot{x}_{k+1} = -\omega_{\mathrm{n}}^2 x_k - [2\xi\omega_{\mathrm{n}} + \omega_{\mathrm{n}}^2\Delta t]\dot{x}_k \\ -\left[2\xi\omega_{\mathrm{n}}(1-\delta)\Delta t + \omega_{\mathrm{n}}^2\left(\frac{1}{2}-\beta\right)(\Delta t)^2\right]\ddot{x}_k + \frac{F_{k+1}}{m}\end{aligned} \tag{3.60}$$

Solving for $\ddot{x}_{k+1}$,

$$\ddot{x}_{k+1} = -\left(\frac{\omega_{\mathrm{n}}^2}{\alpha}\right)x_k - \left(\frac{2\xi\omega_{\mathrm{n}} + \omega_{\mathrm{n}}^2\Delta t}{\alpha}\right)\dot{x}_k - \left(\frac{\gamma}{\alpha}\right)\ddot{x}_k + \left(\frac{1}{m\alpha}\right)F_{k+1} \tag{3.61}$$

in which,

$$\alpha = 1 + 2\xi\omega_{\mathrm{n}}\delta\Delta t + \omega_{\mathrm{n}}^2\beta(\Delta t)^2 \tag{3.62}$$

$$\gamma = 2\xi\omega_{\mathrm{n}}(1-\delta)\Delta t + \omega_{\mathrm{n}}^2\left(\frac{1}{2}-\beta\right)(\Delta t)^2 \tag{3.63}$$

Substituting $\ddot{x}_{k+1}$ into Equations 3.52 and 3.53, x_{k+1} and $\dot{x}_{k+1}$ are given by

$$\begin{aligned}\dot{x}_{k+1} = -\left(\frac{\omega_{\mathrm{n}}^2\delta\Delta t}{\alpha}\right)x_k + \left(\frac{\alpha - 2\xi\omega_{\mathrm{n}}\delta\Delta t - \omega_{\mathrm{n}}^2\delta(\Delta t)^2}{\alpha}\right)\dot{x}_k \\ + \left(\frac{\alpha\Delta t - \delta(\alpha+\gamma)\Delta t}{\alpha}\right)\ddot{x}_k + \left(\frac{\delta\Delta t}{m\alpha}\right)F_{k+1}\end{aligned} \tag{3.64}$$

$$\begin{aligned}x_{k+1} = -\left(\frac{\alpha - \omega_{\mathrm{n}}^2\beta(\Delta t)^2}{\alpha}\right)x_k + \left(\frac{\alpha\Delta t - 2\xi\omega_{\mathrm{n}}\beta(\Delta t)^2 - \omega_{\mathrm{n}}^2\beta(\Delta t)^2}{\alpha}\right)\dot{x}_k \\ + \left(\frac{\frac{1}{2}\alpha(\Delta t)^2 - \beta(\alpha+\gamma)(\Delta t)^2}{\alpha}\right)\ddot{x}_k + \left(\frac{\beta(\Delta t)^2}{m\alpha}\right)F_{k+1}\end{aligned} \tag{3.65}$$

Arranging Equations 3.61, 3.64 and 3.65 in matrix form, a recursive relationship can be obtained as before:

$$\boldsymbol{q}_{k+1} = \boldsymbol{F}_N\boldsymbol{q}_k + \boldsymbol{H}_N F_{k+1} \tag{3.66}$$

in which

$$\boldsymbol{q}_i = \begin{Bmatrix} x_i \\ \dot{x}_i \\ \ddot{x}_i \end{Bmatrix}; \quad \boldsymbol{H}_N = \left\{\frac{1}{m\alpha}\right\}\begin{Bmatrix} \beta(\Delta t)^2 \\ \delta\Delta t \\ 1 \end{Bmatrix} \tag{3.67}$$

$$\boldsymbol{F}_N = \frac{1}{\alpha}\begin{bmatrix} \alpha - \omega_{\mathrm{n}}^2\alpha(\Delta t)^2 & \Delta t - 2\xi\omega_{\mathrm{n}}\beta(\Delta t)^2 - \omega_{\mathrm{n}}^2\beta(\Delta t)^3 & \frac{1}{2}\alpha(\Delta t)^2 - \beta(\alpha+\gamma)(\Delta t)^2 \\ -\omega_{\mathrm{n}}^2\delta\Delta t & \alpha - 2\xi\omega_{\mathrm{n}}\delta\Delta t - \omega_{\mathrm{n}}^2\delta(\Delta t)^2 & \alpha\Delta t - \delta(\alpha+\gamma)\Delta t \\ -\omega_{\mathrm{n}}^2 & -2\xi\omega_{\mathrm{n}} - \omega_{\mathrm{n}}^2\Delta t & -\gamma \end{bmatrix} \tag{3.68}$$

For constant average acceleration between two time stations, the values of $\delta = 1/2$ and $\beta = 1/4$.

3.4.3 Time Domain Analysis in State Space

The state-space equation for the SDOF system for earthquake excitation can be written as:

$$\dot{\boldsymbol{Z}} = \boldsymbol{A}\boldsymbol{Z} + \boldsymbol{f}_g \tag{3.69}$$

in which

$$\boldsymbol{A} = \begin{bmatrix} 0 & 1 \\ -\dfrac{k}{m} & -\dfrac{c}{m} \end{bmatrix}; \qquad \boldsymbol{f}_g = \begin{Bmatrix} 0 \\ -\ddot{x}_g \end{Bmatrix}; \qquad \boldsymbol{Z} = \begin{Bmatrix} x \\ \dot{x} \end{Bmatrix} \tag{3.70}$$

The solution to Equation 3.69 may be written in the standard form as:

$$\boldsymbol{Z}(t) = \boldsymbol{e}^{\boldsymbol{A}(t-t_0)}\boldsymbol{Z}(t_0) + \boldsymbol{e}^{\boldsymbol{A}t}\int_{t_0}^{t} \boldsymbol{e}^{-\boldsymbol{A}s}\boldsymbol{f}_g(s)\mathrm{d}s \tag{3.71}$$

in which t_0 is the initial time.

To obtain a step-by-step solution, $t_{k+1} = t$, $t_k = t_0$, and $\Delta t = t_{k+1} - t_k$ are assumed. Then,

$$\boldsymbol{Z}_{k+1} = \boldsymbol{e}^{\boldsymbol{A}\Delta t}\boldsymbol{Z}_k + \boldsymbol{e}^{\boldsymbol{A}t_{k+1}}\int_{t_k}^{t_{k+1}} \boldsymbol{e}^{-\boldsymbol{A}s}\boldsymbol{f}_g(s)\,\mathrm{d}s \tag{3.72}$$

The integration is performed numerically for the given digitized accelerations. This integration may be performed numerically in two ways leading to the following two expressions for $\boldsymbol{Z}_{k+1}$ [4].

$$\boldsymbol{Z}_{k+1} = \boldsymbol{e}^{\boldsymbol{A}\Delta t}\boldsymbol{Z}_k + \Delta t\boldsymbol{e}^{\boldsymbol{A}\Delta t}\boldsymbol{f}_{gk} \tag{3.73}$$

$$\boldsymbol{Z}_{k+1} = \boldsymbol{e}^{\boldsymbol{A}\Delta t}\boldsymbol{Z}_k + \boldsymbol{A}^{-1}(\boldsymbol{e}^{\boldsymbol{A}\Delta t} - \boldsymbol{I})\boldsymbol{f}_{gk} \tag{3.74}$$

The first one assumes that the forcing function is a series of delta functions within the time interval Δt. The second one assumes constant forcing function within the time interval. As Equation 3.74 involves an inversion procedure, Equation 3.73 is preferred to determine $\boldsymbol{Z}_{k+1}$. Once $\boldsymbol{Z}_{k+1}$ is obtained, the displacement and velocity at time step $k+1$ are known. They are used directly in the second-order equation of motion to obtain the acceleration at the time step $k+1$. To start the integration, the initial values of $\boldsymbol{Z}_k$ are to be defined or specified. In the above equations, computation of $\boldsymbol{e}^{\boldsymbol{A}t}$ is accomplished by the standard procedure of finding the eigen values and eigen vectors of $\boldsymbol{A}$. It can easily be shown that $\boldsymbol{e}^{\boldsymbol{A}t}$ may be determined by

$$\boldsymbol{e}^{\boldsymbol{A}t} = \phi\boldsymbol{e}^{\bar{\lambda}t}\phi^{-1} \tag{3.75}$$

in which ϕ is the eigen matrix of $\boldsymbol{A}$ and $\boldsymbol{e}^{\bar{\lambda}t}$ is a diagonal matrix having diagonal elements as $e^{\lambda_i t}$, in which λ_i is the ith eigen value.

3.4.4 Frequency Domain Analysis Using Fourier Transform

The frequency domain analysis, which is not strictly valid for earthquake excitations, can be used to obtain a good estimate of the rms and peak response of the SDOF system as mentioned before. To obtain the response, the irregular time history of ground motion is decomposed into its frequency components (harmonic components) and the SDOF is analyzed for each harmonic component. Responses obtained for each harmonic component are superimposed to obtain the final response. For this purpose, a pair of Fourier integrals is used. The pair of Fourier integrals for the arbitrary time history of ground acceleration

may be written as:

$$\ddot{x}_g(i\omega) = \frac{1}{2\pi}\int_{-\alpha}^{\alpha} \ddot{x}_g(t)\mathrm{e}^{-i\omega t}\mathrm{d}t \tag{3.76}$$

$$\ddot{x}_g(t) = \int_{-\alpha}^{\alpha} \ddot{x}_g(i\omega)\mathrm{e}^{i\omega t}\mathrm{d}\omega \tag{3.77}$$

The first integral gives the frequency components of the time history of ground acceleration in complex form, while the second integral retrieves back the time history from the complex frequency components. For practical applications, the time history is of finite duration (T) and, therefore, discrete forms of the Fourier transforms as given below are used with the finite duration of the time history [5].

$$\ddot{x}_{gk} = \frac{1}{N}\sum_{r=0}^{N-1} \ddot{x}_{gr}\mathrm{e}^{-i(2\pi kr/N)} \tag{3.78}$$

$$\ddot{x}_{gr} = \sum_{k=0}^{N-1} \ddot{x}_{gk}\mathrm{e}^{-i(2\pi kr/N)} \tag{3.79}$$

in which N is the discrete number of values of $\ddot{x}_g(t)$ sampled at a Δt time interval, termed $\ddot{x}_{gr}\ (r = 1 \ldots N)$; $\ddot{x}_{gk}\ (k = 1 \ldots N)$ are the discrete values of complex quantities denoting amplitude and phase of the kth harmonic sampled at a $\Delta\omega$ frequency interval; $T = (N-1)\Delta t$, T being the finite duration of the acceleration time history.

The computation of the pair of Fourier transforms using a discrete Fourier transform technique has been coded effectively and is popularly known as fast Fourier transform (FFT) and inverse fast Fourier transform (IFFT). FFT performs the first integral and IFFT performs the second one. Sampled values of the time history (having N discrete ordinates) are given as input to FFT. The output provides N discrete values of complex numbers, out of which $N/2$ values are complex conjugates of the other $N/2$ values. The sampling interval $(\Delta\omega)$ of the output is $2\pi/T$, where T is the duration of the time history. Harmonic components of the time history start with frequency $(\omega_i = 0)$ to $\omega_i = [(N/2)-1]\Delta\omega$ at an interval of $\Delta\omega$. If $a_j + b_j$ is the value of the jth complex quantity for the frequency ω_j, the amplitude, frequency, and phase angle of the jth harmonic are $(a_j^2 + b_j^2)^2$, ω_j, and $\theta_j = \tan^{-1}\left(b_j/a_j\right)$. Note that if the input time history is to be retrieved, then N complex numbers including the complex conjugates are to be given as inputs to the IFFT (Equation 3.79).

If $h_j(i\omega)$ is the complex frequency response function of the SDOF at frequency ω_j, then the response due to jth frequency component of the excitation is:

$$x_j(t) = h_j(i\omega)\ddot{x}_{gj}(i\omega)\mathrm{e}^{i\omega_j t} \tag{3.80}$$

in which

$$h(i\omega)_j = [(\omega_\mathrm{n}^2 - \omega_j^2) + 2i\xi\omega_\mathrm{n}\omega_j]^{-1}$$

The total response is obtained by summing up the responses $x_j(t)$, $j = 1 \ldots N/2$. This operation is performed using FFT and IFFT as given in the following steps:

1. Sample $\ddot{x}_g(t)$ at an interval of Δt to obtain N discrete values of the time history having a duration T (preferably $N = 2^n$, where n is an integer).
2. Input $\ddot{x}_{gr}\ (r = 1 \ldots N)$ in FFT.

3. Consider first $N/2$ values of the output from FFT; calculate the cut-off frequency ω_c as $\omega_c = [(N/2)-1]2\pi/T$, where T is the duration of the time history.
4. Obtain the complex frequency response function $h_j(i\omega)$ of the SDOF for $j=0$ to $(N/2-1)$ at frequencies $\omega_j = 0$ to $(N/2-1)\Delta\omega$.
5. Obtain $x_j(i\omega) = h_j(i\omega)\ddot{x}_{gj}(i\omega), j = 0 \ldots (N/2-1)$.
6. Obtain the complex conjugate of $x_j(i\omega)$, such that $x_j(i\omega), j = N/2$ is the complex conjugate of $x_j(i\omega)$, $j = (N/2-1)$ and $x_j(i\omega), j = N-1$ is the complex conjugate of $x_j(i\omega), j=0$.
7. Input $x_j(i\omega), \quad j = 0 \ldots N-1$ in IFFT; output will be N values of $x(t)$ sampled at Δt.

Frequency domain analysis using Fourier transform provides a relationship between the impulse response functions $h(\tau)$ and the complex frequency response function $h(i\omega)$. In time domain analysis using the Duhamel integral

$$x(t) = \int_{-\alpha}^{t} p(\tau)\, h(t-\tau)\mathrm{d}\tau \tag{3.81}$$

in which $p(\tau)$ is the impulse at time τ and $h(t-\tau)$ is the impulse response function for unit impulse response applied at time τ.

In frequency domain analysis, $x(t)$ is given by

$$x(t) = \frac{1}{2\pi}\int_{-\alpha}^{\alpha} h(i\omega)\ddot{x}_g(i\omega)\mathrm{e}^{i\omega t}\mathrm{d}\omega \tag{3.82}$$

Utilizing these two expressions of $x(t)$, a relationship between function $h(t)$ and the complex frequency response function $h(i\omega)$ can be established as [5]:

$$h(i\omega) = \int_{-\alpha}^{\alpha} h(t)\mathrm{e}^{-i\omega t}\mathrm{d}t \tag{3.83}$$

$$h(t) = \frac{1}{2\pi}\int_{-\alpha}^{\alpha} h(i\omega)\mathrm{e}^{i\omega t}\mathrm{d}t \tag{3.84}$$

Thus, $h(t)$ and $h(i\omega)$ form a Fourier transform pair.

Example 3.7

A single bay inclined portal frame with properties as shown in Figure 3.11 is subjected to El Centro earthquake ground acceleration with sampled values given in Appendix 3.C. Find the response (x) of the frame by using the Duhamel integral, Newmark's β-method, state-space time integration method, and frequency domain analysis using FFT. Assume zero initial conditions, that is, $x(0) = 0$, $\dot{x}(0) = 0$, and $\xi = 0.05$.

Solution: $\Delta t = 0.02$s; $\omega_n = 12.24\,\mathrm{rad\,s^{-1}}$; $\omega_d = \omega_n\sqrt{1-\xi^2} = 12.23\,\mathrm{rad\,s^{-1}}$

Duhamel integral–The constants work out to be (Equations 3.38–3.45)

$$C_1 = 0.98; \qquad C_2 = 3.448 \times 10^{-4}; \qquad C_3 = -9.65 \times 10^{-3}; \qquad C_4 = 9.77 \times 10^{-3}$$

$$D_1 = -0.05; \qquad D_2 = 0.987; \qquad D_3 = -5.48 \times 10^{-3}; \qquad D_4 = 5.99 \times 10^{-3}$$

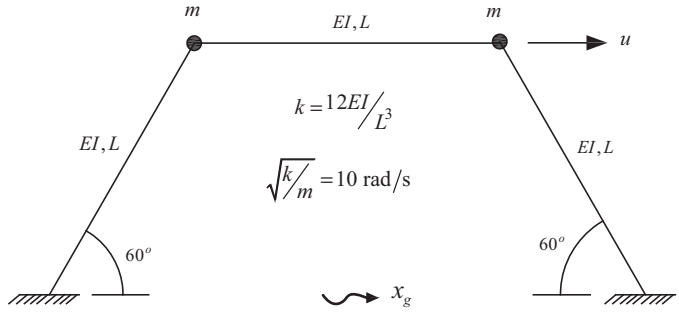

Figure 3.11 Inclined portal frame

Using the above values of the constants, $\boldsymbol{A}$ and $\boldsymbol{H}$ are determined as:

$$\boldsymbol{A} = \begin{bmatrix} 0.0150 & -0.0312 & -0.0257 \\ -0.5980 & 0.9696 & -0.0146 \\ -1.5153 & 3.4804 & 0.0436 \end{bmatrix} \quad \boldsymbol{H} = \begin{bmatrix} 0.0098 \\ 0.0060 \\ -1.0960 \end{bmatrix}$$

Using the recursive Equation 3.49, $\boldsymbol{q}$ for time stations $0-14\Delta t$ are given in Table 3.1.

Table 3.1 Comparison of displacement (m) response obtained by different methods

Time (s)	Duhamel	Newmark	State-space	Frequency domain
0	0	0	0	0.0016
0.02	0	0	0	0.0010
0.04	0	0	0	0.0004
0.06	−0.0001	−0.0001	−0.0001	−0.0003
0.08	−0.0001	−0.0001	−0.0001	−0.0009
0.1	−0.00 025	−0.0002	−0.0002	−0.0015
0.12	−0.0003	−0.0002	−0.0002	−0.0020
0.14	−0.0004	−0.0004	−0.0004	−0.0024
0.16	−0.0005	−0.0005	−0.0005	−0.0027
0.18	−0.0006	−0.0006	−0.0006	−0.0027
0.2	−0.00 075	−0.0007	−0.0007	−0.0028
0.22	−0.0009	−0.0009	−0.0009	−0.0028
0.24	−0.0012	−0.0010	−0.0010	−0.0026
0.26	−0.0013	−0.0012	−0.0012	−0.0023
0.28	−0.0015	−0.0013	−0.0013	−0.0019
Displacement over duration (30 s)				
Rms (m)	0.0150	0.0149	0.0149	0.0150
Peak (m)	0.0791	0.0784	0.0784	0.0754

Newmark's β-method–Using $\delta = 1/2$ and $\beta = 1/4$, $\boldsymbol{F}_n$ and $\boldsymbol{H}_n$ are obtained as

$$\boldsymbol{F}_n = \begin{bmatrix} 0.9854 & 0.0196 & 0.0001 \\ -1.4601 & 0.9589 & 0.0097 \\ -146.0108 & -4.1124 & -0.0265 \end{bmatrix} \quad \boldsymbol{H}_n = \begin{bmatrix} 0.0001 \\ 0.0097 \\ 0.9735 \end{bmatrix}$$

Using the recursive Equation 3.66, $\boldsymbol{q}$ for time stations $0-14\Delta t$ are given in Table 3.1.

State-space time integration–

$$\boldsymbol{A} = \begin{bmatrix} 0 & 1 \\ -37.50 & -1.2247 \end{bmatrix}$$

$$\phi = \begin{bmatrix} -0.0161 - 0.16045i & -0.0161 + 0.16045i \\ 0.9869 & 0.9869 \end{bmatrix}$$

$$e^{\bar{\lambda}\Delta T} = \begin{bmatrix} 0.9805 - 0.1201i & 0 \\ 0 & 0.9805 - 0.1201i \end{bmatrix}$$

$$e^{A\Delta T} = \begin{bmatrix} 0.9926 & 0.0197 \\ -0.7390 & 0.9684 \end{bmatrix}$$

Using Equation 3.73, $\boldsymbol{Z}$ for time stations $0 - 14\Delta t$ and are shown in Table 3.1.

Frequency domain analysis–

$$\Delta\omega = \frac{2\pi}{T} = \frac{2\pi}{30} = 0.2093 \text{ rad s}^{-1}$$

For $\omega_i = 0 - 17\Delta\omega$, $h_i(\omega)$ and $\ddot{x}_{gi}(\omega)$ are given in Table 3.2. After using steps 1–7, the responses obtained are shown for time stations $0 - 14\Delta t$ in Table 3.1.

Table 3.2 Frequency components of ground acceleration, frequency response function, and frequency contents of response for a few frequency steps ($\Delta\omega = 0.2093 \text{ rad s}^{-1}$)

Frequency	$\ddot{X}_{gj}(\omega)$ (m s^{-2})		$h_j(\omega)$ (m N^{-1})		$X_j(\omega)$ (m)	
	R	*I*	*R*	*I*	*R*	*I*
0	1.0979	0	0.0067	0	−0.0076	0
$\Delta\omega$	−1.009	−0.5237	0.0067	0	−0.0064	0.0050
$2\Delta\omega$	0.9244	−0.744	0.0067	0	−0.0301	−0.0089
$3\Delta\omega$	−2.4291	−0.4405	0.0067	0	−0.0236	0.0166
$4\Delta\omega$	4.4541	1.3565	0.0067	0	0.1214	0.0743
$5\Delta\omega$	0.7064	−6.87 521	0.0067	−0.0001	0.1012	−0.154
$6\Delta\omega$	3.4768	−2.4575	0.0067	−0.0001	0.1534	0.0591
$7\Delta\omega$	−0.1803	−19.3454	0.0068	−0.0001	0.1313	−0.0253

It is seen from the table that the responses obtained by the Duhamel integration, Newmark's β-method, and state-space integrations are nearly the same for time stations $0 - 14\Delta t$. The same parameters obtained by the frequency domain analysis are slightly different than others. However, rms and peak values of the responses obtained by all methods are nearly the same. Time histories of displacements obtained by different methods are shown in Figure 3.12(a–d). It is seen from the figure that the time history of displacement obtained by the frequency domain analysis is little different than that obtained by other methods.

3.5 Response Analysis for Multi-Degrees of Freedom (MDOF) Systems

The response analysis for the SDOF system described in Section 3.4 can be easily extended to multi-degrees of freedom systems. The analysis procedures remain the same for both single-point and

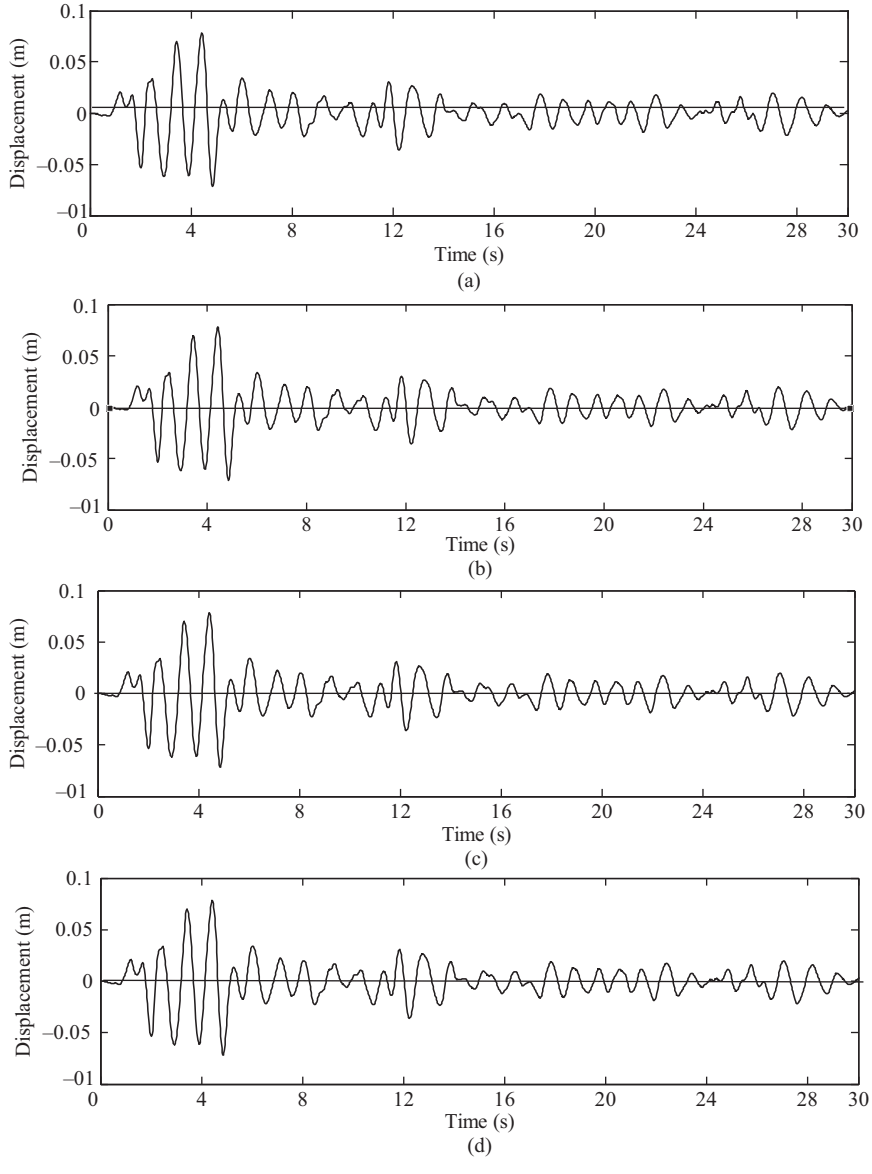

Figure 3.12 Time histories of displacements obtained by different methods: (a) frequency domain FFT analysis; (b) Newmark's β-method; (c) Duhamel integral; (d) state-space analysis

multi-point excitations. Two types of analysis are possible, namely, direct analysis and modal analysis. In the direct analysis, explicit knowledge of the damping matrix is required. For the linear analysis with Rayleigh damping ($\boldsymbol{C} = \alpha\boldsymbol{M} + \beta\boldsymbol{K}$), the modal analysis is used, wherever possible, as it needs only modal damping to be specified, which is generally assumed to be the same for all modes and is equal to the specified material damping.

3.5.1 Direct Analysis

In the direct analysis, the equation of motion, Equation 3.19 at the $k+1$th time step takes the form

$$\boldsymbol{M}\ddot{\boldsymbol{X}}_{\boldsymbol{k}+1} + \boldsymbol{C}\dot{\boldsymbol{X}}_{\boldsymbol{k}+1} + \boldsymbol{K}\boldsymbol{X}_{\boldsymbol{k}+1} = -\boldsymbol{M}\boldsymbol{r}\ddot{\boldsymbol{X}}_{\boldsymbol{g}\boldsymbol{k}+1} \tag{3.85}$$

in which $\boldsymbol{r}$ is the influence coefficient matrix or vector, which can be defined for both the single-point and multi-point excitations described in Section 3.3; $\boldsymbol{M}$, $\boldsymbol{C}$, and $\boldsymbol{K}$ are the same as $\boldsymbol{M}_{ss}$, $\boldsymbol{C}_{ss}$, and $\boldsymbol{K}_{ss}$, respectively; $\ddot{\boldsymbol{X}}_{\boldsymbol{g}\boldsymbol{k}+1}$ is a single time history of ground motion or is a vector consisting of several time histories of acceleration depending upon the type of excitation. Direct analysis is possible using both time domain and frequency domain analysis. In the time domain, both Duhamel integration and Newmark's β-method can be used. However, use of Duhamel integration for direct analysis of multi-degrees of freedom systems is not popular because it is somewhat complicated. Therefore, Duhamel integration is generally used in modal time domain analysis. On the other hand, Newmark's β-method is popular for both direct analysis and modal analysis in the time domain.

Newmark's β-Method: For the use of Newmark's β-method, Equations 3.52 and 3.53 are written with $\boldsymbol{X}_{\boldsymbol{k}+1}, \dot{\boldsymbol{X}}_{\boldsymbol{k}+1}$ as vector quantities denoting the responses of the MDOF system. Equations 3.52 and 3.53 are rewritten as:

$$\dot{\boldsymbol{X}}_{k+1} = \dot{\boldsymbol{X}}_k + (1-\delta)\,\ddot{\boldsymbol{X}}_k\Delta t + \ddot{\boldsymbol{X}}_{k+1}\delta\Delta t \tag{3.86}$$

$$\boldsymbol{X}_{k+1} = \boldsymbol{X}_k + \dot{\boldsymbol{X}}_k\Delta t + \left(\frac{1}{2}-\beta\right)(\Delta t)^2\ddot{\boldsymbol{X}}_k + \beta(\Delta t)^2\ddot{\boldsymbol{X}}_{k+1} \tag{3.87}$$

Substituting for $\dot{\boldsymbol{X}}_{k+1}$ and $\boldsymbol{X}_{k+1}$ into Equation 3.85,

$$\begin{aligned}\boldsymbol{M}\ddot{\boldsymbol{X}}_{k+1} &+ \boldsymbol{C}\{\dot{\boldsymbol{X}}_k + (1-\delta)\ddot{\boldsymbol{X}}_k\Delta t + \ddot{\boldsymbol{X}}_{k+1}\delta\Delta t\} \\ &+ \boldsymbol{K}\left\{\boldsymbol{X}_k + \dot{\boldsymbol{X}}_k\Delta t + \left(\frac{1}{2}-\beta\right)(\Delta t)^2\ddot{\boldsymbol{X}}_k + \beta(\Delta t)^2\ddot{\boldsymbol{X}}_{k+1}\right\} = -\boldsymbol{M}\boldsymbol{r}\ddot{\boldsymbol{X}}_{gk+1}\end{aligned} \tag{3.88}$$

Rearranging Equation 3.88:

$$\begin{aligned}\{\boldsymbol{M} + \boldsymbol{C}\delta\Delta t + \boldsymbol{K}\beta\Delta t^2\}\ddot{\boldsymbol{X}}_{k+1} = &-\boldsymbol{K}\boldsymbol{X}_k - \{\boldsymbol{K}\Delta t + \boldsymbol{C}\}\dot{\boldsymbol{X}}_k \\ &-\left\{\boldsymbol{C}(1-\delta)\Delta t + \boldsymbol{K}\left(\frac{1}{2}-\beta\right)\Delta t^2\right\}\ddot{\boldsymbol{X}}_k - \boldsymbol{M}\boldsymbol{r}\ddot{\boldsymbol{X}}_{gk+1}\end{aligned} \tag{3.89a}$$

$$\ddot{\boldsymbol{X}}_{k+1} = -\boldsymbol{G}^{-1}\boldsymbol{K}\,\boldsymbol{X}_k - \boldsymbol{G}^{-1}\{\boldsymbol{C}+\boldsymbol{K}\Delta t\}\dot{\boldsymbol{X}}_k - \boldsymbol{G}^{-1}\left\{\boldsymbol{C}(1-\delta)\Delta t + \boldsymbol{K}\left(\frac{1}{2}-\beta\right)\Delta t^2\right\}\ddot{\boldsymbol{X}}_k - \boldsymbol{G}^{-1}\boldsymbol{M}\boldsymbol{r}\ddot{\boldsymbol{X}}_{gk+1} \tag{3.89b}$$

Substituting Equation 3.89b into Equations 3.86 and 3.87,

$$\begin{aligned}\dot{\boldsymbol{X}}_{k+1} = &-\delta\Delta t\boldsymbol{G}^{-1}\boldsymbol{K}\,\boldsymbol{X}_k + [I - \boldsymbol{G}^{-1}\{\boldsymbol{C}+\boldsymbol{K}\Delta t\}\delta\Delta t]\dot{\boldsymbol{X}}_k \\ &+ \left[(1-\delta)\Delta t\,I - \boldsymbol{G}^{-1}\left\{\boldsymbol{C}(1-\delta)\Delta t + \boldsymbol{K}\left(\frac{1}{2}-\beta\right)\Delta t^2\right\}\delta\Delta t\right]\ddot{\boldsymbol{X}}_k \\ &-\delta\Delta t\boldsymbol{G}^{-1}\boldsymbol{M}\boldsymbol{r}\ddot{\boldsymbol{X}}_{g\,k+1}\end{aligned} \tag{3.90}$$

$$\begin{aligned}\boldsymbol{X}_{k+1} = &[I - \alpha\Delta t^2\boldsymbol{G}^{-1}\boldsymbol{K}]\boldsymbol{X}_k + [I\Delta t - \boldsymbol{G}^{-1}\{\boldsymbol{C}+\boldsymbol{K}\Delta t\}\beta\Delta t^2]\dot{\boldsymbol{X}}_k \\ &+ \left[\left(\frac{1}{2}-\beta\right)\Delta t^2\,I - \boldsymbol{G}^{-1}\left\{\boldsymbol{C}(1-\delta)\Delta t + \boldsymbol{K}\left(\frac{1}{2}-\beta\right)\Delta t^2\right\}\alpha\Delta t^2\right]\ddot{\boldsymbol{X}}_k \\ &-\beta\Delta t^2\,\boldsymbol{G}^{-1}\boldsymbol{M}\boldsymbol{r}\,\ddot{\boldsymbol{X}}_{g\,k+1}\end{aligned} \tag{3.91}$$

in which

$$\boldsymbol{G} = \boldsymbol{M} + \delta \boldsymbol{C}\Delta t + \beta \boldsymbol{K}\Delta t^2$$

Assuming $\delta = 1/2$ and $\beta = 1/4$, the usual values adopted for δ and β, Equations 3.89–3.91 can be written in recursive form as:

$$\boldsymbol{Q}_{k+1} = \boldsymbol{F}_N \boldsymbol{Q}_k + \boldsymbol{H}_N \ddot{\boldsymbol{X}}_{gk+1} \tag{3.92}$$

in which

$$\boldsymbol{Q}_k = \left[\boldsymbol{X_k} \quad \dot{\boldsymbol{X}}_{\boldsymbol{k}} \quad \ddot{\boldsymbol{X}}_{\boldsymbol{k}} \right]^T$$

and

$$\boldsymbol{F}_N = \begin{bmatrix} I - \dfrac{\boldsymbol{S}\Delta t^2}{4} & I\,\Delta t - \{\boldsymbol{Q} + \boldsymbol{S}\Delta t\}\dfrac{\Delta t^2}{4} & I\,\dfrac{\Delta t^2}{4} - \left\{\dfrac{\boldsymbol{Q}\Delta t}{2} + \dfrac{\boldsymbol{S}\Delta t^2}{4}\right\}\dfrac{\Delta t^2}{4} \\ -\dfrac{\boldsymbol{S}\Delta t}{2} & I - \{\boldsymbol{Q} + \boldsymbol{S}\Delta t\}\dfrac{\Delta t}{2} & I\,\dfrac{\Delta t}{2} - \left\{\dfrac{\boldsymbol{Q}\Delta t}{2} + \dfrac{\boldsymbol{S}\Delta t^2}{4}\right\}\dfrac{\Delta t}{2} \\ -\boldsymbol{S} & -\{\boldsymbol{Q} + \boldsymbol{S}\Delta t\} & -\left\{\dfrac{\boldsymbol{Q}\Delta t}{2} + \dfrac{\boldsymbol{S}\Delta t^2}{4}\right\} \end{bmatrix} \tag{3.93}$$

$$\boldsymbol{S} = \boldsymbol{G}^{-1}\boldsymbol{K}; \qquad \boldsymbol{Q} = \boldsymbol{G}^{-1}\boldsymbol{C}; \qquad \boldsymbol{T} = \boldsymbol{G}^{-1}\boldsymbol{M}r; \qquad \boldsymbol{H}_N = \begin{Bmatrix} -\boldsymbol{T}\dfrac{\Delta t^2}{4} \\ -\boldsymbol{T}\dfrac{\Delta t}{2} \\ -\boldsymbol{T} \end{Bmatrix} \tag{3.94}$$

The size of the $\boldsymbol{F}_N$ matrix is $3n \times 3n$ and that of the $\boldsymbol{H}_N$ matrix is $3n \times m$; in which n is the number of degrees of freedom and m is the number of different support excitations.

Frequency Domain Analysis using Fourier Transform: The method outlined for an SDOF system can be readily extended to an MDOF system. For single-point excitation, the influence coefficient matrix $\boldsymbol{r}$ in Equation 3.85 is a vector and the right-hand side of the equation is a force vector of the form

$$\boldsymbol{P}_g = -\{m_1 m_2 \ldots m_n\}^T \ddot{\boldsymbol{x}}_g \tag{3.95}$$

in which m_i is the mass associated with the ith degree of freedom in the direction of ground motion.

For a multi-point excitation system having, for example, n lumped masses and 3 support excitations, P_g is given by:

$$\boldsymbol{P}_g = -\boldsymbol{M}r\ddot{\boldsymbol{X}}_g = -\{m_1(r_{11}\ddot{x}_{g1} + r_{12}\ddot{x}_{g2} + r_{13}\ddot{x}_{g3}),\ m_2(r_{21}\ddot{x}_{g1} + r_{22}\ddot{x}_{g2} + r_{23}\ddot{x}_{g3}), \ldots\}^T \tag{3.96}$$

in which $\boldsymbol{M}$ is a diagonal matrix, $\boldsymbol{r}$ is a matrix of size $n \times 3$, and $\ddot{\boldsymbol{X}}_g$ is a vector of 3×1.

Extending the method of finding $x(t)$ for SDOF to MDOF systems

$$\boldsymbol{X}_j(i\omega) = \boldsymbol{H}_j(i\omega)\boldsymbol{P}_{gj}(i\omega) \tag{3.97}$$

in which $\boldsymbol{X}_j(i\omega)$ is the frequency component of displacement response vector due to the jth frequency component of the excitation vector $\boldsymbol{P}_g$; $\boldsymbol{H}(i\omega)_j$ is the frequency response function matrix given by:

$$\boldsymbol{H}_j(i\omega) = [\boldsymbol{K} - \boldsymbol{M}\omega_j^2 + i\boldsymbol{C}\omega_j]^{-1} \tag{3.98}$$

Using the same steps for the calculation as mentioned in Section 3.4.4, the response vector $\boldsymbol{X}(t)$ is obtained with the help of FFT and IFFT.

Example 3.8

For the multi-bay portal frame, shown in Figure 3.7, find the displacement responses $\boldsymbol{u}_1$ and $\boldsymbol{u}_2$ by using direct integration (Newmark's β-method) for the El Centro earthquake. Assume that the time delay between the supports is 5 s; $k/m = 100\,(\text{rad s}^{-1})^2$, and the percentage critical damping as 5%.

Solution: As the time delays between the supports are considered to 5 s, the duration of the records of $\ddot{x}_{g1}, \ddot{x}_{g2}$, and $\ddot{x}_{g3}$ is taken to be 40 s. Time history records are constructed from 30 s records of El Centro by adding zeros as given below:

(i) for $\ddot{x}_{g1}$, the last 10 s of record have zero values
(ii) for $\ddot{x}_{g2}$, the first 5 s and the last 5 s of records have zero values
(iii) for $\ddot{x}_{g3}$, the first 10 s of records have zero values.

Referring to Example 3.4, the equation of motion for the frame can be written as:

$$\begin{bmatrix}1 & 0\\ 0 & 2\end{bmatrix} m \begin{Bmatrix}\ddot{x}_1\\ \ddot{x}_2\end{Bmatrix} + \left\{\alpha m \begin{bmatrix}1 & 0\\ 0 & 2\end{bmatrix} + \beta \begin{bmatrix}3 & -3\\ -3 & 9\end{bmatrix} k\right\} \begin{Bmatrix}\dot{x}_1\\ \dot{x}_2\end{Bmatrix} + k \begin{bmatrix}3 & -3\\ -3 & 9\end{bmatrix} \begin{Bmatrix}\ddot{x}_1\\ \ddot{x}_2\end{Bmatrix}$$
$$= -\frac{m}{3} \begin{bmatrix}1 & 0\\ 0 & 2\end{bmatrix} \begin{bmatrix}1 & 1 & 1\\ 1 & 1 & 1\end{bmatrix} \begin{Bmatrix}\ddot{x}_{g_1}\\ \ddot{x}_{g_2}\\ \ddot{x}_{g_3}\end{Bmatrix}$$

For the given value of $k/m = 100$, the first two frequencies are determined as $\omega_1 = 12.25\,\text{rad s}^{-1}$; $\omega_2 = 24.49\,\text{rad s}^{-1}$. With these values of ω_1 and ω_2, the values of α and β are calculated as $\alpha = 0.8161$; $\beta = 0.0027$.

Direct integration method–Assuming $\Delta t = 0.02$ s, $\delta = 1/2$ and $\beta = 1/4$, G is obtained from Equation 3.91b. Then $\boldsymbol{S}$, $\boldsymbol{Q}$, and $\boldsymbol{T}$ are computed using Equation 3.94. The value of $\boldsymbol{Q}_{K+1}$ is obtained from the recursive equation, Equation 3.92 in which $\boldsymbol{F}_n$ and $\boldsymbol{H}_n$ are computed as

$$\boldsymbol{F}_n = \begin{bmatrix} 0.9712 & 0.0272 & 0.0193 & 0.0006 & 0.0001 & 0.0\\ 0.0132 & 0.9581 & 0.0003 & 0.0192 & 0.0 & 0.0001\\ -2.8171 & 2.7143 & 0.9281 & 0.0611 & 0.0096 & 0.0003\\ 1.3572 & -4.1751 & 0.0302 & 0.8973 & 0.0002 & 0.0094\\ -281.7651 & 271.4872 & -7.1831 & 6.1402 & -0.0432 & 0.0343\\ 135.7433 & -417.5091 & 3.0701 & -10.2531 & 0.0171 & -0.0602 \end{bmatrix}$$

$$\boldsymbol{H}_n = \begin{bmatrix} -0.0 & -0.0 & -0.0\\ -0.0 & -0.0 & -0.0\\ -0.0033 & -0.0033 & -0.0033\\ -0.0032 & -0.0032 & -0.0032\\ -0.3301 & -0.3301 & -0.3301\\ -0.3182 & -0.3182 & -0.3182 \end{bmatrix}$$

With the above matrices and $\{x\}$, $\{\dot{x}\}$ as zero

$$\ddot{\boldsymbol{x}}_0 = [\,0 \quad 0\,]^T$$

$$\boldsymbol{Q}_{\Delta t}^T = [\,-0.0 \quad -0.0 \quad -0.0002 \quad -0.0002 \quad -0.0204 \quad -0.0197\,]$$

$$\boldsymbol{Q}_{2\Delta t}^T = [\,-0.0 \quad -0.0 \quad -0.0005 \quad -0.0005 \quad -0.0113 \quad -0.0086\,]$$

The time histories of responses (u_1 and u_2) obtained are shown in Figure 3.13(a and b).

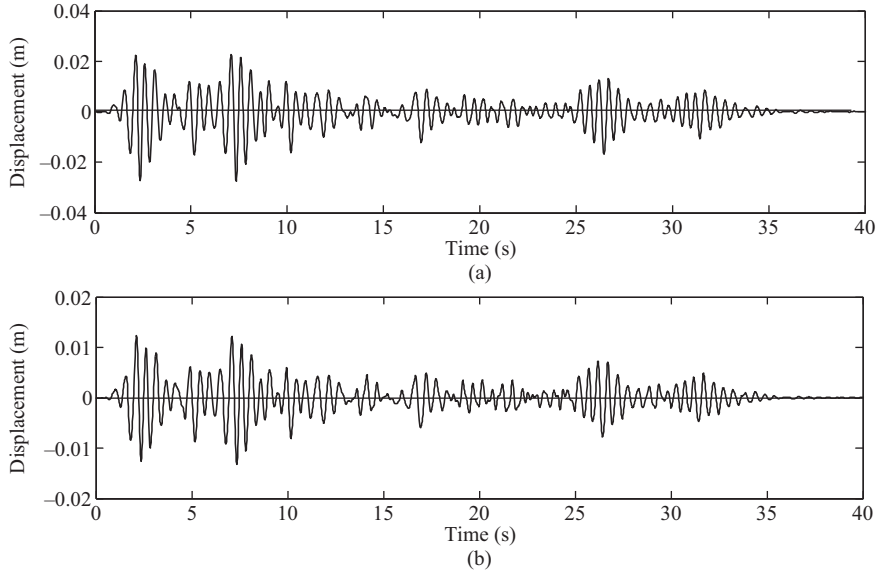

Figure 3.13 Displacements obtained by direct integration method: (a) displacement u_1; and (b) displacement u_2

It is seen from the figure that after 30 s, the time histories of the responses gradually decay to almost zero at 40 s. The reason for this is attributed to: (i) the time delay between the excitations at the three supports; and (ii) the total duration of 40 s of earthquake excitations at the supports are generated only from the 30 s of the actual earthquake record by putting zeros in appropriate places, such as, the tail end of the record.

Example 3.9

For the pitched roof portal frame shown in Figure 3.8, obtain the displacement responses corresponding to the sway degrees of freedom (4 and 5) shown in the figure for the El Centro earthquake. Consider two cases: (1) the same excitations at both supports and (ii) excitations with a time delay of 5 s between the two supports. Assume $\sqrt{EI/mL^3} = 2$ rad s^{-1} and the percentage critical damping is 5%. Use direct integration in the time domain (Newmark's β-method).

Solution: Referring to Examples 3.3 and 3.4, the mass and stiffness matrices of the frame corresponding to the sway degrees of freedom (4, 5) are

$$\boldsymbol{M} = \begin{bmatrix} 2.50 & 1.67 \\ 1.67 & 2.50 \end{bmatrix} m$$

$$\boldsymbol{K} = \frac{EI}{L^3} \begin{bmatrix} 19.56 & 10.49 \\ 10.49 & 129 \end{bmatrix}$$

$$\boldsymbol{r} = \begin{bmatrix} 0.479 & 0.331 \\ -0.131 & 0.146 \end{bmatrix}$$

Assuming $\sqrt{EI/mL^3} = 2$, the natural frequencies are $\omega_1 = 5.58$ rad s^{-1}; $\omega_2 = 18.91$ rad s^{-1}. The values of α and β are calculated as $\alpha = 0.4311$ and $\beta = 0.0041$, respectively, for 5% modal damping. With these values of α and β, the $\boldsymbol{C}$ matrix is obtained as before.

With the above matrices, and $\Delta t = 0.02$ s, and $\boldsymbol{x}$, $\dot{\boldsymbol{x}}$ as zero
For case (i):

$$\ddot{\boldsymbol{x}}_0 = [0 \quad 0]^T$$

$$\boldsymbol{Q}_{\Delta t}^T = [-0.0 \quad -0.0 \quad -0.0005 \quad -0.0 \quad -0.0491 \quad -0.0009]$$

$$\boldsymbol{Q}_{2\Delta t}^T = [-0.0 \quad -0.0 \quad -0.0013 \quad -0.0 \quad -0.0275 \quad -0.0005]$$

For case (ii):

$$\{\ddot{x}\}_0 = [0 \quad 0]^T$$

$$Q_{\Delta t}^T = [-0.0 \quad -0.0 \quad -0.0003 \quad 0.0001 \quad -0.0291 \quad 0.0077]$$

$$Q_{2\Delta t}^T = [-0.0 \quad -0.0 \quad -0.0007 \quad 0.0002 \quad -0.0153 \quad 0.0032]$$

Note that for case (ii) the time history of ground motion is taken to be of 35 s duration and excitations at the two supports are different to that obtained in the problem in Example 3.8. The time histories of displacements (4) and (5) are shown in Figure 3.14(a–d). It is seen from the figure that the effect of the time delay between the two supports is more for the vertical displacement of the crown. The maximum value of the displacement of DOF 5 is more for the case of the time delay between the support excitations. For the horizontal sway displacement, the opposite effect is observed. The maximum response is more for the case of no time delay. Thus, the effect of the time delay could be different for different responses.

***State-space solution*:** The state space solution for the SDOF system given in Section 3.4.3 may be extended to the MDOF system by simply increasing the size of the matrices and the vectors. For an MDOF system having n degrees of freedom, the size of matrix $\boldsymbol{A}$ is $2n \times 2n$ and that of the vector $\boldsymbol{z}$ is $2n \times 1$. Note that the excitation vector $\boldsymbol{f}_g$ is also of size $2n \times 1$ and depends upon the type of excitation. For a single point excitation f_g takes the form

$$\boldsymbol{f}_g = \begin{Bmatrix} 0 \\ -\boldsymbol{r} \end{Bmatrix} \ddot{x}_g \tag{3.99}$$

in which $\boldsymbol{r}$ is the influence coefficient vector of size $n \times 1$, $\ddot{x}_g$ is the specified time history of support acceleration.

For a multi-point excitation system, $\boldsymbol{f_g}$ is given by:

$$\boldsymbol{f}_g = \begin{Bmatrix} 0 \\ \boldsymbol{p}_g \end{Bmatrix} \tag{3.100}$$

in which $\boldsymbol{p}_g$ is a vector of size $n \times 1$ and is obtained as:

$$\boldsymbol{p}_g = -\boldsymbol{r}\ddot{\boldsymbol{x}}_g$$

in which $\boldsymbol{r}$ is the influence coefficient matrix of size $n \times s$; $\ddot{\boldsymbol{x}}_g$ is a vector of acceleration time histories of supports of size $s \times 1$; and s is the number of supports.

In the frequency domain, the state-space equation may be solved for an MDOF system by considering the equation

$$\dot{\boldsymbol{z}} = \boldsymbol{A}\dot{\boldsymbol{z}} + \boldsymbol{f}_g \tag{3.101}$$

in which

$$\boldsymbol{A} = \begin{bmatrix} \boldsymbol{0} & \boldsymbol{I} \\ -\boldsymbol{K}\boldsymbol{M}^{-1} & -\boldsymbol{C}\boldsymbol{M}^{-1} \end{bmatrix}; \quad \boldsymbol{f}_g = \begin{Bmatrix} 0 \\ \boldsymbol{p}_g \end{Bmatrix}; \quad \boldsymbol{z} = \begin{Bmatrix} x \\ \dot{x} \end{Bmatrix}; \quad \text{and} \quad \boldsymbol{p}_g = -\boldsymbol{r}\ddot{\boldsymbol{x}}_g \tag{3.102}$$

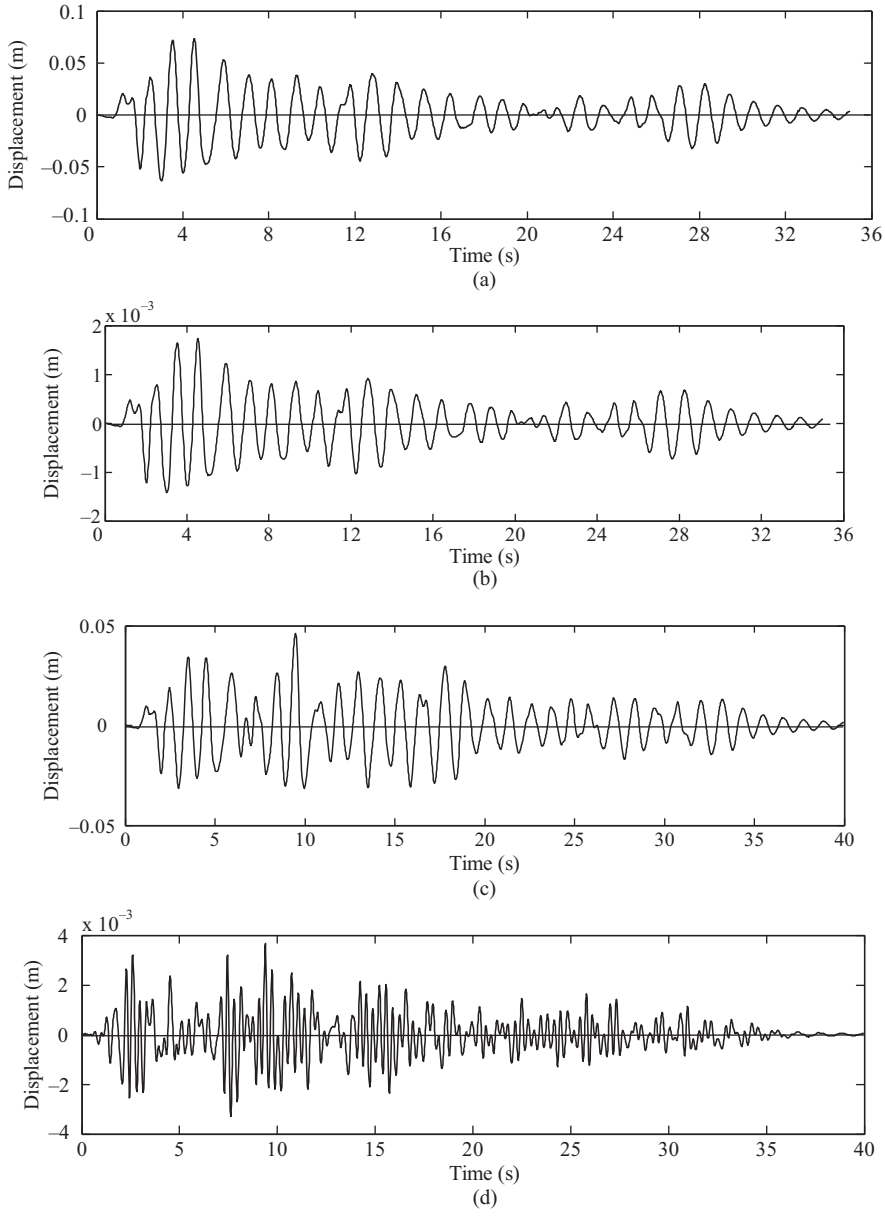

Figure 3.14 Time histories of displacements for the degrees of freedom 4 and 5: (a) without time delay for DOF 4; (b) without time delay for DOF 5; (c) with time delay for DOF 4; and (d) with time delay for DOF 5

By decomposing $\boldsymbol{f}_g$ in a complex Fourier series, let the jth frequency component of $\boldsymbol{f}_g$ be $\boldsymbol{f}_{gj}(i\omega)$. Then, the jth frequency component of the response is given by:

$$\boldsymbol{z}_j(i\omega) = \boldsymbol{H}_j(i\omega)\boldsymbol{f}_{gj}(i\omega) \tag{3.103}$$

$$\boldsymbol{H}_j(i\omega) = [\hat{\boldsymbol{I}}\omega - \boldsymbol{A}]^{-1} \tag{3.104}$$

in which $\hat{\boldsymbol{I}}$ is a diagonal matrix with $i(=\sqrt{-1})$ as diagonal elements. Using the same steps used in the Fourier method of response analysis, $\boldsymbol{z}(t)$ may be obtained.

The equation of motion in terms of absolute responses can be solved in the time domain, frequency domain, and in state space in the same way as described in Section 3.5.1. The right-hand side of Equation 3.15 is converted into an excitation load vector $\boldsymbol{P}_g$ of the form

$$\boldsymbol{P}_g = -(\boldsymbol{K}_{sg}\boldsymbol{x}_g + \boldsymbol{C}_{sg}\dot{\boldsymbol{x}}_g) \tag{3.105}$$

Note that $\boldsymbol{P}_g$ is of the size $n \times 1$; $\boldsymbol{K}_{sg}$ and $\boldsymbol{C}_{sg}$ are of the size $n \times s$; $\boldsymbol{x}_g$ and $\dot{\boldsymbol{x}}_g$ are, respectively, the time histories of displacements and velocities of size $s \times 1$; s is the number of supports. Note that $\boldsymbol{C}_{sg}$ is set to zero in most cases.

Example 3.10

A segment of a pipeline supported on soil is modeled as shown in Figure 3.15. Find the displacement responses corresponding to the dynamic degrees of freedom (1, 2 and 3) using (i) the frequency domain state-space solution and (ii) the frequency domain solution for the second-order equation of motion for El Centro earthquake. Take $3EI/mL^3 = 16\,(\text{rad s}^{-1})^2$; spring stiffness $K_s = 48m$, and $C_s = 0.6m$. Consider the damping ratio to be 2%.

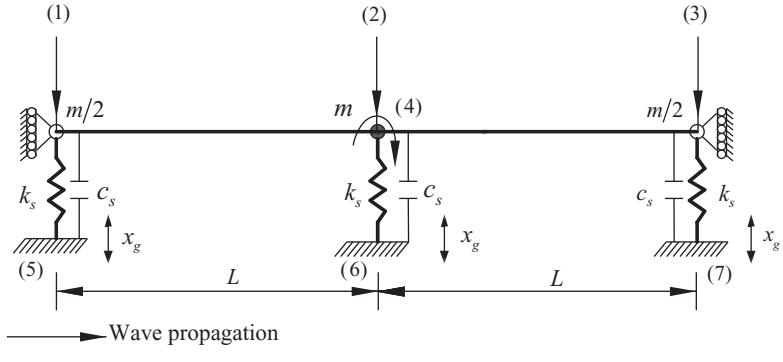

Figure 3.15 Segment of a pipeline supported on soft soil and modeled as spring-dashpot system

Solution: Condensed stiffness matrix corresponding to the dynamic degrees of freedom is

$$\boldsymbol{K} = \begin{bmatrix} 56 & -16 & 8 \\ -16 & 80 & -16 \\ 8 & -16 & 56 \end{bmatrix} m$$

The natural frequencies are $\omega_1 = 8.1\,\text{rad s}^{-1}$, $\omega_2 = 9.8\,\text{rad s}^{-1}$ and $\omega_3 = 12.2\,\text{rad s}^{-1}$.

Considering the first two natural frequencies, the values of α and β are:

$$\alpha = 0.1761 \quad \text{and} \quad \beta = 0.0022$$

The damping matrix for the structure is $\boldsymbol{C} = \alpha\boldsymbol{M} + \beta\boldsymbol{K}$.

The total damping matrix for the soil structure system is:

$$\overline{\boldsymbol{C}} = \begin{bmatrix} 0.813 & -0.035 & 0.017 \\ -0.035 & 0.952 & -0.035 \\ 0.017 & -0.035 & 0.813 \end{bmatrix} m$$

State space solution–

$$\boldsymbol{A} = \begin{bmatrix} 0.0 & 0.0 & 0.0 & 1.0 & 0.0 & 0.0 \\ 0.0 & 0.0 & 0.0 & 0.0 & 1.0 & 0.0 \\ 0.0 & 0.0 & 0.0 & 0.0 & 0.0 & 1.0 \\ -112.0 & 16.0 & -16.0 & -1.622 & 0.035 & -0.035 \\ 32.0 & -80.0 & 32.0 & 0.070 & -0.952 & 0.070 \\ -16.0 & 16.0 & -112.0 & -0.035 & 0.035 & -1.622 \end{bmatrix} \qquad \boldsymbol{f}_g = \begin{Bmatrix} 0 \\ 0 \\ 0 \\ -1 \\ -1 \\ -1 \end{Bmatrix} \ddot{x}_g$$

For $\omega = 4 \times 0.2093 = 0.8372\,\text{rad s}^{-1}$

$$\boldsymbol{H}(i\omega) = \begin{bmatrix} 0.0152-0.0078i & 0.0014+0.0014i & -0.0012-0.0007i & 0.0096-0.0001i & 0.0018 & -0.0009 \\ 0.0041+0.0022i & 0.0131+0.0116i & 0.0049+0.0028i & 0.0035-0.0001i & 0.0014-0.0002i & 0.0035-0.0001i \\ -0.0012-0.0007i & 0.0014+0.0014i & 0.0156+0.0078i & -0.0009 & 0.0018 & 0.0096-0.0001i \\ -1.0061+0.0132i & -0.0012+0.0012i & 0.0006-0.0011i & 0.0001+0.0081i & 0.0015i & -0.0007i \\ -0.0024+0.0041i & -1.0097+0.0112i & -0.0024+0.0042i & 0.0001+0.0032i & 0.0001-0.0117i & 0.0001+0.0031i \\ 0.0006-0.0011i & -0.0012+0.0012i & -1.0066+0.0131i & -0.0007i & 0.0015i & 0.0001+0.0081i \end{bmatrix}$$

$$\boldsymbol{f}_g(\omega) = \begin{bmatrix} 0.0 \\ 0.0 \\ 0.0 \\ -54.206-33.894i \\ -54.206-33.894i \\ -54.206-33.894i \end{bmatrix}$$

and hence,

$$\boldsymbol{z}(\omega) = \begin{bmatrix} -0.574-0.347i \\ -1.153-0.697i \\ -0.574-0.347i \\ 0.291-0.481i \\ 0.584-0.966i \\ 0.291-0.481i \end{bmatrix}$$

For the solution of second-order differential equation

$$\boldsymbol{H}(i\omega) = [\boldsymbol{K} - \boldsymbol{M}\omega^2 + i\overline{\boldsymbol{C}}\omega]^{-1} \qquad \boldsymbol{P}_g = \begin{Bmatrix} -1 \\ -1 \\ -1 \end{Bmatrix} m\ddot{x}_g$$

For $\omega = 0.8372\,\text{rad s}^{-1}$

$$\boldsymbol{H}(i\omega) = \begin{bmatrix} 0.0191-0.0003i & 0.0035-0.0001i & -0.0018 \\ 0.0035-0.0001i & 0.0142-0.0002i & 0.0035-0.0001i \\ -0.0018 & 0.0035-0.0001i & 0.0192-0.0003i \end{bmatrix} \qquad \boldsymbol{p}_g(\omega) = \begin{Bmatrix} -27.103-16.947i \\ -54.206-33.894i \\ -27.103-16.947i \end{Bmatrix} m$$

$$\boldsymbol{X}(\omega) = \begin{Bmatrix} -0.671-0.405i \\ -0.962-0.581i \\ -0.671-0.405i \end{Bmatrix}$$

Time histories of displacements for the degrees of freedom (1) and (2) obtained by the two methods are shown in Figures 3.16 and 3.17. It is seen from the figures that both methods provide almost the same responses.

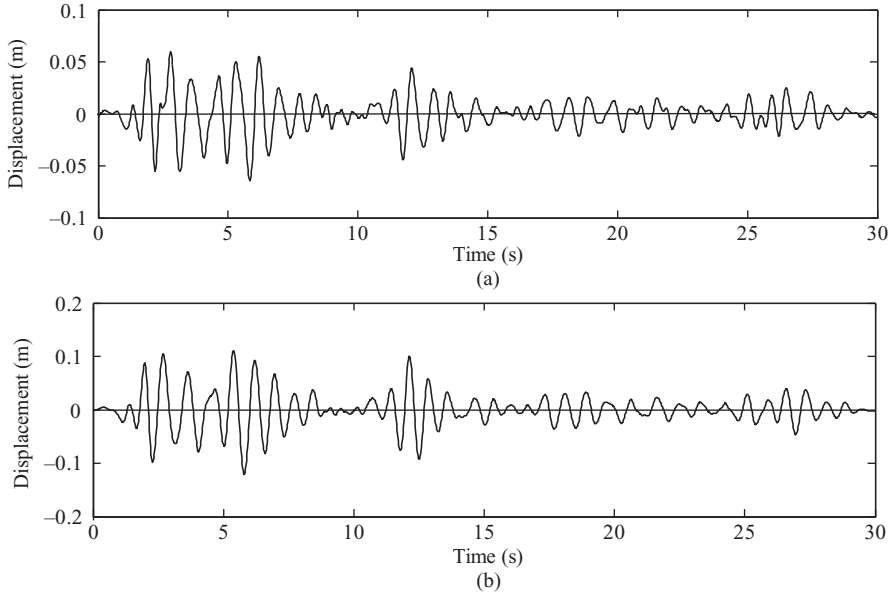

Figure 3.16 Time histories of displacements for degrees of freedom 1 and 2 obtained by frequency domain analysis: (a) displacement for DOF 1; and (b) displacement for DOF 2

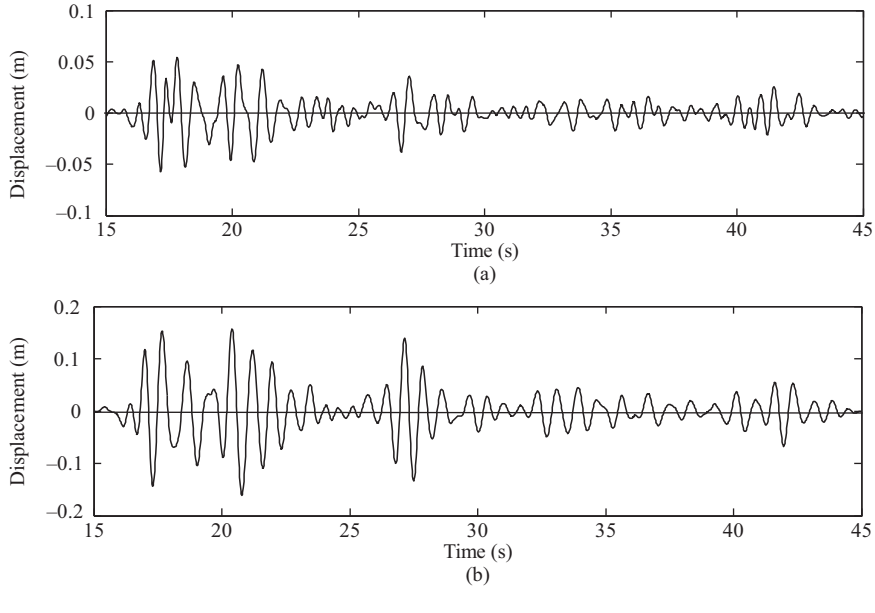

Figure 3.17 Time histories of displacements for degrees of freedom 1 and 2 obtained by frequency domain state-space solution: (a) displacement for DOF 1; and (b) displacement for DOF 2

3.5.2 Modal Analysis

In the modal analysis, the equation of motion, Equation 3.85, is decoupled into a set of n uncoupled equations of motion using the normal mode theory. Each uncoupled equation of motion represents an SDOF system.

The normal mode theory is well explained in all textbooks on structural dynamics. For the sake of completeness, a brief outline of the normal mode theory used in the context of earthquake excitation is presented below.

Normal mode theory stipulates that the response of an MDOF system is a weighted summation of its undamped mode shapes. The weighting functions are functions of time and are known as generalized co-ordinates (are also called modal co-ordinates). Thus, the displacement response of Equation 3.85 may be written as:

$$\boldsymbol{X} = \phi \boldsymbol{z} \tag{3.106}$$

where

$\boldsymbol{X}$ is the vector of displacement of size $n \times 1$
ϕ is the mode shape matrix of size $n \times m$
$\boldsymbol{z}$ is the vector of generalized co-ordinates
m is the number of modes considered in the analysis.

Substituting for $\boldsymbol{X}$ in Equation 3.85 and pre-multiplying by ϕ^T, Equation 3.85 becomes

$$\phi^T \boldsymbol{M}\phi\ddot{\boldsymbol{z}} + \phi^T \boldsymbol{C}\phi\dot{\boldsymbol{z}} + \phi^T \boldsymbol{K}\phi\boldsymbol{z} = -\phi^T \boldsymbol{M}\boldsymbol{r}\ddot{\boldsymbol{X}}_g \tag{3.107}$$

Using the orthogonality condition of mode shapes,

$$\phi^T \boldsymbol{M}\phi = \bar{\boldsymbol{M}}\ ; \qquad \phi^T \boldsymbol{K}\phi = \bar{\boldsymbol{K}} \tag{3.108}$$

in which $\bar{\boldsymbol{M}}$ and $\bar{\boldsymbol{K}}$ are diagonal matrices. Assuming C to be Rayleigh damping, that is, mass and stiffness proportional

$$\boldsymbol{C} = \alpha \boldsymbol{M} + \beta \boldsymbol{K} \tag{3.109}$$

and

$$\phi^T \boldsymbol{C}\phi = \bar{\boldsymbol{C}} \tag{3.110}$$

in which $\bar{\boldsymbol{C}}$ also becomes a diagonal matrix. This type of damping is also known as classical damping. By virtue of $\bar{\boldsymbol{M}}$, $\bar{\boldsymbol{K}}$, and $\bar{\boldsymbol{C}}$ being diagonal matrices, Equation 3.107 is converted into a set of n uncoupled equations of motion of the form

$$\overline{m}_i \ddot{z}_i + \overline{c}_i \dot{z}_i + \overline{k}_i z_i = -\phi_i^T \boldsymbol{M}\boldsymbol{r}\ddot{\boldsymbol{x}}_g; \quad i = 1 \ldots m \tag{3.111}$$

in which

$$\overline{m}_i = \phi_i^T \boldsymbol{M}\phi_i; \overline{c}_i = \phi_i^T \boldsymbol{C}\phi_i$$

$$\overline{k}_i = \phi_i^T \boldsymbol{K}\phi_i; \quad \omega_i^2 = \frac{\overline{k}_i}{\overline{m}_i}; \quad \overline{c}_i = 2\xi_i \omega_i \overline{m}_i \tag{3.112}$$

in which ξ_i is the modal damping ratio.

Equation 3.111 can, therefore, be written as:

$$\ddot{z}_i + 2\xi\omega_i \dot{z}_i + \omega_i^2 z_i = -\sum_{k=1}^{s} \lambda_{ik} \ddot{x}_{gk} \quad (i = 1 \ldots m) \tag{3.113}$$

in which λ_{ik} is the ith mode participation factor for the kth support excitation and is given by

$$\lambda_{ik} = \frac{\phi_i^T \boldsymbol{M} \boldsymbol{r}_k}{\phi_i^T \boldsymbol{M} \phi_i} \tag{3.114}$$

in which $\boldsymbol{r}_k$ is the kth column of the $\boldsymbol{r}$ matrix and $\ddot{x}_{gk}$ is the kth element of the vector $\ddot{\boldsymbol{x}}_g$ consisting of s number of excitations.

For $s = 1$, Equation 3.113 represents the equation for a single-point excitation system.

In general, Equation 3.113 represents m SDOF systems subjected to excitations given by the right-hand side of the equation of motion. For the specified time histories of excitations $\ddot{x}_{gk}$, each of the SDOF systems given by Equation 3.113 can be solved for z_i using Duhamel integration or Newmark's integration method, or frequency domain analysis using a Fourier series. Once $z_i (i = 1 \ldots m)$ are obtained, $\boldsymbol{X}$ can be determined from Equation 3.106.

Example 3.11

For the simplified model of a cable stayed bridge, shown in Figure 3.9, obtain the displacement responses corresponding to the dynamic degrees of freedom (1, 2, and 3) shown in the figure for the El Centro earthquake with 5 s time delay between the supports. Use modal time history (with Newmark's β-method) and modal frequency domain (with FFT) analyses with the percentage critical damping taken as 5%.

Solution: From Example 3.6, the mass matrix, the stiffness matrix corresponding to the dynamic degrees of freedom, and the $\boldsymbol{r}$ matrix are taken as:

$$\boldsymbol{K} = \begin{bmatrix} 684 & 0 & -149 \\ 0 & 684 & 149 \\ -149 & 149 & 575 \end{bmatrix} m \qquad \boldsymbol{M} = \begin{bmatrix} 20 & 0 & 0 \\ 0 & 20 & 0 \\ 0 & 0 & 60 \end{bmatrix} m$$

$$\boldsymbol{r} = \frac{1}{10} \begin{bmatrix} 5.318 & 0.031 & -0.002 & -0.318 \\ -0.318 & -0.002 & 0.031 & 5.318 \\ 1.416 & 0.008 & -0.008 & -1.416 \end{bmatrix}$$

As a time delay of 5 s is considered between the supports, a total of 45 s of excitation is considered at each support. As explained in Example 3.8, $\ddot{x}_{g1}$ will have the first 30 s as the actual El Centro record and the last 15 s will consist of zeros. $\ddot{x}_{g3}$ will have first 10 s as zeros followed by 30 s of the actual record, and the last 5 s of the record will be zeros. Similarly, $\ddot{x}_{g2}$ and $\ddot{x}_{g4}$ may be constructed.

The natural frequency and mode shapes are:

$$\omega_1 = 2.86 \text{ rad s}^{-1} \qquad \omega_2 = 5.85 \text{ rad s}^{-1} \qquad \omega_3 = 5.97 \text{ rad s}^{-1}$$

$$\phi_{\mathbf{1}}^T = [-0.036 \quad 0.036 \quad -0.125]$$

$$\phi_{\mathbf{2}}^T = [0.158 \quad 0.158 \quad 0]$$

$$\phi_{\mathbf{3}}^T = [-0.154 \quad 0.154 \quad 0.030]$$

Using the mode shapes, the first modal equation is

$$\ddot{z}_1 + 2\eta\omega_1 \dot{z}_1 + \omega_1^2 z_1 = -\frac{\phi_{\mathbf{1}}^T \boldsymbol{M} \boldsymbol{r}}{\phi_{\mathbf{1}}^T \boldsymbol{M} \phi_{\mathbf{1}}} \begin{Bmatrix} \ddot{x}_{g1} \\ \ddot{x}_{g2} \\ \ddot{x}_{g3} \\ \ddot{x}_{g4} \end{Bmatrix}$$

$$p_{g1} = [\,1.474 \quad 0.008 \quad -0.0061 \quad 1.474\,] \begin{Bmatrix} \ddot{x}_{g1} \\ \ddot{x}_{g2} \\ \ddot{x}_{g3} \\ \ddot{x}_{g4} \end{Bmatrix}$$

Similarly, the other two modal equations are obtained.

Time histories of p_{g1}, p_{g2}, and p_{g3} are shown in Figure 3.18(a–c). It may be seen that the time histories of the generalized forces are of 45 s duration without having successive zero values either at the beginning or at the end of the time histories.

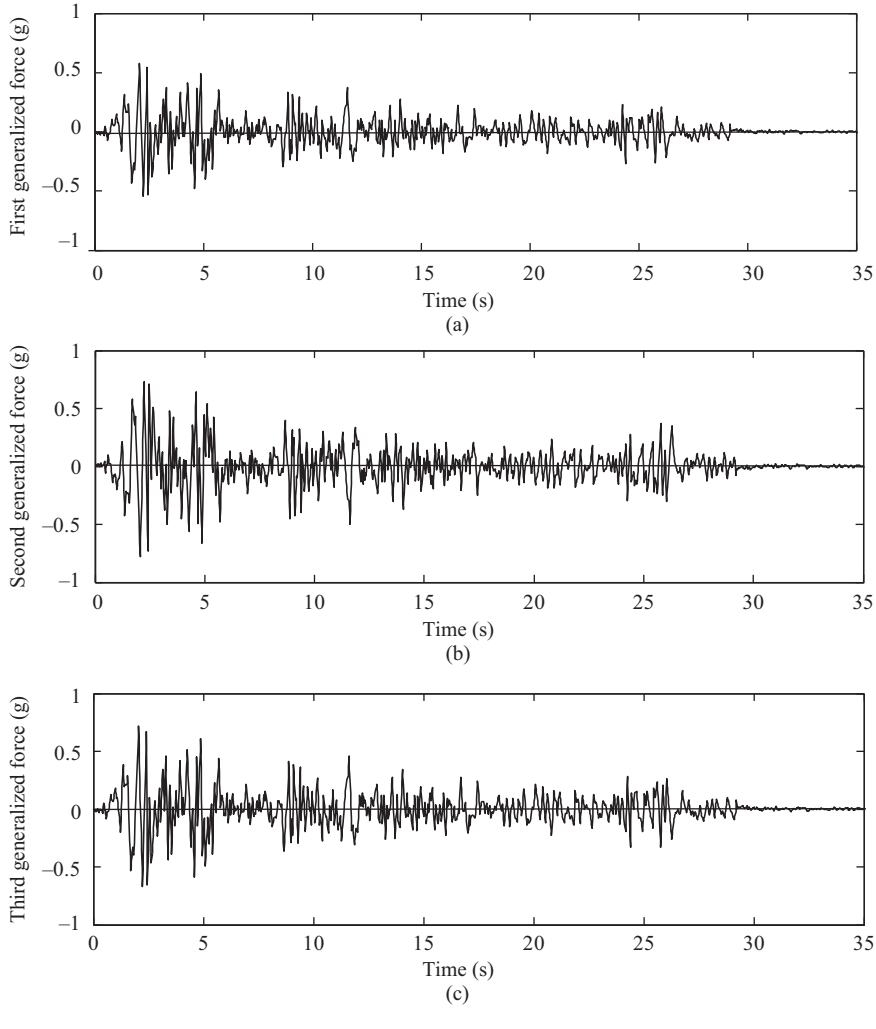

Figure 3.18 Time histories of generalized forces normalized with modal mass: (a) first generalized force (p_{g1}); (b) second generalized force (p_{g2}); and (c) third generalized force (p_{g3})

The modal equations may be solved like single degree of freedom systems. Thus, the three modal equations are solved by Newmark's β-method and frequency domain analysis using FFT. Using zero initial conditions for z_1, z_2, and z_3 and $\Delta t = 0.02$s, the time histories of z_1, z_2, and z_3 are shown in Figure 3.19(a–c). It may be seen from the figure that the generalized displacements begin to die down after 30 s as expected.

The rms and peak values of the generalized displacements obtained by modal time history and frequency domain solution are compared in Table 3.4.

It is seen from Tables 3.3 and 3.4 that the two methods of analysis provide nearly the same results.

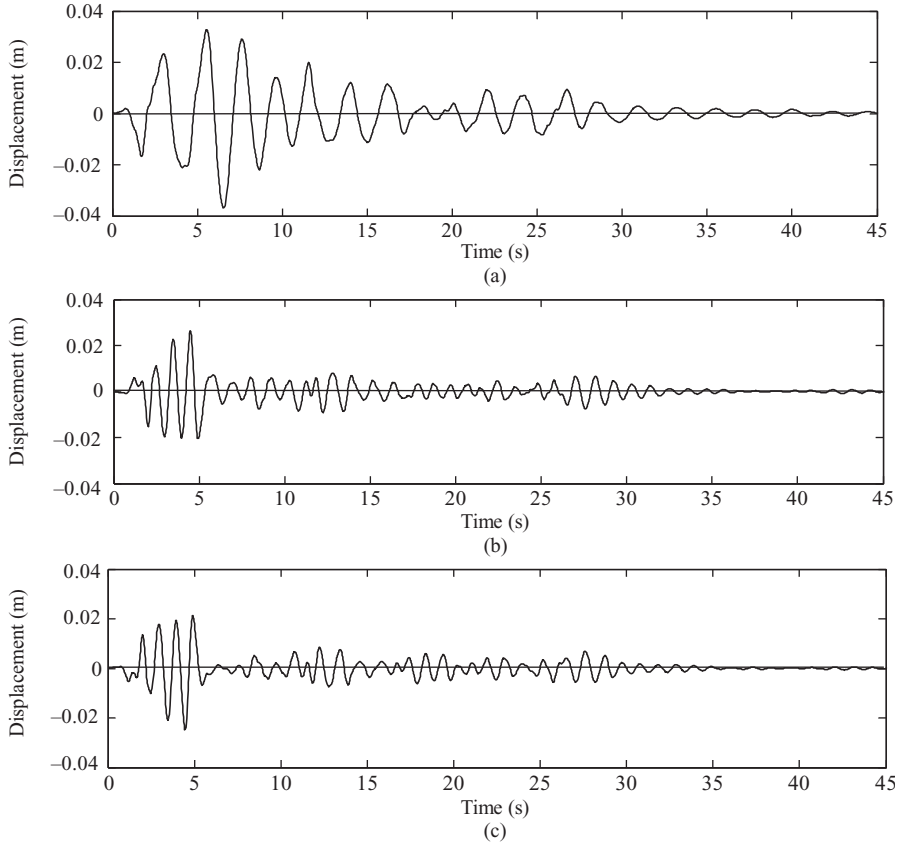

Figure 3.19 Time histories of generalized displacements: (a) first generalized displacement (z_1); (b) second generalized displacement (z_2); and (c) third generalized displacement (z_3)

3.5.3 Size Reduction

One of the advantages of the modal analysis procedure is that the size of the problem can be drastically reduced without compromising much on the accuracy of the results. It has been observed that consideration of the first few modes in Equation 3.113 gives results of sufficient accuracy; contributions

Table 3.3 Results of a few frequency steps for frequency domain modal analysis ($\Delta\omega = 0.139\,\mathrm{rad\,s^{-1}}$)

Variables	ω						
	0	$2\Delta\omega$	$3\Delta\omega$	$4\Delta\omega$	$5\Delta\omega$	$6\Delta\omega$	$7\Delta\omega$
h_{z1}	0.122	0.1228–0.0006i	0.1237–0.0012i	0.1252–0.0019i	0.1273–0.0026i	0.1302–0.0034i	0.1339–0.0043i
p_{g1}	−0.183	0.1305–0.0456i	$0.2943 + 0.3703i$	−0.7413–0.2186i	$0.2102 + 0.9755i$	$-0.8876 + 2.7771i$	$2.9898 + 1.8799i$
z_1	0.022	$-0.0161 + 0.0057i$	−0.0368–0.0454i	$0.0932 + 0.0261i$	−0.0293–0.1237i	0.1062–0.3646i	−0.4084–0.2389i
h_{z2}	0.029	0.0293–0.0001i	0.0293–0.0001i	0.0294–0.0002i	0.0295–0.0003i	0.0297–0.0004i	0.0298–0.0004i
p_{g2}	0.305	$-0.1453 + 0.0828i$	−0.2723–0.5062i	$1.2288 + 0.3644i$	−0.4603–1.1269i	1.6648–3.1453i	−4.9548–3.1031i
z_2	−0.008	0.0042–0.0024i	$0.0081 + 0.0148i$	−0.0362–0.0104i	$0.0139 + 0.0331i$	$-0.0482 + 0.0939i$	$0.1492 + 0.0905i$
h_{z3}	0.028	0.0281–0.0001i	0.0281–0.0001i	0.0282–0.0002i	0.0283–0.0003i	0.0285–0.0003i	0.0286–0.0004i
p_{g3}	−0.226	0.1612–0.0564i	$0.3636 + 0.4574i$	−0.9155–0.2698i	$0.2596 + 1.2046i$	$-1.0963 + 3.4293i$	$3.6921 + 2.3224i$
z_3	0.006	$-0.0045 + 0.0016i$	−0.0103–0.0128i	$0.0259 + 0.0074i$	−0.0077–0.0341i	0.0301–0.0981i	−0.1067–0.0651i

Table 3.4 Comparison of generalized displacements

Solution	z_1		z_2		z_3	
	Rms (m)	Peak (m)	Rms (m)	Peak (m)	Rms (m)	Peak (m)
Time history	0.0091	0.0369	0.0048	0.0261	0.0044	0.0249
Frequency domain	0.009	0.0368	0.0049	0.0265	0.0044	0.0250

of higher modes to the response are not generally significant. This is the case because more energy is required to excite higher modes that have higher frequencies and, generally, the energy contents of excitations at higher frequencies are low. Furthermore, the mode participation factors given by Equation 3.114 become smaller with a higher number of modes. Therefore, only the first few equations $m < n$ are solved to obtain the response, thereby reducing the size of the problem. The number of equations to be solved is equal to the number of modes whose contributions are considered to be significant in the analysis.

However, the number of modes to be considered depends upon the nature of excitation, dynamic characteristics of the structure, and the response quantity of interest. For structures having well separated natural frequencies, the first few modes (up to 5) may be sufficient to obtain the displacement response fairly accurately. For structures having closely spaced frequencies, such as asymmetric tall buildings, suspension or cable stayed bridges, a higher number of modes may have to be considered to obtain good estimates of the responses.

Generally, more number of modes are also required to obtain good estimates of bending moments or stresses compared with that required for displacements. This is the case because higher modes contribute more to the curvature and therefore, contribute more to the bending response. One index, which is widely used to determine the number of modes to be considered in the analysis, is the mass participation factor defined by:

$$\rho_i = \frac{\sum_{r=1}^{n} m_r \phi_{ir}}{M} \tag{3.115}$$

where

m_r is the mass attached to rth degree of freedom
ϕ_{ir} is the ith mode shape coefficient for the rth degree of freedom
M is the total mass of the structure.

The number of modes, m, to be considered in the analysis, is determined such that

$$\sum_{i=1}^{m} \rho_i \approx 1 \quad (\text{within } 5\%) \tag{3.116}$$

One approach, termed the mode acceleration approach [6, 7], has been developed for obtaining a good estimate of any response quantity (moment or displacement) using a lesser number of modes.

Consider the case of single-point excitation. Equation 3.113 can be written as:

$$z_i = \frac{1}{\omega_i^2}\left[-\lambda_i \ddot{x}_g\right] - \frac{1}{\omega_i^2}\left[\ddot{z}_i + 2\xi\omega_i \dot{z}_i\right] \tag{3.117}$$

Let ϕ_i be the ith mode shape coefficient for a response quantity $R(t)$, then

$$R(t) = -\sum_{i=1}^{m} \frac{\phi_i}{\omega_i^2} \lambda_i \ddot{x}_g - \sum_{i=1}^{m} \frac{1}{\omega_i^2} (\ddot{z}_i + 2\xi\omega_i \dot{z}_i)\phi_i \tag{3.118}$$

$$= \overline{R}(t) - \sum_{i=1}^{m} \frac{1}{\omega_i^2} (\ddot{z}_i + 2\xi\omega_i \dot{z}_i)\phi_i \tag{3.119}$$

$\overline{R}(t)$ is obtained by considering m to be equal to n, n being the number of dynamic degrees of freedom.

$\overline{R}(t)$ may be viewed as the response obtained by applying $-M r \ddot{X}_g$ quasi-statically, that is, by ignoring the effects of structural acceleration and velocity on the structure. This can be proved as below.

The quasi-static equation may be written as:

$$\boldsymbol{K}\boldsymbol{X}(t) = -\boldsymbol{M}\boldsymbol{r}\ddot{\boldsymbol{x}}_g(t) \tag{3.120}$$

Using modal transformation, Equation 3.120 can be written as:

$$\phi^{\boldsymbol{T}}\boldsymbol{K}\phi\, \boldsymbol{z}(t) = -\phi^{\boldsymbol{T}}\boldsymbol{M}\boldsymbol{r}\, \ddot{\boldsymbol{x}}_g(t) \tag{3.121}$$

Equation 3.121 is the same as the set of uncoupled equations, given by Equation 3.107 in which $\ddot{z}_i$ and $\dot{z}_i$ are omitted and, therefore, z_i given by Equation 3.121 is the quasi-static response of the ith SDOF system and is given by:

$$z_i = \frac{-\lambda_i \ddot{x}_g}{\omega_i^2} \tag{3.122}$$

As $\overline{R}(t)$ may be written as a weighted summation of all mode shapes (that is, $m = n$)

$$\overline{R}(t) = \sum_{i=1}^{n} \phi_i z_i = -\sum_{i=1}^{n} \phi_i \frac{\lambda_i \ddot{x}_g}{\omega_i^2} \tag{3.123}$$

Thus, the solution for $R(t)$ consists of two steps:

1. Solution of $\overline{R}(t)$ obtained by the quasi-static analysis of the structure for the earthquake force $-\boldsymbol{M}\boldsymbol{r}\ddot{\boldsymbol{x}}_g$.
2. Solution of modal equations to obtain $\sum_{i=1}^{m} \frac{1}{\omega_i^2} (\ddot{z}_i + 2\xi\omega_i \dot{z}_i)\phi_i$.

The second step of the solution may be obtained by finding z_i from Equation 3.117 and then writing

$$\frac{1}{\omega_i^2} (\ddot{z}_i + 2\xi\omega_i \dot{z}_i) = \left(\frac{-\lambda_i \ddot{x}_g}{\omega_i^2} - z_i \right) \tag{3.124}$$

The contribution of the second part of the solution from higher modes to the response $R(t)$ is very small. This is the case because for higher modes, frequencies are very high and relative displacements are very small. Because of these reasons, only the first few modes may be considered for the second part of the solution.

It has been found that mode acceleration approach provides better responses with a smaller number of modes compared with those obtained by the usual mode summation approach. The reason for this is that the first part of the response considers contributions from all modes, while the contributions of higher modes on the second part of the response are very small. In particular, responses such as bending moments and shear forces at any cross-section of the structure can be obtained more accurately with a limited number of modes using the mode acceleration approach.

3.5.4 Computation of Internal Forces

The determination of displacement and acceleration responses of the structure is straight forward using normal mode theory. However, the bending moment and shear forces at any section of the structure cannot be directly obtained. They are calculated from displacement responses of the structure and the stiffness properties of the member. One way to obtain bending responses directly by weighted summation of mode

shapes is to determine the mode shape coefficients for the bending moment or any other response quantity of interest. For this purpose, the structure may be statically analyzed for each mode with a static load given by:

$$\boldsymbol{P}_i = \boldsymbol{M}\phi_i\omega_i^2; \quad i = 1 \ldots m \tag{3.125}$$

where m is the number of modes being considered. The analysis provides a value of the bending moment or the response quantity of interest. This value is the mode shape coefficient for the bending moment in the ith mode. If displacement mode shape coefficients are replaced by the mode shape coefficient in the usual mode superposition technique or mode accelerations approach, the bending moment or the response quantity of interest can be directly obtained as displacements.

When modal analysis is not used, that is, the responses are obtained by direct analysis, the response quantities such as bending moment and shear forces are obtained from the element stiffness properties and the dynamic displacements. While displacements for the dynamic degrees of freedom are directly obtained from the dynamic response analysis, those of the degrees of freedom that were condensed out are determined separately by using the condensation relationship.

It should be noted that modal analysis is not applicable for solving absolute displacements using Equation 3.15. The reason for this is that normal modes are defined with respect to the relative displacement of the structure with respect to the fixed supports. Therefore, if the advantage of the modal analysis is to be taken in finding the absolute displacements of the dynamic degrees of freedom, then Equation 3.19 is solved using the normal mode theory and support displacements are added to the relative displacements.

3.5.5 Modal Analysis in Time Domain for State-Space Equation

The state-space equation, Equation 3.20, can also be solved by the using modal analysis technique. Let the eigen values and eigen vectors of matrix $\boldsymbol{A}$ be denoted by λ_i and ϕ_i $(i = 1 \ldots 2n)$; ϕ_i is a vector of size $2n$. Expressing $\boldsymbol{Z}(t)$ as a weighted summation of mode shapes, $\boldsymbol{Z}(t)$ can be written as:

$$\boldsymbol{Z}(t) = \phi\boldsymbol{q} \tag{3.126}$$

in which ϕ is a $2n \times 2n$ matrix and $\boldsymbol{q}$ is a vector of size $2n$. Equation 3.20 can then be written in the form of

$$\phi\dot{\boldsymbol{q}} = \boldsymbol{A}\phi\boldsymbol{q} + \boldsymbol{f}_g \tag{3.127}$$

Pre-multiplying the left and right sides of Equation 3.127 by ϕ^{-1}, the following equation is obtained.

$$\phi^{-1}\phi\dot{\boldsymbol{q}} = \phi^{-1}\boldsymbol{A}\phi\boldsymbol{q} + \phi^{-1}\boldsymbol{f}_g \tag{3.128}$$

As $\phi^{-1}\phi$ is an identity matrix of size $2n \times 2n$ and $\phi^{-1}\boldsymbol{A}\phi$ is the diagonal eigen value matrix of size $2n \times 2n$, and $\phi^{-1}\boldsymbol{f}_g$ becomes a vector $\overline{\boldsymbol{f}}_g$ of size $2n$, Equation 3.128 is reduced to a set of $2n$ uncoupled equations of motion in state space. The ith uncoupled equation takes the form

$$\dot{q}_i = \lambda_i q_i + \overline{f}_{gi} \quad (i = 1 \ldots 2n) \tag{3.129}$$

in which λ_i is the ith eigen value and $\overline{f}_{gi}$ is the ith modal load.

The solution of Equation 3.129 is obtained as described in Section 3.4.3.

To start the integration, the initial value of q_k has to be specified. This is obtained by specifying $\boldsymbol{Z}_0$ and then obtaining $\boldsymbol{q}_0$ as:

$$\boldsymbol{q}_0 = \phi^{-1}\boldsymbol{Z}_0 \tag{3.130}$$

3.5.6 Modal Analysis in Frequency Domain for State-Space Equation

When state-space modal analysis is carried out in the frequency domain, Equation 3.129 is solved in the frequency domain. For this purpose, f_{g_i} is Fourier synthesized using FFT and $q_i(t)$ is obtained using the Fourier analysis technique given in Section 3.4.4. Note that $h_j(\omega)$ is given by:

$$h_j(\omega) = (i\omega - \lambda_1)^{-1} \tag{3.131}$$

Once $q_i(t)$ is obtained, $\boldsymbol{Z}(t)$ may be obtained using Equation 3.126.

Example 3.12

For the multi-storey frame shown in Figure 3.20, obtain the shear at the base of the right-side column for the El Centro earthquake. Obtain the response quantity of interest in the time domain using: (i) the mode summation approach, (ii) the mode acceleration approach; and (iii) the modal state-space analysis. Assume $k/m = 100\ (\text{rads}^{-1})^2$ and percentage critical damping as 5%.

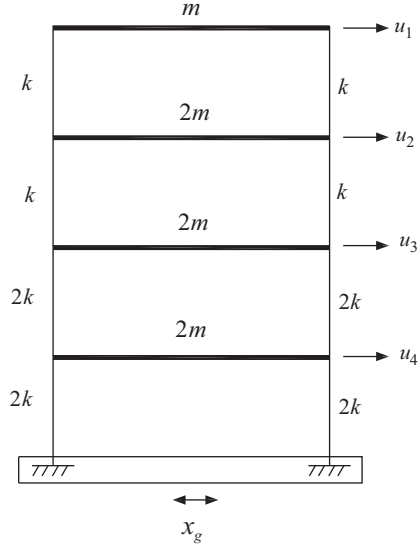

Figure 3.20 Multi-storey frame

Solution: Stiffness and mass matrices for the frame are:

$$\boldsymbol{K} = \begin{bmatrix} 2 & -2 & 0 & 0 \\ -2 & 4 & -2 & 0 \\ 0 & -2 & 6 & -4 \\ 0 & 0 & -4 & 8 \end{bmatrix} k \qquad \boldsymbol{M} = \begin{bmatrix} 1 & 0 & 0 & 0 \\ 0 & 2 & 0 & 0 \\ 0 & 0 & 2 & 0 \\ 0 & 0 & 0 & 2 \end{bmatrix} m$$

The mode shapes and frequencies are: $\omega_1 = 5.06\ \text{rad s}^{-1}$; $\omega_2 = 12.57\ \text{rad s}^{-1}$; $\omega_3 = 18.65\ \text{rad s}^{-1}$; and $\omega_4 = 23.5\ \text{rad s}^{-1}$.

$$\phi_1^T = [-1.0 \quad -0.871 \quad -0.520 \quad -0.278]$$

$$\phi_2^T = [-1.0 \quad -0.210 \quad 0.911 \quad 0.752]$$

$$\phi_3^T = [-1.0 \quad 0.738 \quad -0.090 \quad -0.347]$$

$$\phi_4^T = [1.0 \quad -0.843 \quad 0.268 \quad -0.145]$$

Table 3.5 First four mode shapes

ϕ_1	ϕ_2	ϕ_3	ϕ_4
$0.0158 + 0.0131i$	$0.0158–0.0131i$	$-0.1562–0.1859i$	$-0.1562 + 0.1859i$
$-0.0583–0.0507i$	$-0.0583 + 0.0507i$	$0.2263 + 0.2857i$	$0.2263–0.2857i$
$0.1835 + 0.1607i$	$0.1835–0.1607i$	$-0.0267–0.0381i$	$-0.0267 + 0.0381i$
$-0.2175–0.1906i$	$-0.2175 + 0.1906i$	$-0.1064–0.1345i$	$-0.1064 + 0.1345i$
$-0.0490 + 0.0013i$	$-0.0490–0.0013i$	$0.4525–0.0131i$	$0.4525 + 0.0131i$
$0.1843–0.0007i$	$0.1843 + 0.0007i$	-0.6796	-0.6796
$-0.5818 + 0.0002i$	$-0.5818–0.0002i$	$0.0866 + 0.0051i$	$0.0866–0.0051i$
0.6896	0.6896	$0.3199 + 0.0002i$	$0.3199–0.0002i$

Using the first two frequencies, the damping coefficients are: $\alpha = 0.3608$; $\beta = 0.0057$.

$$\boldsymbol{C} = \alpha\boldsymbol{M} + \beta\boldsymbol{K} = m\begin{bmatrix} 1.500 & -1.140 & 0.0 & 0.0 \\ -1.140 & 3.001 & -1.140 & 0.0 \\ 0.0 & -1.140 & 4.141 & -2.280 \\ 0.0 & 0.0 & -2.280 & 5.281 \end{bmatrix}$$

For state-space analysis, matrix $\boldsymbol{A}$ is given as:

$$\boldsymbol{A} = \begin{bmatrix} 0.0 & 0.0 & 0.0 & 0.0 & 1.0 & 0.0 & 0.0 & 0.0 \\ 0.0 & 0.0 & 0.0 & 0.0 & 0.0 & 1.0 & 0.0 & 0.0 \\ 0.0 & 0.0 & 0.0 & 0.0 & 0.0 & 0.0 & 1.0 & 0.0 \\ 0.0 & 0.0 & 0.0 & 0.0 & 0.0 & 0.0 & 0.0 & 1.0 \\ -2.0 & 1.0 & 0.0 & 0.0 & -1.454 & 0.567 & 0.0 & 0.0 \\ 2.0 & -2.0 & 1.0 & 0.0 & 1.134 & -1.495 & 0.567 & 0.0 \\ 0.0 & 1.0 & -3.0 & 2.0 & 0.0 & 0.567 & -2.062 & 1.134 \\ 0.0 & 0.0 & 2.0 & -4.0 & 0.0 & 0.0 & 1.134 & -2.630 \end{bmatrix}$$

The first four eigen values of $\boldsymbol{A}$ are: $\lambda_1 = -1.793 + 1.571i$; $\lambda_2 = -1.793 - 1.571i$; $\lambda_3 = -1.157 + 1.461i$; $\lambda_4 = -1.157 - 1.461i$; corresponding eigen vectors are shown in Table 3.5.

Mode superposition method–Using the zero initial condition, the solution for the first two modal equations are obtained by Newmark's β-method. Results for the first few time steps using contributions of the first two modes only are given in Table 3.6.

Mode acceleration method–Equation 3.124 is written as:

$$\eta_{bi} = \frac{1}{\omega_i^2}(\ddot{z}_i + 2\xi\omega_i z_i) = \left(-\frac{\lambda_i \ddot{x}_g}{\omega_i^2} - z_i\right) \tag{3.132}$$

η_{bi} for the first two modes, x_4, and M for a few time steps are shown in Table 3.7.

Modal state-space solution–Using Equation 3.73 to solve the first four uncoupled equations of motion, Equation 3.129, the results for the first few time steps are shown in Table 3.8.

Table 3.6 Responses obtained by mode superposition method

Response	Time (s)					
	0	0.02	0.04	0.06	0.08	0.1
z_1	0	0	0.0001	0.0002	0.0003	0.0004
z_2	0	0	0	−0.0001	−0.0001	−0.0001
$u_4(m)$	0	0	−0.0001	−0.0002	−0.0002	−0.0003
V (in terms of mass m)	0	0	−0.0211	−0.0221	−0.0431	−0.0621

Table 3.7 Responses obtained by mode acceleration method

Response	Time (s)					
	0	0.02	0.04	0.06	0.08	0.1
η_{b1}	0	0.0033	−0.0014	0.0019	3.2519e-004	0.0036
η_{b2}	0	−1.9204e-004	8.1083e-005	−1.1126e-004	−1.9204e-005	−2.1185e-004
u_4 (m)	0	0	−0.0001	−0.00 012	−0.0002	−0.0003
V (in terms of mass m)	0	0	−0.021	−0.024	−0.042	−0.061

The time histories of the shear V obtained by the three methods are shown in Figure 3.21(a–c). It is seen from the figure that all three methods provide nearly the same time histories of the moment. This is the case because the frequencies of the structure are well separated.

3.5.7 Computational Steps for MATLAB® Programming

Using MATLAB, seismic responses of the MDOF system can be carried out by adopting either the time domain or frequency domain approach including modal analysis and state-space formulation. Computational steps are detailed below:

I. **Computation of Basic Elements**

1. *Generation of influence coefficient matrix* $\boldsymbol{r}$ *or* $\boldsymbol{I}$

(i) Stiffness matrix $\boldsymbol{K}$ is arranged such that the degrees of freedom to be condensed out (δ_c) appear at the end, that is, $\boldsymbol{K}$ is partitioned as:

$$\boldsymbol{K} = \left[\begin{array}{c|c} \boldsymbol{K}_{dd} & \boldsymbol{K}_{dc} \\ \hline \boldsymbol{K}_{cd} & \boldsymbol{K}_{cc} \end{array}\right] \tag{3.133}$$

in which $\boldsymbol{K}_{cc}$ is the matrix corresponding to the δ_c degrees of freedom; $\boldsymbol{K}_{dd}$ is that corresponding to dynamic degrees of freedom; $\boldsymbol{K}_{cd}$ and $\boldsymbol{K}_{dc}$ are coupling matrices.

(ii) Condensed stiffness matrix $\boldsymbol{K}_d$ corresponding to dynamic degrees of freedom δ_d is obtained as:

$$\boldsymbol{K}_d = \boldsymbol{K}_{dd} - \boldsymbol{K}_{dc}\boldsymbol{K}_{cc}^{-1}\boldsymbol{K}_{cd} \tag{3.134}$$

(iii) Condensed stiffness matrix $\boldsymbol{K}_d$ is arranged such that support degrees of freedom appear at the end, that is, $\boldsymbol{K}_d$ is partitioned as:

$$\boldsymbol{K}_d = \left[\begin{array}{c|c} \boldsymbol{K}_{nnd} & \boldsymbol{K}_{nsd} \\ \hline \boldsymbol{K}_{snd} & \boldsymbol{K}_{ssd} \end{array}\right] \tag{3.135}$$

Table 3.8 Responses obtained by modal state-space analysis

Response	Time (s)					
	0	0.02	0.04	0.06	0.08	0.1
q_1	0	−2.2742e-4 − 1.1751e-4i	−2.7956e-4 − 2.7672e-4i	−1.5686e-4 − 3.9251e-4i	−1.1375e-4 − 5.0055e-4i	−1.5377e-4 − 6.4285e-4i
q_2	0	−2.2742e-4 + 1.1751e-4i	−2.7956e-4 + 2.7672e-4i	−1.5686e-4 + 3.9251e-4i	−1.1375e-4 + 5.0055e-4i	−1.5377e-4 + 6.4285e-4i
q_3	0	6.5931e-4 + 2.5793e-4i	9.0182e-4 + 6.2974e-4i	7.1469e-4 + 9.5577e-4i	0.0008 + 0.0013i	0.0010 + 0.0018i
q_4	0	6.5931e-4 − 2.5793e-4i	9.0182e-4 − 6.2974e-4i	7.1469e-4 − 9.5577e-4i	0.0008–0.0013i	0.0010–0.0018i
u_4 (m)	0	0	−0.00 011	−0.00 012	−0.00 023	−0.00 029
V (in terms of mass m)	0	0	−0.021	−0.023	−0.046	−0.061

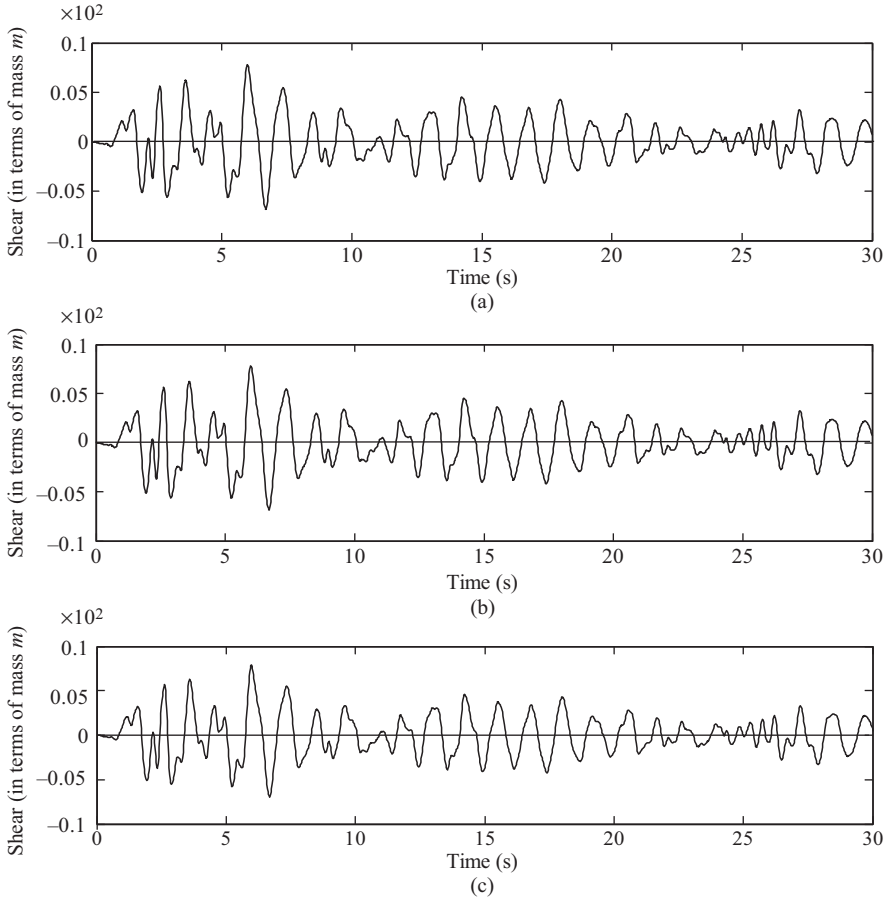

Figure 3.21 Time histories of shear V obtained by the three methods: (a) mode acceleration method; (b) Newmark's β-method; and (c) state-space method

in which $\boldsymbol{K}_{nnd}$ is the matrix corresponding to non-support degrees of freedom; $\boldsymbol{K}_{ssd}$ is that corresponding to support degrees of freedom; $\boldsymbol{K}_{snd}$ and $\boldsymbol{K}_{nsd}$ are coupling matrices.

(iv) Influence coefficient matrix $\boldsymbol{r}$ is obtained as:

$$\boldsymbol{r} = -\boldsymbol{K}_{nnd}^{-1}\boldsymbol{K}_{nsd} \tag{3.136}$$

(v) For uniform support excitations the $\boldsymbol{I}$ matrix may be generated separately by arranging 1 and 0 in the vector or matrix form as explained in Section 3.3.1. Alternatively, the $\boldsymbol{I}$ matrix may be constructed from the $\boldsymbol{r}$ matrix by considering that all support excitations are the same. Note that the stiffness matrix to be used for the dynamic analysis is $\boldsymbol{K}_{nnd}$.

(vi) Once the $\boldsymbol{r}$ matrix is obtained, it is possible to obtain any other response of the structure due to unit displacement to any support DOF (keeping other support DOF locked) by the usual static analysis.

2. *Generation of mass matrix* $\boldsymbol{M}$ *corresponding to the dynamic degrees of freedom*
   (i) Masses corresponding to the dynamic degrees of freedom are to be identified and obtained using lumped mass approximation or consistent mass approximation.
   (ii) Inertia coupling between different dynamic degrees of freedom is to be properly accounted for, as explained in Section 3.3.1.
3. *With* $\boldsymbol{K}_{nnd}$ *and* $\boldsymbol{M}$ *specified explicitly, the following quantities are obtained depending upon the analysis to be performed*
   (i) Mode shapes and frequencies for modal analysis.
   (ii) First two frequencies to obtain $\boldsymbol{C}$ matrix for direct analysis, that is, $\boldsymbol{C} = \alpha\boldsymbol{M} + \beta\boldsymbol{K}$.
   (iii) Matrix $\boldsymbol{A}$ given by Equation 3.102 for state-space analysis and eigen values and eigen vectors of matrix $\boldsymbol{A}$.

II. **Time Domain Analysis**

1. *Direct analysis*
   (i) Form **C** matrix as mentioned above.
   (ii) Choose Δt appropriately and sample the given time history of ground acceleration at time interval Δt, if required (by interpolation).
   (iii) Form $\boldsymbol{G}$ matrix (defined along with Equations 3.90 and 3.91) and obtain $\boldsymbol{G}^{-1}$.
   (iv) Obtain the response vector at time $t + \Delta t$ using Equations 3.92–3.94.
   (v) Obtain δ_c from the dynamic degrees of freedom δ_d by

$$\delta_c = -\boldsymbol{K}_{cc}^{-1}\boldsymbol{K}_{cd}\delta_d. \tag{3.137}$$

   (vi) Obtain stress (moment, shear force, and so on) response quantities of interest at every time step.
2. *State-space analysis*
   (i) Choose Δt as before.
   (ii) Use eigen values and eigen vectors of $\boldsymbol{A}$ to obtain $\boldsymbol{e}^{\boldsymbol{A}t}$ using Equation 3.75.
   (iii) Use Equation 3.73 or 3.74 to obtain the response vector at each time step.
   (iv) Follow steps (v) and (vi) of Direct Analysis to obtain the stress response.
3. *Modal analysis*
   (i) Using mode shapes and frequencies obtain $\boldsymbol{\lambda}_{ik}$ (Equation 3.114) and $\sum \boldsymbol{\lambda}_{ik}\ddot{\boldsymbol{x}}_{gk}$ (Equation 3.113).
   (ii) Choose Δt as before.
   (iii) Solve for $Z_i (i = 1 \ldots m)$ using Duhamel integration (Equations 3.49–3.51) or Newmark's β-method (Equations 3.66–3.68); m is the number of modes. Zero initial condition, that is, $\dot{Z}_{i0}$ and Z_{i0} are assumed to be zero.
   (iv) Obtain $\boldsymbol{X}(t)$ using Equation 3.106.
   (v) Obtain stress response as given in steps (v) and (vi) of Direct Analysis. Alternatively, obtain the stress response using the mode shape coefficient for the response quantity of interest (stress) as described in Section 3.5.3.
4. *Modal state-space analysis*
   (i) Find the ith modal load $\bar{\boldsymbol{f}}_{gi} (i = 1 \ldots 2n)$.
   (ii) q_i is obtained using Equation 3.129 in which λ_i is the eigen value of matrix $\boldsymbol{A}$ (I.3.iii).
   (iii) Δt is chosen as before and the zero initial condition is used to solve Equation 3.129.
   (iv) Obtain $\boldsymbol{Z}(t)$ using Equation 3.126 and stress responses are obtained using steps (v) and (vi) of Direct Analysis.
5. *Mode acceleration approach*
   (i) Obtain $\overline{R}(t)$ by solving Equation 3.120 statically.
   (ii) Obtain Z_i as given in Modal Analysis (II.3.iii).
   (iii) Obtain response quantity $R(t)$ using Equation 3.119; ϕ_i is the mode shape coefficient for the response quantity of interest (obtained by the procedure given in Section 3.5.4).

III. **Frequency Domain Analysis**

1. *Direct analysis*
   (i) Choose sampling interval Δt for the ground motion time histories and take FFT of the sampled time history.
   (ii) Take half of the sampled outputs from FFT (that is, $N/2$ values, if N values are input to FFT).
   (iii) Find $\boldsymbol{P}(\omega) = -\boldsymbol{M}\boldsymbol{r}\ddot{x}_g(\omega)$; $\ddot{x}_g(\omega)$ are the outputs from FFT at an interval of $\Delta\omega = 2\pi/T$, T being the length of the time history; note that $\boldsymbol{P}(\omega)$ is a vector, each element of the vector changes with $\omega\{0, \Delta\omega, [(N/2)-1]\Delta\omega\}$.
   (iv) Obtain $\boldsymbol{H}(\omega) = [\boldsymbol{K}-\boldsymbol{M}\boldsymbol{\omega}^{\boldsymbol{2}} + i\boldsymbol{C}\boldsymbol{\omega}]^{-1}$; ω is taken at an interval of $\Delta\omega$ starting from zero to $\omega = [(N/2)-1]\Delta\omega$.
   (v) Obtain $\boldsymbol{X}(\omega) = \boldsymbol{H}(\omega)\boldsymbol{P}(\omega)$; each element of the vector varies with $\omega\{0, \Delta\omega, [(N/2)-1]\Delta\omega\}$. Add $N/2$ complex numbers to the series of numbers that are complex conjugates of the first set of $N/2$ numbers in the manner explained in Section 3.4.4.
   (vi) Take IFFT of the vector $\boldsymbol{X}(\omega)$ generated as above to obtain $\boldsymbol{X}(t)$.
   (vii) Obtain the stress responses as before.
2. *State-space analysis*
   (i) Choose sampling interval Δt appropriately.
   (ii) Take FFT of the vector $\boldsymbol{p}_g(t)$ as mentioned before and form the vector $\boldsymbol{f}_g(\omega)$ (Equation 3.102).
   (iii) Obtain $\boldsymbol{H}(\omega) = [\boldsymbol{I}\omega-\boldsymbol{A}]^{-1}$ (Equation 3.104) for $\omega\{0, \Delta\omega, [(N/2)-1]\Delta\omega\}$.
   (iv) Obtain $\boldsymbol{Z}(\omega) = \boldsymbol{H}(\omega)\boldsymbol{f}_g(\omega)$ and arrange elements of $\boldsymbol{Z}(\omega)$ in the same way as mentioned in step III.1.(v) of Direct Analysis.
   (v) Take IFFT of $\boldsymbol{Z}(\omega)$ to obtain $\boldsymbol{Z}(t)$.
3. *Modal analysis*
   (i) Choose sampling interval Δt appropriately.
   (ii) Obtain the modal load $p_i(t) = -\sum \boldsymbol{\lambda}_{ik}\ddot{\boldsymbol{x}}_{gk}$ (Equation 3.113), sample it at Δt and take the FFT of it to obtain $p_i(\omega)$.
   (iii) Obtain $\boldsymbol{h}_i(\omega)$ (Equation 3.80) for $\omega\{0, \Delta\omega, [(N/2)-1]\Delta\omega\}$.
   (iv) Obtain $Z_i(\omega) = h_i(\omega)p_i(\omega)$ and obtain $Z_i(t)$ by IFFT of $Z_i(\omega)$ as explained before.
   (v) Obtain $\boldsymbol{X}(t) = \phi\boldsymbol{Z}(t)$ and other stress quantities of interest as mentioned in step (v) of the Modal Analysis in Time Domain.
4. *Modal state-space analysis*
   (i) Choose sampling interval Δt appropriately.
   (ii) Obtain $\bar{\boldsymbol{f}}_g = \phi^{-1}\boldsymbol{f}_g$; $\bar{f}_{gi}$ is the ith element of $\bar{\boldsymbol{f}}_g$.
   (iii) Obtain the FFT of $\bar{f}_{gi}$.
   (iv) Obtain $h_j(\omega) = (i\omega-\boldsymbol{\lambda}_j)^{-1}$ (Equations 3.131 and 3.129).
   (v) Obtain $q_j(\omega) = h_j(\omega)\bar{f}_{gi}(\omega)$ and take IFFT of $q_j(\omega)$ to obtain $q_j(t)$.
   (vi) Obtain $\boldsymbol{Z}(t) = \phi\boldsymbol{q}(t)$.

Exercise Problems

(Use standard programs like MATLAB, SAP2000 and ABAQUAS to solve the problems; you may also use your own program developed using the methods presented in the chapter.)

3.13 Find the effective mass and stiffness of the structure corresponding to the dynamic degree of freedom x shown in Figure 3.22. All members are assumed as inextensible. Shear stiffness $12EI/l^3$ for the member AB is k. The shear stiffness of other members are given in terms of k. If the damping ratio is assumed as 0.05 and k/m is assumed as 200 $(\text{rad s}^{-1})^2$, find the peak and rms displacements

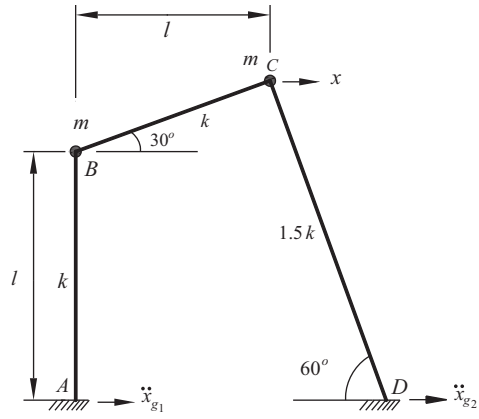

Figure 3.22 Inclined portal frame (idealized as SDOF)

of x for the El Centro earthquake by: (i) Duhamel integral; (ii) frequency domain analysis using FFT; and (iii) state-space analysis in the time domain.

3.14 A rigid pipe embedded within non-uniform soil is modeled as a lumped mass system as shown in Figure 3.23. The soil stiffness and damping are modeled with springs and dash pots. If the soil damping ratio is assumed to be 0.06 and k/m is assumed as 50 $(\text{rad s}^{-1})^2$, then find the peak and rms responses of y and θ to the El Centro earthquake by: (i) direct frequency domain analysis using FFT, and (ii) direct time domain analysis using Newmark's β-method.

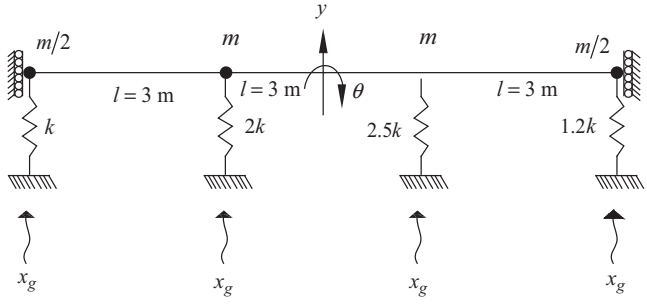

Figure 3.23 Pipe embedded within non-uniform soil

3.15 Figure 3.24 shows the stick model for a building shear frame. Shear stiffness coefficients are shown in the figure. The base of the frame is subjected to both rotational and translational ground motions. Using the direct frequency domain analysis, find the peak values of moment at the base and displacement of the top mass. Take the ground motion as the El Centro earthquake and the rotational component of ground motion as the translational component divided by 50. Take $k/m = 50\ (\text{rad s}^{-1})^2$ and the damping ratio as 0.02.

3.16 Figure 3.25 shows a two-storey shear frame that is subjected to different excitations at the three supports produced due to an arbitrarily assumed time lag in the earthquake ground motion. Obtain the peak and rms values of the top displacement for El Centro ground motion by: (i) direct time domain analysis using Newmark's β-method, and (ii) state-space analysis in the time domain. Assume $k/m = 60(\text{rad s}^{-1})^2$; the time lag between supports as 2.5s; and the modal damping ratio as 0.05.

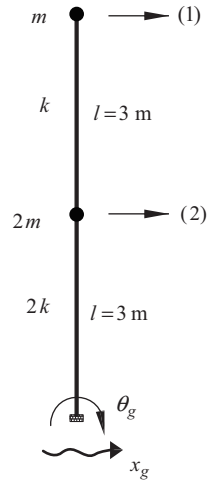

Figure 3.24 Stick model for shear building frame

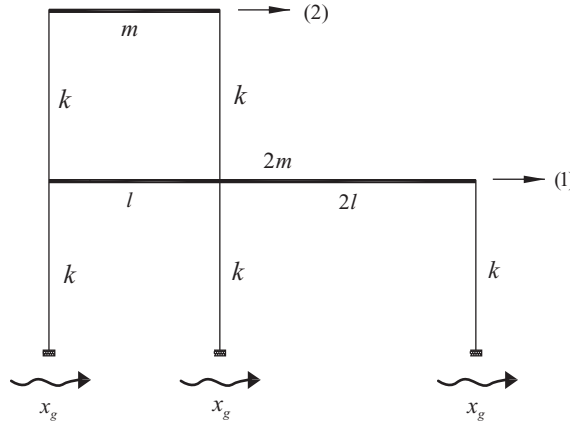

Figure 3.25 Three bay shear frame

3.17 For the frame with a secondary system attached to the top floor as shown in Figure 3.26, find the peak value of the displacement of the mass of the secondary system for different support excitations as shown in the figure by: (i) direct frequency domain analysis using FFT, and (ii) state-space analysis in the frequency domain. Assume: earthquake ground motions as the El Centro earthquake; time lag as 5 s; $k/m = 60(\text{rad s}^{-1})^2$; and damping ratio for the frame and secondary system as 0.02. Compare the result with that obtained for no time lag, that is, the same excitations at the supports.

3.18 Using the modal time domain and frequency domain analyses, find the peak values of the displacement of the top floor and the first-storey drift of the frame shown in Figure 3.27 for El Centro earthquake excitation. Compare between the results obtained by considering contributions

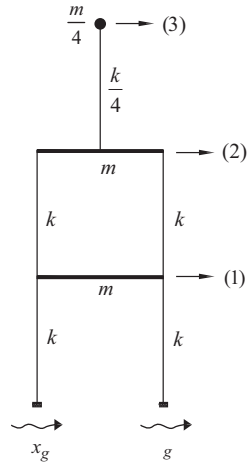

Figure 3.26 Frame with a secondary system

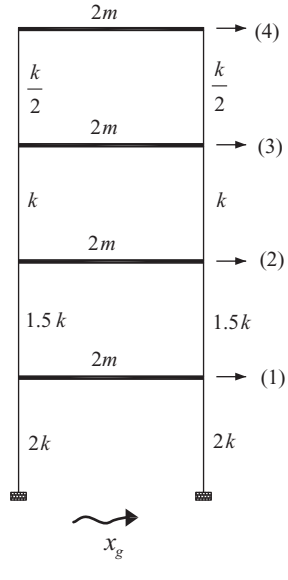

Figure 3.27 Four-storey shear frame

of the first two modes only and all modes. Also, find the times at which the peak values of the top-storey displacement takes place when only two modes are considered and when all modes are considered. Assume the modal damping ratio as 0.05 and $k/m = 40(\text{rad s}^{-1})^2$.

3.19 Using the modal time domain analysis, find the rms and peak values of the dynamic degrees of freedom of a simplified model of a cable stayed bridge shown in Figure 3.28. Use the El Centro

earthquake with time lag between supports 4 and 5 as 2.5 s, 5 and 6 as 5 s, and 6 and 7 as 2.5 s. Assume the following relationships: $AE/l_1 = 12EI/s^3$; $m_1 = {}^1/_3 m$; $12EI/s^3 m = 20(\text{rad s}^{-1})^2$; and the modal damping ratio as 0.05; $(EI)_{tower} = 0.25(EI)_{deck} = 0.25\ EI$; $\left(\frac{AE}{410}\right)_{deck} = 0.8\ \left(\frac{AE}{l_1}\right)_{cable}$; $s = 125$; l_1 is the cable length joining the top of the tower to the end of the bridge; m_1 as the mass lumped at the top of the tower and m as the mass lumped at the centre of the bridge.

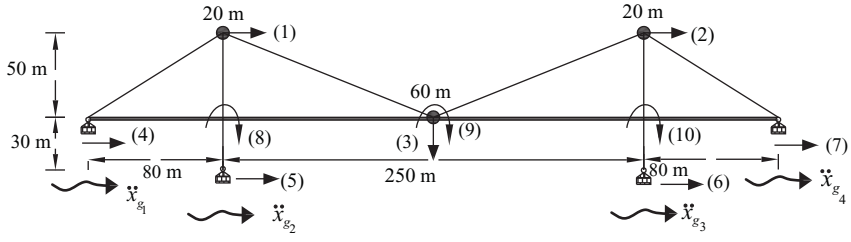

Figure 3.28 Model of a three span cable stayed bridge

3.20 A six-storey shear frame, as shown in Figure 3.29, is subjected to El Centro ground motion. Using the mode acceleration method, find the rms and peak values of the top floor and the first-floor displacements shown in the figure. For the analysis, consider contributions of the first three modes only. Compare the results of the mode acceleration method with those of the mode superposition method considering the contributions of all modes. Assume the modal damping ratio to be 0.05 and $k/m = 40(\text{rad s}^{-1})^2$.

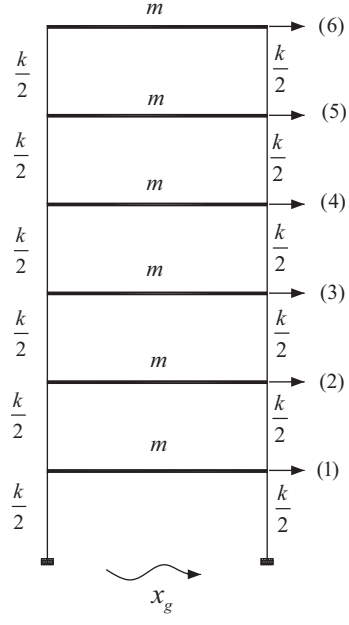

Figure 3.29 Six-storey shear frame

3.21 A two-storey 3D frame with rigid slab, as shown in Figure 3.30, is subjected to the El Centro earthquake. Using the mode acceleration method, find the peak values of the rotation and x displacement of the first floor and y displacement of its top floor. Lateral stiffness of the columns are the same in both directions. Total mass lumped at each floor is taken as m and the mass moment of inertia corresponding to the torsional degree of freedom is taken as $ml^2/6$. Assume the modal damping ratio as 0.05; $k/m = 80(\text{rad s}^{-1})^2$; $m = 10\,000\,\text{kg}$ and $l = 3\,\text{m}$. Consider first three modes for the response calculation and evaluate the accuracy of the results.

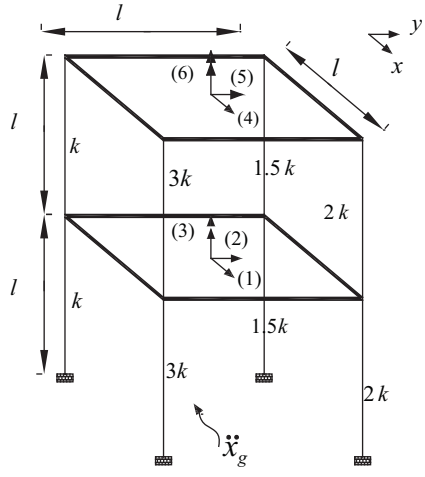

Figure 3.30 Two-storey 3D frame

3.22 A rigid slab is supported by three columns as shown in Figure 3.31. Columns are rigidly connected to the slab and have the same lateral stiffness k in both directions. Total mass of the slab is m and $k/m = 80(\text{rad s}^{-1})^2$. Find the time histories of displacements of the degree of freedom when the base of the structure is subjected to two-component ground motion as shown in the figure. Take $\ddot{x}_{xg}$ as the El Centro earthquake and assume $\ddot{x}_{yg} = {}^1\!/_2\ddot{x}_{xg}$. Use direct time domain analysis by employing Newmark's β-method.

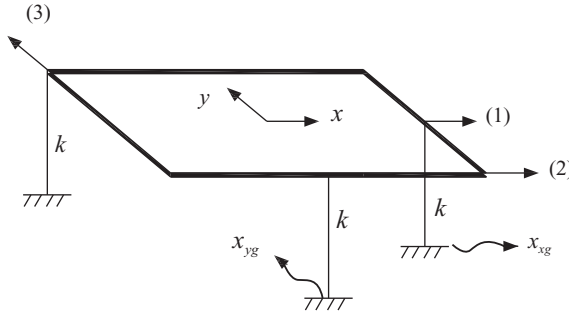

Figure 3.31 Rigid slab supported on three columns

Appendix 3.A Direct Generation of Mass and Stiffness Matrices using the Method of Virtual Work

Mass and stiffness matrices can be generated using the method of virtual work. For certain structures, such as inclined portal frames, the method may prove to be more convenient compared with other approaches. For illustration, the structures shown in Examples 3.2–3.4 are considered.

The method consists of two steps. In the first step, unit displacement or unit acceleration is given to a particular DOF keeping other degrees of freedom locked. As a result, the internal (elastic) or inertial forces generated in the structure are calculated. In the second step, a virtual displacement is given to the DOF for which the stiffness or mass inertia coefficient is to be evaluated keeping other degrees of freedom locked. The stiffness or inertia coefficient is then obtained from the virtual work equation.

Example 3.2

Figure 3.32 shows the steps involved in the computation of inertia coefficients m_{11}, m_{21}, and m_{31}. In Figure 3.32b, unit acceleration is given to the DOF 1. The inertia forces generated in the mass are shown in the same figure. If a virtual displacement Δ is given to the DOF 1, then the displacements at the corners will be Δ (as shown in Figure 3.32c) and the central mass will move by $\Delta/2$ in the directions of the arrows as shown in the same figure; it will also undergo a rotational movement of Δ/L.

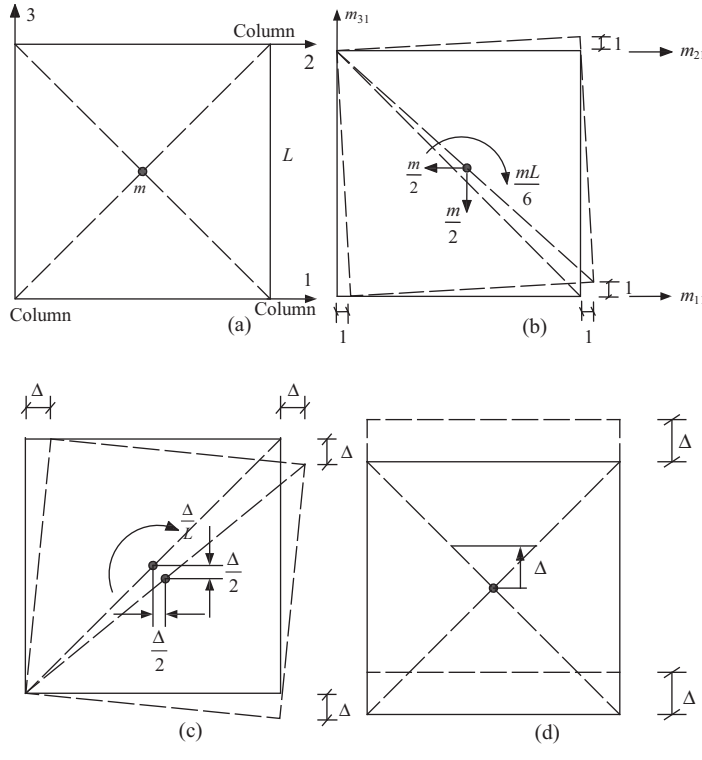

Figure 3.32 Calculation of m_{11}, m_{21}, and m_{31}: (a) DOF 1, 2, and 3; (b) unit acceleration given to DOF 1; (c) virtual displacement given to DOF 2; and (d) virtual displacement given to DOF 3

The virtual work equation gives

$$m_{11}\Delta - \frac{m}{2}\frac{\Delta}{2} - \frac{m}{2}\frac{\Delta}{2} - \frac{m\Delta}{6} = 0 \tag{3.138a}$$

$$m_{11} = \frac{m}{2} + \frac{m}{6} = \frac{4m}{6} \tag{3.138b}$$

If a virtual displacement Δ is given to the DOF 2 as shown in Figure 3.32c, then the virtual work equation gives

$$m_{21}\Delta = \frac{m}{2}\frac{\Delta}{2} - \frac{m}{2}\frac{\Delta}{2} - \frac{m\Delta}{6} \tag{3.139a}$$

$$m_{21} = -\frac{m}{6} \tag{3.139b}$$

If a virtual displacement Δ is given to the DOF 3 as shown in Figure 3.32d, then the virtual work equation gives

$$m_{31}\Delta - \frac{m}{2}\Delta = 0 \tag{3.140a}$$

$$m_{31} = \frac{m}{2} \tag{3.140b}$$

Example 3.3

Figure 3.33 shows the steps involved in the computation of inertia coefficient m_{11} and m_{21} for DOF 1 and 2. In Figure 3.33b, unit acceleration is given to the DOF 1, while the DOF 2 is locked. Resulting inertia forces generated in different masses are shown in the same figure. The mass inertia coefficients m_{11} and m_{21} at the DOF 1 and 2 are also shown. In Figure 3.33c, a virtual displacement of Δ is applied to the DOF 1 keeping the DOF 2 locked. The virtual work equation provides

$$m_{11}\Delta + m_{21} \times 0 - 2m\Delta - \frac{m}{2}\Delta = 0 \tag{3.141a}$$

$$m_{11} = \frac{5}{2}m = 2.5m \tag{3.141b}$$

In Figure 3.33d, a virtual displacement of Δ is applied to the DOF 2 keeping the DOF 1 locked. The virtual work equation provides

$$m_{11} \times 0 + m_{21}\Delta - \frac{m}{2}\frac{2\Delta}{3} - m\frac{4\Delta}{3} = 0 \tag{3.142a}$$

$$m_{21} = \frac{5}{3}m \tag{3.142b}$$

In Figure 3.34a, unit acceleration is given to the DOF 2 keeping the DOF 1 locked. Resulting inertia forces generated in different masses are shown in the same figure. In Figure 3.34b, a virtual displacement

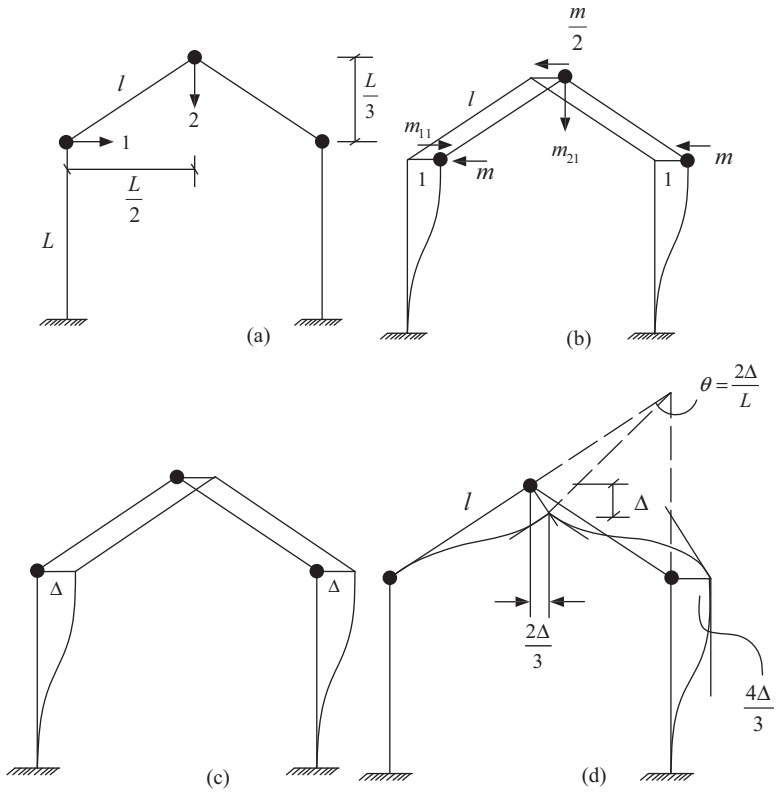

Figure 3.33 Calculation of m_{11} and m_{21}: (a) DOF 1 and 2; (b) unit acceleration given to DOF 1; (c) virtual displacement (Δ) given to DOF 1; and (d) virtual displacement given to DOF 2

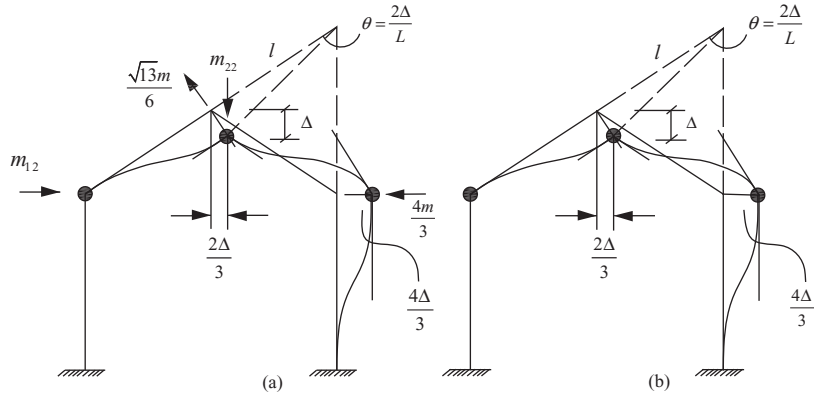

Figure 3.34 Calculation of m_{22}: (a) unit acceleration given to DOF 2; and (b) virtual displacement given to DOF 2

Δ is given to the DOF 2 keeping the DOF 1 locked. The virtual work equation provides

$$m_{22}\Delta - \frac{\sqrt{13}m}{6}\frac{\sqrt{13}}{6}2\Delta - \frac{4m}{3}\frac{4\Delta}{3} = 0 \tag{3.143a}$$

$$m_{22} = \left(\frac{26}{36} + \frac{16}{9}\right)m = \frac{45}{18}m = \frac{5}{2}m = 2.5m \tag{3.143b}$$

Example 3.4

Figure 3.8a shows the kinematic degrees of freedom 1–5 for the frame. The stiffness matrix for the frame in the partitioned form is given in the solution for the probem in Example 3.4. Here the derivation of k_{33}, k_{35}, and k_{55} are shown using the method of virtual work.

In Figure 3.35a,

$$M_1 = M_2 = M_3 = \frac{6EI}{l}\theta = \frac{36EI}{\sqrt{13}L} \times \frac{2}{L} = \frac{72EI}{\sqrt{13}L^2}; M_4 = M_5 = \frac{6EI}{L^2}\frac{4}{3} = \frac{8EI}{L^2}$$

$$F_3 = F_2 = F_1 = \frac{M_1 + M_2}{l}; \qquad F_4 = \frac{M_4 + M_5}{L}$$

For virtual displacement of Δ given to the DOF 5, the virtual work equation provides

$$k_{55}\Delta = F_1 \times \frac{2\Delta}{L} \times \frac{\sqrt{13}L}{6} + F_3 \times \frac{2\Delta}{L} \times \frac{\sqrt{13}L}{6} + F_4\frac{4\Delta}{3} \tag{3.144a}$$

$$k_{55} = \frac{2(M_1 + M_2)}{L} + \frac{2(M_1 + M_3)}{L} + \frac{4(M_4 + M_5)}{3L} = \frac{8M_1}{L} + \frac{8M_4}{3L} = \frac{8}{\sqrt{13}} \times \frac{72EI}{L^3} + \frac{64EI}{3L^3} = \frac{181EI}{L^3} \tag{3.144b}$$

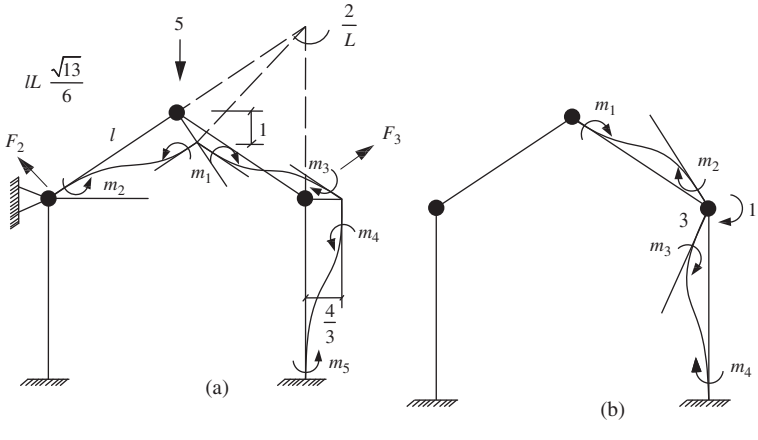

Figure 3.35 Calculation of k_{33}, k_{35}, and k_{55}: (a) unit displacement given to the DOF 5; and (b) unit rotation given to the DOF 3

For virtual rotation of θ given to the DOF 3, the virtual work equation provides

$$k_{35}\theta = M_3\theta - M_4\theta \tag{3.145a}$$

$$k_{35} = \frac{72EI}{\sqrt{13}L^2} - \frac{8EI}{L^2} \approx \frac{12EI}{L^2} \tag{3.145b}$$

In Figure 3.35b,

$$M_2 = \frac{4EI}{l} = \frac{24EI}{\sqrt{13}L};\ M_3 = \frac{4EI}{L}$$

For virtual rotation of θ, the virtual work equation provides

$$k_{33}\theta = M_2\theta + M_3\theta \tag{3.146a}$$

$$k_{33} = \frac{24EI}{\sqrt{13}L} + \frac{4EI}{L} = \frac{38.4EI}{3.6L} \tag{3.146b}$$

Appendix 3.B Derivation of the Response over the Time Interval Δt in Duhamel Integration

(i) Response due to Constant Force F_0 over the Time Interval t

$$\begin{aligned}
x_p(t) &= \left(\frac{F_0}{m\omega_\mathrm{d}}\right)\int_0^t \mathrm{e}^{-\zeta\omega_\mathrm{n}(t-s)}\sin\omega_\mathrm{d}(t-s)\mathrm{d}s \\
&= \frac{F_0}{m\omega_\mathrm{d}}\left[\frac{\omega_\mathrm{d}\mathrm{e}^{-\zeta\omega_\mathrm{n}(t-s)}\cos\omega_\mathrm{d}(t-s) + \zeta\omega_\mathrm{n}\mathrm{e}^{-\zeta\omega_n(t-s)}\sin\omega_\mathrm{d}(t-s)}{\omega_\mathrm{n}^2}\right]_{s=0}^{s=t} \\
&= \frac{F_0}{k\omega_\mathrm{d}}\left[\omega_\mathrm{d} - \omega_\mathrm{d}\mathrm{e}^{-\zeta\omega_\mathrm{n}t}\cos\omega_\mathrm{d}t - \zeta\omega_\mathrm{n}\mathrm{e}^{-\zeta\omega_\mathrm{n}t}\sin\omega_\mathrm{d}t\right] \\
&= -\left(\frac{F_0}{k}\right)\mathrm{e}^{-\zeta\omega_\mathrm{n}t}\cos\omega_\mathrm{d}t - \left(\frac{\zeta F_0}{k\sqrt{1-\zeta^2}}\right)\mathrm{e}^{-\zeta\omega_\mathrm{n}t}\sin\omega_\mathrm{d}t\left(\frac{F_0}{k}\right)
\end{aligned} \tag{3.147}$$

$$\begin{aligned}
\dot{x}_p(t) &= \left(\frac{F_0}{m}\right)\int_0^t \mathrm{e}^{-\zeta\omega_\mathrm{n}(t-s)}\left[\cos\omega_\mathrm{d}(t-s) - \left(\frac{\zeta}{\sqrt{1-\zeta^2}}\right)\sin\omega_\mathrm{d}(t-s)\right]\mathrm{d}s \\
&= \frac{F_0}{m}\left[\frac{-\omega_\mathrm{d}\mathrm{e}^{-\zeta\omega_\mathrm{n}(t-s)}\sin\omega_\mathrm{d}(t-s) + \zeta\omega_\mathrm{n}\mathrm{e}^{-\zeta\omega_\mathrm{n}(t-s)}\cos\omega_\mathrm{d}(t-s)}{\omega_\mathrm{n}^2}\right. \\
&\quad \left. - \frac{\zeta\omega_\mathrm{n}\mathrm{e}^{-\zeta\omega_\mathrm{n}(t-s)}\sin\omega_\mathrm{d}(t-s) + \zeta^2\omega_\mathrm{n}\mathrm{e}^{-\zeta\omega_\mathrm{n}(t-s)}\cos\omega_\mathrm{d}\dfrac{(t-s)}{\sqrt{1-\zeta^2}}}{\omega_\mathrm{n}^2}\right]_{s=0}^{s=t} \\
&= \frac{F_0}{k}\left[-\left(\frac{\omega_\mathrm{n}}{\sqrt{1-\zeta^2}}\right)\mathrm{e}^{-\zeta\omega_\mathrm{n}(t-s)}\sin\omega_\mathrm{d}(t-s)\right]_{s=0}^{s=t} \\
&= -\left(\frac{\omega_\mathrm{n}\dfrac{F_0}{k}}{\sqrt{1-\zeta^2}}\right)\mathrm{e}^{-\zeta\omega_\mathrm{n}t}\sin\omega_\mathrm{d}t
\end{aligned} \tag{3.148}$$

Combining Equations 3.147 and 3.148 with the homogeneous solutions given in Equations 3.29 and 3.30, it follows that

$$x(t) = \left(x_0 - \frac{F_0}{m}\right)e^{-\zeta\omega_n t}\cos\omega_d t + \left[\frac{\zeta\omega_n\left(x_0 - \frac{F_0}{k}\right) + \dot{x}_0}{\omega_n\sqrt{1-\zeta^2}}\right]e^{-\zeta\omega_n t}\sin\omega_d t + \left(\frac{F_0}{k}\right) \tag{3.149}$$

$$\dot{x}(t) = \dot{x}_0 e^{-\zeta\omega_n t}\cos\omega_d t - \left[\frac{\omega_n\left(x_0 - \frac{F_0}{k}\right) + \xi\dot{x}_0}{\sqrt{1-\zeta^2}}\right]e^{-\zeta\omega_n t}\sin\omega_d t \tag{3.150}$$

(ii) Response due to Triangular Variation of Force (F_s) within Time Interval t_0

The force at any time s given by

$$F_s = \frac{F_0}{t_0}s \tag{3.151}$$

Using the convolution integral

$$x_p(t) = \int_0^t \left(\frac{F_0}{m\omega_d t_0}\right)s e^{-\zeta\omega_n(t-s)}\sin\omega_d(t-s)\mathrm{d}s \tag{3.152}$$

$$\dot{x}_p(t) = \int_0^t \left(\frac{F_0}{mt_0}\right)s e^{-\zeta\omega_n(t-s)}\left[\cos\omega_d(t-s) - \left(\frac{\zeta}{\sqrt{1-\zeta^2}}\right)\sin\omega_d(t-s)\right]\mathrm{d}s \tag{3.153}$$

First, consider the displacement response as given in Equation 3.152. Performing the integration gives

$$\begin{aligned} x_p(t) &= \int_0^t \left(\frac{F_0}{m\omega_d t_0}\right)s e^{-\zeta\omega_n(t-s)}\sin\omega_d(t-s) \\ &= \frac{F_0}{m\omega_d t_0}\left\{\frac{e^{-\zeta\omega_n(t-s)}}{(\omega_d^2+\zeta^2\omega_n^2)^2}\left[\left(-2\zeta\omega_n\omega_d + (\omega_d^2+\zeta^2\omega_n^2)\omega_d s\right)\cos\omega_d(t-s)\right.\right. \\ &\qquad \left.\left. + (\omega_d^2 - \zeta^2\omega_n^2 + (\omega_d^2+\zeta^2\omega_n^2)\zeta\omega_n s)\sin\omega_d(t-s)\right]\right\}_{s=0}^{s=t} \end{aligned} \tag{3.154}$$

Simplifying Equation 3.154, it follows that

$$x_p(t) = \left(\frac{2\zeta F_0}{k\omega_n t_0}\right)e^{-\zeta\omega_n t}\cos\omega_d + \left[\frac{F_0(2\zeta^2-1)}{k\omega_n t_0\sqrt{1-\zeta^2}}\right]e^{-\zeta\omega_n t}\sin\omega_d t + \left(\frac{F_0}{kt_0}\right)t - \left(\frac{2\zeta F_0}{k\omega_n t_0}\right) \tag{3.155}$$

The velocity follows from the integration of Equation 3.153 which gives

$$\begin{aligned}\dot{x}_p(t) &= \int_0^t \left(\frac{F_0}{mt_0}\right) s\mathrm{e}^{-\zeta\omega_\mathrm{n}(t-s)}\cos\omega_\mathrm{d}(t-s)\mathrm{d}s - \frac{\zeta}{\sqrt{1-\zeta^2}}\int_0^t \left(\frac{F_0}{mt_0}\right) s\mathrm{e}^{-\zeta\omega_\mathrm{n}(t-s)}\sin\omega_\mathrm{d}(t-s)\mathrm{d}s \\ &= \frac{F_0}{mt_0}\left(\frac{\mathrm{e}^{-\zeta\omega_\mathrm{n}(t-s)}}{(\omega_\mathrm{d}^2+\zeta^2\omega_\mathrm{n}^2)^2}\left\{[(\omega_\mathrm{d}^2+\zeta^2\omega_\mathrm{n}^2)+(\omega_\mathrm{d}^2+\zeta^2\omega_\mathrm{n}^2)\zeta\omega_\mathrm{n}s]\cos\omega_\mathrm{d}(t-s)\right.\right. \\ &\qquad \left.\left. + \left[2\zeta\omega_\mathrm{n}\omega_\mathrm{d} - (\omega_\mathrm{d}^2+\zeta^2\omega_\mathrm{n}^2)\omega_\mathrm{d}s\right]\sin\omega_\mathrm{d}(t-s)\right\}\right)_{s=0}^{s=t} \\ &\quad - \frac{\zeta}{\sqrt{1-\zeta^2}}\frac{F_0}{mt_0}\left(\frac{\mathrm{e}^{-\zeta\omega_\mathrm{n}(t-s)}}{(\omega_\mathrm{d}^2+\zeta^2\omega_\mathrm{n}^2)^2}\left\{[-2\zeta\omega_\mathrm{n}\omega_\mathrm{d}+(\omega_\mathrm{d}^2+\zeta^2\omega_\mathrm{n}^2)\omega_\mathrm{d}s]\cos\omega_\mathrm{d}(t-s)\right.\right. \\ &\qquad \left.\left. + \left[(\omega_\mathrm{d}^2+\zeta^2\omega_\mathrm{n}^2)+(\omega_\mathrm{d}^2+\zeta^2\omega_\mathrm{n}^2)\zeta\omega_\mathrm{n}s\right]\sin\omega_\mathrm{d}(t-s)\right\}\right)_{s=0}^{s=t}\end{aligned} \tag{3.156}$$

Simplifying Equation 3.156 gives

$$x_p(t) = \left(\frac{F_0}{kt_0}\right)\mathrm{e}^{-\zeta\omega_\mathrm{n}t}\cos\omega_\mathrm{d}t - \left[\frac{\zeta}{\sqrt{1-\zeta^2}} - \frac{F_0}{kt_0}\right]\mathrm{e}^{-\zeta\omega_\mathrm{n}t}\sin\omega_\mathrm{d}t + \left(\frac{F_0}{kt_0}\right) \tag{3.157}$$

Substituting $t = t_0 = \Delta t$ and $F_0 = F_{k+1} - F_k$, Equations 3.155 and 3.157 are given as:

$$\begin{aligned}x_p(\Delta t) &= \left[\frac{2\zeta(F_{k+1}-F_k)}{k\omega_\mathrm{n}\Delta t}\right]\mathrm{e}^{-\zeta\omega_\mathrm{n}\Delta t}\cos\omega_\mathrm{d}\Delta t \\ &\quad + \left[\frac{(F_{k+1}-F_k)(2\zeta^2-1)}{k\omega_\mathrm{n}\Delta t\sqrt{1-\zeta^2}}\right]\mathrm{e}^{-\zeta\omega_\mathrm{n}\Delta t}\sin\omega_\mathrm{d}\Delta t + \left[\frac{F_{k+1}-F_k}{k}\right] - \frac{2\zeta(F_{k+1}-F_k)}{k\omega_\mathrm{n}\Delta t}\end{aligned} \tag{3.158}$$

$$\begin{aligned}\dot{x}_p(\Delta t) &= -\left[\frac{F_{k+1}-F_k}{k\Delta t}\right]e^{-\zeta\omega_\mathrm{n}\Delta t}\cos\omega_\mathrm{d}\Delta t \\ &\quad - \left[\frac{\zeta}{\sqrt{1-\zeta^2}}\frac{(F_{k+1}-F_k)}{k\Delta t}\right]\mathrm{e}^{-\zeta\omega_\mathrm{n}\Delta t}\sin\omega_\mathrm{d}\Delta t + \left[\frac{F_{k+1}-F_k}{k\Delta t}\right]\end{aligned} \tag{3.159}$$

Similarly, substituting $x_0 = x_k$, $\dot{x}_0 = \dot{x}_k$, $t = \Delta t$, and $F_0 = F_k$ into Equations 3.149 and 3.150

$$x(\Delta t) = -\left[x_k - \frac{F_k}{k}\right]\mathrm{e}^{-\zeta\omega_\mathrm{n}\Delta t}\cos\omega_\mathrm{d}\Delta t + \left[\frac{\omega_\mathrm{n}\zeta\left(x_k - \dfrac{F_k}{k}\right) + \dot{x}_k}{\omega_\mathrm{n}\sqrt{1-\zeta^2}}\right]\mathrm{e}^{-\zeta\omega_\mathrm{n}\Delta t}\sin\omega_\mathrm{d}\Delta t + \left(\frac{F_k}{k}\right) \tag{3.160}$$

$$\dot{x}(\Delta t) = \dot{x}_k e^{-\zeta\omega_n \Delta t}\cos\omega_d \Delta t - \left[\frac{\omega_n\left(x_k - \frac{F_k}{k}\right) + \zeta\dot{x}_k}{\sqrt{1-\zeta^2}}\right] e^{-\zeta\omega_n \Delta t}\sin\omega_d \Delta t \tag{3.161}$$

Adding the responses due to the constant force F_k and the triangular variation of force $F_{k+1} - F_k/\Delta t$ s over the time interval Δt, that is, adding Equations 3.158–3.161 and then separating out the terms containing x_k, $\dot{x}_k$, F_{k+1}, F_{k+1}, x_{k+1}, and $\dot{x}_{k+1}$, the responses are given as:

$$x_{k+1} = C_1 x_k + C_2 \dot{x}_k + C_3 F_k + C_4 F_{k+1} \tag{3.162}$$

$$\dot{x}_{k+1} = D_1 x_k + D_2 \dot{x}_k + D_3 F_k + D_4 F_{k+1} \tag{3.163}$$

in which expressions for C_1, C_2, D_1, D_2, and so on, are given by Equations 3.38–3.45.

Note that in arriving at the expressions given by Equations 3.162 and 3.163, homogeneous parts of the solution are considered (once) only with constant variation of force F_k over the time interval Δt.

Appendix 3.C Digitized Values of the Ground Acceleration of El Centro Earthquake

Table 3.9 contains ground acceleration data for the El Centro earthquake.

Table 3.9 Ground acceleration (in g unit) data for the El Centro earthquake, sampled at $\Delta t = 0.02$ s (read row wise)

0	0.0062	0.0036	0.001	0.0042	0.0074	0.0107	0.0067
0.0027	−0.0013	0.0036	0.0085	0.0133	0.0071	0.0009	0.0041
0.0022	0.0002	0.0044	0.0085	0.0127	0.0168	−0.0034	−0.0235
−0.0097	0.0041	0.0052	0.0162	0.0273	0.0383	0.024	0.0098
0.0094	0.0091	0.0088	−0.0048	−0.0183	−0.0318	−0.033	−0.0561
−0.0445	−0.0328	−0.0314	−0.03	−0.0286	−0.0271	−0.0404	−0.0536
−0.0669	−0.0801	−0.0672	−0.0542	−0.0413	−0.0418	−0.0423	−0.0238
−0.0053	0.0131	0.0316	0.0501	0.0685	0.087	0.0444	0.0018
−0.0409	−0.0835	−0.1261	−0.1688	−0.1266	−0.0845	−0.0873	−0.0902
−0.093	−0.0915	−0.0899	−0.093	−0.096	−0.1266	−0.0751	−0.0236
0.0279	0.0795	0.131	0.1825	0.234	0.2158	0.1975	0.1793
0.1611	0.1429	0.1584	0.1739	0.1296	0.0854	0.0412	−0.0031
−0.0473	−0.0916	−0.1358	−0.18	−0.2243	−0.2685	−0.3128	−0.2455
−0.1782	−0.1109	−0.0437	0.0236	0.0909	0.1582	0.2254	0.2927
0.2276	0.1624	0.0972	0.0321	−0.0331	−0.0982	−0.1634	−0.2286
−0.2937	−0.0041	0.2855	0.2195	0.1536	0.0877	0.0218	−0.0441
0.018	0.0801	0.1422	0.2042	0.1861	0.168	0.135	0.102
0.0689	0.0359	0.0029	−0.0301	−0.0055	0.0191	0.0437	0.0635
0.0832	0.1029	0.0578	0.0128	−0.0323	−0.0773	−0.0349	0.0076
0.05	0.0099	−0.0301	−0.0702	−0.1103	−0.1503	−0.111	−0.0717
−0.0323	0.007	−0.0623	−0.1316	−0.2009	−0.1224	−0.044	0.0345
0.1129	0.1914	0.1207	0.05	−0.0207	−0.0914	−0.0261	0.0392
0.1045	0.1698	0.1107	0.0516	−0.0076	0.0104	0.0284	0.0465
0.0645	0.0198	−0.0248	−0.0695	−0.0403	−0.0111	0.0028	0.0168
0.0307	−0.0223	−0.0754	−0.1285	−0.1815	−0.1407	−0.1	−0.0592
−0.0184	0.0224	−0.0098	−0.0419	−0.0211	−0.0002	0.0206	−0.0143
−0.0493	−0.0842	−0.1192	−0.1541	−0.1891	−0.224	−0.178	−0.132

Table 3.9 (*Continued*)

−0.0859	−0.0399	0.0061	0.0521	0.0982	0.1442	0.0957	0.0472
−0.0014	0.0504	0.1022	0.154	0.2058	0.2576	0.1667	0.0759
−0.015	−0.1058	−0.1967	−0.0666	0.0636	0.0164	−0.0308	−0.0779
−0.1251	−0.1723	−0.2194	−0.2666	−0.1555	−0.0444	0.0667	0.1778
0.1419	0.1059	0.07	0.0341	0.0948	0.1556	0.2163	0.1795
0.1426	0.1058	0.0689	0.032	0.0652	0.0984	0.1316	0.1014
0.0712	0.041	0.0108	−0.0195	0.0435	0.1065	0.1695	0.1022
0.0348	−0.0325	−0.0999	−0.0712	−0.0426	−0.014	0.0146	−0.0199
−0.0544	−0.0889	−0.1234	−0.1579	−0.1924	−0.145	−0.0977	−0.0503
−0.0029	−0.0191	−0.0354	−0.0516	−0.041	−0.0305	−0.0285	−0.0265
0.0247	0.0174	0.0217	0.0261	0.0041	−0.0178	−0.0398	−0.0617
−0.0237	0.0143	0.0524	0.0238	−0.0047	−0.0332	−0.0055	0.0223
0.0067	−0.009	−0.0246	−0.0403	−0.0559	−0.0179	0.0201	0.0045
−0.0112	−0.0021	0.0069	0.0049	0.0028	0.0007	−0.0052	−0.0112
0.0035	0.0183	0.033	0.0477	0.0298	0.0119	−0.006	−0.0239
0.0135	0.0108	0.0081	0.0054	0.008	0.0106	−0.0068	−0.0241
−0.0415	−0.0589	−0.0762	−0.0936	−0.0609	−0.0283	0.0044	0.0371
0.0174	−0.0023	−0.0219	0.0176	0.0571	0.0367	0.0163	−0.0041
−0.0245	−0.0449	−0.0203	0.0042	0.0288	0.015	0.0177	0.0205
0.0078	−0.0049	−0.0176	−0.0303	−0.0181	−0.0058	0.0064	−0.0247
−0.0558	−0.0397	−0.0235	−0.0074	0.0088	0.0038	−0.0013	−0.0063
−0.0113	−0.0257	−0.04	−0.0544	−0.0428	−0.0313	−0.0683	−0.0553
−0.0422	−0.0292	−0.0161	−0.0031	0.01	0.0231	0.0361	0.0492
0.0239	−0.0014	−0.0266	−0.003	0.0206	0.0442	0.0677	0.0566
0.0455	0.0344	0.0329	0.0315	0.03	0.0319	0.0338	0.0357
0.0132	−0.0092	−0.0317	−0.0294	−0.0304	−0.0313	−0.0254	−0.0195
−0.0135	−0.0076	−0.0142	−0.0208	0.0149	0.0507	0.0865	0.1223
0.158	0.1274	0.0968	0.0661	0.0355	0.0049	0.0041	0.0034
0.0026	−0.0581	−0.1188	−0.1796	−0.1181	−0.0567	0.0047	0.0661
0.1275	0.0821	0.0367	0.0685	0.1002	−0.0345	−0.1692	−0.135
−0.1008	−0.0666	−0.0325	−0.0358	−0.0391	−0.0051	0.0289	0.063
0.097	0.131	0.0581	−0.0147	−0.0876	−0.1604	−0.0598	0.0408
0.0152	−0.0104	−0.036	−0.0617	−0.0873	−0.0533	−0.0192	0.0148
0.0488	0.0829	0.0493	0.0157	−0.0179	−0.0515	−0.085	−0.0664
−0.0478	−0.0291	−0.0105	0.0081	−0.0031	0.0291	0.0613	−0.0023
−0.0659	−0.0397	−0.0136	0.0125	0.0079	0.0297	0.0514	0.0231
−0.0053	−0.0337	−0.062	−0.0904	−0.1188	−0.0829	−0.047	−0.0112
0.0247	0.0606	0.0395	0.0184	0.0437	0.069	0.0943	0.1195
0.0623	0.0051	−0.0522	−0.0306	−0.0091	0.0124	0.0339	0.0322
0.0305	0.0288	0.0443	0.0597	0.0752	0.0906	0.0563	0.022
−0.0123	0.0067	0.0256	0.0446	0.0154	−0.0138	−0.0429	−0.0721
−0.0391	−0.0062	0.0267	0.0596	0.036	0.0123	−0.0113	−0.035
−0.0066	0.0217	0.05	0.0783	0.0678	0.0573	0.0468	0.0364
0.0259	0.0571	0.0884	0.1196	0.0988	0.0779	0.0571	0.0362
0.0153	−0.0055	−0.0264	−0.0473	−0.0681	−0.089	−0.1098	−0.113
−0.1162	−0.1194	−0.1226	−0.1619	−0.2012	−0.1541	−0.1071	−0.0601
−0.0131	0.0339	0.0809	0.0743	0.0677	0.0612	0.0857	0.1102
0.1347	0.1194	0.1041	0.0888	0.0736	0.0786	0.0836	0.0887
0.0609	0.0331	0.0054	−0.0224	−0.0534	−0.0395	−0.0257	−0.0118
−0.0199	−0.028	−0.0612	−0.0346	−0.0079	−0.0485	−0.0357	−0.0229
−0.033	−0.0184	−0.0038	0.0108	0.0254	0.0142	0.003	−0.0082
0.0045	0.0173	0.0301	0.0429	0.0212	−0.0004	−0.0221	−0.0437
−0.0357	−0.0277	−0.0196	−0.0116	−0.024	−0.0364	−0.0487	−0.0577
−0.0667	−0.0756	−0.0846	−0.0935	−0.0616	−0.0296	0.0023	0.0343
0.0432	0.052	0.0312	0.0103	−0.0105	−0.0314	−0.0522	0.0018
0.0559	0.0195	−0.0169	−0.0533	−0.0118	0.0297	0.0713	0.1128
0.071	0.0292	−0.0126	0.0119	0.0364	0.0345	0.0326	0.0182
0.0038	0.0034	−0.0214	−0.0461	−0.0709	−0.0956	−0.1204	−0.0816
−0.0428	−0.004	0.0348	0.0736	0.1124	0.0762	0.04	0.0038

(*continued*)

Table 3.9 (*Continued*)

0.0028	0.0018	−0.0541	0.0464	0.0512	0.0561	0.0609	0.0657
0.0705	0.0265	−0.0175	−0.0614	−0.1054	−0.1494	−0.1235	−0.0976
−0.0717	−0.0458	−0.0199	0.006	0.0319	0.0084	−0.0151	−0.0386
−0.0621	−0.0326	−0.0031	0.0264	0.0117	−0.0029	0.0033	0.0095
0.0157	0.022	0.0413	0.0607	0.0801	0.0341	−0.0119	−0.0128
−0.0138	−0.0517	−0.025	0.0018	0.0286	0.0554	0.0822	0.0172
−0.0478	−0.0203	0.0071	0.0345	−0.0052	−0.0449	−0.0845	−0.0683
−0.052	−0.0358	−0.0195	−0.0033	0.013	0.0293	0.0108	−0.0077
−0.0261	−0.0055	0.0151	0.0357	0.0563	0.031	0.0057	−0.0195
−0.002	0.0156	−0.01	−0.0357	−0.0613	−0.0469	−0.0325	−0.0485
−0.0645	−0.0804	−0.0489	−0.0173	0.0143	0.0459	0.0775	0.0466
0.0157	−0.0152	−0.001	0.0132	0.0274	0.0416	0.0558	0.0371
0.0183	−0.0004	−0.0191	−0.0042	0.0108	0.0257	0.0407	0.0179
−0.005	−0.0086	−0.0366	−0.0645	−0.0255	0.0135	0.0526	0.0916
0.0577	0.0238	−0.0101	−0.0439	−0.0106	−0.0183	−0.026	−0.0338
−0.0246	−0.0153	−0.0061	−0.0099	−0.0137	0.0146	0.0429	0.034
0.0206	0.0072	−0.0062	−0.0196	0.0075	0.0346	0.0334	0.0322
0.031	0.0236	0.0161	0.0096	0.0032	−0.0033	0.0216	−0.019
−0.0597	−0.1003	−0.077	−0.0536	−0.0303	−0.0069	0.0165	0.0191
0.0217	0.0244	0.0177	−0.002	−0.0217	−0.0027	0.0162	0.0352
0.0542	0.0732	0.0609	0.0485	0.0362	−0.0014	0.0451	0.04
0.0349	0.0298	0.0356	0.0413	0.0471	0.0529	0.0485	0.0442
0.0398	0.0354	0.0311	0.006	−0.019	−0.044	−0.0691	−0.0941
−0.076	−0.0579	−0.0398	−0.0216	−0.0035	0.0146	0.0099	0.0051
0.0004	−0.0043	−0.0091	−0.0117	−0.0149	−0.0182	−0.0215	−0.0096
0.0022	0.014	0.0033	−0.0075	−0.0182	−0.0072	0.0038	0.0147
0.0257	0.01	−0.0058	−0.0215	−0.0012	0.0192	0.0395	0.0277
0.0159	0.0042	0.0019	−0.0003	−0.0025	−0.0048	−0.007	−0.0092
−0.0115	−0.0137	−0.0172	−0.0206	−0.0241	−0.0276	−0.0311	−0.0345
−0.0413	−0.048	−0.0349	−0.0219	−0.0088	0.0042	0.0173	0.007
−0.0033	−0.0136	0.0129	0.0393	0.0658	0.0473	0.0288	0.0102
−0.0083	−0.0268	−0.0453	−0.031	−0.0166	−0.0022	0.0122	0.0263
0.0404	0.0545	0.0319	0.0093	−0.0133	−0.014	−0.0148	−0.0155
−0.0413	−0.0263	−0.0114	0.0036	0.0185	0.0335	0.0306	0.0277
0.0286	0.0296	0.0305	0.0038	−0.0229	−0.0497	−0.0375	−0.0253
−0.0131	−0.0009	0.0112	0.0234	0.0356	0.0103	−0.0151	−0.0404
−0.0657	−0.0511	−0.0364	−0.0218	−0.0072	0.0075	0.0221	0.0368
0.0392	0.0418	0.0442	0.0467	0.0491	0.0446	0.04	0.0282
0.0164	0.0046	−0.0072	−0.0011	0.005	0.0111	0.0172	−0.0021
−0.0213	−0.0406	−0.0598	−0.079	−0.0686	−0.0582	−0.0478	−0.0373
−0.0251	−0.0129	−0.0006	0.0116	0.0239	0.0361	0.0483	0.0292
0.01	−0.0091	−0.0283	−0.0475	−0.0666	−0.0477	−0.0288	−0.0099
0.009	0.028	0.0469	0.0241	0.0013	−0.0215	−0.0443	−0.0671
−0.0488	−0.0306	−0.0124	0.0058	0.0241	0.0423	0.0605	0.0787
0.097	0.0633	0.0296	−0.0041	−0.0377	−0.0714	−0.0589	−0.0463
−0.0337	−0.0317	−0.0297	−0.0277	−0.0039	0.0199	0.0031	−0.0138
−0.0306	−0.0475	−0.0644	−0.0503	−0.0363	−0.0223	−0.0083	0.0058
0.0198	0.0265	0.0331	0.0398	0.0465	0.0532	0.0347	0.0162
0.0159	0.0157	0.0154	0.0073	−0.0008	−0.0089	0.0007	0.0103
0.0199	0.0295	0.0391	0.0341	0.0291	0.0241	0.0302	0.0362
0.0423	0.0484	0.0544	0.0605	−0.0052	−0.0708	−0.0622	−0.0535
−0.0448	−0.0361	−0.0361	−0.0361	−0.036	−0.0173	0.0014	0.0201
0.0388	0.0575	0.0349	0.0122	−0.0105	−0.0331	−0.0558	−0.0442
−0.0325	−0.0209	−0.0093	0.0023	−0.002	−0.0064	−0.0108	−0.0152
−0.0118	−0.0083	−0.0049	−0.0015	0.0019	0.0005	−0.0009	0.0111
0.0232	0.0352	0.0473	0.0593	0.0713	0.0279	−0.0155	−0.0589
−0.0497	−0.0406	−0.0314	−0.0308	−0.0301	−0.0295	−0.0183	−0.0071
0.0042	0.0154	0.0266	0.0378	0.0292	0.0205	0.0229	0.0253
0.0277	0.03	0.0324	0.0134	−0.0055	−0.0245	−0.0217	−0.0189
−0.0161	−0.0133	−0.0124	−0.0115	−0.0017	0.0082	0.018	0.0278

Table 3.9 (*Continued*)

0.0376	0.0475	0.0368	0.0261	0.0154	0.0047	−0.006	−0.0166
−0.0077	0.0013	0.0103	0.0193	0.0283	−0.0049	−0.0382	−0.023
−0.0078	0.0074	0.0227	0.0069	−0.0088	−0.0245	−0.0402	−0.0559
−0.0286	−0.0013	0.0259	0.0532	0.0352	0.0171	−0.0009	−0.019
−0.0371	−0.0224	−0.0077	0.007	0.0217	0.0364	0.0511	0.0657
0.0804	0.0303	−0.0199	−0.07	−0.1202	−0.0848	−0.0494	−0.014
0.0214	0.0568	0.0922	0.1276	0.0354	−0.0568	−0.0471	−0.0374
−0.0278	−0.0181	−0.0084	−0.0358	−0.0632	−0.0605	−0.0578	−0.0551
−0.0596	−0.064	−0.0454	−0.0268	−0.0081	0.0105	0.0291	0.0308
0.0324	0.0341	0.0357	0.0449	0.054	0.0632	0.0723	0.0815
0.0354	−0.0107	−0.0568	−0.0461	−0.0353	−0.0246	−0.0139	−0.0349
−0.056	−0.0771	−0.0618	−0.0466	−0.0314	−0.0162	−0.001	0.009
0.0191	0.0291	0.0392	0.0492	0.0593	0.0693	0.0794	−0.0019
−0.0831	−0.069	−0.0548	−0.0407	−0.052	−0.0632	−0.0745	−0.0857
−0.097	−0.0667	−0.0364	−0.0061	0.0242	0.0545	0.0848	0.1151
0.1453	0.0855	0.0257	−0.0342	−0.094	−0.0697	−0.0453	−0.0209
0.0035	0.0278	0.0522	−0.0046	−0.0614	−0.1182	−0.0977	−0.0772
−0.0567	−0.0363	−0.0158	0.0047	0.0252	0.0457	0.0662	0.0866
0.1071	0.1276	0.1079	0.0881	0.0684	0.0486	0.0393	0.03
0.0207	0.0114	0.0077	0.0039	0.0002	−0.0035	−0.0072	−0.0109
−0.0077	−0.0044	−0.0012	0.0021	0.0053	−0.0082	−0.0216	−0.0351
−0.0485	−0.062	−0.0495	−0.037	−0.0245	−0.012	0.0005	0.0047
0.009	0.0133	0.0176	0.0219	0.0087	−0.0045	−0.0177	−0.0309
−0.0223	−0.0137	−0.0052	0.0034	0.012	0.0206	0.0141	0.0076
0.0011	0.0081	0.0151	0.0221	0.0168	0.0115	0.0062	0.0135
0.0207	0.028	0.0352	0.0425	0.0339	0.0254	0.0168	0.0083
−0.0003	−0.0088	−0.0012	0.0063	0.0139	0.02	0.0261	0.0322
0.0383	0.0444	0.0357	0.027	0.0183	0.0096	0.0008	−0.0131
−0.027	−0.0409	−0.0276	−0.0143	−0.0009	0.0124	0.0257	0.0166
0.0074	−0.0017	−0.0109	−0.0201	−0.0292	−0.0384	−0.024	−0.0095
0.0049	0.0193	0.0337	0.0201	0.0066	−0.0069	−0.0205	−0.034
−0.0261	−0.0182	−0.0104	−0.0025	−0.0006	0.0013	0.0031	0.005
0.0098	0.0146	0.0078	0.0009	−0.0059	0.0034	0.0126	0.0219
0.0312	0.0405	0.0266	0.0126	−0.0013	−0.0152	−0.0292	−0.0431
−0.0354	−0.0277	−0.0201	−0.0124	−0.0047	0.003	0.0107	0.0097
0.0086	0.0075	0.0065	0.0121	0.0177	0.0233	0.029	0.0346
0.0273	0.02	0.0128	−0.0335	−0.0062	−0.0061	−0.006	−0.006
−0.0059	−0.0058	−0.0058	−0.0057	−0.0057	−0.0056	−0.0055	−0.0055
−0.0054	−0.0053	−0.0053	−0.0052	−0.0052	−0.0051	−0.005	−0.005
−0.0049	−0.0048	−0.0048	−0.0047	−0.0047	−0.0046	−0.0045	−0.0045
−0.0044	−0.0044	−0.0043	−0.0042	−0.0042	−0.0041	−0.004	−0.004
−0.0039	−0.0039	−0.0038	−0.0037	−0.0037	−0.0036	−0.0035	−0.0035
−0.0034	−0.0034	−0.0033	−0.0032	−0.0032	−0.0031	−0.0031	−0.003
−0.0029	−0.0029	−0.0028	−0.0027	−0.0027	−0.0026	−0.0026	−0.0025
−0.0024	−0.0024	−0.0023	−0.0022	−0.0022	−0.0021	−0.0021	−0.002
−0.0019	−0.0019	−0.0018	−0.0017	−0.0017	−0.0016	−0.0015	−0.0015
−0.0014	−0.0014	−0.0013	−0.0012	−0.0012	−0.0011	−0.0011	−0.001
−0.0009	−0.0009	−0.0008	−0.0007	−0.0007	−0.0006	−0.0006	−0.0005
−0.0004	−0.0004	−0.0003	−0.0002	−0.0002	−0.0001	−0.0001	0

Appendix 3.D Simulink Diagrams

Simulink diagrams for the solution of multi-degrees of freedom system under multi-support earthquake excitation are shown in Figures 3.36 and 3.37 for the problem in Example 3.9. In Figure 3.36, Simulink

diagram for the solution using the state-space formulation is presented, while in Figure 3.37 the solution of the second-order differential equation is presented. The out puts of the solutions are displacement, velocity, and acceleration sampled at the time interval of Δt. They are stored in files 1–3.

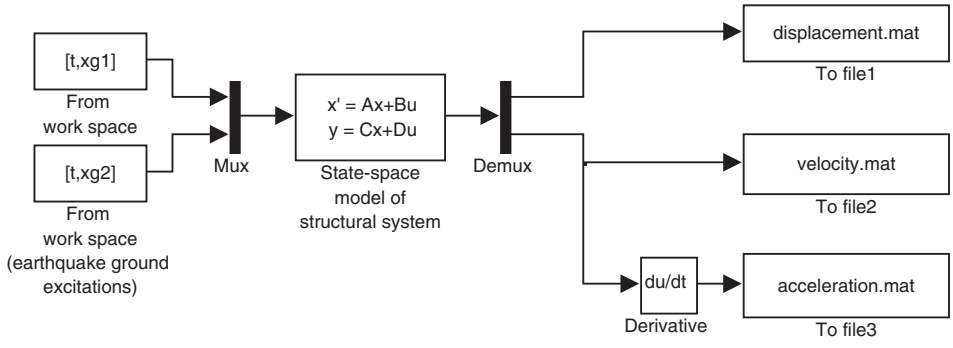

Figure 3.36 Simulink diagram for the solution of the state-space equation

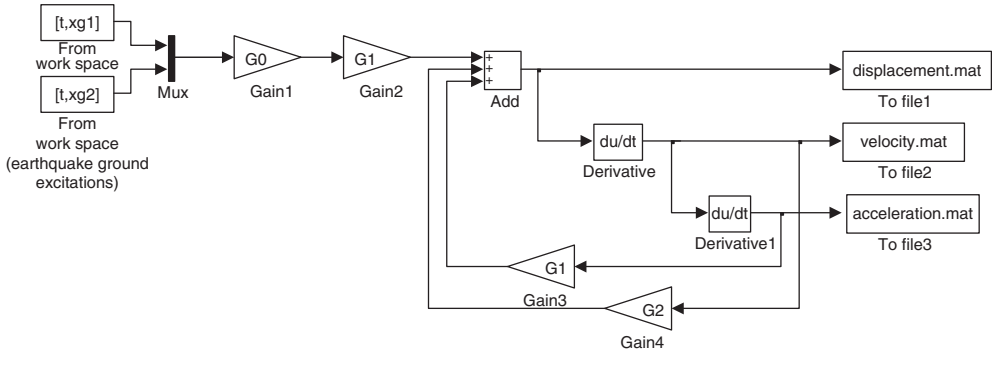

Figure 3.37 Simulink diagram for the solution of the second-order equation

Example 3.9

Solve Example 3.9 using the Simulink toolbox of MATLAB® by (a) state-space solution and (b) solution of second-order differential equations.

Solution:

$$\boldsymbol{M} = \begin{bmatrix} 2.5 & 1.67 \\ 1.67 & 2.5 \end{bmatrix} m$$

$$\boldsymbol{K} = 4\begin{bmatrix} 19.56 & 10.49 \\ 10.49 & 129 \end{bmatrix} m$$

$$\boldsymbol{r} = \begin{bmatrix} 0.479 & 0.331 \\ -0.131 & 0.146 \end{bmatrix}$$

$\boldsymbol{C}$ matrix is generated with $\alpha = 0.431$ and $\beta = 0.0041$. Excitations at the two supports are generated as explained in Example 3.9, each of duration 35 s.
State-space solution–

$$\boldsymbol{A} = \begin{bmatrix} \boldsymbol{0} & \boldsymbol{I} \\ -\boldsymbol{K}\boldsymbol{M}^{-1} & -\boldsymbol{C}\boldsymbol{M}^{-1} \end{bmatrix}_{4\times 4} \quad \boldsymbol{B} = \begin{bmatrix} 0 \\ -\boldsymbol{r} \end{bmatrix}_{4\times 2}$$

where $\boldsymbol{D}$ = null matrix (4×2) and $\boldsymbol{C}$ = diagonal identity matrix (4×4).
Solution of the second-order equation–

$$G0 = r \quad G1 = MK^{-1} \quad G2 = CK^{-1}$$

References

1. Clough, R.W. and Penzien, J. (1993) *Dynamics of Structures*, 2nd edn, McGraw Hill, Inc., New York.
2. Datta, T.K. and Sood, A.M. (1983) On the efficiency of some recently developed integration algorithms for offshore structures. *Journal of Energy Resources Technology, Transactions of ASME*, **1**, 73–78.
3. Bathe, K.J. and Wilson, E.L. (1976) *Numerical Methods in Finite Element Analysis*, Prentice Hall, Englewood Cliffs, NJ.
4. Hart, G.C., Wong, K.K.F., and Wong, K. (2000) *Structural Dynamics for Structural Engineers*, John Wiley & Sons, New York.
5. Newland, D.E. (1975) *An Introduction to Random Vibration and Spectral Analysis*, Longman, London and New York.
6. Hurty, W.C. and Rubinstein, M.F. (1964) *Dynamics of Structures*, Prentice Hall, Englewood Cliffs, NJ.
7. Chopra, A.K. (2001) *Dynamics of Structures, Theory and Applications to Earthquake Engineering*, 2nd edn, Prentice Hall, Englewood Cliffs, NJ.

4

Frequency Domain Spectral Analysis

4.1 Introduction

Frequency domain spectral analysis is performed in order to obtain the responses of structures subjected to random/stochastic excitations. It is one of the most popular techniques for random vibration analysis of structures in the frequency domain and is strictly applicable for linear systems. However, for non-linear systems, the method of analysis has also been extended by applying suitable linearization techniques and is found to work satisfactorily for mildly non-linear systems. The popularity of the method is primarily due to its simplicity and elegance.

When the dynamic excitations are modeled as stationary random processes, they are characterized by the moments of their probability density functions (PDFs), which remain invariant with the shift in time. For most of the structural engineering problems, the second moment of the PDF, that is, the mean square value of the process is of interest and, therefore, the second-order stationarity is sufficient for modeling random dynamic excitations such as wind, earthquake, and wave forces. This permits the use of frequency domain spectral analysis to find the responses of linear structural systems subjected to these forces.

In this chapter, the spectral analysis of structures for earthquake forces is developed without going into the rigors of the theory of random vibration analysis. The objective of this treatment is to enable one to use the spectral analysis of structures for earthquake forces without being a specialist in random vibration analysis. The development of the method uses simple concepts, such as, the stationary random process, auto correlation, and power spectral density functions, cross correlation and cross power spectral density functions, ergodicity, and Fourier transforms. These concepts will first be introduced.

4.2 Stationary Random Process

A random process is one that deals with a number of random variables. For example, a fluctuating component of wind velocity sampled at 2 s intervals between 12:00 and 12.15 p.m. every day for 365 days will constitute a random process. In this process, there will be 451 random variables; each random variable can assume 365 values. The random variables can be designated as $x(0), x(2), x(4), x(6) \ldots, x(900)$; $x(0)$ and $x(900)$ being the velocities measured at 12:00 and 12.15 noon respectively. Thus, the random variation of wind velocity in a year between 12 and 12.15 p.m. can be represented by a random process $x(t)$

Seismic Analysis of Structures T.K. Datta

having random variables $x(t_1), x(t_2) \ldots, x(t_n)$ with $n = 451$ and $t_1 = 0$. The sample size for each variable is 365. In order to characterize a random process, the sample size should ideally be infinity. In practice, this cannot be realized. Therefore, a sample size as large as possible is considered. If the random variables $x(0), x(2), x(4), x(6) \ldots, x(900)$ are connected by a single function of time t, then the random process is called a parametric random process (with parameter t). It is also called a stochastic process as the parameter involved is the time. To characterize a stochastic process, the number of samples constituting the ensemble should be infinity and each sample should also be of infinite duration. Again, for practical purposes, the number of the sample size and duration of each sample should be as large as possible to characterize the process.

An ensemble of time histories of a stochastic process $x(t)$ is shown in Figure 4.1. As shown in the figure, $x(t_1), x(t_2) \ldots, x(t_n)$ and so on are the random variables that can assume any value across the ensemble. A stationary stochastic process (of order two) is one for which the ensemble mean square value remains invariant with the time shift τ. This means that the mean square value of $x(t_1)$ across the ensemble is equal to that of $x(t_2)$, in which $t_2 = t_1 + \tau$ for any value of τ. Thus, a stationary stochastic process can be represented by a unique mean square value, which is the ensemble mean square value. If the mean square value is obtained after deducting the ensemble mean (which also remains invariant with the time shift) from the values of the random variables, then it is called the variance. For example, if the random variable is $x(t)$, then the variance is

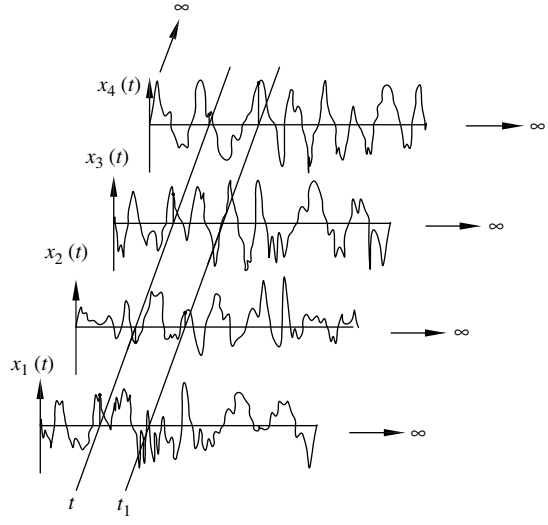

Figure 4.1 An ensemble of time histories of stochastic process $x(t)$

$$\sigma_x^2 = E\left[\{x(t_1) - \bar{x}(t_1)\}^2\right]$$

in which $E[\,]$ denotes the expectation or average of the value and $\bar{x}(t_1)$ is the ensemble mean of $x(t_1)$. In this case, the stationary process is characterized by a unique value of the variance (σ_x^2). Clearly, for a zero mean process the variance is equal to the mean square value.

A stationary process is called an ergodic process if the ensemble mean square value (or variance) is equal to the sample mean square value (or variance). that is,

$$\sigma_x^2 = \sigma_{x_i}^2 \; i = 1 \ldots N$$

in which N is the number of sample s, i denotes ith sample, and

$$\sigma_{x_i}^2 = \frac{1}{T}\int_0^T [x(t) - \bar{x}(t_1)]_i^2 \mathrm{d}t$$

If a stochastic process is an ergodic process, then any sample time history, taken from the ensemble, represents the second-order statistics (that is, mean square value, variance, and second moment of PDF, and so on) of the stochastic process. For the ergodic process, the development of the frequency domain spectral analysis is simple, and will be explained subsequently.

4.3 Fourier Series and Fourier Integral

Any arbitrary function $x(t)$ can be decomposed into a number of harmonic functions using the well-known equation:

$$x(t) = \frac{a_0}{2} + \sum_{k=1}^{\alpha}\left(a_k \cos\frac{2\pi kt}{T} + b_k \sin\frac{2\pi kt}{T}\right) \tag{4.1}$$

$$a_k = \frac{2}{T}\int_{-\frac{T}{2}}^{\frac{T}{2}} x(t)\cos\frac{2\pi kt}{T}\mathrm{d}t; \qquad a_0 = \frac{2}{T}\int_{-\frac{T}{2}}^{\frac{T}{2}} x(t)\mathrm{d}t \tag{4.2}$$

$$b_k = \frac{2}{T}\int_{-\frac{T}{2}}^{\frac{T}{2}} x(t)\sin\frac{2\pi kt}{T}\mathrm{d}t \tag{4.3}$$

T is the duration of $x(t)$, and it is assumed that $x(t)$ has a periodicity of T, that is, $x(t+T) = x(t)$. Using Equations 4.2 and 4.3, it is possible to write Equation 4.1 in the form

$$x(t) = \frac{a_0}{2} + \sum_{k=1}^{\alpha}\left[\frac{\Delta\omega}{\pi}\int_{-\frac{T}{2}}^{\frac{T}{2}} x(t)\cos(\omega_k t)\mathrm{d}t\right]\cos(\omega_k t) + \sum_{k=1}^{\alpha}\left[\frac{\Delta\omega}{\pi}\int_{-\frac{T}{2}}^{\frac{T}{2}} x(t)\sin(\omega_k t)\mathrm{d}t\right]\sin(\omega_k t) \tag{4.4}$$

in which $\Delta\omega = 2\pi/T$ and $\omega_k = 2\pi kt/T$.

For $T \to \alpha$, $\Delta\omega \to \mathrm{d}\omega$ and Σ becomes an integral. Therefore,

$$x(t) = \frac{a_0}{2} + \int_{\omega=0}^{\alpha}\frac{\mathrm{d}\omega}{\pi}\left\{\int_{-\alpha}^{\alpha} x(t)\cos(\omega t)\mathrm{d}t\right\}\cos(\omega t) + \int_{\omega=0}^{\alpha}\frac{\mathrm{d}\omega}{\pi}\left\{\int_{-\alpha}^{\alpha} x(t)\sin(\omega t)\mathrm{d}t\right\}\sin(\omega t) \tag{4.5}$$

Putting

$$A(\omega) = \frac{1}{2\pi}\int_{-\alpha}^{\alpha} x(t)\cos(\omega t)\mathrm{d}t \tag{4.6a}$$

$$B(\omega) = \frac{1}{2\pi}\int_{-\alpha}^{\alpha} x(t)\sin(\omega t)\mathrm{d}t \tag{4.6b}$$

which gives

$$x(t) = 2\int_{\omega=0}^{\alpha} A(\omega)\cos(\omega t)\mathrm{d}\omega + 2\int_{\omega=0}^{\alpha} B(\omega)\sin(\omega t)\mathrm{d}\omega \tag{4.7a}$$

Recognizing that terms within the integration are even functions of ω, Equation 4.7a may be written as

$$x(t) = \int_{-\alpha}^{\alpha} A(\omega)\sin\omega t\,\mathrm{d}\omega + \int_{-\alpha}^{\alpha} B(\omega)\sin\omega t\,\mathrm{d}\omega \tag{4.7b}$$

A negative frequency does not have a physical significance, but is a useful mathematical artifice introduced to represent the form of the Fourier integral pairs in compact form.

Introducing the complex harmonic function

$$\mathrm{e}^{-i\omega t} = \cos(\omega t) - i\sin(\omega t) \tag{4.8}$$

An equation may be written as:

$$x(\omega) = A(\omega) - iB(\omega) = \frac{1}{2\pi}\int_{-\alpha}^{\alpha} x(t)\mathrm{e}^{-i\omega t}\mathrm{d}t \tag{4.9}$$

in which $x(\omega)$ is a complex quantity. Using Equations 4.8 and 4.9, Equation 4.7b can be written as:

$$x(t) = \int_{-\alpha}^{\alpha} x(\omega)\mathrm{e}^{i\omega t}\mathrm{d}\omega \tag{4.10}$$

In the above derivation, it is assumed that $a_0 = 0$. Equations 4.9 and 4.10 are known as Fourier transform pair of integrals. For a Fourier integral to be strictly valid for any arbitrary function, the following condition has to be satisfied:

$$\int_{-\alpha}^{\alpha} |x(t)|\mathrm{d}t < \alpha \tag{4.11}$$

However, this condition can be relaxed under many circumstances. For engineering applications, Equations 4.9 and 4.10 are solved using discrete Fourier transform (DFT). The equivalent forms of the Fourier integral in DFT are [1]

$$x_k(\omega) = \frac{1}{N}\sum_{r=0}^{N-1} x_r \mathrm{e}^{-i\left(\frac{2\pi kr}{N}\right)} \tag{4.12}$$

$$x_r(t) = \sum_{k=0}^{N-1} x_k \mathrm{e}^{i\left(\frac{2\pi kr}{N}\right)} \tag{4.13}$$

Fast Fourier algorithms (FFT and IFFT) are based on DFT. In FFT, $x(t)$ is sampled at an interval of Δt and discrete values of $x(t)$, that is, x_r, are provided as inputs. The number of values should preferably be $N = 2^n$, with n as an integer number. FFT solves Equation 4.12 and gives 2^n complex numbers. If these complex numbers are provided as inputs to IFFT, $x(t)$ is retrieved as 2^n discrete values sampled at Δt by solving Equation 4.13. Of the ($N = 2^n$) complex numbers, the last set of $N/2$ numbers are complex conjugates of the first set. For more details about FFT and IFFT, standard textbooks on the subject may be referred to.

Once x_k is determined from the FFT, Fourier amplitudes can be determined from

$$A_k = 2\sqrt{(c_k^2 + d_k^2)} \quad k = 1, 2 \ldots \frac{N}{2} - 1 \tag{4.14}$$

in which $x_k = c_k + id_k$, and

$$A_0 = c_0 \tag{4.15}$$

Note that in FFT, A_0 need not be zero as assumed in the heuristic development of a Fourier integral from a Fourier series. In certain versions of FFT, x_r is divided by N, that is, Equations 4.12 and 4.13 are used. In this instance, Equations 4.14 and 4.15 remain valid. In other versions such as in MATLAB®, x_r is divided by $N/2$. In that situation

$$A_k = \sqrt{(c_k^2 + d_k^2)} \tag{4.16}$$

$$A_0 = \frac{c_0}{2} \tag{4.17}$$

According to Parsavel's theorem, the mean square value of $x(t)$ as given by Equation 4.1 is:

$$\frac{1}{T}\int_0^T x(t)^2 \mathrm{d}t = \frac{a_0^2}{4} + \frac{1}{2}\sum(a_k^2 + b_k^2) \tag{4.18}$$

if $x(t)$ is expanded using DFT,

$$\frac{1}{T}\int_0^T x(t)^2 \mathrm{d}t = \frac{1}{N}\sum_{r=0}^{N-1} x_r^2 = \sum_{k=0}^{N-1} |x_k|^2 \tag{4.19}$$

Equation 4.18 may be interpreted as: mean square value of $x(t) = (\text{mean value})^2 +$ half of the sum of the amplitude squares of the harmonics. Equation 4.19 may be interpreted as: mean square value of $x(t) =$ the sum of absolute square values of the FFT of $x(t)$, provided FFT is obtained by dividing $x(t)$ by N (not $N/2$). The details of the Fourier series analysis both in the real and in the complex domain, and the Fourier integral and DFT are available in many standard textbooks [1].

4.4 Auto Correlation and Cross Correlation Functions

The auto correlation function denotes the correlation between two random variables separated by a time lag of τ of a stochastic process $x(t)$. Let $x(t_1)$ and $x(t_2 = t_1 + \tau)$ be the two random variables. The auto correlation function for the process $x(t)$ is given by:

$$R_{xx}(\tau) = E[x(t_1)x(t_1 + \tau)] \tag{4.20}$$

where $E[\,]$ stands for the expected value, that is, the average of the products across the ensemble. It is clear from Equation 4.20 that for $\tau = 0$, $R_{xx}(\tau) = R_{xx}(0) =$ mean square value of the process and the two variables are perfectly correlated. As τ increases, it is expected that the correlation will decrease. Figure 4.2 shows the autocorrelation function of the stochastic process $x(t)$. Note that the autocorrelation function is a function of only the time separation τ and from Equation 4.20, it can easily be seen that $R_{xx}(\tau) = R_{xx}(-\tau)$, which is also depicted in Figure 4.2.

The cross correlation function between two random processes $x(t)$ and $y(t)$ may similarly be defined as:

$$R_{xy}(\tau) = E[x(t_1)y(t_1 + \tau)] \tag{4.21}$$

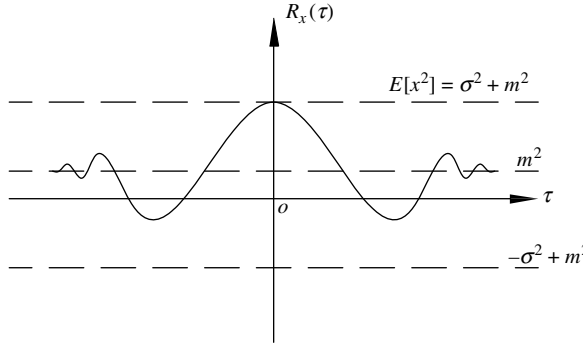

Figure 4.2 Auto correlation function of the stochastic process $x(t)$

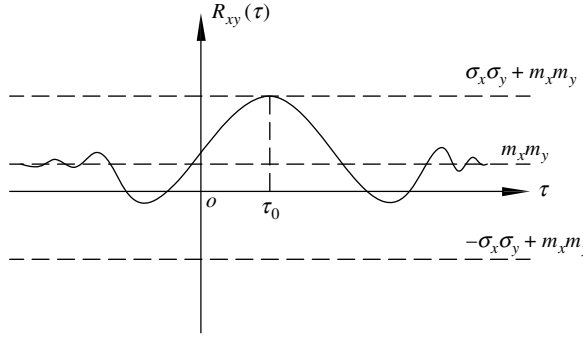

Figure 4.3 Cross correlation function between two stochastic processes $x(t)$ and $y(t)$

As with the auto correlation function, the cross correlation function is a measure of the correlation between two processes. Figure 4.3 shows the cross correlation function between two random processes. It follows from Equation 4.21 that

$$R_{xy}(\tau) = R_{yx}(-\tau)$$

4.5 Power Spectral Density Function (S_{xx}) and Cross Power Spectral Density Function (S_{xy})

Correlation functions and power spectral density functions form Fourier transform pairs as given below.

$$S_{xx}(\omega) = \frac{1}{2\pi}\int_{-\infty}^{\infty} R_{xx}(\tau)\mathrm{e}^{-iw\tau}\mathrm{d}\tau \tag{4.22}$$

$$S_{xy}(\omega) = \frac{1}{2\pi}\int_{-\infty}^{\infty} R_{xy}(\tau)\mathrm{e}^{-iw\tau}\mathrm{d}\tau \tag{4.23}$$

$$R_{xx}(\tau) = \int_{-\infty}^{\infty} S_{xx}(\omega) e^{iw\tau} dw \tag{4.24}$$

$$R_{xy}(\tau) = \int_{-\infty}^{\infty} S_{xy}(\omega) e^{iw\tau} dw \tag{4.25}$$

From Equation 4.23, it follows that $S_{yx}(\omega)$ is the complex conjugate of $S_{xy}(\omega)$.

Referring to Equation 4.24, for $\tau = 0$

$$R_{xx}(0) = r_x^2 = \int_{-\infty}^{\infty} S_{xx}(\omega) d\omega = E[x^2] \tag{4.26a}$$

Similarly,

$$R_{xy}(0) = \int_{-\alpha}^{\alpha} S_{xy}(\omega) d\omega = E[xy] \tag{4.26b}$$

in which r_x^2 is the mean square value of the process; $E[\,]$ indicates the expected value, that is, the average or mean value. Equation 4.26a provides a physical meaning of the power spectral density function. The area under the curve of the power spectral density function is equal to the mean square value of the process. In other words, the power spectral density function may be defined as the frequency distribution of the mean square value. At any frequency ω, the shaded area as shown in Figure 4.4 is the contribution of that frequency to the mean square value. If the square of $x(t)$ is considered to be proportional to the energy of the process [as in $E(t) = {}^1\!/_2 K x(t)^2$], then the power spectral density function of a stationary random process in a way denotes the distribution of the energy of the process with frequency. For random vibration analysis of structures in the frequency domain, the power spectral density function (PSDF) forms an ideal input because of two reasons:

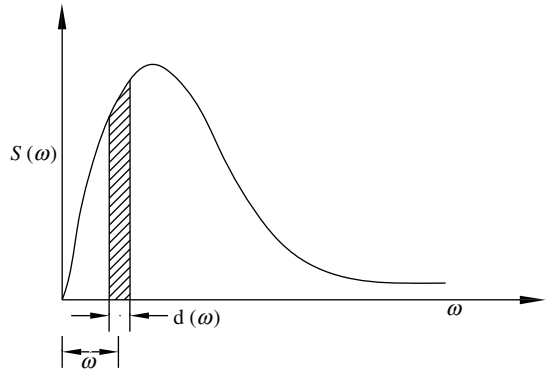

Figure 4.4 Shaded area at frequency ω contributing to the mean square value

i. A second-order stationary random process is uniquely defined by its mean square value.
ii. Distribution of the mean square value with frequency helps in ascertaining the contribution of each frequency content (energy) to the overall response.

The concept of power spectral density function can be explained in simpler terms if the ergodicity is assumed for the random process. In that case, any sample time history of the ensemble represents the mean square value of the process. If a sample time history $x(t)$ is considered, then use of Fourier transform and Parsavel's theorem (Equation 4.18) gives

$$\text{Mean square value} = r_x^2 = \frac{1}{T}\int_0^T x(t)^2 \mathrm{d}t = \frac{a_0^2}{4} + \sum \frac{1}{2}(a_k^2 + b_k^2) = \sum_{k=0}^{N-1} |x_k|^2 \tag{4.27a}$$

for

$$T \to \infty, \quad |x_k|^2 = S_{xx}\mathrm{d}\omega \tag{4.27b}$$

$$\sum |x_k|^2 = \int_0^\infty S_{xx}\mathrm{d}\omega \tag{4.27c}$$

For a zero mean process, $a_0 = 0$ and the mean square value becomes equal to the variance. The variance of the process is then the sum of the discrete ordinates shown in Figure 4.5a. As $T \to \infty$, $2\pi/T \to 0$ and therefore, for a sufficiently large value of T, the ordinates become more packed as shown in Figure 4.5b. If the kth ordinate is divided by $\mathrm{d}\omega = 2\pi/T$, then the shaded areas as shown in Figure 4.5c are obtained. The sum of such shaded areas ($k = 1$ to $N/2$) will result in the variance. A smooth curve passing through the points in Figure 4.5c would then define the PSDF of the process, according to Equations 4.26a, 4.27b and 4.27c.

This definition of PSDF using the assumption of ergodicity is useful in the development of the spectral analysis technique for single-point excitation with a limited knowledge of the theory of random vibration. Note that if $a_0 \neq 0$, then also this definition holds good and the area under the curve gives the mean square value of the process.

While a physical significance can be attached to the PSDF, no such physical significance can be attached to the cross PSDF. However, some physical significance of the cross power spectral density function can be understood from the effect of this function between two stochastic excitations on a response quantity of interest. Consider a simply supported beam with two harmonic excitations as shown in Figure 4.6. The phase lag ϕ between the two excitations is a measure of the degree of correlation between the two and it varies with the variation of ϕ. For $\phi = 0$, the two excitations are perfectly correlated and they are additive. Furthermore, the bending moment at the center of the beam is maximum. For $\phi = 225°$, the two excitations are subtractive, and the bending moment at the center will be minimum Thus, for different values of ϕ, that is the degree of correlation between the two excitations, the response of the beam will be different. If these two excitations are replaced by two random excitations $p_1(t)$ and $p_2(t)$, then it is obvious from the above explanation that the response of the beam will not only depend upon the power spectral density functions S_{p1p1} and S_{p2p2}, but also upon the cross power spectral density functions S_{p1p2} and S_{p2p1}, which denote the degree of correlation between the two.

4.6 Power Spectral Density Function (PSDF) Matrix

Now, consider a stochastic process $y(t)$ to be a weighted summation of two stochastic processes given by:

$$y = a_1 x_1 + a_2 x_2 = [a_1\ a_2]\begin{Bmatrix} x_1 \\ x_2 \end{Bmatrix} \tag{4.28}$$

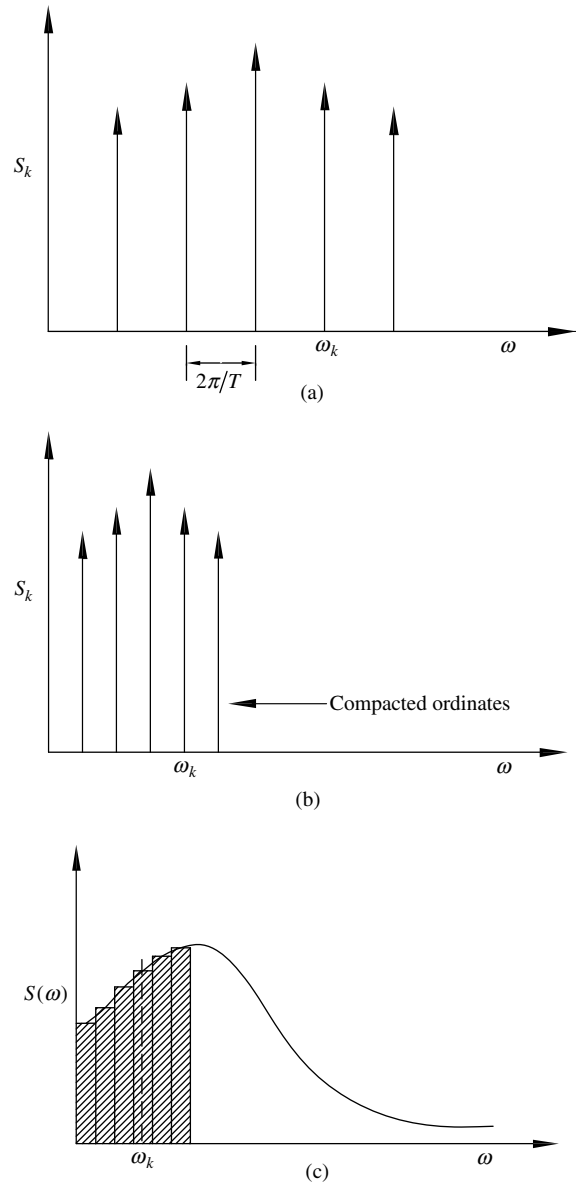

Figure 4.5 Generation of power spectral density function from a Fourier spectrum: (a) $S_k = |X_k|^2$ at kth frequency; (b) S_k at closer frequencies; and (c) kth ordinate of the power spectral density function

If y were equal to $a_1 x_1$ only, then it is clear that $E\,[y^2] = a_1^2 E\,[x_1^2]$. As y is a linear weighted summation of two stochastic processes x_1 and x_2, it is easy to show that

$$\begin{aligned} E[y^2] &= a_1^2 E[x_1^2] + a_2^2 E[x_2^2] + a_1 a_2 E[x_1 x_2] + a_2 a_1 E[x_2 x_1] \\ &= a_1^2 E[x_1^2] + a_2^2 E[x_2^2] + a_1 a_2 E[x_1 x_2] + a_2 a_1 E[x_2 x_1] \end{aligned} \tag{4.29}$$

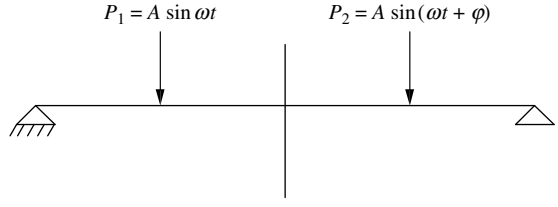

Figure 4.6 A simply supported beam with two harmonic excitations

Using Equations 4.26a and 4.26b, Equation 4.29 may be written as:

$$\int_{-\alpha}^{\alpha} S_{yy}(\omega)d\omega = a_1^2 \int_{-\alpha}^{\alpha} S_{x_1x_1}(\omega)\mathrm{d}\omega + a_2^2 \int_{-\alpha}^{\alpha} S_{x_2x_2}(\omega)\mathrm{d}\omega + a_1a_2 \int_{-\alpha}^{\alpha} S_{x_1x_2}(\omega)\mathrm{d}\omega + a_2a_1 \int_{-\alpha}^{\alpha} S_{x_2x_1}(\omega)\mathrm{d}\omega \tag{4.30}$$

or

$$\int_{-\alpha}^{\alpha} S_{yy}(\omega)\mathrm{d}\omega = \int_{-\alpha}^{\alpha} [a_1^2 S_{x_1x_1}(\omega) + a_2^2 S_{x_2x_2}(\omega) + a_1a_2 S_{x_1x_2}(\omega) + a_2a_1 S_{x_2x_1}(\omega)]\,\mathrm{d}\omega \tag{4.31}$$

As the PSDF of a stochastic process is always a function of ω, ω within the brackets is omitted from the notation of the PSDF henceforth, for brevity. Thus, from Equation 4.31 it follows that

$$S_{yy} = a_1^2 S_{x_1x_1} + a_2^2 S_{x_2x_2} + a_1a_2 S_{x_1x_2} + a_2a_1 S_{x_2x_1} = \{\, a_1 \quad a_2 \,\} \begin{bmatrix} S_{x1x1} & S_{x1x2} \\ S_{x2x1} & S_{x2x2} \end{bmatrix} \begin{Bmatrix} a_1 \\ a_2 \end{Bmatrix} \tag{4.32a}$$

or

$$\mathrm{S_{yy}} = \boldsymbol{a}\boldsymbol{S_{xx}}\boldsymbol{a}^{\boldsymbol{T}} \tag{4.32b}$$

in which $\boldsymbol{S_{xx}}$ is the PSDF matrix for the vector $\boldsymbol{x} = \begin{bmatrix} x_1 & x_2 \end{bmatrix}^T$ and $\boldsymbol{a} = \begin{bmatrix} a_1 & a_2 \end{bmatrix}^T$. Note that the diagonal terms of the PSDF matrix are the PSDFs of x_1 and x_2, and the off diagonal terms are the cross PSDFs between the two. For single to single variable transformation such as $y = \mathrm{a}x$, Equation 4.32b simplifies to

$$\mathrm{S_y} = a^2 S_x \tag{4.33}$$

Equation 4.32b can be easily extended to establish the relationship between PSDFs of two stochastic vectors $\boldsymbol{y}(t)$ and $\boldsymbol{x}(t)$. For example, if $\boldsymbol{y}(t)$ and $\boldsymbol{x}(t)$ are related by:

$$\boldsymbol{y}(t)_{n\times 1} = \boldsymbol{A}_{n\times m}\boldsymbol{x}(t)_{m\times 1} \tag{4.34}$$

then PSDF matrices $\boldsymbol{S_{yy}}$ and $\boldsymbol{S_{xx}}$ are related by:

$$\boldsymbol{S_{yy}} = \boldsymbol{A}\boldsymbol{S_{xx}}\boldsymbol{A}^T \tag{4.35}$$

Extending it further, if $\boldsymbol{y}(t)$ is related to processes $\boldsymbol{x}_1(t)$ and $\boldsymbol{x}_2(t)$ as:

$$\boldsymbol{y}(t) = \boldsymbol{A}_{n\times m}\boldsymbol{x}_1(t)_{m\times 1} + \boldsymbol{B}_{n\times r}\boldsymbol{x}_2(t)_{r\times 1} \tag{4.36}$$

then, $\boldsymbol{S}_{yy}$ is given by

$$\boldsymbol{S}_{yy} = \boldsymbol{A}\boldsymbol{S}_{x_1x_1}\boldsymbol{A}^T + \boldsymbol{B}\boldsymbol{S}_{x_2x_2}\boldsymbol{B}^T + \boldsymbol{A}\boldsymbol{S}_{x_1x_2}\boldsymbol{B}^T + \boldsymbol{B}\boldsymbol{S}_{x_2x_1}\boldsymbol{A}^T \tag{4.37}$$

$\boldsymbol{S}_{x_1x_2}$ and $\boldsymbol{S}_{x_2x_1}$ have the sizes of $m \times r$ and $r \times m$, respectively.

Another relationship that is of interest in spectral analysis of structures is the cross power spectral density function between $\boldsymbol{y}$ and $\boldsymbol{x}$, that is, $\boldsymbol{S}_{yx}$ and $\boldsymbol{S}_{xy}$. For the relationship between $\boldsymbol{y}$ and $\boldsymbol{x}$ given by Equation 4.34, it can be easily shown that $\boldsymbol{S}_{xy}$ is given by:

$$\boldsymbol{S}_{xy} = \boldsymbol{A}\boldsymbol{S}_{xx} \tag{4.38}$$

in which $\boldsymbol{S}_{xy}$ is a matrix of size $m \times n$; $\boldsymbol{S}_{yx} = \boldsymbol{S}_{xy}^T$. If $\boldsymbol{S}_{xy}$ is a complex matrix, then $\boldsymbol{S}_{yx} = \boldsymbol{S}_{xy}^{*T}$. For a single to single variable transformation, Equation 4.38 becomes $S_{\mathrm{xy}} = aS_{xx}$.

4.7 PSDFs and Cross PSDFs of the Derivatives of the Process

The derivatives of the PSDF and cross PSDF, especially the first two derivatives, are useful in the spectral analysis of structures. Therefore, they are derived below.

If $x(t)$ is a stationary random process, the PSDFs of the derivatives of the process and cross PSDFs between the original and derivatives of the process are obtained using the simple rules of differentiation and Fourier transforms. The auto correlation of the process $R_x(\tau)$ is the ensemble average of $x(t)$ and $x(t+\tau)$, that is,

$$R_x(\tau) = E[x(t)x(t+\tau)] \tag{4.39}$$

If $x_r(t)x_r(t+\tau)$ is the product for the rth sample, then differentiation of the product with respect to τ gives

$$\frac{\mathrm{d}}{\mathrm{d}\tau}\{x_r(t)x_r(t+\tau)\} = x_r(t)\frac{\mathrm{d}}{\mathrm{d}\tau}x_r(t+\tau) = x_r(t)\dot{x}_r(t+\tau) \tag{4.40a}$$

Thus,

$$\frac{\mathrm{d}}{\mathrm{d}\tau}\{R_x(\tau)\} = E\left[x(t)\dot{x}(t+\tau)\right] \tag{4.40b}$$

As ensemble averages are independent of time t, it is possible to write

$$E\left[x(t)\dot{x}(t+\tau)\right] = E\left[x(t-\tau)\dot{x}(t)\right] \tag{4.41}$$

or

$$\frac{\mathrm{d}}{\mathrm{d}\tau}\{R_x(\tau)\} = E\left[x(t-\tau)\dot{x}(t)\right] \tag{4.42}$$

From Equation 4.42, it is clear that

$$\frac{\mathrm{d}^2}{\mathrm{d}\tau^2}\{R_x(\tau)\} = -E[\dot{x}(t-\tau)\dot{x}(t)] = -R_{\dot{x}}(\tau) \tag{4.43}$$

Differentiating the inverse Fourier transform relationship between $R_x(\tau)$ and S_x given by Equation 4.24, the following relationships are obtained:

$$\frac{\mathrm{d}}{\mathrm{d}\tau}\{R_x(\tau)\} = \int_{-\alpha}^{\alpha} i\omega S_x \mathrm{e}^{i\omega\tau}\mathrm{d}\omega \tag{4.44}$$

and

$$\frac{\mathrm{d}^2}{\mathrm{d}\tau^2}\{R_x(\tau)\} = -\int_{-\alpha}^{\alpha} \omega^2 S_x \mathrm{e}^{i\omega\tau}\mathrm{d}\omega \tag{4.45}$$

use of Equations 4.43 and 4.45, gives

$$R_{\dot{x}}(\tau) = \int_{-\alpha}^{\alpha} \omega^2 S_x \mathrm{e}^{i\omega\tau}\mathrm{d}\omega \tag{4.46}$$

or

$$R_{\dot{x}}(\tau) = \int_{-\alpha}^{\alpha} S_x \mathrm{e}^{i\omega\tau}\mathrm{d}\omega = \int_{-\alpha}^{\alpha} \omega^2 S_x \mathrm{e}^{i\omega\tau}\mathrm{d}\omega \tag{4.47}$$

or

$$S_{\dot{x}} = \omega^2 S_x \tag{4.48}$$

Proceeding further in this way, it can be shown that

$$S_{\ddot{x}} = \omega^2 S_{\dot{x}} = \omega^4 S_x \tag{4.49}$$

4.8 Single Input Single Output System (SISO)

Consider the SDOF system as shown in Figure 4.7. The equation of motion for the system can be written as:

$$m\ddot{x} + c\dot{x} + kx = p(t) \tag{4.50}$$

in which $p(t)$ is a stationary stochastic process represented by its PSDF S_p. It is further assumed that the process is also an ergodic process. Any sample time history of $p(t)$, therefore, can be considered to obtain the PSDF of $p(t)$ as described earlier. With these assumptions, $p(t)$ is Fourier synthesized using FFT. If $p(\omega)$ is the FFT of $p(t)$, then the frequency contents $x(\omega)$ of the response $x(t)$ can be written as:

$$x(\omega) = h(\omega)p(\omega) \tag{4.51a}$$

in which $h(\omega) = (-m\omega^2 + k + ic\omega)^{-1}$. If $p(t)$ is produced due to the support accelerations $\ddot{x}(t)$, then $p(t) = -m\ddot{x}_g(t)$ and the equation of motion becomes (Chapter 3, Equation 3.1):

$$\ddot{x} + 2\xi\omega_n\dot{x} + \omega_n^2 = -\ddot{x}_g \quad \text{(after dividing by } m\text{)} \tag{4.51b}$$

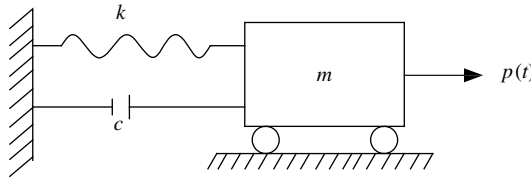

Figure 4.7 A single degree freedom system

$$h(\omega) = (\omega_{\mathrm{n}}^2 - \omega^2 + 2i\xi\omega_{\mathrm{n}}\omega)^{-1} \tag{4.51c}$$

$$p(\omega) = -\ddot{x}_g(\omega) \tag{4.51d}$$

A sample time history of the stationary random process $x(t)$ can be obtained by IFFT of $x(\omega)$, that is,

$$x(t) = \int_{-\infty}^{\infty} x(\omega)\mathrm{e}^{i\omega t}\mathrm{d}\omega \tag{4.52}$$

$x(t)$ is also an ergodic process as the system is assumed to be linear, and therefore the probabilistic nature of the output will be the same as that of the input. From Equation 4.51a, it is possible to write

$$x(\omega)x(\omega)^* = h(\omega)h(\omega)^* p(\omega)p(\omega)^* \tag{4.53a}$$

or

$$|x(\omega)|^2 = |h(\omega)|^2|p(\omega)|^2 \tag{4.53b}$$

Using Equation 4.19, the mean square value of $x(t)$ may be given by:

$$\frac{1}{T}\int_0^T x(t)^2\mathrm{d}t = \frac{1}{N}\sum_{r=0}^{N-1} x_r{}^2 = \sum_{k=0}^{N-1} |x_k|^2 = \sum |x(\omega)|^2 \tag{4.54}$$

Using Equation 4.53b, Equation 4.54 can be written as:

$$\frac{1}{T}\int_0^T x(t)^2\mathrm{d}t = \sum |h(\omega)|^2|p(\omega)|^2 \tag{4.55}$$

for $T \to \alpha$, use of Equations 4.27a and 4.27c in Equation 4.55 leads to

$$\frac{1}{T}\int_0^T x(t)^2\mathrm{d}t = r_x^2 = \int_0^{\infty} |h(\omega)|^2 S_p\mathrm{d}\omega \tag{4.56}$$

Using Equation 4.26a, the above equation can also be written as:

$$\int_0^{\omega} S_x(\omega)\mathrm{d}\omega = \int_0^{\omega} |h(\omega)|^2 S_p\mathrm{d}\omega \tag{4.57}$$

or

$$S_x(\omega) = |h(\omega)|^2 S_p \tag{4.58}$$

or

$$S_x(\omega) = h(\omega)S_p h^*(\omega) \tag{4.59}$$

if $p(\omega) = -\ddot{x}_g(\omega)$ (Equation 4.51d), then S_p is replaced by $S_{\ddot{x}g}$, that is, the PSDF of the support acceleration. Equations 4.58 and 4.59 provide the relationship between the PSDF of response $x(t)$ and that of excitation $p(t)$.

If ergodicity is assumed, then the relationships given by Equations 4.48 and 4.49 can also be proved making use of Equations 4.51 and 4.58 in the following way.

If $x(t)$ is assumed to be an ergodic process, then the frequency contents of velocity can be related to those of displacement as

$$\dot{x}(\omega) = i\omega x(\omega) \tag{4.60}$$

Using Equations 4.51a, 4.58 and 4.38, the following relationships can be then established:

$$S_{\dot{x}} = \omega^2 S_x \tag{4.61}$$

$$S_{x\dot{x}} = i\omega S_x; \qquad S_{\dot{x}x} = -i\omega S_x \tag{4.62}$$

Similarly, the following relationships can also be developed:

$$\ddot{x}(\omega) = -\omega^2 x(\omega) \tag{4.63}$$

$$S_{\ddot{x}} = \omega^4 S_x \tag{4.64}$$

$$S_{x\ddot{x}} = -\omega^2 S_x; \qquad S_{\ddot{x}x} = -\omega^2 S_x \tag{4.65}$$

If the process $\boldsymbol{x}$ is a vector, the above relationships can be generalized to

$$\boldsymbol{S}_{\dot{\boldsymbol{x}}} = \omega^2 \boldsymbol{S}_{\boldsymbol{x}} \tag{4.66}$$

$$\boldsymbol{S}_{\ddot{\boldsymbol{x}}} = \omega^4 \boldsymbol{S}_{\boldsymbol{x}} \tag{4.67}$$

$$\boldsymbol{S}_{\boldsymbol{x}\dot{\boldsymbol{x}}} = i\omega \boldsymbol{S}_{\boldsymbol{x}}; \qquad \boldsymbol{S}_{\dot{\boldsymbol{x}}\boldsymbol{x}} = -i\omega \boldsymbol{S}_{\boldsymbol{x}}^{\boldsymbol{T}} \tag{4.68}$$

$$\boldsymbol{S}_{\boldsymbol{x}\ddot{\boldsymbol{x}}} = -\omega^2 \boldsymbol{S}_{\boldsymbol{x}}; \qquad \boldsymbol{S}_{\ddot{\boldsymbol{x}}\boldsymbol{x}} = -\omega^2 \boldsymbol{S}_{\boldsymbol{x}}^{\boldsymbol{T}} \tag{4.69a}$$

As $\boldsymbol{S}_{\boldsymbol{x}}$ is a symmetric matrix, it is found that

$$\boldsymbol{S}_{\boldsymbol{x}\dot{\boldsymbol{x}}} + \boldsymbol{S}_{\dot{\boldsymbol{x}}\boldsymbol{x}} = 0 \tag{4.69b}$$

Example 4.1

For the frame of the problem in Example 3.7, shown in Figure 3.11, obtain a plot of the PSDF of the displacement x and also, find the rms value of the displacement for the support excitation represented by the PSDF of ground acceleration (for the El Centro earthquake) given in Appendix 4.A.

Solution: For the above problem, $\omega_n = 12.24\ \text{rad s}^{-1}$ and $\Delta\omega = 0.209\ \text{rad s}^{-1}$. The digitized values of the PSDF given in Appendix 4.A are obtained from the El Centro earthquake record by considering it as a sample time history of an ergodic process. As the problem is effectively an SDOF system, $h(\omega)$ is given by Equation 4.51c and the use of Equation 4.58 gives the PSDF of the displacement.

The PSDF of excitation is shown in Figure 4.8 and the plot of the absolute value square of the frequency response function (Equation 4.51c) for the displacement x is shown in Figure 4.9. It is seen from the figure that the curve peaks at the natural frequency of the system. The PSDF of the displacement x is shown in Figure 4.10. It is seen from the figure that the PSDF of displacement also peaks at the natural frequency of the system, not at the frequency where the peak of the PSDF of excitation occurs. Note that the possible positions of the peaks of the PSDF of response are: (i) where the peaks of the plot of the absolute value square of the frequency response function occur, that is, at the points of the natural frequencies of the structure, and (ii) where the peaks of the excitations occur.

The rms value of the displacement x = square root of the area under the PSDF curve = 0.014 m.

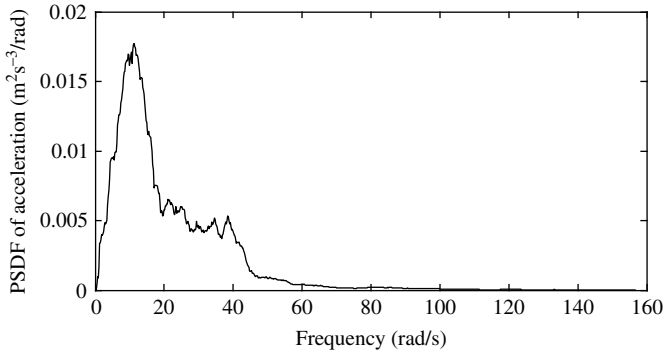

Figure 4.8 Power spectral density function (PSDF) for El Centro earthquake acceleration

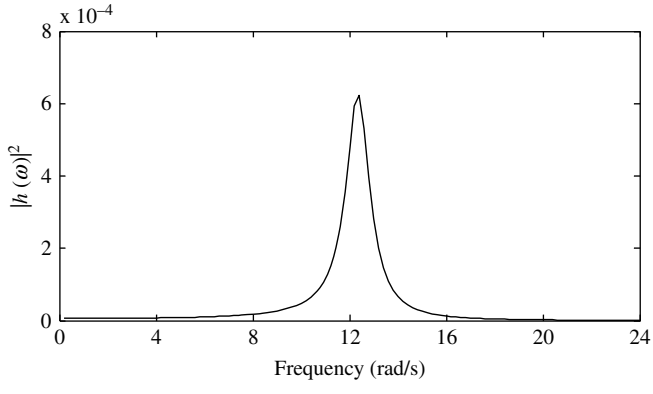

Figure 4.9 Variation of absolute square of frequency response function with frequency

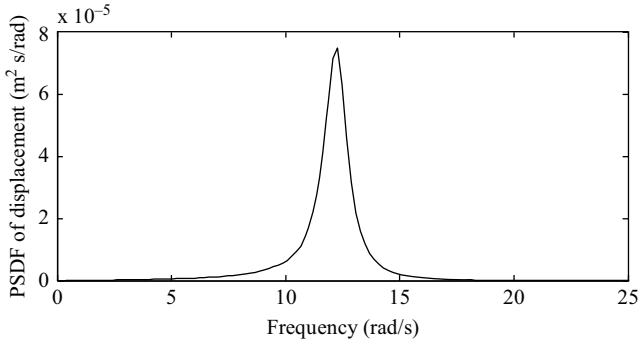

Figure 4.10 PSDF of displacement $x(t)$

The rms value obtained from the time history analysis is 0.015 m (Chapter 3, Example 3.7), which matches well with the above rms value.

4.9 MDOF System with Single-Point and Multi-Point Excitations

4.9.1 Single-Point Excitation

For multi-storey buildings, towers, chimneys, and other tall structures under single-point earthquake excitations, the equations of motion may be written as:

$$\boldsymbol{M}\ddot{\boldsymbol{x}} + \boldsymbol{C}\dot{\boldsymbol{x}} + \boldsymbol{K}\boldsymbol{x} = -\boldsymbol{M}\boldsymbol{I}\ddot{x}_g = \boldsymbol{P}(t) \tag{4.70}$$

Extending Equation 4.51a to the MDOF system

$$\boldsymbol{x}(\omega) = \boldsymbol{H}(\omega)\boldsymbol{P}(\omega) \tag{4.71}$$

in which $\boldsymbol{H}(\omega)$ is the complex frequency response function matrix described in Chapter 3. As the system is linear, $\boldsymbol{x}(\omega)$ is a vector of stationary random processes if $\boldsymbol{P}(\omega)$ is also a vector of a stationary random process. The vector of a stationary random process is characterized by a power spectral density matrix, that is, PSDF matrix as explained earlier. Thus, the PSDF matrix for $\boldsymbol{x}(\omega)$ is denoted by $\boldsymbol{S}_{xx}$ in which the PSDF of the ith process is $S_{x_i x_i}$, that is, the ith diagonal element and the element $S_{x_i x_j}$ is the cross power spectral density function between the ith and jth processes of the vector $\boldsymbol{x}(\omega)$.

Using Equations 4.35 and 4.71, $\boldsymbol{S}_{xx}$ and $\boldsymbol{S}_{pp}$ are related by:

$$\boldsymbol{S}_{xx} = \boldsymbol{H}(\omega)\boldsymbol{S}_{pp}\boldsymbol{H}(\omega)^{*\boldsymbol{T}} \tag{4.72}$$

Note that * indicates a complex conjugate and it appears in Equation 4.72 because $\boldsymbol{H}(\omega)$ is a complex matrix. For real matrices, Equation 4.35 holds good. Simplification of Equation 4.72 for SISO (single input single output) leads to the same expression as given by Equation 4.59. As all PSDFs and frequency response function matrices are invariably functions of frequency, ω within the brackets is omitted from them in subsequent derivations.

From Equation 4.70, $\boldsymbol{P}(\omega)$ is given by:

$$\boldsymbol{P}(\omega) = -\boldsymbol{M}\boldsymbol{I}\ddot{x}_g(\omega) \tag{4.73}$$

in which $\boldsymbol{M}$ is the mass matrix. Using Equation 4.35, $\boldsymbol{S}_{pp}$ is given by

$$\boldsymbol{S}_{pp} = \boldsymbol{M}\boldsymbol{I}\boldsymbol{I}^{\boldsymbol{T}}\boldsymbol{M}^{\boldsymbol{T}}S_{\ddot{x}_g} \tag{4.74}$$

in which $S_{\ddot{x}_g}$ is the PSDF of the single ground acceleration input $\ddot{x}_g$. Substituting for $\boldsymbol{S}_{pp}$ in Equation 4.72; $\boldsymbol{S}_{xx}$ is obtained as:

$$\boldsymbol{S}_{xx} = \boldsymbol{H}\boldsymbol{M}\boldsymbol{I}\boldsymbol{I}^{\boldsymbol{T}}\boldsymbol{M}^{\boldsymbol{T}}\boldsymbol{H}^{*\boldsymbol{T}}S_{\ddot{x}_g} \tag{4.75}$$

The cross PSDF between the response and the excitation is given by:

$$\boldsymbol{S}_{x_{g_x}} = -\boldsymbol{H}\boldsymbol{M}\boldsymbol{I}S_{\ddot{x}_g} \tag{4.76}$$

Example 4.2

For the frame of the problem in Example 3.8, shown in Figure 3.7, obtain the PSDFs of displacements u_1, and u_2 for perfectly correlated ground motion at the three supports represented by the PSDF of acceleration given in Appendix 4.A.

Solution: From Example 3.8, the mass, stiffness and damping matrices are reproduced below.

$$\boldsymbol{M} = \begin{bmatrix} 1 & 0 \\ 0 & 2 \end{bmatrix} m \quad \boldsymbol{C} = 0.816 \begin{bmatrix} 1 & 0 \\ 0 & 2 \end{bmatrix} m + 0.0027 \begin{bmatrix} 3 & -3 \\ -3 & 9 \end{bmatrix} k \quad K = \begin{bmatrix} 3 & -3 \\ -3 & 9 \end{bmatrix} k$$

$$\boldsymbol{H} = [\boldsymbol{K}\text{-}\boldsymbol{M}\omega^2 + i\boldsymbol{C}\omega]^{-1}; \quad \frac{k}{m} = 100; \quad \boldsymbol{I}^T = \{\, 1 \quad 1 \,\}$$

$$\omega_1 = 12.25 \text{ rad s}^{-1} \qquad \omega_2 = 24.49 \text{ rad s}^{-1}$$

The PSDF matrix of displacement is obtained by using Equation 4.75. The diagonal elements of the matrix provide the PSDFs of u_1 and u_2. The plots of the PSDFs of displacements u_1 and u_2, are shown Figure 4.11 (a and b). It is seen from the figure that the peaks of the PSDFs of displacements occur near the first frequency of the structure. This means that the contribution of the first mode to the response is significantly higher than the other mode. The rms values of the displacements u_1 and u_2 are 0.0154 and 0.0078 m, respectively.

4.9.2 Multi-Point Excitation

For multipoint excitations,

$$\boldsymbol{S}_{xx} = \boldsymbol{HMrS}_{\ddot{x}_g} \boldsymbol{r}^T \boldsymbol{M}^T \boldsymbol{H}^{*\,T} \tag{4.77}$$

$$\boldsymbol{S}_{\ddot{x}_g x} = -\boldsymbol{HMrS}_{\ddot{x}_g} \tag{4.78}$$

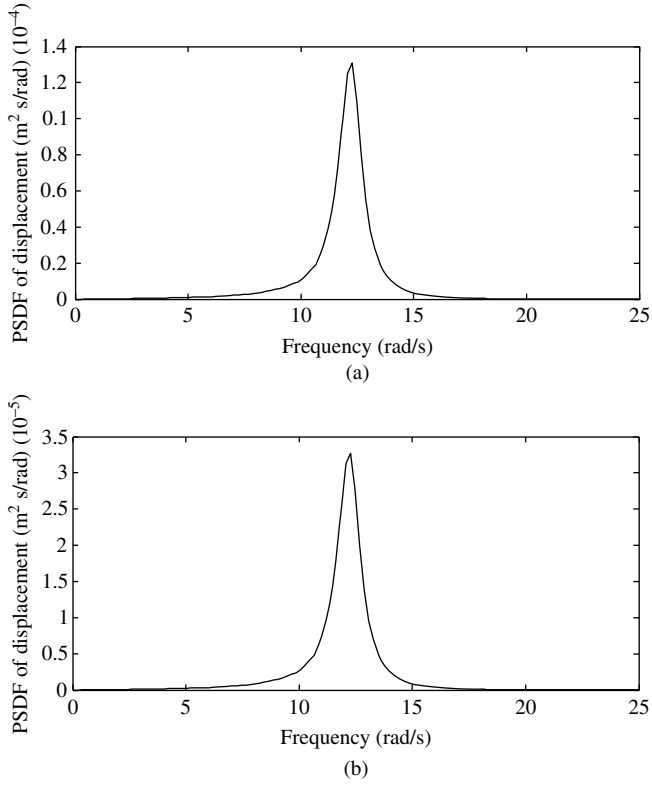

Figure 4.11 PSDFs of displacements: (a) for u_1; and (b) for u_2

where

$\boldsymbol{S}_{\ddot{x}_g}$ is a matrix of size $s \times s$ (number of supports)
r is a matrix of size $n \times s$
$\boldsymbol{H}$ is a matrix of $n \times n$.

In many applications, all displacement responses x may not be of interest. Thus, the frequency response function matrix $\bar{\boldsymbol{H}}$ of interest is derived from the system frequency response function matrix $\boldsymbol{H}$ by appropriately selecting the elements of the matrix $\boldsymbol{H}$. For such systems, Equation 4.77 is revised as:

$$\boldsymbol{S}_{\boldsymbol{xx}} = \bar{\boldsymbol{H}}_{m\times n}\boldsymbol{M}\boldsymbol{r}\boldsymbol{S}_{\ddot{\boldsymbol{x}}_g}\boldsymbol{r}^{\boldsymbol{T}}\boldsymbol{M}^{\boldsymbol{T}}\bar{\boldsymbol{H}}^{*\boldsymbol{T}}_{n\times m} \tag{4.79}$$

in which m is the number of displacements of interest.

The relationships given by Equations 4.75–4.78 can be formally proved, without the assumption of ergodicity, using the auto correlation and cross correlation functions of excitations, establishing their relationship with those of responses with the help of the impulse response function (that is, IFFT of h), and taking their Fourier transforms. Proofs are available in standard textbooks [1–3]. As the readers are not expected to be well acquainted with the theory of random vibrations, these proofs are not given here. Instead, a simpler approach (with the assumption of ergodicity) is adopted here to arrive at the relationships given by Equations 4.75–4.78.

Example 4.3

a. For the same problem as in Example 4.2, find the PSDFs of displacements u_1 and u_2 and their rms values when the excitations are assumed to be partially correlated with a time lag of 5 s between the supports. Use the correlation function given by Equation 2.91.
b. For the problem in Example 3.9, shown in Figure 3.8, obtain the PSDFs of displacements corresponding to the degrees of freedom 4 and 5. Consider two cases – (i) perfectly correlated excitation and (ii) partially correlated excitations at the two supports for an arbitrarily assumed time lag of 5 s. Use the correlation function given by Equation 2.91. For both problems, use the PSDF of excitation given in Appendix 4.A.

Solution:

a. From Example 3.8, $\boldsymbol{r}$ matrix is taken as:

$$\boldsymbol{r} = \frac{1}{3}\begin{bmatrix} 1 & 1 & 1 \\ 1 & 1 & 1 \end{bmatrix}$$

Using Equation 4.77, the PSDFs and rms values of displacements are obtained. Note that in Equation 4.77, $S_{\ddot{x}g}$ is a matrix of support excitations. For this problem, it is a 3×3 matrix, elements of the matrix are represented by $coh(i,j)S_{\ddot{x}g}$, in which i and j denote the two supports and $S_{\ddot{x}g}$ is the PSDF of the ground acceleration. $coh(i,j)$ is calculated by Equation 2.93, that is,

$$coh(i,j) = \exp\left(-\frac{|r_{ij}|\omega}{2\pi v_s}\right)$$

In obtaining $coh(i,j)$, r_{ij}/v_s is replaced by the time lag between the supports i and j. Thus, for this problem $\boldsymbol{S}_{\ddot{x}\boldsymbol{g}}$ is given by:

$$\boldsymbol{S}_{\ddot{x}\boldsymbol{g}} = \begin{bmatrix} 1 & \rho_1 & \rho_2 \\ \rho_1 & 1 & \rho_1 \\ \rho_2 & \rho_1 & 1 \end{bmatrix} S_{\ddot{x}g} \qquad \rho_1 = \exp\left(-\frac{5\omega}{2\pi}\right); \qquad \rho_2 = \exp\left(-\frac{10\omega}{2\pi}\right)$$

The PSDFs and cross PSDFs are shown in Figure 4.12(a–d). It is seen from Figure 4.12d that the imaginary component of the cross PSDFs between u_1 and u_2 is very small. The rms values of displacements u_1 and u_2 are 0.0089 and 0.0045 m, respectively. These values are much smaller than those for the case of fully correlated excitation (Example 4.2). This is expected, as the lack of correlation between excitations at the supports generally reduces the displacement response. The rms values are compared with those of the time history analysis carried out in Chapter 3 [time histories shown in Figure 3.13(a and b)]. The rms values obtained from time history analysis are 0.0092 m for u_1 and 0.0048 m for u_2, which match well with those obtained by the spectral analysis.

b. From the problem in Example 3.9, the mass, stiffness, and $\boldsymbol{r}$ matrices are reproduced below.

$$\boldsymbol{M} = \begin{bmatrix} 2.5 & 1.67 \\ 1.67 & 2.5 \end{bmatrix} m \qquad \omega_1 = 5.58\,\text{rad s}^{-1}; \qquad \omega_2 = 18.91\,\text{rad s}^{-1}$$

$$\boldsymbol{K} = \frac{EI}{L^3}\begin{bmatrix} 19.56 & 10.5 \\ 10.5 & 129 \end{bmatrix} \qquad \sqrt{\frac{EI}{mL^3}} = 2 \qquad \alpha = 0.431; \quad \beta = 0.004$$

$$\boldsymbol{r} = \begin{bmatrix} 0.479 & 0.331 \\ -0.131 & 0.146 \end{bmatrix} \qquad \boldsymbol{C} = \alpha\boldsymbol{M} + \beta\boldsymbol{K}$$

Matrix $\boldsymbol{H}$ is obtained as before (Example 4.2). Using Equation 4.77, the PSDF matrices of displacement are obtained. The elements of the PSDF matrices at $\omega = 5.58\,\text{rad s}^{-1}$ (first natural frequency of the structure) are given below.

Fully correlated excitation	Partially correlated excitation
$\begin{bmatrix} 0.6336 & 0.0146 \\ 0.0146 & 0.0003 \end{bmatrix} 10^{-3}$	$\begin{bmatrix} 0.3176 & 0.0073 \\ 0.0073 & 0.0002 \end{bmatrix} 10^{-3}$

The plots of the PSDFs of displacement are shown in Figures 4.13 and 4.14. The PSDFs of displacements are shown for both cases, that is, for perfectly correlated (case i) and partially correlated (case ii) excitations. It is seen from the figures that there is a difference in the nature of the PSDFs between the two cases for displacement corresponding to DOF 5. For the case i, the PSDF is characterized by a single peak (Figure 4.14a) while for the case ii, it is characterized by two peaks (Figure 4.14b). The first peak occurs at the first natural frequency, while the second peak occurs at the second natural frequency of the structure. For DOF 4, the PSDFs are characterized by a single peak occurring at the first frequency of the structure for both cases [Figure 4.13(a and b)]. The rms values of the displacements are:

Corresponding to DOF 4 = 0.0237 m (perfectly correlated) and 0.0168 m (partially correlated)

Corresponding *to* DOF 5 = 0.0005 m (perfectly correlated) and 0.0009 m (partially correlated)

4.9.3 Determination of the PSDF of Absolute Displacement

Once the PSDFs of displacements (relative) are obtained, the PSDF matrices of absolute (total) displacements are determined by adding the ground displacements to the relative displacements, that is,

$$\boldsymbol{x_a} = \boldsymbol{I}\boldsymbol{x} + \boldsymbol{r}\boldsymbol{x_g} \tag{4.80}$$

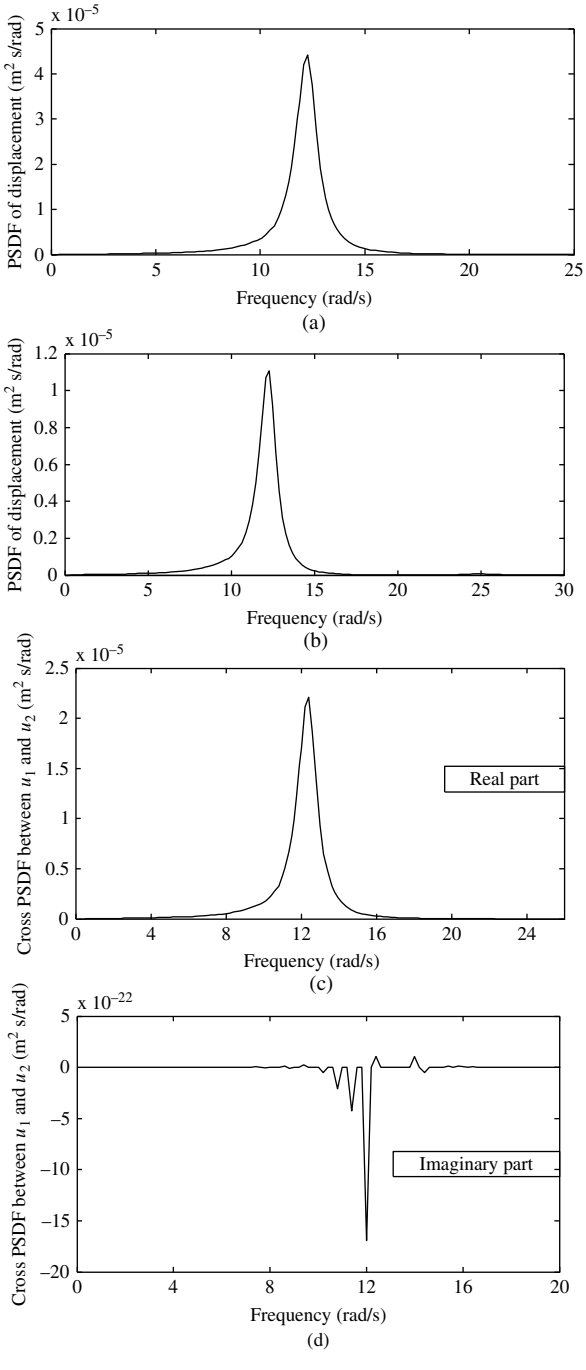

Figure 4.12 PSDFs and cross PSDF of responses: (a) displacement u_1; (b) displacement u_2; (c) real part; and (d) imaginary part of cross PSDF between u_1 and u_2

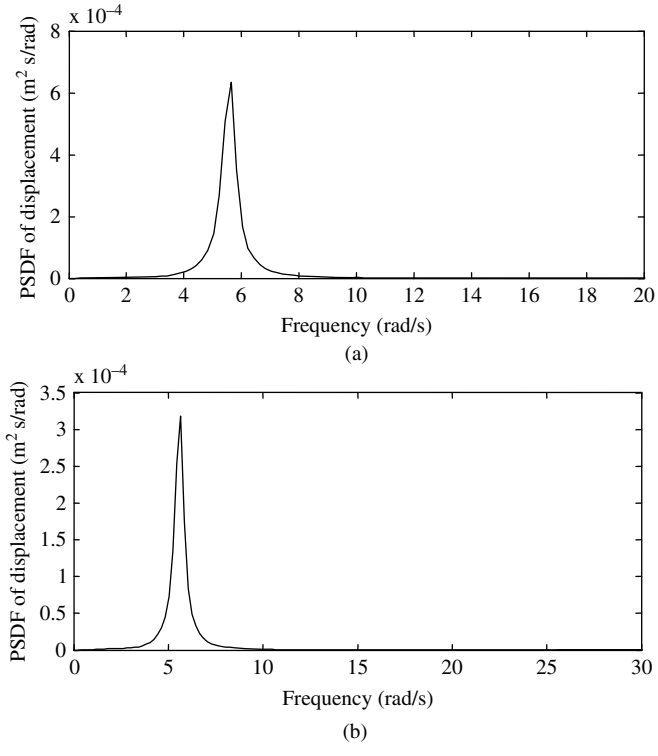

Figure 4.13 PSDFs of displacement for DOF 4: (a) without time lag; and (b) with time lag

Using Equation 4.36, the PSDF matrix $\boldsymbol{S}_{x_a}$ of absolute displacements may be written as:

$$\boldsymbol{S}_{x_a} = \boldsymbol{S}_{xx} + \boldsymbol{r}\boldsymbol{S}_{x_g}\boldsymbol{r}^{\boldsymbol{T}} + \boldsymbol{I}\boldsymbol{S}_{xx_g}\boldsymbol{r}^{\boldsymbol{T}} + \boldsymbol{r}\boldsymbol{S}_{x_g x}\boldsymbol{I}^{\boldsymbol{T}} \tag{4.81}$$

in which $\boldsymbol{I}$ is a diagonal matrix of unity; $\boldsymbol{S}_{xx_g}$ is the cross PSDF between the relative displacement and ground displacement. In Equation 4.81, $\boldsymbol{S}_{x_g}$ can be obtained from $\boldsymbol{S}_{\ddot{x}_g}$ using Equation 4.49. $\boldsymbol{S}_{x_g x}$ is determined using the relationship between $\boldsymbol{x}(\omega)$ and $\boldsymbol{x_g}(\omega)$, that is,

$$\boldsymbol{x}(\omega) = -\boldsymbol{H}\boldsymbol{M}\boldsymbol{r}\ddot{\boldsymbol{x}}_{\boldsymbol{g}}(\omega) = \boldsymbol{H}\boldsymbol{M}\boldsymbol{r}\omega^2\boldsymbol{x_g}(\omega) \tag{4.82}$$

Using Equation 4.38, $\boldsymbol{S}_{xx_g}(\omega)$ may be written as:

$$\boldsymbol{S}_{x_g x} = \boldsymbol{H}\boldsymbol{M}\boldsymbol{r}\omega^2\boldsymbol{S}_{x_g} \quad \text{and} \quad \boldsymbol{S}_{xx_g} = \boldsymbol{S}_{x_g x}^{T} \tag{4.83}$$

Example 4.4

For the same problem as in Example 4.3, find the PSDFs of absolute displacements corresponding to the DOF 4 and 5 for the case of partially correlated excitation.

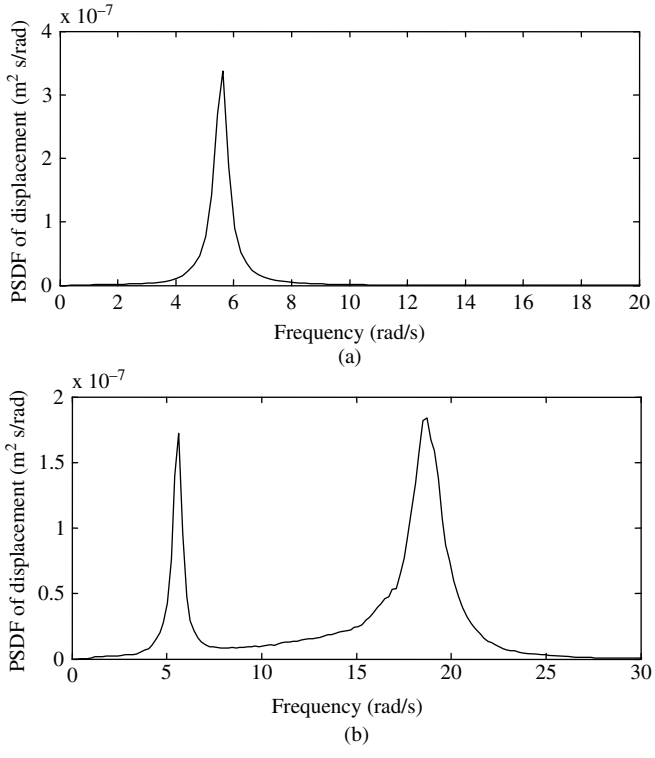

Figure 4.14 PSDFs of displacement for DOF 5: (a) without time lag; and (b) with time lag

Solution: Let $\boldsymbol{x}$ and $\ddot{\boldsymbol{x}}_g$ represent

$$\boldsymbol{x}^T = [x_4 \quad x_5] \quad \text{and} \quad \ddot{\boldsymbol{x}}_{\boldsymbol{g}}^{\boldsymbol{T}} = [\ddot{x}_{g1} \quad \ddot{x}_{g2}]$$

in which $\ddot{x}_{g1}$ and $\ddot{x}_{g2}$ are the support excitations produced due to partially correlated ground motions. Using Equation 4.83, $\boldsymbol{S}_{\boldsymbol{x}_g\boldsymbol{x}}$ is given by:

$$\boldsymbol{S}_{\boldsymbol{x}_g\boldsymbol{x}} = \boldsymbol{HMr}\omega^2\boldsymbol{S}_{\boldsymbol{x}_g} = \boldsymbol{HMr}\omega^{-2}\boldsymbol{S}_{\ddot{\boldsymbol{x}}_g} \tag{4.84}$$

in which $\boldsymbol{H}$, $\boldsymbol{M}$, and $\boldsymbol{r}$ matrices are given in Exercise 4.3; $\boldsymbol{S}_{\ddot{\boldsymbol{x}}_g}$ and $\boldsymbol{S}_{\boldsymbol{x}_g\boldsymbol{x}}$ are given as:

$$\boldsymbol{S}_{\ddot{\boldsymbol{x}}_g} = \begin{bmatrix} c_{11} & c_{21} \\ c_{12} & c_{22} \end{bmatrix} S_{\ddot{x}_g}; \qquad c_{ij} = coh(i,j) \tag{4.85}$$

which is obtained by Equation 2.91.

$$\boldsymbol{S}_{\boldsymbol{x}_g\boldsymbol{x}} = \begin{bmatrix} S_{x_{g1}x_4} & S_{x_{g2}x_4} \\ S_{x_{g1}x_5} & S_{x_{g2}x_5} \end{bmatrix} \tag{4.86}$$

Using Equation 4.81, an $\boldsymbol{S}_{\boldsymbol{xa}}$ matrix of size 2×2 is calculated, in which $\boldsymbol{S}_{\boldsymbol{xx}}$ is obtained from Exercise 4.3. The diagonal terms of the matrix provide the PSDFs of the absolute values of $\boldsymbol{x_4}$ and $\boldsymbol{x_5}$, which are plotted in Figure 4.15(a and b). The rms values of absolute displacements of $\boldsymbol{x_4}$ and $\boldsymbol{x_5}$ are 0.052 and 0.015 m,

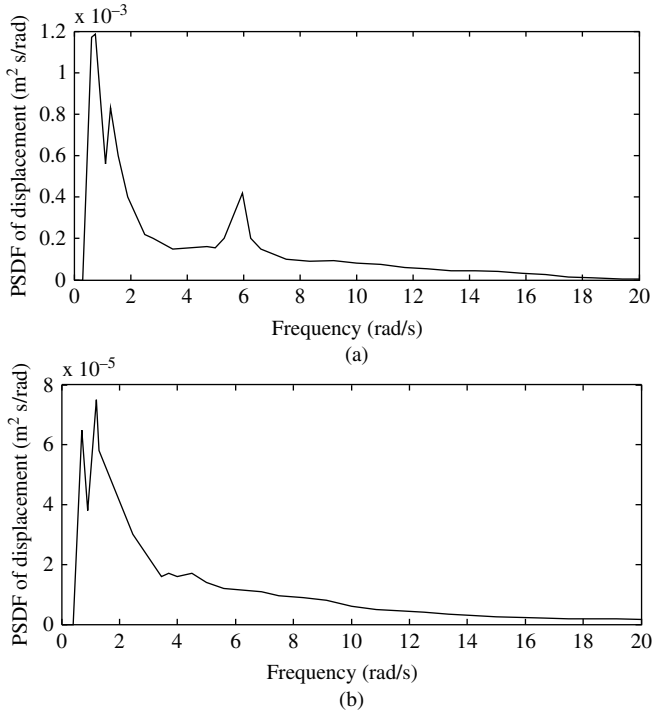

Figure 4.15 PSDFs of absolute displacements with time lag: (a) for DOF 4; and (b) for DOF 5

respectively. It is seen that these values are much higher than those of the relative displacements obtained in the problem in Example 4.3.

4.10 PSDF Matrix of Member End Forces

In dynamic analysis, the dynamic degrees of freedom are not the same as the kinematic degrees of freedom. Many degrees of freedom are condensed out to obtain the desired dynamic degrees of freedom. Consider a simple frame as shown in Figure 4.7. $\boldsymbol{x}$ is the vector of dynamic degrees of freedom, that is, sway degrees of freedom and θ as that of the condensed out degrees of freedom (rotations θ at the joints). θ is related to $\boldsymbol{x}$ by:

$$\theta = \boldsymbol{A}\boldsymbol{x} \tag{4.87}$$

in which matrix $\boldsymbol{A}$ is obtained by a matrix condensation procedure.

Using Equations 4.35 and 4.38, $\boldsymbol{S_{\theta\theta}}$ and $\boldsymbol{S_{\theta x}}$ can be written as:

$$\boldsymbol{S}_{\theta\theta} = \boldsymbol{A}\boldsymbol{S}_{\boldsymbol{xx}}\boldsymbol{A}^{\boldsymbol{T}} \tag{4.88}$$

$$\boldsymbol{S}_{\boldsymbol{x}\theta} = \boldsymbol{A}\boldsymbol{S}_{\boldsymbol{xx}} \quad \text{and} \quad \boldsymbol{S}_{\theta\boldsymbol{x}} = \boldsymbol{S}_{\boldsymbol{x}\theta}^{\boldsymbol{T}} \tag{4.89}$$

Now, consider the column *i–j* in Figure 3.7. The displacements at the ends of the column are represented by the vector

$$\delta = [x_i \theta_i x_j \theta_j]^T \tag{4.90}$$

Let the elemental stiffness matrix corresponding to the above degrees of freedom be $\boldsymbol{K}$, so that member end forces $\boldsymbol{f}$ are denoted by:

$$\boldsymbol{f} = \boldsymbol{K\delta} \tag{4.91}$$

The PSDF matrix of the member end forces is then given by:

$$\boldsymbol{S_{ff}} = \boldsymbol{K S_{\delta\delta} K^T} \tag{4.92}$$

in which the elements of the matrix $\boldsymbol{S}_{\delta\delta}$ are appropriately selected from those of matrices $\boldsymbol{S_{xx}}$, $\boldsymbol{S_{\theta\theta}}$, $\boldsymbol{S_{\theta x}}$, and $\boldsymbol{S_{x\theta}}$.

Note that if $\boldsymbol{\delta}$ does not correspond to local co-ordinates of the member, then δ is further transformed into $\bar{\boldsymbol{\delta}}$, the displacement vector in local coordinates by:

$$\bar{\boldsymbol{\delta}} = \boldsymbol{T}\delta \tag{4.93}$$

in which T is the transformation matrix and $\boldsymbol{S_{ff}}$ is then obtained as:

$$\boldsymbol{S_{ff}} = \boldsymbol{K S_{\bar{\delta}\bar{\delta}} K^T} = \boldsymbol{K T S_{\delta\delta} T^T K^T} \tag{4.94}$$

Example 4.5

For the problem in Example 3.10, shown in Figure 3.15, find the PSDFs of the relative displacements for 1 and 2. Also, find the PSDF of the bending moment at the center of the pipe.

Solution: The stiffness and the damping matrices of the soil structure system are taken from exercise in Example 3.10 as below.

$$\boldsymbol{K} = \begin{bmatrix} 56 & -16 & 8 \\ -16 & 80 & -16 \\ 8 & -16 & 56 \end{bmatrix} m \qquad \bar{\boldsymbol{C}} = \begin{bmatrix} 0.813 & -0.035 & 0.017 \\ -0.035 & 0.952 & -0.035 \\ 0.017 & -0.035 & 0.811 \end{bmatrix} m$$

$$\omega_1 = 8.0 \text{ rad s}^{-1};\ \omega_2 = 9.8 \text{ rad s}^{-1} \text{ and } \omega_3 = 12.0 \text{ rad s}^{-1}$$

Following the same procedure as described before, the PSDFs of displacements 1 and 2 are obtained and are shown in Figure 4.16(a and b). It is seen from Figure 4.16a that the PSDF of the displacement of the end of the pipe is characterized by two peaks. The first peak occurs at the first natural frequency and the second peak occurs at the third natural frequency of the structure. The PSDF of the displacement at the center of the pipe is characterized by a single peak occurring at the first natural frequency of the structure (Figure 4.16b).

To find the PSDF of the bending moment, the rotation θ at the center of the pipe is obtained as below (using the condensation relationship).

Let x_1, x_2, and x_3 be the displacements of the DOF 1, 2, and 3 denoted by

$$\boldsymbol{x}^T = [\, x_1 \quad x_2 \quad x_3 \,]$$

Then,

$$\theta = \frac{3}{4L}[\, -1 \quad 0 \quad 1 \,]\boldsymbol{x} = \boldsymbol{Ax}$$

Using Equations 4.88 and 4.89, $\boldsymbol{S_{\theta\theta}}$ and $\boldsymbol{S_{x\theta}}$ are obtained below for a frequency of $\omega = 8 \text{ rad s}^{-1}$.

$$\boldsymbol{S}_{\theta\theta} = 0; \qquad \boldsymbol{S_{x\theta}} = 0$$

Note that the $\boldsymbol{S_{xx}}$ required to calculate the above quantities are obtained corresponding to the absolute displacements of the DOF 1, 2, and 3. They are obtained following the procedure described in the

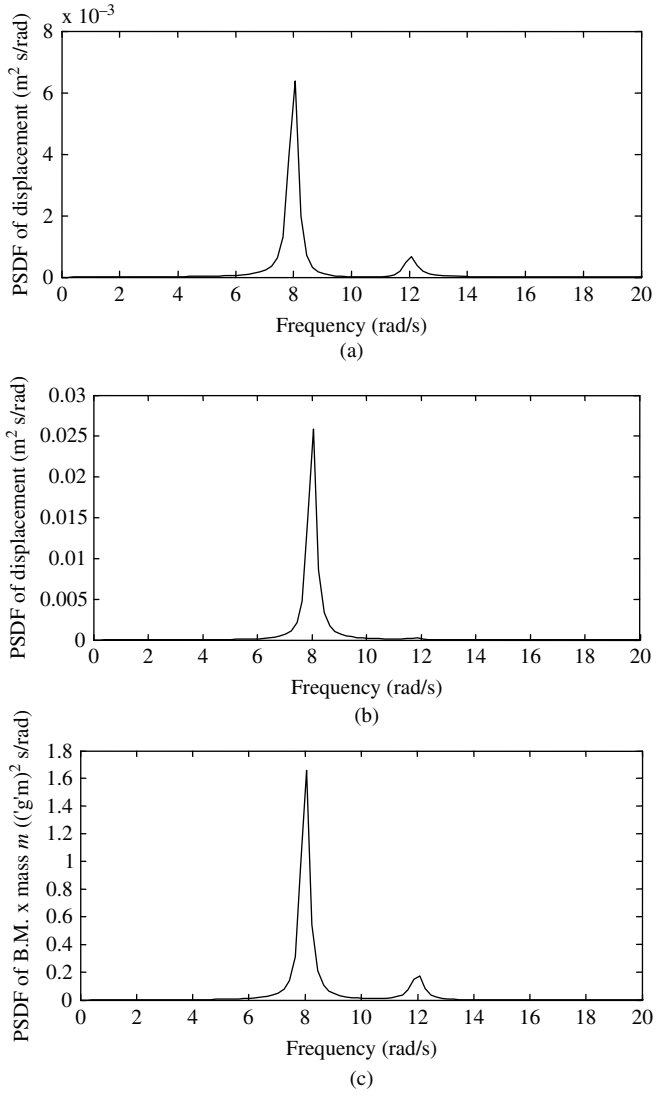

Figure 4.16 PSDFs of responses: (a) displacement for DOF 1; (b) displacement for DOF 2; and (c) bending moment at the center of the pipe

Example 4.4. Both $\boldsymbol{S}_{\theta\theta}$ and $\boldsymbol{S}_{\boldsymbol{x\theta}}$ are found to be zero as the excitation is perfectly correlated, and therefore, the rotation at the center of the pipe is zero. Thus, the displacement vector given by Equation 4.90 is

$$\delta = [x_1, \theta_1, x_2, 0]^T$$

Taking advantage of the zero bending moment at the end support, the matrix $\boldsymbol{K}_{\boldsymbol{e}}$ for the element between DOF 1 and 2 is modified (so that θ_1 is not required for calculating of the bending moment at the center). Using Equation 4.92, the PSDF of the bending moment at the center is obtained and is shown in

Figure 4.16c. It is seen that the PSDF of the bending moment is characterized by two peaks like that observed for the PSDF of x_1. The rms values of relative displacements x_1, x_2 and the bending moment at the center of the pipe are obtained as 0.0637 m, 0.1192 m and 1.1037 times the mass m.

4.11 Modal Spectral Analysis

Modal spectral analysis has the advantage that it does not require the generation of a C matrix. Additionally, computational effort may be reduced by truncating the number of modes to a limited few depending upon the type of problem.

Consider the case of multi-point excitation. The modal equation for the system can be written as:

$$\bar{m}_i\ddot{\bar{q}} + 2\xi_i\omega_i\bar{m}_i\dot{z}_i + \bar{m}_i\omega_i^2 z_i = -\boldsymbol{\varphi}_i^T\boldsymbol{M}\boldsymbol{r}\ddot{x}_g \tag{4.95}$$

or

$$\ddot{\bar{q}} + 2\xi_i\omega_i\dot{z}_i + \omega_i^2 z_i = \frac{-\boldsymbol{\varphi}_i^T\boldsymbol{M}\boldsymbol{r}}{\bar{m}_i}\ddot{x}_g = p_i \quad i = 1\ldots r \tag{4.96}$$

where

$\bar{m}_i = \boldsymbol{\varphi}_i^T\boldsymbol{M}\varphi_i$
$\boldsymbol{r}$ = the influence coefficient matrix of size $m \times n$
ω_i and ξ_i = the frequency and modal damping ratio of the ith mode

The generalized coordinate $z_i(\omega)$ can be related to $p_i(\omega)$ by:

$$z_i(\omega) = h_i(\omega)p_i(\omega) \quad i = 1\ldots r \tag{4.97a}$$

in which

$$p_i(\omega) = \frac{-\boldsymbol{\varphi}_i^T\boldsymbol{M}\boldsymbol{r}\ddot{\boldsymbol{x}}_{\boldsymbol{g}}(\omega)}{\bar{m}_i} \tag{4.97b}$$

Thus, elements of the PSDF matrix of z may be obtained as:

$$S_{z_iz_j} = \frac{h_i h_j^{*i}}{\bar{m}_i\bar{m}_j}\boldsymbol{\varphi}_{\boldsymbol{i}}^{\boldsymbol{T}}\boldsymbol{M}\boldsymbol{r}\boldsymbol{S}_{\ddot{\boldsymbol{x}}_{\boldsymbol{g}}}\boldsymbol{r}^{\boldsymbol{T}}\boldsymbol{M}^{\boldsymbol{T}}\varphi_{\boldsymbol{j}} \quad i = 1\ldots r, \quad j = 1\ldots r \tag{4.98}$$

With the $\boldsymbol{S}_{zz}$ matrix obtained as above, PSDF of the displacement matrix is derived using the modal transformation matrix, that is, $\boldsymbol{x} = \boldsymbol{\phi}\boldsymbol{z}$ and is given by:

$$\boldsymbol{S}_{\boldsymbol{xx}} = \boldsymbol{\phi}\boldsymbol{S}_{\boldsymbol{zz}}\boldsymbol{\phi}^{\boldsymbol{T}} \tag{4.99}$$

in which $\boldsymbol{\phi}$ is a matrix of size $m \times r$. The PSDF of absolute displacements and member end forces may be obtained by the same procedure as described before.

Example 4.6

For the problem in Example 3.11, shown in Figure 3.9, obtain the PSDF of displacements corresponding to DOF 1 (top of the left tower) and DOF 2 (center of the deck) by modal spectral

analysis for the partially correlated ground acceleration with a time lag of 5 s between the supports. The PSDF of ground acceleration is taken as that given in the Appendix 4.A and use Equation 2.93 as the correlation function.

Solution: The mass, stiffness, and $\boldsymbol{r}$ matrices, and the mode shapes and frequencies of the structure are taken from the exercise in Example 3.11 and are given below for convenience.

$$\boldsymbol{K} = \begin{bmatrix} 684 & 0 & -149 \\ 0 & 684 & 149 \\ -149 & 149 & 575 \end{bmatrix} m \quad \boldsymbol{M} = \begin{bmatrix} 20 & 0 & 0 \\ 0 & 20 & 0 \\ 0 & 0 & 60 \end{bmatrix} m$$

$$\boldsymbol{r} = \frac{1}{10} \begin{bmatrix} 5.318 & 0.031 & -0.002 & -0.318 \\ -0.318 & -0.002 & 0.031 & 5.318 \\ 1.416 & 0.008 & -0.008 & -1.416 \end{bmatrix}$$

$$\omega_1 = 2.86 \text{ rad s}^{-1} \quad \omega_2 = 5.85 \text{ rad s}^{-1} \quad \omega_3 = 5.97 \text{ rad s}^{-1}$$

$$\boldsymbol{\phi}_1^T = [-0.036 \quad 0.036 \quad -0.125]$$

$$\boldsymbol{\phi}_2^T = [0.158 \quad 0.158 \quad 0]$$

$$\boldsymbol{\phi}_3^T = [-0.154 \quad 0.154 \quad 0.030]$$

The PSDFs are calculated using Equations 4.98 and 4.99. The plots of S_{z1z1} and S_{z1z2} (both real and imaginary components) are shown in Figure 4.17(a–c). It is seen from Figure 4.17c that the imaginary part of S_{z1z2} is very small compared with the real part. The PSDFs of displacements corresponding to DOF 1 and 2 are shown in Figure 4.18(a and b). The rms values of displacements obtained from the modal spectral analysis and the direct spectral analysis are compared below.

	Modal	Direct
rms value of displacement for DOF 1	0.0139 m	0.0138 m
rms value of displacement for DOF 2	0.0150 m	0.0151 m

4.12 Spectral Analysis Using the State-Space Formulation

When the state-space equation (Equation 3.101, Chapter 3) is used, the PSDF matrix of responses, $\boldsymbol{S}_{zz}$ is obtained as:

$$\boldsymbol{S}_{zz} = \boldsymbol{H}\boldsymbol{S}_{f_g f_g}\boldsymbol{H}^{*T} \tag{4.100a}$$

$$\boldsymbol{H} = [\hat{\boldsymbol{I}}\omega - \boldsymbol{A}]^{-1} \tag{4.100b}$$

in which $\hat{\boldsymbol{I}}$ is a diagonal matrix with $i\left(\sqrt{-1}\right)$ as diagonals; $\boldsymbol{S}_{f_g f_g}$ is the PSDF matrix of the $\boldsymbol{f}_g$. Note that the PSDF matrix S_{zz} contains $S_{x\dot{x}}$ and $S_{\dot{x}x}$ terms. Addition of these terms turns out to be zero because of Equation 4.69b. For the state-space modal analysis, eigen values and eigen vectors of matrix $\boldsymbol{A}$ are used to decouple the equation of motion and the same modal spectral analysis technique described in Section 4.11 is used.

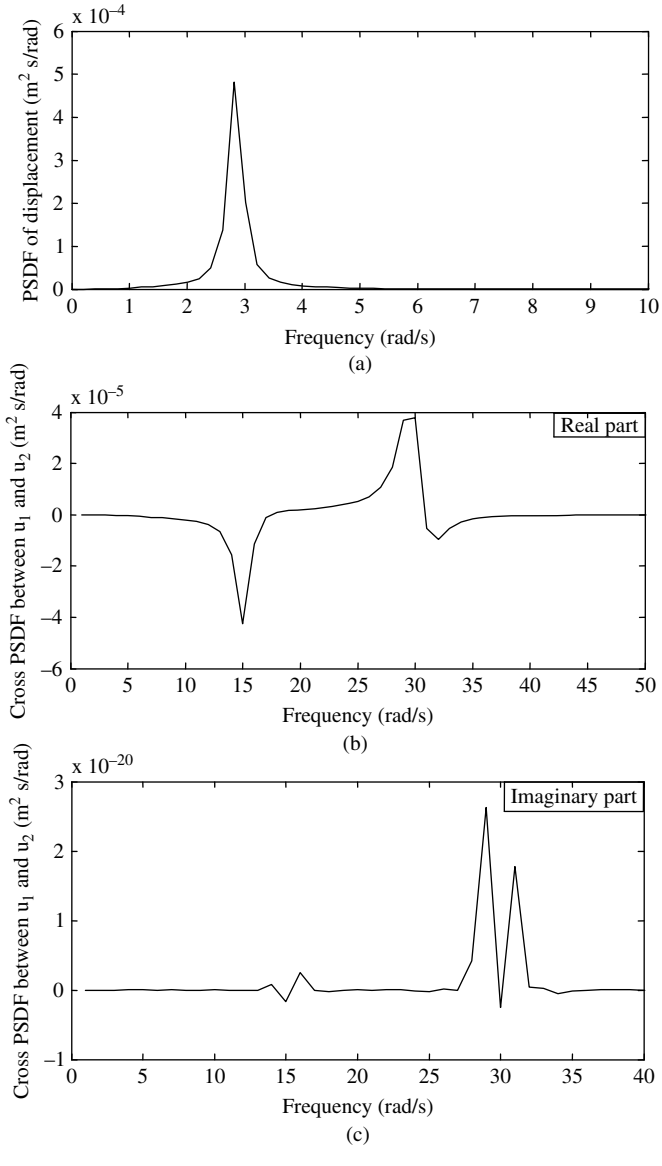

Figure 4.17 PSDF and cross PSDF of generalized displacements: (a) first generalized displacement; (b) real part; and (c) imaginary part of cross PSDF between first- and second-generalized displacement

Example 4.7

For the exercise in Example 3.12, shown in Figure 3.20, determine the PSDFs of the top- and the first-floor displacements using the state-space spectral analysis for perfectly correlated ground acceleration represented by the PSDF given in Appendix 4.A.

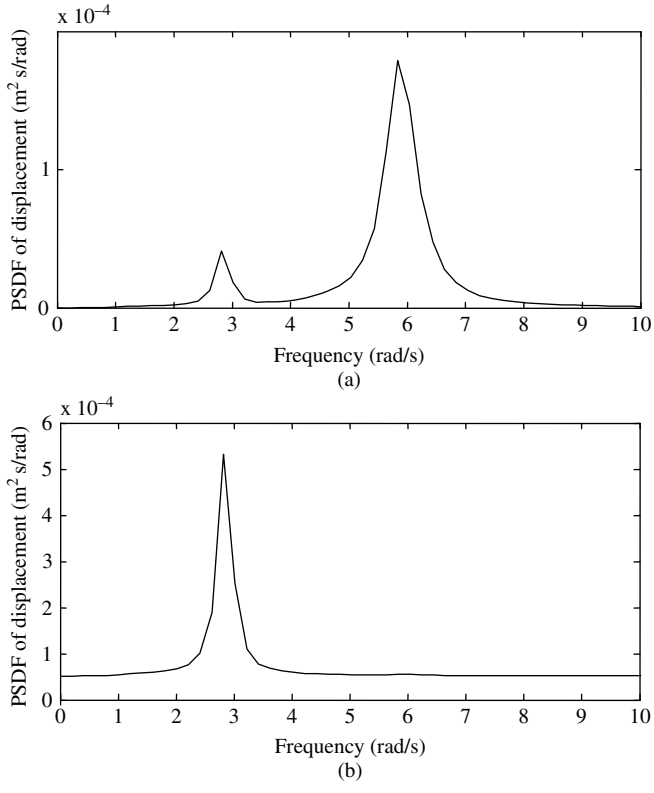

Figure 4.18 PSDFs of displacements: (a) top of the left tower; and (b) center of the deck

Solution: The mass and stiffness matrices and the modal properties are given in the example problem 3.12. For convenience, A is reproduced below.

$$A = \begin{bmatrix} 0.0 & 0.0 & 0.0 & 0.0 & 1 & 0.0 & 0.0 & 0.0 \\ 0.0 & 0.0 & 0.0 & 0.0 & 0.0 & 1 & 0.0 & 0.0 \\ 0.0 & 0.0 & 0.0 & 0.0 & 0.0 & 0.0 & 1 & 0.0 \\ 0.0 & 0.0 & 0.0 & 0.0 & 0.0 & 0.0 & 0.0 & 1 \\ -2.0 & 1.0 & 0.0 & 0.0 & -1.454 & 0.567 & 0.0 & 0.0 \\ 2.0 & -2.0 & 1.0 & 0.0 & 1.134 & -1.495 & 0.567 & 0.0 \\ 0.0 & 1.0 & -3.0 & 2.0 & 0.0 & 0.567 & -2.062 & 1.134 \\ 0.0 & 0.0 & 2.0 & -4.0 & 0.0 & 0.0 & 1.134 & -2.630 \end{bmatrix}$$

Equations 4.100a and 4.100b are used to calculate the PSDFs of the displacements. The PSDFs are shown in Figure 4.19(a and b). The rms values of displacements obtained by the direct, modal and state-space spectral analyses are compared below.

	Modal	Direct	State-space
rms value of displacement for DOF 1	0.0903 m	0.0907 m	0.0905 m
rms value of displacement for DOF 4	0.0263 m	0.0259 m	0.0264 m

(4.101)

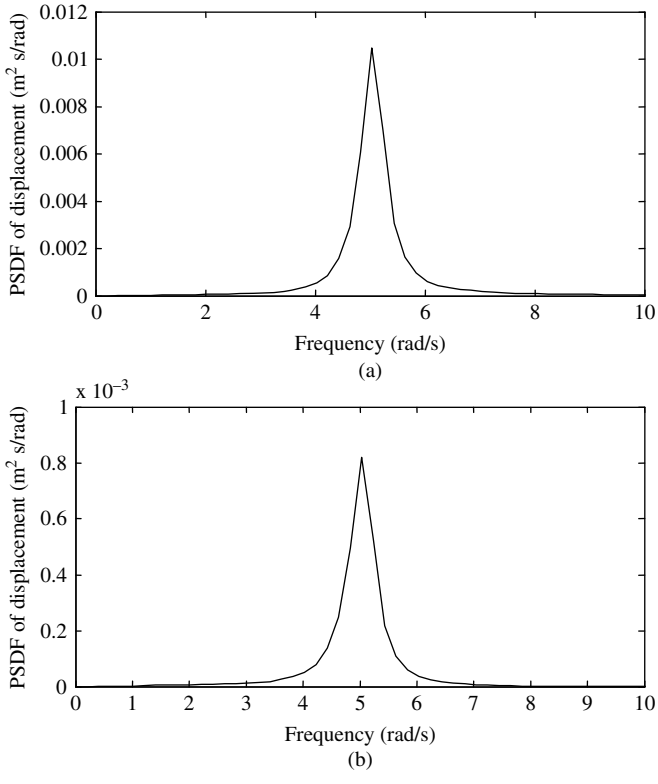

Figure 4.19 PSDFs of displacements: (a) top storey; and (b) first storey

4.13 Steps for Developing a Program for Spectral Analysis in MATLAB® for Multi-Support Excitation

I. Computation of the "Basic Elements" as given in step I of Section 3.5.7 is common for both frequency domain spectral analysis and the deterministic time history analysis.
II. Mode shape coefficient for any response quantity of interest is found out as outlined in Section 3.5.4.
III. Find the $\boldsymbol{H}$ matrix for the structure and then, use Equations 4.75, 4.77, 4.79 or 4.100a to obtain the PSDF matrices of displacement responses.
IV. Cross PSDFs between the displacement and ground acceleration are obtained using Equations 4.76 and 4.78.
V. PSDF matrix of absolute displacements can be obtained using Equations 4.81 and 4.83.
VI. PSDF matrix of member end forces is obtained using Equations 4.92 or 4.94.
VII. For modal spectral analysis, h_i for the ith mode is obtained by the standard method. Elements of the PSDF matrix of generalized co-ordinates are obtained using Equation 4.98 and the PSDF matrix of displacements is obtained by Equation 4.99.

VIII. If the state-space formulation is used, the Equations 4.100a and 4.100b are used to obtain the PSDF matrix of the state vector.

Exercise Problems

(Use standard programs like MATLAB, SAP2000 and ABAQUAS to solve the problems; you may also use your own program developed using the methods presented in the chapter.)

4.8 For Exercise 3.1 (Chapter 3), obtain the plot of the PSDF of the relative displacement x for the PSDF of ground acceleration, as given in Appendix 4.A, the same for the two supports. Compare between the rms values of the response with that of the time history analysis.

4.9 A suspended span of a submarine pipeline is modeled as shown in Figure 4.20. Assuming 5% modal damping, obtain a closed form expression for the PSDF of the relative displacement x. Assume the PSDF of ground acceleration to be the same at the two supports and represented by a white noise with constant PSDF S_0. The cross spectral density function between supports 1 and 2 is given by $S_{g_1 g_2} = S_0 e^{-i\omega T}$ and the equivalent stiffness corresponding to the DOF x is k with $k/m = 100\ (\text{rad s}^{-1})^2$.

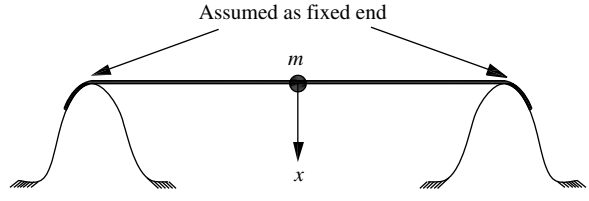

Figure 4.20 Suspended span of submarine pipeline

4.10 For the exercise problem 3.14, obtain plots of $S_{yy}(\omega)$ and $S_{y\theta}(\omega)$ (both real and imaginary components) assuming: (i) the same PSDF of excitations at all supports (given in Appendix 4.A); (ii) the same PSDF but partially correlated at the supports. For the latter, assume the same correlation function given by Equation 2.93 having a time lag of 2.5 s between supports.

4.11 For the problem in Exercise 3.16, find the rms values of the top relative displacement and the drift between the first and the second story. Assume the time lag between the supports as 2.5 s. Take the correlation function and the PSDF as being thesame as those given in Exercise 4.10.

4.12 For the problem in Exercise 3.17, find the rms values of the absolute displacement of the secondary system and the base shear for perfectly correlated support excitations represented by the PSDF given in Appendix 4.A.

4.13 Using the modal spectral analysis, find the peak values of the displacement (relative) of the top floor and the first-storey drift of the frame of Exercise 3.18 for perfectly correlated ground excitations represented by the PSDF given in Appendix 4.A.

4.14 Using the modal and state-space spectral analyses, find the rms value of the deflection of the center of the deck for Exercise 3.19. Compare the results for the two cases: (i) perfectly correlated excitations at the supports and (ii) partially correlated excitations with a time lag between supports as 2.5 s. Take the PSDF of ground excitation (horizontal) as that given in Appendix 4.A and use the correlation function used in the Example 4.10.

4.15 For Exercise 3.21, find the rms values of displacements and rotations of the top floor of the 3D tall building using modal spectral analysis. Also, obtain a plot of $S_{x\theta}$ (both real and imaginary components). Take the excitation as the ground motion, represented by the PSDF given in Appendix 4.A, applied in the x direction.

4.16 For the shear frame shown in Exercise 3.20, compare between the rms values of absolute accelerations of the top floor and the bending moment at the base obtained by the direct, modal, and state-space spectral analyses. Take the same PSDF of excitation that is used for other problems.

Appendix 4.A Digitized Values of the PSDF of the Ground Acceleration of El Centro Earthquake

Table 4.1 provides the digitized values of the PSDF of the El Centro earthquake assuming it to be a sample of an ergodic process.

Table 4.1 Digitized values of the PSDF ($m^2\,s^{-3}\,rad^{-1}$) of the El Centro earthquake acceleration record given in Appendix 3.C at a frequency interval of $0.201\,rad\,s^{-1}$ (read row wise)

1.13E-09	1.18E-05	0.000 442	0.000 988	0.000 889	0.001 664	0.003 397	0.003 424
0.003 678	0.003 996	0.003 952	0.004 042	0.004 172	0.004 598	0.004 859	0.00 476
0.004 837	0.005 039	0.006 083	0.006 752	0.007 215	0.007 957	0.009 187	0.009 486
0.009 495	0.009 453	0.00 958	0.009 357	0.009 875	0.00 995	0.009 948	0.010 551
0.011 874	0.012 146	0.012 598	0.012 623	0.012 785	0.013 486	0.013 679	0.014 088
0.014 443	0.015 289	0.015 662	0.015 695	0.016 283	0.016 527	0.01 647	0.016 974
0.016 915	0.016 163	0.016 505	0.016 887	0.017 107	0.016 297	0.017 287	0.017 635
0.017 721	0.017 499	0.017 407	0.016 865	0.016 892	0.01 687	0.016 661	0.016 164
0.015 786	0.01 516	0.015 281	0.015 223	0.014 571	0.014 381	0.014 092	0.013 486
0.012 894	0.012 197	0.012 068	0.011 422	0.011 184	0.011 426	0.011 143	0.01 104
0.010 975	0.010 439	0.010 034	0.00 904	0.008 627	0.007 367	0.007 553	0.007 548
0.007 526	0.007 497	0.007 216	0.006 954	0.006 939	0.006 338	0.005 555	0.005 697
0.005 693	0.005 349	0.005 371	0.005 753	0.005 758	0.006 063	0.006 076	0.006 178
0.006 208	0.006 529	0.006 415	0.006 492	0.00 633	0.006 146	0.006 274	0.006 089
0.005 879	0.005 512	0.005 444	0.005 621	0.006 008	0.005 549	0.005 581	0.005 741
0.005 616	0.005 639	0.005 809	0.006 023	0.005 955	0.006 023	0.00 582	0.005 826
0.005 825	0.005 725	0.005 212	0.005 057	0.004 741	0.004 972	0.004 751	0.004 684
0.004 239	0.004 228	0.004 429	0.004 322	0.004 339	0.00 418	0.00 425	0.004 388
0.004 321	0.004 439	0.004 938	0.004 633	0.004 544	0.004 661	0.004 437	0.00 458
0.00 457	0.004 398	0.004 191	0.004 313	0.004 156	0.004 184	0.004 279	0.00 426
0.004 232	0.004 281	0.004 535	0.004 609	0.004 446	0.004 574	0.004 569	0.00 456
0.004 897	0.004 699	0.004 756	0.004 916	0.005 171	0.005 106	0.004 746	0.004 671
0.004 559	0.003 994	0.004 021	0.004 019	0.003 808	0.003 891	0.00 373	0.003 925
0.004 045	0.004 299	0.0045	0.004 725	0.004 882	0.004 768	0.00 499	0.005 341
0.0053	0.005 008	0.004 745	0.004 847	0.004 557	0.004 345	0.004 361	0.004 107
0.003 937	0.003 906	0.00 365	0.003 391	0.003 462	0.00 343	0.003 439	0.003 451
0.003 334	0.003 193	0.003 192	0.003 166	0.003 039	0.003 043	0.002 859	0.002 728
0.002 496	0.002 265	0.002 102	0.001 922	0.001 849	0.001 654	0.001 376	0.001 367
0.00 136	0.001 389	0.001 215	0.001 197	0.00 121	0.001 147	0.001 028	0.001 001
0.001 006	0.001 009	0.001 018	0.000 901	0.0009	0.000 929	0.000 907	0.000 875
0.000 911	0.000 934	0.000 926	0.000 913	0.000 871	0.00 092	0.000 965	0.000 928
0.000 849	0.000 819	0.00 084	0.000 914	0.000 939	0.000 866	0.000 835	0.000 858
0.000 826	0.000 808	0.000 836	0.000 818	0.000 822	0.000 798	0.000 781	0.000 753
0.000 729	0.00 073	0.000 734	0.000 729	0.000 717	0.000 726	0.00 071	0.00 072
0.000 702	0.000 681	0.000 716	0.000 715	0.000 648	0.000 595	0.0006	0.000 573
0.000 527	0.000 501	0.000 449	0.000 432	0.000 439	0.00 043	0.000 409	0.000 409
0.000 421	0.000 402	0.000 402	0.000 384	0.000 386	0.000 393	0.000 395	0.000 411
0.000 417	0.000 422	0.000 441	0.000 422	0.000 414	0.000 436	0.000 389	0.000 368
0.00 037	0.000 337	0.000 341	0.000 352	0.000 362	0.000 356	0.000 354	0.000 373

Table 4.1 (*Continued*)

0.000 378	0.000 364	0.000 334	0.000 338	0.000 334	0.000 368	0.000 368	0.000 336
0.000 326	0.000 326	0.000 326	0.000 334	0.000 334	0.000 343	0.000 316	0.000 302
0.000 295	0.000 271	0.000 268	0.000 268	0.000 244	0.00 024	0.000 248	0.000 241
0.00 024	0.000 238	0.000 225	0.000 227	0.000 228	0.000 238	0.000 228	0.000 226
0.000 228	0.000 217	0.000 205	0.000 203	0.000 168	0.000 174	0.000 176	0.000 187
0.000 185	0.000 186	0.000 186	0.000 184	0.00 017	0.000 167	0.00 017	0.000 171
0.000 173	0.00 017	0.000 171	0.000 171	0.000 172	0.000 165	0.000 159	0.000 158
0.000 167	0.000 171	0.000 162	0.000 164	0.000 153	0.000 142	0.00 014	0.000 133
0.000 142	0.000 146	0.000 157	0.000 169	0.000 167	0.000 167	0.000 169	0.000 174
0.000 173	0.000 169	0.000 166	0.000 169	0.000 186	0.000 181	0.000 179	0.000 181
0.000 189	0.000 194	0.000 194	0.000 196	0.000 214	0.00 022	0.000 219	0.000 211
0.0002	0.000 204	0.000 199	0.000 201	0.000 201	0.000 223	0.000 233	0.000 232
0.000 231	0.000 224	0.000 213	0.000 211	0.000 218	0.000 206	0.000 198	0.000 199
0.000 192	0.00 019	0.000 187	0.00 017	0.000 187	0.000 192	0.000 188	0.000 192
0.000 195	0.000 205	0.000 213	0.000 195	0.00 019	0.000 189	0.000 185	0.000 188
0.000 184	0.000 185	0.000 188	0.000 184	0.000 172	0.000 162	0.000 154	0.000 153
0.000 149	0.00 015	0.000 149	0.000 139	0.000 135	0.000 133	0.000 128	0.000 128
0.00 013	0.00 014	0.000 146	0.000 128	0.000 125	0.000 135	0.000 136	0.000 128
0.000 119	0.000 109	0.00 011	0.000 114	0.000 115	0.000 116	0.000 114	0.000 121
0.000 122	0.00 013	0.000 133	0.000 125	0.000 124	0.000 124	0.000 121	0.000 123
0.000 123	0.000 127	0.00 013	0.000 128	0.00 013	0.000 133	0.000 132	0.000 131
0.000 124	0.000 122	0.000 123	0.000 125	0.000 116	0.000 103	0.000 101	0.000 101
0.000 102	0.0001	9.75E-05	9.91E-05	0.000 104	0.000 102	0.000 101	0.000 104
9.63E-05	9.43E-05	9.11E-05	8.88E-05	8.87E-05	8.80E-05	8.82E-05	8.62E-05
8.30E-05	8.25E-05	8.38E-05	8.27E-05	8.26E-05	8.53E-05	8.52E-05	8.27E-05
7.84E-05	7.38E-05	6.87E-05	6.78E-05	6.72E-05	6.98E-05	7.38E-05	7.34E-05
7.68E-05	7.58E-05	7.64E-05	7.88E-05	8.30E-05	7.87E-05	7.28E-05	6.88E-05
6.84E-05	6.85E-05	6.87E-05	6.96E-05	6.94E-05	6.60E-05	6.58E-05	6.56E-05
6.41E-05	6.56E-05	6.65E-05	6.57E-05	6.15E-05	6.07E-05	6.02E-05	6.08E-05
6.16E-05	6.21E-05	6.32E-05	6.71E-05	6.41E-05	5.93E-05	6.16E-05	5.73E-05
5.71E-05	5.50E-05	4.67E-05	4.18E-05	3.77E-05	3.69E-05	3.85E-05	3.92E-05
4.25E-05	4.27E-05	4.28E-05	4.31E-05	4.30E-05	4.23E-05	4.01E-05	3.94E-05
3.71E-05	3.53E-05	3.45E-05	4.05E-05	4.00E-05	3.95E-05	3.99E-05	4.13E-05
4.34E-05	4.35E-05	3.88E-05	4.00E-05	4.18E-05	3.95E-05	4.19E-05	4.50E-05
4.81E-05	5.08E-05	5.25E-05	5.35E-05	5.33E-05	5.26E-05	5.16E-05	4.91E-05
5.21E-05	5.29E-05	5.79E-05	5.78E-05	5.85E-05	6.02E-05	6.12E-05	6.04E-05
6.14E-05	6.15E-05	5.90E-05	6.15E-05	6.29E-05	6.37E-05	6.16E-05	5.89E-05
5.76E-05	5.84E-05	5.63E-05	5.62E-05	5.60E-05	5.37E-05	4.99E-05	4.40E-05
4.15E-05	3.96E-05	3.89E-05	3.93E-05	4.00E-05	3.96E-05	3.89E-05	3.62E-05
3.52E-05	3.02E-05	3.20E-05	3.16E-05	2.98E-05	2.89E-05	2.98E-05	2.89E-05
2.88E-05	2.54E-05	2.65E-05	2.88E-05	2.91E-05	3.26E-05	3.20E-05	3.35E-05
3.32E-05	3.36E-05	3.35E-05	3.30E-05	3.30E-05	3.56E-05	3.95E-05	3.98E-05
4.00E-05	4.22E-05	4.19E-05	4.00E-05	4.07E-05	4.15E-05	4.19E-05	4.13E-05
4.21E-05	4.35E-05	4.39E-05	4.46E-05	4.66E-05	4.56E-05	4.79E-05	4.68E-05
4.78E-05	4.54E-05	4.22E-05	4.23E-05	3.85E-05	4.09E-05	3.99E-05	4.01E-05
4.07E-05	4.14E-05	4.17E-05	4.19E-05	4.01E-05	3.61E-05	3.59E-05	3.61E-05
3.39E-05	3.36E-05	3.39E-05	3.42E-05	3.33E-05	3.25E-05	3.22E-05	3.17E-05
2.88E-05	2.81E-05	2.74E-05	2.59E-05	2.72E-05	2.75E-05	2.78E-05	2.87E-05
2.73E-05	2.65E-05	2.56E-05	2.73E-05	2.47E-05	2.52E-05	2.44E-05	2.36E-05
2.20E-05	2.28E-05	2.36E-05	2.27E-05	2.39E-05	2.46E-05	2.45E-05	2.71E-05
2.96E-05	2.98E-05	2.89E-05	3.01E-05	2.98E-05	2.98E-05	3.14E-05	3.14E-05
3.15E-05	3.18E-05	3.34E-05	3.27E-05	3.06E-05	3.01E-05	2.80E-05	2.84E-05
2.92E-05	2.76E-05	2.60E-05	2.64E-05	2.63E-05	2.64E-05	2.59E-05	2.53E-05
2.59E-05	2.60E-05	2.79E-05	2.90E-05	2.91E-05	3.14E-05	2.95E-05	2.78E-05
2.84E-05	2.83E-05	2.76E-05	2.76E-05	2.81E-05	2.72E-05	2.73E-05	2.73E-05
2.69E-05	2.54E-05	2.50E-05	2.55E-05	2.60E-05	2.72E-05	2.70E-05	2.65E-05
2.73E-05	2.78E-05	2.85E-05	2.99E-05	2.99E-05	3.00E-05	2.99E-05	2.83E-05
2.88E-05	2.82E-05	2.63E-05	2.62E-05	2.40E-05	2.33E-05	2.37E-05	2.32E-05

References

1. Newland, D.E. (1975) *An Introduction to Random Vibration and Spectral Analysis*, Longman, London and New York.
2. Lin, Y.K. (1967) *Probabilistic Theory of Structural Dynamics*, McGraw Hill, Inc., New York.
3. Nigam, N.C. (1983) *Introduction to Random Vibration*, MIT Press, Cambridge, London.

5

Response Spectrum Method of Analysis

5.1 Introduction

In Chapter 2, different types of seismic inputs were described. Among them, the response spectrum of an earthquake is considered as a very useful input for the seismic analysis of structures and is directly used for the response spectrum method of analysis of structures, which is favored by earthquake engineers for a number of reasons. Firstly, the method provides a technique for performing an equivalent static lateral load analysis of structures for earthquake forces. Secondly, it allows a clear understanding of the contributions of different modes of vibration to the overall seismic response of structures. Thirdly, it offers a simplified method for finding the design forces for the members of structures for earthquake forces. Finally, it is also useful in the approximate evaluation of the reliability and safety of structures under earthquake forces.

The response spectrum method of analysis is not an exact method of analysis in the sense that its results are not identical with those of the time history analysis presented in Chapter 3. However, for most of the cases, the results are accurate enough for structural design applications. Apart from this drawback, there are other limitations to the method, namely: (i) it is strictly applicable for linear analysis and (ii) it cannot be applied as such for the case of multi-support excitations. However, the method has been extended for the latter with additional approximations.

In this chapter, development of the response spectrum method of analysis is first presented for single-point excitation, and then its extension to multi-point excitations is briefly described. At the end of the chapter, the equivalent lateral load analysis as specified in earthquake codes is presented and codal provisions regarding the base shear coefficient and response spectrums of a few codes are given for a comparative time study.

5.2 Concept of Equivalent Lateral Force and Response Spectrum Method of Analysis

The equivalent lateral force for an earthquake is a unique concept used in earthquake engineering. The concept is attractive because it converts a dynamic analysis into partly dynamic and partly static analyses for finding the maximum displacement (or stresses) induced in the structure due to earthquake excitation. For seismic resistant design of structures, these maximum stresses are of interest only, not the time history of stresses. The equivalent lateral force for an earthquake is defined as a set of lateral static forces which

Seismic Analysis of Structures T.K. Datta

will produce the same peak response of the structure as that obtained by the dynamic analysis of the structure (Chapter 3) under the same earthquake. This equivalence is restricted only to a single mode of vibration of the structure, that is, there a set of lateral force exist for each mode of vibration.

The equivalent (static) lateral force for an earthquake is obtained by carrying out a modal analysis of structures, and then a static analysis of the structure with equivalent (static) lateral force in each mode of vibration is performed to obtain the desired responses. The entire procedure is known as the response spectrum method of analysis and is developed using the following steps.

1. A modal analysis of the structure is carried out to obtain the mode shapes, frequencies, and mode participation factors for the structure.
2. An equivalent static load is derived to get the same response as the maximum response obtained in each mode vibration, using the acceleration response spectrum of the earthquake.
3. The maximum modal responses are combined to find the total maximum response of the structure.

There are no approximations involved in the first two steps. Only the third one involves approximations. As a result, the response spectrum method of analysis is called an approximate method of analysis. The approximation introduces some errors into the computed response. The magnitude of the error depends upon the problem (both the type of structure and the nature of earthquake excitation). However, seismic response analysis of a number of structures have shown that for most practical problems, the response spectrum method of analysis estimates reasonably good responses for use in design.

The method is primarily developed for single-point excitation with a single-component earthquake. However, the method could be extended to multi-point – multi-component earthquake excitations with certain additional assumptions. Furthermore, response spectrum method of analysis is derived for classically damped structures. Therefore, its application to non-classically damped structural systems is not strictly valid. However, with some other simplifying assumptions, the method has been used for non-classically damped systems.

5.3 Response Spectrum Analysis for Single-Point Excitation

5.3.1 Development of the Method

The equation of motion for an MDOF system with single-point excitation is rewritten below.

$$\boldsymbol{M}\ddot{\boldsymbol{x}} + \boldsymbol{C}\dot{\boldsymbol{x}} + \boldsymbol{K}\boldsymbol{x} = -\boldsymbol{M}\boldsymbol{I}\ddot{x}_g \tag{5.1}$$

Using modal transformation, Equation 5.1 can be written as a number of uncoupled equations of motion representing a set of SDOF systems:

$$\ddot{z}_i + 2\xi_i\omega_i z_i + \omega_i^2 z_i = -\lambda_i \ddot{x}_g \quad i = 1 \ldots m \tag{5.2}$$

in which

$$\lambda_i = \frac{\boldsymbol{\varphi}_i^T \boldsymbol{M}\boldsymbol{I}}{\boldsymbol{\varphi}_i^T \boldsymbol{M}\boldsymbol{\varphi}_i}$$

and $\boldsymbol{\varphi}_i$ is the ith mode shape and m is the number of modes being considered.

The response of the system in the ith mode is given by:

$$\boldsymbol{x}_i = \boldsymbol{\phi}_i z_i \tag{5.3}$$

The elastic force on the system in the ith mode is then specified as:

$$\boldsymbol{f}_{si} = \boldsymbol{K}\boldsymbol{x}_i = \boldsymbol{K}\boldsymbol{\phi}_i z_i \tag{5.4}$$

As the undamped mode shape $\boldsymbol{\phi}_i$ satisfies the following equation

$$\boldsymbol{K}\boldsymbol{\phi}_i = \omega_i^2 \boldsymbol{M}\boldsymbol{\phi}_i \tag{5.5}$$

Equation 5.4 can be written as:

$$\boldsymbol{f_{si}} = \omega_i^2 \boldsymbol{M}\boldsymbol{\phi}_i z_i \tag{5.6}$$

The maximum elastic force developed in the ith mode is then

$$\boldsymbol{f_{si}}_{\max} = \boldsymbol{M}\boldsymbol{\phi_i}\omega_i^2 z_{i\max} \tag{5.7}$$

Now, referring to the development of response spectrums of an earthquake (given in Chapter 2) $z_{i\max}$ may be written as:

$$z_{i\max} = \lambda_i S_{\mathrm{d}_i}(\omega_i, \xi_i) \tag{5.8}$$

in which $S_{\mathrm{d}_i}(\omega_i, \xi_i)$ denotes the ordinate of the displacement response spectrum for the ground acceleration $\ddot{x}_g$ corresponding to a damping of ξ_i and a time period of $T_i = 2\pi/\omega_i$.

As the pseudo acceleration spectrum $S_{\mathrm{a}} = \omega^2 S_{\mathrm{d}}$, Equation 5.7 may be written as:

$$\boldsymbol{f_{si}}_{\max} = \lambda_i \boldsymbol{M}\boldsymbol{\phi_i} S_{\mathrm{a}_i} = \boldsymbol{P}_{\mathrm{e}_i} \tag{5.9}$$

Using Equation 5.4, $\boldsymbol{x_i}_{\max}$ can be written as

$$\boldsymbol{x_i}_{\max} = \boldsymbol{K}^{-1}\boldsymbol{f_{si}}_{\max} = \boldsymbol{K}^{-1}\boldsymbol{P}_{\mathrm{e}_i} \tag{5.10}$$

Equation 5.3 together with Equation 5.10 forms the basis of the response spectrum method of analysis for an earthquake. It may be interpreted in the following way.

If the MDOF system subjected to a single-point ground excitation $\ddot{x}_g$ is assumed to vibrate only in the ith mode, that is, the contribution of the ith mode is only considered in evaluating the response, then the maximum displacement of the response of the system can be obtained by analyzing the system statically under an equivalent static load $\boldsymbol{P}_{\mathrm{e}_i}$.

From Equation 5.9, it is evident that there an equivalent lateral load vector $\boldsymbol{P}_{\mathrm{e}_i}$ exists for each mode of vibration. Furthermore, a pseudo acceleration response spectrum (loosely termed an acceleration response spectrum) of an earthquake is required to obtain this load vector. Because of this reason, this method of analysis is known as the response spectrum method of analysis. As the equivalent lateral load is defined for each mode of vibration, it is also called the modal response spectrum method of analysis. To obtain $\boldsymbol{P}_{\mathrm{e}_i}$ using Equation 5.9, it is seen that $\boldsymbol{\phi}_i$ and λ_i are required in addition to the acceleration response spectrum. Therefore, a modal analysis has to be performed for determining frequencies, mode shapes, and mode participation factors for the structure. Subsequently, a static analysis of the structure under the equivalent lateral load is required to obtain the maximum response in each mode of vibration.

As the contributions of responses from different modes of variation constitute the total response, the total maximum response is obtained by combining the modal quantities. This combination is done in an approximate manner because the actual dynamic analysis is now replaced by an equivalent static analysis. The number of modes to be considered in the analysis is decided based on the total mass participation factor discussed in Chapter 3.

5.3.2 Modal Combination Rules

The maximum responses obtained in each mode of vibration are generally combined using three different types of modal combination rules, namely: (i) ABSSUM, (ii) SRSS, and (iii) CQC.

5.3.2.1 ABSSUM

ABSSUM stands for absolute sum of maximum values of response. Thus, if x is the response quantity of interest then

$$x = \sum_{i=1}^{m} |x_i|_{\max} \tag{5.11}$$

in which $|x_i|_{\max}$ is the absolute maximum value of response in the ith mode of vibration. The combination rule gives an upper bound to the computed value of the total response for two reasons: (i) it assumes that the modal peak responses occur at the same time; and (ii) it ignores the algebraic sign of the response. The actual time history analysis shows that the peak responses (considering both negative and positive peaks) occur at different times in different modes. Also, the total peak response occurs at a time different to those of the modal peaks, as illustrated in Figure 5.1. Thus, the combination rule provides a conservative estimate of the total peak response, and therefore it is not very commonly used in the seismic design of structures.

5.3.2.2 SRSS

In SRSS, square root of sum of squares, the response x is given by:

$$x = \sqrt{\sum_{i=1}^{m} x_{i\max}^2} \tag{5.12}$$

The modal peak responses are squared, summed up, and then the square root of the sum is taken to obtain the total peak response. This combination rule generally provides a good estimate of the total peak response for structures with well separated natural frequencies. When the natural frequencies are not very well separated, the error in estimation of the total peak response becomes considerable. The underlying meaning of Equation 5.12 is that the modal peak responses are assumed to be independent random variables. However, there is always some degree of correlation between the modal responses, which may be very small, and hence can be ignored when the natural frequencies are well separated.

5.3.2.3 CQC

The CQC, complete quadratic combination rule, is a generalization of the SRSS rule and is applicable for a wider class of structures. It is specifically used for structures having closely spaced frequencies. The response x is given by:

$$x = \sqrt{\sum_{i=1}^{m} x_i^2 + \sum_{i=1}^{m}\sum_{j=1}^{m} \rho_{ij} x_i x_j} \tag{5.13}$$

The second term in the above expression is valid for $i \neq j$. Thus, the second term includes the effect of correlation between modal peak responses through the correlation coefficient terms ρ_{ij}. It is obvious that $0 \leq \rho_{ij} \leq 1$. If x_i and x_j are of opposite sign, then $\rho_{ij} x_i x_j$ becomes negative. Therefore, CQC may provide less response than that provided by SRSS. Different expressions for the correlation coefficient ρ_{ij} have been proposed in the literature. Here, two widely used expressions are given for the case when all modal dampings are assumed to be the same (that is, $\xi_i = \xi_j = \xi$). The first one was proposed by Rosenblueth and Elordy [1] and is given as:

$$\rho_{ij} = \frac{\xi^2 (1+\beta_{ij})^2}{(1-\beta_{ij})^2 + 4\xi^2 \beta_{ij}} \tag{5.14}$$

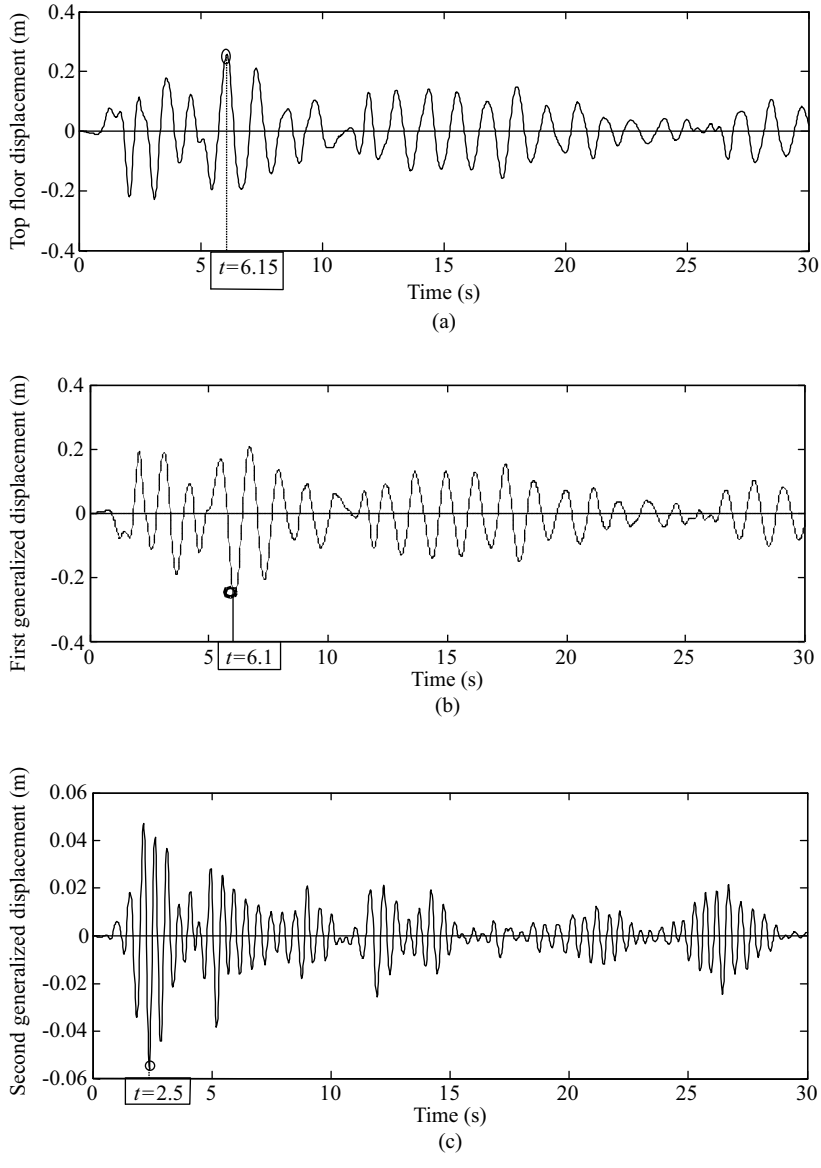

Figure 5.1 Time histories of displacement of the problem in Example 3.12: (a) top-storey displacement; (b) first generalized displacement; and (c) second generalized displacement

in which $\beta_{ij} = \omega_i/\omega_j$. The second one was proposed by Der Kiureghian [2] and is given as:

$$\rho_{ij} = \frac{8\xi^2(1+\beta_{ij})\beta_{ij}^{3/2}}{(1-\beta_{ij})^2 + 4\xi^2\beta_{ij}(1+\beta_{ij})^2} \tag{5.15}$$

The plots of the two expressions are shown in Figure 5.2. It is seen from the figure that both expressions provide almost the same value, especially near $\beta_{ij} = 1$. Furthermore, for a small damping ($\xi < 0.1$), the

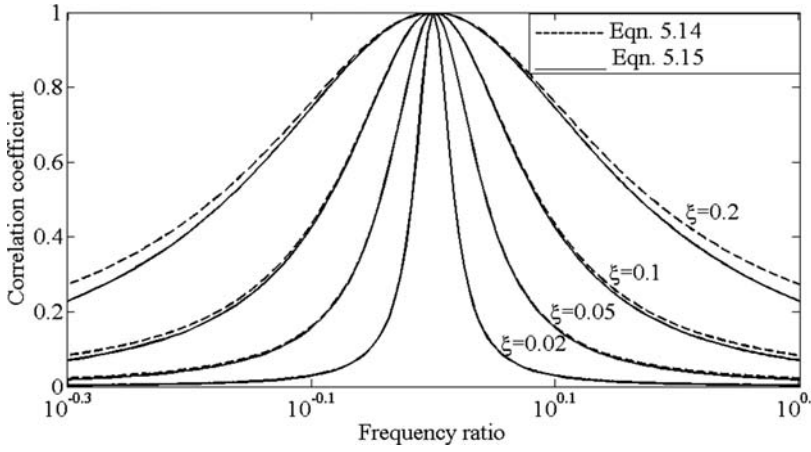

Figure 5.2 Variation of correlation coefficient ρ_{ij} with the modal frequency ratio ω_i/ω_j; abscissa scale is logarithmic

value of ρ_{ij} rapidly decreases as β_{ij} moves away from unity. Thus, for well separated natural frequencies, ρ_{ij} may be ignored as it is assumed in the SRSS combination rule.

SRSS and CQC rules for the combination of peak modal responses are best derived assuming a future earthquake to be a stationary random process (Chapter 4). As both the design response spectrum and power spectral density function (PSDF) of an earthquake represent the frequency contents of ground motion, a relationship exists between the two. This relationship is investigated for the smoothed curves representing the two, which show the averaged characteristics of many ground motions. If the ground motion is assumed to be a stationary random process, then the generalized coordinate in each mode of vibration is also a random process. Therefore, there a cross correlation (represented by cross PSDF) between the generalized coordinates of any two modes is present. Because of this, it is reasonable to assume that a correlation coefficient ρ_{ij} exists between the two modal peak responses. Derivation of ρ_{ij} (Equation 5.15) as given by Der Kiureghian [2] is based on the above concept.

There have been several attempts to establish a relationship between the PSDF and the response spectrum of ground motion. Here, a relationship proposed by Der Kiureghian and Neuenhofer [3] is adopted for use and is given by:

$$S_{\ddot{x}_g}(\omega) = \frac{\omega^{\theta+2}}{\omega^{\theta} + \omega_{ff}^{\theta}} \left[\frac{2\xi\omega}{\pi} + \frac{4}{\pi\tau}\right] \left[\frac{D(\omega,\xi)}{p_0(\omega)}\right]^2 \tag{5.16a}$$

$$p_0(\omega) = \sqrt{2\ln\left(\frac{2.8\omega\tau}{2\pi}\right)} \tag{5.16b}$$

where

$D(\omega, \xi)$ is the displacement response spectrum ordinate for damping ratio ξ and $T = 2\pi/\omega$
ω is the frequency
τ is the duration of the earthquake
$p_0(\omega)$ is the peak factor for the response to white noise, which is given in terms of ω, ξ and τ [4]
ω_{ff} and θ are two constants, some reasonable values, which may be taken, are 0.705 and 3, respectively
$S_{\ddot{x}_g}(\omega)$ is the PSDF of ground acceleration.

Both the CQC and SRSS rules provide good estimates of peak response for wide band earthquakes with durations much greater than the time period of the structure. Because of the underlying principle of

random vibration in deriving the combination rules, the peak responses would be better termed as the mean peak response or expected peak value of response.

Example 5.1

Compare between the PSDFs obtained from the smoothed displacement response spectrum (Equation 5.16a) and the Fourier spectrum of the El Centro earthquake.

Solution: Figure 5.3 shows the PSDFs obtained by Equation 5.16a using the displacement response spectrum of the El Centro earthquake and the smooth PSDF obtained from the Fourier spectrum of the same earthquake (refer to Section 4.5). It is seen from the figure that both PSDFs compare well. Thus, Equation 5.16a can be used to obtain response spectrum compatible PSDFs.

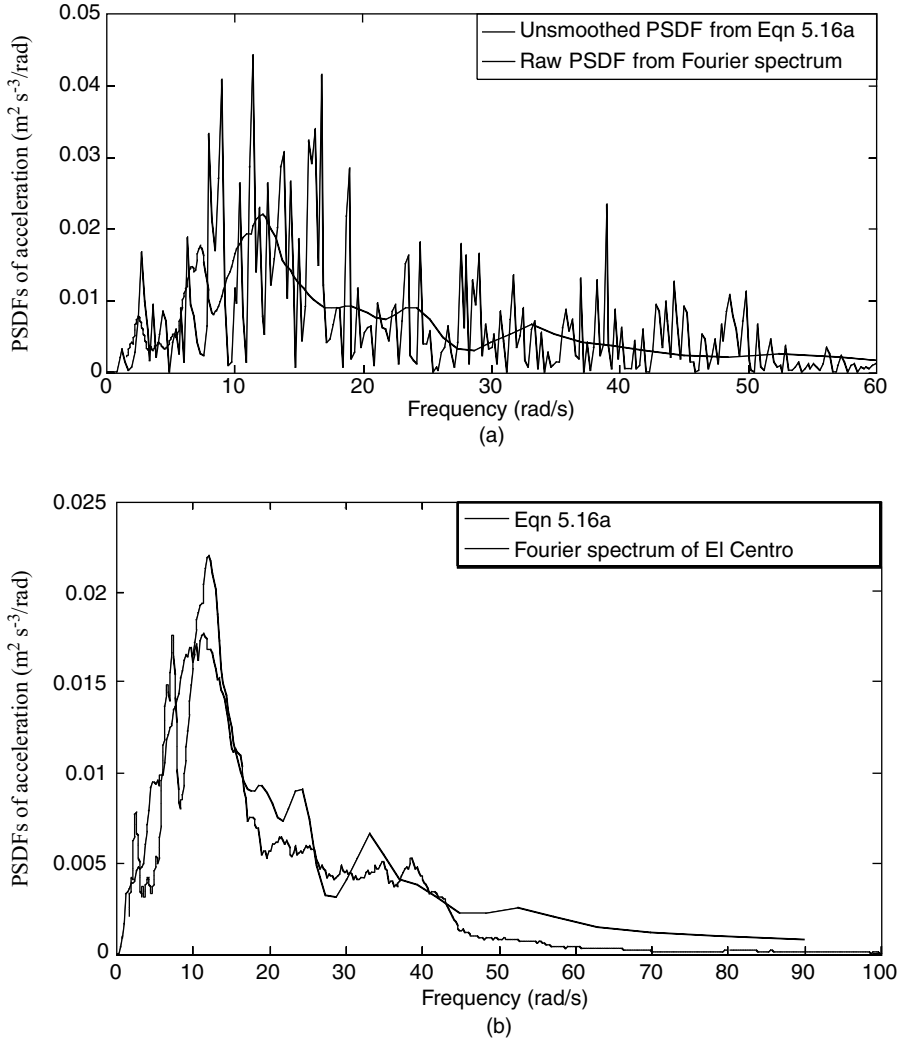

Figure 5.3 Comparison between the PSDFs obtained by Equation 5.16a and the Fourier spectrum of the El Centro earthquake: (a) unsmoothed; and (b) 21-point smoothed

5.3.3 Application to 2D Building Frames, Chimneys, and Stacks

The dynamic degrees of freedom of these structures are considered as the sway degrees of freedom and are obtained by condensing out the rotational degrees of freedom. The single component of an earthquake is assumed to act in the direction of the sway degrees of freedom. The response spectrum method of analysis of these structures can be carried out using the following steps.

1. Identify all kinematic degrees of freedom.
2. Generate a stiffness matrix $\boldsymbol{K}$ of the structure corresponding to the kinematic degrees of freedom.
3. Apply unit loads at the desired dynamic degrees of freedom (that is, sway degrees of freedom) one at a time to generate the flexibility matrix ($\boldsymbol{F}$) corresponding to the dynamic degrees of freedom. Also, the desired response quantities (moments, shear forces, and so on.) are determined for each position of the unit load and are arranged in the form of an influence coefficient matrix $\boldsymbol{R}$ of size $m \times n$, where m is the number of response quantities of interest and n is the number of sway degrees of freedom.
4. Form the diagonal mass matrix $\boldsymbol{M}$ corresponding to sway degrees of freedom and solve for the eigen value problem with $\boldsymbol{M}$ and $\boldsymbol{F}$.
5. For the ith mode, find λ_i (Equation 5.2), and then obtain $\boldsymbol{P}_{e_i}$ (Equation 5.9). For building frames, λ_i may be simplified to:

$$\lambda_i = \frac{\sum_{r=1}^{N} W^r \phi_{ir}}{\sum_{r=1}^{N} W^r (\phi_{ir})^2} \tag{5.17}$$

   in which W^r is the weight of the rth floor and ϕ_{ir} is the mode shape coefficient for the rth floor in the ith mode.
6. Obtain $R_j = RP_{ej} (j = 1 \ldots r)$, in which r is the number of modes considered, R is the influence coefficient matrix explained above, and R_j is the modal peak response vector of size m.
7. Use either the SRSS or CQC rule for combining the modal peak responses.

Example 5.2

For the frame shown in Figure 3.20 (Example 3.12), find the mean peak values of top displacement, base shear, and inter-storey drift between the first and second floors using the response spectrum method of analysis and make a comparison between the results obtained by SRSS, CQC, ABSSUM, and time history analysis by considering two modes only, and by considering all modes. Use the digitized smoothed response spectrum of the El Centro earthquake given in Appendix 5.A.

Solution: Applying the steps given in Section 5.3.3, the lateral load and the response quantities of interest are obtained. The frequencies and mode shapes for the problem are given below.

$$\omega_1 = 5.061 \,\text{rad}\,\text{s}^{-1}; \omega_2 = 12.560 \,\text{rad}\,\text{s}^{-1}; \omega_3 = 18.646 \,\text{rad}\,\text{s}^{-1}$$

$$\begin{aligned}
\phi_{\mathbf{1}}^T &= [-1 \quad -0.871 \quad -0.520 \quad -0.278] \\
\phi_{\mathbf{2}}^T &= [-1 \quad -0.210 \quad 0.911 \quad 0.752] \\
\phi_{\mathbf{3}}^T &= [-1 \quad 0.738 \quad -0.090 \quad -0.347] \\
\phi_{\mathbf{4}}^T &= [1 \quad -0.843 \quad 0.268 \quad -0.145]
\end{aligned}$$

The results of the response spectrum method of analysis are shown in Table 5.1. It is seen from the table that ABSSUM provides much higher values compared with the others. Responses obtained by SRSS and CQC are nearly the same; those of SRSS are on the higher side. The results obtained by CQC compare well with those of time history analysis. As the modes are well separated, SRSS and CQC rules of combination

Table 5.1 Comparison of peak responses obtained by different approaches

Approach	Displacement (m)		Base shear in terms of mass (m)		Drift (m)	
	2 modes	All modes	2 modes	All modes	2 modes	All modes
SRSS	0.9171	0.917	1006.558	1006.658	0.221	0.221
CQC	0.9121	0.905	991.172	991.564	0.214	0.214
ABSSUM	0.9621	0.971	1134.546	1152.872	0.228	0.223
Time history	0.8921	0.893	980.098	983.332	0.197	0.198

provide nearly the same results. In addition, it is seen that contributions of higher modes to the response are not significant as the mass participation factor given by Equation 3.115 for the first two modes is nearly 0.9.

5.3.4 Application to 3D Tall Buildings

For 3D tall buildings subjected to a single-component earthquake, the principal direction of the building is aligned with the direction of ground motion, as shown in Figure 5.4(a and b).

Analysis is performed for ground motion applied to each principal direction separately, and the worst combination of response quantities are considered for the design. The following steps are adopted for the analysis.

1. Assume the floors as rigid diaphragms and find the center of mass of each floor.
2. Dynamic degrees of freedom at the center of mass of each floor are considered as two translations (in the principal directions) and a rotation about a vertical axis. If the centers of masses of the floors do not

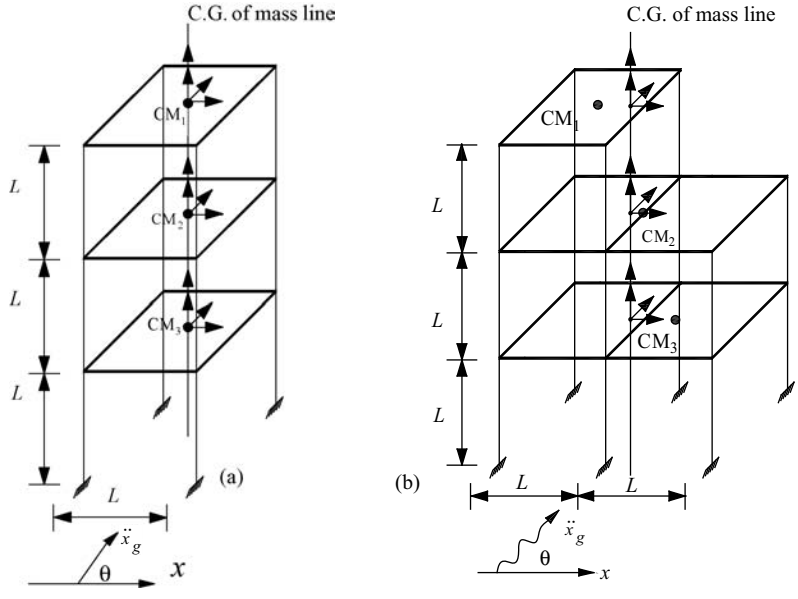

Figure 5.4 Dynamic degrees of freedom for asymmetric 3D tall buildings: (a) center of masses in one vertical axis; (b) center of masses at different vertical axes

lie on one vertical axis, find the c.g of the vertical lines for the centers of masses. Dynamic degrees of freedom are then defined at the points where this vertical axis intersects the floors (Figure 5.4b).
3. Apply unit loads corresponding to each dynamic degrees of freedom one at a time as in the previous case, and solve the 3D building statically to find the flexibility matrix.
4. Carry out steps 4–7 as in the previous case.

Example 5.3

For the 3D frame shown in Figure 3.30 (exercise in Example 3.9), find the mean peak values of top displacements, torque at the first floor, and the two shear forces V_x and V_y at the base of the column A using the response spectrum method of analysis and compare between the results obtained by SRSS, CQC, and time history analysis by taking all modes. Use the digitized values of the response spectrum of the El Centro earthquake given in Appendix 5.A.

Solution: Following the steps given in Section 5.3.4, the results of the response spectrum method of analysis are obtained and are shown in Table 5.2. The natural frequencies of the frame are obtained as:

$$\omega_1 = 13.516\,\text{rad s}^{-1};\ \omega_2 = 15.138\,\text{rad s}^{-1};\omega_3 = 38.731\,\text{rad s}^{-1};$$

$$\omega_4 = 39.633\,\text{rad s}^{-1};\omega_5 = 45.952\,\text{rad s}^{-1};\omega_6 = 119.187\,\text{rad s}^{-1}$$

It is seen from the table that there is a difference between the results obtained by the SRSS and CQC rules of combination. The SRSS rule provides higher responses. This is the case because the natural frequencies of the structure are not well separated. The results obtained by the CQC combination rule are closer to those of the time history analysis; the latter provides less responses.

Table 5.2 Comparison of peak responses obtained by different approaches

Approach	Displacement (m)		Torque (rad)	V_x (N)	V_y (N)
	(1)	(2)	(3)		
SRSS	0.1431	0.0034	0.0020	214 547	44 081
CQC	0.1325	0.0031	0.0019	207 332	43 376
Time history	0.1216	0.0023	0.0016	198 977	41 205

5.4 Response Spectrum Analysis for Multi-Support Excitations

5.4.1 Development of the Method

The response spectrum method of analysis has been developed for single-point excitation with single-component ground motion. Therefore, the concept and the derivation of the method are not valid for multi-support excitation. However, there are many practical problems where the assumption of single-point excitation is not correct. They include long pipelines, networks of pipelines, dams, continuous bridges, and spatially long structures. Depending upon the distance between the supports, the ground motions at the various supports of a structure could be different in terms of their rms values, phases, and frequency contents. A travelling train of an earthquake wave moving with a shear wave velocity of V_s produces different excitations at different supports that have the same frequency contents but have phase differences (time lag). If the support excitations are assumed as random processes, then they form a set of partially correlated random excitations having the same PSDF. Thus, the excitations at the supports are characterized by a single response spectrum, which bears a relationship with the PSDF as given by

Equation 5.16. The effect of a time lag or phase shift or lack of correlation between the excitations is included by defining a correlation function (Chapter 4).

Development of the response spectrum method of analysis for multi-support excitation follows the principles of random vibration analysis and has been presented by Der Kiureghian and Neuenhofer [3]. The derivation of the method is somewhat complex and cannot be understood without a good knowledge of the theory of random vibration. Therefore, it is not included here. However, some of the important features of the development of the method and its use are as follows.

i. It is assumed that the future earthquake ground motions may be represented by an averaged smooth response spectrum and an averaged smooth PSDF of ground motion, both obtained from an ensemble of time history records.
ii. The lack of correlation between the ground motions at two points is represented by a coherence function (as that given by Equation 2.93).
iii. All peak factors, that is, the peak factor in each mode and the peak factor for the total response, are assumed to be the same [3]. Several expressions for peak factors are available in the literature. One expression, which is widely used, is given in Chapter 2 [5] and may be used here.
iv. A relationship between the ordinates of the displacement response spectrum $S_{\mathrm{d}}(\omega, \xi)$ and those of the PSDF of acceleration $S_{\ddot{g}}(\omega)$ of ground motion is established, as given by Equation 5.16.
v. The mean peak value of any response quantity of interest, r (which may be displacement or bending moment or shear force) consists of two parts (Chapter 3), namely: (a) pseudo static response due to the displacements of the supports and (b) dynamic response of the structure due to the motion of the structure with respect to the supports.
vi. Equations of motion in terms of relative displacements are written as given by Equation 3.19 (Chapter 3).
vii. The normal mode transformation provides m sets of uncoupled equations (equal to the number of modes considered) with the right-hand side of each equation containing an acceleration term, which is the weighted sum of the support accelerations. Thus, a typical modal equation is written in the form

$$\ddot{z}_i + 2\xi\omega_i\dot{z}_i + \omega_i^2 z_i = \sum_{k=1}^{s} \beta_{ki}\ddot{u}_k \quad i = 1 \ldots m \tag{5.18}$$

in which s is the number of supports and β_{ki} is given by:

$$\beta_{ki} = \frac{\boldsymbol{\phi}_i^T \boldsymbol{M} \boldsymbol{R}_k}{\boldsymbol{\phi}_i^T \boldsymbol{M} \boldsymbol{\phi}_i} \tag{5.19}$$

where $\boldsymbol{R}_k$ is the influence coefficient vector representing the displacements at the non-support dynamic degrees of freedom produced due to unit displacement given to the kth support only. The method for finding this vector is explained in Chapter 3. If the response of the SDOF oscillator (Equation 5.18) to $\ddot{u}_k$ alone is $\bar{z}_{ki}$, then

$$z_i = \sum_{k=1}^{s} \beta_{ki}\bar{z}_{ki} \tag{5.20}$$

viii. Introducing the quasi-static component of the response, the total value of any response (r) quantity of interest at any instant of time t is given by:

$$r(t) = \sum_{k=1}^{s} a_k u_k(t) + \sum_{i=1}^{m} \bar{\phi}_i z_i(t) \tag{5.21}$$

in which a_k is the response quantity of interest for unit displacement in the direction of ground motion applied at the kth support only, and $\bar{\phi}_i$ is the ith mode shape coefficient for the response

quantity of interest. Substituting for z_i in Equation 5.21

$$r(t) = \sum_{k=1}^{s} a_k u_k(t) + \sum_{i=1}^{m} \bar{\phi}_i \sum_{k=1}^{s} \beta_{ki} \bar{z}_{ki} \tag{5.22}$$

In matrix form, Equation 5.22 may be written as:

$$r(t) = \boldsymbol{a}^T \boldsymbol{u}(t) + \boldsymbol{\phi}_\beta^T \bar{\boldsymbol{z}}(t) \tag{5.23}$$

in which $\boldsymbol{a}$ is a coefficient vector of size s denoting the response quantity of interest for unit displacements applied at the supports (one at a time); $\boldsymbol{u}(t)$ is the vector of ground displacements at the support $\boldsymbol{s}$ at time t; $\boldsymbol{\phi}_\beta$ and $\bar{z}$ are the vectors of size $m \times s$, respectively and are of the form shown below (for $s = 2$ and $m = 3$):

$$\boldsymbol{\phi}_\beta^T = [\, \bar{\varphi}_1\beta_{11} \quad \bar{\varphi}_1\beta_{21} \quad \bar{\varphi}_1\beta_{31} \quad \bar{\varphi}_2\beta_{21} \quad \bar{\varphi}_2\beta_{22} \quad \bar{\varphi}_2\beta_{32} \,] \tag{5.24a}$$

$$\bar{\boldsymbol{z}}^T = \{\, \bar{z}_{11} \quad \bar{z}_{21} \quad \bar{z}_{31} \quad \bar{z}_{11} \quad \bar{z}_{22} \quad \bar{z}_{32} \,\} \tag{5.24b}$$

ix. Assuming $r(t)$, $\boldsymbol{u}(t)$, and $\bar{\boldsymbol{z}}(t)$ to be stationary random processes, the PSDF of $r(t)$, S_{rr} may be written as (Chapter 4):

$$S_{rr} = \boldsymbol{a}^T \boldsymbol{S}_{\boldsymbol{uu}} \boldsymbol{a} + \boldsymbol{\phi}_\beta^T \boldsymbol{S}_{\bar{z}\bar{z}} \boldsymbol{\phi}_\beta + \boldsymbol{a}^T \boldsymbol{S}_{\boldsymbol{u}\bar{\boldsymbol{z}}} \boldsymbol{\phi}_\beta + \boldsymbol{\phi}_\beta^T \boldsymbol{S}_{\bar{z}\boldsymbol{u}} \boldsymbol{a} \tag{5.25}$$

in which $\boldsymbol{S}_{\boldsymbol{uu}}$ is the PSDF matrix of support displacements $\boldsymbol{u}$ of size $s \times s$ and $\boldsymbol{S}_{\bar{z}\bar{z}}$ is the PSDF matrix of generalized displacements $\bar{\boldsymbol{z}}$ of size $ms \times ms$; $\boldsymbol{S}_{\boldsymbol{u}\bar{\boldsymbol{z}}}$ is the cross PSDF matrix between vectors $\boldsymbol{u}$ and $\bar{\boldsymbol{z}}$ of size $s \times ms$; and $\boldsymbol{S}_{\bar{z}\boldsymbol{u}}$ is the complex conjugate of $\boldsymbol{S}_{\boldsymbol{u}\bar{\boldsymbol{z}}}$.

x. Performing integration of Equation 5.25 over the entire range of frequencies, writing the mean peak value of response $r(t)$ as peak factor multiplied by the standard derivation of the response and assuming all peak factors to be the same, the following expression for the mean peak response of $r(t)$ may be obtained:

$$E\Big[\max|r(t)|\Big] = [\boldsymbol{b}^T \boldsymbol{\ell}_{\boldsymbol{uu}} \boldsymbol{b} + \boldsymbol{b}^T \boldsymbol{\ell}_{\boldsymbol{u}\bar{\boldsymbol{z}}} \boldsymbol{\phi}_{\boldsymbol{\beta D}} + \boldsymbol{\phi}_{\boldsymbol{\beta D}}^T \boldsymbol{\ell}_{\bar{z}\bar{z}} \boldsymbol{\phi}_{\boldsymbol{\beta D}} + \boldsymbol{\phi}_{\boldsymbol{\beta D}}^T \boldsymbol{\ell}_{\bar{z}\boldsymbol{u}} \boldsymbol{b}]^{1/2} \tag{5.26}$$

in which

$$\boldsymbol{b}^T = [a_1 u_{p_1} \; a_2 u_{p_2} \; a_3 u_{p_3} \ldots a_S u_{p_S}] \tag{5.27a}$$

$$\boldsymbol{\phi}_{\boldsymbol{\beta D}}^T = \big[\, \bar{\phi}_1\beta_{11}D_{11} \quad \bar{\phi}_1\beta_{21}D_{21} \quad \cdots \quad \bar{\phi}_1\beta_{s1}D_{s1} \ldots \bar{\phi}_m\beta_{11}D_{1m} \quad \cdots \quad \cdots \quad \bar{\phi}_m\beta_{s1}D_{sm} \,\big] \tag{5.27b}$$

$$D_{ij} = D_i(\omega_j, \xi_j) \quad i = 1, \ldots, s; \quad j = 1, \ldots, m \tag{5.27c}$$

In Equations 5.26 and 5.27a–5.27c, $u_{p_i} (i = 1, 2, ..., s)$ is the peak ground displacement at the ith support, D_{ij} is the ordinate of the displacement response spectrum for the ground motion at support i corresponding to time period $T_j = 2\pi/\omega_j$; $\boldsymbol{\ell}_{\boldsymbol{uu}}$ is the correlation matrix between the displacements at the supports and is of size $s \times s$; $\boldsymbol{\ell}_{\boldsymbol{u}\bar{\boldsymbol{z}}}$ is the correlation matrix between the displacements at the supports and modal displacement $\bar{z}_{ki}$ and is of size $s \times ms$; $\boldsymbol{\ell}_{\bar{\boldsymbol{z}}\boldsymbol{u}}$ is the transpose of $\boldsymbol{\ell}_{\boldsymbol{u}\bar{\boldsymbol{z}}}$; $\boldsymbol{\ell}_{\bar{z}\bar{z}}$ is the correlation matrix between the modal displacements $\bar{z}_{ki}$ and $\bar{z}_{ij}$. The elements of the correlation matrices are given by:

$$\ell_{u_i u_j} = \frac{1}{\sigma_{u_i}\sigma_{u_j}} \int_{-\alpha}^{\alpha} S_{u_i u_j}(\omega) \mathrm{d}\omega \tag{5.28}$$

$$\ell_{u_i\bar{z}_{kj}} = \frac{1}{\sigma_{u_i}\sigma_{\bar{z}_{kj}}} \int_{-\alpha}^{\alpha} h_j^* S_{u_i\ddot{u}_k}(\omega)\mathrm{d}\omega \tag{5.29}$$

$$\ell_{\bar{z}_{ki}\bar{z}_{lj}} = \frac{1}{\sigma_{\bar{z}_{ki}}\sigma_{\bar{z}_{lj}}} \int_{-\alpha}^{\alpha} h_i h_j^* S_{\ddot{u}_k\ddot{u}_l}(\omega)\mathrm{d}\omega \tag{5.30}$$

in which h_i is the frequency response function of the ith modal equation.

For a single component travelling wave train of an earthquake,

$$S_{u_iu_j} = \frac{1}{\omega^4} S_{\ddot{u}_i}^{1/2} S_{\ddot{u}_j}^{1/2} coh(i,j) = \frac{coh(i,j)}{\omega^4} S_{\ddot{u}_g} \tag{5.31}$$

$$S_{u_i\ddot{u}_k} = \frac{1}{\omega^2} S_{\ddot{u}_i}^{1/2} S_{\ddot{u}_k}^{1/2} coh(i,k) = \frac{coh(i,k)}{\omega^2} S_{\ddot{u}_g} \tag{5.32}$$

$$S_{\ddot{u}_k\ddot{u}_l} = S_{\ddot{u}_k}^{1/2} S_{\ddot{u}_l}^{1/2} coh(k,l) = coh(k,l) S_{\ddot{u}_g} \tag{5.33}$$

in which $S_{\ddot{u}_i}$ is the PSDF of ground acceleration at support i; $coh(i,j)$ is the coherence function between the ground motions at supports i and j; $S_{\ddot{u}_g}$ is the PSDF of ground acceleration of the travelling wave train.Various forms of $coh(i,j)$ have been given in Chapter 2. Computation of the elements of the correlation matrix given by Equations 5.28–5.30 requires $S_{\ddot{u}_g}(\omega)$ and a coherence function as evident from Equations 5.31–5.33. Further, in Equation 5.27c, $D_{ij} = D(\omega_j, \xi_j)$, that is, $D_{11} = D_{21} = D_{S1}$, and so on, for a single travelling wave train. For a specified displacement response spectrum, $S_{\ddot{u}_g}(\omega)$ is obtained from Equation 5.16. Therefore, additional input required for the case of multi-support excitation is the coherence function between ground motions at any two supports.

xi. If only the expected peak value of the relative displacement (not the total displacement) is required, then the third term of Equation 5.26 is retained only.

It can be seen from Equations 5.26–5.33 that the determination of the mean peak value of responses by the response spectrum method of analysis for multi-support excitation requires: (i) response spectra of the excitations at the supports (Equation 5.27c) and (ii) correlation matrices $\boldsymbol{\ell_{uu}}$, $\boldsymbol{\ell_{u\bar{z}}}$, and $\boldsymbol{\ell_{\bar{z}\bar{z}}}$, which consider the effect of spatial correlation between the excitations at the supports. For a single component travelling wave train of an earthquake, the above inputs consist of describing a correlation function (such as in Equation 2.93) and the PSDF of ground acceleration. The latter is approximated from the displacement response spectrum of the earthquake by Equations 5.16a and 5.16b. As the approximations involved in describing the PSDF affect only the correlation matrices $\boldsymbol{\ell_{uu}}$, $\boldsymbol{\ell_{u\bar{z}}}$, and $\boldsymbol{\ell_{\bar{z}\bar{z}}}$ (Equations 5.28–5.33), only a slight error is introduced into the computation of the mean peak value of the response from Equation 5.26.

5.4.2 Steps for Developing Program in MATLAB®

1. Matrix $\boldsymbol{r}$ is constructed as given in Section 3.5.7 (part I.1.iv).
2. From the matrix $\boldsymbol{r}$, the vector $\boldsymbol{R}_k (k = 1 \text{ to } s)$ is extracted; in which s is the number of supports.
3. β_{ki} is obtained from Equation 5.19 for $k = 1$ to s, and $i = 1$ to m in which m is the number of modes.
4. $\boldsymbol{\phi}_\beta^T$ and $\boldsymbol{\phi}_{\beta D}^T$ are obtained using Equations 5.24a and 5.27b for a response quantity of interest. $\boldsymbol{\phi}_\beta^T$ and $\boldsymbol{\phi}_{\beta D}^T$ for other response quantities of interest are similarly obtained and stored. Note that $\boldsymbol{\phi}_i$ is obtained by the procedure given in Section 3.5.4.

5. The coefficient vector $\boldsymbol{a}$ is generated for any response quantity of interest following the procedure outlined in Section 3.5.6 (part I.1.vi). $\boldsymbol{a}$ for other response quantities of interest are similarly obtained and stored.
6. The vector $\boldsymbol{b}$ is obtained using Equation 5.27a; u_{p_i} is obtained from Equations 2.19a–2.19c for the PSDF of ground displacement at the support $\left(S_{ug} = S_{\ddot{u}g}/\omega^4\right)$; $S_{\ddot{u}g}$ is obtained using Equation 5.16a for a given displacement response spectrum (derived from the acceleration response spectrum) of an earthquake.
7. The matrices $\ell_{\boldsymbol{uu}}$, $\ell_{\boldsymbol{u\bar{z}}}$, and $\ell_{\bar{z}\bar{z}}$ are determined using Equations 5.28–5.30, which provide the expressions for the elements of the above matrices. Note that h_i is the complex frequency response function for the modal equation given by Equation 5.18, and Equations 5.31–5.33 are used to obtain the expressions for $S_{\ddot{u}i\,\ddot{u}j}$, $S_{u_i\ddot{u}j}$, and $S_{u_iu_j}$. Integrations of Equations 5.28–5.30 are numerically carried out and the cross terms, such as $\ell_{\bar{z}_{kj}u_i}$, are taken as the conjugate of $\ell_{u_i\bar{z}_{kj}}$.
8. The mean peak value of the response is obtained by using Equation 5.26 and step (xi) of Section 5.4.1, if appropriate.

Example 5.4

For the problem in Example 3.8, shown in Figure 3.7, find the mean peak value of the displacements u_1 and u_2 using the response spectrum method of analysis. Take the response spectrum of the El Centro earthquake and assume a time delay between the supports of 5 s. Use the correlation function given by Equation 2.93 and the digitized values of the response spectrum of the El Centro earthquake given in Appendix 5.A.

Solution: An acceleration response spectrum compatible PSDF of the El Centro ground motion is shown in Figure 5.3. This PSDF and the correlation function are used to calculate the correlation matrices $\ell_{\boldsymbol{uu}}$, $\ell_{\boldsymbol{u\bar{z}}}$, and $\ell_{\bar{z}\bar{z}}$. Following steps 1–8 as given above, the quantities required for calculating the expected peak value of the responses are given as below.

$$\boldsymbol{\phi} = \begin{bmatrix} 1 & 1 \\ 0.5 & -1 \end{bmatrix}; \quad \bar{\phi} = \begin{bmatrix} 1 & 1 \\ 0.5 & -1 \end{bmatrix}; \quad r = \frac{1}{3}\begin{bmatrix} 1 & 1 & 1 \\ 1 & 1 & 1 \end{bmatrix};$$

$$w_1 = 12.24 \text{ rad s}^{-1}; \quad w_2 = 24.48 \text{ rad s}^{-1}$$

$$\boldsymbol{a^T} = \frac{1}{3}\begin{bmatrix} 1 & 1 & 1 \\ 1 & 1 & 1 \end{bmatrix}; \quad \boldsymbol{\phi}_\beta^T = \begin{bmatrix} \bar{\varphi}_{11}\beta_{11} & \bar{\varphi}_{11}\beta_{21} & \bar{\varphi}_{11}\beta_{31} & \bar{\varphi}_{12}\beta_{12} & \bar{\varphi}_{12}\beta_{22} & \bar{\varphi}_{12}\beta_{32} \\ \bar{\varphi}_{21}\beta_{11} & \bar{\varphi}_{21}\beta_{21} & \bar{\varphi}_{21}\beta_{31} & \bar{\varphi}_{22}\beta_{12} & \bar{\varphi}_{22}\beta_{22} & \bar{\varphi}_{22}\beta_{32} \end{bmatrix}$$

$$\boldsymbol{\phi}_{\beta D} = \begin{bmatrix} 0.0259 & 0.0259 & 0.0259 & -0.0015 & -0.0015 & -0.0015 \\ 0.0129 & 0.0129 & 0.0129 & 0.0015 & 0.0015 & 0.0015 \end{bmatrix}$$

$$D_{11} = D_{21} = D_{31} = D(\omega_1 = 12.24) = 0.056 \text{ m};$$
$$D_{12} = D_{22} = D_{32} = D(\omega_2 = 24.48) = 0.011 \text{ m}$$

$$coh(i,j) = \begin{bmatrix} 1 & \rho_1 & \rho_2 \\ \rho_1 & 1 & \rho_1 \\ \rho_2 & \rho_1 & 1 \end{bmatrix}; \quad \rho_1 = \exp\left(\frac{-5\omega}{2\pi}\right); \quad \rho_2 = \exp\left(\frac{-10\omega}{2\pi}\right)$$

With the above quantities, the correlation matrices are calculated as follows.

$$\ell_{\boldsymbol{uu}} = \begin{bmatrix} 1 & 0.873 & 0.765 \\ 0.873 & 1 & 0.873 \\ 0.765 & 0.873 & 1 \end{bmatrix};$$

$$\ell_{u\bar{z}} = \begin{bmatrix} 0.0382 & 0.0061 & 0.0027 & 0.0443 & 0.0062 & 0.0029 \\ 0.0063 & 0.0387 & 0.0063 & 0.0068 & 0.0447 & 0.0068 \\ 0.0027 & 0.0063 & 0.0387 & 0.0029 & 0.0068 & 0.0447 \end{bmatrix}$$

and

$$\ell_{\bar{z}\bar{z}} = \begin{bmatrix} 1 & 0.0008 & 0.0001 & 0.0142 & 0.0007 & 0.0001 \\ 0.0008 & 1 & 0.0008 & 0.0007 & 0.0142 & 0.0007 \\ 0.0001 & 0.0008 & 1 & 0.0001 & 0.0007 & 0.0142 \\ 0.0142 & 0.0007 & 0.0001 & 1 & 0.0007 & 0.0001 \\ 0.0007 & 0.0142 & 0.0007 & 0.0007 & 1 & 0.0007 \\ 0.0001 & 0.0007 & 0.0142 & 0.0001 & 0.0007 & 1 \end{bmatrix}$$

Using Equation 5.26, mean peak values of the response quantities are determined. The responses are obtained as:

- Mean peak value of total displacement of $u_1 = 0.106$ m
- Mean peak value of total displacement of $u_2 = 0.099$ m
- Mean peak value of relative displacement of $u_1 = 0.045$ m
- Mean peak value of relative displacement of $u_2 = 0.022$ m

For perfectly correlated ground motion, Equation 5.26 may be used for finding the mean peak value of the response. In that case, ℓ_{uu}, $\ell_{u\bar{z}}$, and $\ell_{\bar{z}\bar{z}}$ matrices only need to be changed in order to make the ground motions the same at all supports and to remove the correlation between any two modes. For the problem above, the matrices take the following values:

$$\ell_{uu} = \begin{bmatrix} 1 & 0 & 0 \\ 0 & 1 & 0 \\ 0 & 0 & 1 \end{bmatrix}; \quad \ell_{u\bar{z}} = \text{null matrix}$$

and

$$\ell_{\bar{z}\bar{z}} = \begin{bmatrix} 1 & 1 & 1 & 0 & 0 & 0 \\ 1 & 1 & 1 & 0 & 0 & 0 \\ 1 & 1 & 1 & 0 & 0 & 0 \\ 0 & 0 & 0 & 1 & 1 & 1 \\ 0 & 0 & 0 & 1 & 1 & 1 \\ 0 & 0 & 0 & 1 & 1 & 1 \end{bmatrix}$$

Using the above correlation matrices, the mean peak values of the relative displacements of u_1 and u_2 are obtained as 0.078 and 0.039 m, respectively. The response spectrum method of analysis for single-support excitation for the same problem provides these responses as 0.079 and 0.041 m, respectively. The time history analysis of the same problem (Example 3.10 without the time lag) gives these values as 0.081 and 0.041 m, respectively.

Example 5.5

Find the values of mean peak displacement and bending moment at the center of the pipeline, shown in Figure 3.15, for the El Centro earthquake. Assume a time lag of 2.5 s between the supports. Use the correlation function given by Equation 2.93 and use the digitized values of the response spectrum of the El Centro earthquake given in Appendix 5.A.

Solution: For the bending moment, the quantities required for the calculation of mean peak values are given below (taken from Example 3.10).

$$\boldsymbol{\phi} = \begin{bmatrix} 0.5 & -1 & 1 \\ 1 & 0 & -0.5 \\ 0.5 & 1 & 1 \end{bmatrix}; \quad \bar{\boldsymbol{\phi}} = \begin{bmatrix} 1 & 0 & -0.5 \\ 8mL & 16mL & -24mL \end{bmatrix}$$

$$\boldsymbol{r} = \begin{bmatrix} 1 & 0.002 & -0.152 \\ -0.026 & 1 & -0.026 \\ -0.152 & 0.002 & 1 \end{bmatrix}; \quad \boldsymbol{C} = \begin{bmatrix} 0.8139 & -0.0361 & 0.0182 \\ -0.0361 & 0.9562 & -0.0361 \\ 0.0182 & -0.0361 & 0.8139 \end{bmatrix} m$$

$$w_1 = 8.1 \text{ rad s}^{-1}; w_2 = 9.8 \text{ rad s}^{-1}; w_3 = 12.2 \text{ rad s}^{-1}$$

$$a^T = \begin{bmatrix} -0.026 & 1 & -0.026 \\ 16.42mL & 0 & 16.42mL \end{bmatrix}$$

m and L are shown in Figure 3.15.

$$\boldsymbol{\phi}_{\beta}^{\boldsymbol{T}} = \begin{bmatrix} \bar{\boldsymbol{\phi}}_{11}\beta_{11} & \bar{\boldsymbol{\phi}}_{11}\beta_{21} & \bar{\boldsymbol{\phi}}_{11}\beta_{31} & \bar{\boldsymbol{\phi}}_{12}\beta_{12} & \bar{\boldsymbol{\phi}}_{12}\beta_{22} & \bar{\boldsymbol{\phi}}_{12}\beta_{32} & \bar{\boldsymbol{\phi}}_{13}\beta_{13} & \bar{\boldsymbol{\phi}}_{13}\beta_{23} & \bar{\boldsymbol{\phi}}_{13}\beta_{33} \\ \bar{\boldsymbol{\phi}}_{21}\beta_{11} & \bar{\boldsymbol{\phi}}_{21}\beta_{21} & \bar{\boldsymbol{\phi}}_{21}\beta_{31} & \bar{\boldsymbol{\phi}}_{22}\beta_{12} & \bar{\boldsymbol{\phi}}_{22}\beta_{22} & \bar{\boldsymbol{\phi}}_{22}\beta_{32} & \bar{\boldsymbol{\phi}}_{23}\beta_{13} & \bar{\boldsymbol{\phi}}_{23}\beta_{23} & \bar{\boldsymbol{\phi}}_{23}\beta_{33} \end{bmatrix}$$

$$\boldsymbol{\phi}_{\beta D}^{\boldsymbol{T}} = \begin{bmatrix} 0.0093 & 0.0501 & 0.0093 & 0 & 0 & 0 & -0.0095 & 0.0109 & -0.0095 \\ 0.0093 & 0.0501 & 0.0093 & -0.0696 & 0 & 0.0696 & -0.0576 & 0.0654 & -0.0576 \end{bmatrix}$$

$$D_{11} = D_{21} = D_{31} = D(\omega_1 = 8.1) = 0.0621 \text{ m};$$
$$D_{12} = D_{22} = D_{32} = D(\omega_2 = 9.8) = 0.0606 \text{ m};$$
$$D_{13} = D_{23} = D_{33} = D(\omega_3 = 12.2) = 0.0548 \text{ m}$$

$$coh(i,j) = \begin{bmatrix} 1 & \rho_1 & \rho_2 \\ \rho_1 & 1 & \rho_1 \\ \rho_2 & \rho_1 & 1 \end{bmatrix}; \quad \rho_1 = \exp\left(\frac{-2.5\omega}{2\pi}\right); \quad \rho_2 = \exp\left(\frac{-5\omega}{2\pi}\right)$$

Because of the soil damping of $C_s = 0.6$ m included in the damping matrix, $\boldsymbol{C}$, $\boldsymbol{\phi}^{\boldsymbol{T}}\boldsymbol{C}\boldsymbol{\phi}$ does not become a diagonal matrix. The modal damping ratios required for performing the response spectrum analysis are approximately determined by ignoring the off-diagonal terms of the $\boldsymbol{\phi}^{\boldsymbol{T}}\boldsymbol{C}\boldsymbol{\phi}$ matrix. The resulting modal damping ratios are calculated as $\xi_1 = 0.0811$, $\xi_2 = 0.0812$, and $\xi_3 = 0.0823$. As there is not much difference between the three, a uniform damping ratio of 0.08 is adopted for all three modes.

With the above quantities, the correlation matrices are calculated as shown below.

$$\boldsymbol{\ell}_{\boldsymbol{uu}} = \begin{bmatrix} 1 & 0.9342 & 0.8735 \\ 0.9342 & 1 & 0.9342 \\ 0.8735 & 0.9342 & 1 \end{bmatrix}$$

$$\boldsymbol{\ell}_{\boldsymbol{u\bar{z}}} = \begin{bmatrix} 0.0562 & 0.0231 & 0.0122 & 0.0451 & 0.0184 & 0.0098 & 0.0442 & 0.0147 & 0.0078 \\ 0.0231 & 0.0562 & 0.0231 & 0.0184 & 0.0451 & 0.0184 & 0.0147 & 0.0442 & 0.0147 \\ 0.0122 & 0.0231 & 0.0562 & 0.0098 & 0.0184 & 0.0451 & 0.0078 & 0.0147 & 0.0442 \end{bmatrix}$$

and

$$\boldsymbol{\ell}_{\boldsymbol{\bar{z}\bar{z}}} = \begin{bmatrix} 1 & 0.0524 & 0.0051 & 0.3913 & 0.0207 & 0.0030 & 0.0746 & 0.0099 & 0.0021 \\ 0.0524 & 1 & 0.0524 & 0.0207 & 0.3913 & 0.0207 & 0.0099 & 0.0746 & 0.0099 \\ 0.0051 & 0.0524 & 1 & 0.0030 & 0.0207 & 0.3913 & 0.0021 & 0.0099 & 0.0746 \\ 0.3913 & 0.0207 & 0.0030 & 1 & 0.0278 & 0.0025 & 0.2895 & 0.0109 & 0.0017 \\ 0.0207 & 0.3913 & 0.0207 & 0.0278 & 1 & 0.0278 & 0.0109 & 0.2895 & 0.0109 \\ 0.0030 & 0.0207 & 0.3913 & 0.0025 & 0.0278 & 1 & 0.0017 & 0.0109 & 0.2895 \\ 0.0746 & 0.0099 & 0.0021 & 0.2895 & 0.0109 & 0.0017 & 1 & 0.0148 & 0.0014 \\ 0.0099 & 0.0746 & 0.0099 & 0.0109 & 0.2895 & 0.0109 & 0.0148 & 1 & 0.0148 \\ 0.0021 & 0.0099 & 0.0746 & 0.0017 & 0.0109 & 0.2895 & 0.0014 & 0.0148 & 1 \end{bmatrix}$$

Using Equation 5.26, the mean peak values of the response quantities are determined. The responses are obtained as:

- Mean peak value of the total displacement at the center = 0.1152 m
- Mean peak value of the bending moment at the center = 3.253 (multiplied by mass m)
- Mean peak value of the relative displacement at the center = 0.055 m

5.5 Cascaded Analysis of Secondary Systems using Response Spectrum Method

Secondary systems are smaller (and lighter) structures attached to the main structure. Examples of secondary systems are the piping systems, mechanical fittings, small towers, and so on, mounted on a main industrial structure. In nuclear and chemical industries, seismic qualification of such secondary systems is of great interest. Therefore, seismic response analysis of such secondary structures is routinely carried out. The seismic analysis of the entire structure including the secondary structures is faced with two major problems, namely, (i) the degrees of freedom become prohibitively large, and (ii) the entire system becomes non-classically damped for which modal analysis or the response spectrum method of analysis cannot be used directly. In order to circumvent these difficulties, cascaded analysis has been introduced and it has become very popular for the seismic analysis of secondary structures (systems). In cascaded analysis, the interaction effect between the secondary and the main structures is ignored. Two systems are analyzed separately. Input for the secondary system is constructed from the response of the main system (analyzed separately). In this regard, the concept of the floor response spectrum is a useful concept for defining the input for the cascaded analysis of the secondary system using the response spectrum method of analysis.

If a secondary system is mounted on the floor of a building, as shown in Figure 5.5a, then the secondary system can be analyzed separately using the response spectrum method of analysis. The input to the

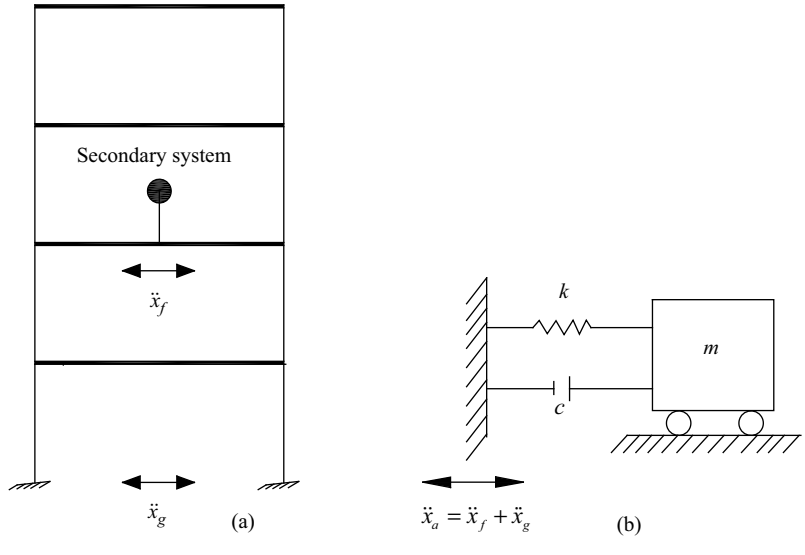

Figure 5.5 Cascaded analysis for a secondary system: (a) secondary system mounted on a floor on a building frame; and (b) SDOF is to be analyzed to obtain floor response spectrum

secondary system is the pseudo acceleration response spectrum of the floor. It is constructed by finding the displacement response of an SDOF attached to the floor to the base motion of the building. If $\ddot{x}_f$ is the acceleration of the floor produced due to the base acceleration, $\ddot{x}_g$, then the absolute acceleration of the floor is obtained as $\ddot{x}_a = \ddot{x}_f + \ddot{x}_g$.

The displacement response of the oscillator is obtained for the support acceleration as $\ddot{x}_a$, shown in Figure 5.5b. From the maximum displacement of the oscillator for varying periods, the pseudo acceleration response spectrum is determined. This is called the floor response spectrum and is used for the response spectrum method of analysis of the secondary system.

Example 5.6

For Example 3.5, find the mean peak displacement of the oscillator for the El Centro earthquake using cascaded analysis. Assume the damping coefficient for the secondary system (oscillator) to be $\xi = 0.02$ and that for the main system (frame) to be 0.05. Compare the result with that of the time history analysis of the total system.

Solution: Figure 5.6 shows the floor displacement response spectrum that is taken as the input for the secondary system (oscillator). The floor displacement response spectrum is obtained by analyzing an SDOF system of varying time period for $\xi = 2\%$, subjected to the time history of absolute acceleration of the floor on which the secondary system is mounted. From the floor displacement response spectrum, the floor acceleration response spectrum can be easily constructed. However, for the present problem, it is easy to obtain the maximum displacement of the secondary system (which is an SDOF system) from the displacement response spectrum itself. Time period of the SDOF is $T = 2\pi/\sqrt{60} = 0.811$ s. From Figure 5.6, the maximum displacement corresponding to $T = 0.811$ s is 0.8635 m.

The maximum displacement of the top mass obtained from the time history analysis of the total system is 0.9163 m, which compares fairly well with the response spectrum method of analysis. Note that the damping matrix for the total system is obtained by assuming Rayleigh damping for the frame (main system) and then, combining the damping of the secondary system with the main system.

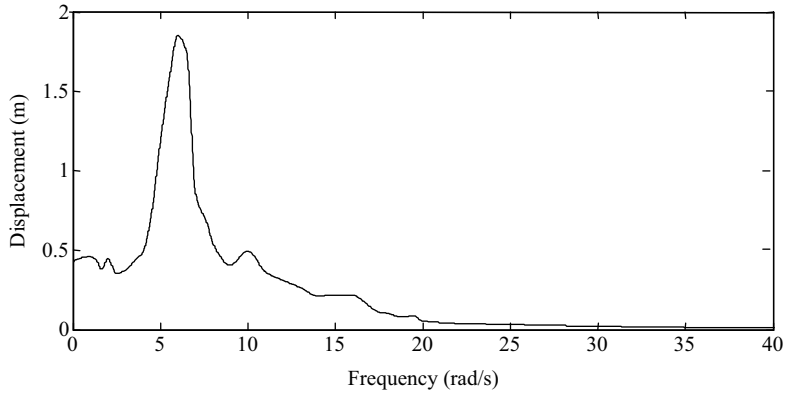

Figure 5.6 Floor displacement response spectrum

5.6 Approximate Modal Response Spectrum Method of Analysis

For secondary systems and other structural systems, where structural components have different types of damping, the response spectrum method of analysis cannot be used directly. However, if different types of damping present in the system are small, an approximate response spectrum method of analysis can be performed. For this, the damping matrix of the entire structural system is derived by assembling damping matrices of the substructures (each substructure has one type of damping only). Note that the coupling terms between the damping matrices of the substructures are assumed to be zero. The overall damping matrix of the system, thus constructed, does not become diagonal under modal transformation, that is, $\boldsymbol{\phi}^T \boldsymbol{C} \boldsymbol{\phi}$ is not a diagonal matrix, in which $\boldsymbol{\phi}$ is the undamped mode shapes of the entire structural system and $\boldsymbol{C}$ is the overall damping matrix. In the approximate modal response spectrum method, the off-diagonal terms of the transformed damping matrix are ignored and an approximate modal damping ratio for each mode of vibration is computed. The response spectrum method of analysis is then carried out as described previously.

5.7 Seismic Coefficient Method

As described in the preceding section, the response spectrum method of analysis allows the designer to use a set of equivalent lateral forces for each mode of vibration and carry out a static analysis to obtain a good estimate of the mean peak response of the structure. The term equivalent lateral load analysis of tall structures, such as buildings, chimneys, towers, and so on, is not only used for the response spectrum method of analysis of structures, but also for another very popular method of analysis called the seismic coefficient method prescribed in different codes. Most of the codes refer to three types of analysis for earthquake forces, namely: (i) Response Spectrum Analysis (RSA), (ii) Response History Analysis (RHA), and (iii) Seismic Coefficient Method of Analysis. In this section, the concept of the seismic coefficient method prescribed in different codes is first presented. Next, the codal provisions given in some of the codes for performing seismic coefficient methods of analysis are discussed. Finally, a comparison of the results of some example problems obtained by the seismic coefficient method, response spectrum method, and time history analysis is shown.

5.7.1 Outline of the Method

The seismic coefficient method obtains a set of equivalent lateral forces for an earthquake using some empirical formulae for a ground supported structure and analyzes it to find the seismic forces induced in the members of the structure. In this method, the total weight of the structure is multiplied by a coefficient, known as the seismic coefficient, to obtain the total base shear of the structure that is distributed as a set of lateral forces along the height of the structure. This distribution of lateral force bears a resemblance (but not the same) with that for the fundamental mode of the structure in RSA. It is obtained by an empirical formula that varies from code to code. The method of analysis consists of the following steps.

(i) Maximum base shear is obtained as:

$$V_b = W \times C_h \tag{5.34}$$

in which, W is the total weight of the building; C_h is a seismic coefficient that depends on the fundamental time period of the structure.

(ii) The lateral load along the height of the structure is distributed such that the sum of the lateral loads is equal to the base shear V_b.

Thus,

$$F_i = V_\mathrm{b} \times f(h_i) \tag{5.35}$$

where, F_i is the lateral load corresponding to the ith lateral displacement degree of freedom of the structure and h_i is the height of the point of application of the lateral load above the ground.

(iii) Static analysis of the structure for the lateral forces F_i (*1 to n*) is carried out to find the response quantities of interest.

Different codes of practice have different provisions for the value of the seismic coefficient C_h and the distribution of the lateral load along the height of the structure. Furthermore, the fundamental time period of the structure, especially for buildings, is computed using some empirical formulae, which are derived from prototype measurements/experimental work/approximate analysis. Variation of the seismic coefficient C_h with the time period, T, follows a shape close to the design response spectrum prescribed in the codes.

Although a perfect inter-relationship does not exist between the earthquake structural dynamics and the development of the seismic coefficient method, an approximate relationship can be shown to exist between the two in terms of the computation of the fundamental time period, T, distribution of the lateral forces along the height of the structure, and the computation of the base shear. The approximate relationships are described in the following sections.

5.7.2 Distribution of Lateral Forces

According to the response spectrum method of analysis, the lateral force, F_j, for the jth floor, for first mode of vibration is given by (Equation 5.9):

$$F_j = \lambda_1 \times W_j \times \phi_{j1} \times \frac{S_{a1}}{g} \tag{5.36}$$

From Equation 5.36, it is possible to write

$$\frac{F_j}{\Sigma F_j} = \frac{W_j \times \phi_{j1}}{\Sigma W_j \times \phi_{j1}} \tag{5.37}$$

As $\Sigma F_j = V_b$, F_j may be written as:

$$F_j = V_b \times \frac{W_j \times \phi_{j1}}{\Sigma W_j \times \phi_{j1}} \tag{5.38}$$

If the fundamental mode shape of the building is assumed to be linear, the above equation simplifies to:

$$F_j = V_b \frac{W_j \times h_j}{\Sigma W_j \times h_j} \tag{5.39}$$

in which h_j is the height of the jth floor.

Although the fundamental mode shape is not linear, the above equation may be modified to take the non-linearity into account by writing

$$F_j = V_b \frac{W_j \times h_j^{\,k}}{\Sigma W_j \times h_j^{\,k}} \tag{5.40}$$

in which $k > 1$, for $k = 2$, the fundamental mode shape varies quadratically along the height. Some codes prescribe the variation of the lateral force as a combination of the above two equations. Thus, it is apparent that the seismic co-efficient method of analysis considers only the contribution of the fundamental mode of vibration of the structure in an approximate way.

5.7.3 Computation of the Fundamental Time Period

Most of the codes provide an empirical formula for finding the fundamental time period of the buildings based on experimental and practical observations. However, some of the codes, such as the International

Building Code, USA, and the National Building Code, Canada, allow calculation of the fundamental time period of buildings using a formula which is almost the same as that used for calculating the approximate fundamental time period of a building frame using Rayleigh's method [6].

5.7.4 Computation of the Base Shear

According to the response spectrum method of analysis, the base shear in the ith mode is given by:

$$V_{b_i} = \Sigma F_{ji} = \left(\Sigma W_j \times \phi_{ji} \times \frac{S_{a_i}}{g}\right) \times \lambda_i \tag{5.41}$$

As $W_i^e = \lambda_i \times \Sigma W_j \times \phi_{ji}$, the ith effective weight of the structure (that is, effective weight of the building in the ith mode), V_{b_i} may be written as:

$$V_{b_i} = W_i^e \frac{S_{a_i}}{g} \tag{5.42}$$

Instead of using the SRSS combination rule, if the absolute sum of the response is used to find an upper bound to the response quantity of interest, then

$$V_b \leq \Sigma|(V_b)| \tag{5.43}$$

$$\leq \Sigma \frac{S_{a_i}}{g} W_i^e \quad (i = 1 \text{ to } n) \tag{5.44}$$

If it is assumed that S_{ai}/g for all modes are the same, and is equal to S_{a1}/g, then an upper bound estimate of the base shear is given as:

$$V_b = \frac{S_{a1}}{g} \times W \tag{5.45}$$

The base shear computed by the seismic coefficient method uses a similar formula, with S_{a1}/g replaced by C_h. Thus, the seismic coefficient method is expected to provide a conservative estimate of the base shear.

5.8 Comparison of Some Code Provisions Prescribed by Different Earthquake Codes

Almost all countries have their own codes for seismic analysis and design of structures. It is difficult to compare all of them. In this section, a comparison between the code provisions for the seismic base shear coefficient, calculation of the fundamental time period of buildings, distribution of the lateral force along the height, and the design response spectra given by the following codes is made in order to demonstrate the type of variations that exist between the codes.

1. International Building Code, IBC – 2000 [7]
2. National Building Code of Canada, NBCC – 1995 [8]
3. Euro Code 8 – 1995 [9]
4. New Zealand Code, NZS 4203 – 1992 [10]
5. Indian Code, IS 1893 – 2002 [11]

The codes under consideration prescribe all three types of analysis, namely: the seismic coefficient method, the response spectrum method of analysis, and response time history analysis. The three methods of analysis require three different types of input. The seismic coefficient method requires seismic coefficient C_h for different values of the time period, T. The response spectrum method requires the

pseudo acceleration response spectrum. The time history analysis requires a suitable time history of the ground acceleration. The codes provide design response spectra (either actual or normalized) and a curve showing the variation of C_h with T. No specified time history of ground acceleration as such is provided by any code. However, depending upon the requirement, the codes recommend considering any appropriate time history of ground acceleration for the time history analysis. In the absence of any such recommendation, the design response spectrum compatible time history should be used for the time history analysis.

Apart from the specification of the design response spectrum and the seismic coefficient, the codes specify a few other recommendations in relation to the three analyses mentioned above. They are: (i) effect of soil conditions; (ii) seismicity of a region; and (iii) reduction factor for the seismic design force. The details of these factors are not covered here. The following brief outlines only are provided.

Effect of Soil Conditions As mentioned before, the local soil conditions modify the ground motion significantly. This is included in the response spectrum or the seismic coefficient in a variety of ways in different codes. Some codes specify different response spectrums for different soil conditions, while others use multiplication factors to include this effect.

Seismicity of the Region Different regions are characterized by different PGAs. Therefore, normalized response spectrums are generally preferred so that regional variation of the PGA may be accounted for by multiplying the normalized spectrum by the appropriate value of the PGA. Some codes recommend multiplication of a specified response spectrum by multiplication factors to incorporate the regional seismicity differences. In addition, multiplication factors are used to differentiate between design basis and maximum credible earthquake spectra.

Reduction Factor A design seismic force for which the structure is analyzed is always less than the actual seismic force. The philosophy behind this is to allow the structure to undergo inelastic excursion under the design earthquake for an economic design. It also allows energy dissipation to take place due to hysteretic behavior of the material during inelastic excursion, thereby helping to limit the displacement. In order to realize the effect, the calculated seismic force by the seismic coefficient method or the response spectrum method is multiplied by a reduction factor. Different codes recommend different reduction factors for different types of structures.

5.8.1 International Building Code (2000)

Variation of C_h with T is given for different site classes such as A, B, C, D, E, and F. For the design basis earthquake for site class B, the value of C_h is given as:

$$C_h = \begin{cases} 1.0 & T_1 \leq 0.4 \text{ s} \\ \dfrac{0.4}{T_1} & T_1 \geq 0.4 \text{ s} \end{cases} \tag{5.46}$$

For the same site, the design response spectrum is given by:

$$\frac{A}{g} = \begin{cases} 0.4 + 7.5T_n & 0 \leq T_n \leq 0.08 \text{ s} \\ 1.0 & 0.08 \leq T_n \leq 0.4 \text{ s} \\ \dfrac{0.4}{T_n} & T_n > 0.4 \text{ s} \end{cases} \tag{5.47}$$

The plots of the variations of C_h and A/g with T are shown in Figure 5.7. It is seen from the figure that except for the initial part, the shapes of the two are exactly the same. Furthermore, for almost rigid structures, the seismic coefficient method recommends acceleration values of 0.5–1g to be multiplied with

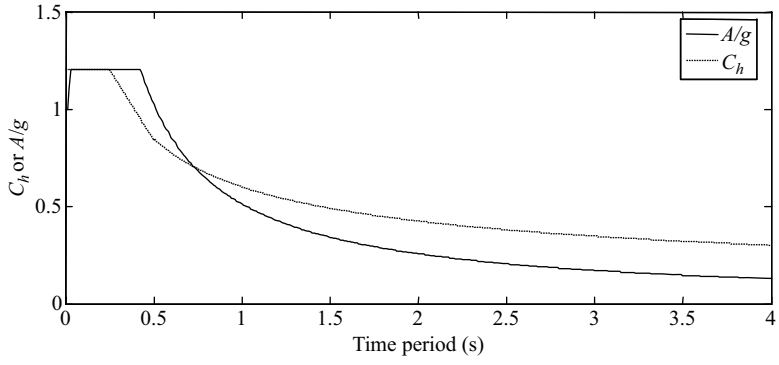

Figure 5.7 Variation of C_h and A/g with time period T

the total mass of the structure to obtain the base shear. For 1–4 storey buildings, the acceleration value is taken to be nearly 1g.

The fundamental natural period of vibration may be computed by the formula:

$$T_1 = 2\pi \left[\frac{\sum_{i=1}^{N} W_i u_i^2}{g \sum_{i=1}^{N} F_i u_i} \right] \tag{5.48}$$

where

W_i is the weight of the ith floor
u_i are the displacements due to static application of a set of lateral forces F_i at floor levels
N is the number of storey.

The distribution of F_i along the height could be any reasonable distribution, not necessarily the same given in the code. The code also provides an alternative empirical formula for calculating the time period.

The distribution of the lateral forces over the height of the building is given as:

$$F_i = V_\mathrm{b} \frac{W_j h_j^k}{\sum_{j=1}^{N} W_j h_j^k} \tag{5.49}$$

in which V_b is the base shear; h_j is the height of the jth storey from the base and k is a coefficient given as:

$$k = \begin{cases} 1 & T_1 \leq 0.5 \text{ s} \\ 0.5(T_1 + 1.5) & 0.5 \leq T_1 \leq 2.5 \text{ s} \\ 2 & T_1 \geq 2.5 \text{ s} \end{cases} \tag{5.50}$$

Using the base shear approach recommended by IBC, the distributions of the lateral forces along the height of a nine-storey frame are determined by Equations 5.49 and 5.50 for time periods corresponding to 0.4, 1, and 2 s. The distributions are shown in Figure 5.8. It is seen from the figure that there is kink in the curve at the eighth floor level. The reason for this is attributed to the sudden reduction in the weight of ninth floor to half the value of the other floors.

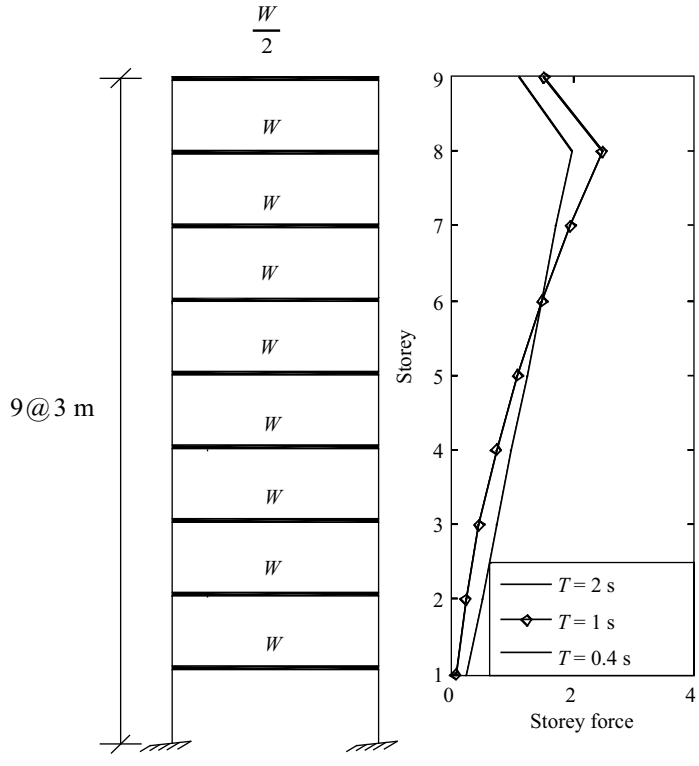

Figure 5.8 Distribution of lateral force along a nine-story building frame

5.8.2 *National Building Code of Canada (1995)*

The seismic coefficient is given by:

$$C_h = \frac{C_e U}{R} \tag{5.51a}$$

$$C_e = U\,\mathrm{SIF} \tag{5.51b}$$

where

C_e is the basic seismic coefficient zone velocity ratio
I and F are importance and foundation factors, respectively
S is the seismic response factor.

S is different for the acceleration related seismic zone (Z_a) and velocity related seismic zone (Z_v). The country is divided into seven zones based on the above two criteria. Figure 5.9 shows the variation of S with T as given in the code.

For $v = 0.4$, I and $F = 1$ and $Z_a = Z_v$, the variations of S and A/g with T are compared in Figure 5.10. Note that $v = 0.4$ corresponds to a peak ground velocity of $0.4\,\mathrm{m\,s^{-1}}$ for which a pseudo acceleration

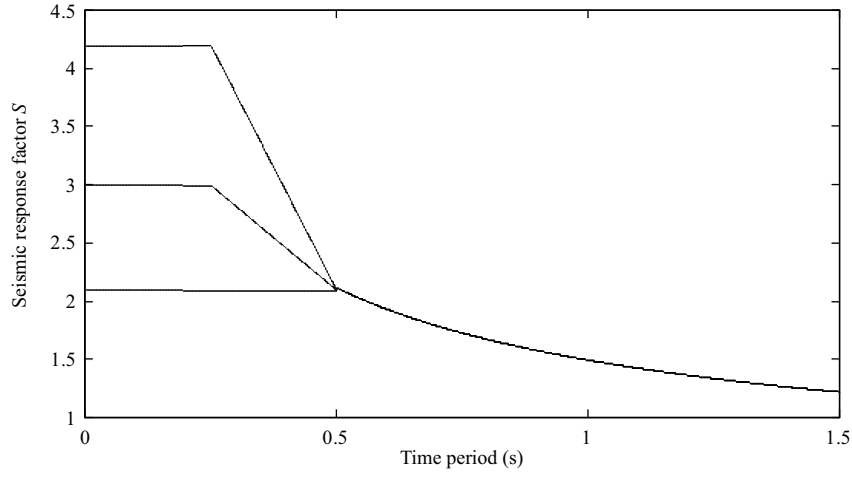

Figure 5.9 Variations of the coefficient S with time period T

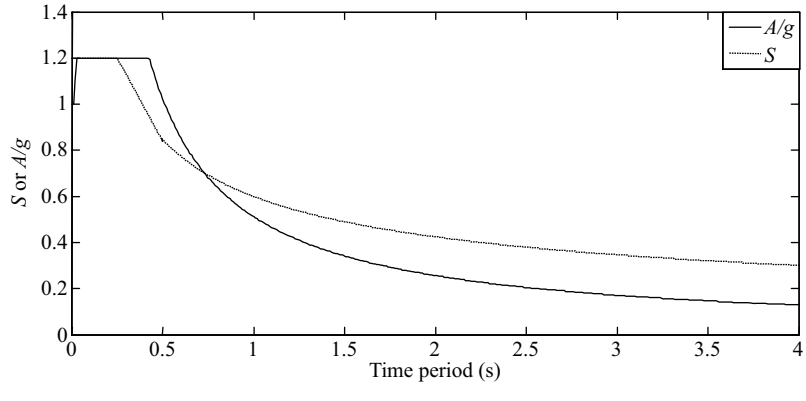

Figure 5.10 Variations of S and A/g with time period T

spectrum (A/g) is drawn. The expression for A/g is given as:

$$\frac{A}{g} = \begin{cases} 1.2 & 0.03 \leq T_{\mathrm{n}} \leq 0.427 \text{ s} \\ \dfrac{0.512}{T_{\mathrm{n}}} & T_{\mathrm{n}} > 0.427 \text{ s} \end{cases} \tag{5.52}$$

In addition to empirical formulae for finding the natural period of vibration of the buildings, the code provides the following formula (similar to Equation 5.49) for estimating the natural period:

$$T_1 = 2\pi \left[\frac{\Sigma_1^N F_i u_i^2}{g \Sigma_1^N F_i u_i} \right]^{1/2} \tag{5.53}$$

in which F_i are the set of lateral forces applied at the floor levels and u_i are the corresponding floor displacements (similar to Equation 5.48).

Unlike the International Building Code, the basic seismic coefficient C_e and A/g differ for most of the time periods. The response spectrum method takes less acceleration value to compute the seismic force for taller buildings (>8 storeys).

The distribution of lateral forces over the height of the building is given by:

$$F_i = (V_b - F_t)\frac{W_i h_i}{\sum_{i=1}^{N} W_i h_i} \tag{5.54}$$

in which F_i is the additional top force applied to the top floor (over and above that calculated by Equation 5.54

$$F_t = \begin{cases} 0 & T_1 \le 0.7 \text{ s} \\ 0.07 T_1 V_b & 0.7 < T_1 < 3.6 \text{ s} \\ 0.25 V_b & T_1 \ge 3.6 \text{ s} \end{cases} \tag{5.55}$$

5.8.3 Euro Code 8 (1995)

The seismic coefficient for base shear is calculated by

$$C_s = \frac{C_e}{q'} \tag{5.56}$$

in which q' is the reduction factor and C_e is expressed as:

$$C_e = \begin{cases} \dfrac{A}{g} & 0 \le T_1 \le T_c \\ \dfrac{A}{g}\left(\dfrac{T_c}{T_1}\right)^{-\frac{1}{3}} & T_1 \ge T_c \end{cases} \tag{5.57}$$

in which T_1 is the fundamental period of the building, T_c is the period at the end of the constant pseudo acceleration region, and A is the pseudo acceleration design spectrum given in the normalized form as:

$$\frac{A}{\ddot{u}_{g_0}} = \begin{cases} 1 + 1.5\dfrac{T_n}{T_b} & 0 \le T_n \le T_b \\ 2.5 & T_b \le T_n \le T_c \\ 2.5\left(\dfrac{T_c}{T_n}\right) & T_c \le T_n \le T_d \\ 2.5\dfrac{T_c T_d}{T_n^2} & T_n \ge T_d \end{cases} \tag{5.58}$$

in which T_n is natural period of an SDOF system; T_b, T_c and T_d denote the period at the beginning of the constant pseudo acceleration, constant pseudo velocity, and constant displacement regions, respectively, of the design spectrum. These period values (T_b, T_c, T_d) for hard, medium, and soft soil conditions are given as: (0.1, 0.4, 3.0) s for the hard soil; (0.15, 0.6, 3.0) s for the medium soil; and (0.2, 0.8, 3.0) s for the soft soil. For soft soil, $A/\ddot{u}_{g_0}$ values given by Equation 5.58 are multiplied by 0.9. The variations $C_e/\ddot{u}_{g_0}$ and $A/\ddot{u}_{g_0}$ with T_1 or T_n are shown in Figure 5.11.

In addition to empirical formulae given for estimating the natural period of the buildings, the code permits the use of Rayleigh's method for the calculation of T_1.

The formula for lateral force F_i is given by:

$$F_i = V_b \frac{W_i \phi_{i1}}{\sum_{i=1}^{N} W_i \phi_{i1}} \tag{5.59}$$

in which ϕ_{i1} is the mode shape coefficient of the ith floor in the first mode. The code also permits the following formula to be used:

$$F_i = V_b \frac{W_i h_i}{\sum_{i=1}^{N} W_i h_i} \tag{5.60}$$

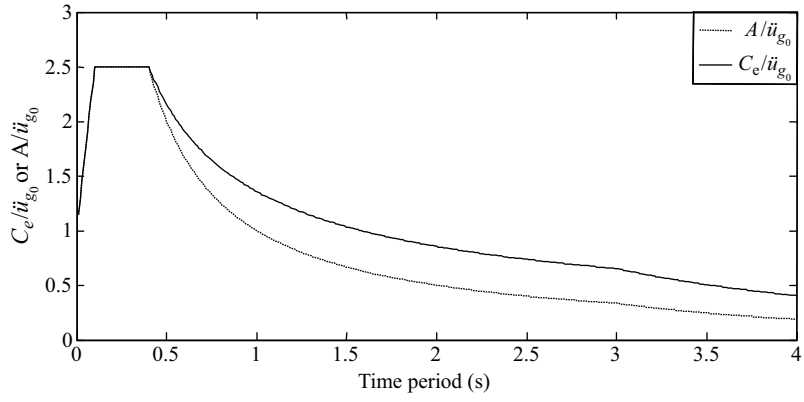

Figure 5.11 Variations of $C_e/\ddot{u}_{g_0}$ and $A/\ddot{u}_{g_0}$ with time period T

5.8.4 New Zealand Code (NZ 4203:1992)

The seismic coefficient and design response curves are the same and are given for different values of the ductility factor. Seismic design forces are calculated for serviceability limit and ultimate load state. The basic acceleration coefficient $C_b(T, \mu)$ is specified for three soil conditions, that is, stiff soil, medium soil, and soft soil. For the serviceability limit, the seismic coefficient is given by:

$$C(T) = C_b(T_1, 1)RzL_s \quad T_1 \geq 0.45 \text{ s} \tag{5.61a}$$

$$= C_b(0.4, 1)RzL_s \quad T_1 \leq 0.45 \text{ s} \tag{5.61b}$$

in which R is the risk factor, z is the zone factor, and L_s is the limit state factor, all given in the code. For the response spectrum method of analysis, T_1 is replaced by T in Equation 5.61a.

The fundamental time period of the structure is computed using Rayleigh's method (Equation 5.48) or from experimental data. The lateral load at each storey level is determined using the same equation as Equation 5.60 multiplied by a factor 0.92. The plot of the variation of C_b with T is shown in Figure 5.12 for $\mu = 1$. Categories 1,2 and 3 denote soft, medium and hard soils respectively.

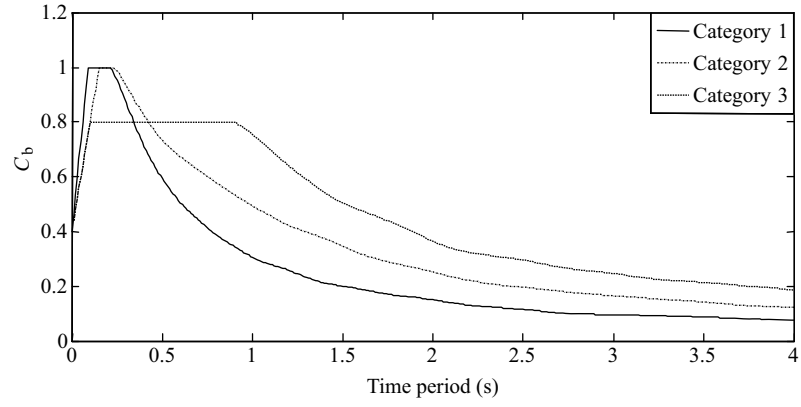

Figure 5.12 Variations of C_b with time period T

5.8.5 Indian Code (IS 1893–2002)

The seismic coefficient for base shear is obtained from the design response spectrum curve, that is, the variation of C_e with T is taken to be the same as that of S_a/g with T. The variation of S_a/g with T is given by:

$$\frac{S_a}{g} = \begin{cases} 1 + 15T & 0 \le T \le 0.1\,\text{s} \\ 2.5 & 0.1 \le T \le 0.4\,\text{s} \\ \dfrac{1}{T} & 0.4 \le T \le 4.0\,\text{s} \end{cases} \quad \text{for hard soil} \tag{5.62}$$

$$\frac{S_a}{g} = \begin{cases} 1 + 15T & 0 \le T \le 0.1\,\text{s} \\ 2.5 & 0.1 \le T \le 0.55\,\text{s} \\ \dfrac{1.36}{T} & 0.55 \le T \le 4.0\,\text{s} \end{cases} \quad \text{for medium soil} \tag{5.63}$$

$$\frac{S_a}{g} = \begin{cases} 1 + 15T & 0 \le T \le 0.1\,\text{s} \\ 2.5 & 0.1 \le T \le 0.67\,\text{s} \\ \dfrac{1.67}{T} & 0.67 \le T \le 4.0\,\text{s} \end{cases} \quad \text{for soft soil} \tag{5.64}$$

The variation of normalized pseudo acceleration, S_a/g with T is shown in Figure 5.13.

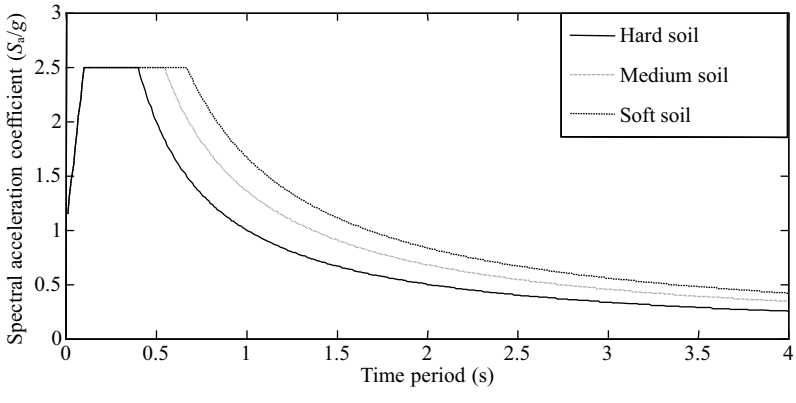

Figure 5.13 Variations of S_a/g with time period T

The fundamental time period of the buildings are obtained by empirical formulae given in the code. The base shear is distributed along the height of the building using a quadratic variation given by:

$$F_j = V_b \frac{W_j h_j^2}{\sum_{j=1}^{N} W_j h_j^2} \tag{5.65}$$

Example 5.7

For the seven-storey frame shown in Figure 5.14, compare the base shears and storey displacements obtained by IBC, NBCC, Euro Code 8, New Zealand Code and Indian Code using the response spectrum method of analysis. Take the contributions of: (i) the first three modes only, and (ii) all modes. Use both SRSS and CQC rules of combination of modal responses.

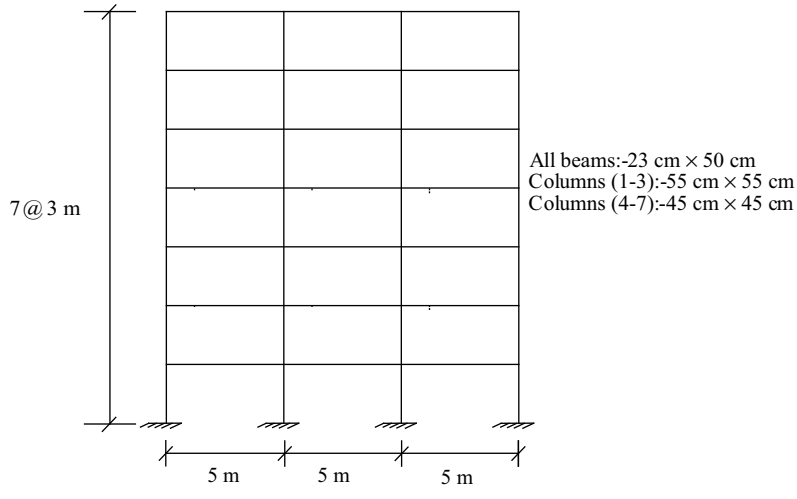

Figure 5.14 A seven-storey building frame for analysis

Solution: In order to maintain the uniformity, all multiplying factors such as importance factor and foundation factor are assumed to be unity. Furthermore, the reduction factor of $R = 3$ is considered, and the maximum value of the spectral acceleration normalized with respect to g is taken as unity for the response spectra given by different codes. This provides a uniform PGA value for different codes under consideration to be 0.4g except the Canadian Code whose PGA turns out to be around 0.65g. The spectral accelerations are considered for the medium soil conditions (not hard rock). Dead load for the beams and columns are obtained by assuming the density of the concrete to be 24 kN m^{-3}; E value of the concrete is assumed to be 2.5×10^7 kN m^{-2}. The effective live loads on the beams are taken as 1.4 kN m^{-1}. For the top three beams, 25% of the live load and for the rest of the beams, 50% of the live load are considered for computing the mass matrix of the structure. The first three time periods of the structure are determined as $T_1 = 0.753$ s, $T_2 = 0.229$ s and $T_3 = 0.111$ s.

It is seen that the first period of the structure is within the range of the falling portion of the spectral acceleration curve. Although the maximum acceleration value is made the same for all codes under comparison, the response spectrum curves are different in different codes in the falling range. As a result spectral accelerations corresponding to the first period of the structure are found to be different for different codes. As the contribution of the first mode predominantly governs the responses, it is expected that differences in the responses obtained by different codes will be different. The results of the analysis are compared in Table 5.3.

Table 5.3 Comparison of results obtained by different codes

Code	Base shear (kN)				First storey displacement (mm)				Top storey displacement (mm)			
	SRSS		CQC		SRSS		CQC		SRSS		CQC	
	3	All	3	All	3	All	3	All	3	All	3	All
IBC	33.51	33.66	33.52	33.68	0.74	0.74	0.74	0.74	10.64	10.64	10.64	10.64
NBCC	35.46	35.66	35.46	35.68	0.78	0.78	0.78	0.78	11.35	11.35	11.35	11.35
NZ 4203	37.18	37.26	37.2	37.29	0.83	0.83	0.83	0.83	12.00	12.00	12.00	12.00
Euro 8	48.34	48.41	48.35	48.42	1.09	1.09	1.09	1.09	15.94	15.94	15.94	15.94
Indian	44.19	44.28	44.21	44.29	0.99	0.99	0.99	0.99	14.45	14.45	14.45	14.45

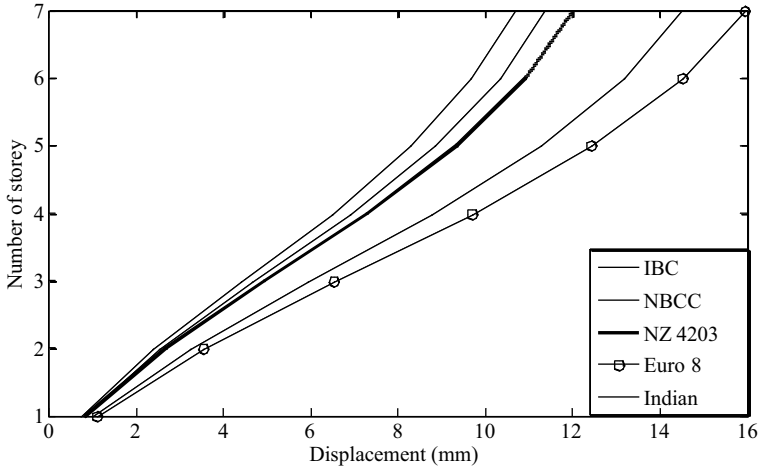

Figure 5.15 Comparison between the storey displacements obtained by different codes

The table shows that the values computed by both SRSS and CQC rules of combination are nearly the same. This is the case because the time periods are widely spaced. Furthermore, it is observed that considering the first three modes provides almost the same responses as those obtained by considering all modes, that is, the contributions of the higher modes are insignificant.

From the table, it is seen that the responses obtained by the Euro Code 8 and the Indian Code are comparable and are greater than those obtained by other codes. The results for IBC and NBCC are again fairly comparable. The New Zealand Code provides higher responses compared with the IBC and NBCC Codes, but are less than those obtained by the Euro Code 8 and the Indian Code. It is interesting to note that the PGA value for the New Zealand Code is higher than the Euro Code 8 and the Indian Code, but the computed responses are still lower than those of the latter. This is the case because the spectral acceleration curve falls more sharply in the falling portion for the New Zealand Code. Figure 5.15 compares the storey displacements obtained by different codes. The figure shows that the storey displacements obtained by different codes vary in a similar way to those observed for other responses (Table 5.3).

Exercise Problems

(Use standard programs like MATLAB®, SAP2000 and ABAQUAS to solve the problems; you may also use your own program developed using the methods presented in the chapter.)

5.8 For the stick model of a building, shown in Figure 3.24, find the mean peak values of the base shear, base moment, and top displacement for the 5% response spectrum of El Centro earthquake. Take the response spectrum for the rotational component of ground motion as $\frac{1}{10}$th of the translational ground motion.

5.9 For the shear frame, shown in Figure 3.29, find the mean peak values of base shear, top displacement, inter-storey drift between the first and second floors, and column moments at the base considering contributions from three modes only and all six modes. Use SRSS, ABSSUM, and CQC rules of combinations and compare the results. Use a 5% response spectrum of the El Centro earthquake as the basic input ground motion. Also, compare the results with those of the time history analysis.

5.10 For the 3D frame, shown in Figure 3.30, find the mean peak values of base shear, top floor displacements, and moments at the base of column A. Take normalized design response spectrum given in IBC (2000) for $\xi = 5\%$ and assume that the angle of incidence of the earthquake is 30° with

the x-axis. Compare the results with those obtained for zero angle of incidence. Use the CQC rule of combination.

5.11 For the simplified model of a cable stayed bridge, shown in Figure 3.28, obtain the mean peak values of the vertical displacement of the center of the deck, base moments of the piers, and the axial forces in the central cables. Assume the time lag between the supports as 5 s, the El Centro earthquake spectrum ($\xi = 5\%$) as seismic input, and correlation function given by Equation 2.93 to be valid. Compare the results with those of the time history analysis.

5.12 For the pipeline, shown in Figure 3.15, find the mean peak values of displacements of the supports for the El Centro earthquake response spectrum. Assume the time lag between supports as 5 s and use Equation 2.93 as the correlation function. Compare the results with those of the time history analysis.

5.13 For the frame with a secondary system, shown in Figure 3.26, find the mean peak value of the displacement of the secondary system by cascaded analysis. Take the El Centro earthquake response spectrum as input excitation with a time lag of 5 s between two supports, and 5 and 2% dampings for primary and secondary systems, respectively. Compare the results with those of the time history analysis.

5.14 For the same secondary system, as above, find the mean peak value of the displacement of the secondary system using an approximate modal response spectrum analysis. Use the El Centro earthquake response spectrum. Compare the results with those of the time history analysis.

5.15 For the frame, shown in Figure 3.27, find the base shear, top-storey displacement, and storey drift between the second and first floor by the seismic coefficient method of analysis using the recommendations of IBC (2000), NBCC (1995), IS1893 (2002), NZ 4203 (1992), and Euro 8. Take $R = 1$, hard soil, and PGA $= 0.2$g.

5.16 For the frame, shown in Figure 3.29, find the mean peak values of the base shear, top-storey displacement, and moments at the bottom of the second storey using the response spectrum method of analysis. Compare the results between those obtained by using the above five codes. Take $R = 1$, hard soil, and PGA $= 0.2$g. In addition, compare the results with those obtained by the seismic coefficient method.

Appendix 5.A Digitized Values of the Acceleration Response Spectrum of El Centro Earthquake

Table 5.4 provides digitized values of the response spectrum of El Centro earthquake.

Table 5.4 Digitized values of the acceleration response spectrum (g) of the El Centro earthquake ($\xi = 5\%$) record given in Appendix 3.C at a time period interval of 0.02 s (read row wise)

0.3128	0.3163	0.3203	0.4945	0.5896	0.6391	0.7502	0.6545
0.7759	0.8677	0.804	0.5864	0.6949	0.8939	0.8041	0.749
0.7797	0.7684	0.7268	0.7243	0.7483	0.781	0.8084	0.825
0.8779	0.9054	0.9025	0.8689	0.8071	0.787	0.7545	0.713
0.6662	0.6171	0.5677	0.5191	0.4733	0.4468	0.4251	0.4454
0.4899	0.5358	0.5678	0.5779	0.5647	0.5275	0.4929	0.498
0.4924	0.4755	0.447	0.4218	0.4039	0.3804	0.3526	0.3226
0.292	0.2672	0.2516	0.2521	0.2541	0.2502	0.2421	0.2317
0.2205	0.2097	0.1997	0.1916	0.1854	0.1814	0.1799	0.1801
0.1814	0.1831	0.1849	0.1863	0.1869	0.1866	0.1856	0.1838
0.1812	0.1775	0.1732	0.1684	0.1631	0.1597	0.1557	0.1501
0.1471	0.1492	0.1501	0.1533	0.1546	0.1544	0.1529	0.1503
0.1467	0.1419	0.1369	0.1351	0.1355	0.1384	0.1414	0.1446
0.1477	0.1507	0.1537	0.1565	0.1589	0.1612	0.1633	0.1651
0.1666	0.1679	0.169	0.1697	0.17	0.1699	0.1696	0.1716
0.1732	0.1745	0.1755	0.1762	0.1765	0.1765	0.1763	0.1757
0.1748	0.1737	0.1722	0.1704	0.1685	0.1663	0.1641	0.1616

(*continued*)

Table 5.4 (*Continued*)

0.1591	0.1567	0.1543	0.1533	0.1525	0.1509	0.1484	0.1451
0.1411	0.1362	0.132	0.129	0.1263	0.1236	0.121	0.1184
0.1158	0.1132	0.1108	0.1085	0.1084	0.1082	0.1081	0.1078
0.1074	0.1069	0.1063	0.1057	0.105	0.1043	0.1035	0.1026
0.1017	0.1007	0.0998	0.0987	0.0977	0.0967	0.0957	0.0948
0.0937	0.0927	0.0916	0.0905	0.0894	0.0883	0.0871	0.0859
0.0847	0.0835	0.0823	0.0811	0.0798	0.0785	0.0773	0.076
0.0747	0.0734	0.0721	0.0708	0.0696	0.0683	0.067	0.0657

References

1. Rosenblueth, E. and Elordy, J. (1969) Response of linear systems to certain transient disturbances. Proceedings of 4th World Conference on Earthquake Engineering, Santiago, Chile, vol. 1.
2. Der Kiureghian, A. (1981) A response spectrum method for random vibration analysis of MDF system. *Earthquake Engineering and Structural Dynamics*, **9**, 419–435.
3. Der Kiureghian, A. and Neuenhofer, A. (1992) Response spectrum method for multi-support seismic excitations. *Earthquake Engineering and Structural Dynamics*, **21**, 713–740.
4. Der Kiureghian, A. (1980) Structural response to stationary excitation. *Journal of Engineering Mechanics, ASCE*, **106**, 1195–1213.
5. Davenport, A.G. (1984) The distribution of largest values of random function with application to gust loading. *Journal of Engineering Mechanics, ASCE*, **28**(4), 187–196.
6. Chopra, A.K. (2001) *Dynamics of Structures, Theory and Application to Earthquake Engineering*, 2nd edn, Prentice Hall, Inc., Englewood Cliffs, NJ, p. 334.
7. International Code Council (2000) International Building Code, Falls Church, VA.
8. Associate Committee on National Building Code (1995) National Building Code of Canada 1995, National Research Council, Ottawa.
9. International Association of Earthquake Engineering (1996) *EUROCODE 8 in Earthquake Resistant Regulation, A World List*, International Association of Earthquake Engineering, Tokyo.
10. New Zealand Code (1992) NZS 4203-1992, Department of Building and Housing, Wellington, New Zealand.
11. Indian Standard (2002) IS 1893-2002 *Criteria for Earthquake Resistant Design of Structures*, Bureau of Indian Standards, New Delhi.

6

Inelastic Seismic Response of Structures

6.1 Introduction

A single degree of freedom system may undergo an inelastic excursion when subjected to a strong support motion such as that produced by severe earthquakes. The inelastic excursion takes place when the restoring force in the spring exceeds or is equal to the yield limit of the spring. For structural systems, it means that the internal stress induced in the material exceeds or is equal to the yield stress of the material. In the earthquake resistant design of structures, the current design philosophy is to design the structures for forces that are much lower than the expected design earthquake forces, so that the structures undergo inelastic deformation and damage under strong earthquakes without collapse. In order to allow the structures to deform sufficiently in the inelastic range, the structural system should have sufficient ductility, which is provided by the reinforcing steel in the case of reinforced concrete structures. In order to properly understand the ductility demand imposed by an earthquake on to a structural system, a study of the inelastic behavior of an SDOF system under earthquake excitation is of great help. For this purpose, the time history analysis of an SDOF system having a non-linear restoring action is required. Similarly, to understand the inelastic behavior of MDOF systems under earthquake forces, non-linear analysis of the MDOF system becomes necessary. Furthermore, non-linear analysis of structures for earthquake forces is required for many other reasons such as the determination of collapse state of structures, seismic risk analysis, and so on. In this chapter, these topics, that is, inelastic seismic response analysis of SDOF and MDOF systems, equivalent non-linear static analysis of MDOF system, and the concepts of ductility and an inelastic response spectrum are presented.

6.2 Non-Linear Analysis of Structures for Earthquake Forces

A number of methods for the linear analysis of structures for earthquake forces have been discussed in the previous chapters. These linear analyses pertain to structural systems which have linear inertia, damping and restoring forces. Whenever the structural system has any or all of the three reactive forces having non-linear variation with the response parameters (that is, displacement, velocity, and acceleration), a set of non-linear differential equations are evolved and need to be solved. The most common non-linearities among the three are the stiffness and the damping non-linearities. In the stiffness non-linearity, two types of non-linearity may be encountered, namely, the geometric non-linearity and the material non-linearity.

Seismic Analysis of Structures T.K. Datta

For the latter, restoring action shows a hysteretic behavior under cyclic loading. For the former no such hysteretic behavior is exhibited; during unloading, the load deformation path follows that of the loading. Figure 6.1 shows the case of load deformation behavior of the non-hysteretic type. Such types of restoring action under cyclic loading are observed for large displacement (small strain) problems.

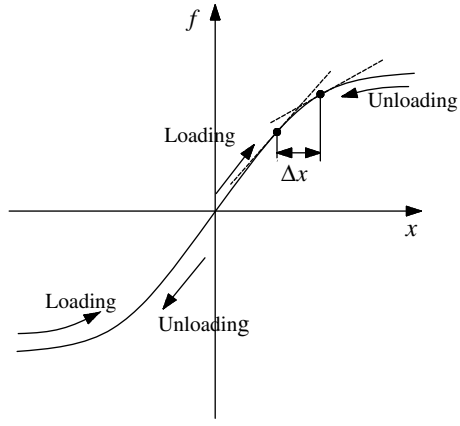

Figure 6.1 Non-linear restoring force (non-hysteretic type)

Figure 6.2 shows the hysteretic behavior of a non-linear restoring force under cyclic loading (material non-linearity). In Figure 6.2(a and b), typical experimental curves of non-linear behavior material under cyclic loading are shown. These experimental curves are often idealized to make them amenable to mathematical modeling. A mathematical model of Figure 6.2b, known as an elasto-plastic model, as shown in Figure 6.2c, is a popular model used to represent the non-linear behavior of many materials. Provided the restoring force remains within the linear range, the unloading path follows that of the loading. When the restoring force is in the plastic state (that is, the horizontal portion of the curve), unloading follows a path parallel to the elastic path, as shown in Figure 6.2c. The mathematical model of Figure 6.2a, popularly known as a bilinear model, as shown in Figure 6.2d, is used to represent the strain hardening characteristics of the material after yielding. The unloading path, after the initial yielding has taken place, is shown in the same figure. A general strain hardening model, which is not idealized as bilinear or trilinear, looks like Figure 6.2(a and b).

Damping non-linearity may be encountered in dynamic problems associated with structural control, offshore structures, and aerodynamics of structures. While most of the damping non-linearities are of a non-hysteretic type, some of the damping non-linearities can exhibit hysteretic behavior. As most structures under earthquake excitation undergo yielding, treatment of material non-linearity exhibiting hysteretic behavior is discussed in this section after giving an introduction to the general non-linear analysis of an SDOF system (without a hysteretic effect) under dynamic excitation.

6.2.1 Equations of Motion

Because the equations of motion for a multi-degrees of freedom system are a set of coupled non-linear differential equations, their solutions are difficult to obtain analytically. Most of the solution procedures are numerical based and obtain the solution by solving the incremental equations of motion. The incremental equations of motion make the problem linear over the small time interval Δt. The solution is

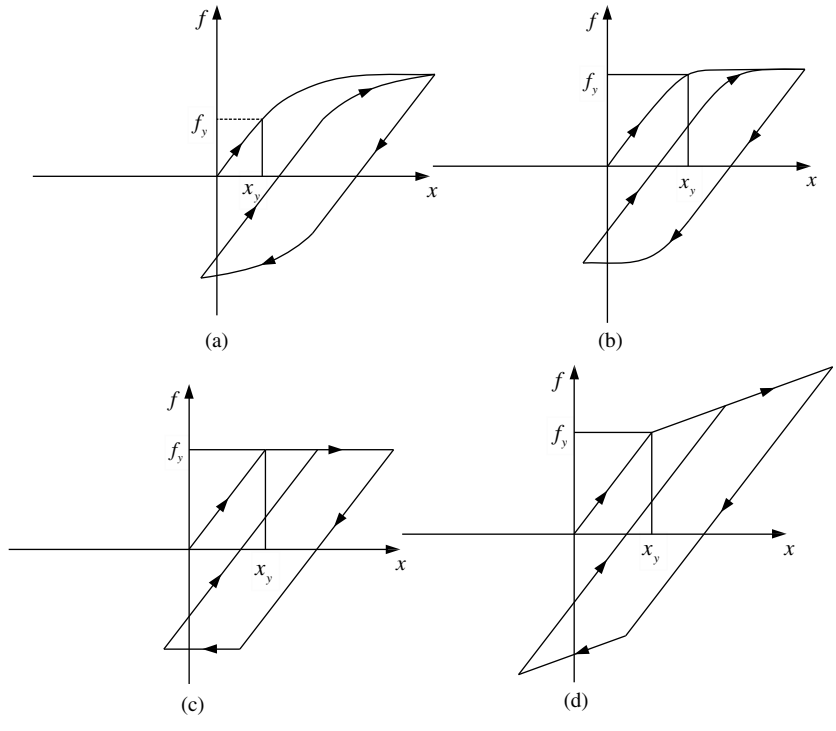

Figure 6.2 Non-linear restoring force (hysteretic type): (a) and (b) variation of force with displacement under cyclic loading; (c) idealized model of force-displacement curve for (b); and (d) idealized model of force-displacement curve for (a)

then determined using the techniques for solving the linear differential equations. However, under certain conditions, iterations are required at each time step in order to obtain the current solution. Incremental equations of motion take the form:

$$\boldsymbol{M}\Delta\ddot{\boldsymbol{x}} + \boldsymbol{C}_t\Delta\dot{\boldsymbol{x}} + K_t\Delta\boldsymbol{x} = -\boldsymbol{M}\boldsymbol{r}\Delta\ddot{\boldsymbol{x}}_g \tag{6.1}$$

where

$\boldsymbol{M}$ is the mass matrix as before
$\boldsymbol{C}_t$ is the damping matrix consisting of elements representing damping coefficients that are used for the current time interval Δt
$\boldsymbol{K}_t$ similarly denotes the stiffness matrix for the current interval Δt
$\Delta\boldsymbol{x}$ represents the incremental displacement vector
$\Delta\ddot{\boldsymbol{x}}_g$ is the incremental ground acceleration vector over the time interval Δt.

6.2.2 *Solution of the Equation of Motion for the SDOF System*

The solution of the equation of motion is obtained in the time domain using the numerical integration scheme. It will be first explained with the help of the SDOF system, and then it will be extended for the MDOF system. For the SDOF system, the equation of motion becomes

$$m\Delta\ddot{x} + c_t\Delta\dot{x} + k_t\Delta x = -m\Delta\ddot{x}_g \tag{6.2}$$

in which c_t and k_t are the initial tangent damping coefficient and the initial tangent stiffness, respectively, at the beginning of the time step. In fact, c_t and k_t should represent the average tangent values as shown in Figure 6.1. As the values of Δx and $\Delta \dot{x}$ are not known in the beginning, an iteration procedure is required to determine these values. If Δt is sufficiently small, then initial tangent values at the start of the time step give results of sufficient accuracy, and therefore the iteration may be avoided. Using Newmark's β-method for numerical integration over the incremental time, Equations 3.52 and 3.53 (Chapter 3) may be written as:

$$\Delta \dot{x} = \Delta t\, \ddot{x}_k + \delta\, \Delta t\, \Delta \ddot{x} \tag{6.3}$$

$$\Delta x = \Delta t\, \dot{x}_k + \frac{(\Delta t)^2}{2} \ddot{x}_k + \beta (\Delta t)^2 \Delta \ddot{x} \tag{6.4}$$

From Equation 6.4, $\Delta \ddot{x}$ is obtained as:

$$\Delta \ddot{x} = \frac{1}{\beta (\Delta t)^2} \Delta x - \frac{1}{\beta \Delta t} \dot{x}_k - \frac{1}{2\beta} \ddot{x}_k \tag{6.5}$$

Substituting the value of $\Delta \ddot{x}$ into Equation 6.3 gives

$$\Delta \dot{x} = \frac{\delta}{\beta \Delta t} \Delta x - \frac{\delta}{\beta} \dot{x}_k + \Delta t \left(1 - \frac{\delta}{2\beta}\right) \ddot{x}_k \tag{6.6}$$

Substituting $\Delta \dot{x}$ and $\Delta \ddot{x}$ into Equation 6.2 gives

$$\overline{k} \Delta x = \Delta p \tag{6.7}$$

in which

$$\overline{k} = k_t + \frac{\delta}{\beta \Delta t} c_t + \frac{1}{\beta (\Delta t)^2} m \tag{6.8a}$$

$$\Delta p = -m \Delta \ddot{x}_g + \left(\frac{m}{\beta \Delta t} + \frac{\delta}{\beta} c_t\right) \dot{x}_k + \left[\frac{m}{2\beta} + \Delta t \left(\frac{\delta}{2\beta} - 1\right) c_t\right] \ddot{x}_k \tag{6.8b}$$

Solution of Equation 6.7 provides the incremental displacement, Δx.

Finally, the responses are obtained as:

$$x_{k+1} = x_k + \Delta x; \quad \dot{x}_{k+1} = \dot{x}_k + \Delta \dot{x}; \quad \ddot{x}_{k+1} = \ddot{x}_k + \Delta \ddot{x} \tag{6.9}$$

In order to get a more accurate value of the acceleration, the acceleration should be calculated from the equation of motion once the displacement and the velocity are determined at a time station.

The above solution is valid provided the damping and restoring force non-linearities follow the same path during loading and unloading. For a geometrically non-linear problem with linear damping, the solution procedure remains the same as above. For material non-linearity with linear damping, which is common in earthquake excitation, the solution procedure becomes different because of the hysteretic behavior of the force-deformation relationship, which represents the restoring action as shown in Figure 6.2c. The solution procedure is then modified and is illustrated for elasto-plastic material behavior.

Elasto-plastic material behavior representing the restoring action is most commonly used in solving non-linear problems associated with the inelastic excursion of structures during an earthquake. For elasto-plastic behavior, $\boldsymbol{c}_t$ is assumed to be constant and k_t is taken either as k or zero depending upon whether the system is elastically loaded and unloaded (unloading follows the path of initial stiffness) or plastically deformed. When the state transition takes place, the stiffness varies within the time step, the dynamic equilibrium is violated, and the unbalanced forces are introduced. The treatment of such state transitions together with the iterative scheme to minimize the unbalanced forces is described below.

6.2.2.1 Elastic to Plastic State

If the system is elastic at the beginning of the time step and remains elastic at the end of the time step, then the computation is not changed and the next time step is started. If it is found that the system has passed from the elastic state to the plastic state, the computations are restarted for that time increment. First, an elastic displacement increment $(\Delta x)_e$ is obtained as a fraction of the displacement increment $(\Delta x)_0$ that was originally calculated as:

$$(\Delta x)_e = a_e(\Delta x)_0 \tag{6.10}$$

in which a_e is a scalar (less than 1) such that the system just reaches yielding. Then, the plastic displacement increment $(\Delta x)_p$ is obtained by using Equation 6.7 for an incremental load of $(1 - a_e)\Delta p$ by setting $k_t = 0$. The final incremental displacement is equal to the sum of the factored displacement and the incremental plastic displacement.

6.2.2.2 Plastic to Plastic State

Once the system enters into the plastic state, it continues to remain in that state until the velocity of the system is positive, that is, the displacement is increasing. Provided the velocity is positive, Δx is obtained using Equation 6.7 with $k_t = 0$. When the velocity at the end of the time interval becomes negative, unloading takes place and the system passes from a plastic to an elastic state within the same time interval. In that case, the computation for the time interval is restarted by considering unloading of the system with elastic stiffness equal to k_t.

6.2.2.3 Plastic to Elastic State

When unloading takes place, the instant at which velocity becomes zero is to be identified. For that, Δx obtained in the original calculation is factored by multiplying by a factor e, so that the factored incremental displacement provides a total displacement of $x(t)$ for which $\dot{x}(t) = 0$. Then, an incremental displacement $(\Delta x)_a$ is obtained using Equation 6.3 with a load increment as $(1 - e)\Delta p$ (with $k_t \neq 0$). The final (Δx) for the time interval is obtained by adding the factored incremental displacement with $(\Delta x)_a$.

Example 6.1

The non-linear property of the spring of an SDOF system shown in Figure 6.3 is elasto-plastic with the maximum spring force given as $0.15mg$ in which m is the mass of the system. The frequency of the system based on the initial stiffness is $10\,\text{rad s}^{-1}$. Find the displacement of the system (i) at 1.52 s, given x, $\dot{x}$, $\ddot{x}$, and f_x at 1.5 s as 0.01315 m, $0.1902\,\text{m s}^{-1}$, $-0.46964\,\text{m s}^{-2}$, and 1.354 N, respectively, and (ii) at 1.64 s, given x, $\dot{x}$, $\ddot{x}$, and f_x at 1.62 s as 0.029818 m, $0.0283\,\text{m s}^{-1}$, $-2.79246\,\text{m s}^{-2}$, and 1.4715 N, respectively, for the El Centro earthquake as excitation. For the computation, take $\Delta t = 0.02$ s, $\xi = 2\%$, $m = 1$ kg, $\delta = 0.5$, and $\beta = 0.25$.

Solution: (i) At time $t = 1.5$ s, $x = 0.01315$ m, $\dot{x} = 0.1902\,\text{m s}^{-1}$, $\ddot{x} = -0.46964\,\text{m s}^{-2}$ and $f_x = 1.354$ N. As $|f_x| < 0.15mg$ and $\dot{x} > 0$, the stiffness of the system is in the elastic (ascending) range.

For the SDOF, $c_t = 2 \times 0.02 \times 10 \times 1 = 0.4\,\text{N s m}^{-1}$; $k_t = 100\,\text{N m}^{-1}$ and therefore, $\overline{k}$ (Equation 6.8a) is calculated as:

$$\overline{k} = 10140\,\text{N m}^{-1}$$

$$\Delta\ddot{x}_g = (\ddot{x}_g)_{t+\Delta t} - (\ddot{x}_g)_t = 0.0312\,\text{g}$$

$$\Delta p\ (\text{Equation 6.8b}) = 37.55\,\text{N}$$

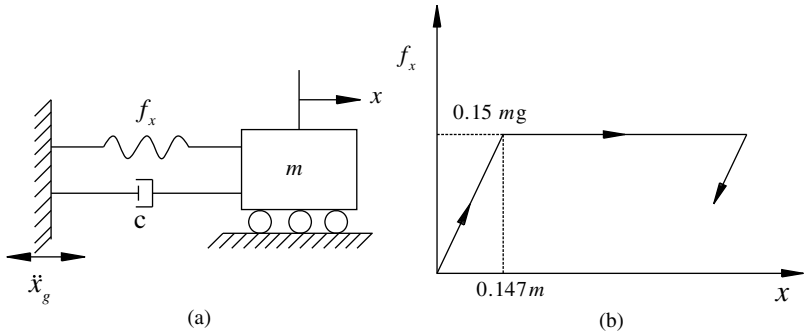

Figure 6.3 Non-linear analysis of SDOF system: (a) SDOF system with non-linear spring; and (b) force-displacement behavior of the spring

Solution of Equation 6.7 gives $\Delta x = 0.0037\,\text{m}$, $\Delta\dot{x} = -0.01\,\text{m s}^{-1}$, $\Delta f = k_t \Delta x = 0.37\,\text{N}$

$$(f_x)_{t+\Delta t} = (f_x)_t + \Delta f = 1.7243\,\text{N}; \quad |f_x| > 0.15mg$$

Therefore, there is a transition point and the system goes from an elastic to a plastic state. The force is brought down to $0.15mg$ by making

$$(f_x)_t + e\Delta x k_t = 0.15mg (e = 0.31761)$$

The value of $\Delta x = \Delta x_1 + \Delta x_2 = e\Delta x + \Delta x_2$, $\Delta x_2 = \Delta x_p$ is obtained by:

$$\overline{k}\Delta x_2 = (1-e)\Delta p; \quad \text{in computing } \overline{k},\ k_t = 0$$

The solution gives $\Delta x_2 = 0.00373\,\text{m}$; $\Delta\dot{x}_2 = -0.00749\,\text{m s}^{-1}$.
Thus,

$$x_{t+\Delta t} = x_t + \Delta x_1 + \Delta x_2 = 0.017254\,\text{m}, \text{ where } \dot{x}_{t+\Delta t} = 0.1827\,\text{m s}^{-1}$$

$$\ddot{x}_{t+\Delta t} = \frac{P_{t+\Delta t} - c_t \dot{x}_{t+\Delta t} - f_{x(t+\Delta t)}}{m} = 0.2789\,\text{m s}^{-2}, \text{ where } f_{x(t+\Delta t)} = f_y = 0.15mg$$

(ii) At time $t = 1.62\,\text{s}$, $\dot{x} > 0$ and $f_x = 0.15\,mg$. Therefore, stiffness of the system is zero and $\overline{k}$ is calculated by setting $k_t = 0$ in Equation 6.8a. Thus,

$$\overline{k} = 10040\,\text{N m}^{-1}; \quad \Delta p = -0.4173\,\text{N}$$

Solution of Equation 6.7 gives

$$\Delta x = -0.000042\,\text{m}; \ \Delta\dot{x} = -0.061\,\text{m s}^{-1}$$

$$\dot{x}_{t+\Delta t} = \dot{x}_t + \Delta\dot{x} = -0.0325\,\text{m s}^{-1} < 0$$

Therefore, there is a transition point and the system is unloaded from a plastic to an elastic state. Using Equation 6.6

$$\Delta\dot{x}_1 = \frac{2}{\Delta t} e\Delta x - 2\dot{x}_t = 0$$

$$e = 7.81; \ \Delta x_1 = e\Delta x = -0.000325\,\text{m}$$

Now, Δx_2 is obtained as:

$$\overline{k}\Delta x_2 = (1-e)\Delta p;\ k_{\mathrm{t}} = 100\ \mathrm{N\,m^{-1}}$$

The solution gives $\Delta x_2 = 0.00028$ m;

$$\Delta x = \Delta x_1 + \Delta x_2 = -4.44 \times 10^{-5}\ \mathrm{m};\ \Delta\dot{x} = -0.061\ \mathrm{m\,s^{-1}};$$
$$\dot{x}_{t+\Delta t} = x_t + \Delta x = 0.0298\ \mathrm{m};\ \dot{x}_{t+\Delta t} = \dot{x}_t + \Delta\dot{x} = -0.033\ \mathrm{m\,s^{-1}};$$
$$\ddot{x}_{t+\Delta t} = \frac{P_{t+\Delta t} - c\dot{x}_{t+\Delta t} - f_{x(t+\Delta t)}}{m} = 3.28\ \mathrm{m\,s^{-2}};\ f_{x(t+\Delta t)} = f_{x\mathrm{t}} - k_{\mathrm{t}}\Delta x_2 = 1.467\ \mathrm{N}$$

Note that if Δt is made very small, then the above corrections for transition points are not required. Accumulated errors remain within a limit.

6.2.3 *Solution of Equations of Motion for the MDOF System without Bidirectional Interaction*

The procedure mentioned above works well for single degree of freedom systems with elasto-plastic force-deformation behavior. It also performs well for the multi-degrees of freedom systems, such as plane frames, in which sections undergoing yielding are predefined. Such a problem is shown in Figure 6.4 for a shear frame. The yield sections and their elasto-plastic force-deformation behavior are also shown in the figure. For the solution of the incremental equations of motion (Equation 6.1), the state of the each yield section is examined at the end of each time step.

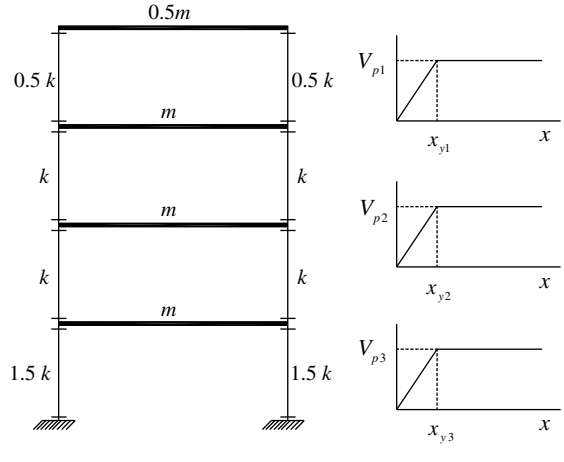

Figure 6.4 Idealized shear frame for analysis with elasto-plastic behavior of columns

Depending upon the states of the yield section of a member, the stiffness of that member is changed and the stiffness matrix of the structure is assembled from the member stiffness matrix to calculate the incremental displacement for the next time step. If required, the calculation is restarted for the current time step with modified stiffness as described for the SDOF system. Note that Equation 6.3 for the SDOF system can be easily extended to the MDOF system by writing it in the matrix form:

$$\overline{\boldsymbol{K}}\Delta\boldsymbol{x} = \Delta\boldsymbol{p} \tag{6.11}$$

in which

$$\overline{\boldsymbol{K}} = \boldsymbol{K}_t + \frac{\boldsymbol{\delta}}{\boldsymbol{\beta}\Delta t}\boldsymbol{C}_t + \frac{1}{\boldsymbol{\beta}(\Delta t)^2}\boldsymbol{M} \tag{6.12a}$$

$$\Delta \boldsymbol{p} = -\boldsymbol{M}\boldsymbol{r}\Delta\ddot{\boldsymbol{x}}_g + \left[\frac{\boldsymbol{M}}{\boldsymbol{\beta}\Delta t} + \frac{\boldsymbol{\delta}}{\boldsymbol{\beta}}\boldsymbol{C}_t\right]\dot{\boldsymbol{x}}_k + \left[\frac{\boldsymbol{M}}{2\boldsymbol{\beta}} + \Delta t\left(\frac{\boldsymbol{\delta}}{2\boldsymbol{\beta}} - 1\right)\boldsymbol{C}_t\right]\ddot{\boldsymbol{x}}_k \tag{6.12b}$$

Example 6.2

A three-storey frame shown in Figure 6.5 is subjected to the El Centro earthquake at the base. Elasto-plastic behavior of the column sections are shown in the same figure. $k/m = 100$; m is assumed to be 1 kg (to simplify the calculation). Find the responses of the top storey of the frame at 3.54 s, given that at 3.52 s, the responses are:

$$\begin{Bmatrix} x_1 \\ x_2 \\ x_3 \end{Bmatrix}_k = \begin{Bmatrix} 0.0169 \\ 0.0066 \\ 0.0107 \end{Bmatrix} \text{m}; \quad \begin{Bmatrix} \dot{x}_1 \\ \dot{x}_2 \\ \dot{x}_3 \end{Bmatrix}_k = \begin{Bmatrix} 0.1870 \\ 0.1106 \\ 0.0689 \end{Bmatrix} \text{m s}^{-1}; \quad \begin{Bmatrix} \ddot{x}_1 \\ \ddot{x}_2 \\ \ddot{x}_3 \end{Bmatrix}_k = \begin{Bmatrix} -2.7713 \\ -2.3492 \\ -2.9660 \end{Bmatrix} \text{m s}^{-2}$$

$$\begin{Bmatrix} f_1 \\ f_2 \\ f_3 \end{Bmatrix}_k = \boldsymbol{f}_k = \begin{Bmatrix} 1.44977 \\ 0.95664 \\ 0.63432 \end{Bmatrix} \text{N}; \; f_i \text{ is the shear force of a column in the } i\text{th storey}$$

$$\boldsymbol{M} = \begin{bmatrix} 1 & 0 & 0 \\ 0 & 1 & 0 \\ 0 & 0 & 1 \end{bmatrix} \text{kg} \quad K_{\text{t}} = \begin{bmatrix} 200 & -100 & 0 \\ -100 & 200 & -100 \\ 0 & -100 & 100 \end{bmatrix} \text{N m}^{-1}$$

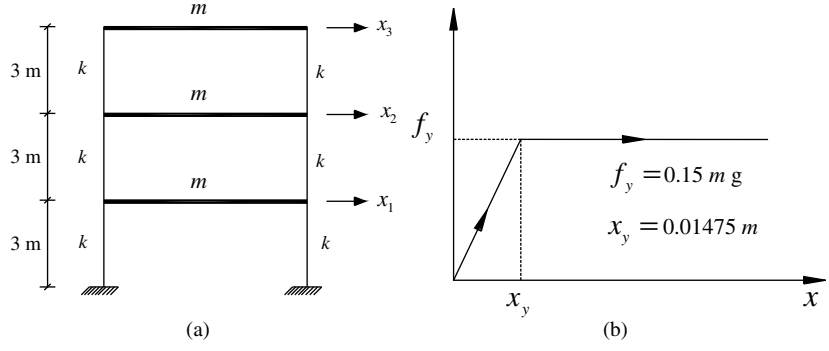

Figure 6.5 Properties of three-storey frame: (a) three-storey frame; and (b) force-displacement curve of the column

From the first two frequencies of the structure, the values of α and β are calculated as 0.1312 and 0.002 364, respectively.

$$\boldsymbol{C}_t = \alpha\boldsymbol{M} + \beta\boldsymbol{K}_{\text{t}} = \begin{bmatrix} 0.6040 & -0.2364 & 0 \\ -0.2364 & 0.6040 & -0.2364 \\ 0 & -0.2364 & 0.3676 \end{bmatrix} \text{N s m}^{-1}$$

Note that the following units are consistently used in the solutions of all example problems in this chapter unless otherwise mentioned:

- mass in kg
- stiffness in $\mathrm{N\,m^{-1}}$
- displacement in m
- velocity in $\mathrm{m\,s^{-1}}$
- acceleration in $\mathrm{m\,s^{-2}}$
- rotation in rad
- rotational velocity and acceleration are in $\mathrm{rad\,s^{-1}}$ and $\mathrm{rad\,s^{-2}}$, respectively
- force in N
- moment in N m
- damping in $\mathrm{N\,s\,m^{-1}}$.

Solution: As

$$\boldsymbol{f}_k = \begin{Bmatrix} 1.44977 \\ 0.95664 \\ 0.63432 \end{Bmatrix} < \begin{Bmatrix} 0.15mg \\ 0.15mg \\ 0.15mg \end{Bmatrix} \text{ and } \dot{x} > 0$$

then the system is in an elastic state and force-displacement behaviors of all columns are in the ascending portion of the of the yield curve shown in Figure 6.5 and therefore,

$$\overline{\boldsymbol{K}} = \boldsymbol{K}_t + \frac{\delta}{\beta \Delta t}\boldsymbol{C}_t + \frac{1}{\beta(\Delta t)^2}\boldsymbol{M} = \begin{bmatrix} 10260 & & sym \\ -124 & 10260 & \\ 0 & -124 & 10137 \end{bmatrix}$$

$$\Delta \ddot{x}_g = 0.5913$$

$$\Delta \boldsymbol{p} = -\boldsymbol{M}\boldsymbol{I}\Delta \ddot{x}_g + \left(\frac{\boldsymbol{M}}{\beta \Delta t} + \frac{\delta}{\beta}\boldsymbol{C}_t\right)\dot{\boldsymbol{x}}_k + \left[\frac{\boldsymbol{M}}{2\beta} + \Delta t\left(\frac{\delta}{2\beta} - 1\right)\boldsymbol{C}_t\right]\ddot{\boldsymbol{x}}_k = \begin{bmatrix} 32.6224 \\ 18.0256 \\ 8.4376 \end{bmatrix}$$

$$\Delta \boldsymbol{x} = \overline{\boldsymbol{K}}^{-1}\Delta \boldsymbol{p} = \begin{bmatrix} 0.0032 \\ 0.0018 \\ 0.0009 \end{bmatrix}$$

and the relative incremental displacements at each floor (drift)

$$= \Delta \overline{x} = \begin{bmatrix} 0.0032 \\ -0.0014 \\ -0.0009 \end{bmatrix};\ \Delta \boldsymbol{f} = k\Delta \overline{\boldsymbol{x}} = \begin{bmatrix} 0.16 \\ -0.07 \\ -0.045 \end{bmatrix}$$

where k is the stiffness of each column.

$$\boldsymbol{f}_{k+1} = \boldsymbol{f}_k + \Delta \boldsymbol{f} = \begin{bmatrix} 1.60977 \\ 0.88664 \\ 0.58932 \end{bmatrix}$$

It is seen that the shear forces for the first storey columns exceed the yield values. Therefore, the displacements for this storey are scaled such that the shear forces in the columns become just equal to or

less than the yield values. Thus,

$$\boldsymbol{f}_k + \boldsymbol{e}\Delta\boldsymbol{f} = \boldsymbol{f}_k + \begin{Bmatrix} e_1(0.16) \\ e_2(-0.07) \\ e_3(-0.045) \end{Bmatrix} \quad k = \begin{Bmatrix} 0.15mg \\ \leq 0.15mg \\ \leq 0.15mg \end{Bmatrix}$$

The solution provides

$$e_1 = 0.136; \quad e_2 = 1 \quad \text{and} \quad e_3 = 1$$

With these values of e_1, e_2, and e_3, the elastic components of displacements, $\Delta\boldsymbol{x}_e = \Delta\boldsymbol{x}_1$ are calculated as:

$$\Delta\boldsymbol{x}_e = \Delta\boldsymbol{x}_1 = \begin{Bmatrix} e_1\Delta x_1 \\ e_1\Delta x_1 + e_2(\Delta x_2 - \Delta x_1) \\ e_1\Delta x_1 + e_2(\Delta x_2 - \Delta x_1) + e_3(\Delta x_3 - \Delta x_2) \end{Bmatrix} = \begin{Bmatrix} \overline{e}_1\Delta x_1 \\ \overline{e}_2\Delta x_2 \\ \overline{e}_3\Delta x_3 \end{Bmatrix} = \begin{Bmatrix} 0.000435 \\ -0.000965 \\ -0.001865 \end{Bmatrix}$$

$$\begin{Bmatrix} \overline{e}_1 \\ \overline{e}_2 \\ \overline{e}_3 \end{Bmatrix} = \begin{Bmatrix} 0.1358 \\ 0.6893 \\ 3.07 \end{Bmatrix}$$

To obtain the second part of the displacement vector, $\Delta\boldsymbol{x}_2$, the $\boldsymbol{K}_t$ matrix is modified as:

$$\boldsymbol{K}_t = \begin{bmatrix} 0 & 0 & 0 \\ 0 & 200 & -100 \\ 0 & -100 & 100 \end{bmatrix}$$

$$\overline{\boldsymbol{K}} = 10^4 \times \begin{bmatrix} 1.006 & & sym \\ -0.0024 & 1.026 & \\ 0 & -0.0124 & 1.0137 \end{bmatrix}$$

$$\overline{\boldsymbol{K}}(\Delta\boldsymbol{x}_2) = \begin{Bmatrix} 1-\overline{e}_1 \\ 1-\overline{e}_2 \\ 1-\overline{e}_3 \end{Bmatrix} \times \Delta\boldsymbol{P} = \begin{Bmatrix} 28.19187 \\ 27.69333 \\ 25.92593 \end{Bmatrix}$$

The solution gives:

$$\Delta\boldsymbol{x}_2 = \begin{Bmatrix} 0.0028 \\ 0.0027 \\ 0.0026 \end{Bmatrix}$$

$$\Delta\boldsymbol{x} = \Delta\boldsymbol{x}_1 + \Delta\boldsymbol{x}_2 = \begin{Bmatrix} 0.00324 \\ 0.0018 \\ 0.00074 \end{Bmatrix}$$

$$\boldsymbol{x}_{k+1} = \boldsymbol{x}_k + \Delta\boldsymbol{x} = \begin{Bmatrix} 0.02009 \\ 0.00833 \\ 0.0114 \end{Bmatrix}$$

$$\Delta\dot{\boldsymbol{x}} = \frac{\delta}{\beta\Delta t}\Delta\boldsymbol{x} - \frac{\delta}{\beta}\dot{\boldsymbol{x}}_k + \Delta t\left(1 - \frac{\delta}{2\beta}\right)\ddot{\boldsymbol{x}}_k = \begin{bmatrix} 0. - 0.0509 \\ -0.0406 \\ -0.0524 \end{bmatrix}$$

$$\dot{\boldsymbol{x}}_{k+1} = \dot{\boldsymbol{x}}_k + \Delta\dot{\boldsymbol{x}} = \begin{bmatrix} 0.1361 \\ 0.07 \\ 0.0165 \end{bmatrix}$$

The incremental forces in the columns are

$$\Delta \boldsymbol{f} = \begin{Bmatrix} e_1(0.16) \\ e_2(-0.07) \\ e_3(-0.045) \end{Bmatrix} + \begin{Bmatrix} 0.00 \\ -0.005 \\ -0.005 \end{Bmatrix} = \begin{Bmatrix} 0.0218 \\ -0.075 \\ -0.05 \end{Bmatrix}$$

Note that the second part of the incremental forces in the columns is calculated by taking the stiffness of the first storey column as zero and that for the other two storeys as k:

$$\boldsymbol{f}_{k+1} = \boldsymbol{f}_k + \Delta \boldsymbol{f} = \begin{Bmatrix} 1.4715 \\ 0.882 \\ 0.584 \end{Bmatrix}$$

$$\ddot{\boldsymbol{x}}_{k+1} = \boldsymbol{M}^{-1}(\boldsymbol{P}_{k+1} - \boldsymbol{C}_t \dot{\boldsymbol{x}}_{k+1} - \boldsymbol{F}_{k+1}) = \begin{bmatrix} -2.289 \\ -1.7018 \\ -2.2825 \end{bmatrix}$$

$\boldsymbol{F}_{k+1}$ is the restoring force vector and is equal to $\boldsymbol{2f}_{k+1}$ (for this problem).

After establishing $\Delta \boldsymbol{x}$, the shear forces in the columns must be checked in order to find if any value has exceeded the yield limit. If so, then a second iteration is required to satisfy the yield condition. For this problem, the yield condition is not violated. Hence, the second iteration is not required.

6.2.4 *Solution of Equations of Motion for the MDOF System with Bidirectional Interaction*

The method of analysis for the SDOF system with elasto-plastic material behavior can be easily extended to multi-storey frames or other structures in which unidirectional forces are induced in the elements. For two component earthquakes, elements of the structures invariably develop internal forces in two orthogonal directions. Even for single component earthquakes, elements of structures such as asymmetric buildings develop forces in two orthogonal directions. Yielding of such elements depends upon the assumed yield criterion, which considers the bidirectional interaction of forces on yielding. If this interaction effect is not included, then yielding of the element takes place in the two directions independent of each other. The effect of bidirectional interaction on the yielding of the elements can be included in the incremental dynamic analysis in the following way.

Consider a one-storey 3D frame as shown in Figure 6.6. The deck is assumed to be rigid and can undergo torsion about a vertical axis. Under unidirectional or bidirectional earthquake excitations, columns translate in both the x- and y-directions. Let $K_{\mathrm{e}x_i}(= 12EI_{x_i}/L_i^3)$ and $K_{\mathrm{e}y_i}(= 12EI_{y_i}/L_i^3)$ of the four columns be different. Similarly, the yield shear capacities of the columns are also different. The elastic stiffness matrix for the system may be written as:

$$\boldsymbol{K}_{\mathrm{e}} = \begin{bmatrix} K_{\mathrm{e}x} & 0 & K_{\mathrm{e}x}e_y \\ 0 & K_{\mathrm{e}y} & K_{\mathrm{e}y}e_x \\ K_{\mathrm{e}x}e_y & K_{\mathrm{e}y}e_x & K_\theta \end{bmatrix} \tag{6.13a}$$

in which

$$K_{\mathrm{e}x} = \sum K_{\mathrm{e}x_i}; \quad K_{\mathrm{e}y} = \sum K_{\mathrm{e}y_i}; \quad K_\theta = \sum K_{\mathrm{e}x_i}e_y + \sum K_{\mathrm{e}y_i}e_x \tag{6.13b}$$

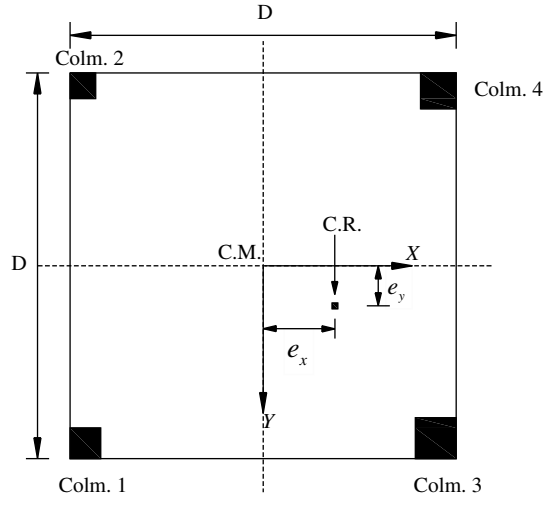

Figure 6.6 Plan of the one-storey 3D frame with a rigid slab

The transient stiffness matrix K_t, which remains constant within a given time interval Δt is given by:

$$\boldsymbol{K}_t = \boldsymbol{K}_e - \boldsymbol{K}_p \tag{6.14}$$

in which $\boldsymbol{K}_p$ is the modification of the stiffness of the system due to yielding of the members. $\boldsymbol{K}_p$ is a matrix similar to the matrix $\boldsymbol{K}_e$ with its elements represented by K_{px}, K_{py}, and $K_{p\theta}$. The modifications of stiffness for the ith element in the x- and y-directions are given by [1]:

$$K_{pxi} = \frac{B_{xi}^2}{G_i}; \quad K_{pyi} = \frac{B_{yi}^2}{G_i}; \quad K_{pxyi} = K_{pyxi} = \frac{B_{xi}B_{yi}}{G_i} \tag{6.15}$$

where

$$G_i = K_{exi}h_{xi}^2 + K_{eyi}h_{yi}^2 \tag{6.16a}$$

$$B_{xi} = K_{exi}h_{xi}; \quad B_{yi} = K_{eyi}h_{yi} \tag{6.16b}$$

$$h_{xi} = \frac{V_{xi}}{V_{pxi}^2}; \quad h_{yi} = \frac{V_{yi}}{V_{pyi}^2} \tag{6.16c}$$

in which V_{pxi} and V_{pyi} are the yield shears in the x- and y-directions, respectively.

Because of the above modification, the $\boldsymbol{K}_t$ matrix takes the form

$$\boldsymbol{K}_t = \begin{bmatrix} K_{ex} - K_{px} & -K_{pxy} & K_{ex}e_y - K_{px}e_{py} \\ -K_{pxy} & K_{ey} - K_{py} & K_{ey}e_x - K_{py}e_{px} \\ K_{ex}e_y - K_{px}e_{py} & K_{ey}e_x - K_{py}e_{px} & K_\theta - K_{p\theta} \end{bmatrix} \tag{6.17}$$

in which

$$K_{px} = \sum K_{pxi}; \quad K_{py} = \sum K_{pyi} \quad K_{pxy} = \sum K_{pxyi} \tag{6.18a}$$

$$K_{p\theta} = \sum K_{pxi}e_{py} + \sum K_{pxi}e_{px} \tag{6.18b}$$

e_{px} and e_{py} are the plastic eccentricities, calculated in the same way as those for elastic eccentricities.

When any of the columns is in the full plastic state which satisfies a yield criterion, the stiffness for that element becomes zero, that is, it does not contribute to the transient stiffness matrix K_t.

During the numerical integration of the incremental equation of motion, the system passes from an elastic state to a plastic state, moves from one plastic state to another, and then passes from a plastic state to an elastic state. Accordingly, the transient stiffness matrix changes following the elasto-plastic property of the element and a specified yield criterion. The elasto-plastic property of the column elements are shown in Figure 6.7.

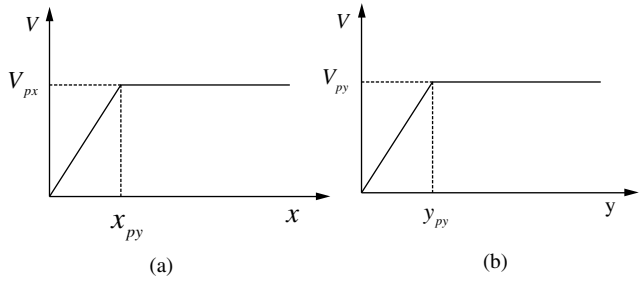

Figure 6.7 Elasto-plastic behavior of the column elements: (a) for x-direction; and (b) for y-direction

The yield criterion could be of different forms for biaxial interaction of yielding of the columns. The most popular yield curve, which represents yielding of the column member, is given by:

$$\varphi_i = \left(\frac{V_{xi}}{V_{\mathrm{p}xi}}\right)^2 + \left(\frac{V_{yi}}{V_{\mathrm{p}yi}}\right)^2 \tag{6.19}$$

For $V_{\mathrm{p}xi} = V_{\mathrm{p}yi}$, the yield curve is represented by a circle. For $V_{\mathrm{p}xi} \neq V_{\mathrm{p}yi}$, the yield curve takes the form of an ellipse. When $\varphi_i < 1$, the element remains in the elastic range; $\varphi_i = 1$ represents the plastic state; and $\varphi_i > 1$ is inadmissible. During the integration of the equation of motion, φ_i is calculated for each element. If φ_i becomes greater than unity for any element, then the state of internal forces is pulled back to satisfy the yield condition. Because of this, the equilibrium of forces is disturbed, and therefore some corrections are required to restore the equilibrium. This requires an iterative process, which is discussed later.

For numerical integration of the equation of motion, the stiffness matrix of the system at the beginning of the time interval Δt is determined with internal forces of the members known at time t. With this stiffness matrix, an incremental displacement ($\Delta \boldsymbol{U}_0$) is calculated using an equation similar to Equation 6.11 (replacing $\Delta \boldsymbol{x}$ by $\Delta \boldsymbol{U}$). With the known values of $\Delta \boldsymbol{U}_0$, internal forces $\Delta \boldsymbol{F}_0$ in the member are computed.

If the system is found to be elastic, both at the beginning and at the end of the time step, then the computed incremental displacement and incremental internal forces are indeed the true displacements and forces. If any element of the system is already in a plastic state at the beginning of the time step and/or passes to another plastic state at the end of the time step, then the incremental displacement ($\Delta \boldsymbol{U}_0$) and internal force ($\Delta \boldsymbol{F}_0$) are the first guesses and should be corrected. With $\Delta \boldsymbol{U}_0$ and $\Delta \boldsymbol{F}_0$, the element forces calculated may very well be found to violate the yield condition, that is, $\varphi_i > 1$. The element forces are then corrected such that the yield condition is not violated. There are several iteration schemes to introduce this correction. The average stiffness predictor-corrector scheme is one of them [2]. In this scheme, the transient stiffness matrix at $t + \Delta t$ is calculated with element forces at $t + \Delta t$ determined using the first guess. Then an average stiffness matrix is obtained for the time interval Δt as

$$\boldsymbol{K}_{\mathrm{ta}} = \frac{1}{2}(\boldsymbol{K}_{t0} + \boldsymbol{K}'_t) \tag{6.20}$$

in which $\boldsymbol{K}_{t0}$ and $\boldsymbol{K}_t'$ are the stiffness matrices calculated at the beginning and at the end of the time interval Δt. The incremental displacements $\Delta \boldsymbol{U}_1$ are obtained with $\boldsymbol{K}_{\text{ta}}$ for the time interval Δt and the incremental forces $\Delta \boldsymbol{F}_1$ for the elements are then calculated. The incremental force vector (restoring) is also calculated as:

$$\Delta \overline{\boldsymbol{F}}_1 = \boldsymbol{K}_{\text{ta}} \Delta \boldsymbol{U}_1 \tag{6.21}$$

The process is repeated until a certain convergence criterion is satisfied, that is,

$$\left|\Delta \overline{\boldsymbol{F}}_{i+1}\right| - \left|\Delta \overline{\boldsymbol{F}}_i\right| \leq \text{ force tolerance} \tag{6.22a}$$

$$\left|\Delta \boldsymbol{U}_{i+1}\right| - \left|\Delta \boldsymbol{U}_i\right| \leq \text{displacement tolerance} \tag{6.22b}$$

When the convergence criteria are satisfied, then forces in the elements are evaluated. If the yield criterion is not satisfied for any element, then the element forces are pulled back such that

$$\boldsymbol{F}_i' = \frac{1}{\sqrt{\varphi_i}} \boldsymbol{F}_i \tag{6.23}$$

in which $\boldsymbol{F}_i$ are the forces before pull back and φ_i is calculated from Equation 6.19. The force vector (restoring) is then re-evaluated. With the new forces, $\boldsymbol{K}_{\text{ta}}$ is again obtained and the process is continued until the yield criterion is satisfied for all elements.

If one or more elements pass from the the elastic state to the plastic state at the end of the time interval Δt, then $\Delta \boldsymbol{U}_0$ is scaled such that the elements remain elastic. Let the scaled $\Delta \boldsymbol{U}_{\text{e}}$ be denoted by:

$$\Delta \boldsymbol{U}_{\text{e}} = a_0 \Delta \boldsymbol{U}_0 \tag{6.24}$$

Next a plastic displacement increment $\Delta \boldsymbol{U}_{\text{p}}$ is calculated corresponding to an effective load vector of $(1 - a_0)\Delta \boldsymbol{p}$. The procedure for calculating $\Delta \boldsymbol{U}_{\text{p}}$ remains the same as described above for elements that pass from one plastic state to the other.

If one or more elements are unloaded from a plastic state to an elastic state, then the plastic work increment $\Delta \boldsymbol{w}_{\text{p}i}$ for the elements are negative for that time step.

The plastic work increment of an element is given by:

$$\Delta \boldsymbol{w}_{\text{p}i} = F_i \Delta \boldsymbol{U}_{\text{p}i} \tag{6.25}$$

in which $\Delta \boldsymbol{U}_{\text{p}i}$ is the plastic displacement increment of element i which in turn is given by:

$$\Delta \boldsymbol{U}_{\text{p}i} = \Delta \boldsymbol{U}_i - \boldsymbol{K}_{\text{e}i}^{-1} \Delta \boldsymbol{F}_i \tag{6.26}$$

in which $\Delta \boldsymbol{U}_i$ is the total displacement increment of element i and $K_{\text{e}i}$ is its elastic stiffness. When an element is found to have unloaded from a plastic state, its stiffness within that time step is assumed to be the same as its elastic stiffness.

Example 6.3

A single-storey 3D frame as shown in Figure 6.8 is subjected to the El Centro earthquake record at the base along the x-direction.

Assume: $D = 3.5\,\text{m}$; $h = 3.5\,\text{m}$; $(M_{\text{p}x} = M_{\text{p}y} = M_{\text{p}})_{\text{A}} = M_0$; $(M_{\text{p}})_{\text{B}} = (M_{\text{p}})_{\text{D}} = 1.5M_0$; $(M_{\text{p}})_{\text{C}} = 2M_0$; $(k_x = k_y = k)_{\text{A}} = k_0$; $k_{\text{B}} = k_{\text{C}} = 1.5k_0$; $k_{\text{C}} = 2k_0$; $k_0/m = 50$ in which $m_x = m_y = m = 620\,\text{kg}$; mass moment of inertia $= mD^2/6$; $(V_{\text{p}})_{\text{A}} = 152.05\,\text{N}$; and damping of the system as zero. Find the initial stiffness matrix of the system and show the procedure for calculating the stiffness matrix at time $t = 1.38\,\text{s}$, given that at $t = 1.36\,\text{s}$:

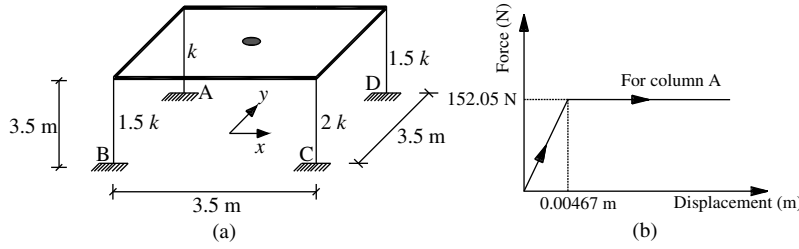

Figure 6.8 Properties of the 3D frame: (a) 3D frame; and (b) force-displacement curve of column A

$$\begin{Bmatrix} U_x \\ U_y \\ \theta \end{Bmatrix}_k = \begin{Bmatrix} 0.00336 \\ 0.00037 \\ 0.00003 \end{Bmatrix} \cdots \begin{Bmatrix} \dot{U}_x \\ \dot{U}_y \\ \dot{\theta} \end{Bmatrix}_k = \begin{Bmatrix} 0.13675 \\ 0.00345 \\ 0.00311 \end{Bmatrix} \cdots \begin{Bmatrix} \ddot{U}_x \\ \ddot{U}_y \\ \ddot{\theta} \end{Bmatrix}_k = \begin{Bmatrix} -0.16679 \\ -0.11434 \\ -0.06153 \end{Bmatrix}$$

$$\boldsymbol{F}_k = \begin{Bmatrix} V_x \\ V_y \\ V_\theta \end{Bmatrix}_k = \begin{Bmatrix} 627.27 \\ 70.888 \\ 773.51 \end{Bmatrix} \quad \begin{matrix} V_{Ax} = 102.83 & V_{Ay} = 10.10 \\ V_{Bx} = 154.24 & V_{By} = 19.56 \\ V_{Dx} = 158.66 & V_{Dy} = 15.15 \\ V_{Cx} = 211.54 & V_{Cy} = 26.08 \end{matrix}$$

$\ddot{x}_{gk} = -0.08613$g. Consider the effect of bi-directional interaction on yielding columns.

Solution: Initial stiffness matrix is determined using Equations 6.13a and 6.13b

$$K_{ex} = \sum K_{exi} = 6k_0; \quad K_{ey} = \sum K_{eyi} = 6k_0; \quad K_\theta = \sum \frac{KD^2}{4} = 3k_0(3.5)^2$$

$$\boldsymbol{K}_e = \begin{bmatrix} 186000 & 0 & 54250 \\ 0 & 186000 & 54250 \\ 54250 & 54250 & 1139250 \end{bmatrix}$$

To determine the stiffness matrix at $t = 1.38$ s, the yield condition for all column members are checked for $t = 1.36$ s:

$$\varphi_i = \left(\frac{V_{xi}}{V_{pxi}}\right)^2 + \left(\frac{V_{yi}}{V_{pyi}}\right)^2$$

$$\varphi_A = 0.462 \quad \varphi_B = 0.465 \quad \varphi_C = 0.491 \quad \varphi_D = 0.488$$

As none of the columns has yielded, $\boldsymbol{K}_t = \boldsymbol{K}_e$

$$\overline{\boldsymbol{K}} = \boldsymbol{K}_t + \frac{\delta}{\beta\Delta t}\boldsymbol{C}_t + \frac{1}{\beta(\Delta t)^2}\boldsymbol{M} = \boldsymbol{K}_t + 10000\boldsymbol{M} = \begin{bmatrix} 638.6 & sym & \\ 0 & 638.6 & \\ 5.425 & 5.425 & 1379.76 \end{bmatrix} \times 10^4$$

$$\Delta\boldsymbol{p} = -\boldsymbol{M}\Delta\ddot{x}_g + \left(\frac{\boldsymbol{M}}{\beta\Delta t} + \frac{\delta}{\beta}\boldsymbol{C}_t\right)\dot{\boldsymbol{U}}_k + \left[\frac{\boldsymbol{M}}{2\beta} + \Delta t\left(\frac{\delta}{2\beta} - 1\right)\boldsymbol{C}_t\right]\ddot{\boldsymbol{U}}_k = \begin{bmatrix} 16282 \\ 286 \\ 612 \end{bmatrix}$$

$$\Delta\boldsymbol{U} = \overline{\boldsymbol{K}}^{-1}\Delta\boldsymbol{p} = \begin{bmatrix} 0.0025 \\ 0.000001 \\ 0.000001 \end{bmatrix} \text{ and } \Delta\boldsymbol{F} = \boldsymbol{K}_t\Delta\boldsymbol{U} = \begin{bmatrix} 476.1 \\ 10.2 \\ 181.2 \end{bmatrix}$$

$$\boldsymbol{U}_{k+1} = \boldsymbol{U}_k + \Delta\boldsymbol{U} = \begin{Bmatrix} 0.0059 \\ 0.0004 \\ 0.0001 \end{Bmatrix}$$

$$\boldsymbol{F}_{k+1} = \boldsymbol{F}_k + \Delta\boldsymbol{F} = \begin{Bmatrix} 1103.36 \\ 81.09 \\ 954.75 \end{Bmatrix}; \quad \begin{matrix} V_{\mathrm{A}x} = 183.89 & V_{\mathrm{A}y} = 13.52 \\ V_{\mathrm{B}x} = 275.84 & V_{\mathrm{B}y} = 20.27 \\ V_{\mathrm{D}x} = 275.84 & V_{\mathrm{D}y} = 20.27 \\ V_{\mathrm{C}x} = 367.79 & V_{\mathrm{C}y} = 27.03 \end{matrix}$$

$$\varphi_i = \left(\frac{V_{xi}}{V_{\mathrm{p}xi}}\right)^2 + \left(\frac{V_{yi}}{V_{\mathrm{p}yi}}\right)^2$$

$$\varphi_{\mathrm{A}} \simeq 1.47 \quad \varphi_{\mathrm{B}} \simeq 1.47 \quad \varphi_{\mathrm{C}} \simeq 1.47 \quad \varphi_{\mathrm{D}} \simeq 1.47$$

Thus, all the columns do not satisfy the yield criterion, and therefore $\Delta\boldsymbol{U}$, ΔV_{xi}, and ΔV_{yi} have to be recalculated by pulling back the internal forces of the members such that they satisfy the yield criterion.

$$e_{\mathrm{A}} = \sqrt{\frac{1}{\varphi_{\mathrm{A}}}} \simeq 0.824 \quad e_{\mathrm{B}} = \sqrt{\frac{1}{\varphi_{\mathrm{B}}}} \simeq 0.824 \quad e_{\mathrm{D}} = \sqrt{\frac{1}{\varphi_{\mathrm{D}}}} \simeq 0.824 \quad e_C = \sqrt{\frac{1}{\varphi_{\mathrm{C}}}} \simeq 0.824$$

With the e values calculated as above, the forces in the columns are pulled back (Equation 6.23) so that the yield condition is satisfied for each column. Accordingly, the displacements of each column are scaled. From the scaled displacements of the columns, the displacements at the centers of mass of the system are calculated and are given by:

$$\Delta\boldsymbol{U}_e = \begin{bmatrix} 0.254 \\ 0.00122 \\ 0.00124 \end{bmatrix} \times 10^{-5}; \ \overline{\boldsymbol{e}} \text{ is calculated as } \simeq \begin{bmatrix} 0.83 \\ 0.83 \\ 0.83 \end{bmatrix} \times 10^{-3} \text{ in which } \overline{e}_x = \frac{\Delta U_{xe}}{\Delta U_x}, \text{ and so on.}$$

$$\Delta\boldsymbol{p}_2 = (1 - \overline{e})\Delta\boldsymbol{p} = \begin{bmatrix} 16268.57 \\ 285.76 \\ 631.48 \end{bmatrix}$$

$$e_x = e_y = \frac{\sum K_i x_i}{\sum K_i} = 0.29167$$

$$h_{xi} = \frac{V_{xi}}{V_{\mathrm{p}xi}^2}; \quad \begin{matrix} h_{x\mathrm{A}} = 0.00795 \\ h_{x\mathrm{B}} = 0.0053 \\ h_{x\mathrm{D}} = 0.0053 \\ h_{x\mathrm{C}} = 0.00398 \end{matrix} \qquad h_{yi} = \frac{V_{yi}}{V_{\mathrm{p}yi}^2}; \quad \begin{matrix} h_{y\mathrm{A}} = 0.00059 \\ h_{y\mathrm{B}} = 0.00039 \\ h_{y\mathrm{D}} = 0.00039 \\ h_{y\mathrm{C}} = 0.00029 \end{matrix}$$

$$B_{xi} = K_{\mathrm{e}xi} h_{xi}; \quad \begin{matrix} B_{x\mathrm{A}} = 246.56 \\ B_{x\mathrm{B}} = 246.56 \\ B_{x\mathrm{D}} = 246.56 \\ B_{x\mathrm{C}} = 246.56 \end{matrix} \qquad B_{yi} = K_{\mathrm{e}yi} h_{yi}; \quad \begin{matrix} B_{y\mathrm{A}} = 18.12 \\ B_{y\mathrm{B}} = 18.12 \\ B_{y\mathrm{D}} = 18.12 \\ B_{y\mathrm{C}} = 18.12 \end{matrix}$$

$$G_i = K_{\mathrm{e}xi} h_{xi}^2 + K_{\mathrm{e}yi} h_{yi}^2; \quad \begin{matrix} G_{\mathrm{A}} = 1.972 \\ G_{\mathrm{B}} = 1.314 \\ G_{\mathrm{D}} = 1.314 \\ G_{\mathrm{C}} = 0.98 \end{matrix}$$

Considering the first guess for the incremental responses, the modification of the tangent stiffness matrix for yielding is obtained as:

$$K_{\mathrm{p}xi} = \frac{B_{xi}^2}{G_i} \quad K_{\mathrm{p}yi} = \frac{B_{yi}^2}{G_i} \quad K_{\mathrm{p}\theta} = \frac{D^2}{2}\sum K_{\mathrm{p}} \quad K_{\mathrm{p}xyi} = K_{\mathrm{p}yxi} = \frac{B_{xi}B_{yi}}{G_i}$$

$$\begin{array}{llll} K_{\mathrm{p}x\mathrm{A}} = 30833.45 & K_{\mathrm{p}y\mathrm{A}} = 166.55 & K_{\mathrm{p}xy\mathrm{A}} = 1690.14 & K_{\mathrm{p}\theta\mathrm{A}} = 189875 \\ K_{\mathrm{p}x\mathrm{B}} = 46250.17 & K_{\mathrm{p}y\mathrm{B}} = 249.83 & K_{\mathrm{p}xy\mathrm{B}} = 3802.82 & K_{\mathrm{p}\theta\mathrm{B}} = 284812.5 \\ K_{\mathrm{p}x\mathrm{D}} = 46250.17 & K_{\mathrm{p}y\mathrm{D}} = 249.83 & K_{\mathrm{p}xy\mathrm{D}} = 3802.82 & K_{\mathrm{p}\theta\mathrm{D}} = 284812.5 \\ K_{\mathrm{p}x\mathrm{C}} = 61666.9 & K_{\mathrm{p}y\mathrm{C}} = 333.1 & K_{\mathrm{p}xy\mathrm{C}} = 6760.574 & K_{\mathrm{p}\theta\mathrm{C}} = 379750 \end{array}$$

$$K_{\mathrm{p}x} = \sum K_{\mathrm{p}xi} = 185000 \quad K_{\mathrm{p}y} = \sum K_{\mathrm{p}yi} = 999.30 \quad K_{\mathrm{p}xy} = \sum K_{\mathrm{p}xyi} = 16056 \quad K_{\mathrm{p}\theta} = \sum K_{\mathrm{p}\theta i} = 1139250$$

$$e_{x\mathrm{p}} = \frac{\sum K_{\mathrm{p}yi}x_i}{\sum K_{\mathrm{p}yi}} = 0.2917 \quad e_{y\mathrm{p}} = \frac{\sum K_{\mathrm{p}xi}y_i}{\sum K_{\mathrm{p}xi}} = 0.2917$$

The modified tangent stiffness matrix is given as:

$$\boldsymbol{K}_{\mathrm{t}} = \boldsymbol{K}_{\mathrm{e}} - \boldsymbol{K}_{\mathrm{p}}$$

$$\boldsymbol{K}_{\mathrm{t}} = \begin{bmatrix} 1.0 & sym & \\ -16.06 & 185 & \\ 0.29 & 53.96 & 0 \end{bmatrix} \times 10^3$$

$$\overline{\boldsymbol{K}} = \boldsymbol{K}_{\mathrm{t}} + \frac{\delta}{\beta\Delta t}\boldsymbol{C}_t + \frac{1}{\beta(\Delta t)^2}\boldsymbol{M} = \boldsymbol{K}_{\mathrm{t}} + 10000\boldsymbol{M} = 10^5 \times \begin{bmatrix} 62 & sym & \\ -0.16 & 63.85 & \\ 0 & 0.54 & 126.6 \end{bmatrix}$$

$$\Delta\boldsymbol{U_2} = \overline{\boldsymbol{K}}^{-1}\Delta\boldsymbol{p_2} = \begin{bmatrix} 0.0026 \\ 0.0001 \\ 0.00 \end{bmatrix} \quad \Delta\boldsymbol{U}_{\mathrm{p}x} = \begin{Bmatrix} 0.002598 \\ 0.002598 \\ 0.002602 \\ 0.002602 \end{Bmatrix} \quad \Delta\boldsymbol{U}_{\mathrm{p}y} = \begin{Bmatrix} 0.0000983 \\ 0.0001018 \\ 0.0000983 \\ 0.0001018 \end{Bmatrix}$$

$$\Delta\boldsymbol{U} = \Delta\boldsymbol{U}_{\mathrm{e}} + \Delta\boldsymbol{U}_2 = \begin{bmatrix} 0.002602 \\ 0.0001 \\ 0.000001 \end{bmatrix}$$

$$\Delta\boldsymbol{V}_{\mathrm{p}i} = \begin{bmatrix} K_{\mathrm{e}x} - K_{\mathrm{p}x} & -K_{\mathrm{p}xy} \\ -K_{\mathrm{p}xy} & K_{\mathrm{e}y} - K_{\mathrm{p}y} \end{bmatrix}_i \begin{bmatrix} \Delta U_{\mathrm{p}x} \\ \Delta U_{\mathrm{p}y} \end{bmatrix}_i$$

Revised shear forces in the column are obtained by adding the plastic components of the shear forces as calculated above with shear forces determined after pulling back to the yield surface (for satisfying the yield condition). The resulting revised shear forces are:

$$\begin{array}{ll} V_{\mathrm{A}x} = 151.913 & V_{\mathrm{A}y} = 9.78 \\ V_{\mathrm{B}x} = 228.043 & V_{\mathrm{B}y} = 11.54 \\ V_{\mathrm{D}x} = 227.745 & V_{\mathrm{D}y} = 11.37 \\ V_{\mathrm{C}x} = 303.471 & V_{\mathrm{C}y} = 10.98 \end{array}$$

$$\varphi_i = \left(\frac{V_{xi}}{V_{\mathrm{p}xi}}\right)^2 + \left(\frac{V_{yi}}{V_{\mathrm{p}yi}}\right)^2$$

$$\varphi_{\mathrm{A}} = 1.002 \quad \varphi_{\mathrm{B}} = 1.002 \quad \varphi_{\mathrm{C}} = 1.0 \quad \varphi_{\mathrm{D}} = 1.00$$

Because the yield condition is practically satisfied for all columns, no further iteration is required. Therefore, the calculated value of $\boldsymbol{K}_t$ is used to obtain the response for the next incremental time step at $t = 1.38$ s.

6.3 Inelastic Earthquake Analysis of Multi-Storey Building Frames

The multi-storey building frames idealized as 2D frames can be analyzed for earthquake excitations in the inelastic range without too much complexity. For 3D building frames, the effect of bidirectional interaction on yielding of the columns may have to be considered if the columns are weaker than the beams. This leads to some complexity and more computational effort. This interaction effect is well understood for the elasto-plastic property of the material. For other non-linear material characteristics, this interaction effect is difficult to incorporate in a theoretical framework. Therefore, the procedure to perform the non-linear seismic analysis of multi-storey frames will be discussed for the elasto-plastic material property with bidirectional interaction and for other (materially) non-linear systems, without this interaction effect.

For a 2D frame with elasto-plastic properties of the frame elements, potential sections where plastic hinges can form are identified and the moment–rotation relationship for each section is specified as elasto-plastic. During the integration of the incremental equation of motion, moments at the potential sections of hinge formation are checked. When $|M| = M_p$ (the plastic moment capacity of the section), a plastic hinge is formed at that section. For the next time interval, the stiffness matrix of the frame is generated by assuming an ordinary hinge at that section. If $|M| > M_p$ at any section at the end of a time interval, then $|M|$ is set equal to M_p and the stiffness matrix of the frame is generated as described above. The response for the time interval is then re-evaluated with the average of the stiffness matrices at the beginning of the time interval and at the end (with $|M|$ set equal to M_p). This correction is not generally required if the time step is taken as sufficiently small, because the accumulated error is then very small. The calculation for the next time interval is then carried out.

At the end of each time interval, the velocity response at each potential section of hinge formation is checked. If unloading takes place at a plastic hinge (indicated by the reversal of the sign of velocity) at the end of a time interval, then for the subsequent time steps the section is assumed to behave elastically until plastification again takes place.

Example 6.4

For the three-storey frame with elasto-plastic columns shown in Figure 6.9a, find the time history of the moment at A and the corresponding (shear) force-displacement plot for the El Centro earthquake. If the force-displacement backbone curve for the columns is modeled as that shown in Figure 6.9b, then compare the results with those obtained for the elasto-plastic model.

Solution: The frame is modeled in SAP2000, which requires force-displacement back bone curves for the potential yield sections of the columns. They are shown in Figure 6.9. The integration is performed with $\Delta t = 0.02$ s.

The time history of the moment at A and the force-displacement plot of section A are shown in Figures 6.10 and 6.11, respectively for elasto plastic condition. It is seen from Figure 6.10 that the value of the moment at A reaches the yield moment ($V_p \times l/2 = 519.34$ kN m) and stays at the same value over a certain duration of time. Figure 6.11 shows the elasto-plastic nature of the hysteretic loops, as expected.

In Figure 6.12, the time history of moment at A for the bilinear back bone curve is shown. It is seen that the moments do not remain constant for a duration of time, but change at each time step. Figure 6.13 shows the bilinear characteristics of hysteretic curve for the force-displacement relationship.

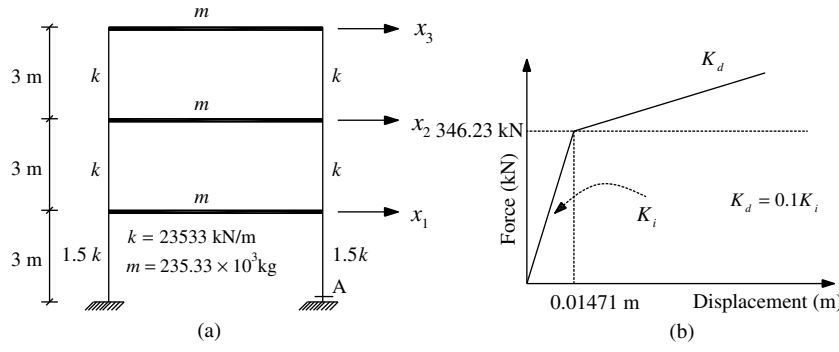

Figure 6.9 Properties of the three-storey frame: (a) three-storey frame; and (b) force-displacement curve of column

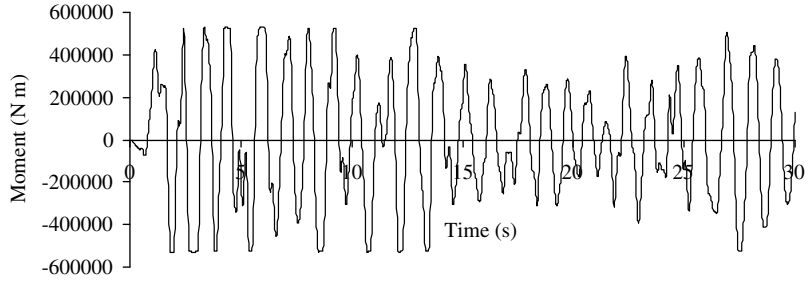

Figure 6.10 Time history of moment at A

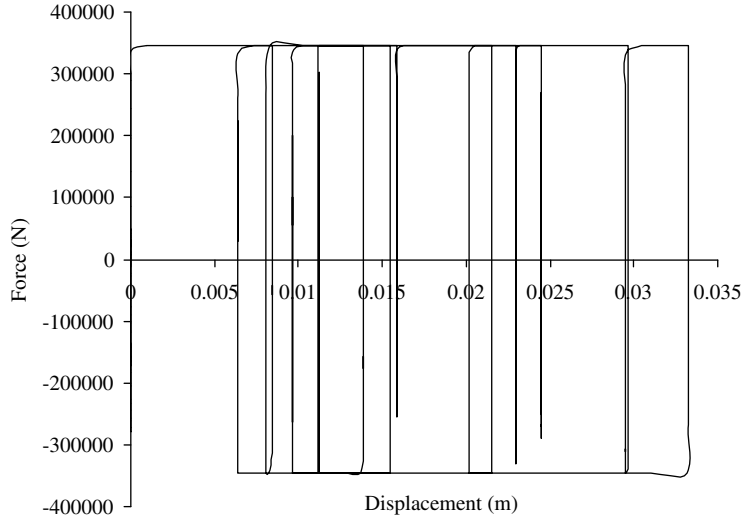

Figure 6.11 Shear force-displacement plot at A

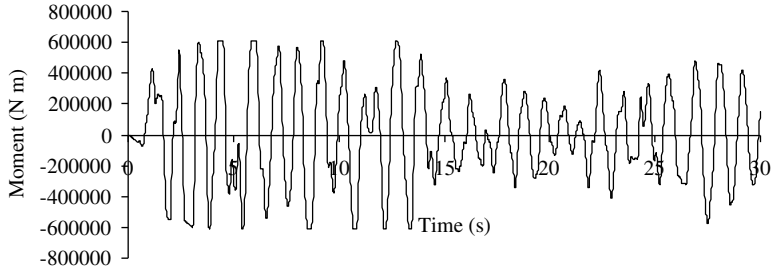

Figure 6.12 Time history of bending moment at A

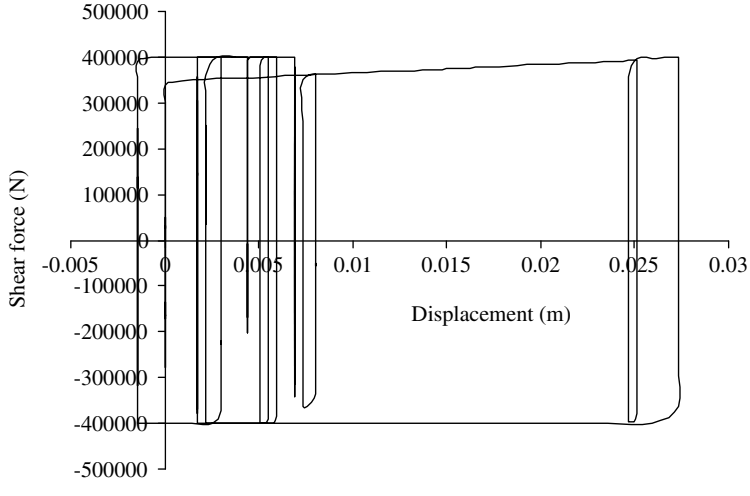

Figure 6.13 Shear force-displacement plot at A

When the non-linear moment–rotation relationship, as shown in Figure 6.14, is considered instead of the elasto-plastic one, the tangent stiffness matrix for each time interval is calculated by considering the slope of the curve corresponding to the beginning of the time interval, as explained in Figure 6.1. When unloading takes place at the potential section of yielding, the section behaves elastically having a stiffness property equal to the initial tangent stiffness of the moment–rotation curve. For ease of computation, slopes of the back bone curve for different values of force or moment may be given as inputs to the program. The slope for the in between values is obtained by interpolation. If the back bone curve is bilinear, two (pre- and post-yield) slopes are given as input. The stiffness of the system is calculated using one slope or the other depending upon its state.

Yielding with bilinear interaction takes place for column elements in 3D frames. If it is assumed that the columns are weaker than the beams, then the top and bottom sections of the columns become the sections for potential hinge formation. During the integration of the incremental equation of motion, the tangent stiffness matrix for a time interval is written as:

$$\boldsymbol{K}_{\mathrm{t}} = \boldsymbol{K}_{\mathrm{e}} - \boldsymbol{K}_{\mathrm{p}} \tag{6.27}$$

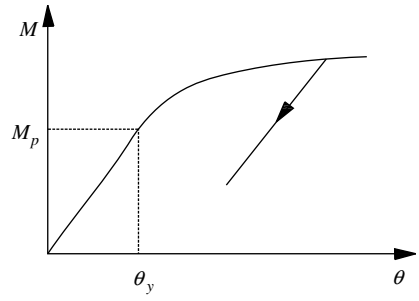

Figure 6.14 Non-linear moment–rotation relationship (not idealized by straight lines)

in which $\boldsymbol{K}_e$ is the condensed stiffness matrix of the frame corresponding to dynamic degrees of freedom and $\boldsymbol{K}_p$ is the assembled correction matrix due to the plastification of potential sections in the columns. Non-zero elements of the matrix $\boldsymbol{K}_p$ are arranged in such a way that they correspond to the degrees of freedom which are affected by the plastification of column sections. Non-zero elements are computed using Equations 6.15 and 6.16. The incremental solution procedure remains the same as that described for inelastic analysis with bidirectional interaction on yielding described previously. If the 3D frame is a weak beam–strong column system, then bilinear interaction on yielding is not required as the beams undergo only one way (vertical) bending. The analysis procedure remains the same as that of the 2D frame.

Note that for both 3D and 2D analyses, rotational degrees of freedom are condensed out if the mass moments of inertia for the skeletal members are ignored and point mass lumping is assumed.

If rotational degrees are condensed out, then incremental rotations at the ends of the members are obtained from the incremental displacement using the relationship between the displacements and rotations. Rotational stiffness of the members are modified at the end of the time interval if plastification or

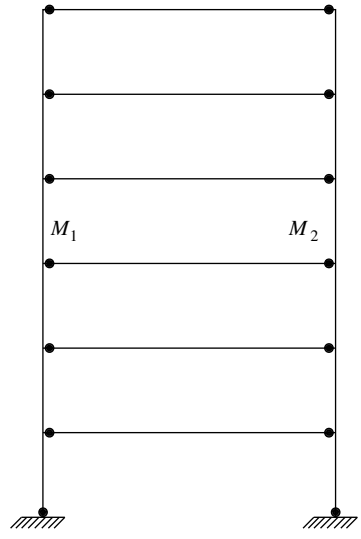

Figure 6.15 Weak beam–strong column frame with potential sections for hinge formation

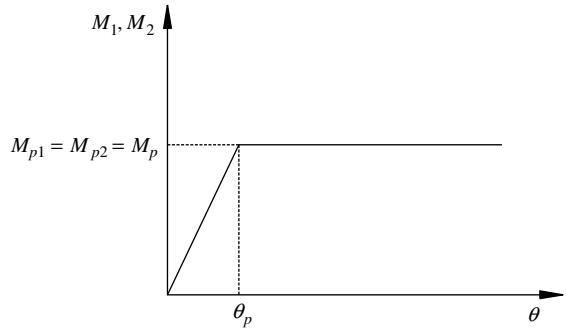

Figure 6.16 Idealized moment–rotation relationship of elasto-plastic beam

unloading takes place. The full stiffness matrix is then assembled and rotational degrees of freedom are condensed out to obtain the tangent stiffness matrix to be used for the next time step.

The procedure is illustrated for a framed structure like that shown in Figure 6.15, but having only two storeys. Column and beam length are equal to l. Δ_1 and θ_1 stand for top storey displacement and joint rotation. The frame is assumed to be a weak beam–strong column system. Therefore, beam ends are potential sections for yielding. The sections that undergo yielding are shown in the figure. The moment–rotation relationship for the sections is shown in Figure 6.16. The sections, other than the ones that are marked, remain elastic. Furthermore, it is assumed that masses are point lumped, that is, there is no mass moment of inertia and all members are inextensible. Considering anti-symmetric bending, the elastic stiffness matrix corresponding to the kinematic degrees of freedom is given by:

$$\boldsymbol{K} = \left[\begin{array}{cc|cc} k & -k & -\frac{kl}{2} & -\frac{kl}{2} \\ -k & 2k & \frac{kl}{2} & 0 \\ \hline -\frac{kl}{2} & \frac{kl}{2} & \frac{kl^2}{2}(\alpha_1 + 0.67) & \frac{kl^2}{6} \\ -\frac{kl}{2} & 0 & \frac{kl^2}{6} & \frac{kl^2}{2}(\alpha_2 + 1.33) \end{array}\right] \left\{\begin{array}{c} \Delta_1 \\ \Delta_2 \\ \theta_1 \\ \theta_2 \end{array}\right\} \tag{6.28a}$$

in which

$$\frac{12EI_c}{l^3} = k; \quad \frac{EI_{b_1}}{EI_c} = \alpha_1, \quad \frac{EI_{b_2}}{EI_c} = \alpha_2$$

The condensed stiffness matrix corresponding to the sway degrees of freedom is

$$\overline{\boldsymbol{K}}_\Delta = \boldsymbol{K}_\Delta - \boldsymbol{K}_{\Delta\theta}\boldsymbol{K}_\theta^{-1}\boldsymbol{K}_{\theta\Delta} \tag{6.28b}$$

in which $\overline{\boldsymbol{K}}_\Delta$ is the condensed stiffness matrix corresponding to the sway degrees of freedom; $\boldsymbol{K}_\Delta$, $\boldsymbol{K}_{\theta\Delta}$, and so on, are the partitioned matrices according to Δ and $\boldsymbol{\theta}$ degrees of freedom. From Equation 6.28a, it may easily be shown that

$$\boldsymbol{K}_\theta^{-1} = \frac{6}{kl^2}\begin{bmatrix} 3(\alpha_1 + 0.67) & 1 \\ 1 & 3(\alpha_2 + 1.33) \end{bmatrix}^{-1} \tag{6.29a}$$

$$\boldsymbol{\theta} = \frac{3}{l}\begin{bmatrix} 1 & -1 \\ 1 & 0 \end{bmatrix}\begin{bmatrix} 3(\alpha_1 + 0.67) & 1 \\ 1 & 3(\alpha_2 + 1.33) \end{bmatrix}^{-1}\Delta \tag{6.29b}$$

Substituting for $\boldsymbol{K}_{\theta}^{-1}$, $\boldsymbol{K}_{\theta\Delta}$, and so on, into Equation 6.28b, $\overline{\boldsymbol{K}}_{\Delta}$ is obtained as;

$$\overline{\boldsymbol{K}}_{\Delta} = k\begin{bmatrix}1 & -1\\ -1 & 2\end{bmatrix} - \frac{3k}{l}\begin{bmatrix}-1 & -1\\ 1 & 0\end{bmatrix}\begin{bmatrix}3(\alpha_1+0.67) & 1\\ 1 & 3(\alpha_2+1.33)\end{bmatrix}^{-1}\begin{bmatrix}1 & -1\\ 1 & 0\end{bmatrix} \tag{6.30}$$

The equation of motion for the frame may be written as:

$$\boldsymbol{M}\Delta\ddot{\boldsymbol{x}} + \boldsymbol{C}\Delta\dot{\boldsymbol{x}} + \overline{\boldsymbol{K}}_{\Delta t}\Delta\boldsymbol{x} = -\boldsymbol{M}\boldsymbol{I}\Delta\ddot{x}_g \tag{6.31}$$

in which

$$\boldsymbol{M} = m\begin{bmatrix}\frac{1}{2} & 0\\ 0 & 1\end{bmatrix} \quad \boldsymbol{C} = \alpha\overline{\boldsymbol{K}}_{\Delta 0} + \beta\boldsymbol{M} \tag{6.32}$$

$\overline{\boldsymbol{K}}_{\Delta 0}$ is the initial tangent stiffness matrix and is given by Equation 6.30, computed when the entire system is elastic. When the system is unloaded, the tangent stiffness matrix is equal to $\overline{\boldsymbol{K}}_{\Delta 0}$. For the time interval Δt starting from t_i, the computation of responses requires $\overline{\boldsymbol{K}}_{\Delta t}$ to be obtained for time t_i. Assume that the responses for the previous time interval are $\Delta\boldsymbol{x}_{i-1}$, $\Delta\dot{\boldsymbol{x}}_{i-1}$, ΔM_{1i-1}, ΔM_{2i-1}. Then,

$$\boldsymbol{x}_i = \boldsymbol{x}_{i-1} + \Delta\boldsymbol{x}_{i-1}; \quad \dot{\boldsymbol{x}}_i = \dot{\boldsymbol{x}}_{i-1} + \Delta\dot{\boldsymbol{x}}_{i-1} \tag{6.33a}$$

$$M_{1i} = M_{1i-1} + \Delta M_{1i-1}; \quad M_{2i} = M_{2i-1} + \Delta M_{2i-1} \tag{6.33b}$$

M_{1i} and M_{2i} are the bending moments at the ends of the beams at time t_i.

Computation of ΔM_{1i-1} and ΔM_{2i-1} requires the responses $\Delta\theta_{1i-1}$ and $\Delta\theta_{2i-1}$, which are not directly obtained from the solution of the incremental equation of motion. They are obtained using the relationship given by Equation 6.29b. To determine $\Delta\theta$, α values in Equations 6.29a and 6.29b are obtained as:

$$\alpha_1 = \frac{r_{1i-1}l}{6EI_c} \text{ and } \alpha_2 = \frac{r_{2i-1}l}{6EI_c}$$

in which

$$r_{1i-1} = \frac{M_{1i-1}}{\theta_{1i-1}} \text{ and } r_{2\,i-1} = \frac{M_{2i-1}}{\theta_{2i-1}}$$

Once $\Delta\boldsymbol{\theta}$ is known, ΔM_{1i-1} and ΔM_{2i-1} can be determined because $M_{1i-1} = r_{1i-1}\,\theta_{1i-1}$ and $M_{2i-1} = r_{2i-1}\,\theta_{2i-1}$. With the values of M_{1i} and M_{2i} known, $r_{1i} = M_{1i}/\theta_{1i}$ and $r_{2i} = M_{2i}/\theta_{2i}$ can be obtained. α_1 and α_2 are then calculated as $\alpha_1 = r_{1i}l/6EI_c$ and $\alpha_2 = r_{2i}l/6EI_c$ and the tangent stiffness matrix $\overline{K}_{\Delta t}$ for time t_i is obtained using Equation 6.30.

When the moment–rotation relationship for the beam is assumed to be elasto-plastic, then α_1 and α_2 are set to zero for $|M_1| = M_{p_1}$ and $|M_2| = M_{p_2}$, respectively at the beginning of any time interval. When unloading takes place, α_1 and α_2 are calculated based on the elastic stiffness of the beam given by Equation 6.28a.

Example 6.5

The three-storey strong column–weak beam frame, shown in Figure 6.17, is subjected to El Centro earthquake excitation. The elasto-plastic behavior of the beams are also shown in the same figure. Find the stiffness matrix of the frame corresponding to sway DOF at $t = 1.36$ s, given the response quantities shown in Table 6.1.

Solution: It is seen from the table that moments at sections 1 and 6 reach the yield moment. Therefore, the stiffness contributions (rotational) of the beams at these sections are taken as zero. For the next increment

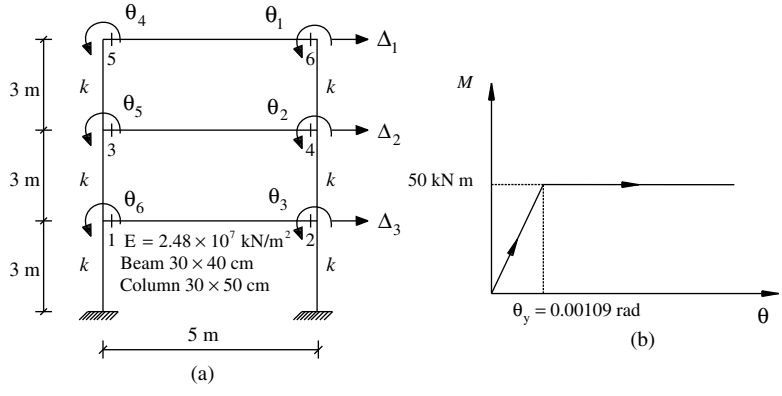

Figure 6.17 Properties of the three-storey frame: (a) three-storey frame; and (b) force-displacement curve

Table 6.1 Response quantities at $t = 1.36$ s. Yield moment for the beams is 50 kN m

Section	Time step (s)	x (m)	$\dot{x}$ (m s^{-1})	$\ddot{x}$ (m s^{-2})	θ (rad)	$\dot{\theta}$ (rad s^{-1})	$\ddot{\theta}$ (rad s^{-2})	M (kN m)
1	1.36	0.00293	0.0341	−1.2945	0.00109	0.013	−0.452	50
3	1.36	0.00701	0.0883	−2.8586	0.000946	0.014	−0.297	−23.18
5	1.36	0.00978	0.1339	−3.4814	0.000529	0.009127	−0.098	42.89
2	1.36	0.00293	0.0341	−1.2945	0.00109	0.013	−0.452	−50
4	1.36	0.00701	0.0883	−2.8586	0.000946	0.014	−0.297	23.18
6	1.36	0.00978	0.1339	−3.4814	0.000529	0.009127	−0.098	−42.89

of time, the stiffness matrix for the system is computed by considering hinges at sections where yieldings have taken place. After the total stiffness matrix is obtained as described above (Equation 6.28a), the stiffness matrix is condensed to only the sway degrees of freedom. The total stiffness matrix and the condensed stiffness matrix are given below:

$$K = 4.83 \times 10^4 \times \begin{bmatrix} 1.067 & & & & & & & & \\ -1.067 & 2.133 & & & & sym & & & \\ 0 & -1.067 & 2.133 & & & & & & \\ 0.8 & -0.8 & 0 & 2.4 & & & & & \\ 0.8 & 0 & -0.8 & 0.8 & 4 & & & & \\ 0 & 0.8 & 0 & 0 & 0.8 & 3.2 & & & \\ 0.8 & -0.8 & 0 & 0.4 & 0 & 0 & 2.4 & & \\ 0.8 & 0 & -0.8 & 0 & 0.4 & 0 & 0.8 & 4 & \\ 0 & 0.8 & 0 & 0 & 0 & 0 & 0 & 0.8 & 3.2 \end{bmatrix} \begin{matrix} \Delta_1 \\ \Delta_2 \\ \Delta_3 \\ \theta_1 \\ \theta_2 \\ \theta_3 \\ \theta_4 \\ \theta_5 \\ \theta_6 \end{matrix}$$

$$K_\Delta = 4.83 \times 10^4 \times \begin{bmatrix} 0.4451 & & sym \\ -0.6177 & 1.276 & \\ 0.2302 & -1.0552 & 1.811 \end{bmatrix} \begin{matrix} \Delta_1 \\ \Delta_2 \\ \Delta_3 \end{matrix}$$

6.4 Pushover Analysis

Pushover analysis is popular in earthquake engineering, as is the response spectrum method of analysis. As the latter is a good equivalent static analysis (substitute) for the elastic dynamic analysis of structures to a given earthquake, likewise pushover analysis is a good equivalent non-linear static analysis (substitute) for the inelastic dynamic analysis of structures for the earthquake. Pushover analysis provides a load versus deflection curve of the structure starting from the state of rest to the ultimate failure of the structure. The load is representative of the equivalent static load of a mode (generally taken as the fundamental mode) of the structure and may be conveniently taken as the total base shear of the structure. Similarly, the deflection may represent the deflection of any storey and may be conveniently selected as the top-storey deflection.

Pushover analysis could be force controlled or displacement controlled. In the force control, the total lateral force is applied in increments. For each increment of the load, the stiffness matrix of the structure may have to be changed, once the structure passes from the elastic state to the inelastic state. In the displacement control, the displacement of the top storey of the structure is incremented, such that the required horizontal force pushes the structure laterally proportional to the fundamental horizontal translational mode of the structure in the direction of the lateral load. As in force controlled pushover analysis, the stiffness matrix of the structure may have to be changed for each increment of displacement. The displacement controlled pushover analysis is generally preferred over the force controlled one because the analysis could be carried out up to the desired level of the displacement.

The displacement controlled pushover analysis is explained with the help of an example of a building frame. Consider the building frame shown in Figure 6.18. The fundamental mode shape is also shown in the same figure. For the analysis, the following input data are required in addition to those shown in the figure: (i) the assumed collapse mechanism (for example Figure 6.15); (ii) moment–rotation relationship for the sections that are assumed to yield (for example Figure 6.16); (iii) the fundamental mode shape; (iv) the limiting displacement, if displacement at the complete collapse is not desired; and (v) rotational capacity of the plastic hinges.

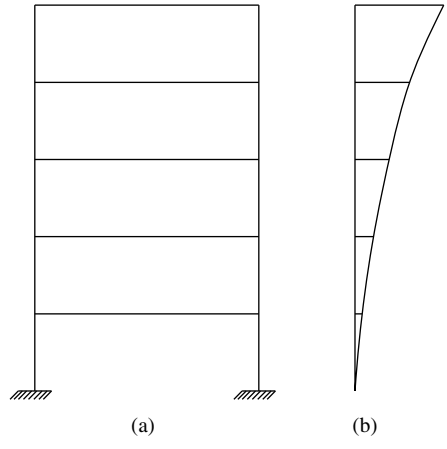

Figure 6.18 Example frame for pushover analysis: (a) bare frame; and (b) fundamental mode shape of the frame

The analysis is carried out in the following steps:

i. Choose a suitable increment $\delta\Delta_1$ for the displacement to be applied at the top of the frame.
ii. Give the first increment of displacement at the top and find the corresponding displacements at other floor levels by multiplying it with the mode shape coefficients, that is, $\delta\Delta_1^r = \delta\Delta_1 \times \phi^r$, in which $\delta\Delta_1^r$ is the displacement increment of the rth floor and ϕ^r is the mode shape coefficient for the rth floor.
iii. Obtain the load vector $\Delta \boldsymbol{p} = \boldsymbol{K}\boldsymbol{\delta}\Delta_1$ in which $\boldsymbol{K}$ is the elastic stiffness matrix of the frame and $\boldsymbol{\delta}\Delta_1$ is the incremental displacement vector corresponding to lateral degrees of freedom. From the load vector, obtain ΔV_{B1} in which ΔV_{B1} is the incremental base shear.
iv. The top displacement is incremented in this manner and $V_{Bn} = \sum_{i=1}^{n} \Delta V_{Bi}$ is obtained for any stage (n) for the top-floor displacement, $\Delta_n = \sum_{i=1}^{n} \delta\Delta_i$.
v. At the end of each increment of displacement, moments are checked at each potential location of the plastic hinges shown in the figure. For this purpose, θ_n at the ends of the beam are calculated using the following relationship $\boldsymbol{\theta}_n = -\boldsymbol{K}_{\theta\theta}^{-1}\,\boldsymbol{K}_{\theta\Delta}\Delta_n$ in which $\boldsymbol{K}_{\theta\theta}$ and $\boldsymbol{K}_{\theta\Delta}$ are the partitioned matrices used in the standard matrix condensation procedure to condense out rotations, and Δ_n is the lateral displacement vector of the frame. If the moments at the potential sections of yielding reach the yield moment, plastic hinges are assumed to form at those sections. For the subsequent displacement increment, the stiffness matrix of the frame is modified by assuming ordinary hinges at those sections.
vi. Whenever a plastic hinge is formed at a section, rotation at the hinge is calculated for the subsequent displacement increment, and the total rotation in the hinge at any stage (n) is checked for the assumed rotation capacity. If the rotation at any hinge exceeds its rotation capacity, then the displacement increment is discontinued. A rotational hinge failure (partial collapse) preceeds the assumed mechanism of failure. Assumption of unlimited rotation capacity in the plastic hinge is generally made in order to avoid such a partial collapse.
vii. The load-deflection curve (V_B versus Δ) is traced up to the final collapse or up to the specified displacement level.

Example 6.6

Carry out an equivalent static non-linear analysis of a seven-storey frame shown in Figure 6.19 by displacement control pushover analysis for the elasto-plastic backbone curves given in the same figure. The properties of the frame are given in Table 6.2.

Solution: The first mode shape for the structure is shown in Figure 6.20. SAP2000 is used to obtain the displacement control pushover analysis. The moment-rotation curve for the yield sections is shown in Figure 6.19b (with a specified rotational capacity). For a given displacement at the top, the displacements at other floors are obtained using the first mode shape.

The plot of base shear versus top-storey displacement is shown in Figure 6.21. The sequence of the formation of hinges is shown in Figure 6.22. In Table 6.3, plastic hinges formed at different displacement stages are shown. It is seen from Figure 6.22 that the frame collapses before an adequate number of hinges are formed in the structure. This is so because joint failure takes place at the joint, where four hinges are formed, much before the complete mechanism of failure. Furthermore, it is observed from Figure 6.21 that the load suddenly drops at certain values of the displacement. The reason for such drops is attributed to the inputs given to SAP2000 for the analysis. In SAP, the moment–rotation curve for a yield section is not specified exactly as elasto-plastic, but mildly bilinear as shown in Figure 6.19b. As a result, yield

Table 6.2 Properties of the seven-storey frame: $E = 2.48 \times 10^7$ kN m^{-2}; mass at each floor level is calculated by lumping appropriate masses at each floor; C and B stand for columns and beams respectively

Cross section	Location	b (mm)	$\underline{d}$ (mm)	M_y (kN m)	θ_y (rad)	θ_{max} (rad)
C1	Ground, first, second	400	400	168.9	9.025e-3	0.0271
C2	Third, fourth, fifth and sixth	300	300	119.15	0.0133	0.0399
B1	Ground, first, second	400	500	205.22	6.097e-3	0.0183
B2	Third, fourth, fifth and sixth	300	300	153.88	8.397e-3	0.0252

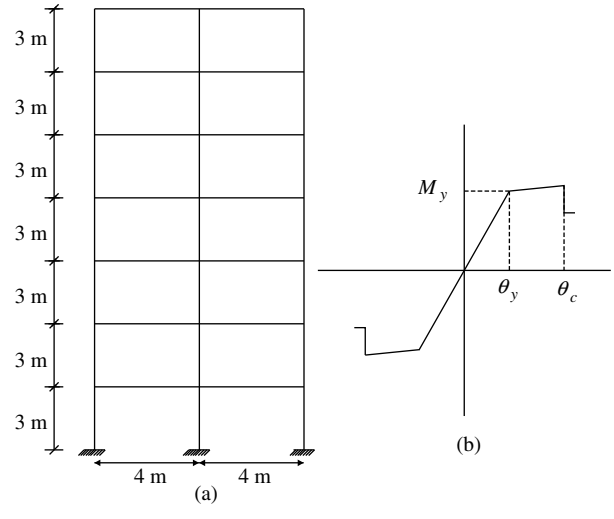

Figure 6.19 Properties of the seven-storey frame: (a) seven-storey frame; and (b) moment-rotation curve for beams

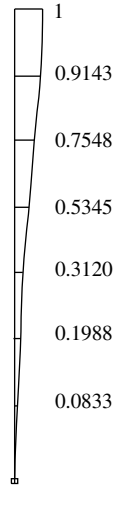

Figure 6.20 First mode shape of the frame

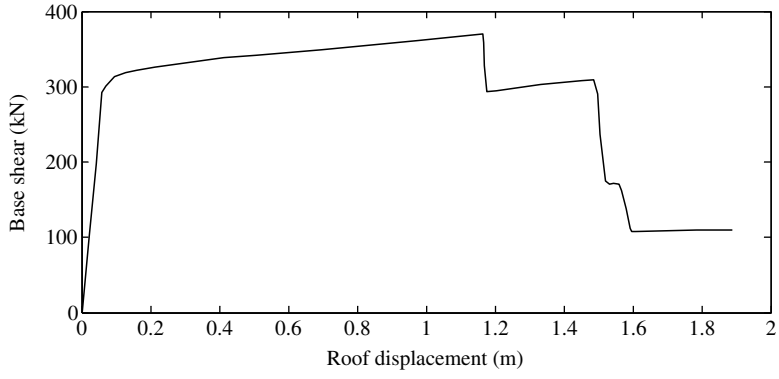

Figure 6.21 Variation of base shear with top floor displacement

sections continue to take moment after the initial yielding, until the final rotational capacity of the section is reached. The stiffness of the structure suddenly drops leading to a drop of the load carrying capacity of the structure, when the rotational capacity of a yield section or those of a number of yield sections are reached.

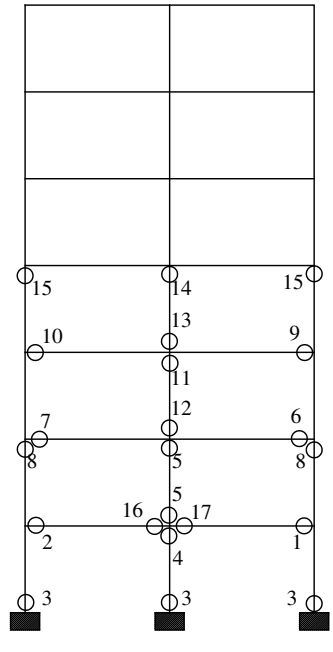

Figure 6.22 Sequence of the formation of hinges

Table 6.3 Sequence of formation of hinges at different displacement stages

Δ (m)	Base shear (kN)	Plastic hinges at section
0.110891	316.825	1
0.118891	317.866	1,2
0.134891	319.457	1,2,3
0.142891	320.006	1,2,3,4
0.150891	320.555	1,2,3,4,5
0.174891	322.201	1,2,3,4,5,6
0.190891	323.299	1,2,3,4,5,6,7
0.206891	324.397	1,2,3,4,5,6,7,8
0.310891	331.498	1,2,3,4,5,6,7,8,9
0.318891	332.035	1,2,3,4,5,6,7,8,9,10
0.334891	333.11	1,2,3,4,5,6,7,8,9,10,11
0.350891	334.185	1,2,3,4,5,6,7,8,9,10,11,12
0.518891	342.546	1,2,3,4,5,6,7,8,9,10,11,12,13
0.534891	343.207	1,2,3,4,5,6,7,8,9,10,11,12,13,14
0.622891	346.843	1,2,3,4,5,6,7,8,9,10,11,12,13,14,15
1.448699	307.822	1,2,3,4,5,6,7,8,9,10,11,12,13,14,15,16
1.456699	308.225	1,2,3,4,5,6,7,8,9,10,11,12,13,14,15,16,17

6.5 Concepts of Ductility and Inelastic Response Spectrum

As shown in the elastic response spectrum method of analysis, the base shear induced in a single portal frame is:

$$V_b = mS_a = \frac{WS_a}{g} \tag{6.34}$$

where W is the weight of the mass and S_a is pseudo acceleration response spectrum ordinate corresponding to the natural period and damping of the system. If the system is designed for a base shear much lower than V_b, for example, V_b/R, where R could be 3–4, then the system will be deformed beyond the limit of elastic behavior for the design earthquake whose spectrum is used to obtain the value of S_a/g. Under this earthquake, the system will vibrate in a different way than it would have vibrated if it were designed for V_b. The nature of vibration will depend upon the material behavior represented by its force deformation characteristics under cyclic loading. This force deformation behavior is discussed in Section 6.2. For such non-linear force-deformation behavior of the materials, the equation of motion is written in incremental form and solved for each time step assuming the stiffness of the system to remain the same within the increment, as explained previously. In order to explain the concept of ductility and other related parameters, two SDOF systems, one with elasto-plastic material behavior and the other with a corresponding elastic (linear) material behavior are considered as shown in Figure 6.23.

6.5.1 Ductility

The ductility factor is defined as:

$$\mu = \frac{x_m}{x_y} \tag{6.35a}$$

where x_m is the maximum absolute displacement of the elasto-plastic system during the earthquake and x_y is the yield displacement. The ductility factor is always greater than unity and is a measure of the deformation of the system beyond the yield limit. An associated factor, known as the yield reduction factor, R_y is defined as the inverse of $\overline{f}_y$, in which $\overline{f}_y$ is the normalized yield strength of the elasto-plastic system (Figure 6.23) given by:

$$\overline{f}_y = \frac{f_y}{f_0} = \frac{x_y}{x_0} \tag{6.35b}$$

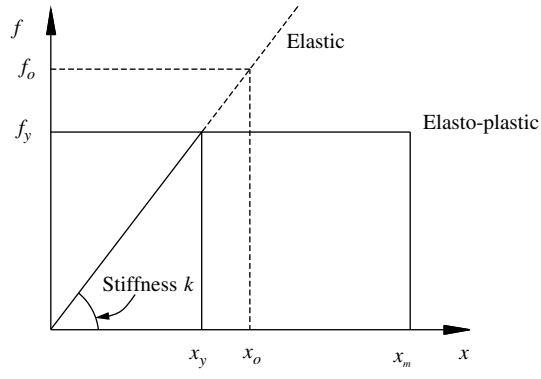

Figure 6.23 Elasto-plastic system and corresponding elastic system

f_0 is defined as the strength (or restoring force $= kx_0$) of the SDOF system if it were to remain within the elastic limit during an earthquake. A normalized strength of less than unity implies that the SDOF system will deform beyond its elastic limit. If $\overline{f} = 1$, it denotes an elasto-plastic SDOF system with $f_y = f_0$ so that the system does not deform beyond the elastic limit. A system designed with $R_y = 2$ means that the strength of the SDOF system is halved compared with that for which the system would have remained within an elastic limit during the earthquake.

The ratio between the peak deformations x_m and x_0 of the elasto-plastic system and the corresponding elastic system may be written as a function of μ and R_y as

$$\frac{x_m}{x_0} = \frac{x_m}{x_y} \times \frac{x_y}{x_0} = \mu \overline{f}_y = \frac{\mu}{R_y} \tag{6.36}$$

With the above definitions, the equation of motion of the elasto-plastic SDOF system may be rewritten as:

$$\ddot{x} + 2\xi\omega_n \dot{x} + \omega_n^2 x_y \overline{f}(x, \dot{x}) = -\ddot{x}_g \tag{6.37}$$

in which $\overline{f}(x, \dot{x}) = f(x, \dot{x})/f_y$; ω_n is the natural frequency of the system based on its initial stiffness, and ξ is the damping ratio used to define the damping in the elastic range. Assuming that the deformation goes in the inelastic range, the equation of motion can be written in terms of a ductility ratio, that is,

$$\ddot{\mu} + 2\xi\omega_n \dot{\mu} + \omega_n^2 \overline{f}(\mu, \dot{\mu}) = -\omega_n^2 \frac{\ddot{x}_g}{a_y} \tag{6.38}$$

in which $x(t) = \mu(t)x_y$; $a_y = f_y/m$ is the acceleration of the mass necessary to produce the yield force. μ depends upon three parameters ω_n, ξ, and a_y for a given $\ddot{x}_g$ and form of $\overline{f}(\mu, \dot{\mu})$. As $a_y = f_y/m = \omega_n^2 x_0 \overline{f}_y$, the parameter a_y is replaced by $\overline{f}_y$.

For different levels of $\overline{f}_y$, the time histories of the response for an elasto-plastic SDOF model will be different and will give different values of the peak displacement. For example, for $\overline{f}_y = 1$, the responses remain within elastic limits. In many instances, the peak displacement observed for $\overline{f}_y = 1$ is more than $\overline{f}_y < 1$. However, this is not always true. The reason for the lower value of the peak response in the elastic-plastic case is the energy dissipation due to hysteresis produced by cyclic excitation leading to increased equivalent damping in the system. The opposing effect, which increases the displacement, is the decreased equivalent stiffness of the system as cyclic effect continues in the inelastic range. The most important effect of reduction of $\overline{f}_y$ is on the drift (permanent deformation) that takes place at the end of the earthquake. The less the value of $\overline{f}_y$, the more the system is forced to stay in the inelastic state and more becomes the drift. The ductility can be easily calculated from $x_m/x_0 (= \mu/R_y)$ if peak deformations of an elasto-plastic system with a specified $\overline{f}_y$ and the corresponding elastic system are known.

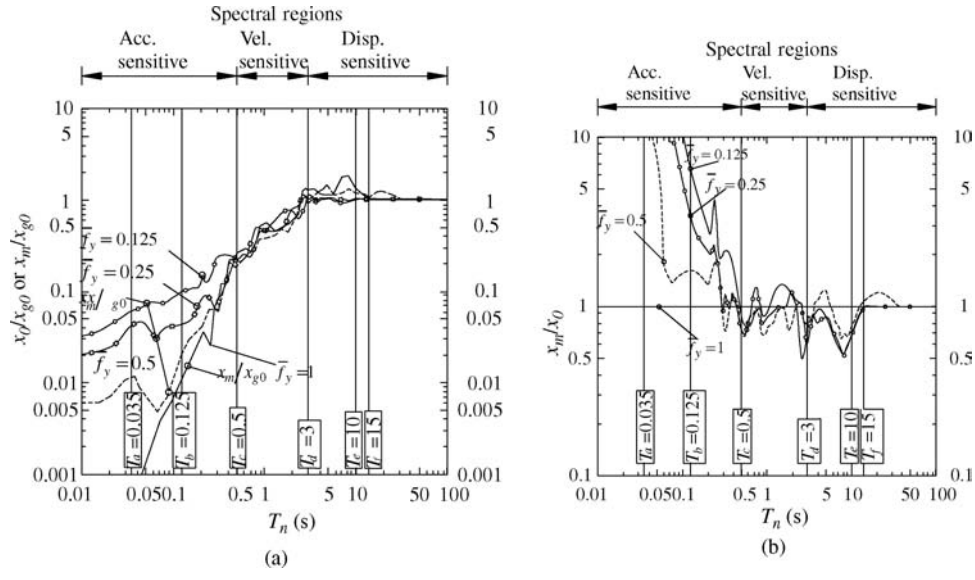

Figure 6.24 Response of an SDOF system for El Centro ground motion for different values of T_n: (a) normalized peak deformations for elasto-plastic system and elastic system; and (b) ratio of the peak deformations

The effects of time period $T_n = \frac{2\pi}{\omega_n}$ on μ, x_m, x_0, and $\bar{f}_y$ are illustrated with the help of Figure 6.24 drawn for the El Centro earthquake. The figure shows the following:

i. For long period structures, x_m and x_0 are nearly the same and are almost independent of $\bar{f}_y$, that is, displacements of elasto-plastic and elastic systems are nearly the same. Furthermore, peak deformation is equal to peak ground displacement, independent of $\bar{f}_y$ and $\mu = R_y$.
ii. In the velocity sensitive region, $x_m \neq x_0$; may be smaller or larger than x_0; affected by $\bar{f}_y$ (not to a great extent); μ may be smaller or larger than R_y.
iii. In the acceleration sensitive region, x_m is greater than x_0 and x_m increases with decreasing $\bar{f}_y$ and decreasing period. μ can be much greater than R_y. Thus, for a very short period structure, the ductility demand imposed on the structure may be very large even though the system could have a strength only slightly less than the corresponding elastic system.

These observations are found to be valid for many cases of ground motions; only the *D-A-V* zones may vary from ground motion to ground motion.

6.5.2 *Inelastic Response Spectrum*

The inelastic response spectrum is plotted for

$$D_y = x_y \quad V_y = \omega_n x_y \quad A_y = \omega_n^2 x_y \tag{6.39}$$

where D_y is the yield deformation of the elasto-plastic system. A plot of D_y against T_n for a fixed value of μ is known as the yield deformation response spectrum. Similarly, plots of V_y and A_y are, respectively, termed pseudo velocity and pseudo acceleration spectra. These spectra are called inelastic response spectra, and also ductility spectra. Because of the relationship between D_y, V_y, and A_y, they can be plotted

in a tripartite plot. The yield strength of the elasto-plastic system, f_y, is given by

$$f_y = mA_y \tag{6.40}$$

Yield strength for a specified ductility is difficult to obtain. Reverse is possible. However, using an interpolation technique the yield strength for a specified ductility can be determined and a ductility spectrum can be constructed. The procedure may be summarized as follows.

i. For specified T_n and ξ, obtain the response of the elasto-plastic system for a number of $\bar{f}_y$ values less than equal to 1. Each response analysis will give a value of μ. Choose $\bar{f}_y$ such that the μ values thus obtained are in the vicinity of the desired μ value. Note that f_0 is obtained as kx_0, where x_0 is the maximum elastic response for the specified time history.
ii. From the set of the pair of $\bar{f}_y$ and μ values, interpolate the desired μ value and the corresponding $\bar{f}_y$ value.
iii. Using this $\bar{f}_y$ value, obtain the response of the elasto-plastic system and find μ. If the value of μ is very close to that which was obtained from interpolation, then the process may be stopped. Otherwise, a pair of better interpolated values may be obtained and the process is repeated.
iv. For different values of T_n, the steps can be repeated to obtain the ductility curve as shown in Figure 6.25. Note that $w = mg$.

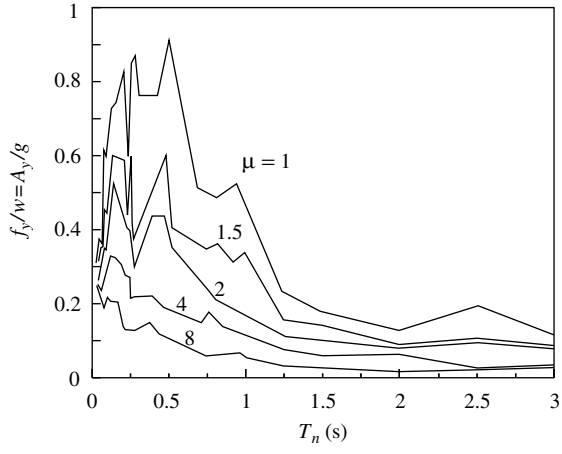

Figure 6.25 Constant ductility spectrum for elasto-plastic systems ($\mu = 1, 1.5, 2, 4, 8$)

From the ductility spectrum, it is possible to obtain the yield strength to limit the ductility demand to an allowable value for given T_n and ξ. Peak deformation is $x_m = \mu x_y$ and $x_y = f_y/k = A_y/\omega_n^2$. With the knowledge of the ductility spectrum for $\mu = 1$, it is possible to plot $\bar{f}_y$ versus T_n for different values of μ. This provides a direct idea about the strength reduction required for a particular ductility. Such a plot is shown in Figure 6.26.

The effect of damping ratio from 0.02 to 0.01 is marginal on the ductility curve especially in the acceleration and displacement zones of the spectrum. In the velocity zone the effect is observed, which is reduced for higher values of μ. It may be noted that the effect of yielding cannot be considered in terms of a fixed amount of equivalent damping.

From the nature of the plot of $\bar{f}_y$ with T_n for several earthquake records, researchers have provided several idealized forms of the variation of $\bar{f}_y$ with T_n. One such simple relationship is given by the

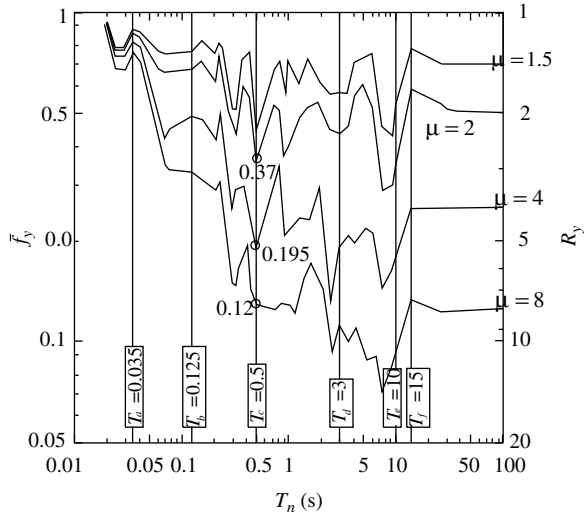

Figure 6.26 Variation of $\bar{f}_y$ with T_n ($\mu = 1, 1.5, 2, 4, 8$)

following and is shown in Figure 6.27.

$$\bar{f}_y = \begin{cases} 1 & T_n < T_a \\ (2\mu - 1)^{-1/2} & T_b < T_n < T_c \\ \mu^{-1} & T_n > T_c \end{cases} \tag{6.41}$$

T_a, T_b, T_c, and so on are those used for the elastic design spectrum.

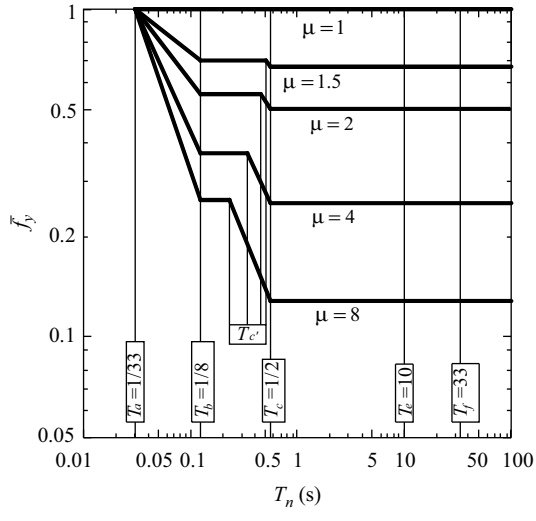

Figure 6.27 Idealized variation of $\bar{f}_y$ with T_n

As yield strength reduction factor $R_y = 1/\overline{f}_y$, it is possible to construct an idealized inelastic design spectrum for a particular value of μ from the elastic design spectrum. This inelastic design spectrum compares well with many inelastic spectra for real earthquakes when smoothed. Construction of the inelastic design spectrum for a given value of μ from the elastic design spectrum is illustrated with the help of the example below.

Example 6.7

Construct an inelastic design spectrum in a tripartite plot for $\mu = 2$ for the given elastic design spectrum (Figure 2.22; 50th percentile; Chapter 2).

Solution: It is presumed that the elastic design spectrum $a - b - c - d - e - f$ shown in Figure 6.28a has been developed as explained in Section 2.5.4 (Chapter 2). From this elastic design spectrum, the inelastic design spectrum $a' - b' - c' - d' - e' - f'$ is obtained as shown below.

1. Divide the constant-*A* ordinate of segment *b*–*c* by $R_y = \sqrt{2\mu - 1}$ to obtain the segment $b' - c'$.
2. Divide the constant-*V* ordinate of segment $c - d$ by $R_y = \mu$ to obtain the segment $c' - d'$.
3. Divide the constant-*D* ordinate of segment $d - e$ by $R_y = \mu$ to obtain the segment $d' - e'$.
4. Divide the ordinate at f by $R_y = \mu$ to obtain f'. Join points f' and e'. Draw $D_y = x_{g0}/\mu$ for $T_n > 33$ s.
5. Take the ordinate a' of the inelastic spectrum at $T_n = 1/33$ s as equal to that of point a of the elastic spectrum. Join points a' and b'.
6. Draw $A_y = \ddot{x}_{g0}$ for $T_n < 1/33$ s.

The resulting inelastic response spectrum is shown in the Figure 6.28b.

6.6 Ductility in a Multi-Storey Structure

For a single degree of freedom system, an inelastic response spectrum/ductility spectrum can be directly used for designing the system (that is, to determine the yield strength to be provided) for a specified ductility. Once it is designed, then the maximum displacement of the elasto-plastic system obtained from the time history analysis is found to be exactly the same as μu_y. However, this is not the case for the multi-storey structures. Firstly, it is very difficult to obtain design yield strength for all members of the structure corresponding to a uniform ductility factor. Secondly, even if it could be done for some simplified cases, the ductility demands imposed by the earthquake (as obtained from time history analysis) could be widely different from one member to the other, and for some members may far exceed the designed (uniform) ductility.

Some studies on multi-storey frames are discussed here in order to show the variation of ductility demands of different members of the frame when it is designed using the inelastic response spectrum for a specified (design) ductility [3]. Building frames of 5, 10, 20 and 40 storeys idealized as shear frames with uniform floor mass are considered for study. The fundamental time periods of these frames are selected as 0.8, 1.6, 3.5 s, respectively. The lateral force and storey shears for the frames are obtained by the seismic coefficient method in terms of base shear V_b. The value of V_{by} is obtained from the inelastic response spectrum of the El Centro earthquake for a specified ductility.

The storey stiffness is obtained using the following considerations:

i. Base shear coefficient for the specified time period and damping using code provisions.
ii. Static application of lateral forces, assuming the structure to be elastic and storey drifts to be equal resulting in a linearly varying deflection with height.

The storey yield shears are obtained from V_{by} and the storey shear distribution as given in the code.

These frames were analyzed assuming elasto-plastic behavior of the storey shear versus storey displacement under the El Centro earthquake time history. The storey ductility demands were obtained from the analysis and results were analyzed. The results show that:

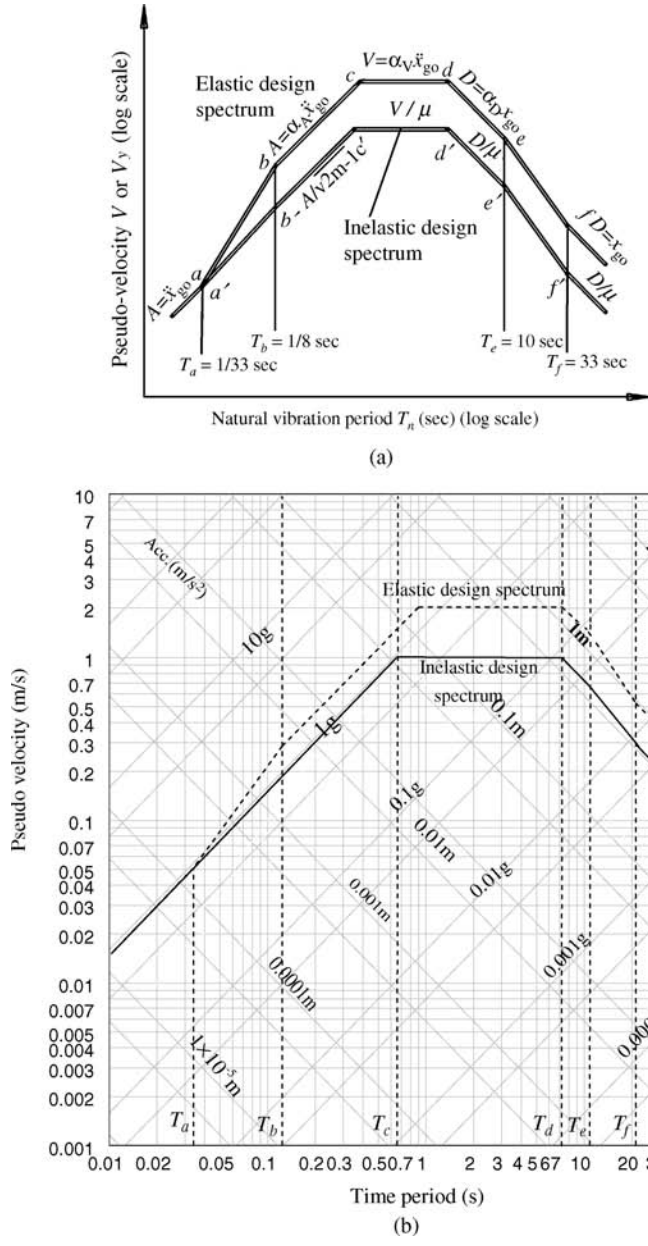

Figure 6.28 Construction of inelastic design spectrum: (a) illustration of the method; and (b) inelastic design spectrum for $\mu = 2$

i. For taller buildings, the ductility demands are larger in the upper and lower storeys and decrease in the middle storeys.
ii. The deviation of storey ductility demands from the allowable (design) ductility demand increases for taller buildings.

iii. In general, the ductility demand is maximum at the first storey and could be 2–3 times the allowable ductility.

In order that the ductility demand in the first storey remains within the allowable limit, V_{by}, as obtained from the inelastic spectrum, should be increased. An idea of how much the increase should be can be made from the ratio between the V_{by} of the multi-storey building and that of the corresponding SDOF system for the allowable ductility. The corresponding SDOF system has the same natural period as that of the first mode of the building frame. The mass and V_{by} of the SDOF system are the same as the total mass and design V_{by} of the multi-storey frame. A detailed discussion is given in reference [3].

In general, an increase of base shear over and above the design base shear by some percentage tends to keep the ductility demand imposed by the earthquake within the stipulated limit.

Exercise Problems

(Use standard programs like MATLAB®, SAP2000 and ABAQUAS to solve the problems; you may also use your own program developed using the methods presented in the chapter.)

6.8 An SDOF system has a non-linear spring having the bilinear force-displacement characteristics as shown in Figure 6.29. Find the time histories of relative displacement and acceleration of the mass for the El Centro earthquake. Also, find the ductility ratio. Take $\xi = 5\%$ and $m = 10$ kg.

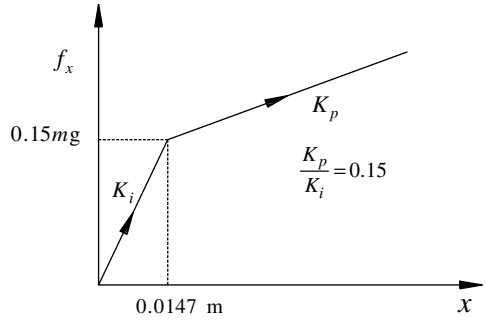

Figure 6.29 Force-displacement curve of the non-linear spring

6.9 A five-storey frame as shown in Figure 6.30 is subjected to the El Centro earthquake. The columns are weaker than the beams and have the non-linear properties as shown in the figure. Find (i) the envelope of the peak relative displacements of the floors; (ii) the time history of the base shear; and (iii) the stiffness matrix of the system at time $t = 6.2$ s. Assume $\xi = 5\%$.

6.10 A three-storey 3D frame with rigid diaphragms, shown in Figure 6.31, is subjected to the El Centro earthquake acting along the x-direction. The elasto-plastic force-deformation characteristics of the columns are also shown in the same figure. Find (i) the time histories of rotation and x-displacement of the top floor; (ii) the time histories of base shears of column A; (iii) the ductility demand of the column A at each floor level; and (iv) the stiffness matrix of the system at time $t = 7$ s. Assume $\xi = 5\%$. To perform the analysis, the effect of bi-directional interaction on yielding of the columns may be ignored. However, to compute the stiffness matrix at $t = 7$ s, this interaction effect should be included and the responses obtained from the no interaction analysis at $t = 7$ s may be used.

6.11 For the frame shown in Figure 6.30, find the top-floor response spectrum (for 5% damping), and compare it with that if the columns are assumed to be un-yielding. Also, find the ductility demand of

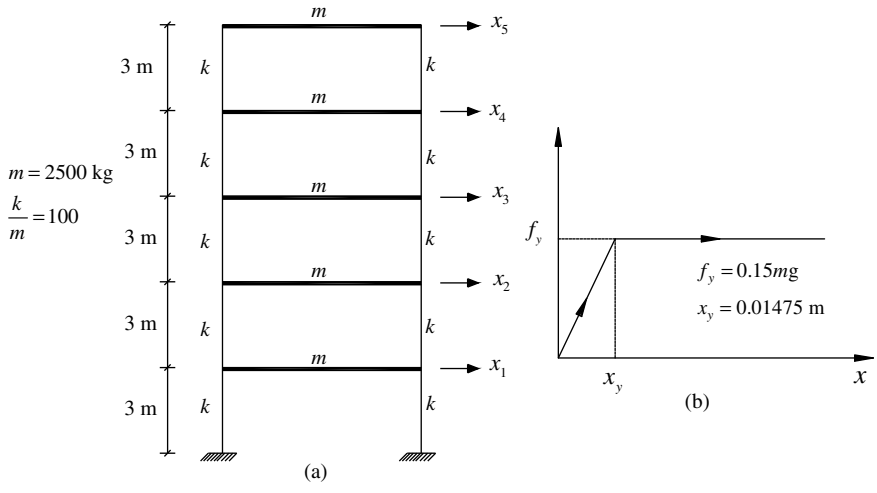

Figure 6.30 Properties of the five-storey frame: (a) five-storey frame; and (b) force-displacement curve of the columns

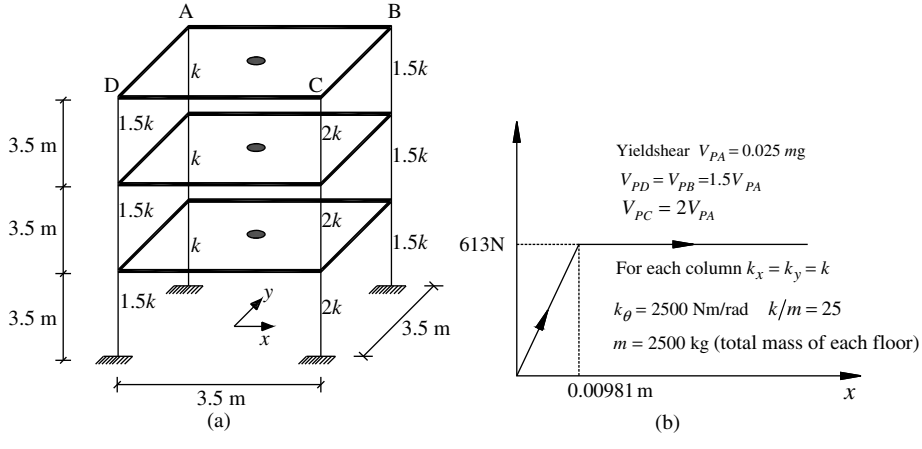

Figure 6.31 Properties of 3D frame: (a) three-storey frame; and (b) force-displacement curve of column

each floor. [HINT: the floor response spectrum is the plot of pseudo acceleration of an SDOF attached to the floor with its time period for a given value of ξ.]

6.12 A five-storey strong column–weak beam frame, shown in Figure 6.32, is subjected to the El Centro earthquake. The mass at each floor level is $m = 2500$ kg. The potential locations of the plastic hinges in the beams are shown in the same figure along with the moment–rotation backbone curves. Obtain the time histories of (i) the top floor relative displacement; (ii) the base shear of the column A; (iii) the moment–rotation plot for section B; and (iv) ductility demand of each beam.

6.13 Using the displacement control pushover analysis, obtain the plots of base shear versus top displacement of the frames shown in Figure 6.32 (with changed beams and columns cross sections) and Figure 6.30. Changed cross sections are: all columns– 40 × 40 cm and all beams– 30 × 30 cm.

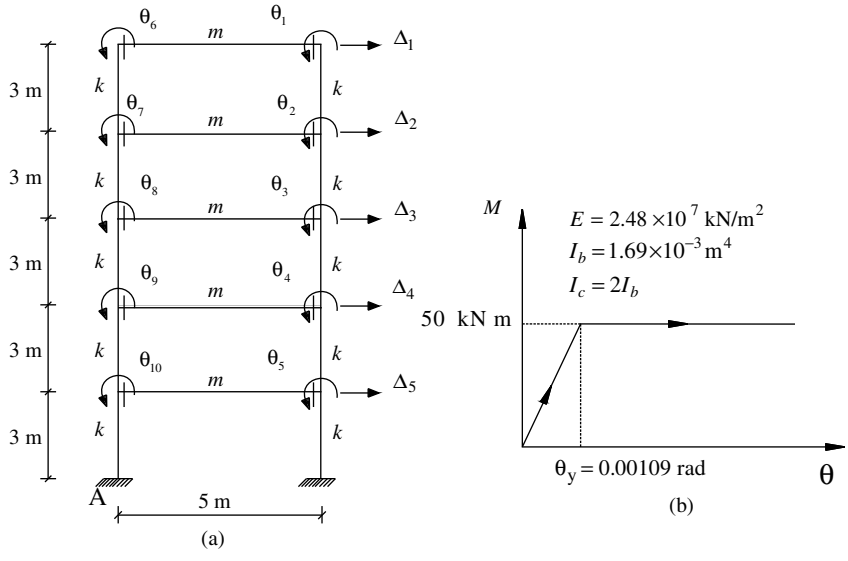

Figure 6.32 Properties of the five-storey frame: (a) five-storey frame; and (b) moment-rotation curve of the beams

Floor masses are not changed. Take the values of M_y, θ_y and θ_{max} from Table 6.4, which can be interchanged between beams and columns. For the other problem (that is, Figure 6.30), take the shear displacement capacity as three times the yield value. Also, show the formation of hinges at different displacement stages. [NOTE: for pushover analysis, the flat portion of the elasto-plastic curve is replaced by a line with a very mild slope.]

Table 6.4 Properties of the five-storey frame

Member	Cross section (mm)	M_y (kN m)	θ_y (rad)	θ_{max} (rad)
Beam	300×300	153.88	8.397e-3	0.0252
Column	400×400	168.9	9.025e-3	0.0271

6.14 Construct an inelastic design response spectrum in tripartite plot for $\mu = 2$, 3 and 4 for the idealized elastic response spectrum of the El Centro earthquake (Figure 2.17; Chapter 2). Compare the inelastic design response spectra with the actual inelastic response spectrums of the El Centro earthquake for $\mu = 2$ and 4 (for $\xi = 5\%$).

References

1. Tso, W.K. and Sadek, A.W. (1985) Inelastic seismic response of eccentric structures. *Journal of Earthquake Engineering and Structural Dynamics*, **13**(2), 255–269.
2. Shakib, H. and Datta, T.K. (1993) Inelastic response of torsionally coupled system to an ensemble of non stationary ground motion. *Engineering Structure*, **15**(1), 13–20.
3. Chopra, A.K. (2001) *Dynamics of Structures: Theory and Application to Earthquake Engineering*, 2nd edn, Prentice Hall, Inc., Englewood Cliffs, NJ.

7

Seismic Soil Structure Interaction

7.1 Introduction

For the seismic analysis of overground and underground structures, consideration of the soil–structure interaction becomes extremely important when the soil or the foundation medium is not very firm. During earthquake excitation, the structure interacts with the surrounding soil imposing soil deformations. These deformations, in turn, cause the motion of the supports or the interface region of the soil and the structure to be different to that of the free field ground motion. These interactions substantially change the response of the structure. For very stiff soil, this change is extremely small and can be neglected. Therefore, consideration of base fixity remains a valid assumption for overground structures constructed on firm soil. Similarly, the effect of soil–structure interaction on long buried structures. such as pipelines, within firm soil is negligible as it takes the same profile as that of the soil during the earthquake motion.

In order to understand the soil–structure interaction problem properly, it is necessary to have some knowledge of the earthquake wave propagation through the soil medium for two main reasons. Firstly, the dynamic characteristics of the input ground motion to the structure depend upon the modification of the bedrock motion as it propagates through the soil. Thus, the knowledge of wave propagation through the soil medium is essential to understand ground motion modifications due to soil properties. Secondly, the knowledge of the vibration characteristics of the soil medium due to wave propagation is important in relation to the determination of the soil impedance functions and fixing the boundaries for a semi-infinite soil medium, when the wave propagation analysis is performed by numerical techniques. Therefore, in this chapter, wave propagation through soil is discussed first and then, seismic soil–structure interaction problems are presented.

7.2 Wave Propagation through Soil

Referring to Figure 7.1, it can be easily shown that the unbalanced external forces in the x-direction are in equilibrium with the internal force in the same direction and give

$$\rho \frac{\partial^2 u}{\partial t^2} = \rho \ddot{u} = \frac{\partial \sigma_{xx}}{\partial x} + \frac{\partial \sigma_{xy}}{\partial y} + \frac{\partial \sigma_{xz}}{\partial z} \tag{7.1}$$

in which σ_{xx}, σ_{xz}, and so on are the stresses as shown in the figure and ρ is the mass density of the soil. In a similar way, two more equations of equilibrium can be written for y- and z-directions respectively.

Seismic Analysis of Structures T.K. Datta

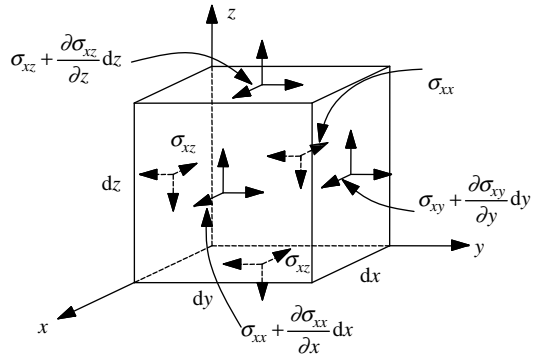

Figure 7.1 Stresses on an infinitesimal cube

Using strain displacement relationships, these three equations can be written in the following form:

$$\rho \ddot{u} = (\lambda + \mu) \frac{\partial \overline{\varepsilon}}{\partial x} + \mu \nabla^2 u \tag{7.2}$$

$$\rho \ddot{v} = (\lambda + \mu) \frac{\partial \overline{\varepsilon}}{\partial y} + \mu \nabla^2 v \tag{7.3}$$

$$\rho \ddot{w} = (\lambda + \mu) \frac{\partial \overline{\varepsilon}}{\partial z} + \mu \nabla^2 w \tag{7.4}$$

where

$\ddot{u}$, $\ddot{v}$, and $\ddot{w}$ are the accelerations in the x-, y- and z-directions, respectively
λ and μ are Lame's constants
$\overline{\varepsilon} = \varepsilon_{xx} + \varepsilon_{yy} + \varepsilon_{zz}$, ε_{xx} is the strain in the x-direction
∇^2 is the Laplace operator.

Solution of the above equations under different boundary conditions provides the ground motions in the x-, y- and z-directions at any point within the soil due to earthquake wave propagation. Note that the two Lame's constants are related to E, G, and γ (Young's modulus, Shear modulus, and Poisson's ratio, respectively) as:

$$E = \frac{\mu(3\lambda + 2\mu)}{\lambda + \mu}; \qquad G = \mu; \qquad \gamma = \frac{\lambda}{2(\lambda + \mu)} \tag{7.5}$$

The above wave equations (Equations 7.2–7.4) in an infinite soil medium can be combined to produce two wave equations. The first type of wave equation is obtained by differentiating Equations 7.2–7.4 with respect to x, y, and z and adding the results to give

$$\rho\left(\frac{\partial^2 \varepsilon_{xx}}{\partial t^2} + \frac{\partial^2 \varepsilon_{yy}}{\partial t^2} + \frac{\partial^2 \varepsilon_{zz}}{\partial t^2}\right) = (\lambda + \mu)\left(\frac{\partial^2 \overline{\varepsilon}}{\partial x^2} + \frac{\partial^2 \overline{\varepsilon}}{\partial y^2} + \frac{\partial^2 \overline{\varepsilon}}{\partial z^2}\right) + \mu\left(\frac{\partial^2 \varepsilon_{xx}}{\partial x^2} + \frac{\partial^2 \varepsilon_{yy}}{\partial y^2} + \frac{\partial^2 \varepsilon_{zz}}{\partial z^2}\right) \tag{7.6}$$

or

$$\rho \frac{\partial^2 \overline{\varepsilon}}{\partial t^2} = (\lambda + \mu)\nabla^2 \overline{\varepsilon} + \mu \nabla^2 \overline{\varepsilon} = (\lambda + 2\mu)\nabla^2 \overline{\varepsilon} \tag{7.7}$$

or

$$\frac{\partial^2 \bar{\varepsilon}}{\partial t^2} = V_P^2 \nabla^2 \bar{\varepsilon}; \qquad V_P = \sqrt{\frac{\lambda + 2\mu}{\rho}} \tag{7.8}$$

This type of wave is called a P wave with V_P as the P wave velocity in a three-dimentional wave propagation. $\bar{\varepsilon}$ is the volumetric strain, which involves no shearing or rotation. Thus, this wave equation describes an irrotational wave having particle motion only in the direction of wave propagation, as shown in Figure 1.8 of Chapter 1. By substituting for λ and μ, V_P can be written as:

$$V_P = \sqrt{\frac{2G(1-\gamma)}{\rho(1-2\gamma)}} \tag{7.9}$$

For one-dimensional wave propagation, Equation 7.8 takes the form

$$\frac{\partial^2 \varepsilon_x}{\partial t^2} = \sqrt{\frac{2G(1-\gamma)}{\rho(1-2\gamma)}} \frac{\partial^2 \varepsilon_x}{\partial x^2} \tag{7.10}$$

or

$$\frac{\partial^2 u}{\partial t^2} = \sqrt{\frac{E}{\rho}} \frac{\partial^2 u}{\partial x^2} \tag{7.11}$$

in which $V_P = \sqrt{E/\rho}$ as γ does not enter in one-dimensional wave propagation.

The second type of wave equation is obtained by eliminating $\bar{\varepsilon}$ from Equations 7.3 and 7.4. Differentiating Equations 7.3 and 7.4 with respect to z and y, respectively, and subtracting one from the other

$$\rho \frac{\partial^2 \theta_x}{\partial t^2} = G \frac{\partial^2 \theta_x}{\partial x^2} \quad \text{or} \quad \frac{\partial^2 \theta_x}{\partial t^2} = V_S^2 \frac{\partial^2 \theta_x}{\partial x^2}; \qquad V_S = \sqrt{\frac{G}{\rho}} \tag{7.12}$$

where

$\theta_x = \left(\frac{\partial w}{\partial y} - \frac{\partial v}{\partial z}\right)$ is the rotation about x-axis

Thus, this wave equation represents distortional wave propagation with rotation about the x-axis. Similar expressions of wave propagation in the y- and z-directions can be obtained with rotations about y- and z-axes, respectively. This wave is called an S wave or shear wave with shear wave velocity, V_S. Particle motion in this wave propagation takes place on a plane perpendicular to the direction of wave propagation (Figure 1.8). S waves generally have two components, that is, S-H and S-V waves. If the particle motion takes place only in horizontal direction perpendicular to the direction of wave propagation, then it is called an S-H wave. Similarly, an S-V wave has particle motion only in the vertical direction. In general, particle motion can take place in both horizontal and vertical directions. It is usually observed that $V_P > V_S$.

As the earth is not an infinite body, seismic wave propagation within the earth does not follow strictly the above wave propagation equations. While wave propagation well within the earth's crest may nearly follow the above equations, that near the surface allows additional wave equation forms due to the presence of a free surface at the top boundary. The earth in this region is modeled as a semi-infinite body with a planar free surface. Two types of additional wave equations are obtained in this region, one for a Rayleigh wave (named after Rayleigh) and the other for a Love wave. Both waves are called surface waves and they attenuate with distance more slowly than body waves. In Rayleigh waves, all particle motions take place in a vertical plane with an elliptical motion having axes in the vertical direction and in the direction of wave propagation, as shown in Figure 1.8.

The wave equation is derived using two potential functions giving

$$u = \frac{\partial \varphi}{\partial x} + \frac{\partial \psi}{\partial z} \tag{7.13}$$

$$w = \frac{\partial \varphi}{\partial z} - \frac{\partial \psi}{\partial x} \tag{7.14}$$

With the two potential functions defined as above, it can be shown that they satisfy the wave equations similar to those for P and S waves, and a Rayleigh wave is a combination of these two waves [1]. The potential functions satisfy the following equations:

$$\frac{\partial^2 \varphi}{\partial t^2} = V_{\mathrm{p}}^2 \nabla^2 \varphi \tag{7.15}$$

$$\frac{\partial^2 \psi}{\partial t^2} = V_s^2 \nabla^2 \psi \tag{7.16}$$

Solutions of Equations 7.15 and 7.16 provide the particle velocities u and w.

Love waves are essentially S-H waves that are trapped by multiple reflections within a surface layer of material having a lower shear wave velocity than the layers below. The love waves satisfy the wave equations of the S wave. The particle motion and the wave velocity can be obtained by solving this wave equation.

Apart from Rayleigh and Love waves, there are a number of other surface waves, but they are much less significant in terms of ground motions affecting the structures.

7.3 One-Dimensional Wave Propagation and Ground Response Analysis

The influence of local soil conditions in modifying the nature of free field ground motion has long been recognized. This influence is studied by way of ground response analysis, which obtains the response at the free ground surface using wave propagation analysis with bedrock motion as input. According to the dimensionality of the problem, the ground response analysis could be three (3D), two (2D) or one dimensional (1D). Depending upon the site conditions and geometry, it may be decided whether 3D, 2D or 1D ground response analysis would be required. It has been observed that one-dimensional ground response analysis provides a reasonably good estimate of the free field ground motion in many cases. In addition, one dimensional analysis is computationally simple. Because of these reasons, it is mostly used for ground response analysis.

Figure 7.2 shows a schematic view of one-dimensional wave propagation analysis. As wave propagation velocities near the surface of the earth are generally less than those beneath them, inclined rays that strike horizontal boundaries are usually reflected to a more vertical direction. However, horizontal ground motions are of greater importance for seismic input to the structures. As a consequence, one-dimensional wave propagation analysis is based on the assumption that the response of a soil deposit is predominantly governed by S-H waves propagating vertically from the underlying bedrock. The soil and bedrock surfaces are also assumed to extend in the horizontal direction. Some of the definitions associated with the analysis are explained in Figure 7.2.

When the soil deposit behaves linearly, the analysis is simple and the solution of the wave equation (Equation 7.12) can be used to obtain the free field ground motion. However, if the soil deposit behaves non-linearly, which is often the case for strong ground motion, a non-linear or equivalent linear analysis is performed to obtain the ground response. For this purpose, the simple solution of the wave equation cannot be used, and generally more involved analysis using FEM is carried out.

Referring to Figure 7.3, consider a uniform layer of homogeneous elastic soil overlying the rigid bedrock. Harmonic horizontal motion of the bedrock will produce vertically propagating shear waves in

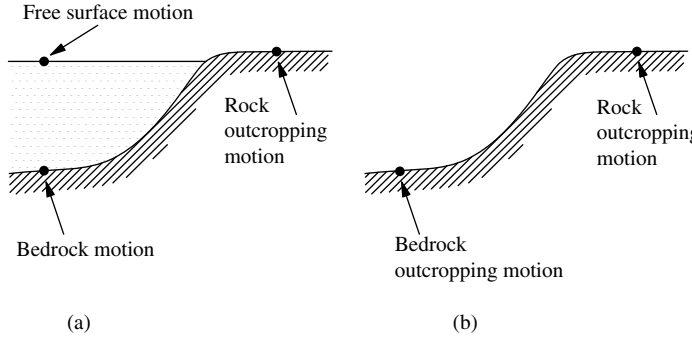

Figure 7.2 Terminologies used in ground response analysis: (a) soil overlying bedrock; and (b) no soil overlying bedrock

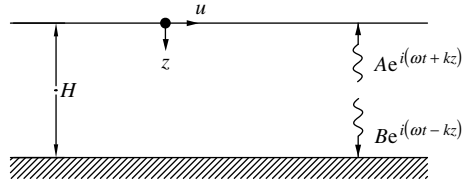

Figure 7.3 One-dimensional wave propagation analysis in linear elastic soil

the soil. For one-dimensional wave propagation equation of the form

$$\frac{\partial^2 u}{\partial t^2} = V_S^2 \frac{\partial^2 u}{\partial z^2} \tag{7.17}$$

the solution for harmonic bedrock motion is given as [1]:

$$u(z,t) = Ae^{i(\omega t + kz)} + Be^{i(\omega t - kz)} \tag{7.18}$$

where ω is the frequency of excitation and $k = \omega/V_S$; A and B are the amplitudes of waves traveling in the upward and downward directions, respectively. As the shear strain must vanish at the free surface

$$G\gamma(0,t) = G\frac{\partial u(0,t)}{\partial z} = 0 \tag{7.19}$$

The above condition provides

$$Gik(A-B)e^{i\omega t} = 0 \tag{7.20}$$

or

$$A = B \tag{7.21}$$

The displacement at any depth $u(z,t)$ then becomes

$$u(z,t) = 2A\cos kz e^{i\omega t} \tag{7.22}$$

Equation 7.22 shows a standing wave of amplitude $2A\cos kz$ where amplitude decreases with depth. Equation 7.22 can be used to obtain the ratio between the amplitudes of displacement

between the top and bottom surface as:

$$R(\omega) = \frac{u_{\max}(0,t)}{u_{\max}(H,t)} = \frac{1}{\cos kH} \tag{7.23}$$

Equation 7.23 shows that if a harmonic ground motion is prescribed at the bottom, then its amplitude will amplify as it travels upward to the surface. $R(\omega)$ also denotes the transfer function for the propagating harmonic wave from rock bed to the free field. The plot of the transfer function is shown in Figure 7.4.

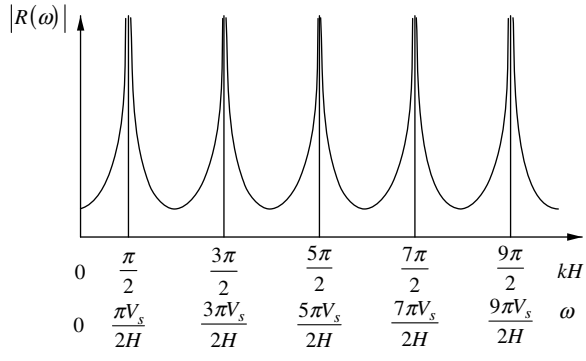

Figure 7.4 Modulus of transfer function for undamped elastic layer

The figure shows that amplifications at frequencies $n\pi V_S/2H (n = 1, 3, 5, \ldots)$ approach infinity. These frequencies are the soil deposit frequencies starting from the fundamental frequency $\pi V_S/2H$. Because of zero damping (considered in the analysis), amplifications approach infinity at resonance points.

If soil damping is considered, the equation of wave propagation takes the form

$$\frac{\partial^2 u}{\partial t^2} = V_S^2 \frac{\partial^2 u}{\partial z^2} + \frac{\eta}{\rho} \frac{\partial^3 u}{\partial z^2 \partial t} \tag{7.24}$$

in which η is defined as the equivalent viscosity given by $\eta = 2G\xi/\omega$ and is the parameter of the Kelvin–Voigt model to represent the stress–strain relationship in shear for soil given by:

$$\tau = G\gamma + \eta \frac{\partial \gamma}{\partial t} \tag{7.25}$$

in which γ and τ are the shear strain and stress, respectively. Equation 7.25 is used to represent the stress–strain relationship because, for the purpose of viscoelastic wave propagation, soils are usually modeled as Kelvin–Voigt solids (that is, materials whose resistance to shearing deformation is an addition of the elastic and viscous components). Furthermore, the equivalent viscosity, η, used in Equation 7.24, is defined to be inversely proportional to frequency in order to make the soil damping ratio to be frequency independent [1]. The relationship between η and ξ at a frequency is derived from the energy dissipation in the soil for harmonic oscillation. The second term on the right side of Equation 7.24 appears due to soil damping, which arises due to the movement of soil particles during shear wave propagation. Solution of the wave equation is of the form

$$u(z,t) = Ae^{i(\omega t + kz)} + Be^{i(\omega t - kz)} \tag{7.26}$$

in which $\overline{k}$ is a complex number having k_1 and k_2 as the real and imaginary parts. Using the same condition of zero shear strain at the free surface, the transfer function $R(\omega)$ can be shown to be [1]:

$$R(\omega) = \frac{1}{\cos \overline{k}H} \tag{7.27}$$

in which $\overline{k}H = \omega H/\overline{V}_S$; $\overline{V}_S$ is the complex shear velocity given by:

$$\overline{V}_s = \sqrt{\frac{\overline{G}}{\rho}}; \qquad \overline{G} = G(1 + i2\xi) \tag{7.28}$$

For small ξ, expanding $(1 + i2\xi)^{1/2}$ in a power series and neglecting higher order terms, it can be shown that

$$\overline{V}_S = \sqrt{\frac{G(1 + i2\xi)}{\rho}} = \overline{V}_S(1 + i\xi) \tag{7.29}$$

Thus,

$$R(\omega) = \frac{1}{\cos\left[\dfrac{\omega H}{V_S}(1 + i\xi)\right]} \tag{7.30}$$

Using $|\cos(a + ib)| = [\cos^2 a + \sin h^2 b]^{\frac{1}{2}}$, the absolute value of the transfer function can be expressed as:

$$|R(\omega)| = \frac{1}{\left[\cos^2\left(\dfrac{\omega H}{V_S}\right) + \left(\dfrac{\xi \omega H}{V_S}\right)^2\right]^{1/2}} \tag{7.31}$$

In the above equation, $\sinh^2 x \approx x^2$ is used, as x is small.

The plot of the absolute value of $R(\omega)$ is shown in Figure 7.5. It is seen from the figure that $|R(\omega)|$ reaches a peak value near the natural frequencies of the soil deposit (that is, $\omega_n = n\pi V_S/2H$; $n = 1, 3, 5 \ldots$) as in the undamped case. The peaks at the natural frequencies have finite values because of the presence of damping. In addition, peaks also decrease with increasing natural frequencies. For the soil deposit, the mode shapes corresponding to the first three natural frequencies are shown in Figure 7.6.

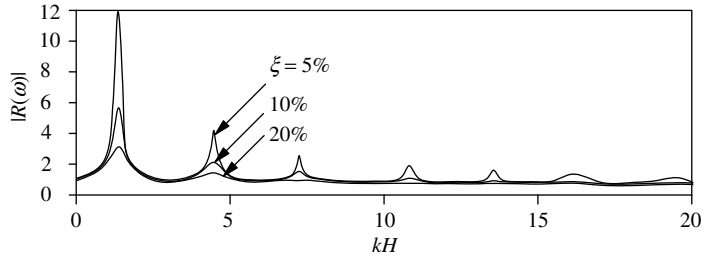

Figure 7.5 Modulus of transfer function for damped elastic layer

7.3.1 Ground Response Analysis Using FFT

With the transfer function known, the free field ground response due to a propagating S-H wave for a specific time history of bedrock motion can be easily obtained using Fourier analysis. The steps to be

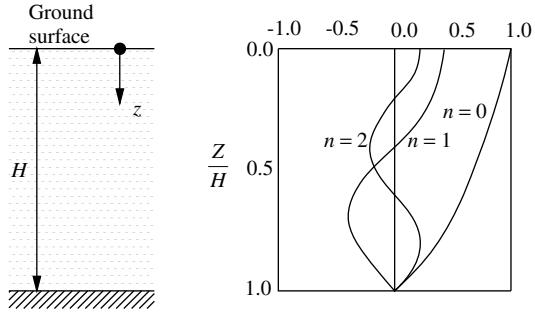

Figure 7.6 Mode shapes corresponding to first three natural frequencies

followed for performing the linear ground response analysis for a specified time history of ground motion are summarized below:

(i) Fourier synthesize the bedrock ground motion using FFT, which gives a set of complex numbers at discrete interval of $\Delta\omega$.
(ii) Take the first half of the numbers (the remaining half of the numbers are complex conjugates of the first half).
(iii) Obtain the values of the transfer function at a frequency interval of $\Delta\omega$ starting from zero.
(iv) Multiply complex numbers of the Fourier transform with the corresponding values of the transfer function.
(v) Multiplied numbers are complex; find complex conjugates of these numbers and sequence them in an order as explained in Chapter 2.
(vi) Take an inverse Fourier transform of the series; the output provides the time history of the ground response.

7.3.2 Ground Response Analysis (Linear and Non-Linear) in the Time Domain

Ground response analysis can also be performed in the time domain. In this method, the soil medium is discretized as a number of shear beam elements as shown in Figure 7.7. Appropriate soil mass is lumped at

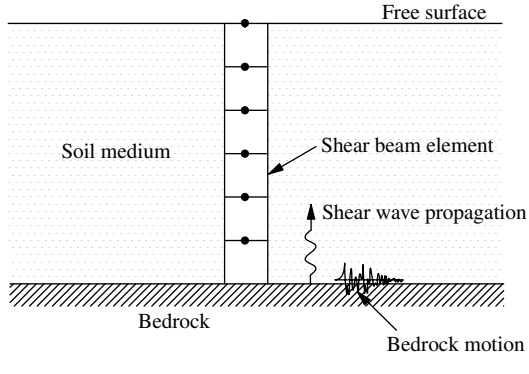

Figure 7.7 Shear beam element for one-dimensional wave propagation analysis

the nodal points. Assuming a reasonable damping ratio for the soil, the following equations of motion are solved numerically to find the time history of response for the top node:

$$\boldsymbol{M}\ddot{\boldsymbol{u}} + \boldsymbol{C}\dot{\boldsymbol{u}} + \boldsymbol{K}\boldsymbol{u} = -\boldsymbol{M}\boldsymbol{I}\ddot{u}_g \tag{7.32}$$

in which $\boldsymbol{M}$, $\boldsymbol{C}$, and $\boldsymbol{K}$ are, respectively, the mass, damping, and stiffness matrices for the equivalent shear beam; $\ddot{u}_g$ is the time history of ground acceleration at the bedrock level; and $\boldsymbol{u}$ is horizontal ground motion. The solution to Equation 7.32, for a specified time history of ground motion by using different methods, has been explained in Chapter 3. To obtain the total (absolute) free field acceleration, the bedrock acceleration is added to the acceleration of the top node.

For strong ground motion, the non-linear behavior of the soil should be taken into account in the ground response analysis. For non-linear response analysis, the equation of motion (Equation 7.32) is modified as:

$$\boldsymbol{M}\ddot{\boldsymbol{u}} + \boldsymbol{C}\dot{\boldsymbol{u}} + \boldsymbol{R}(\boldsymbol{u}) = -\boldsymbol{M}\boldsymbol{I}\ddot{u}_g \tag{7.33}$$

in which $\boldsymbol{R}(\boldsymbol{u})$ is the non-linear force–displacement relationship of the soil under cyclic loading. This non-linear relationship is represented by a backbone curve as explained in Chapter 6. For the case of soil, the backbone curve represents the variation of G with the shear strain of the soil as shown in Figure 7.8a. The non-linear equation of motion is solved numerically to obtain the free (relative) field ground response. The method of analysis is explained in Chapter 6. The free field ground response obtained by the non-linear analysis is generally less than that obtained by the linear analysis. The reason for this is the hysteretic behavior of the non-linear soil under cyclic loading, which provides a force–deformation relationship shown in Figure 7.8b. Because of this hysteretic behavior, more seismic energy is dissipated in addition to that due to the material damping of the soil.

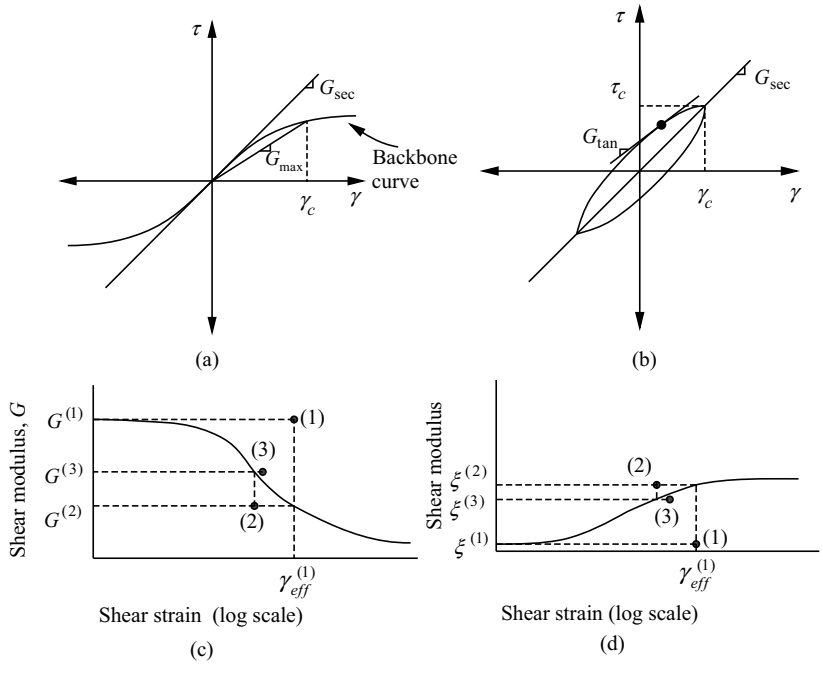

Figure 7.8 Non-linear behavior of the soil: (a) backbone curve; (b) hysteresis loop under cyclic loading; (c) variation of shear modulus with shear strain; and (d) variation of equivalent damping ratio with shear strain

An equivalent linear analysis for the non-linear problem is widely used in ground response analysis. In the equivalent linear analysis, an equivalent shear modulus and an equivalent damping ratio, representing the energy loss in the hysteretic loops, are used in the analysis. The equivalent shear modulus is the average of the shear modulus at every point of the hysteretic curve in Figure 7.8b. It can be approximated by the secant modulus as shown in Figure 7.8a. The equivalent damping ratio at different strain levels are obtained from the area of the loop. As the secant modulus decreases with increasing strain, there is a degradation of the modulus as the strain increases. From cyclic experimental tests, the degradation of the equivalent shear modulus with the level of shear strain has been obtained as shown in Figure 7.8c. Thus, the equivalent linear analysis uses the strain dependent G value as depicted in Figure 7.8c. A reasonable estimate of $G_{\max}$ is taken to be equal to ρV_s^2. The equivalent damping also varies with the strain and can be obtained from laboratory tests. A typical variation of the damping ratio with the shear strain is shown in Figure 7.8d.

The equivalent linear analysis starts with a value of $G_{\max}$ and finds the computed strain in the elements. In the next iteration, a strain compatible modulus (Figure 7.8c) is used to obtain the solution. The process is continued until a convergence (defined by a norm) is achieved. Standard programs are available, such as FLAC for performing both equivalent linear and non-linear one-dimensional wave propagation analysis for a soil medium.

7.4 2D or 3D Response Analysis in the Time Domain

The solution of the one-dimensional wave propagation analysis can be easily extended to 2D or 3D analysis by FEM. Instead of considering one-dimensional shear beam elements, if 2D or 3D elements are considered for the analysis (Figure 7.9), then the responses in two or three directions can be obtained. For 2D analysis, plane strain elements are used. Ground motions are prescribed at the rock bed. For the 3D analysis, eight node brick elements may be used. Appropriate boundaries for the soil medium are to be defined depending upon the topography. 2D or 3D analysis is generally performed for regions with irregular topography and near the ends of a basin. In the central region of the basin having regular topography, 1D wave propagation analysis is sufficient for all practical purposes. Both linear and non-linear analyses are possible for 2D and 3D wave propagation problems. The interaction effect on yielding and improved yield curves may be included in the non-linear analysis. Standard softwares such as ANSYS or ABAQUS can be used for this purpose. Note that responses obtained by 2D or 3D wave propagation analysis for a single component vertically propagating ground motion will give slightly different results than those obtained from 1D wave propagation analysis because of the Poisson effect.

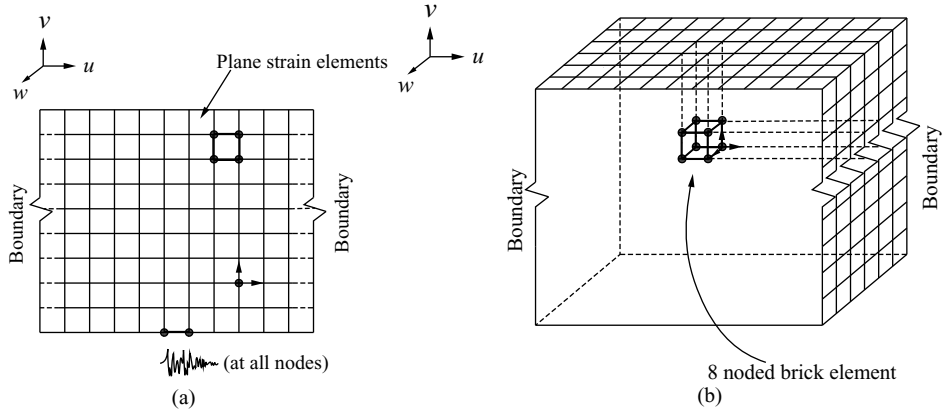

Figure 7.9 FEM idealization of wave propagation in soil medium: (a) 2D approximation; and (b) 3D approximation

Example 7.1

A vertically propagating shear wave travels through a uniform layer of soil deposit that is 50 m thick lying over a rock bed. Take the damping ratio for the soil to be 5%, and three cases of soil properties given by $V_S = 80\,\text{m s}^{-1}$, $\rho = 1600\,\text{kg m}^{-3}$; $V_S = 200\,\text{m s}^{-1}$, $\rho = 1800\,\text{kg m}^{-3}$; and $V_S = 600\,\text{m s}^{-1}$, $\rho = 2000\,\text{kg m}^{-3}$. Find (i) the plots of the ground amplification factor (modulus of transfer function); (ii) the plots of the time histories of relative displacement and absolute acceleration at the surface using 1D wave propagation time history analysis for the El Centro earthquake as bedrock input; (iii) the PGA amplification; and (iv) the free field absolute acceleration response spectra for $V_S = 80\,\text{m s}^{-1}$, $200\,\text{m s}^{-1}$, and the input ground motion.

Solution:

(i) The modulus of transfer function, $|R(\omega)|$, given by Equation 7.31, is plotted for $V_S = 80$, 200, and $600\,\text{m s}^{-1}$ with ξ for soil taken as 5%. The plots are shown in Figures 7.10–7.12. It is seen from the figures that for $V_S = 80\,\text{m s}^{-1}$ (soft soil), the first peak of the transfer function occurs at a much lower frequency compared with the frequencies at which the first peaks of the transfer functions occur for $V_S = 200$ and $600\,\text{m s}^{-1}$. This is the case because the fundamental frequency $(\pi V_S/2H)$ of the soil deposit for $V_S = 80\,\text{m s}^{-1}$ is much lower.

(ii) Time histories of free field displacement (relative to the bedrock) and absolute acceleration obtained by 1D wave propagation analysis (using integration of Equation 7.32 by Newmark's method with $\Delta t = 0.02$ s) are shown in Figures 7.13 and 7.14. It is seen from the figures that the

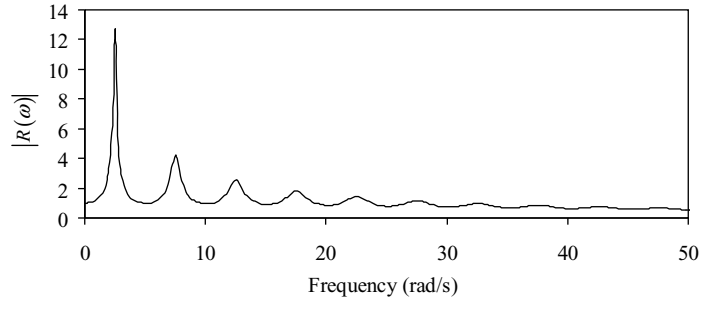

Figure 7.10 Transfer function for $V_S = 80\,\text{m s}^{-1}$

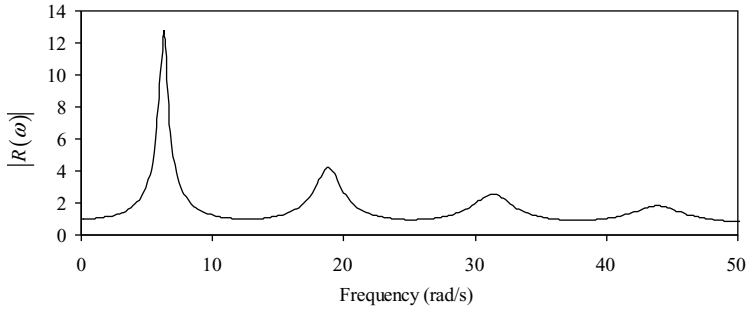

Figure 7.11 Transfer function for $V_S = 200\,\text{m s}^{-1}$

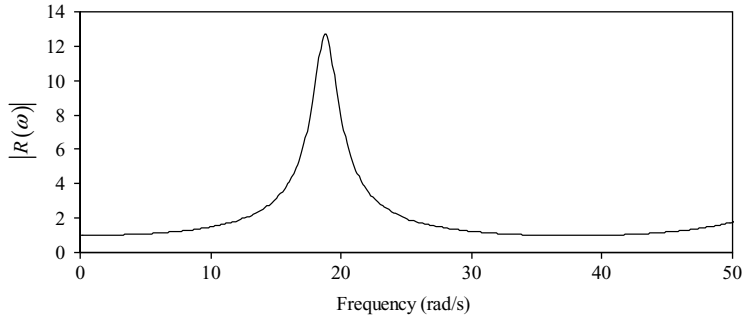

Figure 7.12 Transfer function for $V_S = 600\,\text{m s}^{-1}$

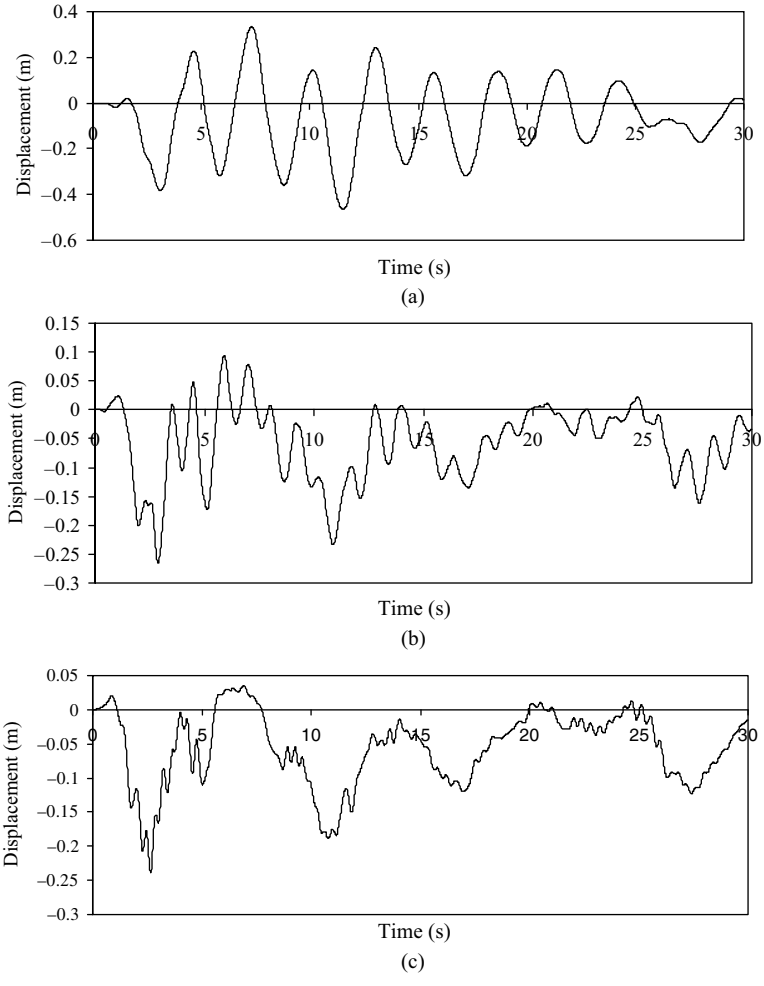

Figure 7.13 Time histories of ground displacement: (a) $V_s = 80\,\text{m s}^{-1}$; (b) $V_s = 200\,\text{m s}^{-1}$; and (c) $V_s = 600\,\text{m s}^{-1}$

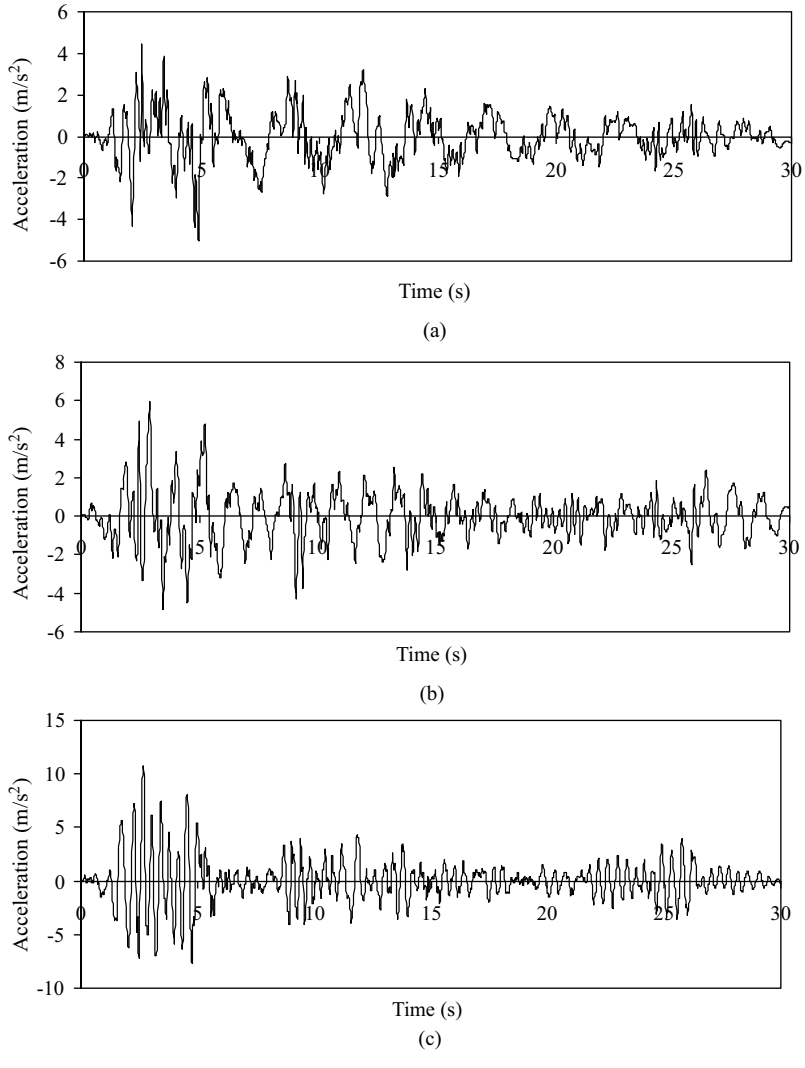

Figure 7.14 Time histories of absolute acceleration: (a) $V_S = 80\,\mathrm{m\,s^{-1}}$; (b) $V_S = 200\,\mathrm{m\,s^{-1}}$; and (c) $V_S = 600\,\mathrm{m\,s^{-1}}$

free field ground displacement is more for $V_S = 80\,\mathrm{m\,s^{-1}}$ (soft soil). Also, the time history of ground displacement for $V_S = 80\,\mathrm{m\,s^{-1}}$ shows a predominant period that is approximately equal to the fundamental period for the soil deposit. This explains the reason why free field ground motion for soft soil shows a narrow band spectrum. The time histories of the absolute ground acceleration show that the accelerations are more for the stiffer soil; PGA is maximum for $V_S = 600\,\mathrm{m\,s^{-1}}$.

(iii) The PGA amplification (p_a), that is, the ratio of peak free field absolute acceleration to the peak rock bed acceleration for the three cases are $p_a = 1.52$ for $V_S = 80\,\mathrm{m\,s^{-1}}$; $p_a = 1.92$ for $V_S = 200\,\mathrm{m\,s^{-1}}$, and $p_a = 3.43$ for $V_S = 600\,\mathrm{m\,s^{-1}}$. Thus, PGA amplification is less for the softer soil.

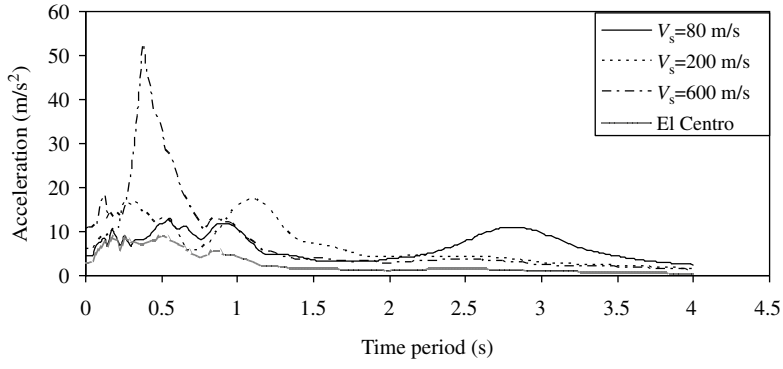

Figure 7.15 Pseudo acceleration response spectra for 5% damping

(iv) The pseudo acceleration response spectra for the free field ground acceleration for $V_S = 80\,\text{m s}^{-1}$; $200\,\text{m s}^{-1}$ and input bedrock acceleration are compared in Figure 7.15. It is seen that the frequency contents of the three response spectra are significantly different showing that the soil characteristic modifies the frequency contents of the ground motion to a great extent.

Example 7.2

For the above problem, compare between the free field responses obtained using 1D and 2D wave propagation analyses.

Solution: Both 1D and 2D analyses are performed using ABAQUS. Plain strain elements have been used for both analyses. In 2D analysis, two degrees of freedom (vertical and horizontal) at each node of the element are considered. For 1D analysis, the vertical degree of freedom is restrained. A soil medium of 100 m (width) and 50 m (depth) is discretized into finite elements of size 5×5 m. The time history of acceleration is applied at the bedrock at every node. The responses are shown for the node at the center of the medium on the ground surface. Time histories of responses are compared in Figures 7.16 and 7.17. It is seen from the figures that some differences exist between the time histories of horizontal responses obtained for the two cases. The reason for these differences is attributed to the Poisson effect. Difference in the ground displacements is pronounced for the soft soil ($V_S = 80\,\text{m s}^{-1}$), while the difference in the ground acceleration is pronounced for the stiff soil ($V_S = 600\,\text{m s}^{-1}$).

Example 7.3

If the soil has the non-linear characteristics modeled by an elasto-plastic stress–strain relationship with yield shear stress $= 40\,960\,\text{N m}^{-2}$; and yield strain $= 0.002$, obtain the free field acceleration for the problem in Example 7.1 for $V_S = 80\,\text{m s}^{-1}$ and compare it with that obtained for the linear soil.

Solution: Response of the non-linear soil can be obtained by incremental time history analysis as explained in Chapter 6. Here, the response is determined using 1D time history analysis with the help of ABAQUS. The input requires stress–strain behavior of the soil in addition to other inputs given for the

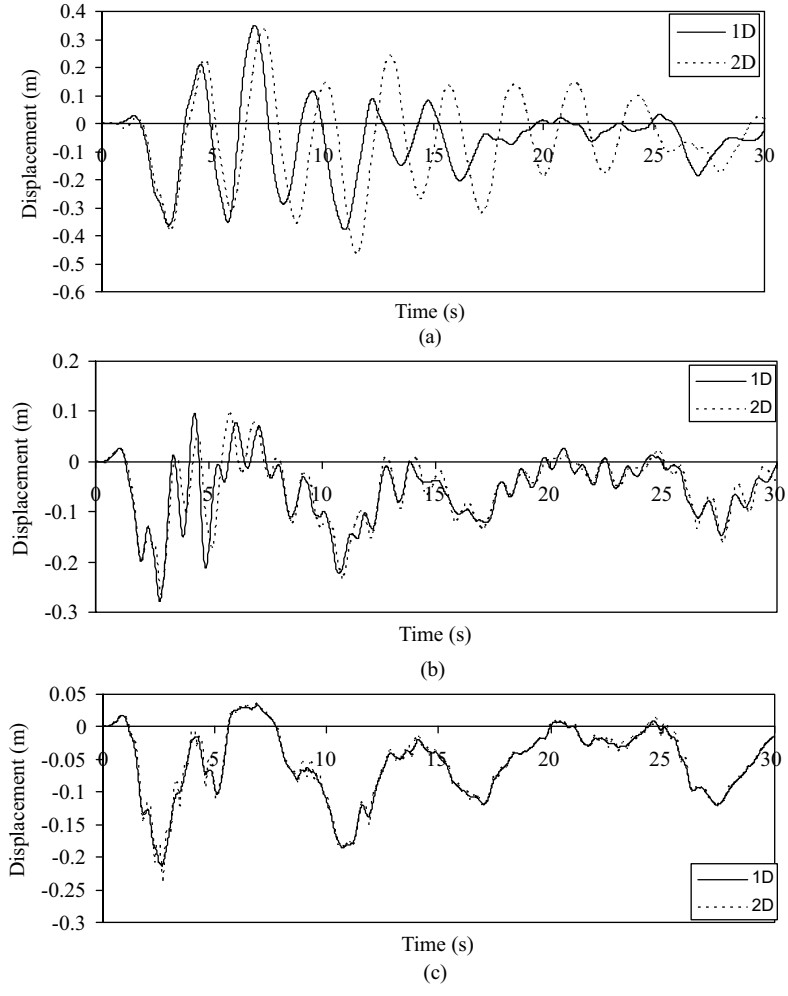

Figure 7.16 Time histories of ground displacement: (a) $V_S = 80\,\mathrm{m\,s^{-1}}$; (b) $V_S = 200\,\mathrm{m\,s^{-1}}$; and (c) $V_S = 600\,\mathrm{m\,s^{-1}}$

Example 7.2. The result of the analysis is shown in Figure 7.18. It is seen from the figure that the free field acceleration for the non-linear soil is less than the corresponding linear soil. The reason for this is attributed to the dissipation of seismic energy due to the hysteretic behavior of the non-linear soil during vibration.

7.5 Dynamic Soil–Structure Interaction

The effect of a dynamic soil–structure interaction depends on the stiffness and mass properties of the structure, the stiffness of the soil, and the damping characteristics of both soil and structure. The dynamic soil–structure interaction consists of two interactions, namely, kinematic interaction and inertial interaction. The kinematic interaction is the result of the stiffness of the structure, while the inertial

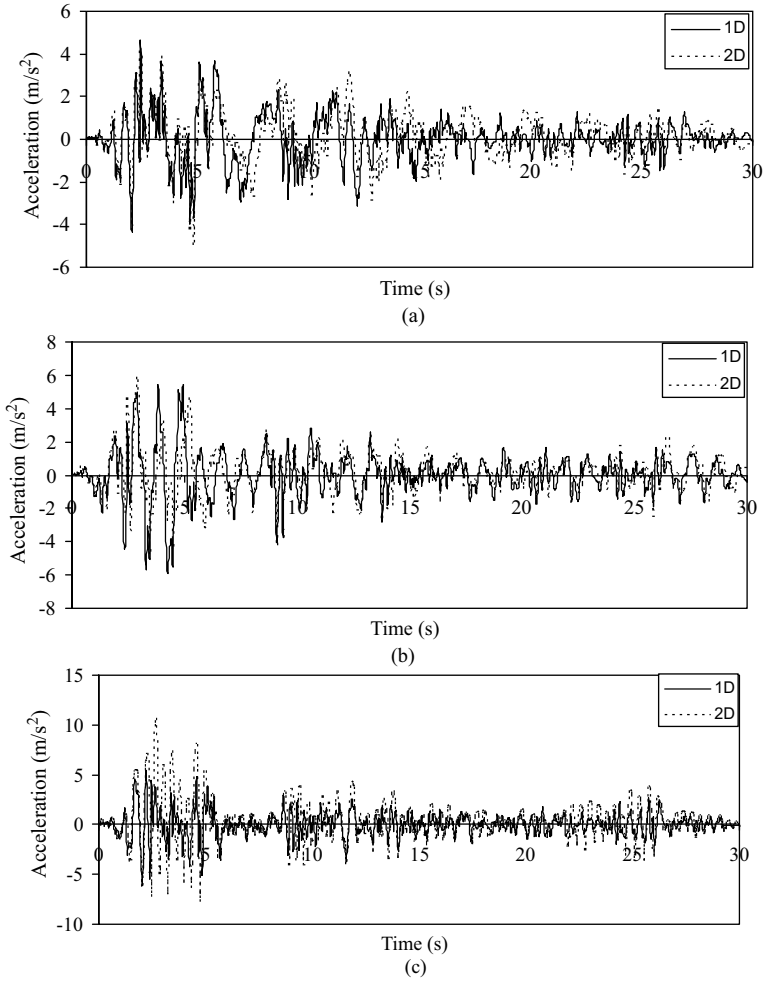

Figure 7.17 Time histories of absolute acceleration: (a) $V_S = 80\,\mathrm{m\,s^{-1}}$; (b) $V_S = 200\,\mathrm{m\,s^{-1}}$; and (c) $V_S = 600\,\mathrm{m\,s^{-1}}$

interaction is the result of the mass of the structure. The kinematic interaction is explained with the help of Figure 7.19(a–d). In Figure 7.19a, the massless mat foundation restrains the vertical movement of the ground motion because of its flexural stiffness. As a result, the mat foundation moves differently than the free field ground motion (that is, the ground motion is away from the foundation). Also, the nature of ground motion in the close vicinity and below the foundation is changed from that of the free field ground motion because of this action. This interaction of the foundation with the ground motion is called the kinematic interaction. Similar examples of kinematic interaction are shown in Figure 7.19(b and c). In Figure 7.19b, a vertically propagating shear wave is restrained by the embedded foundation. In Figure 7.19c, the axial stiffness of the slab prevents the incoherent ground motion produced below the foundation due to the vertically propagating shear wave. The kinematic interaction can also induce rotational movement in a foundation, as shown in Figure 7.19d for vertically propagating purely S waves.

The tau (τ) effect, as explained by Clough and Penzien [2], is another example of kinematic interaction. In Figure 7.20, the horizontally propagating shear wave in the y-direction produces ground motion in the

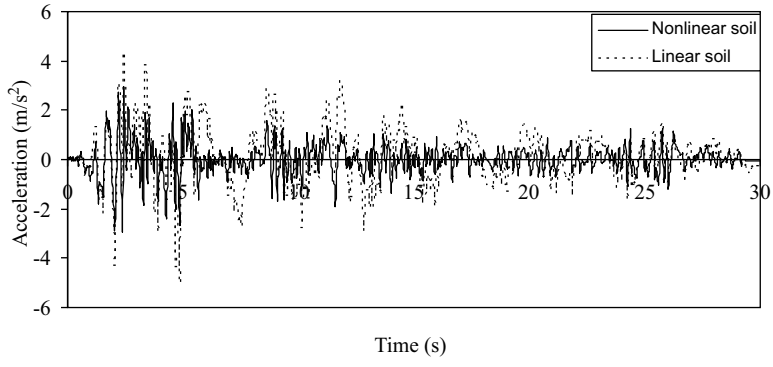

Figure 7.18 Time histories of absolute acceleration for linear and non-linear soil

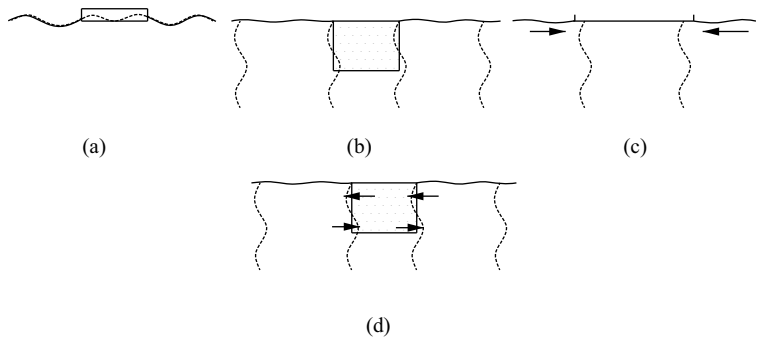

Figure 7.19 Kinematic interaction: (a) vertical motion modified; (b) horizontal motion modified; (c) incoherent ground motion prevented; and (d) rocking motion introduced

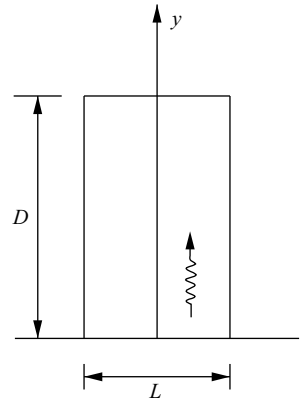

Figure 7.20 Horizontally propagating shear wave in the *y*-direction beneath the rigid slabs

x-direction which varies with y. Because of the rigidity of the slab, this varying motion is restrained and the motion of the slab in the x-direction is different to that of the free field ground motion. If τ is defined as the ratio between the amplitudes of rigid base translational motion and the free field motion for a particular harmonic component, then it is shown that [2]

$$\tau = \frac{1}{\alpha}\sqrt{2(1-\cos\alpha)} \tag{7.34a}$$

$$\alpha = \frac{\omega D}{V_a} = \frac{2\pi D}{\lambda(\omega)} \tag{7.34b}$$

where

$\lambda(\omega) = \frac{2\pi V_a}{\omega}$ is the wavelength
D is the dimension of the base in the y-direction
V_a is the apparent wave velocity in the y-direction.

It is shown that the values of τ decrease from unity at $\alpha = 0$ (and $\lambda \to \infty$) to zero at $\alpha = 2\pi$ (and $\lambda = D$).

This means that if the base dimension of the foundation is very small compared with the wavelength of the ground motion, then the τ effect is negligible. On the other hand, if the base dimension of the foundation is sizable compared with the wavelength of the ground motion, then the τ effect should be considered and the base motion could be much smaller than the free field ground motion.

Inertial interaction is purely caused by the inertia forces generated in the structure due to the movement of the masses of the structure during vibration (Figure 7.21). The inertia forces transmit dynamic forces to the foundation. If the supporting soil is compliant, the foundation will undergo dynamic displacement that would not occur if the soil is very stiff (as assumed for the fixed base condition). Clearly, the dynamic displacement at the foundation–soil interface is the sum total of the free field ground motion, the displacement produced due to kinematic interaction, and the displacement produced due to inertial interaction. As a portion of the soil adjacent to the foundation undergoes vibration produced by the inertial effect, some portion of the energy, imparted to the structure by the ground motion, is lost in moving the adjacent soil mass. The energy travels within the soil in the form of radiating waves and gradually dies

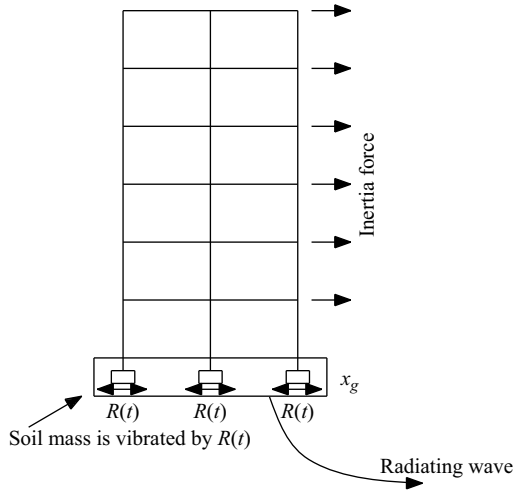

Figure 7.21 Inertial effects

down with distance. This energy loss is popularly known as radiation damping of the soil and is one of the important aspects of the inertial effect. The radiation damping and the resistance of the soil to the movement of the foundation can be obtained theoretically by finding the impedance functions for the soil, described later. All these interaction effects modify both the responses of the structure and the movements of the ground below the foundation and are known as soil–structure interaction effects. Exclusive treatment of the subject is available in reference [3].

7.5.1 Bounded Problem and Idealization of Realistic Problems

Dynamic soil–structure interaction problems can be treated in different ways. Exact or rigorous analysis could be obtained only under certain specific conditions. The most direct approach to solve the problem is to include a layer of the soil along with the structure and use the finite element approach to model the entire system. Such a model is shown in Figure 7.22. If the model can be assumed to be bounded as shown in the figure, the equation of motion takes the usual form, that is,

$$\boldsymbol{M}\ddot{\boldsymbol{V}} + \boldsymbol{C}\dot{\boldsymbol{V}} + \boldsymbol{K}\boldsymbol{V} = -\boldsymbol{M}\boldsymbol{I}\ddot{u}_g \tag{7.35}$$

where

$\boldsymbol{M}$, $\boldsymbol{C}$, and $\boldsymbol{K}$ are the mass, damping, and stiffness matrices, respectively, of the soil–structure system corresponding to the dynamic degrees of freedom
$\boldsymbol{V}$ is the vector of the relative displacements of the degrees of freedom with respect to the base
$\ddot{u}_g$ is the ground motion applied at the base
$\boldsymbol{I}$ is influence coefficient vector (of unity).

For the specified time history of the ground motion at the bed, the equation of motion can be solved either in the time domain or in the frequency domain (by Fourier transform) to obtain the relative displacement vector $\boldsymbol{V}$. The absolute displacement or acceleration vector corresponding to the degrees of freedom may be obtained by adding the ground motion to the relative motions of the degrees of freedom. This approach

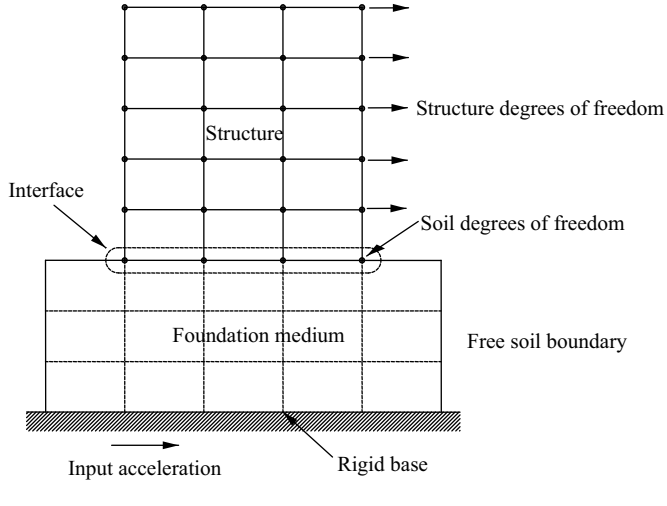

Figure 7.22 FEM modeling of soil-structure as bounded problem

is a direct method of solving the soil–structure interaction problem. However, this has certain disadvantages, which are discussed later.

In the multi-step method, the problem is solved in two stages as shown in Figure 7.23(a and b). In the first stage, the problem of the kinematic interaction is solved in which mass of the superstructure is ignored. The equation of motion takes the form:

$$\overline{\boldsymbol{M}}\ddot{\boldsymbol{V}}_I + \boldsymbol{C}\dot{\boldsymbol{V}}_I + \boldsymbol{K}\boldsymbol{V}_I = -\overline{\boldsymbol{M}}\boldsymbol{I}\ddot{u}_g \tag{7.36}$$

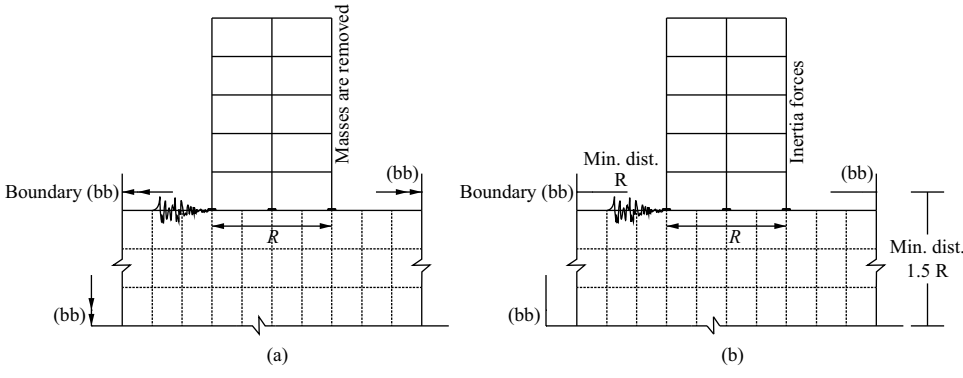

Figure 7.23 Multi-step method: (a) solution for kinematic interaction; and (b) solution for inertial interaction

in which $\overline{\boldsymbol{M}}$ is the mass matrix with masses corresponding to the structure and foundation degrees of freedom set to zero (that is, only soil masses are retained); and $\boldsymbol{V}_I$ is the relative displacements produced at the degrees of freedom. Thus, the elements of the vector of displacements $\{\boldsymbol{V}_I - u_g\}^T$ corresponding to the structural degrees of freedom are the motions that are imparted to the structure due to the ground motion. Owing to the kinematic interaction, the ground motion as such is not imparted to the structure.

If $\boldsymbol{V}_I$ at all structural degrees of freedom are nearly the same and are equal to those at the base of the structure, then kinematic interaction is negligible (that is, no tau effect) and the free field ground motion (that is, the motion at the base of the structure) is transferred as such into the structure.

In the second stage, the problem of the inertial interaction is solved in which the entire mass matrix is considered on the left-hand side of the equation of motion with the effective earthquake force acting only on the structure. Thus, the equation of motion takes the form

$$\boldsymbol{M}\ddot{\boldsymbol{V}}_{II} + \boldsymbol{C}\dot{\boldsymbol{V}}_{II} + \boldsymbol{K}\boldsymbol{V}_{II} = -\boldsymbol{M}_s\{\ddot{\boldsymbol{V}}_I + \boldsymbol{I}\ddot{u}_g\} \tag{7.37}$$

in which $\boldsymbol{M}_s$ is the mass matrix having non-zero elements for only structural degrees of freedom. Note that $\ddot{\boldsymbol{V}}_I$ for structural degrees of freedom are zero as the structure and foundation behave quasi-statically during the solution of the kinematic interaction. The solution provides the response $\boldsymbol{V}_{II}$ produced due to the inertial interaction. The final response of the system is the sum of the responses $\boldsymbol{V}_I$ and $\boldsymbol{V}_{II}$. The total or absolute response is obtained by adding u_g to $\boldsymbol{V}_I$ and $\boldsymbol{V}_{II}$. It can be easily shown that addition of Equations 7.36 and 7.37 leads to original Equation 7.35.

The direct method, as explained above, can be conveniently used for bounded problems in which ground motions are prescribed at the boundaries. The multi-step method can also be used for bounded problem as the prescribed free field ground motion can be expressed in terms of ground motion prescribed at the boundaries. However, most of the soil–structure interaction problems associated with the overground structures are different to those of the bounded problem. The difference is due to:

(i) Mostly the ground motions are prescribed at the free field rather than at the rock bed below.
(ii) The superstructure is constructed over the ground, the ground extending to far distances on all sides except the upward vertical direction.
(iii) The effect of soil–structure interaction on the response of the superstructure is of primary interest; the response of the soil mass below is generally not of great concern. Also, the rock bed may be at a much greater depth and, hence, a bottom boundary (not at the rock bed) may be provided.
(iv) For most of the foundations of the superstructure, the kinematic interaction is small and, therefore, can be neglected. As a result, the soil–structure interaction problem is one of inertial interaction.

The above factors have led to different methods of treatment of soil–structure interaction problems associated with the overground structures. Note that the bounded problem can also be formulated with free field ground motion as input [3]. The second factor above is of crucial importance as infinite soil mass cannot be included in a realistic model. Therefore, the optimum amount of soil mass should be incorporated in the model so as to allow effective dissipation of radiation waves (Figure 7.21). Alternatively, an effective mechanism to absorb radiation energy at the boundaries of the soil mass should be provided to perform the same function. A small selection of methods, both exact and approximate, are discussed here. All these methods solve the problem of the inertial effect only.

7.5.2 Direct Method

In the direct method, soil–structure foundation is modeled together using FEM, as shown in Figure 7.23. The difference between the modeling shown in Figures 7.22 and 7.23 is that the boundary is not fixed and there is no rock bed at the bottom in the latter. The ground motion, as shown in Figure 7.23, is specified at the free field. It is assumed that kinematic interaction is insignificant and the free field ground motion is the motion with which the foundation blocks move. The inertia forces acting on the structure produce vibration in the structure, foundation, and the soil masses, both at the soil–foundation interface and below it. The equation of motion takes the form

$$\boldsymbol{M}\ddot{\boldsymbol{u}} + \boldsymbol{C}\dot{\boldsymbol{u}} + \boldsymbol{K}\boldsymbol{u} = -\boldsymbol{M}_s\boldsymbol{I}\ddot{u}_g \tag{7.38}$$

where

$\boldsymbol{M}$ is the mass matrix for the entire structure–foundation and the soil
$\boldsymbol{C}$ is the damping matrix (material damping) of the structure and the soil
$\boldsymbol{K}$ is stiffness matrix of the entire system
$\boldsymbol{M}_s$ is the mass matrix having non-zero masses for the structural degrees of freedom
$\boldsymbol{I}$ is influence coefficient vector
$\ddot{u}_g$ is the free field ground acceleration
$\boldsymbol{u}$ is the vector of relative displacement with respect to the base.

In Figure 7.23, the soil is modeled as an assemblage of rectangular plane strain elements having two translational degrees of freedom at each node, while the building frame is modeled as an assemblage of

beam elements. As soil elements do not admit rotational DOF, soil structure interface nodes require special consideration, as shown in the figure. The stiffness matrix for the entire system can be generated using the standard assembling procedure. To generate the damping matrix, damping matrices of the structure and the soil are constructed separately from their modal damping ratios assuming them to follow Rayleigh damping. Then, they are combined together to form the total damping matrix by assuming that the coupling terms between the soil and structure are zero. Note that the damping coefficients corresponding to the degrees of freedom of the interface nodes consist of two components, that is, the components from the structural damping and those from the soil damping.

The inertia forces will be transferred to the base (foundation) in the form of a shear force and a moment, which in turn will tend to deform the soil at the soil–structure interface. This vibratory deformation of the soil at the interface propagates in the form of radiation waves through the soil in all directions, giving rise to soil radiation damping. It is this damping which mostly affects the structure-foundation responses. Contribution of the material damping of the soil to the response reduction of the structure-foundation system is very insignificant. Unless these radiation waves travel for sufficient distances, they do not die down. Therefore, the radiation waves reflect back if any boundary is provided at a distance not far away from the structure and introduce error into the calculation of responses. In other words, simulation of the semi-infinite elastic half space of the soil mass by finite element modeling of the dynamic soil–structure interaction problem may become very large. From different numerical studies carried out so far, a good approximation for fixing the boundaries is also shown in Figure 7.23. In order to reduce the size of the problem, the concept of absorbing boundaries has been introduced in the finite element formulation. The purpose of absorbing boundaries (which have dash pots) is to dissipate the radiation energy effectively by placing the boundaries not far away from the structure, thus reducing the size of the problem.

In the direct method, the problem can be solved either in the time domain or in the frequency domain for a specified free field ground motion. If the time histories of ground motion are different at different supports, then also the problem can be solved by modifying the influence co-efficient vector $\{I\}$ used in Equation 7.38. The necessary modifications have been explained in Chapter 3.

Standard software packages are now available to solve dynamic soil–structure interaction problems by direct methods. However, there are a few shortcomings of the direct method of analysis. Firstly, the problem is one of non-classical damping, and therefore a good representation of the damping matrix for the system is difficult. This is further complicated if absorbing boundaries are used. Secondly, a large problem has to be dealt with to find the superstructure responses, which are the main interest. Thirdly, if the superstructure is modeled as a 3D system, then not only does the size of the problem become very large, but also modeling of interface elements becomes complex.

Example 7.4

The stick model, shown in Figure 7.24, is supported on a circular footing resting on a soil having $V_S = 80\ \text{m s}^{-1}$, $\rho = 1600\ \text{kg m}^{-3}$, and $\xi = 5\%$ (for both structure and soil). The foundation has a radius of 1.5 m. Using 2D direct analysis, find the time history of tip displacement (relative) and base rotation for the El Centro earthquake applied at the base of the foundation.

Solution: The FEM modeling of the stick and soil is shown in Figure 7.24. The stick is modeled by beam elements, while the footing and the soil are modeled by plane strain elements. The stick and the footing are connected by the tie element with the rotational DOF locked. Contact surface interaction between the footing and the soil is defined as (i) hard contact in the vertical direction, (ii) friction contact in the tangential direction, and (iii) separation in the vertical direction, which is allowed for tension. The ground motion is applied at the base of the structure. Appropriate boundaries for the soil medium are also shown in the same figure for proper attenuation of radiation waves. Direct integration of the equation of motion for the soil structure system is carried out in ABAQUS.

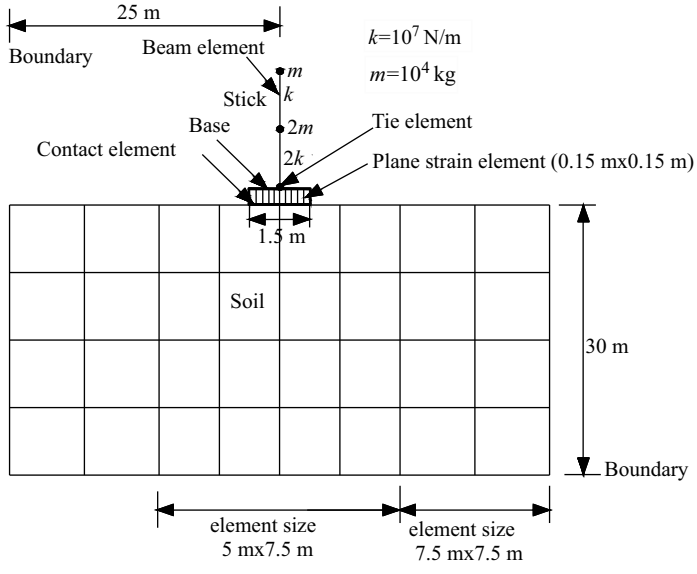

Figure 7.24 FEM modeling of soil–structure system

The results are shown in Figures 7.25–7.27. It is seen from the figures that the top displacement of the stick is more and the bending stress at the base is less for the flexible base than the corresponding response quantities for the fixed base. Also, the base rotation for the flexible base is found to be significant, as the soil is soft.

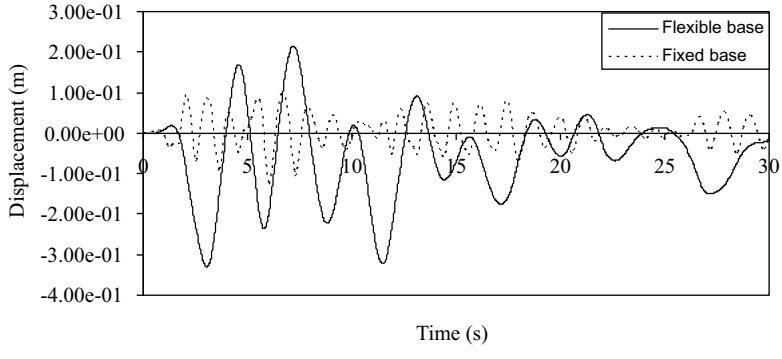

Figure 7.25 Time histories of top displacements of the stick for fixed base and flexible base ($V_S = 80\,\mathrm{m\,s^{-1}}$)

7.5.3 Substructure Method of Analysis

Most of the disadvantages of the direct method of analysis can be removed if the substructure method is employed. In the substructure method of analysis, the two systems, that is, the superstructure and the

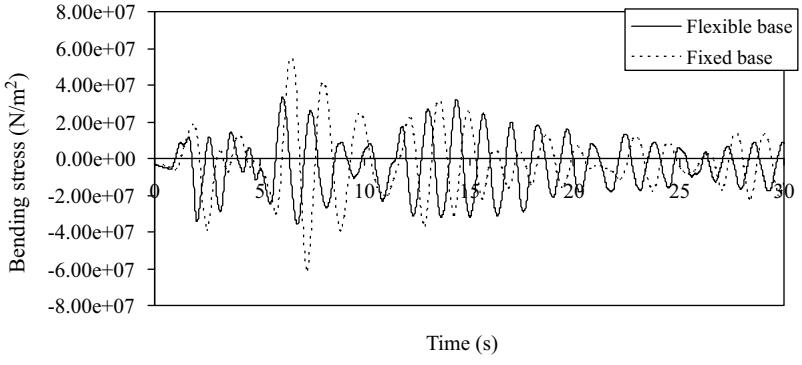

Figure 7.26 Bending stresses at the base for fixed base and flexible base ($V_S = 80\,\mathrm{m\,s^{-1}}$)

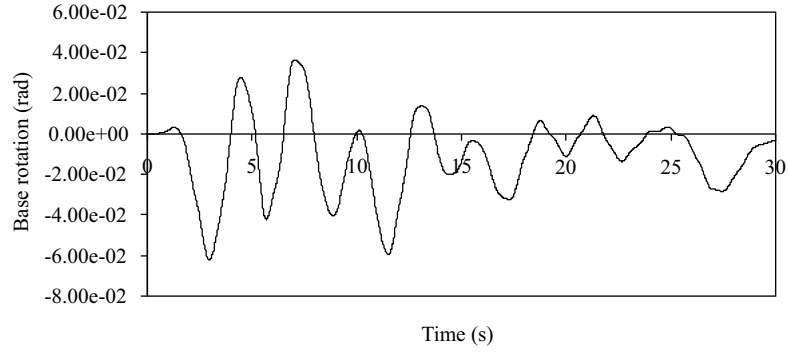

Figure 7.27 Time history of the base rotation for flexible base ($V_S = 80\,\mathrm{m\,s^{-1}}$)

foundation medium, are treated as two independent models. The connection between the two models is established by the interaction forces acting on the interface. The dynamic equilibrium equations are finally written in terms of interface degrees of freedom and solved either in the time domain or in the frequency domain. The foundation medium is treated as an elastic half space for which impedance functions are known. Impedance functions for a massless circular flooring resting on an elastic half space have been derived by many investigators [4, 5] and are available in the form of graphs. For rectangular footings, approximate expressions for impedance functions may be derived from those of the (area) equivalent circular footings. For rigid (massless) circular footings, the impedance function for the elastic half space can be derived analytically by applying complex unit harmonic forces one at a time as shown in Figure 7.28. The resulting displacements of the degrees of freedom of the plate are obtained as complex numbers and are arranged in a column to form a complex flexibility matrix. The inverse of the matrix provides the impedance matrix. In the impedance matrix, coupling terms exist only between the rotation and the translation. Real and imaginary parts of the elements corresponding to a degree of freedom are equal to the soil stiffness and damping corresponding to that degree of freedom. These impedance functions are the key parameters for the substructure method of analysis.

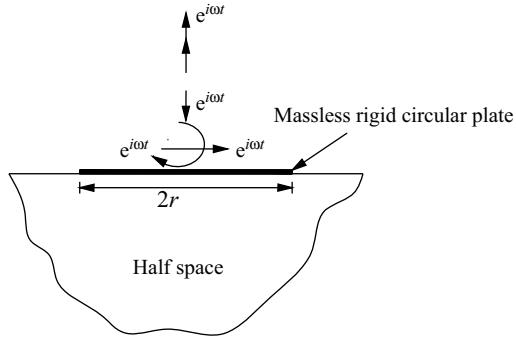

Figure 7.28 Elastic half space solution for soil impedance function

The superstructure is modeled invariably by finite elements. Modeling for the substructure method of analysis is shown in Figure 7.29. For some of the structures, a portion of the soil may be included in the superstructure. For such structures two interfaces are dealt with, one at the free ground surface and the other at the surface between the superstructure and foundation medium as shown in Figure 7.29b.

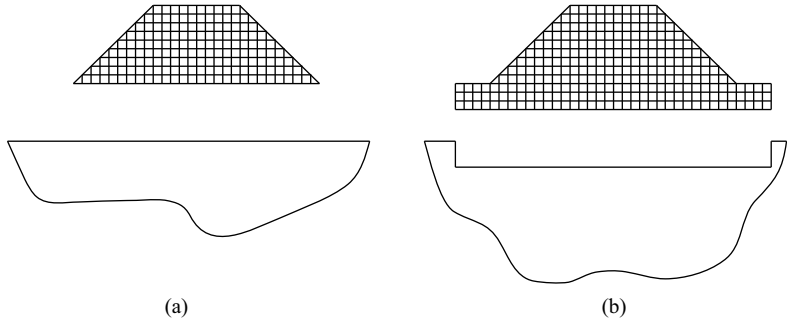

Figure 7.29 Modeling for substructure method of analysis: (a) structure without any soil portion; and (b) structure with a portion of soil attached

The substructure method of analysis is first explained with the single degree of freedom superstructure, before it is extended to the multi-degrees of freedom with multi-point excitation of the superstructure.

7.5.3.1 SDOF Superstructure

Referring to Figure 7.30, the superstructure, which is modeled as an SDOF system, induces two forces at the base, namely, a horizontal shear force and a moment. It is assumed that the base of the SDOF system is attached to a rigid massless plate resting on an elastic half space. At the base, the SDOF will undergo two movements, that is, one translation produced by base shear, and the other a rotation produced by the moment.

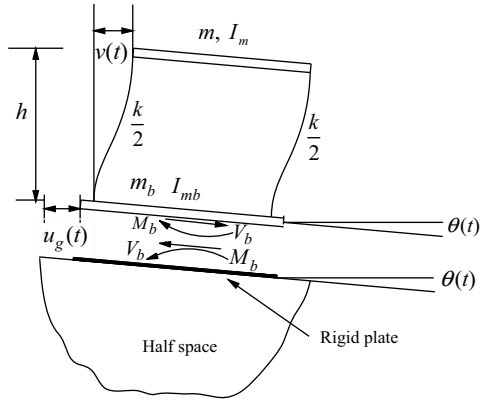

Figure 7.30 Substructure method of analysis for SDOF system

Dynamic stiffness (impedance function) for the rigid massless circular footing of radius r resting on an isotropic homogeneous half space for translation and rotational (rocking) degrees of freedom are represented by a stiffness matrix of the form

$$\boldsymbol{G}_{\mathrm{d}}(\omega) = \begin{bmatrix} G_{vv} & G_{v\theta} \\ G_{\theta v} & G_{\theta\theta} \end{bmatrix} \tag{7.39}$$

in which G_{vv}, $G_{v\theta}$, and so on, are the frequency dependent complex functions. G_{vv}, $G_{v\theta}$, and so on, have real and imaginary parts in the form of

$$G(ia) = G^{\mathrm{R}}(a) + iG^{\mathrm{I}}(a) \tag{7.40}$$

in which R and I denote real and imaginary parts and represent the soil resistance (stiffness) and damping (radiation), respectively. a is the non-dimensional frequency given by:

$$a = \frac{r\omega}{V_{\mathrm{S}}} \tag{7.41}$$

in which V_{S} is the shear wave velocity of the soil mass. Plots of $G^{\mathrm{R}}(a)$ and $G^{\mathrm{I}}(a)$ for the elements of the $\boldsymbol{G}_{\mathrm{d}}(\omega)$ matrix are available in numerous publications, for example, in reference [2].

Let the base displacement and rotation caused by the soil structure interaction be $v(t)$ and $\theta(t)$. Then, the total base motion will be:

$$v^{\mathrm{t}} = v(t) + u_g(t) \tag{7.42}$$

in which $u_g(t)$ is the free field ground displacement, and v^{t} is the total displacement at the base. Referring to Figure 7.30, the equation of motion for the top mass of the SDOF system may be written as:

$$m\ddot{u} + 2m\omega_{\mathrm{n}}\xi\dot{u} + ku + mh\ddot{\theta} + m\ddot{v}^{\mathrm{t}} = 0 \tag{7.43}$$

where

u is the relative displacement of the top mass with respect to the base
h is the column height
k is the total lateral stiffness of the mass with respect to the base
m is the lumped mass at the top
ξ is the percentage critical damping
ω_{n} is the natural frequency of the SDOF, and $\ddot{v}^{t}$ is defined by Equation 7.42.

The interaction forces V_b and M_b between the superstructure and the half space can be written by considering the equilibrium of the superstructure as:

$$m\ddot{u} + mh\ddot{\theta} + (m + m_b)\ddot{v}^t - V_b = 0 \tag{7.44}$$

$$mh\ddot{u} + (mh^2 + I_m + I_{mb})\ddot{\theta} + mh\ddot{v}^t - M_b = 0 \tag{7.45}$$

in which m_b and I_{mb} are the mass and mass moments of inertia of the base mass, respectively.

The interaction forces M_b and V_b are determined by considering the motions of the rigid plate attached to the elastic half space, that is, $u(t)$ and $\theta(t)$. As these forces are obtained with the help of the complex frequency dependent impedance functions as described previously, Equations 7.43–7.45 are written in the frequency domain using a Fourier transform as:

$$g(\omega)u(\omega) - mh\omega^2\theta(\omega) - m\omega^2 v^t(\omega) = 0 \tag{7.46}$$

$$-m\omega^2 u(\omega) - mh\omega^2\theta(\omega) - (m + m_b)\omega^2 v^t(\omega) - V_b(\omega) = 0 \tag{7.47}$$

$$-mh\omega^2 u(\omega) - \bar{I}_m\omega^2\theta(\omega) - mh\omega^2 v^t(\omega) - M_b(\omega) = 0 \tag{7.48}$$

in which $\bar{I}_m = I_m + I_{mb} + mh^2$ and $g(\omega)$ is the inverse of complex frequency response function of an SDOF system. Noting that $V_b(\omega)$ and $M_b(\omega)$ can be written in terms of the impedance matrix $\boldsymbol{G}_d(\omega)$ given by Equation 7.39, the above three equations can be re-arranged in the following form

$$\boldsymbol{K}_g(\omega)\boldsymbol{d}(\omega) = \boldsymbol{M}\ddot{u}_g(\omega) \tag{7.49}$$

where

$\boldsymbol{K}_g(\omega)$ is a frequency dependent complex stiffness matrix of the soil structure system
$\boldsymbol{d}(\omega)$ is the complex frequency components of the displacement vector $[u, v, \theta]^T$
$\ddot{u}_g(\omega)$ is the complex frequency components of the ground acceleration
$\boldsymbol{M} = -[m(m + m_b)\, mh]^T$.

In obtaining the equations in the form of a matrix equation, use is made of the following relationship:

$$\begin{bmatrix} V_b \\ M_b \end{bmatrix} = \boldsymbol{G}_d(\omega)\begin{Bmatrix} u(\omega) \\ \theta(\omega) \end{Bmatrix} \tag{7.50}$$

and $\omega^2 v^t(\omega) = \omega^2 v(\omega) + \ddot{u}_g(\omega)$. Elements of $\boldsymbol{K}_g(\omega)$ are given as:

$$K_{g\,11} = g(\omega); \qquad K_{g\,12} = K_{g\,21} = -\omega^2 m; \qquad K_{g\,13} = K_{g\,31} = -\omega^2 mh \tag{7.51a}$$

$$K_{g\,22} = -\omega^2(m + m_b) + G_{uu}(\omega); \qquad K_{g\,33} = -\omega^2\bar{I}_m + G_{\theta\theta}(\omega) \tag{7.51b}$$

$$K_{g\,23} = K_{g\,32} = -\omega^2 mh + G_{u\theta}(\omega) \tag{7.51c}$$

Solution of Equation 7.49 for each frequency provides the response vector $\boldsymbol{d}(\omega)$ given the Fourier transform of the ground acceleration, $\ddot{u}_g(t)$. Inverse Fourier transform of $\boldsymbol{d}(\omega)$ gives the time histories of the response quantities $u(t)$, $v(t)$, and $\theta(t)$.

7.5.3.2 MDOF System with Multi-Support Excitation

Unlike the SDOF system, the MDOF system with multi-support excitations, as shown in Figure 7.31, is characterized by the presence of a quasi-static component of the response in the total (absolute) response of different degrees of freedom. The quasi-static component of the response is produced due to different ground motions at different supports producing relative support motions. In order to formulate the problem of dynamic soil–structure interaction using the substructure method, the total displacement is written as the sum of three displacement components

$$\boldsymbol{v}^t = \boldsymbol{v}_g + \boldsymbol{v}_r + \boldsymbol{v}_d \tag{7.52}$$

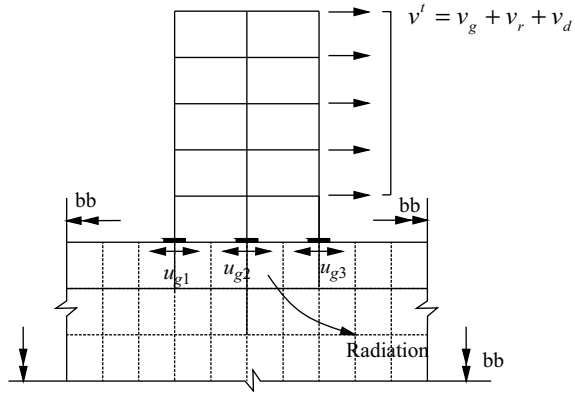

Figure 7.31 Substructure method of analysis for MDOF system with multi-support excitation

where

$\boldsymbol{v}_g$ is the vector of displacements produced at all non-support degrees of freedom produced due to the ground displacements at the supports

$\boldsymbol{v}_r$ is the same due to displacements at the supports for maintaining elastic compatibility between the foundation and the soil

$\boldsymbol{v}_d$ is the vector of the relative dynamic displacements produced at all non-support degrees of freedom due to the inertial action.

The first two displacement vectors are quasi-static in nature and therefore, involve the stiffness of the soil structure system only. A physical interpretation of Equation 7.52 helps in the derivation of the equations of motion and for solving them to obtain the three components of the displacement.

Initially, the free field ground motion tends to move the supports at positions the same as those of the displaced ground beneath the supports. The relative motion between the supports, produced due to different ground motions at different supports, produces elastic forces in the structure. These elastic forces give rise to the development of a set of equal and opposite reactions at the interface between the foundation and the soil. These equal and opposite reactions produce deformations in the interface, thus inducing compatible displacements both in the structure and the soil. In a similar way, the inertia forces developed at the masses associated with each degree of freedom of the structure induce a pair of equal and opposite dynamic forces at the foundation and soil interface. This pair of dynamic forces induces compatible dynamic displacements in the structure and the soil. The dynamic displacement caused in the soil

propagates in the form of a wave within the soil giving rise to the radiation damping in the dynamic soil structure interaction problem, as mentioned previously.

With this background, the equation of motion of the superstructure, shown in Figure 7.31, can be written as:

$$\begin{bmatrix} \boldsymbol{M}_{ss} & \boldsymbol{M}_{sf} \\ \boldsymbol{M}_{fs} & \boldsymbol{M}_{ff} \end{bmatrix} \begin{Bmatrix} \ddot{\boldsymbol{v}}_s^{\mathrm{t}} \\ \ddot{\boldsymbol{v}}_f^{\mathrm{t}} \end{Bmatrix} + \begin{bmatrix} \boldsymbol{C}_{ss} & \boldsymbol{C}_{sf} \\ \boldsymbol{C}_{fs} & \boldsymbol{C}_{ff} \end{bmatrix} \begin{Bmatrix} \dot{\boldsymbol{v}}_s^{t} \\ \dot{\boldsymbol{v}}_f^{\mathrm{t}} \end{Bmatrix} + \begin{bmatrix} \boldsymbol{K}_{ss} & \boldsymbol{K}_{sf} \\ \boldsymbol{K}_{fs} & \boldsymbol{K}_{ff} \end{bmatrix} \begin{Bmatrix} \boldsymbol{v}_s^{\mathrm{t}} \\ \boldsymbol{v}_f^{\mathrm{t}} \end{Bmatrix} = \begin{Bmatrix} 0 \\ \boldsymbol{p}_f^{\mathrm{t}} \end{Bmatrix} \tag{7.53}$$

in which the subscripts s and f refer to the structure and the foundation (base), respectively; $\boldsymbol{p}_f^{\mathrm{t}}$ is the total nodal forces at the base degrees of freedom; the opposite of these forces act on the soil substructure.

In order to obtain the quasi-static components of the responses, that is, $\boldsymbol{v}_g$ and $\boldsymbol{v}_r$, only the stiffness terms of the equation of motion are considered. Let the quasi-static response of non-support degrees of freedom due to ground motion at the supports be denoted by $\boldsymbol{v}_g^f$ and the ground motions at the supports be denoted by $\boldsymbol{v}_g^f = \boldsymbol{u}_g$. Let the quasi-static displacements at non-support degrees of freedom produced due to the compatible displacements at the soil foundation interface be denoted by v_r^s, and the compatible displacements at the supports be denoted by $\boldsymbol{v}_r^f$. Then, the equilibrium of forces at the structure foundation interface written in frequency domain is given by:

$$\boldsymbol{K}_{fs}(\boldsymbol{v}_g^s + \boldsymbol{v}_r^s) + \boldsymbol{K}_{ff}(\boldsymbol{v}_g^f + \boldsymbol{v}_r^f) + \boldsymbol{G}_{ff}\boldsymbol{v}_r^f = 0 \tag{7.54}$$

in which $\boldsymbol{G}_{ff}$ is the impedance matrix for the soil corresponding to the interface degrees of freedom. Note that imaginary part of the impedance matrix is not included as the above equation is written only for quasi-static motion. Simplification of the above equation leads to

$$\boldsymbol{K}_{fs}\boldsymbol{v}_r^s + (\boldsymbol{K}_{ff} + \boldsymbol{G}_{ff})\boldsymbol{v}_r^f = -\boldsymbol{K}_{fs}\boldsymbol{v}_g^s - \boldsymbol{K}_{ff}\boldsymbol{v}_g^f = -\boldsymbol{P}_f \tag{7.55}$$

If the displacements of the non-support degrees of freedom due to the free field ground motion of the supports are only considered, then

$$\boldsymbol{K}_{ss}\boldsymbol{v}_g^s + \boldsymbol{K}_{sf}\boldsymbol{v}_g^f = 0 \tag{7.56}$$

or

$$\boldsymbol{v}_g^s = -\boldsymbol{K}_{ss}^{-1}\boldsymbol{K}_{sf}\boldsymbol{v}_g^f = -\boldsymbol{K}_{ss}^{-1}\boldsymbol{K}_{sf}\boldsymbol{u}_g = \frac{1}{\omega^2}\boldsymbol{K}_{ss}^{-1}\boldsymbol{K}_{sf}\ddot{\boldsymbol{u}}_g \tag{7.57}$$

Substituting for $\boldsymbol{v}_g^s$ given by Equation 7.57 in the right-hand side of Equation 7.55, the following expression for $\boldsymbol{P}_f$ is obtained

$$\boldsymbol{P}_f = -\frac{1}{\omega^2}(\boldsymbol{K}_{ff} - \boldsymbol{K}_{fs}\boldsymbol{K}_{ss}^{-1}\boldsymbol{K}_{sf})\ddot{\boldsymbol{u}}_g \tag{7.58}$$

Thus, $\boldsymbol{v}_r$ can be obtained by solving the following equation

$$\begin{bmatrix} \boldsymbol{K}_{ss} & \boldsymbol{K}_{sf} \\ \boldsymbol{K}_{fs} & \boldsymbol{K}_{ff} + \boldsymbol{G}_{ff} \end{bmatrix} \begin{Bmatrix} \boldsymbol{v}_r^s \\ \boldsymbol{v}_r^f \end{Bmatrix} = \begin{Bmatrix} 0 \\ -\boldsymbol{P}_f \end{Bmatrix} \tag{7.59}$$

Equation 7.59 is obtained by adding Equation 7.60, given below, with Equation 7.55 as there are no external set of forces acting on the structure.

$$\boldsymbol{K}_{ss}\boldsymbol{v}_r^s + \boldsymbol{K}_{sf}\boldsymbol{v}_r^f = 0 \tag{7.60}$$

To determine $\boldsymbol{v}_d$, $\boldsymbol{v}^t$ given by Equation 7.52 is substituted into Equation 7.53 and the equation of motion is rewritten as:

$$\begin{bmatrix} \boldsymbol{M}_{ss} & \boldsymbol{M}_{sf} \\ \boldsymbol{M}_{fs} & \boldsymbol{M}_{ff} \end{bmatrix} \begin{Bmatrix} \ddot{\boldsymbol{v}}_d^s \\ \ddot{\boldsymbol{v}}_d^f \end{Bmatrix} + \begin{bmatrix} \boldsymbol{C}_{ss} & \boldsymbol{C}_{sf} \\ \boldsymbol{C}_{fs} & \boldsymbol{C}_{ff} \end{bmatrix} \begin{Bmatrix} \dot{\boldsymbol{v}}_d^s \\ \dot{\boldsymbol{v}}_d^f \end{Bmatrix} + \begin{bmatrix} \boldsymbol{K}_{ss} & \boldsymbol{K}_{sf} \\ \boldsymbol{K}_{fs} & \boldsymbol{K}_{ff} \end{bmatrix} \begin{Bmatrix} \boldsymbol{v}_d^s \\ \boldsymbol{v}_d^f \end{Bmatrix} = -\begin{bmatrix} \boldsymbol{M}_{ss} & \boldsymbol{M}_{sf} \\ \boldsymbol{M}_{fs} & \boldsymbol{M}_{ff} \end{bmatrix} \begin{Bmatrix} \ddot{\boldsymbol{v}}_a^s \\ \ddot{\boldsymbol{v}}_a^f \end{Bmatrix} - \begin{bmatrix} \boldsymbol{C}_{ss} & \boldsymbol{C}_{sf} \\ \boldsymbol{C}_{fs} & \boldsymbol{C}_{ff} \end{bmatrix} \begin{Bmatrix} \dot{\boldsymbol{v}}_a^s \\ \dot{\boldsymbol{v}}_a^f \end{Bmatrix} - \begin{bmatrix} \boldsymbol{K}_{ss} & \boldsymbol{K}_{sf} \\ \boldsymbol{K}_{fs} & \boldsymbol{K}_{ff} \end{bmatrix} \begin{Bmatrix} \boldsymbol{v}_a^s \\ \boldsymbol{v}_a^f \end{Bmatrix} + \begin{Bmatrix} 0 \\ \boldsymbol{p}_f^t \end{Bmatrix} \tag{7.61}$$

in which $\boldsymbol{v}_a^s = \boldsymbol{v}_g^s + \boldsymbol{v}_r^s$ and $\boldsymbol{v}_a^f = \boldsymbol{v}_g^f + \boldsymbol{v}_r^f$.

The damping terms on the right-hand side of Equation 7.61 make little contribution to effective loading for relatively low structural damping. Considering this fact and using Equation 7.54, Equation 7.61 may be written in frequency domain as:

$$\left\{ -\omega^2 \begin{bmatrix} \boldsymbol{M}_{ss} & \boldsymbol{M}_{sf} \\ \boldsymbol{M}_{fs} & \boldsymbol{M}_{ff} \end{bmatrix} + i\omega \begin{bmatrix} \boldsymbol{C}_{ss} & \boldsymbol{C}_{sf} \\ \boldsymbol{C}_{fs} & \boldsymbol{C}_{ff} \end{bmatrix} + \begin{bmatrix} \boldsymbol{K}_{ss} & \boldsymbol{K}_{sf} \\ \boldsymbol{K}_{fs} & \boldsymbol{K}_{ff} \end{bmatrix} \right\} \begin{Bmatrix} \boldsymbol{v}_d^s \\ \boldsymbol{v}_d^f \end{Bmatrix} = +\omega^2 \begin{bmatrix} \boldsymbol{M}_{ss} & \boldsymbol{M}_{sf} \\ \boldsymbol{M}_{fs} & \boldsymbol{M}_{ff} \end{bmatrix} \begin{Bmatrix} \boldsymbol{v}_a^s \\ \boldsymbol{v}_a^f \end{Bmatrix} + \begin{Bmatrix} 0 \\ \boldsymbol{P}_f^t - \boldsymbol{P}_{rf} \end{Bmatrix} \tag{7.62}$$

in which $\boldsymbol{P}_{rf} = -\boldsymbol{G}_{ff}\boldsymbol{v}_r^f$; $\boldsymbol{P}_f^t - \boldsymbol{P}_{rf}$ may be viewed as the dynamic component of the load acting on the foundation arising due to the dynamic compatibility of displacements at the interface. It may be obtained in a similar way as that for the case of interface compatibility of quasi-static displacement (Equation 7.54), that is,

$$\boldsymbol{P}_f^t - \boldsymbol{P}_{rf} = \boldsymbol{P}_f^d = -\boldsymbol{G}_{ff}\boldsymbol{v}_d^f \tag{7.63}$$

Note that in Equation 7.63, $\boldsymbol{G}_{ff}$ has both real and imaginary components. The imaginary component denotes the radiation damping and it adds on to the overall damping of the system. Equation 7.62 can, therefore, be written in the frequency domain as:

$$\left\{ -\omega^2 \begin{bmatrix} \boldsymbol{M}_{ss} & \boldsymbol{M}_{sf} \\ \boldsymbol{M}_{fs} & \boldsymbol{M}_{ff} \end{bmatrix} + i\omega \begin{bmatrix} \boldsymbol{C}_{ss} & \boldsymbol{C}_{sf} \\ \boldsymbol{C}_{fs} & \boldsymbol{C}_{ff} \end{bmatrix} + \begin{bmatrix} \boldsymbol{K}_{ss} & \boldsymbol{K}_{sf} \\ \boldsymbol{K}_{fs} & \boldsymbol{K}_{ff} + \boldsymbol{G}_{ff} \end{bmatrix} \right\} \begin{Bmatrix} \boldsymbol{v}_d^s \\ \boldsymbol{v}_d^f \end{Bmatrix} = +\omega^2 \begin{bmatrix} \boldsymbol{M}_{ss} & \boldsymbol{M}_{sf} \\ \boldsymbol{M}_{fs} & \boldsymbol{M}_{ff} \end{bmatrix} \begin{Bmatrix} \boldsymbol{v}_a^s \\ \boldsymbol{v}_a^f \end{Bmatrix} \tag{7.64}$$

As $\boldsymbol{v}_a^s$ and $\boldsymbol{v}_a^f$ have been obtained previously, $\boldsymbol{v}_d^s$ and $\boldsymbol{v}_d^f$ can be determined from the solution of Equation 7.64, which requires inversion of a complex matrix for each value of ω. Once $\boldsymbol{v}_d^s$ and $\boldsymbol{v}_d^f$ are solved for different frequencies, the $\boldsymbol{v}^t$ vector can be obtained. Inverse Fourier transform of $\boldsymbol{v}^t$ provides the desired response vector $\boldsymbol{v}^t$.

Steps for Performing the Substructure Method of Analysis

1. Partition the condensed stiffness matrix of the structure–foundation system corresponding to the dynamic DOF according to the structure(s) and foundation(s) DOF (Equation 7.53).
2. Obtain quasi-static component of displacements $\boldsymbol{v}_g^s(\omega)$ of the non-support degrees of freedom using Equation 7.57.
3. Find $\boldsymbol{P}_f$ using Equation 7.58 and then find $\boldsymbol{v}_r^s(\omega)$ and $\boldsymbol{v}_r^f(\omega)$ from the solution to Equation 7.59.
4. Find $\boldsymbol{v}_a^s = \boldsymbol{v}_g^s + \boldsymbol{v}_r^s$ and $\boldsymbol{v}_a^f = \boldsymbol{v}_g^f + \boldsymbol{v}_r^f$; note that $\boldsymbol{v}_g^f$ is the vector of earthquake ground displacement.
5. As $\boldsymbol{v}_a^s$ and $\boldsymbol{v}_a^f$ are known, solve Equation 7.64 by the frequency domain analysis technique using FFT and IFFT (Chapter 3).

Example 7.5

The shear frame, shown in Figure 7.32, is supported by two circular footings of radius 1 m below the two columns. The footing rests on a soil with $V_S = 80\,\text{m s}^{-1}$; $\mu = 1/3$ and $\rho = 1600\,\text{kg m}^{-3}$. Using a substructure technique, find the time histories of the first- and the top-floor displacements (relative to the ground) for the El Centro earthquake acceleration applied at the base. Use a frequency independent impedance function for the soil. Assume $\xi = 5\%$ for the frame.

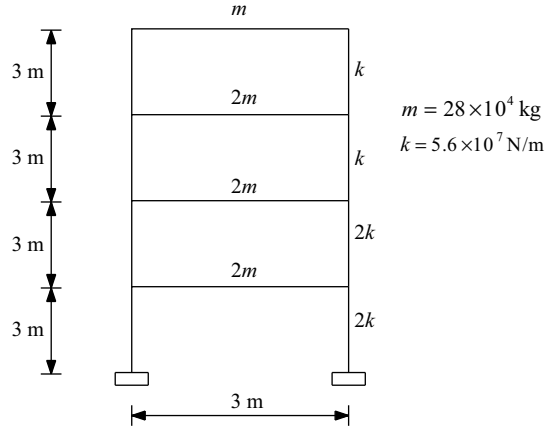

Figure 7.32 Model of the four-storey building frame

Solution: As all the supports are subjected to the same excitation, $\boldsymbol{v}_g^s = \boldsymbol{I}u_g$. The required matrices for the solution are:

$$K_{ss} = \begin{bmatrix} 5.6 & -5.6 & 0 & 0 \\ -5.6 & 11.2 & -5.6 & 0 \\ 0 & -5.6 & 16.8 & -11.2 \\ 0 & 0 & -11.2 & 22.4 \end{bmatrix} \times 10^7\,\text{N m}^{-1}; \qquad K_{sf} = \begin{bmatrix} 0 & 0 \\ 0 & 0 \\ 0 & 0 \\ -11.2 & -16.8 \end{bmatrix} \times 10^7\,\text{N m}^{-1}$$

$$K_{fs} = K_{sf}^T; \quad K_{ff} = \begin{bmatrix} 11.2 & 16.8 \\ 16.8 & 33.6 \end{bmatrix} \times 10^7\,\text{N m}^{-1}; \quad M_{ss} = \begin{bmatrix} 1 & 0 & 0 & 0 \\ 0 & 2 & 0 & 0 \\ 0 & 0 & 2 & 0 \\ 0 & 0 & 0 & 2 \end{bmatrix} \times 28 \times 10^4\,\text{kg}$$

$$\boldsymbol{I} = \begin{bmatrix} 1 & 1 & 1 & 1 \end{bmatrix}^T$$

in which $\boldsymbol{K}_{ff}$ corresponds to base displacement and rotation (DOF).

The frequency independent $\boldsymbol{G}_{ff}$ matrix is (which is formed using coefficients given in Equations 7.69a and 7.69b)

$$\boldsymbol{G}_{ff} = \begin{bmatrix} 98.32 & 6.88 \\ 6.88 & 81.19 \end{bmatrix} \times 10^6 + \boldsymbol{i} \begin{bmatrix} 70.65 & 6.14 \\ 6.14 & 15.35 \end{bmatrix} \times 10^4$$

$\boldsymbol{P}_f(\omega)$ is obtained using Equation 7.58 and finding the FFT of $\ddot{u}_g(t)$. For example, $\boldsymbol{P}_f(\omega)$ for $\omega = 0.418\,\text{rad s}^{-1}$ is obtained as:

$$\boldsymbol{P}_f = \begin{Bmatrix} -2.49 & -i0.766 \\ -0.17 & -i0.0536 \end{Bmatrix} \times 10^9$$

$\boldsymbol{v}_r^s$ and $\boldsymbol{v}_r^f$ are determined by solving Equation 7.59. Note that $\boldsymbol{G}_{ff}$ in Equation 7.59 is taken as the real part of $\boldsymbol{G}_{ff}$.

$$\boldsymbol{v}_a^s = \boldsymbol{v}_g^s + \boldsymbol{v}_r^s = \boldsymbol{I}\boldsymbol{u}_g + \boldsymbol{v}_r^s = -\frac{1}{\omega^2}\boldsymbol{I}\ddot{\boldsymbol{u}}_g(\omega) + \boldsymbol{v}_r^s(\omega)$$

$$\boldsymbol{v}_a^f = -\frac{1}{\omega^2}\boldsymbol{T}\ddot{\boldsymbol{u}}_g(\omega) + \boldsymbol{v}_r^f(\omega) \quad \boldsymbol{T} = \begin{bmatrix} 1 & 0 \end{bmatrix}^T$$

Equation 7.64 is then solved for $\boldsymbol{v}_d^s$ and $\boldsymbol{v}_d^f$, in which

$$C_{ff} = \begin{bmatrix} 70.65 & 6.14 \\ 6.14 & 15.35 \end{bmatrix} \times 10^4 \text{ N s m}^{-1}; \quad G_{ff} = \begin{bmatrix} 98.32 & 6.88 \\ 6.88 & 81.19 \end{bmatrix} \times 10^6 \text{ N m}^{-1};$$

$$C_{ss} = \alpha M_{ss} + \beta K_{ss}; \quad \alpha = 0.3608; \quad \beta = 0.0057$$

$$C_{ss} = \begin{bmatrix} 4.202 & -3.192 & 0 & 0 \\ -3.192 & 8.404 & -3.192 & 0 \\ 0 & -3.192 & 11.596 & -6.384 \\ 0 & 0 & -6.384 & 14.788 \end{bmatrix} \times 10^5 \text{ N s m}^{-1}$$

$$C_{sf} = C_{fs} = M_{fs} = M_{sf} = M_{ff} = 0$$

The total displacements of different degrees of freedom are determined by Equation 7.52 in the frequency domain and taking the IFFT of them. The time histories of relative displacements with respect to ground (that is, $\boldsymbol{v}_d^s + \boldsymbol{v}_r^s$) for the top floor and the first floor are shown in Figures 7.33 and 7.34 respectively. In subsequent problems, these time histories are compared with those obtained by other methods.

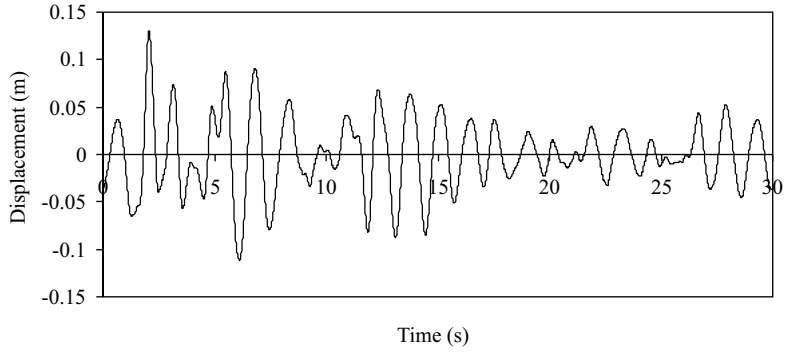

Figure 7.33 Time history of top-floor displacement relative to the ground

7.5.4 Modal Analysis Using the Substructure Technique

The solution to Equation 7.64 provides directly the dynamic displacements of the structure. However, the size of the problem may be large depending upon the degrees of freedom of the superstructure. Further, the damping matrix $\boldsymbol{C}_{ss}$ has to be constructed from the fundamental frequencies of the superstructure. In view

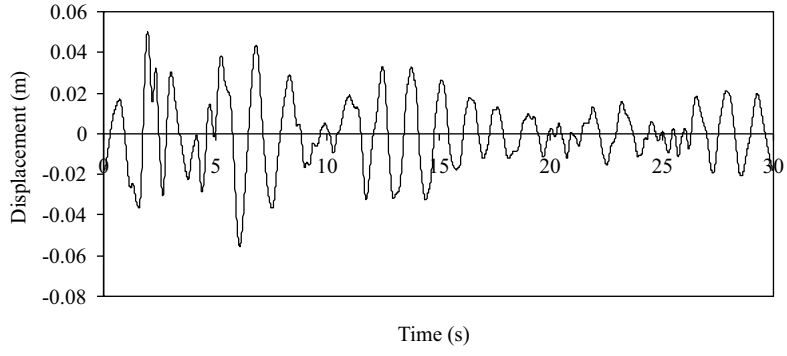

Figure 7.34 Time history of first-floor displacement relative to the ground

of this, a modal analysis can be performed using the frequencies and mode shapes of the superstructure, which leads to the solution of a lower number of coupled equations. The number of equations depends upon the number of modes being considered. Furthermore, the solution only requires the knowledge of the damping ratio of the structure. In order to carry out the analysis, Equation 7.64 is written as:

$$\begin{aligned} &-\omega^2 \boldsymbol{M}_{ss}\boldsymbol{v}_d^s - \omega^2 \boldsymbol{M}_{sf}\boldsymbol{v}_d^f + i\omega \boldsymbol{C}_{ss}\boldsymbol{v}_d^s + i\omega \boldsymbol{C}_{sf}\boldsymbol{v}_d^f + \boldsymbol{K}_{ss}\boldsymbol{v}_d^s + \boldsymbol{K}_{sf}\boldsymbol{v}_d^f \\ &\quad = \omega^2 \boldsymbol{M}_{ss}\boldsymbol{v}_a^s + \omega^2 \boldsymbol{M}_{sf}\boldsymbol{v}_a^f \end{aligned} \tag{7.65a}$$

$$\begin{aligned} &-\omega^2 \boldsymbol{M}_{fs}\boldsymbol{v}_d^s - \omega^2 \boldsymbol{M}_{ff}\boldsymbol{v}_d^f + i\omega \boldsymbol{C}_{sf}\boldsymbol{v}_d^s + i\omega \boldsymbol{C}_{ff}\boldsymbol{v}_d^f + \boldsymbol{K}_{fs}\boldsymbol{v}_d^s + (\boldsymbol{K}_{ff} + \boldsymbol{G}_{ff})\boldsymbol{v}_d^f \\ &\quad = \omega^2 \boldsymbol{M}_{fs}\boldsymbol{v}_a^s + \omega^2 \boldsymbol{M}_{ff}\boldsymbol{v}_a^f \end{aligned} \tag{7.65b}$$

Assuming the superstructure to remain elastic, the dynamic displacement $\boldsymbol{v}_d^s$ of the structure relative to the base (foundation) may be written as a weighted summation of mode shapes of the fixed base structure as:

$$\boldsymbol{v}_d^s = \boldsymbol{\phi}\boldsymbol{z} \tag{7.66}$$

in which $\boldsymbol{\phi}$ is the mode shape matrix of size $n \times m$ and $\boldsymbol{z}$ is a vector of generalized co-ordinates of size m; m is the number of modes considered in the analysis. Substituting for $\boldsymbol{v}_d^s$ into Equations 7.65a and 7.65b and pre-multiplying Equation 7.65a by $\boldsymbol{\phi}^T$, Equations 7.65a and 7.65b may be written as:

$$\begin{aligned} &\left\{ -\omega^2 \begin{bmatrix} \overline{\boldsymbol{M}}_{ss} & \overline{\boldsymbol{M}}_{sf} \\ \overline{\boldsymbol{M}}_{fs} & \boldsymbol{M}_{ff} \end{bmatrix} + i\omega \begin{bmatrix} \overline{\boldsymbol{C}}_{ss} & \overline{\boldsymbol{C}}_{sf} \\ \overline{\boldsymbol{C}}_{fs} & \boldsymbol{C}_{ff} \end{bmatrix} + \begin{bmatrix} \overline{\boldsymbol{K}}_{ss} & \overline{\boldsymbol{K}}_{sf} \\ \overline{\boldsymbol{K}}_{fs} & \boldsymbol{K}_{ff} + \boldsymbol{G}_{ff} \end{bmatrix} \right\} \begin{Bmatrix} \boldsymbol{z} \\ \boldsymbol{v}_d^f \end{Bmatrix} \\ &\quad = \omega^2 \begin{bmatrix} \boldsymbol{\phi}^T \boldsymbol{M}_{ss} & \boldsymbol{\phi}^T \boldsymbol{M}_{sf} \\ \boldsymbol{M}_{fs} & \boldsymbol{M}_{ff} \end{bmatrix} \begin{Bmatrix} \boldsymbol{v}_a^s \\ \boldsymbol{v}_a^f \end{Bmatrix} \end{aligned} \tag{7.67}$$

in which $\overline{\boldsymbol{M}}_{ss} = \boldsymbol{\phi}^T \boldsymbol{M}_{ss}\boldsymbol{\phi}$; $\overline{\boldsymbol{M}}_{sf} = \boldsymbol{\phi}^T M_{sf}$; $\overline{\boldsymbol{M}}_{fs} = M_{fs}\boldsymbol{\phi}$, $\overline{\boldsymbol{C}}_{ss}$, $\overline{\boldsymbol{K}}_{fs}$, and so on, are defined in a similar way.

Equation 7.67 is a coupled matrix equation in the complex domain of size $(m+r) \times (m+r)$, in which m is the number of modes considered for the superstructure and r is the number of support degrees of freedom. Thus, the size of the matrix equation to be solved is greatly reduced by taking advantage of the modal characteristic of the superstructure. The physical meaning of Equation 7.67 is that the motions of the structural degrees of freedom are replaced by a few mode shapes of the structure. For most practical problems, $\boldsymbol{M}_{sf} = \boldsymbol{M}_{fs} = 0$ and $\boldsymbol{C}_{sf} = \boldsymbol{C}_{fs} = 0$. With these simplifications, Equation 7.67 can be written as:

$$[\overline{\boldsymbol{h}} + \overline{\boldsymbol{K}}_{sf}] \begin{Bmatrix} \boldsymbol{z} \\ \boldsymbol{v}_d^f \end{Bmatrix} = \boldsymbol{P}^s \tag{7.68a}$$

$$[\overline{\boldsymbol{K}}_{fs} + \overline{\boldsymbol{K}}_{ff}] \begin{Bmatrix} \boldsymbol{z} \\ \boldsymbol{v}_d^f \end{Bmatrix} = \boldsymbol{P}^f \tag{7.68b}$$

in which $\overline{\boldsymbol{h}}$ is a diagonal matrix with diagonal elements as $\overline{m}_j[(\omega_j^2 - \omega^2) + 2i\xi\omega_j\omega](j = 1 \ldots m)$; ω_j and $\overline{m}_j$ are the jth natural frequency and jth modal mass, respectively; ξ is the modal damping; and $\boldsymbol{P}^s$, $\boldsymbol{P}^f$ and $\overline{\boldsymbol{K}}_{ff}$ are given by:

$$\boldsymbol{P}^s = \omega^2 \boldsymbol{\phi}^T \boldsymbol{M}_{ss} \boldsymbol{v}_a^s \tag{7.68c}$$

$$\boldsymbol{P}^f = \omega^2 \boldsymbol{M}_{ff} \boldsymbol{v}_a^f \tag{7.68d}$$

$$\overline{\boldsymbol{K}}_{ff} = [\boldsymbol{K}_{ff} + \boldsymbol{G}_{ff} + i\omega \boldsymbol{C}_{ff}] \tag{7.68e}$$

Solution of Equations 7.68a and 7.68b provide $\boldsymbol{z}$ and $\boldsymbol{v}_d^f$. Taking the IFFT of $\boldsymbol{z}$ and $\boldsymbol{v}_d^f$, using modal superposition and utilizing Equation 7.52, the total displacement of the dynamic degrees of freedom of the soil–structure system are obtained. Other response quantities of interest are determined from the displacements as explained in Chapter 3.

Example 7.6

Using the modal substructure technique, solve the problem in Example 7.5 and compare the results with those of the direct substructure analysis.

Solution: The first three mode shapes and frequencies of the undamped fixed base structure are given below.

$$\omega_1 = 5.06 \text{ rad s}^{-1}; \quad \omega_2 = 12.57 \text{ rad s}^{-1}; \quad \omega_3 = 18.65 \text{ rad s}^{-1}$$

$$\boldsymbol{\phi}_1^T = [\,1 \quad 0.871 \quad 0.520 \quad 0.278\,]; \quad \boldsymbol{\phi}_2^T = [\,1 \quad 0.210 \quad -0.911 \quad -0.752\,]$$

$$\boldsymbol{\phi}_3^T = [\,1.0 \quad -0.738 \quad 0.090 \quad 0.347\,]$$

Taking the first three modes, the following matrices (Equation 7.67) are obtained.

$$\overline{\boldsymbol{K}}_{ss} = 10^7 \times \begin{bmatrix} 2.305 & 0 & 0 \\ 0 & 17.152 & 0 \\ 0 & 0 & 22.842 \end{bmatrix} \text{N m}^{-1}$$

$$\overline{\boldsymbol{M}}_{ss} = 10^5 \times \begin{bmatrix} 8.992 & 0 & 0 \\ 0 & 10.861 & 0 \\ 0 & 0 & 6.571 \end{bmatrix} \text{kg}$$

$$\overline{\boldsymbol{C}}_{ss} = 10^5 \times \begin{bmatrix} 4.561 & 0 & 0 \\ 0 & 13.721 & 0 \\ 0 & 0 & 15.421 \end{bmatrix} \text{N s m}^{-1}$$

$$\overline{\boldsymbol{K}}_{fs} = \begin{bmatrix} -3.11 & 8.432 & -3.891 \\ -4.672 & 12.612 & -5.842 \end{bmatrix} \times 10^7 \text{N m}^{-1}$$

$$\overline{\boldsymbol{K}}_{sf} = \overline{\boldsymbol{K}}_{fs}^T$$

$\boldsymbol{K}_{ff}$, $\boldsymbol{G}_{ff}$, $\boldsymbol{C}_{ff}$, and so on, remain the same as in the previous problem.

Solution of Equation 7.67 provides the responses $\boldsymbol{z}(\omega)$ and $\boldsymbol{v}_d^f(\omega)$. Using Equation 7.66, $\boldsymbol{v}_d^s(\omega)$ is obtained with the help of $\boldsymbol{z}(\omega)$. After $\boldsymbol{v}_d^s(\omega)$ and $\boldsymbol{v}_d^f(\omega)$ are determined, the rest of the procedure remains

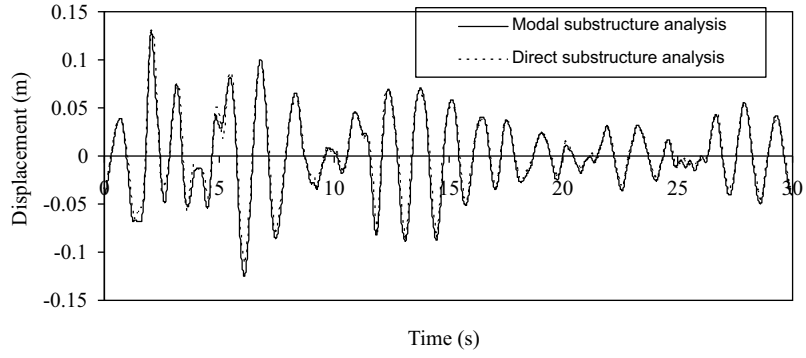

Figure 7.35 Time histories of top-floor displacement relative to the ground obtained by direct substructure and modal substructure analyses

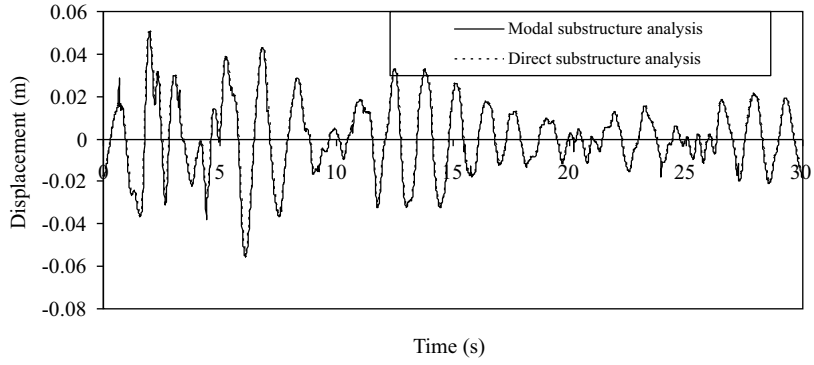

Figure 7.36 Time histories of first-floor displacement relative to the ground obtained by direct substructure and modal substructure analyses

the same as the previous problem. Results are obtained by considering all three modes and are shown in Figures 7.35 and 7.36. It is seen that the modal analysis provides almost the same results as those obtained by the direct substructure analysis.

7.5.5 Equivalent Spring–Dashpot Analysis

In the substructure method of analysis, it is seen that the stiffness and damping corresponding to the foundation degrees of freedom are contributed by both the structure and the soil. The soil components are derived from the frequency dependent impedance functions of the soil, which are readily available for circular rigid mat (weightless) footings. For other types of footings, namely square and rectangular, impedance functions can be approximately determined from the area of an equivalent circle as mentioned previously. Frequency independent impedance functions, which are the values of impedance functions very close to the zero non-dimensional frequency, are also widely used in soil–structure interaction problems. The use of frequency independent impedance functions are popular mainly for two

reasons: (i) it permits a time domain analysis to be performed for soil–structure interaction problems, and (ii) it allows the soil to be replaced by a spring and a dashpot. The stiffness and damping coefficients of the spring and dashpot are obtained from the real and the imaginary parts of the impedance function close to the zero value of a_0, respectively. For circular rigid footings, these values are available in many textbooks. Gazetas [6] provided a very useful series of charts and tables for estimating the spring and dashpot coefficients for a variety of foundation types and soil conditions. For easy reference, the coefficients for a circular rigid mat are given below.

$$k_v = \frac{4Gr}{1-\mu}; \quad k_h = \frac{8Gr}{2-\mu}; \quad k_\phi = 5.3Gr^3; \quad k_\theta = \frac{8Gr^3}{3(1-\mu)}; \quad k_{\theta h} = \frac{0.56Gr^2}{(2-\mu)} \tag{7.69a}$$

$$c_v = \frac{3}{1-\mu}\rho V_S r^2; \quad c_h = \frac{4.6}{2-\mu}\rho V_S r^2; \quad c_\phi = 0.8\rho V_S r^4; \quad c_\theta = \frac{0.4}{1-\mu}\rho V_S r^4; \quad c_{\theta h} = \frac{0.4}{2-\mu}\rho V_S r^3 \tag{7.69b}$$

where

v, h, θ, and φ stand for vertical, horizontal rocking, and torsion, respectively
V_S is the shear wave velocity
G is the shear modulus
ρ is the mass density.

The values given are mostly valid for $\mu = 1/3$.

In equivalent spring–dashpot analysis, the soil–foundation system is replaced by a spring and a dashpot, as shown in Figure 7.37. For the dynamic analysis of the soil–structure system, the stiffness and damping coefficients of the springs and dashpots are included in the stiffness and damping matrices of the total system. The response for the equivalent spring–dashpot analysis can be carried out using the direct integration method (Chapter 3). An approximate modal analysis can also be performed by ignoring the off-diagonal terms of the transformed damping matrix ($\boldsymbol{\phi}^T \boldsymbol{C} \boldsymbol{\phi}$). Note that the undamped mode shapes and frequencies of the systems are determined with the help of the stiffness and mass matrices of the structure obtained by considering the springs at the base. Using these mode shapes, frequencies, and approximate modal damping, a response spectrum analysis of the soil–structure system can also be carried out.

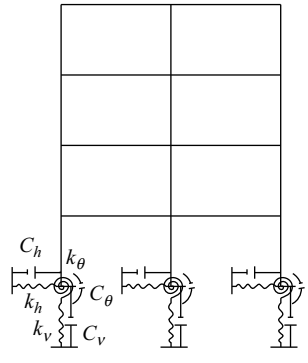

Figure 7.37 Equivalent spring–dashpot analysis

Example 7.7

Consider the frame shown in Figure 7.32. It is assumed that the columns are supported by circular footings of diameter of 1 m resting on a soil having the same properties as those given in the problem in Example 7.5. Determine the stiffness and damping matrices of the soil–structure system by replacing the soil by spring–dashpot and obtain the responses for the El Centro earthquake.

Solution: It is assumed that the members are inextensible and that vertical degrees of freedom are ignored. For 1 m diameter footings, the following values of the spring stiffness and dashpot coefficients are obtained using Equations 7.69(a-b)

$$K_h \text{ (horizontal stiffness) of the spring} = 98.3 \times 10^6 \text{ N m}^{-1}$$

$$K_\theta \text{ (rotational stiffness) of the spring} = 81.19 \times 10^6 \text{ N m rad}^{-1}$$

$K_{\theta h} = 6.88 \times 10^6$; $C_h = 70.65 \times 10^4$ N s m^{-1}; $C_\theta = 15.35 \times 10^4$ N m s rad^{-1}; $C_{\theta h} = 6.14 \times 10^4$

The stiffness matrices of the soil structure system is:

$$K = \begin{bmatrix} 5.6 & -5.6 & 0 & 0 & 0 & 0 \\ -5.6 & 11.2 & -5.6 & 0 & 0 & 0 \\ 0 & -5.6 & 16.8 & -11.2 & 0 & 0 \\ 0 & 0 & -11.2 & 22.4 & -11.2 & -16.8 \\ 0 & 0 & 0 & -11.2 & 21 & 17.5 \\ 0 & 0 & 0 & -16.8 & 17.5 & 41.7 \end{bmatrix} \times 10^7 \text{ N m}^{-1}$$

Matrix C turns out to be the same as that in Example 7.5. The first two undamped natural frequencies of the spring supported frame are $\omega_1 = 4.31$ and $\omega_2 = 10.99$ rad s^{-1}.

The responses obtained by integrating the equation of motion in the time domain for the structure–spring dashpot system subjected to the El Centro earthquake are compared with those obtained for Example 7.5 by the frequency domain substructure technique. The results are shown in Figures 7.38 and 7.39. It is seen from the figures that the time histories of the two analyses differ. Further, rms and peak values of the displacements obtained by the two methods are also not the same. The reason for the difference between the results of the two analyses is that one is obtained in the frequency domain (which does not require any initial conditions) and the other is obtained by time domain analysis (which requires initial conditions to start the integration process).

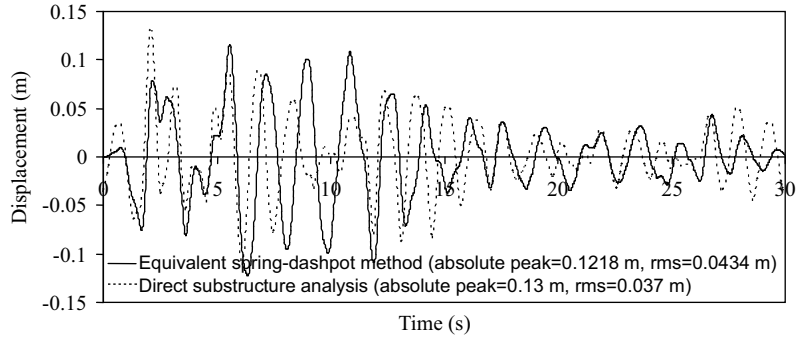

Figure 7.38 Time histories of top-storey displacements obtained by direct substructure and equivalent spring-dashpot analyses

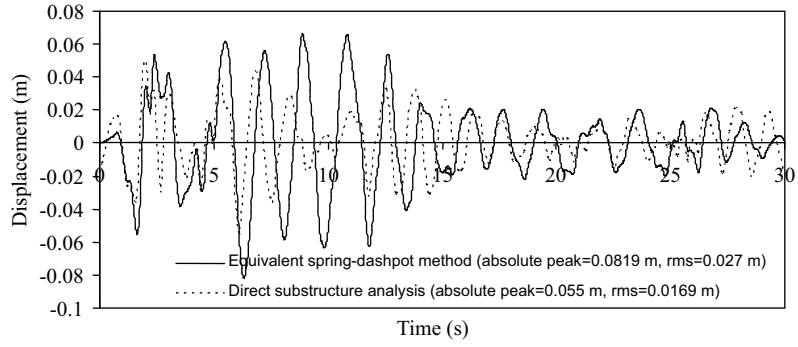

Figure 7.39 Time histories of first-storey displacements obtained by direct substructure and equivalent spring–dashpot analyses

Also, in Figure 7.40 the time history of the top-storey and first-storey displacements for the fixed base conditions are compared with those of the flexible base conditions. It is seen from the figures that the top-storey displacement for the flexible base is, generally, less than that for the fixed base, while the opposite result is observed for the first-storey displacement. Thus, the displacement response of the flexible base

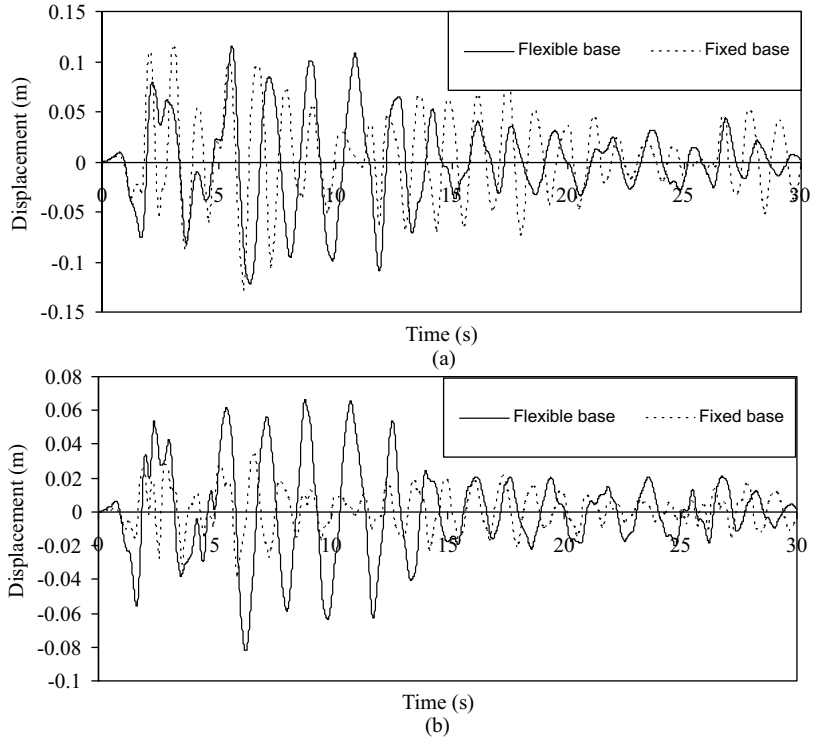

Figure 7.40 Comparison of the time histories of displacements between the fixed base and the flexible base: (a) top storey; and (b) first storey

frame need not necessarily be more compared with the fixed base frame. This is the case because two counteractive effects influence the response of flexible base frame, namely: (i) increase of displacement due to base flexibility; and (ii) decrease of displacement due to radiation damping. The increase or decrease of displacement depends upon the relative contributions of the two on the total response.

7.5.6 Approximate Analysis Using Equivalent Modal Damping

This method of analysis was proposed by Novak [7] and can be used both for time history analysis and the response spectrum method of analysis. It can be explained with the help of a 3D tall building [8]. The equation of motion of a 3D tall building can be written in the usual form:

$$\boldsymbol{M}\ddot{\boldsymbol{x}} + \boldsymbol{C}\dot{\boldsymbol{x}} + \boldsymbol{K}\boldsymbol{x} = -\boldsymbol{M}\boldsymbol{I}\ddot{x}_g \tag{7.70}$$

where

$\boldsymbol{M}$ is the diagonal lumped mass matrix
$\boldsymbol{K}$ is the stiffness matrix corresponding to the dynamic DOF as shown in Figure 7.41
$\boldsymbol{C}$ is the damping matrix not explicitly known but it will be defined in terms of an equivalent modal damping
$\boldsymbol{x}$ is the displacement vector, which also includes the base DOF
$\ddot{x}_g$ is the ground acceleration.

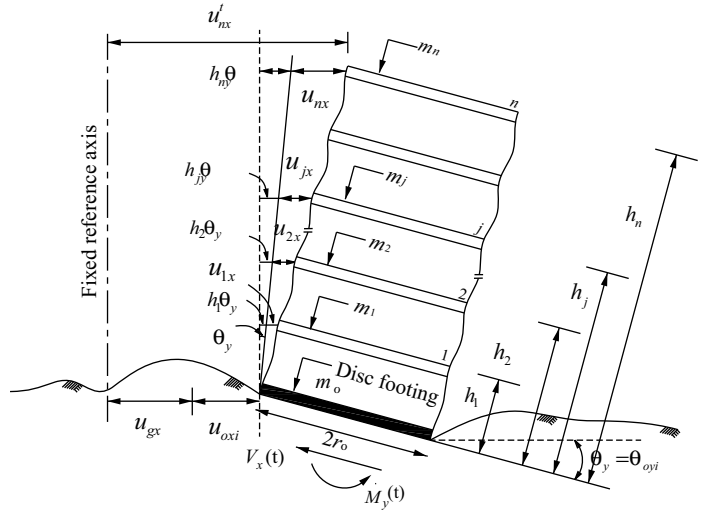

Figure 7.41 Model of flexible base 3D building

Assume that each mass of the building is free to undergo horizontal translations, u_{xi}, u_{yi}, rocking about horizontal axes, θ_{xi}, θ_{yi} and twisting about a vertical axis, θ_{zi}, and that the building and footing are harmoniously vibrating in the ith mode with the natural frequency ω_i. The footing has the following displacements corresponding to base DOF shown for one direction (Figure 7.41) namely, u_{oxi}, θ_{oyi}. For the other direction, similar motions are present, that is, u_{oyi}, θ_{oxi}. In addition, there is a rotation θ_{ozi} about the vertical axis.

In general, the work done W_d by the damping forces $F(x)$, during a period of vibration $T_i = \frac{2\pi}{\omega_i}$ is given by:

$$W_{di} = \int_0^{T_i} F(\dot{x})\mathrm{d}x(t) \tag{7.71}$$

This formula can be used to find the work done by the footing's equivalent damping (dash pots) during the vibration of the building in a natural mode. During harmonic motions, the damping forces acting at the footing are:

$$P(\dot{u}_x) = c_{xx}\dot{u}_{oxi} = c_{xx}u_{oxi}\omega_i \cos(\omega_i \mathrm{t}) \tag{7.72a}$$

$$P(\dot{u}_y) = c_{yy}\dot{u}_{oyi} = c_{yy}u_{oyi}\omega_i \cos(\omega_i \mathrm{t}) \tag{7.72b}$$

$$P(\dot{\theta}_x) = c_{y\theta_x}\dot{\theta}_{oxi}(t) = c_{y\theta_x}\theta_{oxi}\omega_i \cos(\omega_i \mathrm{t}) \tag{7.72c}$$

$$P(\dot{\theta}_y) = c_{x\theta_y}\dot{\theta}_{oyi}(t) = c_{x\theta_y}\theta_{oyi}\omega_i \cos(\omega_i \mathrm{t}) \tag{7.72d}$$

$$M(\dot{u}_x) = c_{\theta_y x}\dot{u}_{oxi}(t) = c_{\theta_y x}u_{oxi}\omega_i \cos(\omega_i \mathrm{t}) \tag{7.72e}$$

$$M(\dot{u}_y) = c_{\theta_x y}\dot{u}_{oyi}(t) = c_{\theta_x y}u_{oyi}\omega_i \cos(\omega_i \mathrm{t}) \tag{7.72f}$$

$$M(\dot{\theta}_x) = c_{\theta_x\theta_x}\dot{\theta}_{oxi}(t) = c_{\theta_x\theta_x}\theta_{oxi}\omega_i \cos(\omega_i \mathrm{t}) \tag{7.72g}$$

$$M(\dot{\theta}_y) = c_{\theta_y\theta_y}\dot{\theta}_{oyi}(t) = c_{\theta_y\theta_y}\theta_{oyi}\omega_i \cos(\omega_i \mathrm{t}) \tag{7.72h}$$

$$T(\dot{\theta}_z) = c_{\theta_z\theta_z}\dot{\theta}_{ozi}(t) = c_{\theta_z\theta_z}\theta_{ozi}\omega_i \cos(\omega_i \mathrm{t}) \tag{7.72i}$$

According to Equation 7.71, the total work done by these forces during a period of vibration is:

$$\begin{aligned} W_{di} = &\int_0^{T_i} c_{xx}u_{oxi}^2\omega_i^2\cos^2(\omega_i t)\mathrm{d}t + \int_0^{T_i} c_{yy}u_{oyi}^2\omega_i^2\cos^2(\omega_i t)\mathrm{d}t + \int_0^{T_i} c_{\theta_x\theta_x}\theta_{oxi}^2\omega_i^2\cos^2(\omega_i t)\mathrm{d}t \\ &+ \int_0^{T_i} c_{\theta_y\theta_y}\theta_{oyi}^2\omega_i^2\cos^2(\omega_i t)\mathrm{d}t + \int_0^{T_i} c_{x\theta_y}\theta_{oyi}u_{oxi}\omega_i^2\cos^2(\omega_i t)\mathrm{d}t \\ &+ \int_0^{T_i} c_{y\theta_x}\theta_{oxi}u_{oyi}\omega_i^2\cos^2(\omega_i t)\mathrm{d}t + \int_0^{T_i} c_{\theta_x y}\theta_{oxi}u_{oyi}\omega_i^2\cos^2(\omega_i t)\mathrm{d}t \\ &+ \int_0^{T_i} c_{\theta_y x}\theta_{oyi}u_{oxi}\omega_i^2\cos^2(\omega_i t)\mathrm{d}t + \int_0^{T_i} c_{\theta_z\theta_z}\theta_{ozi}^2\omega_i\cos^2(\omega_i t)\mathrm{d}t \end{aligned} \tag{7.73}$$

Integration over the period leads to

$$W_{di} = \pi\omega_i^2(c_{xx}u_{oxi}^2 + c_{yy}u_{oyi}^2 + c_{\theta_x\theta_x}\theta_{oxi}^2 + c_{\theta_y\theta_y}\theta_{oyi}^2 + c_{\theta_z\theta_z}\theta_{ozi}^2 + 2c_{\theta_x y}u_{oyi}\theta_{oxi} + 2c_{\theta_y x}u_{oxi}\theta_{oyi}) \tag{7.74}$$

The maximum potential energy of the whole building in the ith mode can be calculated as the maximum kinetic energy ϕ_{pi} given by:

$$\phi_{pi} = \sum_{j=0}^{n}\frac{1}{2}m_{jx}u_{jxi}^2\omega_i^2 + \sum_{j=0}^{n}\frac{1}{2}m_{jy}u_{jyi}^2\omega_i^2 + \sum_{j=0}^{n}\frac{1}{2}I_{jx}\theta_{jxi}^2\omega_i^2 + \sum_{j=0}^{n}\frac{1}{2}I_{jy}\theta_{jyi}^2\omega_i^2 + \sum_{j=0}^{n}\frac{1}{2}I_{jz}\theta_{jzi}^2\omega_i^2 \tag{7.75}$$

where

n is the number of masses
m_{jx} and m_{jy} are the translational masses at the jth floor level in the x- and y-directions, respectively
I_{jx}, I_{jy}, and I_{jz} are the mass moment of inertias of the jth floor about the x-, y- and z-axes, respectively
$j = 0$ indicates the foundations.

The damping ratio η_{gi} of the structure due to the radiation damping of the soil is defined for the response in the ith mode as:

$$\eta_{gi} = \frac{W_{di}}{4\pi\phi_{pi}} \tag{7.76}$$

Substituting W_{di} and ϕ_{pi} from Equations 7.74 and 7.75 into Equation 7.76, gives

$$\eta_{gi} = \left(\frac{1}{2}\overline{m}\omega_i\right)(c_{xx}u_{oxi}^2 + c_{yy}u_{oyi}^2 + c_{\theta_x\theta_x}\theta_{oxi}^2 + c_{\theta_y\theta_y}\theta_{oyi}^2 + c_{\theta_z\theta_z}\theta_{ozi}^2 + 2c_{\theta_{xy}}u_{oyi}\theta_{oxi} + 2c_{\theta_{yx}}u_{oxi}\theta_{oyi}) \tag{7.77}$$

in which $\overline{m}_i$ is the generalized mass given by:

$$\overline{m}_i = \sum_{j=0}^{n}(m_{jx}u_{jxi}^2 + m_{jy}u_{jyi}^2 + I_{jx}\theta_{jxi}^2 + I_{jy}\theta_{jyi}^2 + I_{jz}\theta_{jzi}^2) \tag{7.78}$$

In the above equations, u_{jxi}, u_{jyi}, θ_{jxi}, θ_{jyi}, and θ_{jzi} are the modal displacements of the building, while u_{oxi}, u_{oyi}, and θ_{ozi} are the modal displacements of the footing obtained from the solution of the undamped equation of motion with the equivalent soil stiffness represented by the real part of the impedance function (Equation 7.69); c_{xx}, c_{yy}, $c_{\theta_x\theta_x}$, and so on, are the soil damping constants that can be obtained from the imaginary parts of the impedance functions. The frequency independent constants (Equation 7.69) are considered in the analysis.

The damping due to the soil η_{gi} (determined above) can be added to the other component of damping, that is, the modal damping η_i of the building to obtain the total damping η_i^t:

$$\eta_i^t = \eta_i + \eta_{gi} \tag{7.79}$$

With the equivalent modal damping for the flexible base structure defined as above, the ith modal equation in generalized coordinates can be written as:

$$\ddot{q}_i(t) + 2\eta_i^t\omega_i\dot{q}_i(t) + \omega_i^2 q_i(t) = \frac{p_{i(t)}}{\overline{m}_i} \tag{7.80}$$

where

$q_i(t)$ is the generalized displacements (over dots denote time derivates)
$p_i(t)$ is the generalized force producing a response in the ith mode only
$\overline{m}_i$ is the generalized mass.

Making use of Equation 7.80, an approximate response spectrum method of analysis can also be performed for a given response spectrum of earthquake.

Example 7.8

Using equivalent modal damping for the soil structure interaction problem, solve the problem in Example 7.5 by modal time history analysis and compare the results with those of Example 7.7.

Solution: It is assumed that the members are inextensible, and therefore vertical degrees of freedom are ignored. Frequency independent damping coefficients for the footing are obtained from Equation 7.69 as:

$$C_h = 70.65 \times 10^4 \text{ N s m}^{-1}; \quad C_\theta = 15.35 \times 10^4 \text{ N m s rad}^{-1}; \quad C_{\theta h} = 6.14 \times 10^4$$

The stiffness matrix of the soil–structure system with soil replaced by a spring is

$$K = \begin{bmatrix} 5.6 & -5.6 & 0 & 0 & 0 & 0 \\ -5.6 & 11.2 & -5.6 & 0 & 0 & 0 \\ 0 & -5.6 & 16.8 & -11 & 0 & 0 \\ 0 & 0 & -11 & 22.4 & -11 & -16.8 \\ 0 & 0 & 0 & -11 & 21 & 17.5 \\ 0 & 0 & 0 & -16.8 & 17.5 & 41.8 \end{bmatrix} \times 10^7 \text{ N m}^{-1}$$

Undamped mode shapes and frequencies of the system are: $\omega_1 = 4.31$, $\omega_2 = 10.99$, $\omega_3 = 18.15$, $\omega_4 = 21.61$, $\omega_5 = 27.30$, and $\omega_6 = 125.38 \text{ rad s}^{-1}$.

$$\boldsymbol{\phi}_1^T = [-1 \quad -0.938 \quad -0.760 \quad -0.624 \quad -0.196 \quad -0.169]$$

$$\boldsymbol{\phi}_2^T = [1 \quad 0.475 \quad -0.547 \quad -0.772 \quad -0.321 \quad -0.180]$$

$$\boldsymbol{\phi}_3^T = [1 \quad -0.576 \quad -0.336 \quad 0.313 \quad 0.817 \quad -0.232]$$

$$\boldsymbol{\phi}_4^T = [0.601 \quad -0.500 \quad 0.232 \quad 0.173 \quad -1 \quad 0.531]$$

$$\boldsymbol{\phi}_5^T = [-0.247 \quad 0.393 \quad -1 \quad 0.890 \quad -0.443 \quad 0.613]$$

$$\boldsymbol{\phi}_6^T = [0 \quad -0.0001 \quad 0.003 \quad -0.071 \quad 0.113 \quad 1]$$

Considering last two coefficients of the mode shapes corresponding to base translation and base rotation and using Equation 7.73,

$$W_{d1} = 2.08 \times 10^6; \quad W_{d2} = 3.22 \times 10^7; \quad W_{d3} = 4.73 \times 10^8; \quad W_{d4} = 1.00 \times 10^9;$$
$$W_{d5} = 3.87 \times 10^8; \quad W_{d6} = 8.72 \times 10^9$$

Using Equation 7.75 (with $I_{jx} = m_j \times 3^2/12$ and $I_0 \approx 0$),

$$\boldsymbol{\phi}_{p1} = 1.38 \times 10^7; \quad \boldsymbol{\phi}_{p2} = 9.13 \times 10^7; \quad \boldsymbol{\phi}_{p3} = 2.84 \times 10^8; \quad \boldsymbol{\phi}_{p4} = 4.36 \times 10^8;$$
$$\boldsymbol{\phi}_{p5} = 5.88 \times 10^8; \quad \boldsymbol{\phi}_{p6} = 1.23 \times 10^{10}$$

Using Equation 7.76

$$\eta_{g1} = 0.012; \quad \eta_{g2} = 0.028; \quad \eta_{g3} = 0.133; \quad \eta_{g4} = 0.183; \quad \eta_{g5} = 0.052; \quad \eta_{g6} = 0.056$$

$$\lambda_i = \frac{\boldsymbol{\phi}_i^T M}{\boldsymbol{\phi}_i^T M \boldsymbol{\phi}_i}; \quad \lambda_1 = -1.253; \quad \lambda_2 = -0.347; \quad \lambda_3 = 0.272; \quad \lambda_4 = -0.304;$$
$$\lambda_5 = -0.016; \quad \lambda_6 = 0.959$$

Using the total modal damping ratios obtained by Equation 7.79 and mode participation factors calculated as above, the responses are obtained by considering all modes. The results are compared with those of Example 7.7 in Figures 7.42 and 7.43. It is seen from the figures that the difference between the two results is not very significant; the equivalent modal damping method provides a few more values of the displacements.

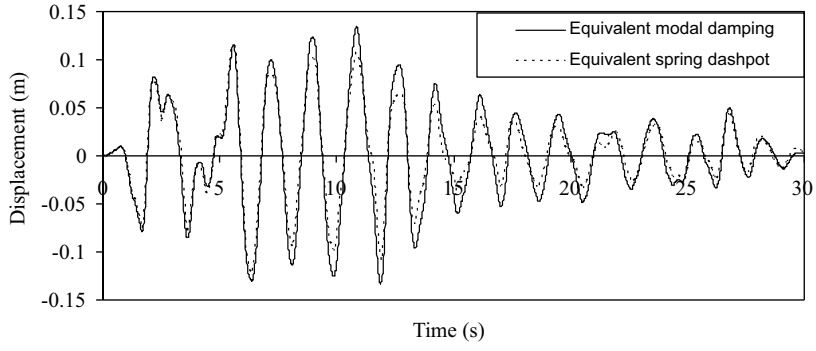

Figure 7.42 Time histories of top-storey displacement obtained by equivalent modal damping and equivalent spring–dashpot analyses

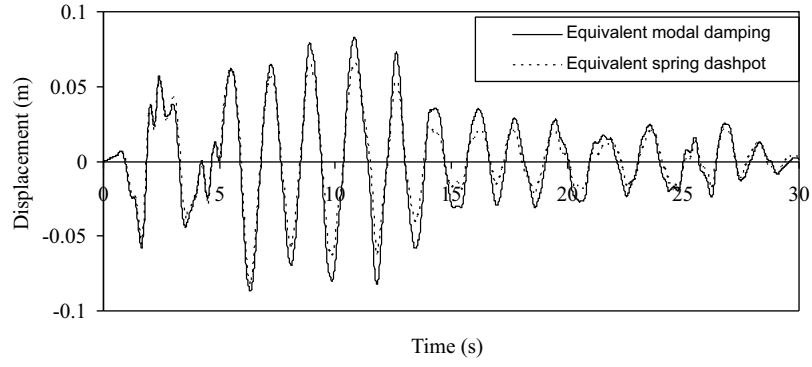

Figure 7.43 Time histories of first-storey displacement obtained by equivalent modal damping and equivalent spring–dashpot analyses

7.6 Soil–Pile Structure Interaction

Many structures are supported by pile foundations in place of isolated footings or mat foundations. The use of pile foundations is dictated primarily by the soil conditions. Large and heavy superstructures on soft soils are generally pile founded. While the length and the size of the piles are mostly governed by the gravity load design, the lateral resistance of the pile to earthquake induced forces on the superstructure is also a major concern. Therefore, all important pile founded structures are analyzed for earthquake forces. For structures with pile foundations, the superstructure may directly rest on the pile cap covering all piles or individual columns of the structure may be directly connected to each pile or a group of piles as shown in Figure 7.44. In the former, the pile cap acts like a raft.

Seismic response analysis of structures including soil-pile-structure interaction can be performed using direct analysis, substructure technique, approximate modal analysis and equivalent spring-dash pot analysis. Analysis procedures are similar to those applied for the soil structure interaction problems except for the additional consideration of the piles. Brief outlines of different procedures are presented below:

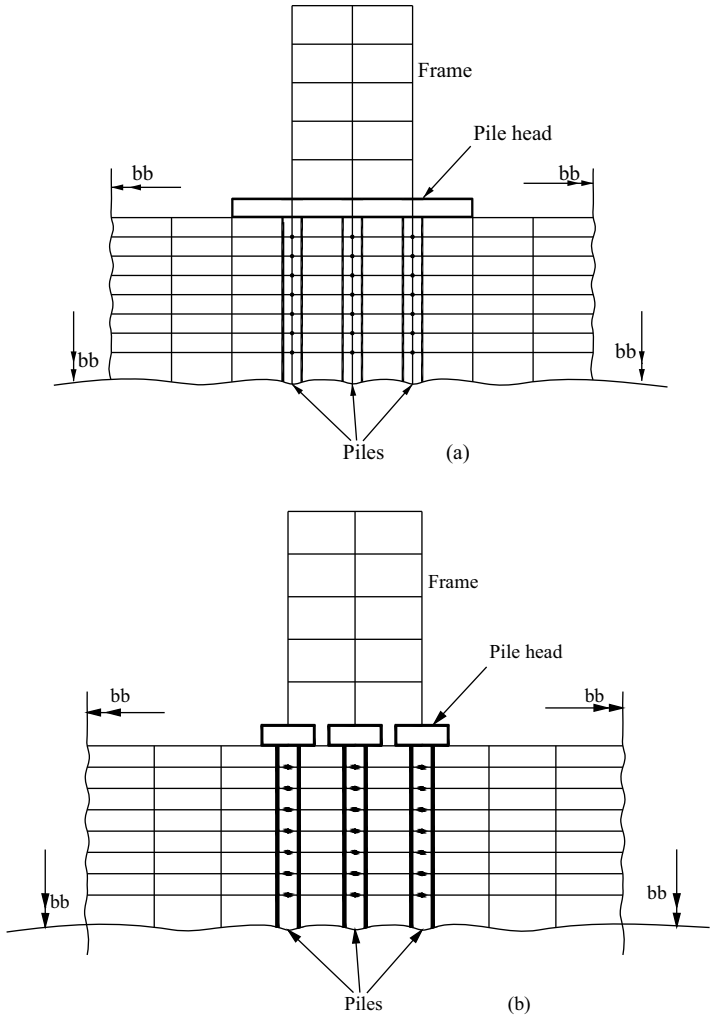

Figure 7.44 Soil–pile structure modeling using FEM: (a) with pile cap as a raft; and (b) with individual piles

7.6.1 Direct Analysis

In the direct analysis, soil, pile, and structure are modeled together using FEM. The soil and the structure are modeled as described previously. Piles are modeled as beam elements and connected to the soil elements using the master-slave DOF or using interface or connecting elements (available in standard software). If the bottom of the piles rest on the rock bed, then the vertical and the horizontal displacements of the piles are prescribed as zero. The boundaries for the soil domain are prescribed as described previously. Pile caps are modeled as beam elements connected to the soil by interface or connecting elements (Figure 7.44). The ground motion is applied at the foundation level.

7.6.2 Substructure Technique

The substructure technique for solving the soil–pile structure interaction problem is similar to that for solving the soil–structure interaction problem. In this case, the impedance functions for the pile head or pile cap are found by a separate analysis of the soil–pile system. Once the impedance functions are obtained, the structure-foundation analysis is solved exactly in the same way as the substructure analysis described previously (Section 7.5.3).

To find the impedance function of the pile head, a finite element model of a single pile or a group of piles, along with the soil, is made as shown in Figure 7.45. The pile head is then subjected to unit complex harmonic forces in the direction of the DOF one at a time in order to obtain a complex flexibility matrix. The inverse of the flexibility matrix gives the impedance function matrix corresponding to the DOF of the pile head. This matrix has coupling terms between the translational and the rotational degrees of freedom. For each value of the frequency, the impedance function matrix is derived and is used to solve the seismic soil–pile structure interaction problem in the frequency domain (Equation 7.64) for a prescribed ground motion at the foundation level. The analysis provides the responses of the superstructure including the displacement of the pile heads or pile cap. With the help of the impedance functions for the pile cap or the pile head, equivalent spring and dash pot coefficients for the soil-pile system can be obtained. Springs and dash pots may be used to replace the soil-pile system at the pile cap level as shown in Figure 7.46.

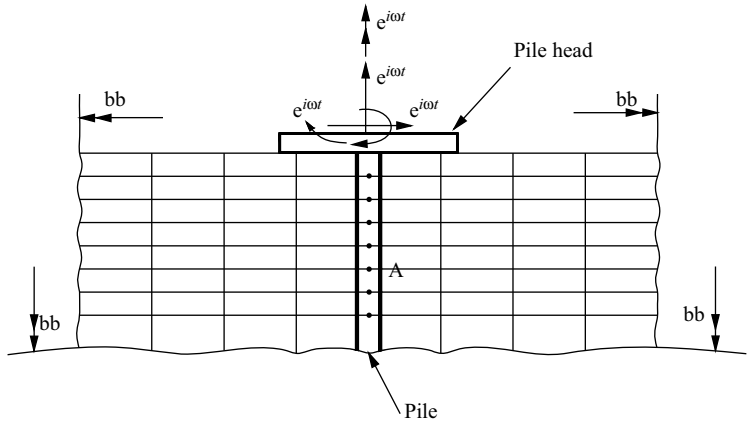

Figure 7.45 Modeling for finding soil–pile impedance

In order to obtain the stresses in the piles, a separate analysis of the soil–pile system is carried out for the time histories of pile head displacements applied to the top nodes of the piles. Alternatively, the response quantities of interest of the piles are stored as a complex frequency response function matrix while impedance functions for the pile head is determined. These may be used to obtain the time history of the response quantity of the interest. For example, say the bending moment at a section A of a pile is required (Figure 7.45). For finding the bending moment at A, following steps may be carried out:

(i) Determine the bending moment at A for unit complex harmonic forces applied at the top of the pile as shown in Figure 7.45. Store the bending moment as a complex number for each frequency.
(ii) Foundation forces are obtained as complex number for each frequency after obtaining the displacements by solving Equation 7.64.
(iii) The bending moment determined from step (i) as a complex quantity, for each harmonic force, is multiplied by the corresponding foundation force (obtained as a complex quantity).
(iv) IFFT of the complex numbers in step (iii) provides the time history of the bending moment at A for a foundation force.

The same steps are repeated for other foundation forces and the corresponding time histories of the bending moment are obtained. The sum of all time histories thus obtained is the final time history of the bending moment at A.

7.6.3 Equivalent Spring–Dashpot Analysis

In this analysis, soil is replaced by springs and dashpots as shown in Figure 7.46. The segment of the pile between two springs is modeled as a beam element and the stiffness matrix for the entire system corresponding to the dynamic degrees of freedom is determined following the standard procedure. Assuming Rayleigh damping, the damping matrix is obtained from the mass and stiffness matrices. Dashpot coefficients are added to the diagonal elements of the damping matrix. The total system (superstructure and the piles with springs and dashpots) is analyzed for the ground motion applied at the foundation level. Analysis may be carried out using the direct time integration method. As the method of analysis is straightforward and the number of degrees of freedom is less as compared with the direct finite element analysis, this method of analysis is preferred for most cases. Furthermore, the non-linear property of the soil can be easily incorporated into the analysis by replacing the linear springs with non-linear springs having the same force-displacement behavior as that of the soil. A non-linear dynamic analysis of the total system is performed using the procedure described in Chapter 6.

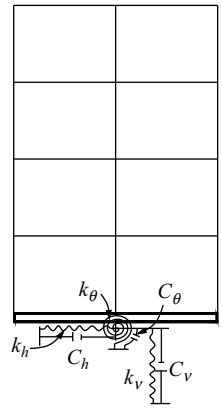

Figure 7.46 Equivalent spring–dashpot model for soil–pile structure interaction

To obtain the frequency independent constants of the springs and dashpots, Equations 7.81 and 7.82 given in the next section may be used. The values of S_u, S_w, $\overline{S}_u$ and $\overline{S}_w$ are obtained from Figure 7.56.

Example 7.9

It is assumed that the building frame of Exercise 7.5 is pile founded in a soft soil medium with $V_S = 80\,\text{m s}^{-1}$ and $\rho = 1600\,\text{kg m}^{-3}$ as shown in Figure 7.47a and is subjected to El Centro ground motion at the base of the building. Other properties of the soil and pile are shown in the same figure. Using the time domain analysis, find the time histories of the top displacement of the frame and the horizontal displacement of the base by: (i) direct analysis, and (ii) replacing the soil by linear springs and dashpots.

Solution: The soil–pile structure system is modeled as shown in Figure 7.47b. The structure and the pile are modeled as beam elements, while the soil and the pile cap are modeled by plane strain elements. Contact elements are used between (i) the soil and the pile, and (ii) the soil and the structure. The same

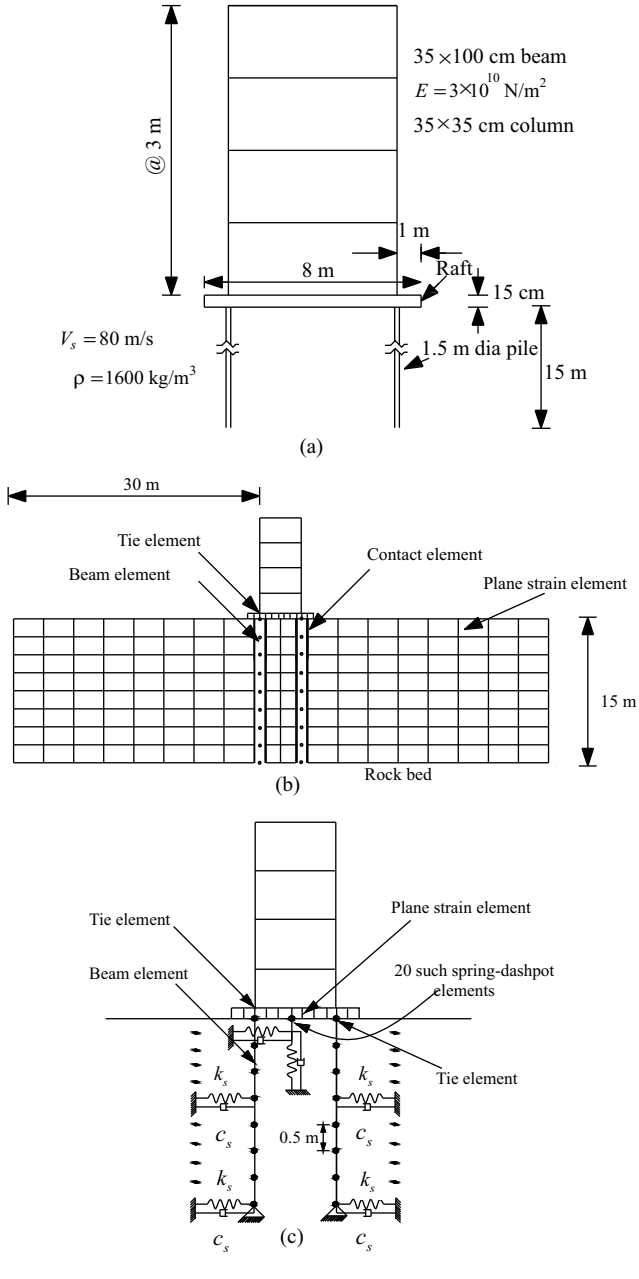

Figure 7.47 Pile founded building frame: (a) properties; (b) modeling of soil–pile frame together; and (c) modeling by replacing soil by spring–dashpot

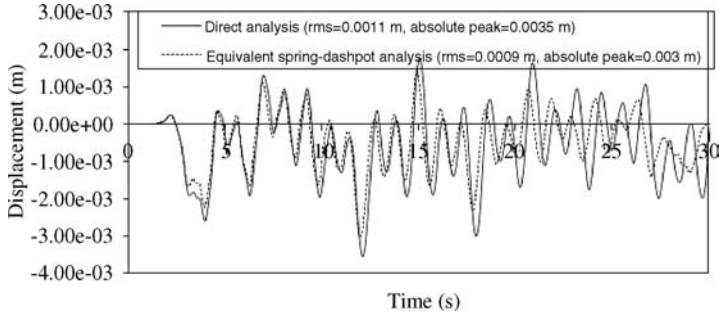

Figure 7.48 Comparison between the time histories of top-storey displacement obtained by the direct method and equivalent spring–dashpot analysis

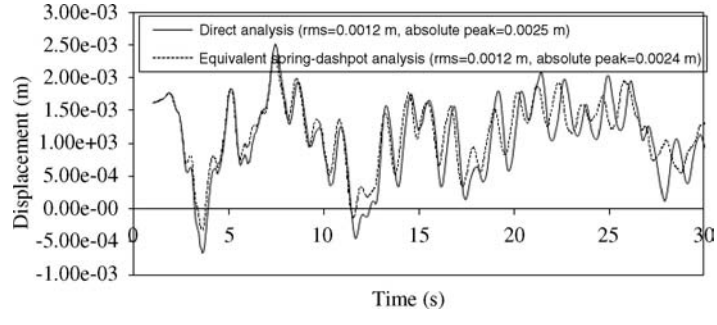

Figure 7.49 Comparison between the time histories of base displacement obtained by the direct method and equivalent spring–dashpot analysis

properties of the contact elements as those mentioned in Exercise 7.4 are used. A tie element is used between the frame and the pile cap. The finite element modeling of the soil–pile structure is shown in Figure 7.47b. The results are obtained by ABAQUAS (for soil, pile and structure damping ratio taken as 5%) and are shown in Figures 7.48 and 7.49.

Figure 7.47c shows the modeling of the pile founded frame, when the soil is replaced by springs and dashpots. The coefficients of the lateral springs and dashpots attached to the piles are calculated using Equations 7.81 and 7.82 (given in Section 7.7.2). For this purpose, the total pile length is divided into five equal segments. The constants S_u and $\overline{S}_u$ are calculated for five segments by considering soil depths as those of the centers of the five segments. The spring and dashpot coefficients are assumed to remain the same within each segment. The coefficients of springs and dashpots attached below the raft are determined using Equation 7.69. The calculation of the constants is as follows.

Pile length is divided into five segments. The depth of the center of each segment and the corresponding values of S_u and $\overline{S}_u$ are obtained as shown in Table 7.1. The spring stiffness and damping constant are

Table 7.1 Depth of centers of segments and corresponding values of S_u and $\overline{S}_u$ for pile lengths

Depth (m)	S_u	$\overline{S}_u$
1.5	3.15	7.3
4.5	3.6	8.2
7.5	3.8	8.5
10.5	3.9	8.9
13.5	4	9

calculated using the following expressions (Equations 7.81 and 7.82 given in Section 7.7.2),

$$K_s = GS_u l; \quad l = 0.5\,\text{m}$$

$$C_s = G\bar{S}_u \frac{rl}{V_S}; \quad r = 0.75\,\text{m}; \quad V_S = 80\,\text{m s}^{-1}$$

The constants of the springs and dashpots attached below the raft are determined as:

$$k_v = \frac{4Gr}{1-\mu}; \quad c_v = \frac{3}{1-\mu}\rho V_S r^2; \quad G = 1.024 \times 10^7\,\text{N m}^{-2}; \quad \mu = 0.38$$
$$k_h = \frac{8Gr}{2-\mu}; \quad c_h = \frac{4.6}{2-\mu}\rho V_S r^2; \quad \rho = 1600\,\text{kg m}^{-3}; \quad r = 4\,\text{m}$$

Calculated values of k_h, c_v, and so on are divided by 20 to obtain the spring and dashpot constants for each of the 20 spring dashpot systems placed below the raft.

The model of Figure 7.47c is analyzed by ABAQUS. The results are also shown in Figures 7.48 and 7.49. It is seen from the figures that the equivalent spring dashpot solution provides responses fairly comparable to those obtained by the direct analysis.

7.7 Seismic Analysis of Buried Structures

Buried structures form a different class of structures for the seismic analysis and design. Examples of buried structures are buried pipelines called lifelines, tunnels, underground liquid storage tanks, underground nuclear shelters, and so on. Seismic behavior of such structures is very different from that of the overground structures in many respects, such as:

i. The inertia forces, which are the main factors for designing the overground structures, are mainly resisted by the surrounding soil in the case of the buried structures.
ii. For the overground structure, it is generally (not always) assumed that the foundation follows the ground motion and, therefore, the relevant response is the relative displacements between the foundations and the structure. In the case of buried pipelines, tunnels, and so on, a relative movement between the pipe and the surrounding soil is expected because of the long length of the structure, and, therefore total displacement of the structure becomes important for finding the stresses in the structure. However, for a simplified analysis it is often assumed that the structure follows the ground deformation produced by the traveling train of the earthquake. Because of this assumption, the buried structures are under deformation control as the stresses induced in the structures are primarily governed by the deformation of the soil due to the earthquake. On the other hand, overground structures are under force control because the inertia forces govern the stresses induced in the structure.
iii. The ground motion is considered as being coherent for most overground structures, while it is considered as incoherent for buried structures such as pipelines because of the phase difference between the excitations at different stations and changes in soil properties along the pipeline.
iv. The buried structures are heavily damped because of the embedment within the soil. As a result, the frequency amplification is insignificant.
v. As the soil mass being replaced by the structure is comparatively very large (with respect to the mass of the structure), the inertial actions of the structure do not contribute much to the response. As a result, a quasi-static analysis may be sufficient in certain instances.

There have been considerable studies on the seismic analysis of buried pipelines and tunnel type structures [9–11]. 3D analysis of buried pipelines using shell elements have also been proposed [10]. The proposed methods of analysis are also applicable to other types of buried structures. In general, it is convenient to divide the analysis of a buried structure into two parts, namely: a plane strain or plane stress

analysis along the cross-section of the structure, and a bending analysis of the structure in the longitudinal direction. With the availability of standard software, both analyses can be easily performed using FEM. As the soil and the structure do not loose contact at any point of time, the option of "no loss of contact" is used in many software packages when the problem is treated as a contact problem between the two mediums. However, the analyses can also be performed without considering it as a contact problem. The salient features of the two analyses are described below.

7.7.1 Plane Strain Analysis

Figure 7.50 shows cross-sections of a tunnel and a buried pipeline. For vertically propagating S waves, the cross-sections of the structures are deformed and two-dimensional stresses are developed in the cross-sections. If the cross-section is large, then seismic excitations differ substantially between the top and the bottom of the cross-sections. In this case, the time history of ground acceleration is preferably prescribed at the rock bed. For smaller cross-sections, variation in the ground motions at different nodes of the cross-section is ignored and the same time histories of excitations are applied at all nodes. In addition, if the buried depth is not large, then the free field ground motion (which is generally known and can be measured) is uniformly applied to all nodes of the structure for most practical cases.

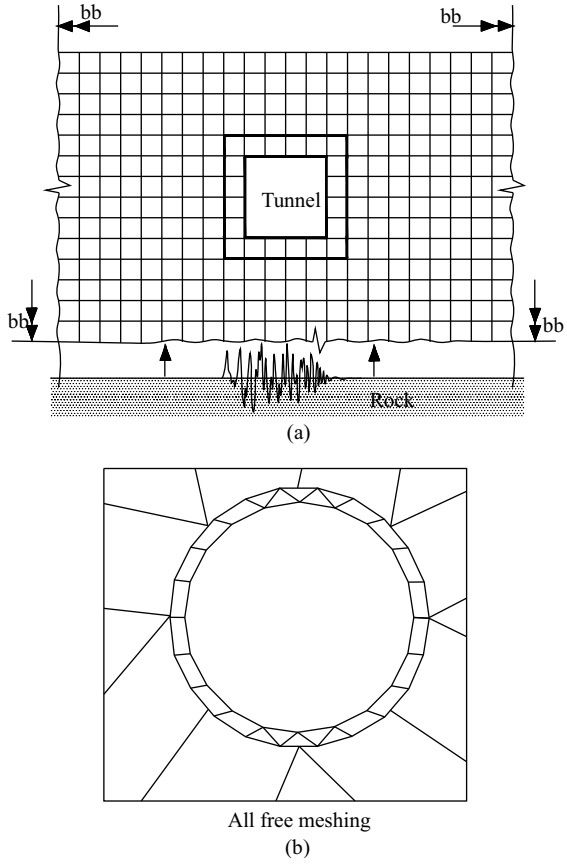

Figure 7.50 Plane strain analysis for the cross-section of buried structures: (a) tunnel; and (b) pipeline

For the analysis, the structure is divided into plane strain elements as for the soil. In order to include the radiation effect properly, the soil boundaries are appropriately selected as discussed previously. Software such as ABAQUS may be used for the analysis. In the case of pipelines, generation of compatible 2D plane strain elements for the soil and structure may be difficult. The option of automatic mesh generation with free meshing, available in most software can be used for such cases. Analysis of a buried pipe line is shown as an example problem for illustration.

Example 7.10

A cross-section of a circular buried pipeline as shown in Figure 7.51a is subjected to vertically propagating earthquake wave, taken as the acceleration of the El Centro earthquake, from the bedrock. The properties of the pipe and soil are shown in the same figure. Find the envelope of maximum stresses of the cross-section of the pipe in the x- and y-directions, and the time history of displacement of the point A. In addition, determine the same time history of displacement by replacing the soil by a spring and dashpot, and by applying a time history of acceleration at the spring supports the same as the free field acceleration at a height of 49.25 m above the rock bed (that is, at the level of the center of the pipeline). Compare the two time histories of the displacements.

Solution: A model of the buried pipeline is shown in Figure 7.51b. Both the soil and structure are modeled by plane strain elements. Contact elements are used between the soil and the pipe. The option of free meshing is used for automatic mesh generation of plane strain elements. The solution is obtained by ABAQUS. The stresses (maximum) in the x- and y-directions are shown in Figures 7.52 and 7.53. It is seen from the figures that maximum stresses are developed in the central region of the pipe cross-section and the stresses are anti-symmetric about the vertical axis through the center of the cross-section. Furthermore, the stresses in the y-direction are much smaller than those in the x-direction, as expected.

The time history of displacement of point A obtained by the direct analysis is shown in Figure 7.54. To obtain the same time history by the equivalent spring–dashpot analysis, the constants of the springs and dashpots are obtained as below.

As the pipe diameter is not very large, the constants of the spring and dashpot at the level of the center of the pipe cross-section are determined and are equally distributed to the total number of springs and dashpots used as shown in Figure 7.51c. To calculate the constants, Equations 7.81 and 7.82 (given in Section 7.7.2) are used. The values of the constants are obtained as $d/r = 5.75/0.75 = 7.66$; for this value of d/r ratio, $S_u = 3.5$ and $\overline{S}_u = 8.1$.

$$K_s = \rho V_s^2 S_u l = 1600 \times 80^2 \times 3.5 \times 1 = 35.84 \times 10^6 \text{N m}^{-1}$$
$$C_s = \rho V_s S_u r l = 1600 \times 80 \times 8.1 \times 0.75 \times 1 = 77.76 \times 10^4 \text{N s m}^{-1}$$

These values of the constants are divided by the number of springs and dashpots in order to obtain individual spring and dashpot coefficients.

The analysis is performed by ABAQUS and the results are compared in Figure 7.54. It is seen from the figure that the two time histories of the displacements do not differ significantly. This shows that a simpler approximate plane stress analysis of the cross-section of the buried pipeline for a vertically propagating earthquake wave can be carried out using an equivalent spring–dashpot model as shown in Figure 7.51c.

7.7.2 Analysis for the Longitudinal Direction

In the longitudinal direction, the structure undergoes a bending action due to (i) the inertia forces developed in the structure, and (ii) the variation of ground displacement along the length of the structure.

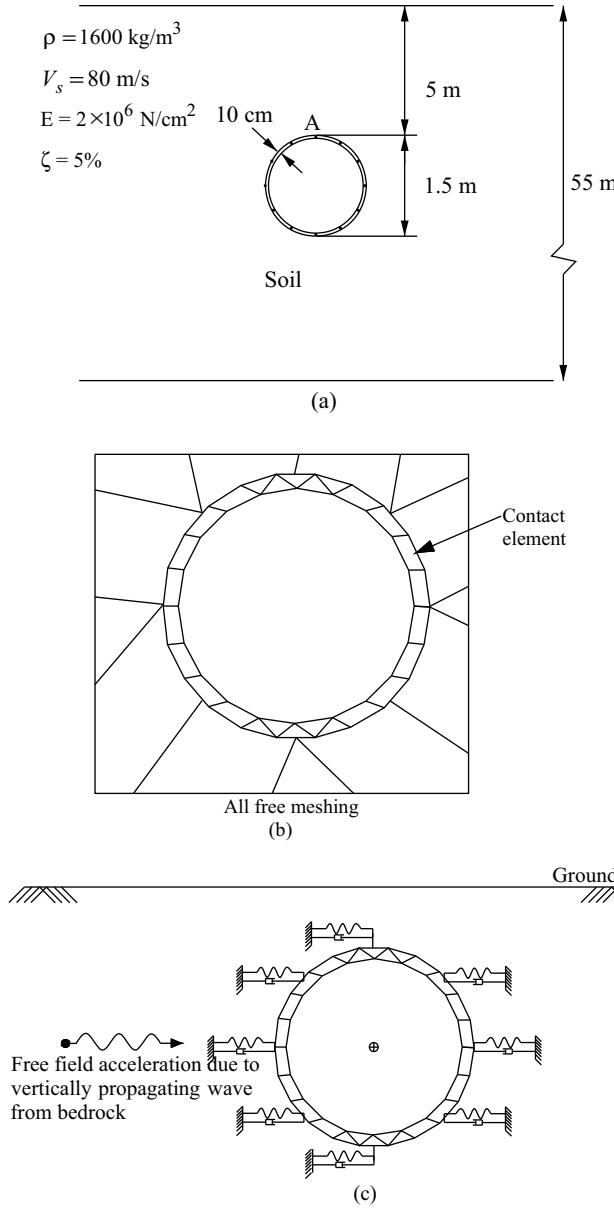

Figure 7.51 Cross-section of a buried pipeline: (a) properties; (b) modeling of soil-pipe together; and (c) modeling by replacing soil by spring–dashpot

If the ground motion is assumed to be the same and perfectly correlated along the length of the structure, then the bending action is due to the former alone. However, for long pipelines and tunnels, the assumption of perfectly correlated homogeneous ground motion is not justified because of the expected variation of soil properties along longitudinal direction of the structure.

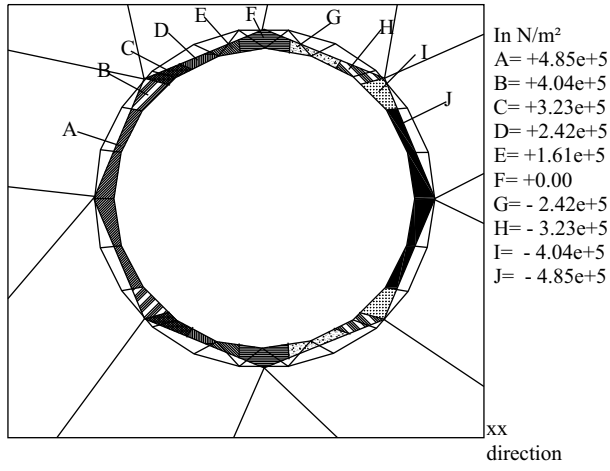

Figure 7.52 Maximum stresses in the *x*-direction

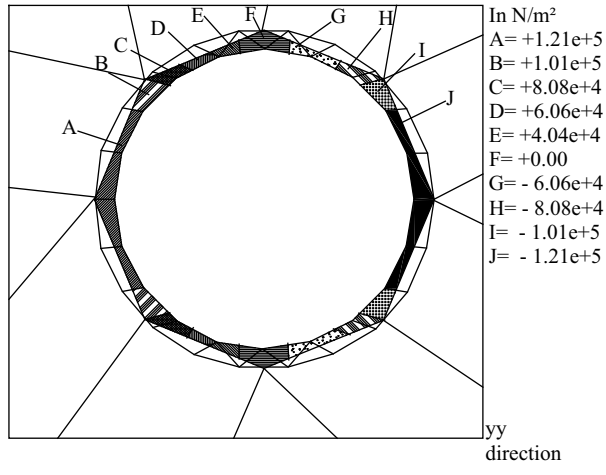

Figure 7.53 Maximum stresses in the *y*-direction

The transverse bending analysis of long lengths of buried pipelines and tunnels for seismic forces has been an interesting topic of research [12–14]. A convenient and widely used method of analysis is presented here.

The analysis replaces the soil by spring–dashpots as shown in Figure 7.55. The spring stiffness and damping coefficients of the dashpots are derived by combining Mindlin's static analysis of the soil pressure at a depth within the soil and the soil impedance functions. The details of the derivation are given in references [12, 13]. The stiffness and damping coefficients of the matrices corresponding to the DOF are coupled unlike the condition of Winkler's bed. However, a simplified analysis can be performed by ignoring the off-diagonal terms and by using the diagonal terms to assign stiffness and

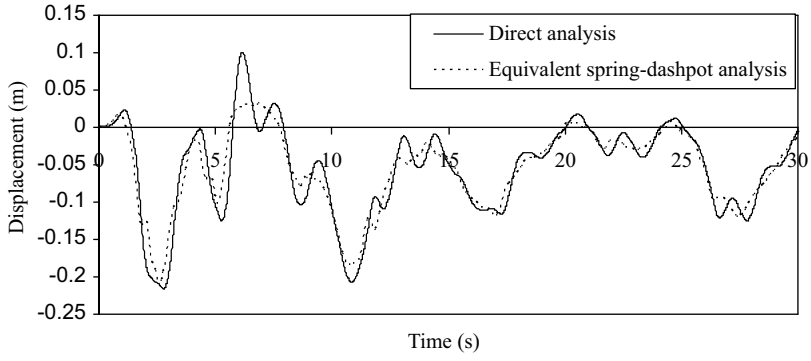

Figure 7.54 Time histories of the displacement at point A obtained by direct analysis and equivalent spring-dashpot analysis

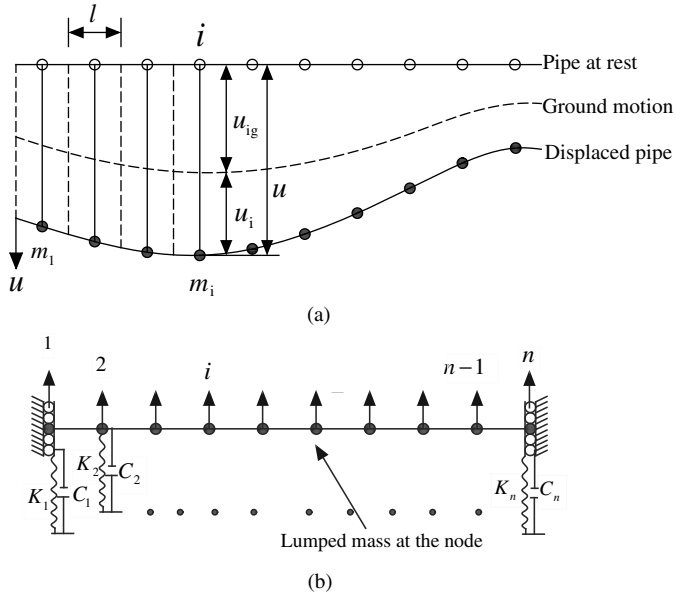

Figure 7.55 Longitudinal pipeline model on springs and dashpots: (a) deformations of soil and pipeline; and (b) spring–dashpot model of the soil pipeline problem

damping coefficients to individual springs and dashpots at the nodes. In this case, the model simplifies to the one given in Example 3.10. The effect of ignoring the off-diagonal terms is illustrated in references [12, 13].

Extensive analysis of buried pipelines to traveling seismic waves has shown that the stresses and deformations in the middle of the pipeline for long lengths remain nearly constant. As a result, long lengths of pipelines are designed for these constant stresses. Keeping this in mind, an adequate length of the pipeline is analyzed for any specified end conditions such that the nature of the end condition does not

change the deformations and stresses of the pipeline in the middle. A rough guideline for the required length is specified as 30–40r; where r is the radius of the pipeline. The element length should be less than $2r$ to obtain good results. Once the pipeline or the tunnel is modeled in this manner, the seismic response analysis of the structure can be performed as described in Chapters 3 and 4.

The pipeline is also subjected to axial vibration along the length of the pipe due to P waves traveling along the pipeline. Analysis as described above can be carried out for axial vibration of the pipeline, with the soil being replaced by equivalent springs and dashpots. The stiffness and damping coefficients of the springs and dashpots are similarly obtained as for the case of transverse oscillation. For a simplified analysis, stiffness and damping coefficients of the springs and dashpots may be obtained by ignoring the off-diagonal terms of the soil stiffness and damping matrices. Figure 7.56 provides the frequency independent stiffness and damping coefficients of the equivalent springs and dashpots for transverse and axial vibrations of buried pipelines [12]. These coefficients may be used to obtain the stiffness and damping coefficients as follows:

$$k_{sl} = G \times S_u \times l; \qquad c_{sl} = G \times \overline{S}_u \times \frac{rl}{V_S} \tag{7.81}$$

$$k_{sa} = G \times S_w \times l \qquad c_{sa} = G \times \overline{S}_w \times \frac{rl}{V_S} \tag{7.82}$$

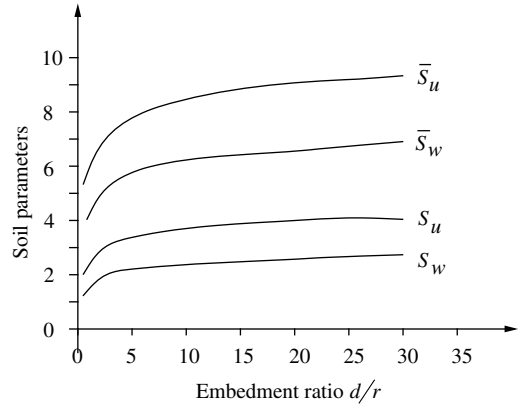

Figure 7.56 Variation of frequency independent spring and damper coefficients with d/r

in which l is the length of the element, r is the radius of the pipe cross-section, and d is the buried depth. For $d \gg r$, $S_u = 4$; $\overline{S}_u = 9$; $S_w = 2.7$ and $\overline{S}_w = 6.7$.

With the help of these coefficients, the stiffness and damping matrices of the buried pipeline for lateral and axial motion can be derived as:

$$K_{sl} = k_{sl}B_l; \qquad C_{sl} = c_{sl}B_l \tag{7.83}$$

$$K_{sa} = k_{sa}B_a; \qquad C_{sa} = c_{sa}B_a \tag{7.84}$$

The matrices B_l and B_a are normalized coefficient matrices and are obtained using Mindlin's equation. The details of the derivation are given in references [12–14]. For ready reference, the matrices for 18 element discretization is given in Appendix 7.A.

Example 7.11

A segment of an underground pipeline is shown in Figure 7.57. For illustrative purposes, the pipeline is divided into four elements. Determine the stiffness and damping matrices for the pipe for axial and lateral vibration. Take *EI* and *EA* values for the pipe cross-section as 10.4×10^5 kN m^{-2} and 6.9×10^6 kN, respectively; $r = 0.5$ m; embedment depth $d = 8$ m; pipe length $= 10$ m; ξ for the pipe $= 5\%$, $V_S = 200$ m s^{-1}; $\rho = 1800$ kg m^{-3}; and lumped masses at the nodes $= 2156$ kg.

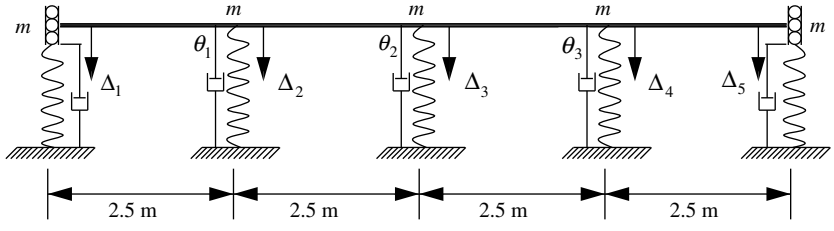

Figure 7.57 Model of a segment of a buried pipeline

Solution: As $d \gg r$, the following values for the coefficients are considered: $S_u = 4$; $\overline{S}_u = 9$; $S_w = 2.7$ and $\overline{S}_w = 6.7$

From Appendix 7.A

$$[B]_l = \begin{bmatrix} 1 & -0.213 & -0.044 & -0.028 & -0.019 \\ & 1 & -0.213 & -0.044 & -0.028 \\ & & 1 & -0.213 & -0.044 \\ & sym & & 1 & -0.213 \\ & & & & 1 \end{bmatrix}$$

$$[B]_a = \begin{bmatrix} 1 & -0.217 & -0.043 & -0.027 & -0.019 \\ & 1 & -0.217 & -0.043 & -0.027 \\ & & 1 & -0.217 & -0.043 \\ & sym & & 1 & -0.217 \\ & & & & 1 \end{bmatrix}$$

Soil stiffness and damping matrices are:

$$G = \rho V_S^2 = 1800 \times 4 \times 10^4 = 72 \times 10^6 \text{ N m}^{-2}$$

$$[K_s]_l = GS_u l[B]_l = 720 \times 10^6 [B]_l \text{ N m}^{-1}$$

$$[K_s]_a = GS_w l[B]_a = 486 \times 10^6 [B]_a \text{ N m}^{-1}$$

From Equations 7.81–7.84

$$[C_s]_l = \frac{72 \times 10^6 \times 9 \times 0.5 \times 2.5}{200}[B]_l = 4.1 \times 10^6 [B]_l \text{ N s m}^{-1}$$

$$[C_s]_a = \frac{72 \times 10^6 \times 6.7 \times 0.5 \times 2.5}{200}[B]_a = 3 \times 10^6 [B]_a \text{ N s m}^{-1}$$

Stiffness matrix for the structure corresponding to the DOF, shown in Figure 7.57, is obtained as:

$$[K]_l = \frac{12EI}{l^3}\begin{bmatrix} \overbrace{\begin{matrix} 1 & & & & \\ -1 & 2 & & & \\ 0 & -1 & 2 & & \\ 0 & 0 & -1 & 2 & \\ 0 & 0 & 0 & -1 & 1 \end{matrix}}^{\bar{K}} & & \begin{matrix} & \\ & \\ & \\ & \\ & \end{matrix} & \left.\begin{matrix} \\ \\ \\ \\ \end{matrix}\right| \Delta \\ \begin{matrix} \frac{l}{2} & 0 & 0 & 0 & 0 \\ 0 & \frac{l}{2} & 0 & 0 & 0 \\ 0 & 0 & \frac{l}{2} & 0 & -\frac{l}{2} \end{matrix} & \begin{matrix} \frac{2}{3}l^2 & & \\ \frac{1}{6}l^2 & \frac{2}{3}l^2 & \\ \frac{1}{6}l^2 & \frac{2}{3}l^2 & \end{matrix} & \left.\begin{matrix} \\ \\ \\ \end{matrix}\right| \theta \end{bmatrix}; \quad M = \begin{bmatrix} m & & & \\ & m & 0 & \\ & & m & \\ & 0 & & m \end{bmatrix}$$

$$[K]_a = \frac{EA}{l}\begin{bmatrix} 1 & & & & \\ -1 & 1 & & sym & \\ 0 & -1 & 1 & & \\ 0 & 0 & -1 & 1 & \\ 0 & 0 & 0 & -1 & 1 \end{bmatrix}$$

$[K_s]_l$ is added to the $\overline{K}$ part of the $[K]_l$ matrix and then rotational degrees of freedom are condensed out. The resulting stiffness matrix is the soil–pipe stiffness matrix. For axial vibration, $[K_s]_a$ is directly added to $[K]_a$. To construct the damping matrix, $[K]_l$ is condensed to eliminate θ degrees of freedom. Assuming Rayleigh damping, $[C]_l$ for the pipe is obtained using the first two frequencies of the soil–pipe system. Note that the eigen value problem cannot be solved without adding spring stiffness to the pipe stiffness matrix. $[C_s]_l$ is added to $[C]_l$ to obtain the damping matrix of the soil–pipe system. In a similar way, a damping matrix for the axial vibration can be determined. Results of the computation are given below.

The first two frequencies of the soil–pipe system and α and β values are:

$$\text{Axial}: \quad \omega_1 = 358.87 \text{ rad s}^{-1}; \quad \omega_2 = 825.7 \text{ rad s}^{-1}; \quad \alpha = 10 \text{ and } \beta \approx 0$$

$$\text{Lateral}: \quad \omega_1 = 370.3 \text{ rad s}^{-1}; \quad \omega_2 = 568.4 \text{ rad s}^{-1}; \quad \alpha = 8.76 \text{ and } \beta \approx 0$$

Soil–pipe lateral stiffness matrix:

$$\overline{\boldsymbol{K}}_l = \begin{bmatrix} 11.97 & -8.66 & -0.53 & -0.21 & 0.08 \\ -8.66 & 19.75 & -8.66 & -0.31 & -1.05 \\ -0.53 & -8.66 & 19.96 & -9.52 & 2.89 \\ -0.21 & -0.31 & -9.52 & 23.17 & -9.52 \\ 0.08 & -1.05 & 2.89 & -9.52 & 11.97 \end{bmatrix} \times 10^8 \text{ N m}^{-1}$$

Soil–pipe axial stiffness matrix:

$$\overline{\boldsymbol{K}}_a = \begin{bmatrix} 32.42 & -28.61 & -0.21 & -0.13 & -0.09 \\ -28.61 & 6 & -28.61 & -0.21 & -0.13 \\ -0.21 & -28.61 & 6 & -28.61 & -0.21 \\ -0.13 & -0.2 & -28.61 & 6 & -28.61 \\ -0.09 & -0.13 & -0.21 & -28.61 & 32.42 \end{bmatrix} \times 10^8 \text{ N m}^{-1}$$

Soil–pipe lateral damping matrix:

$$\overline{C}_l = \begin{bmatrix} 42.57 & -9.95 & -1.81 & -1.15 & -0.78 \\ -9.95 & 43.75 & -9.95 & -1.81 & -1.15 \\ -1.81 & -9.95 & 43.75 & -9.95 & -1.81 \\ -1.15 & -1.81 & -9.95 & 43.75 & -9.95 \\ -0.78 & -1.15 & -1.81 & -9.95 & 42.57 \end{bmatrix} \times 10^5 \text{ N s m}^{-1}$$

Soil–pipe axial damping matrix:

$$\overline{C}_a = \begin{bmatrix} 31.31 & -7.47 & -1.29 & -0.81 & -0.57 \\ -7.47 & 32.24 & -7.47 & -1.29 & -0.81 \\ -1.29 & -7.47 & 32.24 & -7.47 & -1.29 \\ -0.81 & -1.29 & -7.47 & 32.24 & -7.47 \\ -0.57 & -0.81 & -1.29 & -7.47 & 31.31 \end{bmatrix} \times 10^5 \text{ N s m}^{-1}$$

Exercise Problems

(Use standard programs like MATLAB®, SAP2000 and ABAQUAS to solve the problems; you may also use your own program developed using the methods presented in the chapter.)

7.12 A vertically propagating shear wave travels through a soil deposit of 50 m thick lying over a rock bed. The soil deposit consists of two equal layers, the properties of the upper and bottom layers are given as: $V_S = 80 \text{ m s}^{-1}$, $\rho = 1600 \text{ kg m}^{-3}$; and $V_S = 400 \text{ m s}^{-1}$, $\rho = 1800 \text{ kg m}^{-3}$, respectively and $\xi = 5\%$. Find: (i) the plot of the square of the modulus of transfer function for absolute acceleration versus frequency using 1D wave propagation time history analysis; (ii) the PSDF of free field ground acceleration, if a stationary random ground motion represented by double filter PSDF of ground acceleration with $\omega_g = 15 \text{ rad s}^{-1}$, $\xi_g = \xi_f = 0.5$, $\omega_f = 0.1\omega_g$, and $S_0 = 1$ is applied at the rock bed; and (iii) the PGA amplification and the amplification of peak ground displacement

7.13 For the same soil deposit as given above, if the El Centro earthquake is applied at the rock bed, find: (i) the plots of the time histories of relative displacement and absolute acceleration at the surface using 1D time history analysis; (ii) the plots of the same time histories by considering non-linear behavior of the top layer of soil with yield stress = 35000N m^{-2} and yield strain = 0.002; (iii) the PGA amplification for the linear and non-linear cases; and (iv) the difference between the free field response spectra for the linear and non-linear soil conditions. Assume zero damping for the soil.

7.14 The frame shown in Figure 7.32 rests on footings of 1 m diameter. Soil properties are specified by $V_S = 200 \text{ m s}^{-1}$ and $\rho = 1800 \text{ kg m}^{-3}$. Using the method of direct analysis, obtain the time histories of base shear, base rotation, and total displacement of the top storey for the El Centro earthquake applied at the base of the frame. Use beam elements for the superstructure, plane strain elements for the foundation and the soil, and contact elements at the interface between the soil and the structure. Take soil boundaries at appropriate distances for adequate dissipation of the radiation waves.

7.15 Solve the same problem, Exercise 7.14, by considering plane strain elements for both soil and structure. [HINT*:* divide the frame elements into several layers depth wise.]

7.16 Solve the problem in Exercise 7.14 by the substructure technique and compare the results with those of the direct analysis.

7.17 The multi-bay portal frame of Example 3.8 (Figure 3.7; Chapter 3) is supported at the base by circular footings of 1 m diameter resting on a soil having $V_S = 100 \text{ m s}^{-1}$ and $\rho = 1700 \text{ kg m}^{-3}$. Find the displacement responses u_1 and u_2 using the substructure technique. Base masses are equal to $m/10$; $k = 5k_s$, in which k_s is the real part of the impedance function corresponding to the horizontal base degree of freedom; $k/m = 100 \left(\text{rad s}^{-1}\right)^2$. Take the earthquake excitation to be same as that for Example 3.8.

7.18 Solve the problem in Exercise 7.14 using the modal substructure technique and compare the results with those of Exercise 7.16.

7.19 Solve the problem in Exercise 7.14 by replacing the soil by an equivalent spring–dashpot system and compare the results with those of the Exercise 7.16.

7.20 A soil–pile structure system, as shown in Figure 7.47, is subjected to El Centro ground motion at the foundation level. Piles have individual pile heads, not connected to a common one. The columns are directly connected to the pile heads, which are of size 2×2 m. Soil characteristics remain the same as those shown in Figure 7.47. Replacing the soil by equivalent spring–dashpot systems, obtain: (a) the impedance functions for the pile head; and (b) using the same impedance function, find the displacement of the top of the frame and base shear at the pile head by the substructure technique.

7.21 A pipeline of diameter 1 m, as shown in Figure 7.51, is buried at a depth of 5 m in a layer of soil deposit of 20 m. V_S and ρ are given as 200 m s^{-1} and 1800 kg m^{-3}. For the vertically propagating S wave as the El Centro earthquake: (a) find the free field motion at the level of the center of the pipeline; (b) obtain the radial and circumferential stresses at point A of the pipe; (c) obtain the bending moment at the center of the pipeline of length 30 m, assuming fully correlated excitation and pinned support at the two ends; and (d) also, find the rms and peak values of the bending moments at the two adjacent nodes on either side of the center, and compare their values with those at the center.

Appendix 7.A

Normalized coefficient matrix B_l (symmetric matrix; rows are given starting from diagonal element):

$$[B]_l = \begin{bmatrix} \text{Row 1} & +1.0 & -0.2134 & -0.0437 & -0.0277 & -0.0186 & -0.0136 & -0.0104 \\ & -0.0084 & -0.0069 & -0.0058 & -0.005 & -0.0044 & -0.0039 & -0.0035 \\ & -0.0031 & -0.0028 & -0.0026 & -0.0024 & -0.0023 & & \\ \text{Row 2} & +1.0 & -0.2134 & -0.0437 & -0.0277 & -0.0186 & -0.0136 & -0.0104 \\ & -0.0084 & -0.0069 & -0.0058 & -0.005 & -0.0044 & -0.0039 & -0.0035 \\ & -0.0031 & -0.0028 & -0.0026 & -0.0024 & & & \\ \text{Row 3} & +1.0 & -0.2134 & -0.0437 & -0.0277 & -0.0186 & -0.0136 & -0.0104 \\ & -0.0084 & -0.0069 & -0.0058 & -0.005 & -0.0044 & -0.0039 & -0.0035 \\ & -0.0031 & -0.0028 & -0.0026 & & & & \\ & & & & \text{and so on} & & & \end{bmatrix}$$

$$[B]_a = \begin{bmatrix} \text{Row 1} & +1.0 & -0.2169 & -0.0426 & -0.0275 & -0.0189 & -0.0140 & -0.0108 \\ & -0.0086 & -0.007 & -0.0058 & -0.005 & -0.0043 & -0.0038 & -0.0033 \\ & -0.003 & -0.0027 & -0.0025 & -0.0023 & -0.0021 & & \\ \text{Row 2} & +1.0 & -0.2169 & -0.0426 & -0.0275 & -0.0189 & -0.0140 & -0.0108 \\ & -0.0086 & -0.007 & -0.0058 & -0.005 & -0.0043 & -0.0038 & -0.0033 \\ & -0.003 & -0.0027 & -0.0025 & -0.0023 & & & \\ \text{Row 3} & +1.0 & -0.2169 & -0.0426 & -0.0275 & -0.0189 & -0.0140 & -0.0108 \\ & -0.0086 & -0.007 & -0.0058 & -0.005 & -0.0043 & -0.0038 & -0.0033 \\ & -0.003 & -0.0027 & -0.0025 & & & & \\ & & & & \text{and so on} & & & \end{bmatrix}$$

References

1. Kramer, S.L. (1996) *Geotechnical Earthquake Engineering*, Pearson Education Inc., Upper Saddle River, NJ.
2. Clough, R.W. and Penzien, J. (1993) *Dynamics of Structures*, 2nd edn, McGraw Hill, Inc., New York.
3. Wolf, J.P. (1985) *Dynamic Soil Structure Interaction*, Prentice-Hall. Englewood Cliffs, NJ.
4. Veletsos, A.S. and Wei, Y.T. (1971) Lateral and rocking vibrations of footings. *Journal of the Soil Mechanics and Foundation Division, ASCE*, **97**, 1227–1248.
5. Luco, J.E. and Westman, R.A. (1971) Dynamic response of circular footings. *Journal of the Engineering Mechanics Division, ASCE*, **97** (EM5), 1381–1395.
6. Gazetas, G. (1991) Foundation vibrations, Chapter 15, in *Foundation Engineering Handbook*, 2nd edn (ed. H-.Y. Fang), Van Nostrand Reinhold, New York, pp. 553–593.
7. Novak, M. (1974) Effect of soil on structural response to wind and earthquake. *Earthquake Engineering and Structural Dynamics*, **3**, 79–96.
8. Asthana, A.K. and Datta, T.K. (1990) A simplified response spectrum method for random vibration analysis of flexible base building. *Engineering Structures*, **12**, 185–194.
9. Datta, S.K., Shah, A.H., and Wong, K.C. (1984) Dynamic stresses and displacements in buried pipe. *Journal of Engineering Mechanics, ASCE*, **110**, 1451–1465.
10. O'Leary, P.M. and Datta, S.K. (1985) Dynamics of buried pipelines. *Journal of Soil Dynamics and Earthquake Engineering*, **4**, 151–159.
11. Takada, S. and Tanabe, K. (1987) Three dimensional seismic response analysis of buried continuous or jointed pipelines. *Journal of Pressure Vessel Technology, ASME*, **109**, 80–87.
12. Hindy, A. and Novak, M. (1979) Earthquake response of underground pipelines. *Earthquake Engineering and Structural Dynamics*, **7**, 451–476.
13. Hindy, A. and Novak, M. (1980) Pipeline response to random ground motion. *Journal of Engineering Mechanics, ASCE*, **106**, 339–360.
14. Datta, T.K. and Mashaly, E.A. (1986) Pipeline response of random ground motion by discrete model. *Earthquake Engineering and Structural Dynamics*, **14**, 559–572.

8

Seismic Reliability Analysis of Structures

8.1 Introduction

Reliability analysis of structures implies estimation of the limit state probabilities of a structure under adverse/environmental loading for its intended period of use. There is a synonymous nomenclature, called safety, which is used to indicate reliability. However, safety is a more traditional concept, while reliability is a relatively new one and offers a probabilistic meaning to the traditional concept. Similarly, risk analysis and reliability analysis of structures are simultaneously used in many publications to express their probabilities of failure. However, they are not actually one and the same thing. Risk analysis of structures is an extension of the reliability analysis to include the consequences of failure. Typically in the seismic risk analysis of structures, the limit state probability of the structure (obtained from the reliability analysis) is integrated with the seismic risk of the site. An associated term that is used in connection with the seismic reliability or risk analysis of structures is the fragility analysis. Fragility analysis is aimed at finding the probability of failure of structures for different levels of PGA at the site and is closer to the seismic risk analysis of structures. Despite these finer distinctions, seismic risk, reliability, safety, and fragility analysis of structures are used loosely in the literature to denote the seismic probability of failure of structures, failure being defined by different limit state conditions.

The most important aspect of the reliability analysis is the consideration of uncertainties that make structures vulnerable to failure for a predefined limit state. Accuracy of the reliability analysis depends upon how accurately all the uncertainties are accounted for in the analysis. Firstly, it is practically impossible to identify all uncertainties; however, important ones can be identified. Secondly, and most importantly, methods for modeling and analyzing them are not easy and some amount of uncertainty always remains associated with their modeling. Finally, analytical formulation of the limit state surface and integration of the probability density function within the domain of interest are complex resulting in various approximations. As a result, varying degrees of simplifications are made in the reliability analysis leading to the development of different reliability methods. Therefore, it is not possible to obtain the exact probability of failure of a structure for any event except for very simple ones.

In this chapter, seismic reliability analysis of structures is briefly discussed. As the subject is vast and considerable research has taken place in this area, it is not possible to cover the entire subject in one small chapter. Only some of the fundamental concepts of seismic reliability of structures, and a few simpler

Seismic Analysis of Structures T.K. Datta

methods of computing the probability of failure of structures for seismic forces, which are of practical importance, will be discussed.

8.2 Uncertainties

Generally there are three types of uncertainties, which are dominant in seismic reliability analysis, namely: (a) randomness and variability of excitation; (b) statistical uncertainty, which arises due to estimation of parameters describing statistical models; and (c) model uncertainty, which arises due to imperfection of mathematical modeling of the complex physical phenomena. In addition to these uncertainties, there are some others which result from simplification of the problem at hand, for example, non-linear analysis may be replaced by equivalent linear analysis, continuums may be represented by a discrete model with limited degrees of freedom, and so on.

In the main, the uncertainty arising due to (a) is irreducible but those arising due to (b) and (c) can be reduced. For example, collection of more data or samples helps in providing better statistical parameters. Likewise, use of a more refined model may reduce the uncertainty due to (c). Other uncertainties, as mentioned above, may be reduced by performing more rigorous analysis with more sophisticated models of structures. A unified approach for treating statistical and model uncertainties in the reliability analysis is discussed in the literature [1] in which the Bayesian updating rule is described to update model parameters and models by developing likelihood functions. With the help of these functions, posterior parameters or models are obtained from prior ones, which are then supposed to have less uncertainty as they are developed using more data and with more observations.

In the seismic reliability analysis of structures, uncertainties of earthquake or ground intensity parameters are considered to affect the reliability estimates significantly and to assume more importance over other uncertainties. As a result, seismic reliability analysis of structures is found to be mostly carried out by considering the randomness of ground motion, the uncertainties inherent in the occurrence of an earthquake and in defining its different intensity parameters. However, many problems have also been solved in which uncertainties of material behavior and modeling of the physical phenomenon have also been included along with the uncertainties of ground motion and earthquakes. The complexity of the analysis increases manifold as more sources of uncertainties are included.

In the seismic reliability analysis of structures, the randomness of ground motion, the uncertainties of earthquake, and its intensity parameters are included in several ways by considering some or all of the following elements of seismicity:

i. Probability density function (PSDF) of ground motion.
ii. Risk consistent or uniform hazard response spectrum.
iii. Model of the occurrence of an earthquake.
iv. Attenuation laws.
v. Probability density functions of the magnitude of an earthquake, epicentral distance, and sources of an earthquake.
vi. Hazard curve.
vii. Empirical relationships to describe the response spectrum ordinates as a function of magnitude and epicentral distance.

The probabilistic models that are widely used to describe the distributions of different uncertain parameters are uniform distribution, extreme value distribution, log normal distribution, and Poisson distribution. Procedures for performing the reliability analysis vary with the selection of the above elements. When material and other uncertainties are introduced, the procedure for the analysis may significantly differ, for example, stochastic FEM analysis for random loading may be used. However, material and other uncertainties may also be included by simple procedures in an approximate manner. In fact, various levels of approximations are often used to simplify the reliability analysis procedure consistent with the desired accuracy.

8.3 Formulation of the Reliability Problem

Seismic reliability analysis of structures can be formulated in different ways. The formulations can broadly be divided in two groups, namely, time invariant problems and time variant problems. In both, a limit state function is defined which could be based on serviceability criterion or ultimate stress criterion, or some other criterion. The reliability problem seeks to find out the probability of limit state failure, that is, violating the limit state condition. For the time invariant problem, let $g(x) = 0$ describe the limit state function in which x denotes a set of random variables $x_1, x_2, \ldots x_n$ and $g(x) \leq 0$ denotes the failure event. The probability of failure is then defined as:

$$P_f = P[g(x) \leq 0] = \int_D f(x)\mathrm{d}x \tag{8.1}$$

in which $f(x)$ is the joint probability density function of $g(x) = 0$ and the integration is performed over the domain D where $g(x) < 0$. The reliability is defined as:

$$R = 1 - P_f \tag{8.2}$$

Figure 8.1 shows the concept for the special case of two random variables. Integration of a suitable probability density function within the shaded area is the reliability against failure defined by the limit state function, $g(x_1, x_2) = 0$.

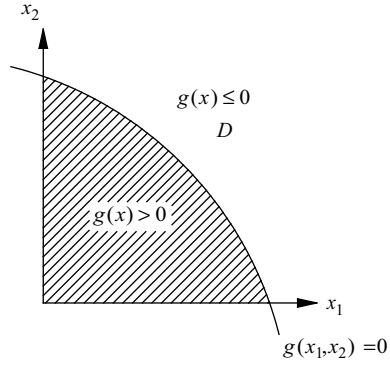

Figure 8.1 Concept of reliability with two random variables

A reliability problem is said to be time variant if the limit state function is also a function of time, that is, the limit state function is defined by $g(\boldsymbol{x}, \boldsymbol{y}(t))$, in which $\boldsymbol{x}$ is a set of random variables and $\boldsymbol{y}(t)$ denotes a vector of stochastic processes. The failure event for such problems may constitute the out crossing of the vector processes, $\boldsymbol{y}(t)$, through the limit state surface $g(\boldsymbol{x}, \boldsymbol{y}) = 0$ as shown in Figure 8.2.

The probability of failure is given by

$$P_f = \int_{0<t\leq T} P[\min g(\boldsymbol{x}, \boldsymbol{y}(t)) \leq 0 | \boldsymbol{x}] f(\boldsymbol{x})\mathrm{d}\boldsymbol{x} \tag{8.3}$$

in which T denotes the structure's lifetime, $f(\boldsymbol{x})$ is the joint probability density function of x, and the conditional probability within brackets is obtained by stochastic analysis of the structure for the random

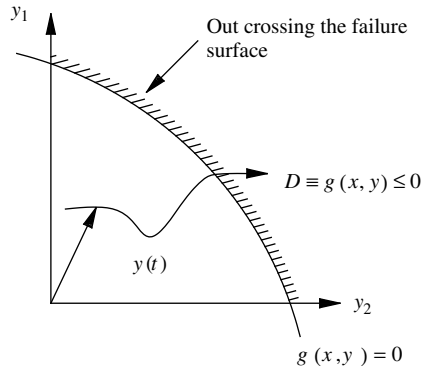

Figure 8.2 Time variant reliability problem

loading $\boldsymbol{y}(t)$. The exact solution of the out crossing analysis is very difficult for two reasons: (i) evaluation of the conditional probability within the bracket, and (ii) determination of the joint probability density function $f(\boldsymbol{x})$. In fact, the latter is also the reason for not being able to obtain the exact integration of Equation 8.3. Therefore, various levels of approximations and assumptions are made in the reliability analysis problems. In particular, different types of seismic reliability analysis of structures have been formulated and solved, which make reasonable approximations to arrive at good estimates of the probability of failure of structures. Before they are described and illustrated with examples, popular methods of finding the probability of failure in structural reliability are described.

8.4 Methods of Finding Probabilities of Failure

There are many methods of finding the probabilities of failure of structures involving functions of random variables. The accuracies of the methods depend upon how correctly the joint probability functions of the random variables are determined and how correctly the integrations such as Equations 8.1 and 8.3 are evaluated. Further, depending upon how the joint probability functions are derived, analytically or numerically, the methods could be classified as analytical methods or numerical methods. Some of the widely used methods in the structural reliability analysis are given in the following sections.

8.4.1 First Order Second Moment Method (FOSM)

In the FOSM, a first order Taylor series approximation of the limit state function is used and only second moment statistics of the random variables are employed to obtain the probability of failure. In its original form, Cornell [2] used two random variables to derive the method. The limit state function is defined as:

$$Z = R - S \tag{8.4}$$

Assuming that R and S are statistically independent normally distributed random variables, Z is also normally distributed. Its mean and covariance are obtained as:

$$\mu_Z = \mu_R - \mu_S \quad \text{and} \quad \sigma_Z^2 = \sigma_R^2 + \sigma_S^2 \tag{8.5}$$

The probability of failure is given by:

$$P_f = P[Z < 0] = P[(R - S) < 0] \tag{8.6}$$

If Z is a normal variate, then it may be easily shown that P_f is given by:

$$P_f = \phi\left(-\frac{\mu_Z}{\sigma_Z}\right) \tag{8.7}$$

in which ϕ is the cumulative distribution function for a standard normal variable.

The ratio of μ_Z/σ_Z is denoted by β and is familiar as the reliability index (safety index) in the theory of reliability. Then, P_f is also popularly expressed as:

$$P_f = \phi(-\beta) \tag{8.8}$$

If the variables R and S are log normally distributed, then the limit state function is defined as:

$$Z = \ln\left(\frac{R}{S}\right) \tag{8.9}$$

Z is again a normal variable, and the probability of failure can be expressed as [3]:

$$P_f = 1 - \phi\left\{\frac{\ln\dfrac{\mu_R}{\mu_S}\sqrt{\dfrac{1+\delta_S^2}{1+\delta_R^2}}}{\sqrt{\ln(1+\delta_R^2)\ln(1+\delta_S^2)}}\right\} \tag{8.10}$$

in which δ_R and δ_S are the coefficient variations of R and S.

The above formulation may be generalized to many random variables, denoted by a vector $\boldsymbol{X}$. Let the performance function be written as:

$$Z = \boldsymbol{G}(\boldsymbol{X}) \tag{8.11}$$

The Taylor series expansion of the performance function about the mean values gives

$$Z = \boldsymbol{G}(\overline{\boldsymbol{X}}) + \sum_{i=1}^{n}\frac{\partial \boldsymbol{G}}{\partial x_i}(x_i - \overline{x}_i) + \frac{1}{2}\sum_{i=1}^{n}\sum_{j=1}^{n}\frac{\partial^2 \boldsymbol{G}}{\partial x_i \partial x_j}(x_i - \overline{x}_i)(x_j - \overline{x}_j) + \cdots \tag{8.12}$$

in which $\overline{x}_i$ is the mean of the variable x_i. Truncating the series at the linear terms, the first-order approximation of the mean and variance of Z are obtained as:

$$\overline{Z} = \boldsymbol{G}(\overline{\boldsymbol{X}}) \tag{8.13}$$

$$\sigma_Z^2 = \sum_{i=1}^{n}\sum_{j=1}^{n}\frac{\partial^2 \boldsymbol{G}}{\partial x_i \partial x_j}\mathrm{cov}(x_i, x_j) \tag{8.14}$$

in which $\mathrm{cov}(x_i, x_j)$ is the covariance of x_i and x_j. If the variables are assumed to be statistically independent, then

$$\sigma_Z^2 = \sum_{i=1}^{n}\left(\frac{\partial \boldsymbol{G}}{\partial x_i}\right)^2 \sigma_{x_i}^2 \tag{8.15}$$

Partial derivatives are obtained at the mean values.

8.4.2 Hasofer–Lind Method

While the method of finding the first order approximate mean and variance using Taylor series expansion about the mean values is valid for a non-linear performance function, the safety index β thus obtained

cannot be directly related to the exact probability of failure. The safety index, β, provides the exact probability of failure when all random variables are statistically independent normal variables and the performance function is a linear combination of the random variables. The Hasofer–Lind method is an improvisation over the FOSM method described earlier [3]. The method is centered around the computation of the design point or the minimum distance of the performance function from the origin. This minimum distance is shown to be the safety index β for the case of normal random variables with linear performance function.

The method uses reduced variables defined as:

$$x_i' = \frac{x_i - \overline{x}_i}{\sigma_{X_i}} \quad (i = 1, \ldots, n) \tag{8.16}$$

Thus, the reduced variable has a zero mean and unit standard derivation. With the help of the reduced variable, the original limit state or performance function $\boldsymbol{G}(\boldsymbol{X}) = 0$ is converted into $\boldsymbol{G}(\boldsymbol{X}') = 0$. The minimum distance, termed β_{HL}, can be expressed as:

$$\beta_{\mathrm{HL}} = [(\boldsymbol{X}_{\mathbf{d}})(\boldsymbol{X}_{\mathbf{d}})^T]^{\frac{1}{2}} \tag{8.17}$$

in which $\boldsymbol{X}_{\mathbf{d}}$ is the minimum distance point on the limit state function and is called the design point or checking point.

The importance of finding β_{HL} can be explained with the help of the linear limit state function of two variables. Consider the limit state function as:

$$Z = R - S = 0 \tag{8.18}$$

The reduced variables are then defined as:

$$R' = \frac{R - \mu_R}{\sigma_R} \tag{8.19}$$

and

$$S' = \frac{S - \mu_S}{\sigma_S} \tag{8.20}$$

Substituting for R and S, the limit state equation may be expressed in terms of R' and S' as:

$$\sigma_R R' - \sigma_S S' + \mu_R - \mu_S = 0 \tag{8.21}$$

In the space of reduced variables, the limit state function can be plotted as shown in Figure 8.3. It is apparent from Figure 8.3 that if the limit state line is near to the origin, the failure region is larger and the probability of failure is increased. The converse is the case for a lesser probability of failure. The minimum distance of the line from the origin is computed as:

$$\beta_{\mathrm{HL}} = \frac{\mu_R - \mu_S}{\sqrt{\sigma_R^2 + \sigma_S^2}} \tag{8.22}$$

Note that β_{HL} is the same as β defined for the normal variables R and S. Thus, β_{HL} can be regarded as a measure of the safety index.

The Hasofer–Lind reliability index can be used to calculate a first-order approximation to the failure probability as $P_f = \phi(-\beta_{\mathrm{HL}})$. This is the integration of the standard normal density along the ray joining the origin and $\boldsymbol{X}_{\mathbf{d}}'$.

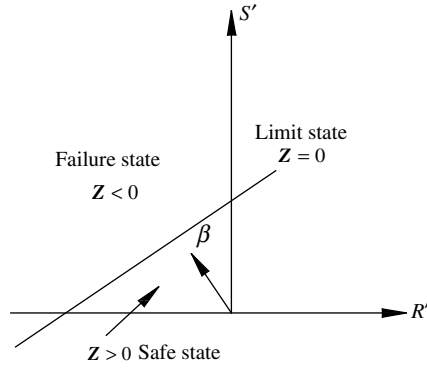

Figure 8.3 Hasofer–Lind reliability index with linear performance function

When the limit state function is non-linear, the computation of the minimum distance becomes an optimization problem, that is,

$$\text{Minimize} \quad D = \sqrt{(\boldsymbol{X}')^T(\boldsymbol{X}')} \tag{8.23}$$

$$\text{Subject to } G(\boldsymbol{X}') = 0 \tag{8.24}$$

Shinozuka [4] obtained an expression for the minimum distance as:

$$\beta_{\text{HL}} = -\frac{\sum_{i=1}^{n} x'_{di}\left(\frac{\partial G}{\partial x'_{di}}\right)}{\sqrt{\sum_{i=1}^{n}\left(\frac{\partial G}{\partial x'_{di}}\right)^2}} \tag{8.25}$$

where the derivatives $\left(\partial G/\partial x'_{di}\right)$ are evaluated at the design point $(x'_{d1}, x'_{d2}, \ldots x'_{dn})$. The design point is given by:

$$x'_{di} = \alpha_{di}\beta_{\text{HL}}; \quad (i = 1, 2, \ldots n) \tag{8.26}$$

where

$$\alpha_{di} = \frac{\left(\frac{\partial G}{\delta x'_{di}}\right)}{\sqrt{\sum_{i=1}^{n}\left(\frac{\partial G}{\partial x'_{di}}\right)^2}}$$

are the direction cosines along the co-ordinate axes x'_i. In the space of original variables, the design point is

$$x'_{di} = \mu_{x_i} - \alpha_{di}\sigma_{x_i}\beta_{\text{HL}} \tag{8.27}$$

The method constructs a linear approximation of the limit state function at the design point, as shown in Figure 8.4. With the β_{HL}, as obtained above, an estimate of P_f is given by $P_f = \phi(-\beta_{\text{HL}})$. If all the variables are not normally distributed, then it is difficult to relate β_{HL} to the exact probability of failure. Rackwitz and Fiessler [5] suggested that an improved estimate of the probability of failure may be obtained by transforming the non-normal variables into equivalent normal variables. They estimated the parameters of the equivalent normal distribution $\mu^N_{x_i}$ and $\sigma^N_{x_i}$ by imposing two conditions, namely: (i) the cumulative distribution functions, and (ii) the probability density functions of the original variables and the equivalent normal variables should be equal at the checking point $\left(x'_{d1}, x'_{d2}, \ldots x'_{dn}\right)$ on the

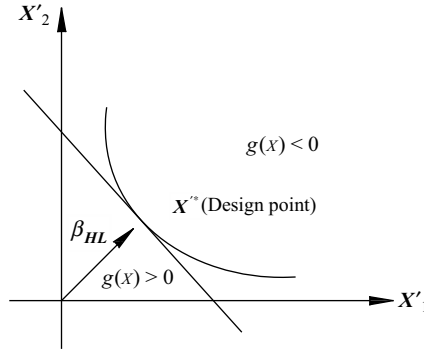

Figure 8.4 Hasofer–Lind reliability index with non-linear performance function

limit state surface. The mean values and the standard deviations of the equivalent normal variables are given by:

$$\sigma_{x_i}^N = \frac{\overline{\phi}\{\phi^{-1}[F_i(x_{di})]\}}{f_i(x_{di})} \tag{8.28}$$

$$\mu_{x_i}^N = x_{di} - \phi^{-1}[F_i(x_{di})]\sigma_{x_i}^N \tag{8.29}$$

in which F_i and f_i are the non-normal cumulative distribution and density functions of x_i; and ϕ and $\overline{\phi}$ are the cumulative distribution and density functions of the standard normal variate, respectively.

With this modification of the random variables, the following algorithm may be used to compute β_{HL}:

i. Assume the initial values of the design point $x_{di}(i = 1, 2, \ldots n)$. To start with, the mean values of the random variables may be considered as the design point.
ii. Obtain the reduced variable $x'_{di} = \frac{(x_{di} - \mu_{x_i})}{\sigma_{x_i}}$.
iii. Evaluate $\left(\frac{\partial \boldsymbol{G}}{\partial x'_{di}}\right)$ and α_{di} at x'_{di}.
iv. Obtain the new design point x_{di} in terms of β_{HL} (use Equation 8.26).
v. Substitute the new x_{di} into the limit state equation $\boldsymbol{G}(\boldsymbol{X}_{\mathbf{d}}) = 0$ and solve for β_{HL}.
vi. Using the β_{HL} value obtained in step (v), evaluate $x'_{di} = -\alpha_{di}\beta_{\text{HL}}$.
vii. Repeat steps (iii)–(vi) until convergence is achieved.
viii. Obtain $\sigma_{x_i}^N$ and $\mu_{x_i}^N$ (use Equations 8.28 and 8.29).
ix. Use Equation 8.27 to obtain the equivalent normal variables in terms of β_{HL}. Note that μ_{xi} and σ_{xi} in Equation 8.27 should be replaced by $\mu_{x_i}^N$ and $\sigma_{x_i}^N$.
x. Solve $\boldsymbol{G}(\boldsymbol{X}_{\mathbf{d}}) = 0$ to obtain β_{HL}.
xi. Obtain $P_f = \phi(-\beta_{\text{HL}})$.

8.4.3 Second Order Reliability Method

The limit state function could be non-linear for many reasons, such as: (i) non-linear relationship between random variables and the limit state function, (ii) transformation of non-normal variables to standard normal variables, and (iii) transformation from correlated to uncorrelated variables. If the limit state function is highly non-linear and the joint probability density function does not decay rapidly as it moves away from the minimum distance point, then a higher order approximation is required for the failure probability computations.

There are many second order reliability methods proposed by various researchers [6, 7] that obtain the P_f by using different assumptions and approximations. One of the popular and easy to apply method is described here.

In this method, the curvature of the limit state function around the minimum distance point is approximated by a quadratic function. Fiessler *et al.* [8] explored the use of various quadratic approximations. A closed form solution for the probability of failure of a region bounded by a quadratic limit state is given by Breitung [9] using asymptotic approximations as [3]:

$$p_f \approx \phi(-\beta) \prod_{i=1}^{n-1} (1+\beta k_i)^{-\frac{1}{2}} \tag{8.30}$$

in which k_i denotes the ith main curvature of the limit state function at the minimum distance point. The main curvature k_i is the ith eigen value of the second derivative matrix $\mathbf{A}$ of the limit state surface at the design point in rotated normal space. The elements of the matrix $\mathbf{A}$ are given by:

$$a_{ij} = \frac{(R\boldsymbol{D}R^T)_{ij}}{|\nabla \boldsymbol{G}(Y^*)|} \quad (i,j = 1,2,\ldots,n-1) \tag{8.31}$$

in which R is the orthogonal transformation matrix for which the nth row is selected to be $Y^*/(Y^{*\,T}Y^*)^{1/2}$. A standard Gram–Schmidt algorithm may be used to determine R; D is the $n \times n$ second derivative matrix of the limit state surface in the standard normal space evaluated at the design point; $\nabla \boldsymbol{G}(\boldsymbol{Y}^*)$ is the gradient vector in the standard normal space.

8.4.4 Simulation Based Reliability Method

Let the performance function or limit state function be given by $g(\boldsymbol{X}) = 0$. The probability of failure P_f is obtained as:

$$P_f = \iint \cdots \int_{g(\boldsymbol{X}) \le 0} f_x(\boldsymbol{X}) \mathrm{d}\boldsymbol{X} \tag{8.32}$$

in which $f_x(\boldsymbol{X})$ is the joint density function of variables $x_1, x_2, \ldots x_n$ and $\mathrm{d}\boldsymbol{X}$ stands for $\mathrm{d}x_1, \mathrm{d}x_2, \mathrm{d}x_3, \ldots, \mathrm{d}x_n$.

The simulation procedure consists of Monte Carlo simulation of basic variables according to their probabilistic characteristics and then feeding them in the limit state function. The number of failures N_f [that is, $g(\boldsymbol{X}) < 0$] is counted for the set of random variables generated. The probability of failure is calculated as:

$$P_f = \frac{N_f}{N} \tag{8.33}$$

in which N is the total number of simulation cycles. The estimated probability of failure depends upon the number of cycles of simulation used. For sufficiently accurate result, a large number of simulations may be needed. Therefore, it is better to approximately compute the variance of the estimated probability of failure. This is done by assuming each simulation cycle to constitute a Bernoulli trial. Therefore, N_f in N trials can be considered to follow a binomial distribution. Variance of the estimated probability of failure can be computed approximately as:

$$\mathrm{var}(P_f) \simeq \frac{(1-P_f)P_f}{N} \tag{8.34}$$

The statistical accuracy of the estimated P_f is measured by the coefficient of variation given by:

$$\text{cov}(P_f) \simeq \frac{\sqrt{\frac{(1-P_f)P_f}{N}}}{P_f} \tag{8.35}$$

The smaller the coefficient of variation, the better the accuracy is. Accordingly, N is decided.

8.5 Seismic Reliability Analysis

Seismic reliability or risk analysis of structures can be performed with different degrees of complexity as outlined previously. Uncertainties that could be considered in the analysis are shown in Figure 8.5. It is practically impossible to consider all uncertainties in one analysis. Further, the estimated probability

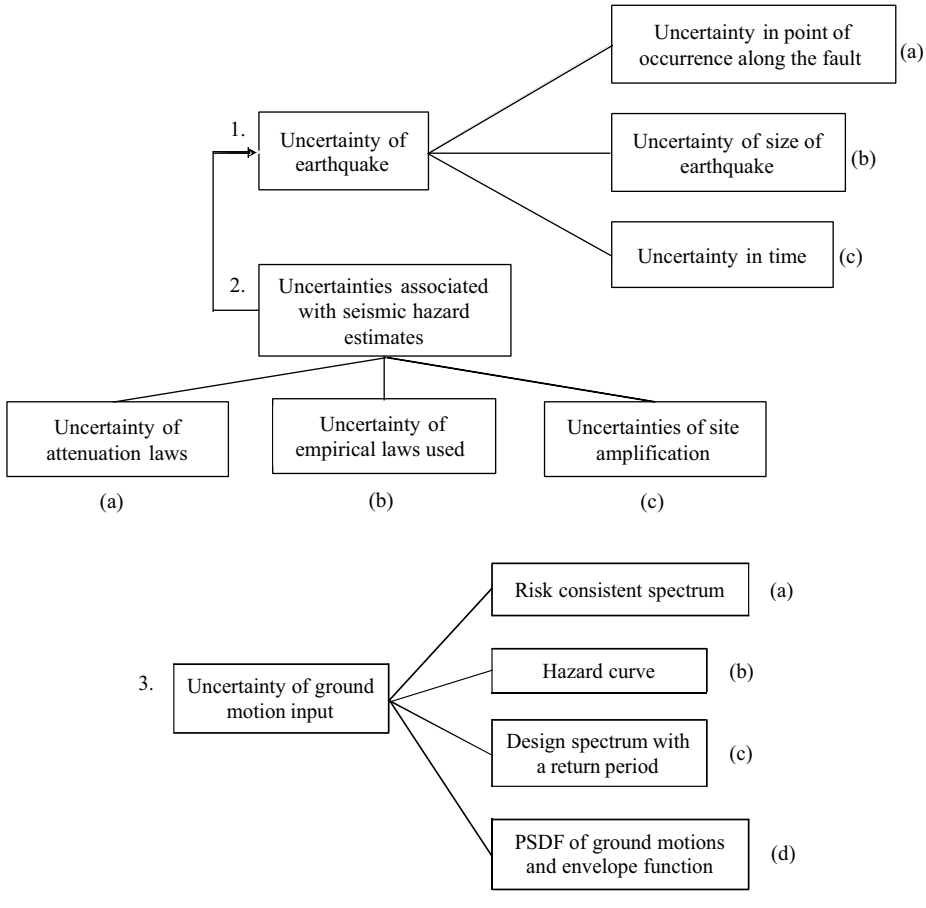

Figure 8.5 Different types of uncertainties in seismic risk analysis

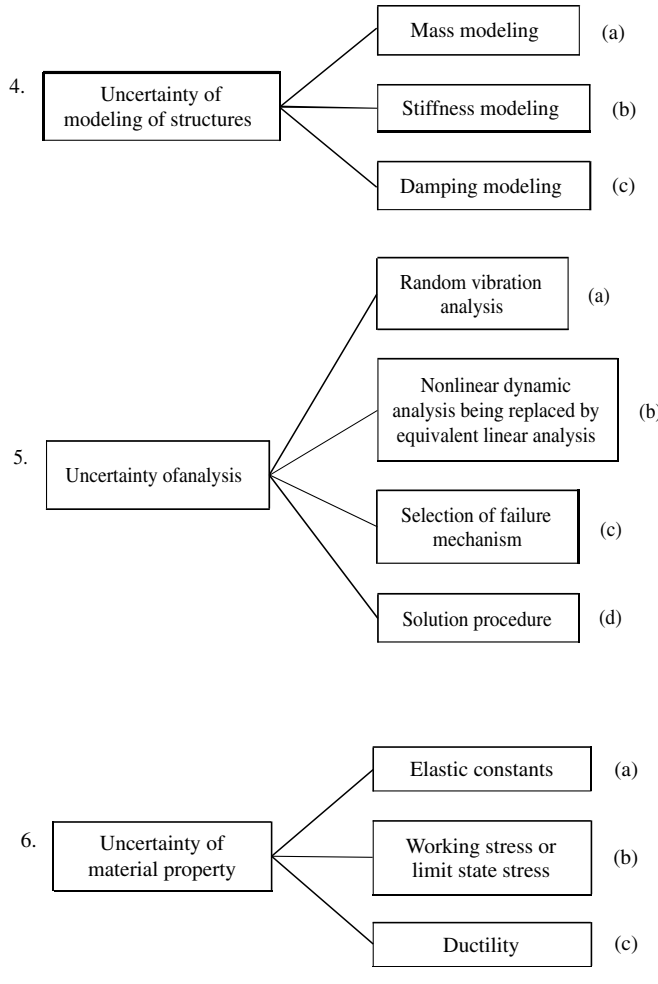

Figure 8.5 (*Continued*)

of failure obtained by any reliability analysis technique cannot be accurate because of the approximations involved in each method. Thus, the calculated seismic reliability is at best a good estimate of the actual reliability of structures against the failure event. In view of this, many simplified seismic reliability analyses have been proposed by various researchers [10, 11]. They are useful in obtaining an estimate of the seismic reliability of structures considering some (but not all) of the uncertainties at a time. Some of them are described here. They include: (i) reliability analysis of structures considering uncertainty of ground inputs only; (ii) reliability analysis of structures using seismic risk parameters of the site; (iii) threshold crossing reliability analysis of structures for deterministic time history of ground motion; (iv) first passage reliability analysis of structures for random ground motions; (v) reliability analysis using damage probability matrix; and (vi) simplified probabilistic risk analysis of structures.

8.5.1 *Reliability Analysis of Structures Considering Uncertainty of Ground Input*

The simplest analysis that can be performed is that of finding the seismic reliability of a structure using a risk consistent spectrum (or uniform hazard spectrum) that considers the uncertainty of ground motion input [uncertainty 3(a)] of Figure 8.5 only. The probability of failure of the structure designed with this spectrum is the exceedance probability of the response spectrum ordinate being used for the design. If a uniform hazard spectrum or risk consistent response spectrum is constructed using seismic hazard analysis, then it is implicit that the analysis also considers uncertainties (2) and (1) of Figure 8.5. Thus, if a rigorous seismic hazard analysis has been performed for a site and the resulting seismic input in the form of a risk consistent spectrum is used in the seismic analysis of the structures, then the uncertainties indicated in (1), (2), and (3a) are mostly included in the reliability estimate. Note that the estimated probability of failure does not include other uncertainties of Figure 8.5 and that the failure of the structure is assumed to take place under the load, determined from the spectrum.

Example 8.1

Consider a multi-storey frame as shown in Figure 8.6. Three alternative designs of the frame are made with the help of three risk consistent response spectrums, which have 10, 5 and 2% probabilities of exceedance in 50 years, respectively. It is assumed that the frame collapses under the earthquake loads obtained by the response spectrums. Determine the probabilities of failure of the frame.

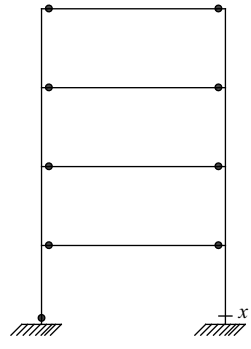

Figure 8.6 Probable mechanism of failure for weak beam–strong column frame under lateral load

Solution: As the frame collapses under the lateral loads determined using the response spectra, the probabilities of exceedance of the response spectrum ordinates are the probabilities of failure of the frame.

The probability of exceedance of at least one or more in t years, for the response spectrum ordinates, is given by the commonly used equation

$$P_e = 1 - \left(1 - \frac{1}{\tau}\right)^t \tag{8.36}$$

in which P_e is the probability of exceedance (PE) in t years and τ is the average recurrence interval. Using the above equation, the average recurrence intervals are calculated as:

- 475 years for 10% PE in 50 years
- 975 years for 5% PE in 50 years
- 2475 years for 2% PE in 50 years

The corresponding probabilities of failure are 2.10×10^{-3}, 1.025×10^{-3} and 4.040×10^{-4}, respectively.

8.5.2 *Reliability Analysis of Structures Using Seismic Risk Parameters of the Site*

Seismic risk analysis of a structure located in a region surrounded by a number of faults may be obtained by integrating the concepts of reliability analysis and seismic risk analysis for the region. Consider a structure in a region as shown in Figure 8.7. There are n earthquake point sources with mean occurrence rate of $\gamma_j (j = 1 \ldots n)$. For each earthquake source, the probability density function of the magnitude of earthquake is given by:

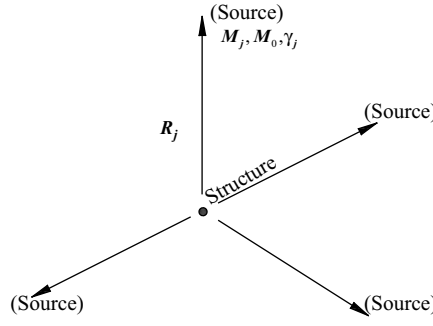

Figure 8.7 Structure in a region surrounded by a number of earthquake sources

$$f_M(m) = \frac{\beta \exp[-\beta(m - m_0)]}{1 - \exp[-\beta(m_j - m_0)]} \tag{8.37}$$

where m_j is the upper limit of the magnitude of earthquake for the jth source. The occurrence of an earthquake in time is assumed to be a Poisson process. The attenuation law for the response spectrum ordinate is given in the form of

$$\text{Log}\, S(T) = a(T) + b(T)M + c(T)\log R \tag{8.38}$$

in which $S(T)$ is the response spectrum ordinates at time period T; $a(T)$, $b(T)$, and $c(T)$ are period dependent constants; M is the magnitude of earthquake; and R is the epicentral distance in kilometers (shortest distance of the site from the rupture length if it is a line source). Other forms of attenuation laws, which are available in the literature, may also be used.

If the material property of the structure is assumed to be deterministic, then the performance function of the structure is a function of the seismic parameters M and R, that is,

$$g(Y) = g(M, R) \tag{8.39a}$$

The lifetime probability of failure of the structure within $(0, t)$ is given by:

$$P[g(M, R) \leq 0] \text{ in } (0, t) \tag{8.39b}$$

If the occurrence of an earthquake is assumed to be a Poisson process with mean occurrence rate γ then

$$P[g(M,R) \leq 0] \text{ in } (0,t) = 1 - \exp\{-\gamma t P[g(M,R) \leq 0]\} \tag{8.40a}$$

$$\approx \gamma t P[g(M,R) \leq 0] \quad \text{for small probabilities} \tag{8.40b}$$

The return period for the failure event is then given by:

$$\overline{T} = \frac{1}{\gamma P[g(M,R) \leq 0]} \tag{8.40c}$$

When more than one source of an earthquake is involved, then the probability of failure is obtained by conditioning on the source and summing up for all sources. In this case, $P[g(M,R_j) \leq 0|E_j]$ is the probability of failure for the earthquake event occurring at source j and

$$P[g(M,R) \leq 0] = \sum_j P[g(M,R_j) \leq 0|E_j]P(E_j) \tag{8.41a}$$

in which

$$P(E_j) = \frac{\gamma_j}{\sum \gamma_j} \tag{8.41b}$$

where R_j is the shortest distance of the site from the rupture length of source j.

The conditional probability of failure is given by:

$$P[g(M,R) \leq 0|E_j] = \int_{m_0}^{m_j} P[g(M,R) \leq 0|E_j, M]f(M)\mathrm{d}M \tag{8.42}$$

The conditional probability is obtained by finding the minimum distance of the performance function (surface) from the origin.

Example 8.2

A two-storey frame, as shown in Figure 8.8, is subjected to earthquake ground motion. The uncertainties of the ground motion in terms of the occurrence and magnitude of the earthquake are to be considered to obtain the probability of failure of the frame. The following data are provided for the analysis.

i. Two-point earthquake sources 1 and 2 exist for the site where the frame is located
ii. $\gamma_1 = 1/\text{year}$; $\gamma_2 = 2/\text{year}$; m_1 (upper limit) $= 7$; m_2 (upper limit) $= 8.5$; m_0 (lower limit for both sources) $= 4$.
iii. Regional seismicity parameter $\beta = 1.5$; $R_1 = 20$ m, and $R_2 = 50$ m.
iv. Use the following attenuation laws for the displacement response spectrum ordinates [11].

$$\overline{S}_1 = 0.01168 \exp(0.82\overline{M})(R+25)^{-1.2} \tag{8.43a}$$

$$\overline{S}_2 = 0.02565 \exp(0.51\overline{M})(R+25)^{-1.34} \tag{8.43b}$$

$$\sigma_{\overline{S}_i} = 0.35 \tag{8.43c}$$

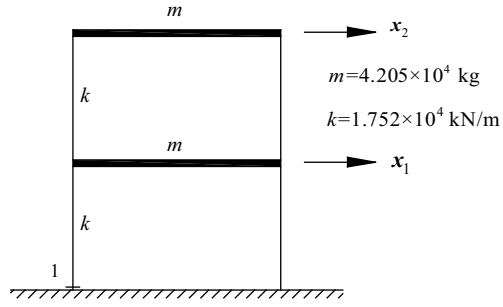

Figure 8.8 A two-storey shear frame

in which $\overline{M}$ is the mean value of earthquake magnitude, R is the epicentral distance in kilometers and $\overline{S}_i$ is the mean value of spectral ordinate in meters for time period T_i.

$$\text{Modal correlation, } \rho_{12} = \rho_{21} = 0.012$$

v. Threshold values for the floor displacement and the storey shear are 64 mm and 623 kN, respectively.

Solution: The frame is analyzed using the response spectrum ordinates given by the attenuation laws shown above. For given values of $\overline{M}$ and R, the attenuation laws provide the mean values of the response spectrum ordinates with a coefficient of variation of 0.35. They are assumed to be log normally distributed.

The responses of the frame are obtained by using the response spectrum method of analysis with CQC rule of combination. Let $r_{\max}$ be the response quantity of interest. Then,

$$r_{\max} = \left[\sum_{i=1}^{2}\sum_{j=1}^{2} \phi_i \phi_j \rho_{ij} S_i S_j\right]^{1/2}$$

in which ϕ_i is the mode shape coefficient for the response. The two frequencies of the frame are $\omega_1 = 12.5$ and $\omega_2 = 33\,\text{rad}\,s^{-1}$ and the mode shape coefficients for top displacement and base shear are:

$$\phi_{d1} = 1.17\,(\text{displacement}) \qquad \phi_{d2} = -0.171\,(\text{displacement})$$

$$\phi_{b1} = 12.67 \times 10^3\,(\text{base shear}) \qquad \phi_{b2} = 4.84 \times 10^3\,(\text{base shear})$$

The performance function may be written as:

$$g(\overline{M}, R) = r_0^2 - \phi_1^2 S_1^2 - 2\rho_{12}\phi_1\phi_2 S_1 S_2 - \phi_2^2 S_2^2$$

Failure surface for given values of $\overline{M}$, R is $g(\overline{M}, R) = 0$.

The plots of the failure surfaces on the S_1 and S_2 axes for displacement and base shear are shown in Figure 8.9. The figure shows that the plots are ellipses with major and minor axes almost coinciding with the S_2 and S_1 axes, respectively. The angle θ of the major and minor axes with respect to the S_1 and S_2 axes may be shown to be as [11]:

$$\theta = \frac{1}{2}\tan^{-1}\left[\frac{4\rho_{12}\phi_1\phi_2}{\phi_1^2 - \phi_2^2}\right]$$

For given values of $\overline{M}$ and R, the minimum distance of the failure surface (plotted on S_1' and S_2' axes; S_1' and S_2' being $S_1 - \overline{S}_1/\sigma_{\overline{S}_1}$ and $S_2 - \overline{S}_2/\sigma_{\overline{S}_2}$, respectively) from the origin is the safety index β. As the

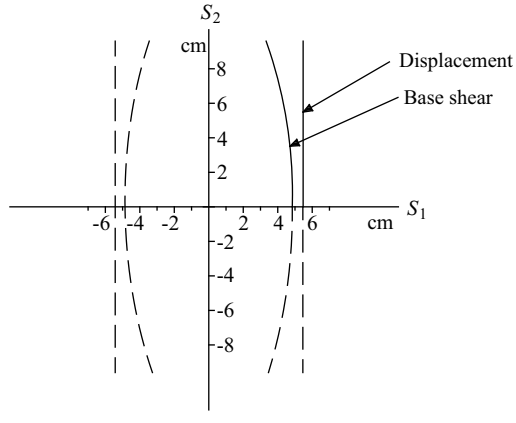

Figure 8.9 Plots of the failure surfaces

minimum distances for both response surfaces nearly coincide with the S_1 axis,

$$\beta = \frac{\ln\left(\frac{S_1}{\overline{S}_1}\right)}{\sigma_{\ln\overline{S}_1}}$$

in which $\ln(\overline{S}_1)$ is the mean value of the response spectrum calculated from the attenuation law given above; $\ln(S_1)$ is the logarithmic value of the minor axis of the ellipse. The probability of failure is given by:

$$P[g(\overline{M}, R) \leq 0 | E_j] = \phi(-\beta)$$

For each source of earthquake (E_j), the computed values of $\phi(-\beta)$ for different assumed values of M and a given value of R are shown in Tables 8.1 and 8.2.

$$d\overline{M} = 0.5 \quad P_{f_{d1}} = \sum \phi(-\beta) f(\tilde{M}) d\overline{M} = 1.38 \times 10^{-3}$$

$$P_{f_{b1}} = \sum \phi(-\beta) f(\overline{M}) d\overline{M} = 0.244 \times 10^{-3}$$

$$d\overline{M} = 0.5 \quad P_{f_{d2}} = \sum \phi(-\beta) f(\overline{M}) d\overline{M} = 1.48 \times 10^{-3}.$$

$$P_{f_{b2}} = \sum \phi(-\beta) f(\overline{M}) d\overline{M} = 1.95 \times 10^{-3}$$

Table 8.1 Results of computation for source-1 ($R = 20$; $\gamma_1 = 1$)

$\overline{M}$	$f(\overline{M})$	Displacement			Base shear		
		$\ln(S_1)$	$\ln(\overline{S}_1)$	$\phi(-\beta)$	$\ln(S_1)$	$\ln(\overline{S}_1)$	$\phi(-\beta)$
4	1.50	−2.91	−5.73	3.8E-16	−3.012	−5.73	3.8E-15
4.5	0.72	−2.91	−5.33	2.4E-12	−3.012	−5.33	1.8E-11
5	0.34	−2.91	−4.92	4.7E-09	−3.012	−4.92	2.5E-08
5.5	0.16	−2.91	−4.51	2.4E-06	−3.012	−4.51	9.3E-06
6	0.076	−2.91	−4.1	3.4E-04	−3.012	−4.1	9.4E-04
6.5	0.036	−2.91	−3.69	0.01	−3.012	−3.69	0.03
7	0.017	−2.91	−3.28	0.14	−3.012	−3.28	0.22

Table 8.2 Results of computation for source-2 ($R = 50$; $\gamma_2 = 2$)

$\overline{M}$	$f(\overline{M})$	Displacement			Base shear		
		$\ln(S_1)$	$\ln(\overline{S}_1)$	$\phi(-\beta)$	$\ln(S_1)$	$\ln(\overline{S}_1)$	$\phi(-\beta)$
4	1.50	−2.91	−6.35	5.1E-23	−3.012	−6.35	5.9E-22
4.5	0.72	−2.91	−5.94	2.4E-18	−3.012	−5.94	3.1E-17
5	0.34	−2.91	−5.53	4.0E-14	−3.012	−5.53	3.2E-13
5.5	0.16	−2.91	−5.12	1.5E-10	−3.012	−5.12	8.7E-10
6	0.076	−2.91	−4.71	1.4E-07	−3.012	−4.71	6.1E-07
6.5	0.036	−2.91	−4.30	3.6E-05	−3.012	−4.30	1.2E-04
7	0.017	−2.91	−3.89	0.002	−3.012	−3.89	0.006
7.5	7.89E-3	−2.91	−3.48	0.05	−3.012	−3.48	0.09
8	3.72E-3	−2.91	−3.07	0.32	−3.012	−3.07	0.43
8.5	1.76E-3	−2.91	−2.66	0.76	−3.012	−2.66	0.84

$$P[g(\overline{M}, R) \leq 0]_d = P_{f_{d1}} \frac{\gamma_1}{\gamma_1 + \gamma_2} + P_{f_{d2}} \frac{\gamma_2}{\gamma_1 + \gamma_2} = 1.45 \times 10^{-3}.$$

$$P[g(\overline{M}, R) \leq 0]_b = P_{f_{b1}} \frac{\gamma_1}{\gamma_1 + \gamma_2} + P_{f_{b2}} \frac{\gamma_2}{\gamma_1 + \gamma_2} = 1.38 \times 10^{-3}.$$

8.5.3 *Threshold Crossing Reliability Analysis of Structures for Deterministic Ground Motion*

The threshold crossing reliability analysis is the out crossing analysis in which exceedance probability of a threshold value of the response is determined. One minus the value of the threshold crossing probability is defined as the threshold crossing reliability of the structure.

Consider a frame that has uncertain properties represented by the uncertainties of the EI values of beams and columns. The time history of excitation is deterministic. The problem is formulated as a time variant reliability problem with a limit state function defined as:

$$g(\boldsymbol{x}, t) = u_0 - u(\boldsymbol{x}, t) \tag{8.44}$$

in which u_0 is the threshold value of the top displacement of a frame and $u(\boldsymbol{x}, t)$ is the top-storey displacement of the frame at any given time, t, which is a function of a number of random variables given by the vector $\boldsymbol{x}$. Assuming the random variables to be independent normally distributed variables, and the Taylor series expansion of the limit state function to be truncated at the first-order term (Equation 8.12), the mean and variance of $g(\boldsymbol{x}, t)$ can be determined as described previously.

The integration of Equation 8.42 is carried out numerically for different assumed values of $\boldsymbol{x}$. As it is assumed that the random variables in $\boldsymbol{x}$ are independent variables, $f(\boldsymbol{x})$ is given by:

$$f(\boldsymbol{x}) = f(x_1) f(x_2) \ldots f(x_n) \tag{8.45}$$

For a particular set of $\boldsymbol{x}$, $g(\boldsymbol{x}, t)$ is a deterministic function and therefore, Equation 8.42 can be written as:

$$P_f = \int_{0<t<T} P[g(\boldsymbol{x}, t) \leq 0 | \boldsymbol{x}] f(\boldsymbol{x}) \mathrm{d}\boldsymbol{x} \tag{8.46}$$

$P[g(\boldsymbol{x}, t) \leq 0]$ can be obtained easily as:

$$P[g(\boldsymbol{x}, t) \leq 0] = \frac{t_u}{T}$$

in which t_u is the total time for which $u(\boldsymbol{x}, t) \geq u_0$.

An alternative formulation for the above problem can be made without conditioning on $\boldsymbol{x}$. The limit state surface $g(\boldsymbol{x}, t) = 0$ will have a different position for different values of $\boldsymbol{x}$ and t. The nearest point of the limit state surface from the origin will give the β value. For this purpose, the Hasofer–Lind algorithm may be used to obtain β_{HL} by iteration. Note that transforming the random variables to normal variables is not required as the variables $\boldsymbol{x}$ are assumed to be normally distributed.

The same problem may be posed as a time invariant reliability problem, if the probability of (material) failure of a section is desired. Consider a column Section-1, as shown in Figure 8.8. The failure is defined by the exceedance of the moment beyond the yield moment of the beam. The maximum bending moment at Section-1 produced by the earthquake is a function of the random variables $\boldsymbol{x}$. The moment capacity of Section-1 is another random variable y, which is assumed to be normally distributed. The limit state function $g(\boldsymbol{x}')$ is then given by:

$$Z = g(\boldsymbol{x}') = y - M(\boldsymbol{x}) \tag{8.47}$$

in which $M(\boldsymbol{x})$ is the moment induced at Section-1 due to an earthquake and $\boldsymbol{x}'$ is the vector of random variables, which contain both $\boldsymbol{x}$ and $\boldsymbol{y}$. Using the Taylor series expansion about the mean value and truncating the series at the first-order term,

$$\overline{Z} = g(\overline{\boldsymbol{x}'}) = \bar{y} - M(\overline{\boldsymbol{x}}) \tag{8.48a}$$

and

$$\sigma_z = \sum_{i=1}^{n} \frac{\partial \boldsymbol{g}}{\partial x_i'} \mathrm{var}(x_i'); \qquad \beta = \frac{\overline{Z}}{\sigma_z} \tag{8.48b}$$

It is assumed that the random variables are independent of each other in the preceeding expressions. A threshold crossing reliability analysis for a frame undergoing inelastic deformation under a given earthquake excitation is solved by Der Kiureghian [10] in which the threshold value is considered for the top displacement of the frame.

Example 8.3

A two-storey frame as shown in Figure 8.10 is subjected to the El Centro earthquake. EI_c and EI_b are assumed to be normally distributed independent random variable with mean values as 5.617×10^7 Nm^2 and 2.509×10^7 Nm^2, respectively, and coefficients of variation as 0.1. The mass of each floor, $m =$ 12 000 kg, is assumed to be deterministic. The threshold value for the top displacement is given as 19 mm. Find the threshold crossing reliability of the frame.

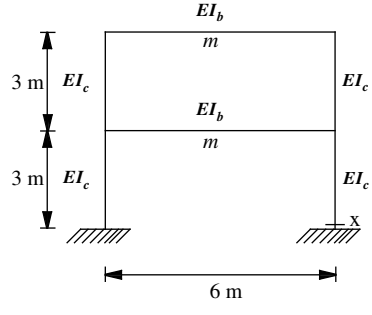

Figure 8.10 A two-storey frame

Solution: The probability of failure is given by Equation 8.46. The random vector $\boldsymbol{x}$ consists of independent variables EI_b and EI_c. Thus,

$$f(\boldsymbol{x}) = f(EI_b)f(EI_c)$$

Ten combinations of EI_b and EI_c values are considered for the analysis. To perform the integration of Equation 8.46 numerically, these values are selected at a regular interval and $f(EI_b)dEI_b$ and $f(EI_c)dEI_c$ are written as $F(EI_c)$ and $F(EI_b)$. Equation 8.46 is then converted into

$$P_f = \sum_{j=1}^{10} P[(g(\boldsymbol{x}, t) \leq 0)_j | \boldsymbol{x}_j] F(EI_b)_j F(EI_c)_j$$

$P[g(\boldsymbol{x}, t) \leq 0]_j$ is obtained by analyzing the frame for the jth combination of EI_b and EI_c values for the earthquake, and finding t_{uj}/T, in which t_{uj} is the total time for which top displacement of the frame remains above the threshold value and $T = 30$ s (duration of earthquake). A sample time history of the top displacement of the frame is shown in Figure 8.11. Computation is performed in tabular form, Table 8.3.

$$P_f = \sum = 9.42 \times 10^{-4}$$

$$\text{Reliability} = 1 - P_f = 0.999$$

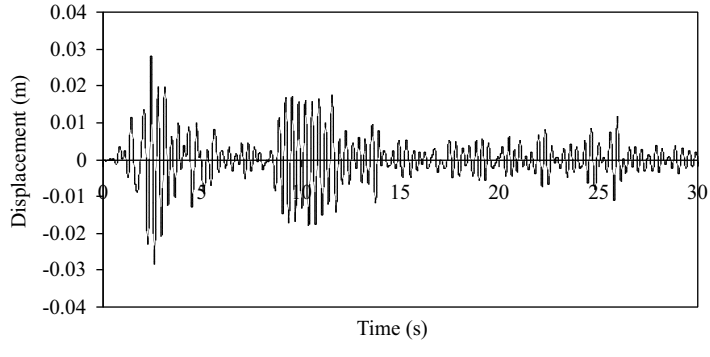

Figure 8.11 A typical time history of the top displacement of the frame

Table 8.3 Results of computation for threshold crossing failure

	1	2	3	4	5	6	7	8	
S. No.	EI_b (Nm^2)	EI_c (Nm^2)	t_u(s)	$\frac{t_{uj}}{T}$	$f(EI_b)$	$f(EI_c)$	$F(EI_b)$	$F(EI_c)$	Product $(4 \times 7 \times 8)$
1	2.13E+07	4.77E+07	0.780	0.0250	5.05E-08	2.26E-08	4.04E-02	3.84E-02	3.88E-05
2	2.21E+07	4.94E+07	0.640	0.0205	7.78E-08	3.41E-08	5.45E-02	5.80E-02	6.48E-05
3	2.28E+07	5.11E+07	0.480	0.0154	1.04E-07	4.70E-08	8.35E-02	7.99E-02	1.03E-04
4	2.36E+07	5.28E+07	0.480	0.0154	1.33E-07	5.91E-08	9.30E-02	1.00E-01	1.44E-04
5	2.43E+07	5.45E+07	0.420	0.0135	1.51E-07	6.78E-08	1.21E-01	1.15E-01	1.88E-04
6	2.51E+07	5.62E+07	0.340	0.0109	1.59E-07	7.10E-08	1.11E-01	1.21E-01	1.46E-04
7	2.58E+07	5.79E+07	0.240	0.0077	1.53E-07	6.78E-08	1.22E-01	1.08E-01	1.02E-04
8	2.66E+07	5.95E+07	0.240	0.0077	1.33E-07	5.97E-08	9.30E-02	1.02E-01	7.28E-05
9	2.73E+07	6.12E+07	0.220	0.0071	1.08E-07	4.78E-08	8.66E-02	8.12E-02	4.99E-05
10	2.81E+07	6.29E+07	0.200	0.0064	7.78E-08	3.49E-08	6.22E-02	5.93E-02	2.36E-05
11	2.89E+07	6.46E+07	0.180	0.0058	5.05E-08	2.32E-08	4.04E-02	3.95E-02	9.26E-06

Example 8.4

For the same problem as above, find the probability of failure of the column section *X,* given that the mean and coefficient of variation of the moment capacity of the section are 361 kN m and 0.1, respectively. Assume moment capacity to be normally distributed.

Solution: For the different combinations of EI_b and EI_c values shown in Table 8.3, the maximum bending moments at X are obtained. Eleven values of maximum bending moments, their mean and standard derivation are given in Table 8.4.

Table 8.4 Bending moment at X for different combinations of EI_b and EI_c

	1	2	3	4	5	6	7	8	9	10	11	$\overline{M}$	σ_M
M (kN m)	214	218	222	224	224	228	230	226	227	225	221	223.54	4.61

$$\beta = \frac{\overline{M}_c - \overline{M}}{\sqrt{\sigma_{M_c}^2 + \sigma_M^2}} = 3.8$$

$$P_f = \phi(-\beta) = 1 \times 10^{-4}$$

8.5.4 *First Passage Reliability Analysis of Structures for Random Ground Motion*

The first passage (excursion) is defined as the event that a random process, for the first time, crosses an upper threshold value or a lower threshold value. The problem is one of finding the probability structure of the random time T when such an event takes place. If the uncertainties of the properties of the structure are considered along with the stochastic nature of the ground motion (uncertainties 6 and 3 of Figure 8.5), then the first passage reliability analysis can be posed as a reliability analysis of the structure for a defined limit state function $g(\boldsymbol{x}, \boldsymbol{y}(t))$, in which $\boldsymbol{x}$ is the vector of random variables representing the uncertainties of the properties of the structure and $\boldsymbol{y}(t)$ is the vector of random ground motion inputs. Thus, the problem requires a time variant reliability analysis in which the limit state function is also a function of time. At every time instant, the limit state function changes. Maximum probability of failure for the first excursion takes place at the earliest instant of time t when the limit state function $g(\boldsymbol{x}, \boldsymbol{y}(t)) = 0$ is nearest to the origin.

Usually, the probability of failure is obtained by conditioning on the random variables $\boldsymbol{x}$ and the problem is formulated as:

$$P_f = \int_{0 \le t \le T} P[\min g(\boldsymbol{x}, \boldsymbol{y}(t)) \le 0 | \boldsymbol{x}] f(\boldsymbol{x}) \mathrm{d}\boldsymbol{x} \tag{8.49a}$$

in which T is the duration of the earthquake. The exact solution of the problem is complex and difficult to find out even for simple linear systems. However, the problem may be solved with certain approximations, which depend upon the desired solution.

For illustration, a simpler problem of the first excursion reliability analysis of a structure subjected to random ground motion $y_g(t)$ is considered with the material property of the structure taken to be deterministic. The intensity/magnitude of an earthquake occurring in the region is also considered to be a random variable. Consider the frame shown in Figure 8.12. Assume the moment at the fixed base is the

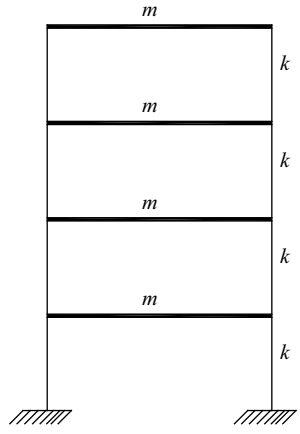

Figure 8.12 Example frame for obtaining the damage probability matrix

response quantity of interest and the probability of first excursion failure for a threshold limit of M_0 is desired. The limit state function is defined as:

$$g(y_g(t)) = M_0 - M(y_g(t)) \tag{8.49b}$$

$$\text{and} \quad P_f = P[g(y_g(t)) \leq 0] \tag{8.49c}$$

The solution to the problem first involves passage analysis of the response in random vibration analysis of structures [12, 13]. The exact solution for the first passage excursion failure is difficult as mentioned previously. However, under certain simplified assumptions, the solution to the problem can be achieved. The important assumptions are [12]:

i. It is assumed that the structure can recover immediately after suffering failure (threshold crossing).
ii. It is assumed that such failures arrive independently, that is, they constitute a Poisson process.
iii. It is assumed that the probability of failure (that is, threshold crossing) within a time interval $[0,t]$ is the distribution function of the random time T (crossing time).

Following the above assumptions, the first excursion reliability analysis can be performed. The analysis requires the zeroth, first and second moment of the response obtained from its PSDF. These moments are defined as (Chapter 4):

$$\lambda_n = \int_0^\infty \omega^n S_m(\omega) \mathrm{d}\omega \tag{8.50}$$

in which $S_m(\omega)$ is the PSDF of the base moment. With these three moments, the following parameters are obtained.

$$\gamma_0 = \frac{1}{2\pi}\sqrt{\frac{\lambda_2}{\lambda_0}} \tag{8.51}$$

and

$$q = \sqrt{1 - \frac{\lambda_1^2}{\lambda_0 \lambda_2}} \tag{8.52}$$

in which γ_0 is defined as the mean rate of zero crossing at positive slope, and q is defined as the dispersion parameter [12].

The mean rate of crossing a specified threshold level M_0 at a positive slope by a stationary zero mean Gaussian process $M(t)$ can be expressed as [12, 13]:

$$\gamma_{M_0} = \gamma_0 \mathrm{e}^{-\frac{\Psi^2}{2}}; \qquad \psi = \frac{M_0}{\sigma_{M_0}} \tag{8.53}$$

in which σ_M is the variance of the moment $M(t)$

It has been confirmed by theoretical and simulation studies that the probability of a stationary response process remaining below a specified barrier decays approximately exponentially with time as given by the relationship [14]

$$L(T) = L_0 \mathrm{e}^{-\alpha T} \tag{8.54}$$

where L_0 is the probability of starting below the threshold, α is the decay rate, and T is the duration of the process. At high barrier levels, L_0 is practically one and the decay rate is given by the following expressions with double barrier (α_{D}) and one sided barrier (α_{S}) respectively [12],

$$\alpha_{\mathrm{D}} = 2\gamma_{M_0} \quad \text{and} \quad \alpha_{\mathrm{S}} = \gamma_{M_0} \tag{8.55}$$

The above relationships are asymptotically exact as the ratio Ψ of the threshold level and the standard derivation of the response becomes large. However, when $\Psi \gg 1$, the Poisson process assumption is no longer valid. In the case of relatively low threshold levels, improved expressions for L_0, α_{D} and α_{S} are given by Vanmarcke [15].

$$L_0 = 1 - \mathrm{e}^{-\frac{\Psi^2}{2}} \tag{8.56}$$

$$\alpha_{\mathrm{D}} = 2\gamma_{M_0} \frac{1 - \mathrm{e}^{-\sqrt{\frac{\pi}{2}}\, q\Psi}}{L_0} \tag{8.57}$$

$$\alpha_{\mathrm{S}} = \gamma_{M_0} \frac{1 - \mathrm{e}^{-\sqrt{2\pi}\, q\Psi}}{L_0} \tag{8.58}$$

The probability of first excursion failure is then given by:

$$P_f = \int P[g(y_g(t)) = M_0 - M(y_g(t)) \leq 0 | \overline{M}] f(\overline{M}) \mathrm{d}\overline{M} \tag{8.59}$$

or

$$P_f = \int P[M(y_g(t)) \geq M_0 | \overline{M}] f(\overline{M}) \mathrm{d}\overline{M} \tag{8.60}$$

$$= \int [(1 - L(T)) | \overline{M}] f(\overline{M}) \mathrm{d}\overline{M} \tag{8.61}$$

in which $L(T)$ is given by Equation 8.54 and $\overline{M}$ is the magnitude of the earthquake. Note that the PSDF of $y_g(t)$ may be expressed in terms of the intensity parameter $\overline{M}$ using the empirical equations given in Chapter 2.

In the above problem, if material uncertainty is included then the limit state function takes the form

$$g(\boldsymbol{x}, y_g(t)) = M_0 - M(\boldsymbol{x}, y_g(t)) \tag{8.62}$$

in which $\boldsymbol{x}$ is the vector of random variables denoting the flexural rigidities of the beams and columns, and M_0 is the threshold value of the column base moment. The probability of first passage failure is obtained by conditioning on both magnitude $\overline{M}$ and $\boldsymbol{x}$, and is given by:

$$P_f = \int P[g(\boldsymbol{x}, y_g(t)) \leq 0 | \overline{M}, \boldsymbol{x}] f(\boldsymbol{x}) f(\overline{M}) \mathrm{d}\boldsymbol{x}\, \mathrm{d}\overline{M} \tag{8.63}$$

If $\boldsymbol{x}$ consists of normally distributed independent random variables, then $f(\boldsymbol{x})$ can be expressed as given by Equation 8.45.

Example 8.5

If the frame shown in Figure 8.8 is subjected to a random ground excitation represented by the double filter PSDF with $\omega_g = 15.7\,\mathrm{rad\,s^{-1}}$, $\eta_g = \eta_f = 0.6$, and $\omega_f = 0.1\omega_g$, find the probability of first passage failure of the frame for a threshold value of top displacement of 12.8 mm. The PDF of the magnitude of the earthquake is given by Equation 8.37; with $\beta = 1.5$, $m_j = 8$, $m_0 = 4$, and the attenuation law for the region is given by Equation 2.44 (Chapter 2) with $R = 75\,\mathrm{km}$.

Solution: The PSDF of ground motion is given by Equation 2.74 (Chapter 2). Considering a cut-off frequency of $30\,\mathrm{rad\,s^{-1}}$, the first three moments of the PSDF, that is, λ_0, λ_1, and λ_2 (Equation 8.50) are obtained as:

$$\lambda_0 = 37S_0; \qquad \lambda_1 = 506S_0; \qquad \lambda_2 = 8980S_0$$

in which S_0 is defined in Equation 2.74

Using Equation 2.19c and duration of the earthquake as 30 s, the peak factor is calculated as 3.27. Thus, PGA $= p\sigma_{\ddot{x}_g}$. Using the attenuation law given by Equation 2.44, the PGA for different values of the magnitude, $\overline{M}$, and the corresponding values of $\sigma_{\ddot{x}_g}$ and S_0 are shown in Table 8.5.

Table 8.5 Results of computation of PGA, $\sigma_{\ddot{x}_g}$ and S_0

$\overline{M}$	PGA (g)	$\sigma_{\ddot{x}_g}$ (g)	$S_0(g^2\,\mathrm{rad\,s^{-1}})$
4	0.0046	0.0014	5.26E-08
4.5	0.007	0.0021	1.24E-07
5	0.0107	0.003	2.90E-07
5.5	0.0163	0.005	6.75E-07
6	0.0248	0.0076	1.56E-06
6.5	0.0374	0.0114	3.54E-06
7	0.0559	0.0171	7.91E-06
7.5	0.0826	0.0253	1.73E-05
8	0.1202	0.0368	3.65E-05

Using the computed values of S_0, the PSDF of the top displacement of the frame is determined using spectral analysis presented in Chapter 4. Calculation of the first passage failure probability for displacement (d) is shown in tabular form in Table 8.6 (Equations 8.50–8.58).

$$P_f = \sum_{i=1}^{9} [1 - L(T)]_i F(\overline{M})_i = 0.00788$$

in which

$$F(\overline{M})_i = f(\overline{M})_i d\overline{M} (d\overline{M} = 0.5)$$

Table 8.6 Results of computation of first passage failure for displacement

$\overline{M}$	λ_0	λ_1	λ_2	γ_0	Ψ	L_0	γ_d	$\alpha_D = 2\gamma_d$	$L(T)$	$f(\overline{M})$
4	9.92E-08	1.27E-06	1.67E-05	2.07	4.06E+01	1	0.00E+00	0.00E+00	1	1.50E+00
4.5	2.34E-07	2.98E-06	3.95E-05	2.07	2.65E+01	1	1.60E-152	3.20E-152	1	7.20E-01
5	5.47E-07	6.98E-06	9.23E-05	2.07	1.73E+01	1	1.89E-65	3.71E-65	1	3.40E-01
5.5	1.27E-06	1.62E-05	2.15E-04	2.07	1.13E+01	1	2.36E-28	4.40E-28	1	1.60E-01
6	2.94E-06	3.75E-05	4.97E-04	2.07	7.46E+00	1	1.68E-12	2.79E-12	1	7.60E-02
6.5	6.68E-06	8.52E-05	1.13E-03	2.07	4.95E+00	1	9.72E-06	1.35E-05	1.000	3.60E-02
7	1.49E-05	1.90E-04	2.52E-03	2.07	3.31E+00	0.996	8.53E-03	9.35E-03	0.752	1.70E-02
7.5	3.26E-05	4.16E-04	5.51E-03	2.07	2.24E+00	0.919	1.68E-01	1.51E-01	0.010	7.89E-03
8	6.88E-05	8.78E-04	1.16E-02	2.07	1.54E+00	0.696	6.29E-01	5.56E-01	0.000	3.72E-03

8.5.5 *Reliability Analysis of Structures Using a Damage Probability Matrix*

Another problem of interest, which is closely associated with the reliability analysis, is the determination of damage probability matrix of structures. In this problem, it is assumed that the material behavior is elasto-plastic and the major damage of a section occurs when the yield moment is reached at that section. Furthermore, it is assumed that the material property is deterministic, but the ground motion is random, with the earthquake intensity parameter also defined as a random variable. Consider the frame, shown in Figure 8.12, and it is desired to construct a damage probability matrix for the moment at the support of the columns.

If the random ground motion is assumed as a stationary Gaussian process, then the response (moment) of the frame is also a stationary Gaussian process so long it is in the elastic range or it just reaches the yield state. As the response is a stationary Gaussian process, a Gumbel type I distribution [12, 13] can be used to express the distribution of its peak value. The probability density of the peak value is given by [16]:

$$f(M) = a' \exp[-a'(M-b') - \exp\{-a'(M-b')\}] \tag{8.64}$$

in which a' and b' are related to the mean (μ_M) and standard deviation (σ_M), respectively, of the peak values $M(T)$ of the process $m(t)$ of duration T as:

$$a' = \frac{\pi}{\sqrt{6}\sigma_M}; \qquad b' = \mu_M - \frac{0.5772}{a'} \tag{8.65a}$$

μ_M and σ_M are given by [17]:

$$\mu_M = \left(K' + \frac{0.5772}{K'}\right)\sigma_m \tag{8.65b}$$

$$\sigma_M = \frac{\pi}{\sqrt{6}K'}\sigma_m \tag{8.65c}$$

$$K' = \sqrt{2\ln\gamma_0 T} \tag{8.65d}$$

in which σ_m is the standard deviation of the process $m(t)$, and γ_0 is the mean rate of the zero crossing of the process $m(t)$ (Equation 8.51).

Using the standard results of integration, the cumulative distribution function may be expressed as:

$$P[M \le M_0] = \exp[-\exp\{-a'(M_0 - b')\}] \tag{8.66}$$

The probabilities of moderate and minor damage may be defined by specifying threshold levels for them. If the threshold level for moderate damage is defined as αM_0, then the probabilities of major (P_1),

moderate (P_2), and minor (P_3) damage, respectively, due to the earthquake intensity parameter I (could be intensity or magnitude or any other parameter) can be calculated as:

$$P_1, I = 1 - P(M \leq M_0) \tag{8.67}$$

$$P_2, I = 1 - P_1, I - P(M \leq \alpha M_0) \tag{8.68}$$

$$P_3, I = 1 - P_1, I - P_2, I \tag{8.69}$$

A damage probability matrix can then be obtained for different intensities of the earthquake.

The damage probability matrix is combined with the annual probability of occurrence$P(I_S \geq I)$ of an earthquakes of different levels of intensity to obtain the annual probability of each damage state, known as the damage index and is obtained as:

$$P_k = \sum_{I=I_L}^{I_U} P[I_S \geq I] P_k, I \quad k = 1, 2, 3 \tag{8.70}$$

in which P_k is the damage index for the kth damage state; I_L and I_U are the lower and upper bounds, respectively, of the earthquake intensity. Mashaly and Datta [16] used an empirical relationship to express standard derivation $\sigma_{\ddot{u}_g}$ (cm/s^2) of ground acceleration in terms of intensity of the earthquake. This enables the PSDF of ground motion to be defined as a function of the intensity of the earthquake as:

$$\sigma_{\ddot{u}_g} = \frac{10^{\left(\frac{I}{3} - 0.5\right)}}{K^*} \tag{8.71}$$

in which

$$K^* = K' + \frac{0.5772}{K'}; \qquad K' = \sqrt{2 \ln(\gamma_0 T)} \tag{8.72}$$

Using attenuation laws such as that given by Equation 2.44 (Chapter 2) and a relationship between the peak and rms values, $\sigma_{\ddot{x}_g}$ can also be related to the magnitude of the earthquake.

Example 8.6

A pipe segment (of radius r_0 and thickness t) is modeled as shown in Figure 8.13. It is assumed that the pipe is subjected to the same (perfectly correlated) ground acceleration at all supports and is represented by the double filter PSDF with: $\omega_g = 15.7\,\text{rad s}^{-1}$; $\eta_g = \eta_f = 0.6$; $\omega_f = 0.1\omega_g$. The same attenuation law used in the previous example is utilized to relate the magnitude of an earthquake with PGA. The properties of the pipe are: $E = 2.1 \times 10^8\,\text{kN m}^{-2}$; $r_0 = 0.685\,\text{m}$; $t/r_0 = 0.0162$; $\xi = 0.05$; $\rho_p = 2500\,\text{kg m}^{-3}$ and $L = 70\,\text{m}$. The value of the spring stiffness $K_s = 8.417 \times 10^3\,\text{kN m}^{-1}$. Find the damage probability matrix and damage indices for the displacement at the center of the pipe for $\overline{M} = 4 - 8$. Maximum allowable displacement $(d_{\max})$ is prescribed as 150 mm. Moderate damage is

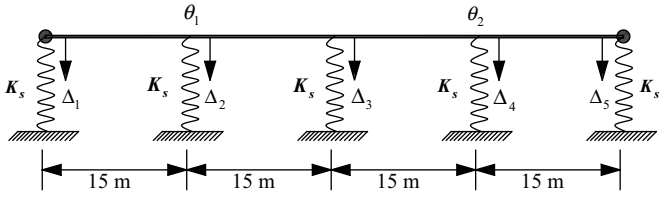

Figure 8.13 A segment of a buried pipeline

considered at displacement $= 0.7\ d_{\max}$. The CDF of the magnitude of the earthquake is given by:

$$F_M(\overline{M} < m) = \frac{1 - \exp[-\beta(m - m_0)]}{1 - \exp[-\beta(m_u - m_0)]}; \quad \text{take } \beta = 1.5; \quad m_u = 8, \quad m_0 = 4$$

Solution: As the same PSDF of ground motion and the attenuation law as that of the previous example problem are considered, the values of S_0 for different values of $\overline{M}$ remain the same as shown in Table 8.6. The PSDF of the displacement at the center of pipe shown in Figure 8.13 is obtained for the random ground motion using the procedure given in Chapter 4. The response quantities of interest and the computation of the damage probability matrix are shown in Table 8.7.

Table 8.7 Results of computation of damage probability matrix

$\overline{M}$	σ_d	γ_0 Eqn. 8.51	μ_D Eqn. 8.65b	σ_D Eqn. 8.65c	a' Eqn. 8.65a	b' Eqn. 8.65a	P_1 Eqn. 8.67	P_2 Eqn. 8.68	P_3 Eqn. 8.69	PE of $\overline{M}$
4	0.0182	3.11	0.058	0.008	165.490	0.055	0.000	0.000	1.000	1.000
4.5	0.024	3.12	0.077	0.010	125.541	0.072	0.000	0.016	0.984	0.471
5	0.0317	3.12	0.102	0.013	95.047	0.096	0.006	0.328	0.666	0.221
5.5	0.0412	3.16	0.132	0.018	73.233	0.124	0.141	0.842	0.016	0.103
6	0.0552	3.14	0.177	0.023	54.621	0.166	0.914	0.086	0.000	0.047
6.5	0.0729	3.15	0.234	0.031	41.374	0.220	1.000	0.000	0.000	0.021
7	0.0962	3.16	0.309	0.041	31.364	0.290	1.000	0.000	0.000	0.009
7.5	0.127	3.16	0.407	0.054	23.758	0.383	1.000	0.000	0.000	0.003
8	0.1676	3.16	0.538	0.071	18.002	0.506	1.000	0.000	0.000	0.000

σ_d = Standard deviation of displacement at the centre. μ_D = Mean peak value of the displacement at the centre. σ_D = Standard deviation of the peak displacement at the centre. PE = Probability of exceedance.

Annual damage index for major damage:

$$(P_1) = \sum_{\overline{M}=4}^{8} (8)(11) = 0.0917$$

Annual damage index for moderate damage:

$$(P_2) = \sum_{\overline{M}=4}^{8} (9)(11) = 0.172$$

Annual damage index for minor damage:

$$(P_3) = \sum_{\overline{M}=4}^{8} (10)(11) = 1.612$$

8.5.6 *Simplified Probabilistic Risk Analysis of Structures*

As discussed previously, it is practically impossible to consider all uncertainties in one analysis in a rigorous way. The complexities involved are unsurmountable. Therefore, an attempt has been made by Shinozuka *et al.* [18] to evolve a simplified procedure for seismic risk analysis of structures in which most of the uncertainties are included in an approximate manner. The method is useful for a preliminary estimate of the probability of failure of structures and can be readily used by practicing engineers. It is widely practiced under the name of a PRA (probability risk analysis) procedure. The simplified PRA of structures for an earthquake presented here is similar to that presented by Shinozuka *et al.* [18] except that the random vibration analysis of the structures is replaced by an equivalent static lateral load analysis

using the risk consistent response spectrum to obtain the expected peak response. The method includes the following uncertainties:

i. Variability of input ground motion (represented by a risk consistent spectrum) is included by a random variable, F_1. Its median value is taken as unity and logarithmic standard deviation β_1 is calculated as $\beta_1 = \ln(r_{84}/r_{50})$; in which r_{84} and r_{50} are the responses of the structure for 84th percentile and mean input response spectrums, respectively.
ii. Variability of the system parameters, including structural and soil properties used in the analysis, is introduced by a random variable F_2. Its median value is unity and β_2 is calculated in a similar way as above.
iii. Uncertainty involved in modeling of the system and in the analytical method is included by a random variable F_3. Its median value is taken as unity and coefficient of variation may be taken between 0.2 and 0.3 [19].
iv. Uncertainty resulting from the actual simulation analysis being replaced by equivalent linear analysis (or other approximate analysis) is included by the random variable F_4 with unit median and the coefficient of variation may be taken as 0.15.
v. Uncertainty in the capacity of the sections of the structure due to ductility (as non-linear analysis is not performed) is included by a random variable F_5. Its median value is taken as $0.6\sqrt{2\mu - 1}$ where μ is the ductility factor and the coefficient of variation may be taken as 0.2 [19].
vi. Uncertainty in the overall capacity of the structure due to the multiple formations of plastic hinges is included by a random variable F_6 with a median value taken as 1.13, and the coefficient of variation may be taken as 0.1.
vii. Uncertainty of material strength leading to variable section capacity is included by the mean section capacity S, and a specified coefficient of variation.

Note that the coefficients of variation given above are taken from reference [19]. Depending upon structures and the construction practices adopted in different countries, the values of these coefficients may vary. These values are best obtained from the statistical analysis of collected data.

For an assumed value of the PGA, the base shear for the frame shown in Figure 8.6 is obtained with the help of the risk consistent normalized response spectrum given in Figure 8.14. The fundamental time period of the frame is obtained using the mean values of the properties of the frame. Furthermore, the base shear is obtained for the 84th percentile response spectrum and β_1 is computed as described in (i) as above.

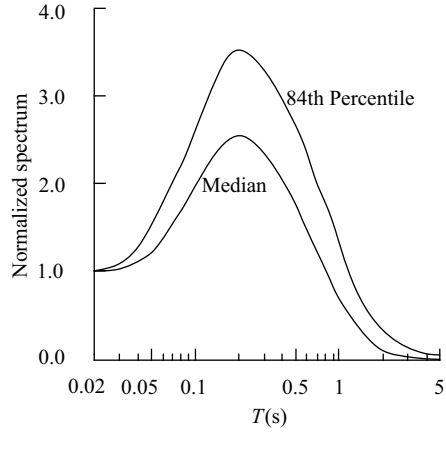

Figure 8.14 Risk consistent response spectrum

In the next step, β_2 is calculated by obtaining the base shear corresponding to the mean plus one standard deviation value of the properties of the frame. Note that the 50th percentile response spectrum is used to calculate the base shear.

In the third step, the equivalent lateral load for the frame is obtained for the base shear calculated in the first step (for the 50th percentile response spectrum) and the response quantity of interest, for example, the moment at a section X as shown in Figure 8.6 is obtained. The response (that is, the moment) $R(a)$ for the section is a random variable given by:

$$R(a) = r(a)F_1F_2F_3F_4 \tag{8.73}$$

in which $r(a)$ is the computed moment at the section X for the assumed value of the PGA (a); F_1, F_2, F_3 and F_4 were defined earlier.

Similarly, the capacity for the section is a random variable, which is a product of three variables, namely:

$$C = S\,F_5\,F_6 \tag{8.74}$$

in which S is the mean value of the moment capacity of the section calculated based on the mean values of the material property with a coefficient of variation as β_7; F_5 and F_6 were defined earlier.

The distributions of the random variables $R(a)$ and C are log normal if all random variables as described above are assumed to be log normal. Using FOSM, the probability of failure P_f for the section is given by:

$$P_f = P[(C - R(a)) \leq 0] = \phi(-\beta) = 1 - \phi(\beta) \tag{8.75}$$

$$\text{in which } \beta = \frac{\ln \dfrac{\overline{C}}{\overline{R}(a)}}{\sqrt{\sigma^2_{\ln R} + \sigma^2_{\ln C}}} \tag{8.76}$$

$\overline{R}(a)$ and $\overline{C}$ are the mean values of $R(a)$ and C, respectively. For small values of $\sigma^2_{\ln R}$ and $\sigma^2_{\ln C}$ it can be shown that:

$$\sigma_{\ln R} \approx Cov(R) \quad \text{and} \quad \sigma_{\ln C} \approx Cov(C)$$

Thus, the denominator of Equation 8.76 can be replaced by:

$$\sqrt{\beta_1^2 + \beta_2^2 + \beta_3^2 + \beta_4^2 + \beta_5^2 + \beta_6^2 + \beta_7^2}$$

The following steps are adopted when performing the analysis:

i. Potential sections of the plastic hinges are identified for the expected mechanisms of failure of the frame (partial or total). This is obtained by a pushover analysis of the frame. The section where the last hinge is formed is noted (for example, X in Figure 8.6).
ii. Assume a value of PGA and obtain the equivalent lateral load.
iii. The load is applied to the frame, and moments at the potential sections for the plastic hinges are obtained. If the moments are less than the mean values of the moment capacities of the sections, then P_f is calculated for each section. The value of P_f for the section X provides the probability of failure of the frame for the assumed value of PGA. If the moments at some sections are greater than their moment capacities, then an incremental analysis is performed with sequential formation of the plastic hinges. For the last increment of loading, the P_f value is calculated for the section X.
iv. Steps (ii) and (iii) are repeated for increased values of PGA until the complete failure takes place for the assumed mechanism of failure.
v. The probabilities of failure thus obtained are conditional probabilities with respect to the assumed value of PGA.

vi. Annual frequencies of exceedance of the PGA values are obtained separately from the seismic hazard curve for the site as explained in Chapter 1.
vii. Using the hazard curve, a curve showing the variation of probability of failure of the frame with the annual frequency of exceedance is obtained. Each point on the curve shows the annual frequency of the probability of failure of the frame corresponding to an assumed failure mode (partial or complete).

Example 8.7

For the frame, shown in Figure 8.15, obtain the fragility curve showing the variation of the probability of failure of the frame with the PGA corresponding to an assumed failure mechanism (partial or complete). Mean values of EI_b, EI_c, and m are shown in the figure. The coefficients of variation for EI_b, EI_c, and m are assumed to be the same and taken as 0.1. The coefficient of variation of the moment capacity of the sections is assumed to be $\beta_7 = 0.15$. The normalized risk consistent spectrum to be used for analysis is shown in Figure 8.14.

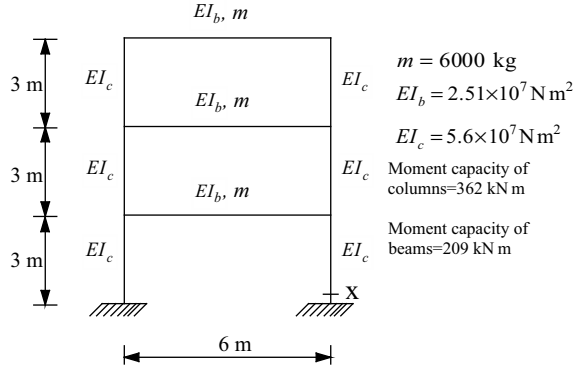

Figure 8.15 A three-storey frame

Solution: A pushover analysis is performed for the frame with mean values of the properties of the frame as shown in Figure 8.15. From the push over analysis, the section where the last hinge that is formed for the collapse of the frame is marked as X in the figure. To obtain the fragility curve, the probability of failure at X for different assumed values of PGA is calculated. A sample calculation for PGA = 200 cm s^{-2} is shown below.

$$\text{Time period for the frame (based on mean values of the properties)} = 0.39\ \text{s}$$

$$\text{The corresponding spectral acceleration } (S_a)_{50} = 400\ \text{cm s}^{-2};\quad (S_a)_{84} = 600\ \text{cm s}^{-2}$$

$$\text{Base shear } (V):\quad (V)_{50} = 72.52\ \text{kN}\quad (V)_{84} = 107.28\ \text{kN}$$

$$\text{Load at different storeys } (P^T):\quad (P^T)_{50} = 46,\ 20.4,\ 5.12\ \text{kN}$$

$$(P^T)_{84} = 69, 30.6, 7.68\ \text{kN}$$

An incremental analysis of the frame with the above loads is performed and moments at X are obtained as $M_{50} = 101.32$ kN m and $M_{84} = 152$ kN m.

$$\beta_1 = \ln\left(\frac{M_{84}}{M_{50}}\right) = 0.405$$

To calculate β_2, M_{84} is determined using the mean plus one standard deviation value of the properties of the frame. Thus, $\beta_2 = \ln\left(\frac{M_{84}}{M_{50}}\right) = \ln\left(\frac{105}{101}\right) = 0.039$

For an assumed ductility of $\mu = 3$, median value of $F_5 = 0.6\sqrt{2\mu - 1} = 1.34$ and median value of $F_6 = 1.13$ (given in step vi). Thus,

$$\overline{R}(200) = M_{50} = 101.32\,\text{kN m}$$

$$\overline{C} = 361 \times 1.34 \times 1.13 = 546.62\,\text{kN m}$$

$$\sqrt{\sigma^2_{\ln R} + \sigma^2_{\ln C}} = \overline{\beta} = \sqrt{\beta_1^2 + \beta_2^2 + \beta_3^2 + \beta_4^2 + \beta_5^2 + \beta_6^2 + \beta_7^2} = 0.548$$

$$\beta = \frac{\ln \overline{C}}{\overline{\ln \overline{R}(200)}} = 3.072; \qquad P_f = \phi(-\beta) = 1.06 \times 10^{-3}$$

Following the above calculation procedure, P_f is determined for each assumed value of PGA. The calculated values are shown in Table 8.8.. The fragility curve showing the variation of P_f with PGA is shown in Figure 8.16.

Table 8.8 Results of computation of the probability of failure

PGA (cm s^{-2})	$M_{50} = \overline{R}$ (kN m)	$\overline{C}$ (kN m)	$\ln(\overline{C}/\overline{R})$	β	P_f
0	0.000	546.63	0	0	0
50	25.33	546.63	3.072	5.599	1.08E-08
100	50.66	546.63	2.378	4.336	7.26E-06
150	75.99	546.63	1.973	3.597	1.6E-04
200	101.32	546.63	1.685	3.072	1.06E-03
250	126.65	546.63	1.462	2.666	3.8E-03
300	151.98	546.63	1.280	2.333	9.8E-03
350	177.31	546.63	1.126	2.052	2.0E-02
400	202.65	546.63	0.992	1.809	3.5E-02
450	227.97	546.63	0.874	1.594	5.5E-02
500	253.30	546.63	0.769	1.402	8.0E-02
550	279.0	546.63	0.672	1.226	1.1E-01
600	304.0	546.63	0.586	1.069	1.42E-01
650	329.0	546.63	0.508	0.925	1.77E-01
700	358.0	546.63	0.423	0.772	2.20E-01

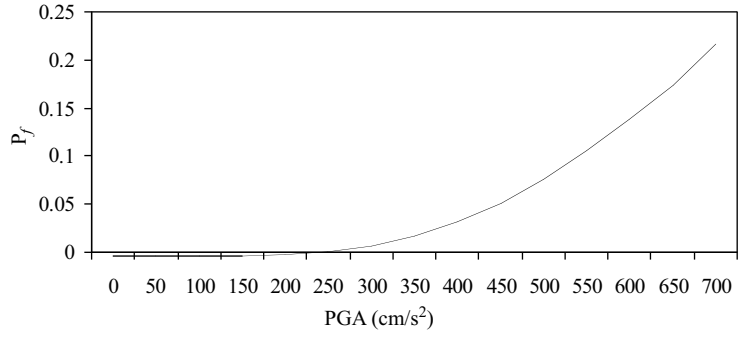

Figure 8.16 Fragility curve for the example frame

Exercise Problems

(Use standard programs like MATLAB®, SAP2000 and ABAQUAS to solve the problems; you may also use your own program developed using the methods presented in the chapter.)

8.8 The three-storey frame shown in Figure 8.17 is designed using the normalized response spectrum shown in Figure. 8.14. It is designed for a PGA of 0.3 g, which has 10% probability of exceedance in 50 years. Assuming the moment capacity of the column at the base and the load calculated from the response spectrum to be a normally distributed random variable, find the probability of failure of the column at the base. Coefficients of variation of the moment capacity and loads are assumed to be 0.15 and the mean value of the moment capacity of the column is assumed to be 362 kN m.

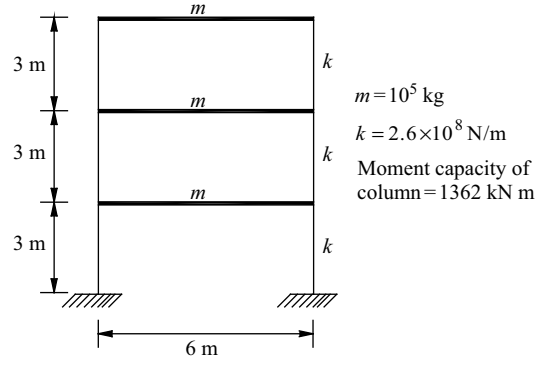

Figure 8.17 A three-storey shear frame

8.9 For the three-storey frame shown in Figure 8.17, find the threshold crossing probabilities of maximum drift and the base moment for the El Centro earthquake, given the threshold crossing values as 3.5 mm, 1050 kNm, respectively.

8.10 For the frame shown in Figure 8.10 and the properties of the frame given in the problem in Example 8.3, find the threshold crossing probability of the base moment for the El Centro earthquake given that: (i) the threshold crossing value is 150 kNm; (ii) columns are stronger than beams such that yielding take place in the beams; (iii) plastic moment capacities of the beams (M_{pb}) and columns (M_{pc}) are normally distributed random variables with mean and coefficient of variation as 100 kNm, 360 kNm and 0.15, respectively; and (iv) yield rotation $= M_{pb}l/6EI_b$.

8.11 The three-storey frame shown in Figure 8.17 is subjected to a random ground excitation represented by the double filter PSDF with $\omega_g = 15.7$ rad s^{-1}; $\eta_g = \eta_f = 0.6$; $\omega_f = 0.1\omega_g$. Find the probability of first excursion failure for the top displacement of the frame for a threshold value of 5 mm. Take the PDF of the magnitude of the earthquake and the attenuation law of the region same as those for problem in Example 8.5.

8.12 If the major damage criterion for the above frame is taken as first-storey drift exceeding 3.5 mm (d_m) and moderate damage as $0.75d_m$, find the damage probability matrix and damage indices considering $I = 6 - 12$. Take the relationship between $\sigma_{\ddot{x}_g}$ and I given by Equation 8.71 and probability of exceedance of I given by Equation 1.33 (Chapter 1).

8.13 The three-storey frame shown in Figure 8.17 is subjected to uncertain ground motion. Uncertainties of the ground motion are represented by:

i. A point earthquake source and a line source as shown in Figure 8.18 with seismic properties as given in the figure; lower bound magnitude for both sources are assumed to be 4 and $\beta = 1.5$.

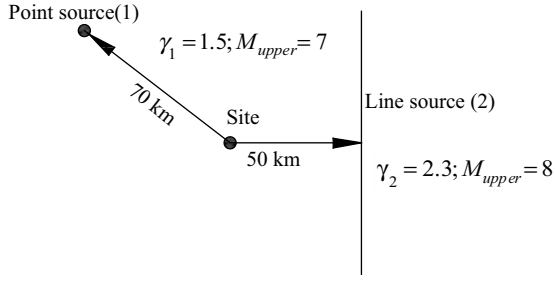

Figure 8.18 Earthquake sources for the site

ii. The site specific response spectrum is given by Equation 8.38 with the constants a, b and c as:

$$a(T_1) = -1.5 \qquad b(T_1) = 0.3 \qquad c(T_1) = 0.15$$

$$a(T_2) = 0.8 \qquad b(T_2) = -0.1 \qquad c(T_2) = 0.1$$

$$a(T_3) = 0.08 \qquad b(T_3) = -0.05 \qquad c(T_3) = 0.04$$

$$\sigma_{\ln s} = 0.3$$

iii. Threshold values of displacement and base moment are 20 mm and 1600 kNm.

Find the probabilities of failure of the frame for the top displacement and the base moment.

8.14 If the beams of the three-storey frame shown in Figure 8.17 are not infinitely rigid but have the flexural rigidity of half of the column flexural rigidity and the floor mass is reduced to 2×10^4 kg, find the fragility curve showing the variation of probability of failure with PGA using the simplified PRA procedure. Use the risk consistent response spectrum to be the same as that shown in Figure 8.14. The mean value of the moment capacity of the beams is 300 kN m with coefficient of variation as 0.15. The value of μ is taken as 3.5. The coefficient of variation for the mass and the *EI* values of the frame is 0.1. The values of mass and *EI* values shown in the figure are their mean values.

References

1. Box, G.E.P. and Tiao, G.C. (1973) *Bayesian Inference in Statical Analysis*, Addison-Wesley, Reading, MA.
2. Cornell, C.A. (1969) A probability based structural code. *Journal of the American Concrete Institute*, **66** (12), 974–985.
3. Halder, A. and Mahaderan, S. (1995) First order and second order reliability method, in *Probabilistic Structural Mechanics Hand Book* (ed. C. Raj Sundararajan) Chapman and Hall, London, pp. 27–52.
4. Shinozuka, M. (1983) Basic analysis of structural safety. *Journal of the Structural Division, ASCE*, **109** (3), 721–740.
5. Rackwitz, R. and Fiessler, B. (1976) Note on Discrete Safety Checking When Using Non-Normal Stochastic Models for Basic Variables. Loads Project Working Session. Cambridge, Massachusetts: Massachusetts Institute of Technology.
6. Tvedt, L. (1990) Distribution of quadratic forms in normal space-application to structural reliability. *Journal of the Engineering Mechanics Division, ASCE*, **116** (6), 1183–1197.
7. Der Kiureghian, A.D., Lin, H.Z., and Hwang, S.F. (1987) Second order reliability approximation. *Journal of Engineering Mechanics Division, ASCE*, **113** (8), 1208–1225.
8. Fiessler, B., Neumann, H.J., and Rackwitz, R. (1979) Quadratic limit states in structural reliability. *Journal of Engineering Mechanics Division, ASCE*, **105** (4), 661–676.
9. Breitung, K. (1984) Asymptotic approximation for multi-normal integrals. *Journal of Engineering Mechanics Division, ASCE*, **110** (3), 357–366.
10. Der Kiureghian, A.D. (1996) Structural reliability methods for seismic safety assessment: A review. *Engineering Structures*, **18** (6), 412–424.

11. Der Kiureghian, A.D. (1981) Seismic risk analysis of structural systems. *Journal of Engineering Mechanics, ASCE*, **107** (6), 1133–1153.
12. Lin, Y.K. (2008) *Probabilistic Theory of Structural Dynamics*, McGraw-Hill, New York.
13. Newland, D.E. (1975) *An Introduction to Random Vibrations and Spectral Analysis*, Longman, London.
14. Crandall, S.H., Chandiramani, K.L., and Cook, R.G. (1966) Some first passage problems in random vibration. *Journal of Applied Mechanics, ASME*, **42** (9), 532–538.
15. Vanmarcke, E.H. (1975) On the distribution of the first passage time for normal stationary random process. *Journal of Applied Mechanics, ASME*, **51** (3), 215–220.
16. Mashaly, E.A. and Datta, T.K. (1989) Seismic risk analysis of buried pipelines. *Journal of Transportation Engineering, ASCE*, **115** (3), 232–252.
17. Davenport, A.G. (1964) Note on the distribution of the largest value of the random function with application to gust loading. *Proceedings of Institute of Civil Engineers*, **28**, 187–196.
18. Shinozuka, M., Mizutani, M., Takeda, M., and Kai, Y. (1989) A Seismic PRA Procedure in Japan and its Application to a Building Performance Safety Estimation Part 3-Estimation of Building and Equipment Performance Safety. Proceedings of ICOSAR 1989, San Francisco, USA, pp. 637–644.
19. Takeda, M., Kai, Y., and Mizutani, M. (1989) A Seismic PRA Procedure in Japan and its Application to a Building Performance Safety Estimation Part 2-Fragility Analysis. Proceedings of ICOSAR 1989, San Francisco, USA, pp. 629–636.

9

Seismic Control of Structures

9.1 Introduction

It is gradually being recognized that effective means of protecting structures from earthquake forces are by way of using various methods of structural control. They are not only effective for mitigating earthquake forces, but also are equally useful in controlling undesirable vibrations of structures produced due to wind and other dynamic excitations. In addition, there are a number of other factors that have emerged in recent years that require the control of the structural response. These factors include increased flexibility of the structural systems, increased safety levels, stringent performance level, and economic considerations. As a result, research in the area of structural control has intensified since the 1980s and many structural control methodologies have been developed, with some now being implemented in practice. Broadly, methods of structural control can be classified as passive and active control methods. In the passive control, the mass or the damping or stiffness or a combination of any two or all are modified by adding some components into the structure. These components are actuated by the movements of the structure and provide control forces according to their dynamic characteristics. No external source of energy is required to activate the system. In the active control, an external source of energy is used to activate the control system by providing an analog signal to it. This signal is generated by the computer following a control algorithm that uses measured responses of the structure. Combination of these two methods of structural control has been used to evolve semi-active and hybrid control methods. While methods of structural control are applicable for all types of dynamic forces, their applications for protecting structures from seismic forces and wind induced vibrations are challenging areas of study and research in civil engineering. In this chapter, some of the widely used passive and active control methodologies for earthquake applications will be discussed. At the end of the chapter, the more promising semi-active controls of structures will be briefly presented.

9.2 Base Isolation

Base isolation of structures is one of the most popular means of protecting structures against earthquake forces. It is a passive control device that is installed between the foundation and the base of the building. For bridges, the base isolators are installed between the deck and the pier, as with bridge bearings. In buildings, the base isolator protects the structure from earthquake forces in two ways: (i) by deflecting the seismic energy and (ii) by absorbing the seismic energy. The seismic energy is deflected by making the base of the building flexible (instead of fixed) in lateral directions, thereby increasing the fundamental time period of the structure. As buildings with longer time periods attract less seismic force (Chapter 5),

Seismic Analysis of Structures T.K. Datta

the isolation system deflects the seismic energy. In particular, high energy in the ground motions at higher mode frequencies are deflected. The seismic energy is absorbed by the isolator because of its non-linear response to earthquake excitation. The (internal) force–displacement curve of isolators under sinusoidal excitation exhibits hysteretic behavior and, therefore, much of the input energy to the isolators is lost in the hysteresis loop. Because of these two properties of the isolators, they have become very attractive passive control devices to be used in the control of seismic response of structures, especially the building structures. Extensive research, both theoretical and experimental, has been carried out in the area of base isolation of structures. As a result of these research projects, many base isolation devices have evolved and implemented in practice. Generally, the base isolators can be grouped under (i) laminated bearings, and (ii) friction bearings. Among the laminated bearings, laminated rubber bearing (LRB), and New Zealand (NZ) rubber bearings are used extensively in practice. Of the friction type, elastic sliding bearings, friction pendulum systems (FPS), resilient friction systems (R-FBI), and pure friction (P-F) systems are popular. The characteristics of these isolators are briefly discussed below [1].

9.2.1 *Laminated Rubber Bearing (LRB)*

The basic components of the LRB are steel and rubber plates built into alternate layers (Figure 9.1a). Generally, an LRB system exhibits high damping capacity, horizontal flexibility, and high vertical stiffness. For low damping rubber bearings, a lateral force–deformation relationship is modeled as linear, as shown in Figure 9.1b. A temperature independent model for the lateral stiffness of the bearing is given

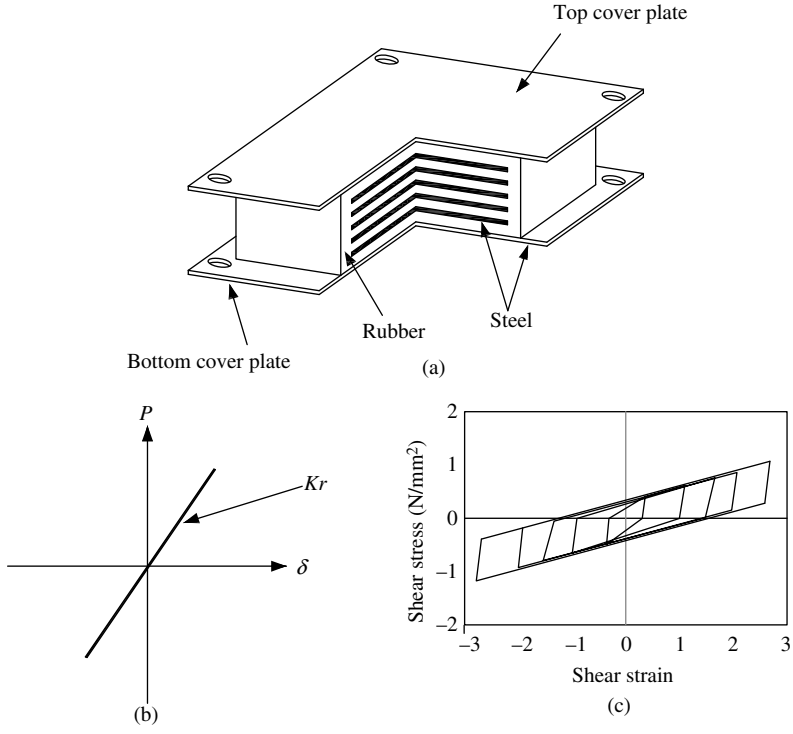

Figure 9.1 Laminated rubber bearing system: (a) section and elements; (b) idealized force deformation behavior for low damping rubber; and (c) idealized force deformation behavior for high damping rubber

by that at 15 °C, that is,

$$K_r = \frac{GA}{H} \tag{9.1}$$

in which G, A, and H are the shear modulus, the cross-sectional area, and the total thickness of the rubber, respectively. The vertical stiffness K_v is given by:

$$K_v = \frac{\alpha A}{H}\left[\frac{E_0(1+2kS_1^2)E_b}{E_0(1+2kS_1^2)+E_b}\right] \tag{9.2}$$

where

S_1 is the primary shape factor (10–15)
k is the correction modulus of rubber hardness (1–0.5)
E_0 and E_b are the longitudinal and the bulk modulus of elasticity, respectively
α is the correction modulus for longitudinal elasticity (0.8–1).

The linear damping coefficient may be taken to be about 10%. For a high damping rubber bearing, the equivalent damping is considerably increased due to the hysteretic effect as shown in Figure 9.1c. It could be of the order of 15–20%.

9.2.2 New Zealand Bearing System

A New Zealand bearing is similar to a laminated rubber bearing, but with a central lead core or rubber core in order to increase the size of the hysteresis loop and, hence, to provide additional dissipation of energy (Figure 9.2a). A typical idealized force–displacement relationship of lead–rubber bearing is shown in Figure 9.2b. The initial stiffness K_u is given by:

$$K_u = \beta K_d \quad \text{in which} \quad \beta = \frac{K_u}{K_d} \tag{9.3}$$

and K_d is given by:

$$K_d = C_d(K_r + K_p) \tag{9.4}$$

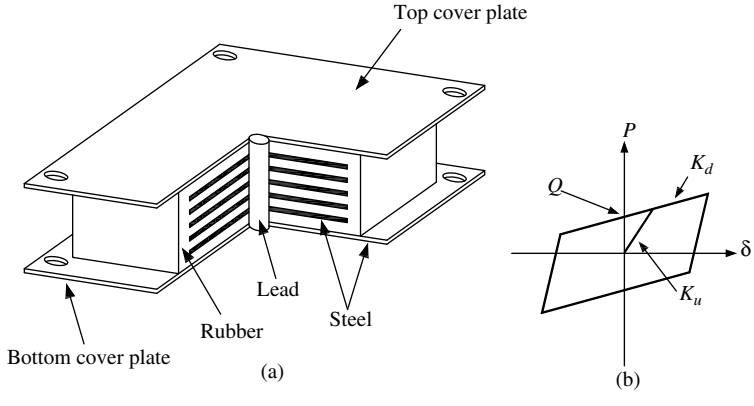

Figure 9.2 Lead rubber bearing (New Zealand system): (a) section and elements; and (b) idealized force deformation behavior

in which

$K_r = \frac{GA}{H}$
$K_p = \alpha \frac{A_p}{H}$
$A_p =$ the area of the flow plug
$\alpha =$ the shear modulus of lead

$$C_d = \left.\begin{matrix} 0.78\,\gamma^{-0.43} \\ \gamma^{-0.25} \\ \gamma^{-0.12} \end{matrix}\right\} \begin{matrix} \gamma < 0.25 \\ 0.25 \le \gamma < 1.0 \\ 1.0 \le \gamma < 2.5 \end{matrix} \tag{9.5}$$

in which γ is the maximum shearing strain.

The yield force, Q, is given by:

$$Q = C_q \sigma_p A_p \tag{9.6}$$

in which σ_p is the yield shear stress of lead,

$$C_q = \left.\begin{matrix} 2.04\,\gamma^{0.41} \\ 1.11\,\gamma^{0.145} \\ 1 \end{matrix}\right\} \begin{matrix} (\gamma \le 0.1) \\ (0.1 < \gamma < 0.5) \\ (\gamma \ge 0.5) \end{matrix} \tag{9.7}$$

The equivalent stiffness (k_{eq}) and damping (ξ_{eq}) for the linear analysis are given by

$$K_{\text{eq}} = \frac{Q}{\gamma H} + K_d \tag{9.8}$$

$$\xi_{\text{eq}} = \frac{2}{\pi} \frac{Q\left\{\gamma H - \dfrac{Q}{(\beta - 1)K_d}\right\}}{K_{\text{eq}}(\gamma H)^2} \tag{9.9}$$

The size of the lead core, diameter (area), thickness, and number of the rubber layers and thin plates are determined using the procedure given in reference [2]. For the convenience of the readers, the essential formulae are given below:

9.2.2.1 Area of Rubber Layer

$$\text{Maximum of}\left(\sigma_c = \frac{P_{DL+LL}}{A_0}, \qquad \gamma_{DL+LL} = 6S\frac{P_{DL+LL}}{E_c A_1} \le \frac{\varepsilon_{\text{b}}}{3}, \quad A_{sf}(\text{reduced}) = \frac{K_r H}{G}\right) \tag{9.10a}$$

in which A_0 and A_1 are the areas of rubber layer, A_{sf} is the load free area [2], γ is the shear strain, S is the shape factor, and ε_{b} is the elongation of rubber at break.

$$\text{Area of lead plug} : A_p = \frac{Q_d}{f_{py}} \tag{9.10b}$$

in which f_{py} is the yield shear stress for lead. Thickness of each rubber layer (circular) can be obtained from

$$S = \frac{\text{loaded} \cdot \text{area}}{\text{load} \cdot \text{free} \cdot \text{area}} = \frac{(\pi d^2/4)}{(\pi d)t} = \frac{d}{4t} \tag{9.10c}$$

where t is the thickness of each rubber layer and d is the diameter of the rubber layer.

$$\text{Number of rubber layers,} \quad N = \frac{H}{t} \quad \text{where} \quad H = \frac{S_d}{\gamma_{\max}} \tag{9.10d}$$

in which S_d is the design displacement and H is the total thickness of the rubber layers.

$$\text{Thickness of steel shim plates} \quad t_s \geq \frac{2(t_i + t_{i+1})(DL + LL)}{A_{re} F_s} \geq 2\,\text{mm} \tag{9.10e}$$

in which

t_i and t_{i+1} are the thicknesses of the rubber layers at the top and the bottom of a steel plate
A_{re} is the area of the steel plate
F_s is the shear yield strength of steel.

9.2.3 Resilient Friction Base Isolation (R-FBI)

The friction base isolator consists of concentric layers of teflon coated plates that are in friction contact with one another, and it contains a central core of rubber (Figure 9.3a). It combines the beneficial effect of friction damping with that of resiliency of rubber. The rubber core distributes the sliding displacement and velocity along the height of the R-FBI bearing. The system provides isolation through the parallel action of friction, damping, and restoring force, and is characterized by natural frequency (ω_b), damping constant (ξ_b), and coefficient of friction (μ). Recommended values of these parameters are $\omega_b = 0.5\pi\,\text{rad}\,\text{s}^{-1}$; $\xi_b = 0.1$, and $0.03 \leq \mu \leq 0.05$. The force deformation behavior of the isolator is shown in Figure 9.3b.

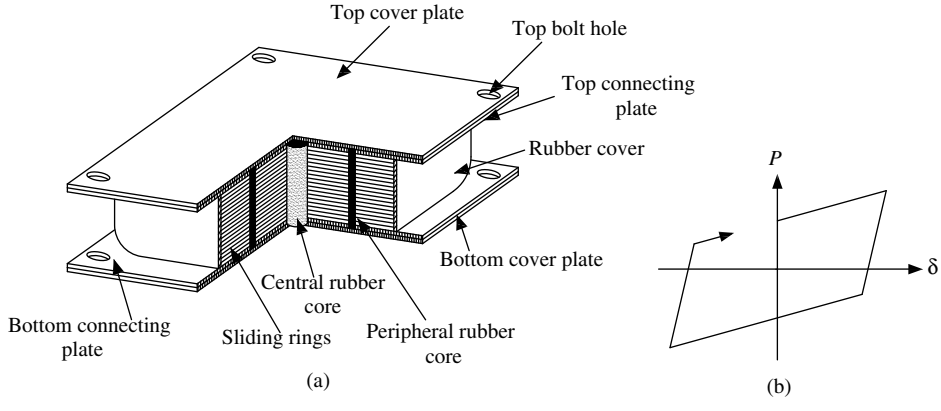

Figure 9.3 Resilient friction based isolator system: (a) section and elements; and (b) idealized force deformation behavior

9.2.4 Pure Friction System

A pure friction (P-F) base isolator is based essentially on the mechanism of sliding friction (Figure 9.4a). The horizontal frictional force offers resistance to motion and dissipates energy. The coefficient of friction depends on the nature of the surface over which the sliding takes place. The force–deformation behavior of the isolator is shown in Figure 9.4b.

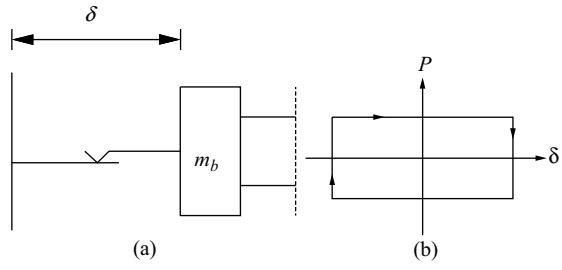

Figure 9.4 Pure friction system: (a) schematic diagram; and (b) idealized force deformation behavior

9.2.5 Elastic Sliding Bearing

This is principally composed of rubber layers, connective steel plates, sliding material, a sliding plate, and a base plate. The sliding material is set between the sliding plate and the connective plate as shown in Figure 9.5(a and b). Under the lateral force, the shearing deformation is limited to the laminated rubber

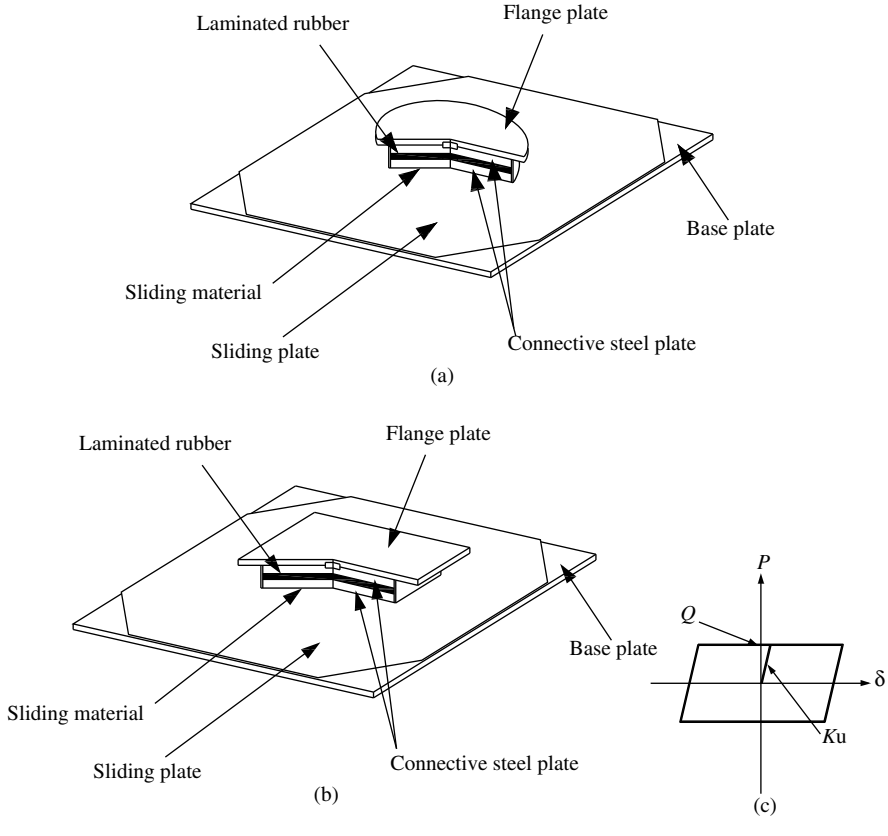

Figure 9.5 Elastic sliding bearing: (a) round type; (b) square type; and (c) idealized force deformation behavior

until the yield force associated with sliding is exceeded. After the yield force has been reached, the bearing assembly slides. Thus, the force–deformation curve takes the shape as shown in Figure 9.5c. The initial stiffness is governed by K_r given by Equation 9.1.

The yield force, Q of the bearing is given by $Q = \mu W$; where W is the vertical force, and μ has stress and velocity dependency and is given by:

$$\mu = [0.0801 - 0.437\exp(-0.005v)]\sigma^{-0.33} \tag{9.11}$$

in which v is the velocity and σ is the stress.

The equivalent stiffness is given by:

$$K_{\text{eq}} = \frac{Q}{\gamma H} \tag{9.12}$$

in which γ is the maximum shearing strain of the rubber.

9.2.6 *Friction Pendulum System (FPS)*

The FPS consists of a concave plate, a slider, sliding material, and a dust proof cover as shown in Figure 9.6a. It is based on the principle of pendulum motion and uses geometry and gravity to achieve the desired seismic isolation. The force–deformation behavior of the isolator is shown in Figure 9.6b. The secondary stiffness, K_2 is given by:

$$K_2 = \frac{W}{2R} \tag{9.13a}$$

$$R = g\left(\frac{T_d}{2\pi}\right)^2 \tag{9.13b}$$

in which W is the vertical load and R is the spherical radius of the sliding surface, and T_d is the target design period. The yield force of the curved plane sliding bearing, Q is determined from

$$Q = \mu W \tag{9.14}$$

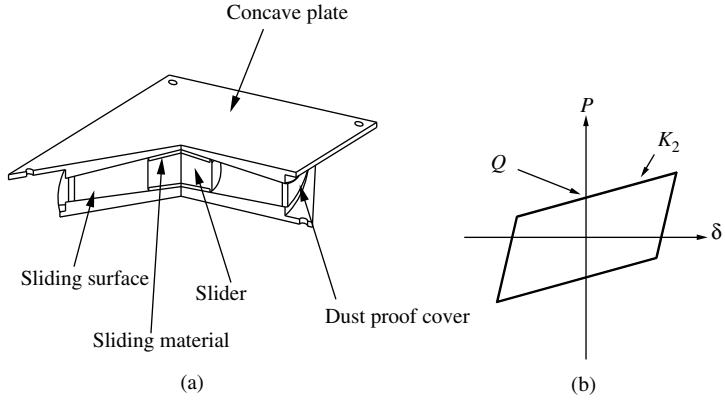

Figure 9.6 Curved plane sliding bearing (FPS): (a) section and elements; and (b) idealized force deformation behavior

in which μ is velocity and stress dependent. One of the empirical formulae to determine μ is given as:

$$\mu = [0.197 - 0.121 \exp(-0.009v)]\sigma^{-0.57} \tag{9.15}$$

in which v is the velocity and σ is the stress.

Equivalent stiffness is obtained as

$$K_{eq} = \frac{Q}{\gamma H} + K_2 \tag{9.16}$$

9.3 Base Isolators and their Characteristics

The load deformation behavior of the isolator is obtained from the experimental test and is modeled for theoretical analysis. The laboratory test is carried out under cyclic loading and the hysteresis loop obtained from the experimental test is used to characterize the isolator stiffness and damping. The isolator's equivalent stiffness envelope and the equivalent damping for different displacement levels are constructed from the experimental results for use in the design.

A general idealized load deformation curve for an isolator is shown in Figure 9.7a. An isolator is termed a linear isolator if the equivalent stiffness envelope is a straight line, as shown in Figure 9.7b. For a non-linear isolator, the equivalent stiffness envelope is not a straight line, but could be bi-linear or tri-linear (Figure 9.7c). The equivalent stiffness (secant stiffness) varies with displacement, and can be obtained for any displacement as shown in Figure 9.7c. Similarly, equivalent damping of a non-linear isolator also varies with deformation level. The equivalent stiffness and damping of an isolator can be computed by:

$$k_{eq} = \frac{F^+ - F^-}{\Delta^+ - \Delta^-} \tag{9.17a}$$

$$\xi_{eq} = \frac{1}{2\pi}\left[\frac{\text{area of loop}}{F_{max}\Delta_{max}}\right] \tag{9.17b}$$

in which Δ is the displacement shown in Figure 9.7a.

Typical variations of equivalent stiffness and damping with displacement are shown in Figure 9.8(a and b). An isolator is designed to have a desired equivalent stiffness and damping characteristics. Empirical expressions for k_{eq} and ξ_{eq} depending upon the material properties and characteristics of the isolator are also given in some texts [1,2]. Some of these expressions are given above.

Example 9.1

For a seven-storey building frame as shown in Figure 9.9, design the lead core laminated rubber bearings that satisfy the required criteria for practical implementation and manufacturing. The response spectrum to be used is shown in Figure 9.10. Take PGA = 0.36g and damping modification coefficient for 10% damping as 0.8.

Solution: The total vertical load on the isolators = 1750 kN. Maximum vertical reaction (R) is found under the interior column after gravity load analysis (dead + live) = 853.76 kN. Fixed base time period (T) of the frame is 0.875 s. A time separation of 3 is considered for the base isolated structure, that is, $T_b = 3T = 2.6$ s.

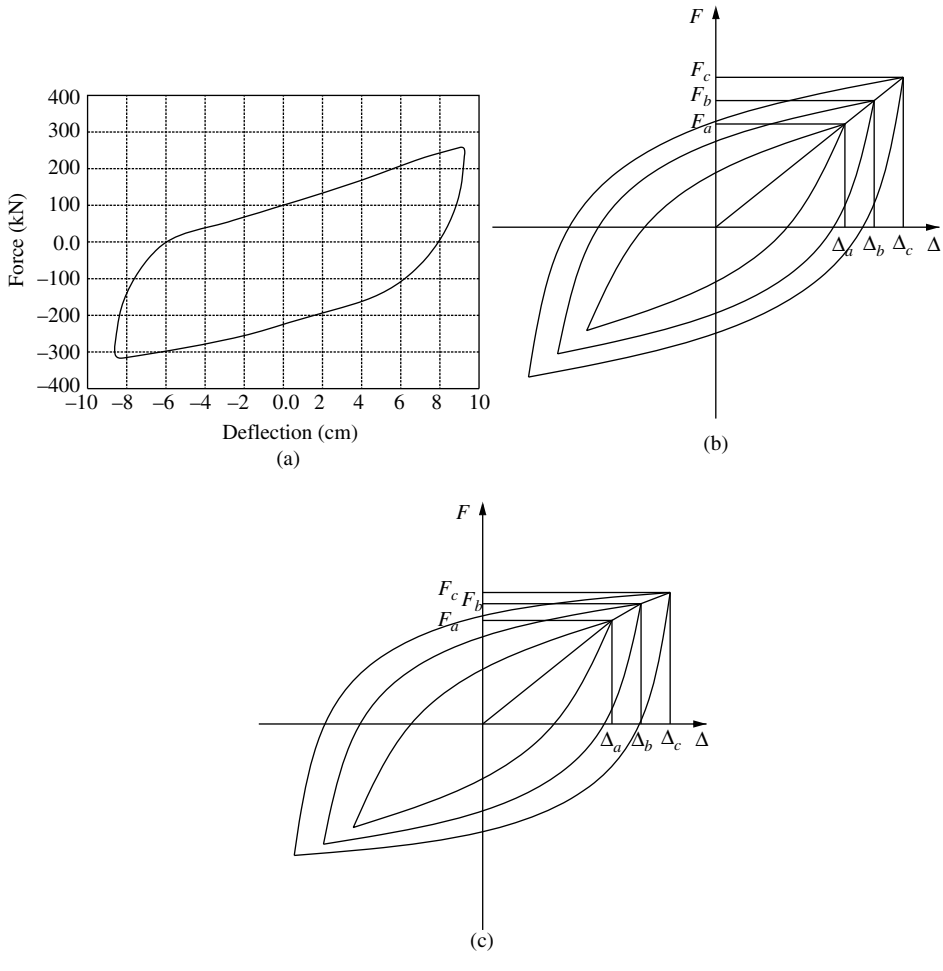

Figure 9.7 Load deformation curve of isolator under cyclic loading: (a) hysteretic curve; (b) linear isolator; and (c) non-linear (bilinear or trilinear, and so on.) isolators

From the maximum vertical reaction R and T_b, the effective stiffness of the isolator is

$$K_{\text{eff}} = \frac{R}{g}\frac{4\pi^2}{T_b^2} = 508.25\ \text{kN m}^{-1}$$

From the given response spectrum shown in Figure 9.10, the design (maximum) displacement of the isolator corresponding to the target time period is (for $\xi_{\text{eff}} = 10\%$),

$$S_d = \frac{S_a T_b^2}{4\pi^2} = 0.186\ \text{m}$$

Referring to Figure 9.11, the energy dissipation per cycle, W_D can be approximately calculated by assuming $Q \approx Q_{\max}$ for a very small post yield stiffness as [2]:

$$W_D = 2\pi K_{\text{eff}} S_d^2 \xi_{\text{eff}} \quad \text{and} \quad W_D = 4Q(S_d - D_y)$$

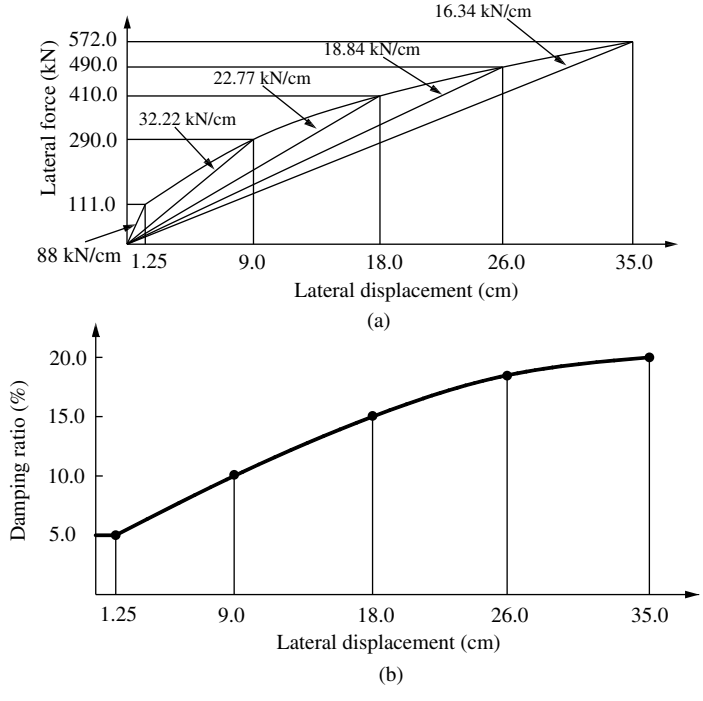

Figure 9.8 Variation of equivalent stiffness and damping with displacement: (a) stiffness variation; and (b) damping variation

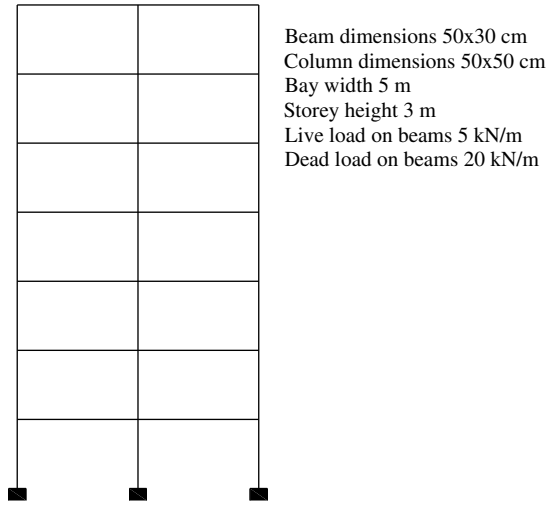

Figure 9.9 Properties of the base isolated frame

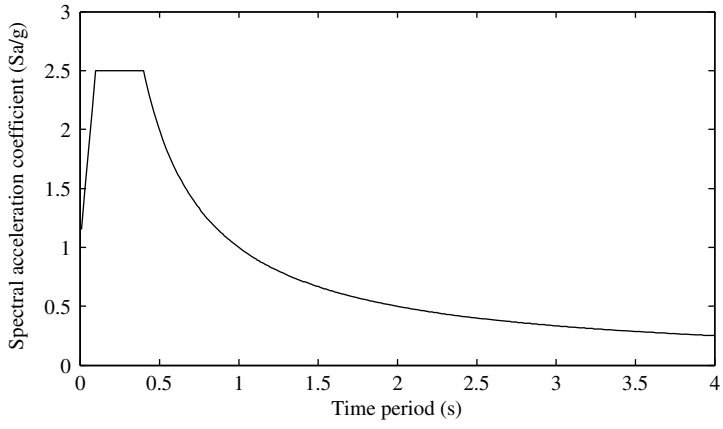

Figure 9.10 Acceleration response spectrum for 5% damping

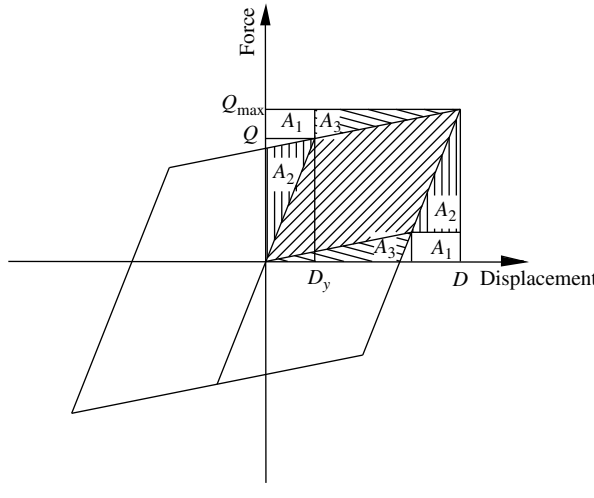

Figure 9.11 Idealized force–deformation plot for the isolator

in which $D_y = Q/K_u - K_d$ and $K_u \approx 10K_d$; K_u and K_d are the pre- and post-yield stiffness.

Neglecting D_y, a first approximation for the short term yield force Q_D is

$$Q_D = \frac{W_D}{4S_d} = \frac{\pi}{2} K_{\text{eff}} \xi_{\text{eff}} S_d = 14.86\,\text{kN}$$

As $S_d = \gamma H$, the post yield horizontal stiffness can be obtained as (Equation 9.8):

$$K_d = K_{\text{eff}} - \frac{Q_D}{S_d} = 428.42\,\text{kN m}^{-1}$$

Using the expression for D_y and the approximate value of K_u as given above, D_y can be calculated as:

$$D_y = \frac{Q_D}{9K_d} = 0.00385\,\text{m} \quad \text{and} \quad F_y = K_u \times D_y = 16.51\,\text{kN}$$

Correcting the first estimate of Q_D for D_y, gives

$$Q = \frac{W_D}{4(S_d - D_y)} = 15.71 \text{ kN}$$

9.3.1 Geometric Design

Assuming the material properties to be:

$$E = 4.45 \times 103 \text{ kN m}^{-2};\ \varepsilon_b = 500\%;\ G = 1.06 \times 10^3 \text{ kN m}^{-2};\ k = 0.57(\text{modification factor})$$

$$\text{Design shear strain } \gamma_{\max} = 50\%;\ \text{effective damping ratio } \xi_{\text{eff}} = 10\%$$

$$\text{Yield strength of lead core } f_{py} = 8.82 \times 10^3 \text{ kN m}^{-2}$$

$$\text{Allowable normal stress } \sigma_c = 7.84 \times 10^3 \text{ kN m}^{-2}$$

$$\text{Yield strength of steel plates } F_y = 2.74 \times 10^5 \text{ kN m}^{-2};\ F_s = 0.6\,F_y = 1.65 \times 10^5 \text{ kN m}^{-2}$$

Using Equations 9.10a–9.10e

$$\text{The lead plug area}, A_p = \frac{Q}{f_{py}} = 1.72 \times 10^{-3} \text{ m}^2;\ d_p = 0.047 \text{ m}$$

Use $d_p = 5$ cm

$$\text{Total height of the rubber layers}, H = \frac{S_d}{\gamma_{\max}} = 0.37 \text{ m}$$

Select the shape factor in such a way that $E(1 + 2kS^2)/G > 400$; $S > 9.09$; use $S = 10$. The compression modulus of rubber-steel composite,

$$E_c = E(1 + 2kS^2) = 511750 \text{ kN m}^{-2}.$$

The effective area A_0 of the bearing based on the allowable normal stress under the vertical load case:

$$\sigma_c = \frac{P_{DL+LL}}{A_0} \leq 7.84 \text{ kN m}^{-2};\ A_0 = 0.11 \text{ m}^2$$

Effective area A_1 from the shear strain condition for the vertical load case:

$$\gamma_{DL+LL} = 6S\frac{P_{DL+LL}}{E_c A_1} \leq \frac{\varepsilon_b}{3}$$

$$A_1 > 0.06 \text{ m}^2$$

K_d is related to K_r by

$$K_d = K_r\left(1 + 12\frac{A_p}{A_0}\right);\ K_r = 360.16 \text{ kN m}^{-1}$$

$$\text{Area of the rubber layer}, A = \frac{K_r H}{G} = 0.126 \text{ m}^2;\ d = 0.40 \text{ m}$$

$$\beta = 2\cos^{-1}\left(\frac{S_d}{d}\right) = 2.18; \quad A_{re} = \frac{d^2}{4}(\beta - \sin\beta) = 0.055 \text{ m}^2$$

$$A = \max(A_0, A_1, A_2) = 0.11 \text{ m}^2\ (A_2 \text{ is the same as } A_{re})$$

$d = 0.32$ m; use $d = 0.50$ m

$$A = 0.196\ \text{m}^2$$

$$\text{Single layer thickness: } S = \frac{d^2/4}{\pi d t} = \frac{d}{4t};\ t = 1.25\ \text{cm}$$

$$\text{Number of layers: } N = \frac{H}{t} = 29.8;\ \text{use } N = 30$$

Steel plate thickness,

$$t_s \geq \frac{2(t_i + t_{i+1})(DL + LL)}{A_{re} F_s} \geq 2\ \text{mm}$$

in which t_i and t_{i+1} are the thicknesses of the rubber layers on the top and the bottom of the steel plate.

Use $t_s = 2.5$ mm

Total height of the isolator, $h = H + N \times t_s + 2$ (cover plate thickness) $= 41.49$ cm.

Diameter of the cover plate is taken as 60 cm > diameter of the rubber core (50 cm).

According to the design shown above, the final dimensions of different components of the base isolator are shown in Figure 9.12.

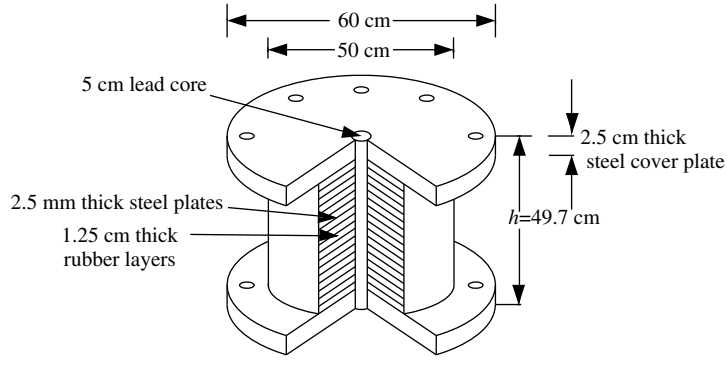

Figure 9.12 Design dimensions of the lead core rubber bearing

9.4 Analysis of Base Isolated Buildings

For the analysis of base isolated buildings, two types of base isolation are considered namely, base isolation at the isolated footings (Figure 9.13) and base isolation with a base slab (Figure 9.14a).

For base isolation at the isolated footings, the bottom end of the column is idealized as shown in Figure 9.13b. The lateral non-linear springs have the force–deformation behavior under cyclic loading the same as that of the isolator. For base isolation with a raft, three reactive forces are assumed to act corresponding to the three degrees of freedom at the center of mass of the raft. These three reactive forces are the resultants of the forces developed in each isolator due to the deformations of the isolators produced by the base motion (Figure 9.14b). These three reactive forces may or may not be coupled depending upon the spatial distribution and characteristics of each isolator. The lower ends of the columns may be assumed to be fixed against rotation about the horizontal axes.

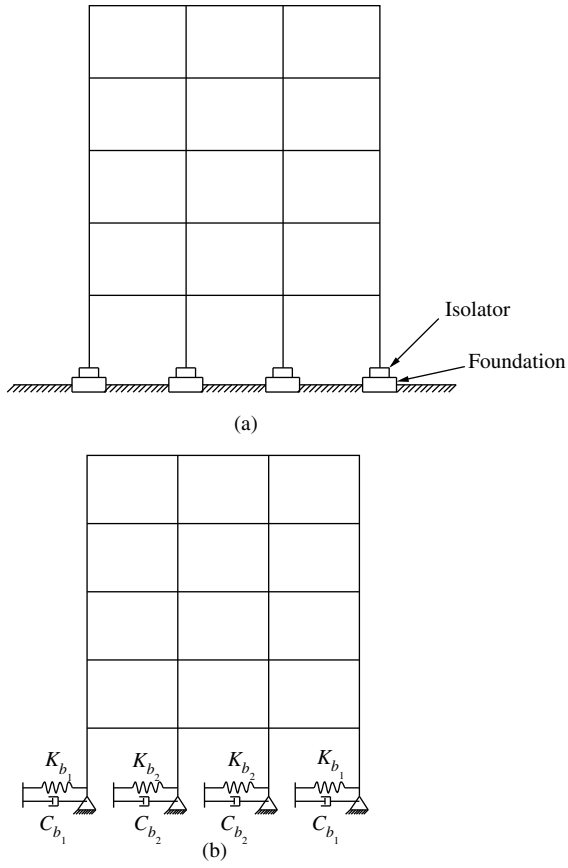

Figure 9.13 Base isolation at the isolated footings: (a) isolators in position; and (b) mathematical model with effective stiffness and damping

9.4.1 Analysis of Base Isolated Buildings with Isolated Footings

Since the force–deformation behavior of the isolators can mostly be idealized as bilinear, the backbone curve of the isolator at the base may be considered as that shown in Figure 9.15b. The other possible variations of the backbone curves are shown in Figure 9.15(c and d). The equation of motion for a multi-storey 2D frame with base flexibility can be written in incremental form of

$$\begin{bmatrix} \boldsymbol{m}_{ss} & \boldsymbol{m}_{sb} \\ \boldsymbol{m}_{bs} & \boldsymbol{m}_{bb} \end{bmatrix} \begin{Bmatrix} \Delta\ddot{\boldsymbol{v}}_s^t \\ \Delta\ddot{\boldsymbol{v}}_b^t \end{Bmatrix} + \begin{bmatrix} \boldsymbol{c}_{ss} & \boldsymbol{c}_{sb} \\ \boldsymbol{c}_{bs} & \boldsymbol{c}_{bb} \end{bmatrix} \begin{Bmatrix} \Delta\dot{\boldsymbol{v}}_s^t \\ \Delta\dot{\boldsymbol{v}}_b^t \end{Bmatrix} + \begin{bmatrix} \boldsymbol{k}_{ss} & \boldsymbol{k}_{sb} \\ \boldsymbol{k}_{bs} & \boldsymbol{k}_{bb} \end{bmatrix} \begin{Bmatrix} \Delta\boldsymbol{v}_s^t \\ \Delta\boldsymbol{v}_b^t \end{Bmatrix} + \begin{bmatrix} 0 & 0 \\ 0 & \overline{\boldsymbol{k}}_{bb} \end{bmatrix} \begin{Bmatrix} \Delta\boldsymbol{v}_s \\ \Delta\boldsymbol{v}_b \end{Bmatrix} = \begin{Bmatrix} 0 \\ 0 \end{Bmatrix} \tag{9.18}$$

in which $\boldsymbol{m}_{ss}$ and $\boldsymbol{m}_{bb}$ are the diagonal matrices corresponding to the non-support ($\boldsymbol{v}_s$) and base ($\boldsymbol{v}_b$) degrees of freedom, respectively. In a similar way, elements of the damping and stiffness matrices may be defined. $\overline{\boldsymbol{k}}_{bb}$ is a diagonal or a non-diagonal matrix of the size equal to the number of base degrees of freedom. Elements of the matrix are determined from the tangent stiffness of the base isolators corresponding to the displacements of the lateral degrees of freedom.

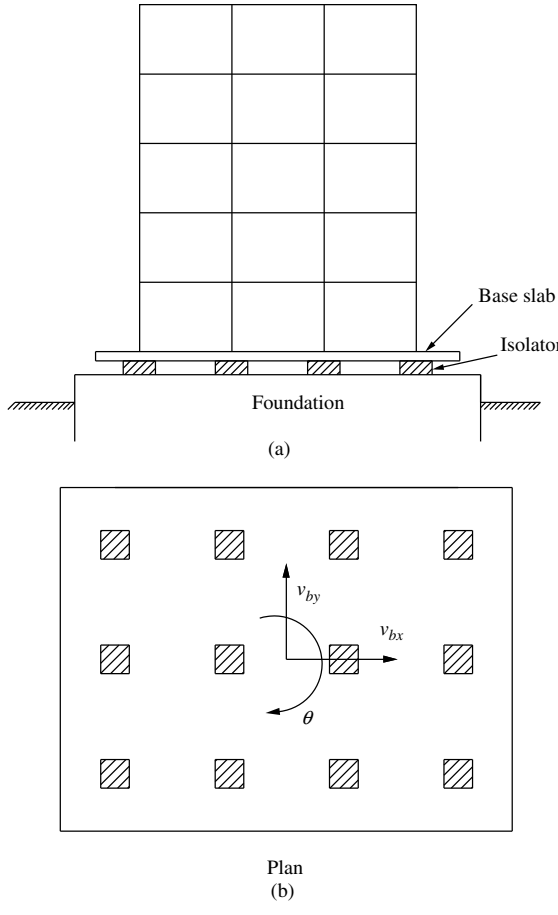

Figure 9.14 Base isolation with a raft: (a) isolators in position; and (b) based degrees of freedom

The total incremental displacements are given by:

$$\Delta \boldsymbol{v}_s^t = \Delta \boldsymbol{v}_s + \Delta \boldsymbol{v}_{sg} \tag{9.19a}$$

$$\Delta \boldsymbol{v}_b^t = \Delta \boldsymbol{v}_b + \Delta \boldsymbol{v}_g \tag{9.19b}$$

in which $\Delta \boldsymbol{v}_s$ and $\Delta \boldsymbol{v}_b$ are the dynamic displacements with respect to the support; $\Delta \boldsymbol{v}_g$ are the ground displacements, and $\Delta \boldsymbol{v}_{sg}$ are the quasi-static displacements produced at the non-support degrees of freedom (DOF) due to the movements of the support DOF. Substituting for $\Delta \boldsymbol{v}_s^t$ and $\Delta \boldsymbol{v}_b^t$ in Equation 9.18 and putting $\boldsymbol{m}_{sb}$ and $\boldsymbol{m}_{bs}$ as zero, the resulting equations of motion become

$$\begin{aligned}
&\begin{bmatrix} \boldsymbol{m}_{ss} & 0 \\ 0 & \boldsymbol{m}_{bb} \end{bmatrix} \begin{Bmatrix} \Delta \ddot{\boldsymbol{v}}_s \\ \Delta \ddot{\boldsymbol{v}}_b \end{Bmatrix} + \begin{bmatrix} \boldsymbol{c}_{ss} & \boldsymbol{c}_{sb} \\ \boldsymbol{c}_{bs} & \boldsymbol{c}_{bb} \end{bmatrix} \begin{Bmatrix} \Delta \dot{\boldsymbol{v}}_s \\ \Delta \dot{\boldsymbol{v}}_b \end{Bmatrix} + \begin{bmatrix} \boldsymbol{k}_{ss} & \boldsymbol{k}_{sb} \\ \boldsymbol{k}_{bs} & \boldsymbol{k}_{bb} + \overline{\boldsymbol{k}}_{bb} \end{bmatrix} \begin{Bmatrix} \Delta \boldsymbol{v}_s \\ \Delta \boldsymbol{v}_b \end{Bmatrix} \\
&= -\begin{bmatrix} \boldsymbol{m}_{ss} & 0 \\ 0 & \boldsymbol{m}_{bb} \end{bmatrix} \begin{Bmatrix} \Delta \ddot{\boldsymbol{v}}_{sg} \\ \Delta \ddot{\boldsymbol{v}}_g \end{Bmatrix} - \begin{bmatrix} \boldsymbol{c}_{ss} & \boldsymbol{c}_{sb} \\ \boldsymbol{c}_{bs} & \boldsymbol{c}_{bb} \end{bmatrix} \begin{Bmatrix} \Delta \dot{\boldsymbol{v}}_{sg} \\ \Delta \dot{\boldsymbol{v}}_g \end{Bmatrix} - \begin{bmatrix} \boldsymbol{k}_{ss} & \boldsymbol{k}_{sb} \\ \boldsymbol{k}_{bs} & \boldsymbol{k}_{bb} \end{bmatrix} \begin{Bmatrix} \Delta \boldsymbol{v}_{sg} \\ \Delta \boldsymbol{v}_g \end{Bmatrix}
\end{aligned} \tag{9.20}$$

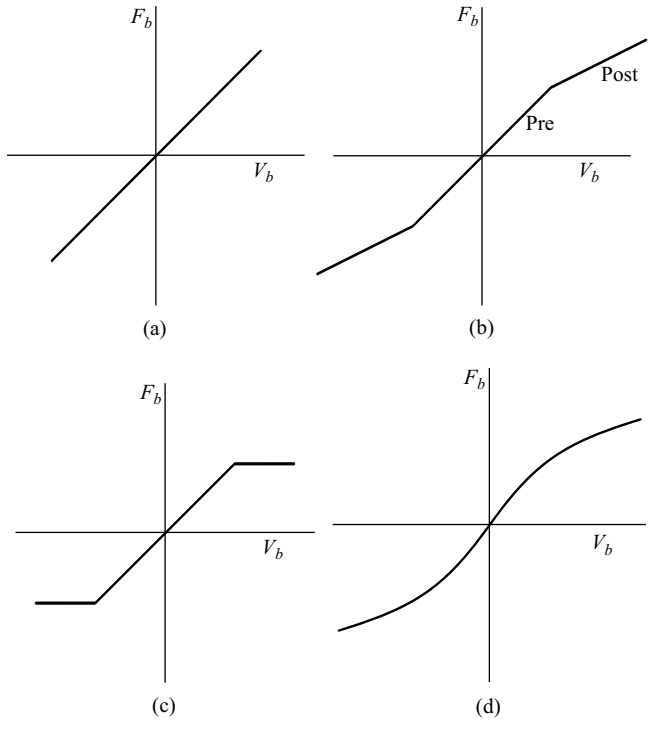

Figure 9.15 Backbone curves for the isolators: (a) linear; (b) bilinear; (c) elastoplastic; and (d) non-linear

Equation 9.20 may be split into two equations:

$$\boldsymbol{m}_{ss}\Delta\ddot{\boldsymbol{v}}_s + \boldsymbol{c}_{ss}\Delta\dot{\boldsymbol{v}}_s + \boldsymbol{c}_{sb}\Delta\dot{\boldsymbol{v}}_b + \boldsymbol{k}_{ss}\Delta\boldsymbol{v}_s + \boldsymbol{k}_{sb}\Delta\boldsymbol{v}_b = -\boldsymbol{m}_{ss}\Delta\ddot{\boldsymbol{v}}_{sg} - \boldsymbol{c}_{ss}\Delta\dot{\boldsymbol{v}}_{sg} - \boldsymbol{c}_{sb}\Delta\dot{\boldsymbol{v}}_g - \boldsymbol{k}_{ss}\Delta\boldsymbol{v}_{sg} - \boldsymbol{k}_{sb}\Delta\boldsymbol{v}_g \quad (9.21)$$

$$\boldsymbol{m}_{bb}\Delta\ddot{\boldsymbol{v}}_b + \boldsymbol{c}_{bs}\Delta\dot{\boldsymbol{v}}_s + \boldsymbol{c}_{bb}\Delta\dot{\boldsymbol{v}}_b + \boldsymbol{k}_{bs}\Delta\boldsymbol{v}_s + (\boldsymbol{k}_{bb} + \overline{\boldsymbol{k}}_{bb})\Delta\boldsymbol{v}_b = -\boldsymbol{m}_{bb}\Delta\ddot{\boldsymbol{v}}_g - \boldsymbol{c}_{sb}\Delta\dot{\boldsymbol{v}}_{sg} - \boldsymbol{c}_{bb}\Delta\dot{\boldsymbol{v}}_g - \boldsymbol{k}_{bs}\Delta\boldsymbol{v}_{sg} - \boldsymbol{k}_{bb}\Delta\boldsymbol{v}_g \quad (9.22)$$

Equation 9.21 can be written as:

$$\boldsymbol{m}_{ss}\Delta\ddot{\boldsymbol{v}}_b + \boldsymbol{c}_{ss}\Delta\dot{\boldsymbol{v}}_s + \boldsymbol{k}_{ss}\Delta\boldsymbol{v}_s + \boldsymbol{k}_{sb}\Delta\boldsymbol{v}_b = -\boldsymbol{m}_{ss}\Delta\ddot{\boldsymbol{v}}_{sg} = -\boldsymbol{m}_{ss}\boldsymbol{r}\Delta\ddot{\boldsymbol{v}}_g \quad (9.23a)$$

in which

$$\boldsymbol{r} = -\boldsymbol{k}_{ss}^{-1}\boldsymbol{k}_{sb} \quad (9.23b)$$

and $\boldsymbol{c}_{sb}$, that is, the coupling term in the damping matrix between support and non-support degrees of freedom, and the effect of damping terms on the right-hand side of the equation are ignored as explained in Chapter 3.

By considering $\boldsymbol{k}_{bs}\Delta\boldsymbol{v}_{sg} + \boldsymbol{k}_{bb}\Delta\boldsymbol{v}_g = 0$ for the quasi-static analysis of the superstructure due to the movement of the supports (isolators not undergoing any dynamic motion), Equation 9.22 can be written as:

$$\boldsymbol{m}_{bb}\Delta\ddot{\boldsymbol{v}}_b + c_{bb}\Delta\dot{\boldsymbol{v}}_b + \boldsymbol{k}_{bs}\Delta\boldsymbol{v}_s + (\boldsymbol{k}_{bb} + \overline{\boldsymbol{k}}_{bb})\Delta\boldsymbol{v}_b = -\boldsymbol{m}_{bb}\Delta\ddot{\boldsymbol{v}}_g \quad (9.24)$$

Equations 9.23a and 9.24 can now be combined to give

$$\begin{bmatrix} \boldsymbol{m}_{ss} & 0 \\ 0 & \boldsymbol{m}_{bb} \end{bmatrix} \begin{Bmatrix} \Delta\ddot{\boldsymbol{v}}_s \\ \Delta\ddot{\boldsymbol{v}}_b \end{Bmatrix} + \begin{bmatrix} \boldsymbol{c}_{ss} & 0 \\ 0 & \boldsymbol{c}_{bb} \end{bmatrix} \begin{Bmatrix} \Delta\dot{\boldsymbol{v}}_s \\ \Delta\dot{\boldsymbol{v}}_b \end{Bmatrix} + \begin{bmatrix} \boldsymbol{k}_{ss} & \boldsymbol{k}_{sb} \\ \boldsymbol{k}_{bs} & \boldsymbol{k}_{bb} + \overline{\boldsymbol{k}}_{bb} \end{bmatrix} \begin{Bmatrix} \Delta\boldsymbol{v}_s \\ \Delta\boldsymbol{v}_b \end{Bmatrix} = -\begin{bmatrix} \boldsymbol{r}\boldsymbol{m}_{ss} \\ \boldsymbol{m}_{bb} \end{bmatrix} \Delta\ddot{\boldsymbol{v}}_g = \boldsymbol{p}(t) \tag{9.25}$$

in which $\boldsymbol{c}_{bb}$ is the linear damping of the isolator. In many problems, $\boldsymbol{c}_{bb}$ is neglected, and therefore the damping matrix consists of the damping matrix of the superstructure. Furthermore, when the ground motion is assumed to be the same for all supports, the influence coefficient matrix becomes a vector of unity. Then, the right-hand side of Equation 9.25 becomes

$$\boldsymbol{p}(t) = -\begin{bmatrix} \boldsymbol{m}_{ss} & 0 \\ 0 & \boldsymbol{m}_{bb} \end{bmatrix} \{\boldsymbol{I}\} \Delta\ddot{v}_g \tag{9.26}$$

in which $\Delta\ddot{v}_g$ is the same ground acceleration at all supports.

9.4.2 Method of Solution

For buildings, the ground motion is generally assumed to be the same for all supports, and therefore Equations 9.25 and 9.26 are solved to find the response of base isolated buildings. The solution of the incremental equation of motion provides $\boldsymbol{v}_s$ and $\boldsymbol{v}_b$. In order to obtain the solution, the incremental equations are solved in the same way as explained in Chapter 6. At each incremental step, $\overline{\boldsymbol{k}}_{bb}$ is only changed depending upon the displacements of the isolators; the rest of the stiffness sub-matrices remain the same as the building frame does not enter into an inelastic state. As the force–displacement behavior of most of the isolators can be idealized as bilinear (including friction isolators), the method of solution outlined in Chapter 6 can be used, with the only change being that beyond the initial yielding, $\overline{\boldsymbol{k}}_{bb}$ is not taken equal to zero but is set to a value depending upon the post- to pre-yielding ratio (< 1).

For the NZ system, which does not exhibit bilinear hysteresis, the same method of solution may be used. During loading, the tangent stiffness of the isolator at the beginning of the increment is used for the incremental time step. During unloading, the initial tangent stiffness of the isolator is used over the incremental time step. Iterations may be required at an incremental time step when the transition from loading to unloading takes place. The procedure is described in Chapter 6.

Example 9.2

The same building frame as shown in Figure 9.9 is subjected to the El Centro earthquake. The columns of the frame are connected to the isolators resting on isolated footings. The backbone curve, that is, the envelope curve showing the force–displacement behavior of the isolators is shown in Figure 9.16. Obtain the time histories of the top displacement of the frame, the base isolator displacement, and the base shear for the right outer column.

Solution: As no moment is transferred to the isolator, the bases of the columns resting on the isolator are assumed to be hinged. The mass of the isolators is taken to be negligible. The stiffness matrix of the frame corresponding to only the sway degrees of freedom is given by:

$$\boldsymbol{K} = \begin{bmatrix} \boldsymbol{K}_{ss} & \boldsymbol{K}_{sb} \\ \boldsymbol{K}_{bs} & \boldsymbol{K}_{bb} \end{bmatrix}$$

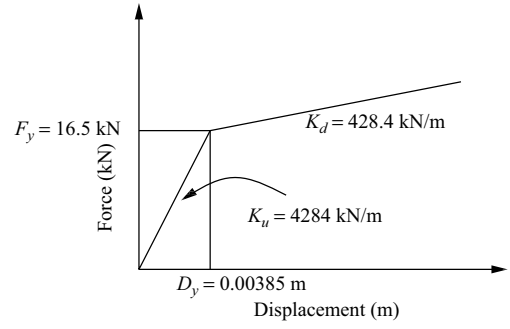

Figure 9.16 Backbone curve of the isolator

$$\boldsymbol{K} = 10^5 x \left[\begin{array}{ccccccc|c} 1.492 & & & & & & & \\ -1.711 & 3.421 & & & & & & \\ 0.281 & -1.992 & 3.421 & & & sym & & \\ -0.085 & 0.313 & -1.742 & 2.84 & & & & \\ -0.172 & 0.221 & -0.221 & -0.96 & 2.281 & & & \\ 0.201 & -0.258 & 0.258 & 0-0.587 & -0.962 & 3.092 & & \\ -0.004 & 0.006 & -0.006 & 0.231 & 0-0.198 & -1.822 & 2.281 & \\ \hline 0 & 0 & 0 & 0 & 0 & 0 & -0.431 & 0.431 \end{array}\right] \text{kN m}^{-1}$$

In forming the above matrix, it is assumed that all column bases move by the same amount at every instant of time, t. Therefore, there is effectively one base degree of freedom at the base. The stiffness matrix for the isolated structure is obtained by adding the total stiffness of the isolators to the last diagonal term. Note that this added stiffness varies with the displacement according to the load displacement behavior of the isolator.

Fundamental time period of fixed base building is computed to be 0.875 s.
Fundamental time period of the isolated structure is assumed to be 2.6 s.
Damping of the isolator is assumed to be 10%.

The $\boldsymbol{C}_{ss}$ matrix for the structure is obtained by assuming Rayleigh damping with coefficients (determined using the first two modes of the structure having $\boldsymbol{K}$ as $\boldsymbol{K}_{ss}$) as $\alpha = 0.6758$; $\beta = 0.00267$. The $\boldsymbol{C}$ matrix of the isolated structure is obtained as:

$$\boldsymbol{C} = \begin{bmatrix} \boldsymbol{C}_{ss} & 0 \\ 0 & \overline{C}_{bb} \end{bmatrix}$$

$$\boldsymbol{C} = 10^4 x \left[\begin{array}{ccccccc|c} 1.9951 & & & & & & & \\ -0.0003 & 1.9952 & & & & & & \\ 0.0001 & -0.0004 & 1.9952 & & & sym & & \\ 0 & 0.0001 & -0.0003 & 1.9952 & & & & \\ 0 & 0 & 0 & -0.0002 & 1.9952 & & & \\ 0 & 0 & 0 & -0.0001 & -0.0002 & 1.9952 & & \\ 0 & 0 & 0 & 0 & 0 & -0.0003 & 1.9952 & \\ \hline 0 & 0 & 0 & 0 & 0 & 0 & 0 & 8.10 \end{array}\right]$$

$\overline{\boldsymbol{C}}_{bb}$ is the effective damping of the isolator for linear analysis. In the case of non-linear analysis, the damping of the isolators is generally taken as that provided by the hysteretic effect. Thus, once the backbone curves of the isolators are specified for non-linear analysis, the $\overline{\boldsymbol{C}}_{bb}$ part of the matrix $\boldsymbol{C}$ is set to zero.

The equation of motion given by Equations 9.25 and 9.26 are solved using numerical integration, explained in Chapter 6. Bi-direction interaction of yielding of isolators is not considered. Here, the integration is performed using SAP 2000 with $\Delta t = 0.02$ sec. The required SAP inputs are

1. Properties of the frame.
2. End connection of the columns with the isolators.
3. Backbone curves of the isolators (force versus displacement envelope curve) in terms of initial stiffness, yield force, and post-yield stiffness ratio.
4. The time history of ground acceleration.

The isolators are placed just below the columns as shown in Figure 9.17.

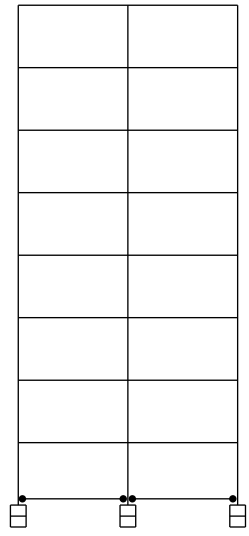

Figure 9.17 Model of the base isolated frame

The time histories of the uncontrolled and controlled (isolated) top floor displacements are shown in Figure 9.18. It is seen from the figure that there is ~46% reduction in top floor displacement. Figure 9.19 compares the time histories of controlled and uncontrolled base shears of the right outer column. It is seen from the figure that there is 80% reduction in the base shear. Figure 9.20 shows the time history of isolator displacements (all isolators have the same time histories). The maximum base displacement is 6.3 cm.

9.4.3 Analysis of Base Isolated Building with Base Slab

A model of a base isolated building with a base slab is shown in Figure 9.14a. The base slab rests over a number of isolators. All isolators may not have the same load-deformation behavior. Therefore, even under unidirectional ground motion, the base slab undergoes three motions at the base as shown in Figure 9.14b. The restoring action to these three motions are provided by the base isolators. The dynamic degrees of freedom of the superstructure are defined as shown in Figure 9.14a. The equations of motion

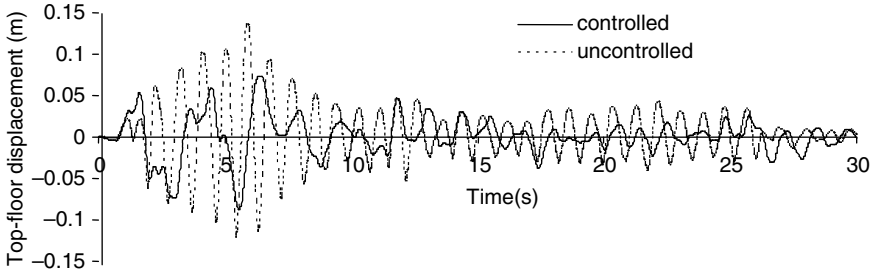

Figure 9.18 Comparison between controlled and uncontrolled top-floor displacements

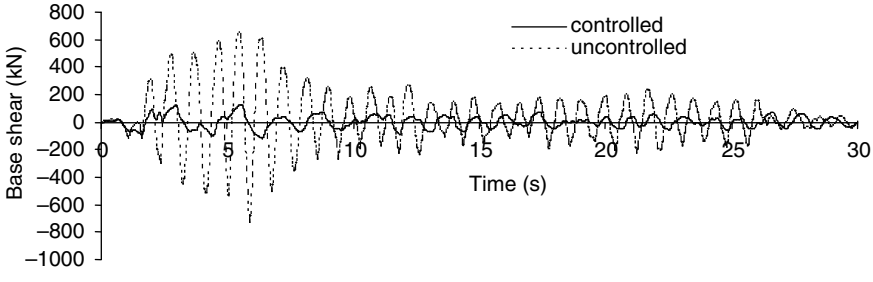

Figure 9.19 Comparison between controlled and uncontrolled base shear

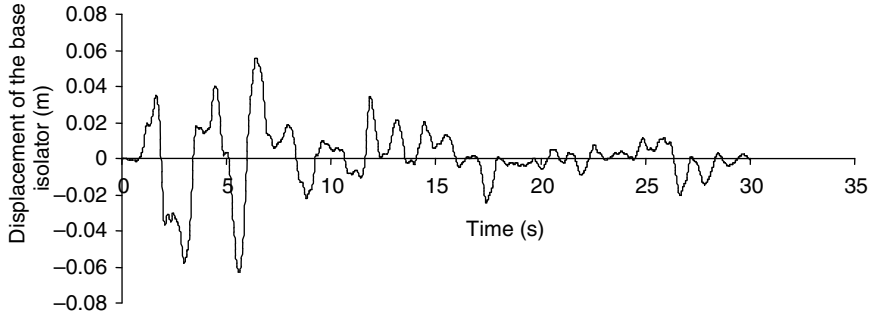

Figure 9.20 Time history of displacement of the base isolator

take the form

$$\boldsymbol{M}\ddot{\boldsymbol{v}}^t + \boldsymbol{C}\dot{\boldsymbol{v}} + \boldsymbol{K}\boldsymbol{v} = 0 \tag{9.27}$$

$$\boldsymbol{M}_b\ddot{\boldsymbol{v}}_{bg} + \boldsymbol{C}\dot{\boldsymbol{v}}_b + \boldsymbol{R} - \overline{\boldsymbol{V}} = 0 \tag{9.28}$$

in which $\boldsymbol{M}$, $\boldsymbol{C}$, and $\boldsymbol{K}$ are, respectively, the mass, damping, and stiffness matrices corresponding to the dynamic degrees of freedom of the superstructure; $\boldsymbol{v}$ is the relative displacement vector of the superstructure with respect to the base slab; $\boldsymbol{v}_b$ is the vector of the displacement of the base slab due to the displacement of the isolators; $\boldsymbol{R}$ is the restoring force vector provided by the isolators; and $\overline{\boldsymbol{V}}$, $\boldsymbol{v}^t$ and

$\boldsymbol{v}_{bg}$ are defined by:

$$\overline{\boldsymbol{V}} = \boldsymbol{C}\dot{\boldsymbol{v}} + \boldsymbol{K}\boldsymbol{v} \tag{9.29}$$

$$\boldsymbol{v}^t = \boldsymbol{v} + \boldsymbol{I}_b\boldsymbol{v}_b + \boldsymbol{I}\boldsymbol{v}_g \tag{9.30a}$$

$$\boldsymbol{v}_{bg} = \boldsymbol{v}_b + \boldsymbol{I}\boldsymbol{v}_g \tag{9.30b}$$

Substituting for $\boldsymbol{v}^t$ and $\boldsymbol{v}_{bg}$ in Equations 9.27 and 9.28, the equations of motion take the form

$$\boldsymbol{M}\ddot{\boldsymbol{v}} + \boldsymbol{C}\dot{\boldsymbol{v}} + \boldsymbol{K}\boldsymbol{v} = -\boldsymbol{M}\boldsymbol{I}\ddot{\boldsymbol{v}}_g - \boldsymbol{M}\boldsymbol{I}_b\ddot{\boldsymbol{v}}_b \tag{9.31}$$

$$\boldsymbol{M}_b\ddot{\boldsymbol{v}}_b + \boldsymbol{C}_b\dot{\boldsymbol{v}}_b + \boldsymbol{R} - \overline{\boldsymbol{V}} = -\boldsymbol{M}_b\boldsymbol{I}\ddot{\boldsymbol{v}}_g \tag{9.32}$$

in which $\boldsymbol{I}$ and $\boldsymbol{I}_b$ are appropriate influence coefficient matrices/vectors; for a two component earthquake $\ddot{\boldsymbol{v}}_g = [\ddot{\boldsymbol{v}}_{gx},\ \ddot{\boldsymbol{v}}_{gy}]$, and for a single component earthquake $\ddot{\boldsymbol{v}}_g$ is a scalar. The restoring force vector $\boldsymbol{R}$ is obtained from the force–deformation behavior of the isolators. The restoring forces F_{xi} and F_{yi} of the ith isolator are given by the relationship

$$\begin{Bmatrix} F_{xi} \\ F_{yi} \end{Bmatrix} = \alpha K_{oi} \begin{Bmatrix} u_{xi} \\ u_{yi} \end{Bmatrix} + (1-\alpha) K_{oi} q_i \begin{Bmatrix} z_{xi} \\ z_{yi} \end{Bmatrix} \tag{9.33}$$

In abbreviated form, Equation 9.33 may be written as:

$$\boldsymbol{F}_i = \alpha K_{oi}\boldsymbol{u}_i + (1-\alpha) K_{oi}\boldsymbol{z}_i q_i \tag{9.34}$$

in which u_{xi} and u_{yi} are the lateral displacements of the ith isolator; z_{xi} and z_{yi} are the hysteretic displacement components of restoring forces in the x- and y-directions, respectively; α is the post- to pre-yielding stiffness ratio; K_{oi} is the initial stiffness $= Q_i/q_i$; Q_i and q_i are the yield force and yield displacement of the ith isolator, respectively; z_{xi} and z_{yi} are the hysteretic displacement components and satisfy the following coupled non-linear differential equations:

$$\boldsymbol{z}_i = \boldsymbol{G}_i\dot{\boldsymbol{u}}_i \tag{9.35a}$$

$$\boldsymbol{G}_i = \begin{bmatrix} A - \beta\,\mathrm{sgn}(\dot{u}_{\mathrm{xi}})|\boldsymbol{z}_{xi}|\boldsymbol{z}_{xi} - \tau\boldsymbol{z}_{xi}^2 & -\beta\,\mathrm{sgn}(\dot{u}_{yi})\big|\boldsymbol{z}_{yi}\big|\boldsymbol{z}_{xi} - \tau\boldsymbol{z}_{yi}\boldsymbol{z}_{xi} \\ -\beta\,\mathrm{sgn}(\dot{u}_{xi})|\boldsymbol{z}_{xi}|\boldsymbol{z}_{yi} - \tau\boldsymbol{z}_{xi}\boldsymbol{z}_{yi} & A - \beta\,\mathrm{sgn}(\dot{u}_{yi})\big|\boldsymbol{z}_{yi}\big|\boldsymbol{z}_{yi} - \tau\boldsymbol{z}_{yi}^2 \end{bmatrix} \tag{9.35b}$$

in which β, τ, and A are the parameters that control the shape and size of the hysteresis loop and sgn denotes signum function.

By properly selecting the parameters Q, q, α, β, τ, and A, the force–deformation behavior of different types of isolators may be modeled. The sum of the initial stiffness of the isolators corresponding to the base degrees of freedom (Figure 9.14b) is

$$K_{bx} = K_{by} = \sum_i K_{oi} \tag{9.36}$$

$$K_{b\theta} = \sum_i K_{oi}x_i^2 + K_{oi}y_i^2 \tag{9.37}$$

The uncoupled base isolation frequencies of the isolator based on initial stiffness are

$$\omega_{bx} = \omega_{by} = \sqrt{\frac{K_{bx}}{\sum_j m_j + M_b}} \tag{9.38}$$

$$\omega_{b\theta} = \sqrt{\frac{K_{b\theta}}{\sum_j m_j r_j^2 + M_b r_b^2}} \tag{9.39}$$

in which j is the floor number; m_j is the floor mass; M_b is the base mass; r_j is the radius of gyration for the jth floor mass; and r_b is the radius of gyration of base mass. The restoring force vector for the three base

degrees of freedom changes with the isolator displacements, which are governed by Equation 9.35a. As a result, the equations of motion are solved in incremental form. The incremental equations may be written as:

$$\boldsymbol{M}\{\Delta\ddot{\boldsymbol{v}}+\boldsymbol{I}_b\Delta\ddot{\boldsymbol{v}}_b\}+\boldsymbol{C}\Delta\dot{\boldsymbol{v}}+\boldsymbol{K}\Delta\boldsymbol{v}=-\boldsymbol{M}\boldsymbol{I}\Delta\ddot{v}_g \tag{9.40}$$

$$\boldsymbol{M}_b\Delta\ddot{\boldsymbol{v}}_b+\boldsymbol{C}_b\Delta\dot{\boldsymbol{v}}_b+\Delta\boldsymbol{R}-\Delta\overline{\boldsymbol{V}}=-\boldsymbol{M}_b\boldsymbol{I}\Delta\ddot{v}_g \tag{9.41}$$

Because the isolator stiffness change with displacements, and also during loading and unloading, $\Delta\boldsymbol{R}$ over the increment is obtained based on the tangent stiffness of the isolator and a pseudo force vector. In general, $\Delta\boldsymbol{R}$ can be split into two parts, that is,

$$\Delta\boldsymbol{R}=\boldsymbol{K}_t\Delta\boldsymbol{v}_b+\Delta\boldsymbol{R}_s \tag{9.42}$$

$\boldsymbol{K}_t$ and $\Delta\boldsymbol{R}_s$ are given by

$$\boldsymbol{K}_t=\sum_i \boldsymbol{T}_i^T\boldsymbol{R}_{ti}\boldsymbol{T}_i \tag{9.43}$$

in which

$$\boldsymbol{R}_{ti}=\text{diag}\,(\alpha K_{oi,}\alpha K_{oi,}) \tag{9.44}$$

$$\boldsymbol{T}_i=\begin{bmatrix}1 & 0 & -y_i\\ 0 & 1 & x_i\end{bmatrix} \tag{9.45}$$

where x_i and y_i are the x and y coordinates of the ith isolator.

Similarly,

$$\Delta\boldsymbol{R}_s=\sum_i \boldsymbol{T}_i^T\boldsymbol{R}_{si}\boldsymbol{T}_i \tag{9.46}$$

in which

$$\boldsymbol{R}_{si}=\text{diag}\,[(1-\alpha)qK_{oi}\Delta z_{xi},\ (1-\alpha)qK_{oi}\Delta z_{yi}] \tag{9.47}$$

As the computation of $\Delta\boldsymbol{R}$ involves the hysteretic displacement component $\Delta\boldsymbol{z}$ of each isolator for incremental displacement vector $\Delta\boldsymbol{v}_b$, an iterative procedure is required at every increment of the solution. The steps of the procedure are summarized at the end of this section [3].

To solve Equations 9.40 and 9.41, Newmark's method is used with incremental vector $\Delta\ddot{\boldsymbol{v}}$ and $\Delta\dot{\boldsymbol{v}}$ given as:

$$\Delta\ddot{\boldsymbol{v}}=a_0\Delta\boldsymbol{v}+a_1\dot{\boldsymbol{v}}(t)+a_2\ddot{\boldsymbol{v}}(t) \tag{9.48}$$

$$\Delta\dot{\boldsymbol{v}}=b_0\Delta\boldsymbol{v}+b_1\dot{\boldsymbol{v}}(t)+b_2\ddot{\boldsymbol{v}}(t) \tag{9.49}$$

in which

$$a_0=\frac{6}{(\Delta t)^2};\ a_1=-\frac{6}{\Delta t};\ a_2=-3;\ b_0=-\frac{3}{\Delta t};\ b_1=-3;\ b_2=-\frac{\Delta t}{2}$$

Similarly, $\Delta\ddot{\boldsymbol{v}}_b$ and $\Delta\dot{\boldsymbol{v}}_b$ can be obtained in terms of $\Delta\boldsymbol{v}_b$, $\dot{\boldsymbol{v}}_b(t)$, and $\ddot{\boldsymbol{v}}_b(t)$; note that $\dot{\boldsymbol{v}}(t)$, $\dot{\boldsymbol{v}}_b(t)$, and so on, denote velocities at the previous time station.

Using Equations 9.48 and 9.49, Equations 9.40 and 9.41 can be written as:

$$\begin{bmatrix}\boldsymbol{K}_{vv} & \boldsymbol{K}_{vv_b}\\ \boldsymbol{K}_{v_bv} & \boldsymbol{K}_{v_bv_b}\end{bmatrix}\begin{Bmatrix}\Delta\boldsymbol{v}\\ \Delta\boldsymbol{v}_b\end{Bmatrix}=\begin{Bmatrix}\Delta\boldsymbol{P}_v\\ \Delta\boldsymbol{P}_{v_b}\end{Bmatrix} \tag{9.50}$$

in which

$$\boldsymbol{K}_{vv} = a_0\boldsymbol{M} + b_0\boldsymbol{C} + \boldsymbol{K} \tag{9.51}$$

$$\boldsymbol{K}_{vv_b} = a_0\boldsymbol{I}_b\boldsymbol{M} \tag{9.52}$$

$$\boldsymbol{K}_{v_bv} = -b_o\boldsymbol{C} - \boldsymbol{K} \tag{9.53}$$

$$\boldsymbol{K}_{v_bv_b} = a_0\boldsymbol{M}_b + b_0\boldsymbol{C}_b + \boldsymbol{K}_t \tag{9.54}$$

$$\Delta\boldsymbol{P}_v = -\boldsymbol{M}\boldsymbol{I}\Delta\ddot{\boldsymbol{v}}_g - [a_1\boldsymbol{M} + b_1\boldsymbol{C}]\dot{\boldsymbol{v}}(t) - [a_2\boldsymbol{M} + b_2\boldsymbol{C}]\ddot{\boldsymbol{v}}(t) - a_1\boldsymbol{M}\boldsymbol{I}_b\dot{\boldsymbol{v}}_b(t) - a_2\boldsymbol{M}\boldsymbol{I}_b\ddot{\boldsymbol{v}}_b\,(t) \tag{9.55}$$

$$\Delta\boldsymbol{P}_{v_b} = -\boldsymbol{M}_b\Delta\ddot{\boldsymbol{v}}_g - [a_1\boldsymbol{M}_b + b_1\boldsymbol{C}_b]\dot{\boldsymbol{v}}_b(t) - [a_2\boldsymbol{M}_b + b_2\boldsymbol{C}_b]\ddot{\boldsymbol{v}}_b\,(t) + b_1\boldsymbol{C}\dot{\boldsymbol{v}}(t) + b_2\boldsymbol{C}\ddot{\boldsymbol{v}}(t) - \Delta\boldsymbol{R}_s \tag{9.56}$$

9.4.3.1 Iteration at Each Time Interval

In order to solve the incremental Equation 9.50 to obtain $\Delta\boldsymbol{v}$ and $\Delta\boldsymbol{v}_b$, ΔR_s is required. The computation of ΔR_s involves $\Delta\boldsymbol{z}$ for the time interval Δt. The Runga–Kutta method is employed to obtain $\Delta\boldsymbol{z}$ iteratively as given below.

i. Assume $(\Delta\boldsymbol{z})_j = 0$ in iteration number $j = 1$.
ii. Substitute $(\Delta\boldsymbol{z})_j$ in Equations 9.46 and 9.47 and solve Equation 9.50 for $\Delta\boldsymbol{v}$ and $\Delta\boldsymbol{v}_b$.
iii. Calculate velocity vector $\dot{\boldsymbol{v}}_b(t + \Delta t)$.
iv. Compute $(\Delta\boldsymbol{z})_{j+1}$ for each isolator by solving Equation 9.35 using the Runga–Kutta method using the following steps:

$$\Delta\boldsymbol{z}_i\ (\text{for } x \text{ and } y) \;=\; \frac{\boldsymbol{K}_{oi} + 2\boldsymbol{K}_{1i} + 2\boldsymbol{K}_{2i} + \boldsymbol{K}_{3i}}{6} \tag{9.57}$$

$$\boldsymbol{K}_{oi} = \Delta t\boldsymbol{G}(\boldsymbol{z}_i)\,\boldsymbol{T}_i^T\dot{\boldsymbol{v}}_b(t) \tag{9.58}$$

$$\boldsymbol{K}_{1i} = \Delta t\boldsymbol{G}\left(\boldsymbol{z}_i + \frac{\boldsymbol{K}_{0i}}{2}\right)\boldsymbol{T}_i^T\dot{\boldsymbol{v}}_b\left(t + \frac{\Delta t}{2}\right) \tag{9.59}$$

$$\boldsymbol{K}_{2i} = \Delta t\boldsymbol{G}\left(\boldsymbol{z}_i + \frac{\boldsymbol{K}_{1i}}{2}\right)\boldsymbol{T}_i^T\dot{\boldsymbol{v}}_b\left(t + \frac{\Delta t}{2}\right) \tag{9.60}$$

$$\boldsymbol{K}_{3i} = \Delta t\boldsymbol{G}\left(\boldsymbol{z}_i + \frac{\boldsymbol{K}_{2i}}{3}\right)\boldsymbol{T}_i^T\dot{\boldsymbol{v}}_b(t + \Delta t) \tag{9.61}$$

in which $\dot{\boldsymbol{v}}_b(t + \Delta t/2)$ is obtained by interpolation.
v. Iteration is continued until convergence is reached. The convergence criterion is specified for each bearing as:

$$\frac{\left|(\Delta\boldsymbol{z}_i)_{j+1}\right| - \left|(\Delta\boldsymbol{z}_i)_j\right|}{\boldsymbol{z}_m} \leq \text{ tolerance} \tag{9.62a}$$

$$\boldsymbol{z}_m = \sqrt{\frac{A}{\beta + \tau}} \tag{9.62b}$$

in which $\boldsymbol{z}_m$ is the maximum value of the hysteretic displacement of the isolator; A, β, and τ are defined earlier.
vi. With $\Delta\boldsymbol{z}_i$ known, $\Delta\boldsymbol{R}_s$ can be obtained from Equations 9.46 and 9.47.

After the incremental displacement vectors $\Delta\boldsymbol{v}$ and $\Delta\boldsymbol{v}_b$ are obtained, $\Delta\boldsymbol{R}$ is obtained from Equation 9.42 and $\boldsymbol{v}(t + \Delta t)$, $\boldsymbol{v}_b(t + \Delta t)$, $\boldsymbol{R}(t + \Delta t)$, $\boldsymbol{z}_i(t + \Delta t)$, and ith isolator forces are computed.

The advantage of modeling the isolator force–deformation behavior by Equations 9.34 and 9.35 is that bidirectional interaction on yielding of isolators for a 3D solution can be included for all cases, that is, bilinear, elasto-plastic, perfectly plastic (friction isolator), and purely hysteretic types. If bidirectional interaction is ignored, then off-diagonal terms of Equation are set to be zero.

Example 9.3

The 3D model of the seven-storey building frame shown in Figure 9.21 is base isolated using a base slab at the base of the columns. The arrangement of the isolators is also shown in the same figure. The backbone curves of the isolators in both directions are the same and are shown in Figure 9.16. Find the time histories

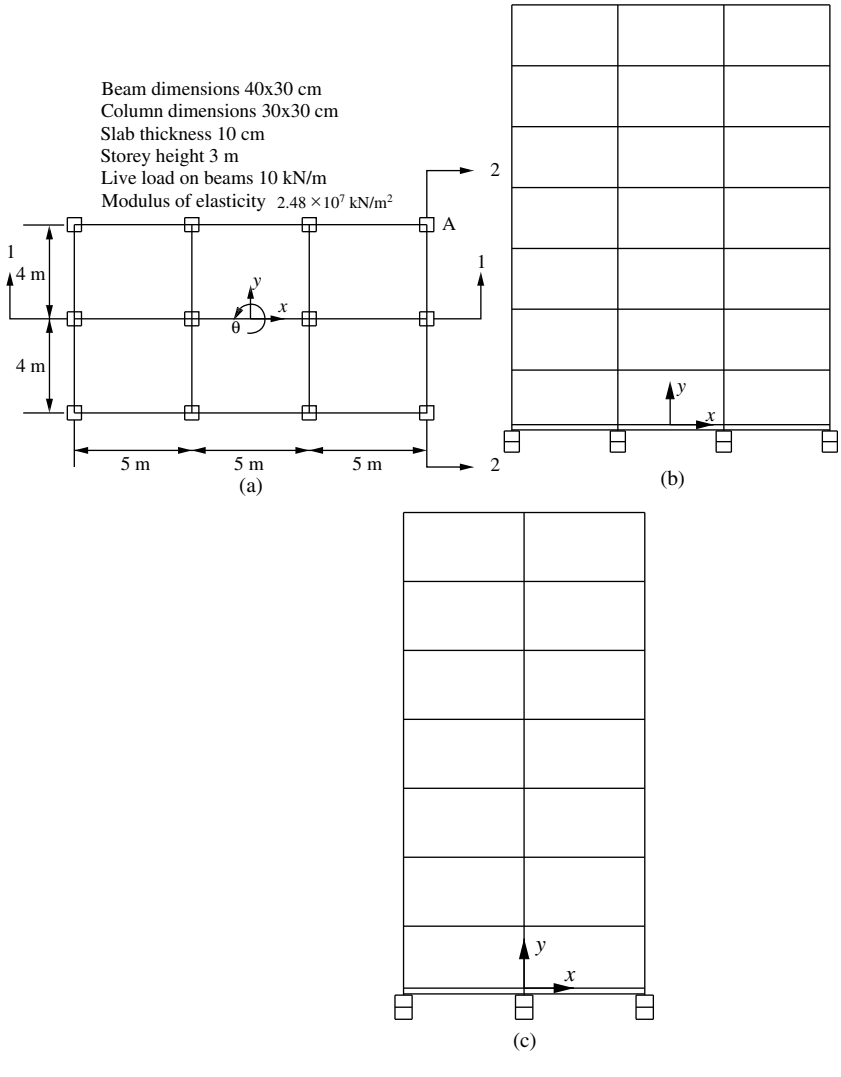

Figure 9.21 3D frame and its properties: (a) plan; (b) frame elevation 1-1; and (c) frame elevation 2-2

of displacements of column A at the top floor level and at the base slab for a two-component earthquake. Take $\ddot{x}_g$ as the El Centro earthquake; and $\ddot{y}_g = \frac{1}{2}\ddot{x}_g$. Ignore bi-directional interaction of the yielding of isolators.

Solution: The ends of the columns are assumed to be rigidly connected to the base slab. The slab has 3 DOF at the center of mass as shown in Figure 9.21. The displacements of the isolators in the x- and y-directions relative to the foundation are governed by the motion of the slab. If the isolators are not symmetrically arranged (geometrically and characteristics wise) about the center of mass, then additional eccentricities at the level of the slab are produced at each time step due to this effect.

As bilinear interactions on yielding of the isolators are ignored here, the problem is solved by using SAP 2000 (which cannot take this interaction into account). Note that the base slab is modeled as a rigid diaphragm. The isolators are placed below the rigid diaphragm and beneath each column. If bilinear interaction is included, then a computer code has to be developed for the iterative method presented in Section 9.4.3.

Figure 9.22(a and b) shows the time histories of responses of the column at the top floor level. The figures also show the responses of the fixed-base structure. It is seen that there is 28% reduction in top displacements (x- and y-translations).

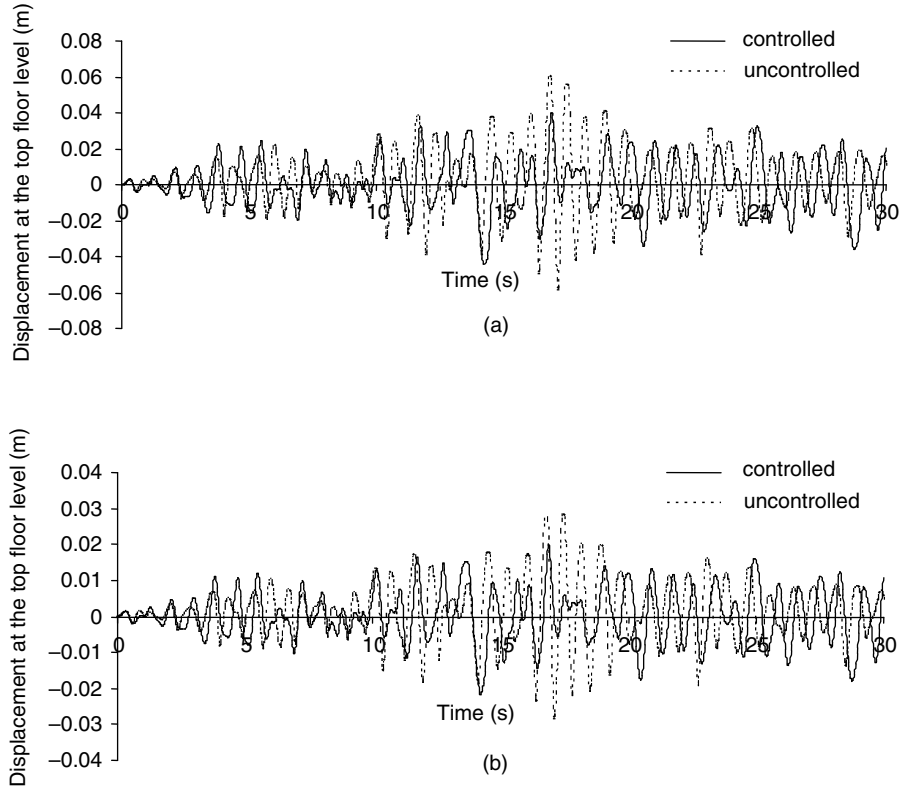

Figure 9.22 Comparison between controlled and uncontrolled displacements of the column at the top floor level: (a) x-direction; and (b) y-direction

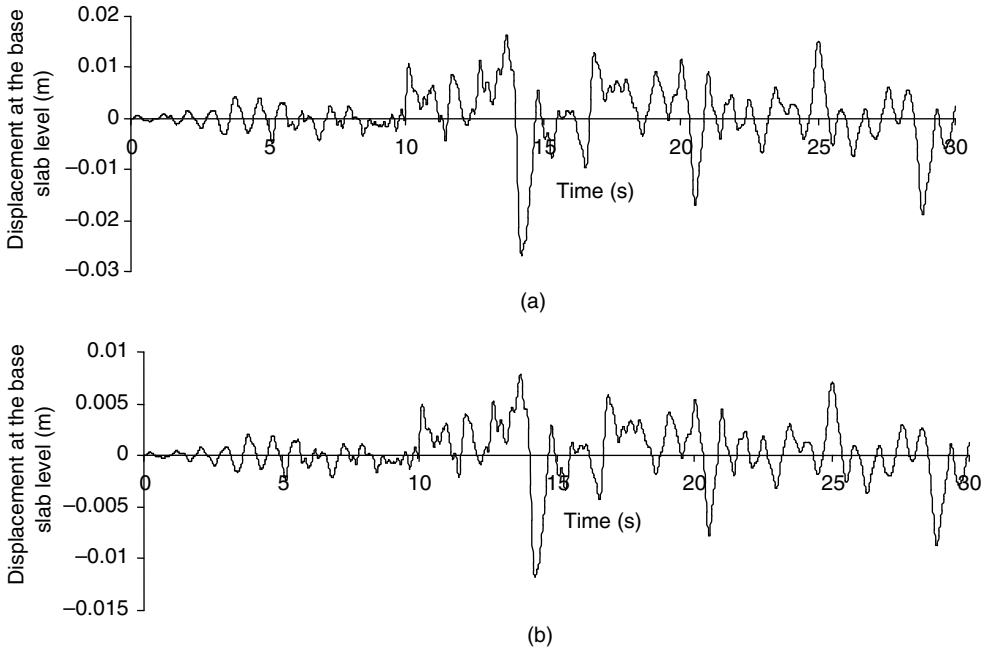

Figure 9.23 Time histories of displacements of the base of the column: (a) *x*-direction; and (b) *y*-direction

Figure 9.23(a and b) shows the time histories of displacements at the base of the column. It is seen from the figures that maximum base displacements in the *x*- and *y*-directions are 0.026 and 0.0113 m, respectively. As the building is symmetric and is supported on a symmetrically placed isolator having the same characteristics, the building vibrated along the *x*- and *y*-directions without any torsional coupling. As expected, the base movement in the *y*-direction is less than that in the *x*-direction.

The force–deformation behaviors of the isolator A in the *x*- and *y*-directions for the entire duration of the earthquake are shown in Figure 9.24. It is seen from the figure that the hysteretic loop for the *x*-direction is bigger than that for the *y*-direction.

9.5 Design of Base Isolated Buildings

The design of base isolated buildings consists of three steps, namely: (i) design of isolator; (ii) design of base isolated building; and (iii) checking of the design by non-linear time history analysis. The last step ensures that the design of base isolator and base isolated building satisfy the desired criteria. Thus, in principle, iterations are involved through steps (i) and (ii) and finally, through steps (i), (ii), and (iii). The iterations are explained in subsequent sections.

The design of an isolator is aimed at finding the required (equivalent) stiffness and damping of the isolator. With a non-linear isolator, which is more common in practice, both parameters depend upon the displacement of the isolator. For design purposes, equivalent stiffness is taken as the secant stiffness corresponding to the desired displacement level. In a preliminary design, estimates of the equivalent stiffness and damping of the isolator are obtained for a given design criterion. The values of these parameters are successively improved by iteration.

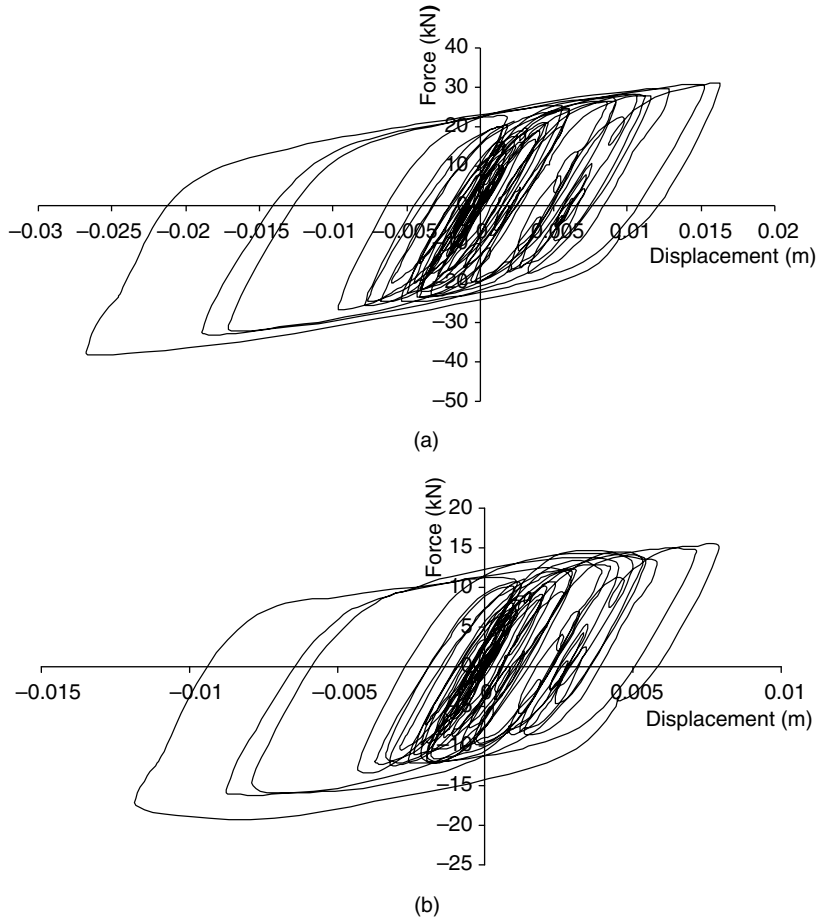

Figure 9.24 Hysteretic behavior of the isolator A: (a) for *x*-direction; and (b) for *y*-direction

9.5.1 Preliminary Design (Design of Isolator and Initial Sizing of the Isolated Structure)

For the preliminary design, the superstructure is assumed to be a rigid block mounted on the isolator so that isolator period can be determined by considering it as a single degree of freedom system. A bi-spectrum is used for the design of the isolator. This spectrum (that is, plot of spectral acceleration versus spectral displacement) is obtained by combining the acceleration response spectrum and the displacement response spectrum. Time period (T) axis being common for both, any point on the bi-spectrum denotes a set of compatible spectral displacement and spectral acceleration, and a corresponding time period. A bi-spectrum is shown in Figure 9.25.

Many criteria could be used for the design of the isolator. However, the following three criteria are generally used: (i) good separation of time periods between the fixed base structure and the base isolated structure; (ii) specified maximum displacement of the isolator; and (iii) specified maximum spectral acceleration of the isolator.

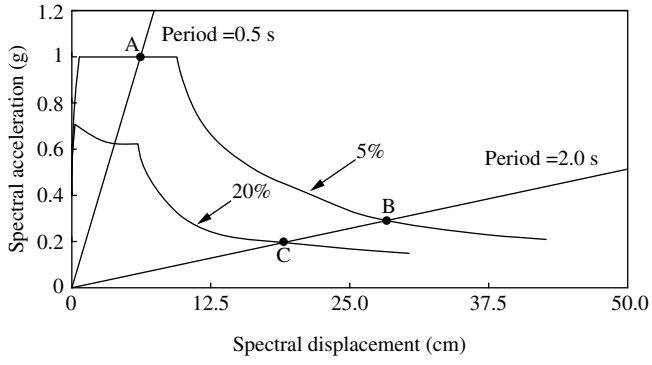

Figure 9.25 Use of design bi-spectrum for isolator design (first criterion)

For the first criterion, the fundamental period (T) of the superstructure as a fixed base is calculated. The isolator period is then obtained as nT so that there is a good separation between the two periods. Typically n is kept around 3–4 and the isolator period is kept above 2 s (as per UBC). Once the time period of the isolator is decided and an equivalent damping of the isolator is assumed, the maximum isolator displacement and the absolute acceleration (spectral acceleration) are obtained from the bi-spectrum, as shown in Figure 9.25. An approximate base shear for the isolated building can be calculated from the spectral acceleration and the total mass of the superstructure. It is possible then to see how much reduction is achieved in the base shear of the isolated building as compared with the fixed base structure by providing the isolator. The equivalent stiffness of the isolator is obtained as $K_{eq} = 4\pi^2 M/(nT)^2$ in which M is the total mass of the building.

A preliminary design for the superstructure (sizing) can be carried out by equally distributing the base shear at all floor levels to obtain the equivalent lateral load. This means that the fundamental mode shape of the isolated structure is taken as unity along the height. The lateral load analysis for the preliminary design of the superstructure may be carried out as per the code provision using 2D or 3D idealization and, if necessary, by incorporating the provision for torsion. For the analysis, the base of the frame is either fixed against rotation or is hinged, vertical motion is restrained and lateral movements are controlled by lateral springs having stiffness equal to the isolator stiffness. If the column ends are connected to isolated footings resting on isolators, then bases are idealized as hinged. If the columns are connected to the base slab, the bases may be fixed against rotation.

For the second criterion, the maximum permissible displacement of the isolator is stipulated from practical considerations. Once the maximum isolator displacement is known, it is possible to obtain the spectral acceleration and the isolator time period from the bi-spectrum, as shown in Figure 9.26 for an assumed value of the equivalent damping of the isolator. The time period is checked against the code provision. With the time period being known, the equivalent stiffness of the isolator can be calculated as before. The preliminary design of the superstructure using lateral load analysis is carried out as described previously.

The third criterion is generally required for buildings that house sensitive equipment and machines requiring stringent control on the floor acceleration. Acceleration control may be required for human comfort as well. For the third criterion, the maximum isolator displacement and time period of the isolator are obtained as shown in Figure 9.27 for an assumed value of the equivalent damping. With the time period known, the equivalent stiffness of the isolator and the preliminary design of the superstructure are obtained as before.

After the preliminary design of the frame and isolators are complete, a response spectrum analysis of the base isolated structure is carried out in order to obtain a better estimate of the isolator displacements.

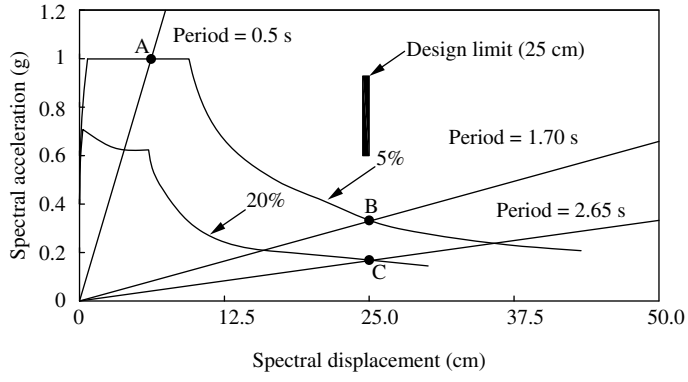

Figure 9.26 Use of design bi-spectrum for isolator design (second criterion)

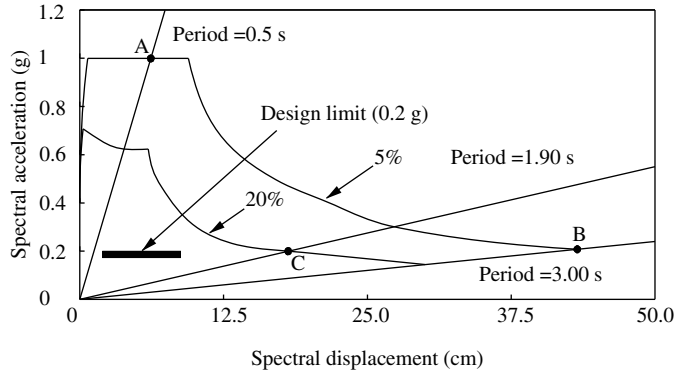

Figure 9.27 Use of design bi-spectrum for isolator design (third criterion)

9.5.2 *Response Spectrum Analysis of Base Isolated Structure*

For the case of isolated footings, Equation 9.24 is modified for the response spectrum analysis. Modification consists of writing c_{bb_i} and k_{bb_i} (elements of diagonal matrices $\boldsymbol{c}_{bb}$ and $\overline{\boldsymbol{k}}_{bb}$) as:

$$\boldsymbol{c}_{bb_i} = \overline{\boldsymbol{c}}_{bb_i} + \boldsymbol{c}_{beq_i} \tag{9.63}$$

$$\overline{\boldsymbol{k}}_{bb_i} = \boldsymbol{k}_{\mathrm{beq}_i} \tag{9.64}$$

in which $\overline{\boldsymbol{c}}_{bb_i}$ is the linear damping of the ith isolator and $\boldsymbol{c}_{\mathrm{beq}_i}$ is the equivalent damping of the ith isolator for the hysteretic effect; similarly, $\boldsymbol{k}_{\mathrm{beq}_i}$ is the equivalent stiffness of the ith isolator. The structural damping matrix $\boldsymbol{c}_{ss}$ is obtained by assuming Rayleigh damping for the structure. As the damping matrix for the building–isolator system is non-classical, the application of normal mode theory gives a non-diagonal damping matrix. By ignoring the off-diagonal terms, a modal damping in each mode of vibration can be computed and the response spectrum method of analysis, as described in Chapter 5, can be carried out.

For the case of base isolation with a base slab, the base of the 3D model of the building is attached to three springs and three dashpots. Referring to Figure 9.14, the spring stiffness are obtained from the

equivalent spring stiffness of each isolator as given below:

$$\overline{\boldsymbol{K}}_{x\text{eq}} = \sum_{i=1}^{n} \boldsymbol{K}_{x\text{eq}_i}; \qquad \overline{\boldsymbol{K}}_{y\text{eq}} = \sum_{i=1}^{n} \boldsymbol{K}_{y\text{eq}_i} \tag{9.65}$$

$$\overline{\boldsymbol{K}}_{\theta\text{eq}} = \sum_{i=1}^{n} \boldsymbol{K}_{x\text{eq}_i} \boldsymbol{y}_i^2 + \boldsymbol{K}_{y\text{eq}_i} \boldsymbol{x}_i^2 \tag{9.66}$$

The damping coefficient of the dashpots can be similarly obtained from the equivalent damping of each isolator.

By assuming three degrees of freedom at each floor level (with floors assumed as rigid diaphragms), equations of motion for the flexible base building can be obtained using standard procedures. The damping matrix for the entire system becomes non-classical. By ignoring the off-diagonal terms of the modal damping matrix, the response spectrum method of analysis can be performed as before.

From the response spectrum method of analysis, mean peak displacements of the base isolators are obtained and are compared with those of the isolator displacements obtained from the preliminary design of the isolators. If the difference between the two is significant, then the isolator characteristics are changed. New equivalent stiffness and damping are computed corresponding to the displacement of the isolators obtained from the response spectrum method of analysis. A corresponding new time period of the isolator is checked against the code provision. The preliminary design and response spectrum analysis are then repeated. The procedure is continued until a convergence is achieved.

9.5.3 Non-Linear Time History Analysis

After completion of the above stage, the isolator characteristics are finalized. The non-linear time history analysis is then performed as mentioned in Section 9.4 for the response spectrum compatible ground motion. Generally, the peak displacements obtained by the time history analysis are less than those of the response spectrum method of analysis. This is the case because damping due to the hysteretic effect is more than the equivalent damping considered in the response spectrum method of analysis. If the maximum base displacement obtained from the time history analysis is found to be very different from that of the response spectrum analysis, then the entire process of preliminary design, response spectrum analysis, and time history analysis are repeated until satisfactory results are obtained.

Example 9.4

The seven-storey building frame as shown in Figure 9.9 is to be base isolated using a base slab. Design the base isolation system and the base isolated structure, starting from the preliminary design to the last stage of non-linear analysis. For seismic analysis, consider 50% of the live load. Use the response spectrum as shown in Figure 9.10 with PGA = 0.36g and damping modification as given in Table 9.1.

Table 9.1 Multiplying factors for damping (spectral ordinates to be multiplied by this factor)

Damping (%)	0	2	5	7	10	15	20	25	30
Factor	3.2	1.4	1	0.9	0.8	0.7	0.6	0.55	0.5

Solution: Total load of the structure = 1575 kN. Fixed base fundamental period of the frame is 0.75 s.

Assuming a time period separation of 3, the fundamental time period of the frame is 2.25 s.

Assuming a damping of 10% for the isolator, the response spectrum provides a value of

$$\frac{S_a}{g} = 0.356 \quad \text{for} \quad T = 2.25\ \text{s}$$

Base shear $(W/g)S_a = 1575 \times 0.356 \times 0.36 = 201.63$ kN (fixed base shear = 756.12 kN).

S_d (maximum base displacement) $= S_a T^2/4\pi^2 = 16$ cm (base displacement from preliminary design).

Isolator is designed for $W = 853.76$ kN (Example 9.1). Assuming the mass of the isolator to be negligible in comparison with the mass of the structure, effective stiffness of the isolator is $K_{\text{eq}} = 4\pi^2 W/gT^2 = 678.63\,\text{kNm}^{-1}$. Assume a pre- to post-yield stiffness ratio of 10.

Using the method for designing isolator as illustrated in Example 9.1,

$$Q_D = \frac{W_D}{4S_d} = \frac{\pi}{2} K_{\text{eff}} \xi_{\text{eff}} S_d = 678.63 \times \frac{\pi}{2} \times 0.1 \times 0.16 = 17.11\,\text{kN}$$

$$K_d = K_{\text{eff}} - \frac{Q_D}{S_d} = 678.63 - \frac{17.1}{0.16} = 571.75\,\text{kN m}^{-1}; \quad D_y = \frac{Q_D}{9K_d} = 0.0033\,\text{m}$$

$$F_y = K_u \times D_y = 10K_d \times D_y = 18.86\,\text{kN}$$

The back bone curve for the isolator is shown in Figure 9.28. It is seen from the figure that for a base displacement of 16 cm, K_{eq} of the isolator is the same as that obtained above.

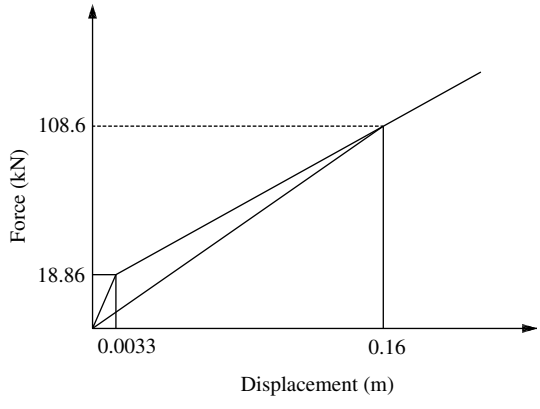

Figure 9.28 Backbone curve for the designed isolator

9.5.3.1 Initial Design

The base shear for the isolated frame is distributed equally to all floors and the base of the frame is horizontally restrained by a spring of stiffness $3K_{\text{eq}}$. A static analysis is carried out to obtain the bending moments and shear forces in beams and columns for the gravity and lateral loads. The bending moment diagram is shown in Figure 9.29. Based on the worst combination of moments, the sizes of column and beam cross-sections are modified (compared with the fixed base frame). Both original cross-sections and the revised ones are shown in Figure 9.30.

9.5.3.2 Response Spectrum Analysis

It is assumed that the changed cross-sections do not significantly change the mass of the frame (that is, vertical load). The response spectrum analysis of the frame with a revised cross-section is carried out by assigning a horizontal spring (of stiffness $3K_{\text{eq}}$) at the base.

As the system becomes non-classically damped because of two different types of damping present in the system, a response spectrum analysis is carried out with an approximate equivalent modal damping calculated for each mode. For this, a damping matrix of the total system is constructed by assuming

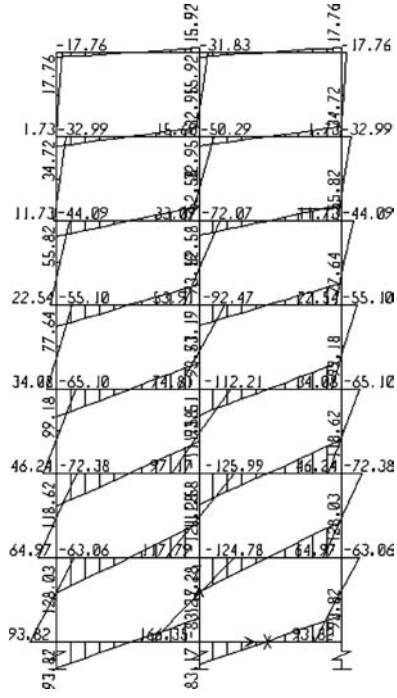

Figure 9.29 Bending moment (kN m) diagram for the initial design of the base isolated frame

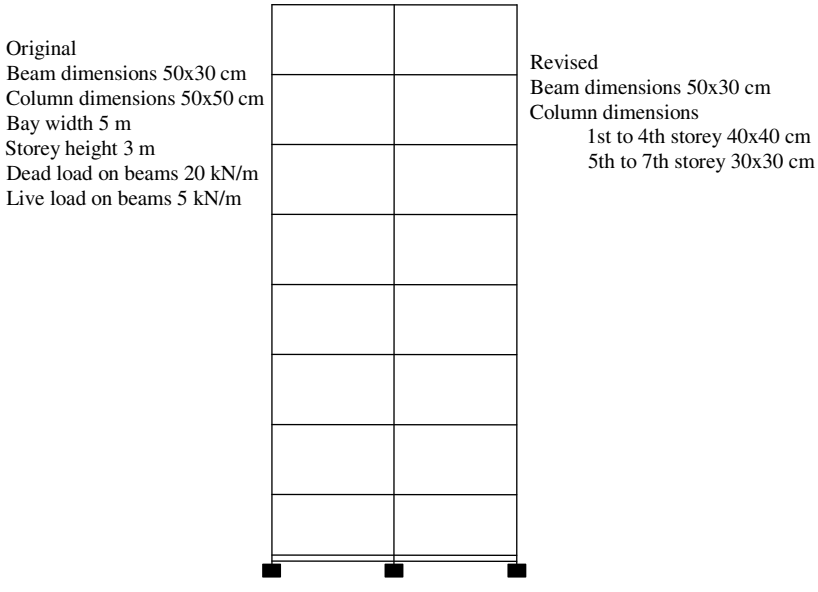

Figure 9.30 The base isolated frame with revised dimensions

Rayleigh damping for the frame with $\alpha = 0.676$ and $\beta = 0.0027$ and the isolator damping (assuming $\xi = 10\%$). The resulting $\boldsymbol{C}$ matrix for the structure isolator system is given below.

$$\boldsymbol{C} = 10^4 \times \begin{bmatrix} 1.3956 & & & & & & & \\ -0.0249 & 1.4297 & & & & sym & & \\ 0.0071 & -0.0339 & 1.4350 & & & & & \\ 0.0009 & 0.0062 & -0.0404 & 1.4447 & & & & \\ -0.0014 & 0.0021 & 0.00093 & -0.0409 & 1.4367 & & & \\ 0.0012 & -0.0027 & 0.0027 & 0.0054 & -0.0348 & 1.4367 & & \\ -0.0028 & 0.0044 & -0.0004 & -0.0036 & 0.0076 & -0.0432 & 1.4541 & \\ 0 & 0 & 0 & 0 & 0 & 0 & 0 & 8.900 \end{bmatrix}$$

The undamped mode shapes and frequencies of the isolated structure modeled by a horizontal spring at the base with stiffness equal to $3K_{eq}$ are obtained. The first two undamped mode shapes of the spring supported frame are:

$$\phi_1^T = [1 \quad 0.986 \quad 0.964 \quad 0.936 \quad 0.90 \quad 0.858 \quad 0.810 \quad 0.770]$$

$$\phi_2^T = [1 \quad 0.736 \quad 0.356 \quad -0.085 \quad -0.508 \quad -0.833 \quad -1.010 \quad -1.050]$$

Using these two mode shapes, the equivalent modal damping in the first two modes, after ignoring the off-diagonal terms of the transformed modal damping matrix, are obtained as $\xi_1 = 0.084$; $\xi_2 = 0.0167$.

By considering the first two modes, the response spectrum analysis is carried out using SAP 2000.The envelope of the bending moment diagram is shown in Figure 9.31. The base displacement is obtained as

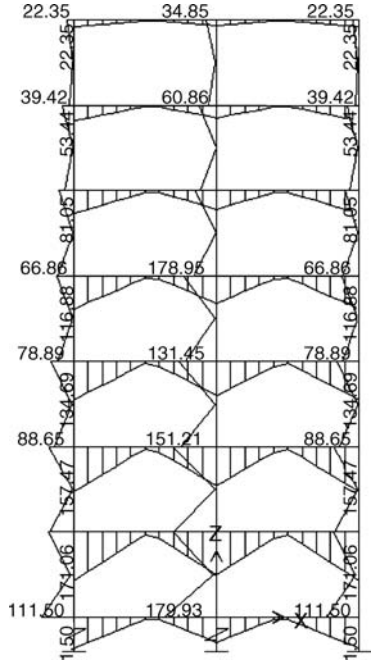

Figure 9.31 Envelope of the bending moment (kN m) diagram obtained from the response spectrum analysis

0.11 m, which is not much different than the base displacement obtained from the preliminary design. Thus, there is no significant change in K_{eq}. If the base displacement obtained by the response spectrum method of analysis is substantially different to the initial displacement, then the isolator backbone curve is to be suitably changed, and the preliminary design and response spectrum analysis are to be repeated until satisfactory results are obtained.

9.5.3.3 Non-Linear Time History Analysis

The frame along with the base slab and isolators shown in Figure 9.30 are analyzed for the response spectrum compatible time history of acceleration shown in Figure 9.32. A backbone curve of the isolator is shown in Figure 9.28. Analysis is carried out using SAP 2000. The envelope of the bending moment is shown in Figure 9.33. It is seen from the figure that the time history analysis provides less bending moments compared with the response spectrum analysis. The time history of the base displacement is shown in Figure 9.34. It is seen from the figure that the maximum base displacement is 0.096 m, little less than the maximum base displacement obtained by the response spectrum method of analysis. If the two displacements are found to be very different, then the entire procedure may have to be repeated starting from the initial design. In this case, the iteration is not needed.

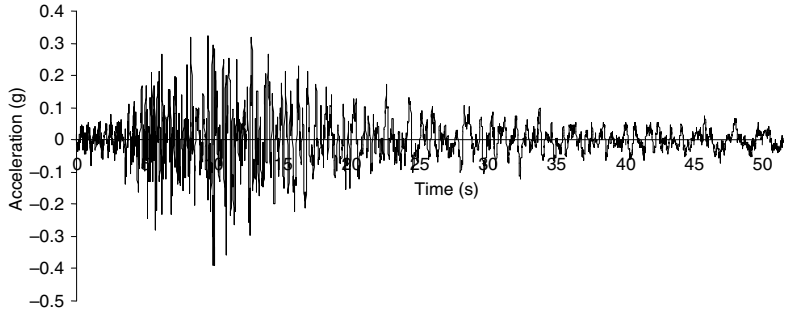

Figure 9.32 Response spectrum compatible simulated time history of the ground acceleration (for PGA = 0.36g)

9.6 Tuned Mass Damper

Tuned mass dampers (TMDs) are passive control devices that are generally installed at the roof tops of buildings to control the responses of buildings produced due to wind or an earthquake. TMDs may be installed in other structures also, such as, flexible bridges (suspension/cable stayed bridges) to control the wind induced vibration [4]. TMDs have been successfully implemented to control the responses of some well known towers (buildings) produced by winds, such as Citicorp Tower, Sydney Tower, and so on.

TMD consists of a mass, a spring, and a damper, which is attached to one side of the building as shown in Figure 9.35. To control the responses in two directions, TMDs may be placed in two directions on the top of a building. Furthermore, by placing the TMDs eccentrically, the torsional response of the building may also be controlled. The most important feature of the TMDs is the tuning of frequencies, that is, the frequency of the TMD is made equal to the fundamental frequency of the structure. Because of various uncertainties inherent in the properties of both the TMD and the structure, perfect tuning is very difficult to achieve. As a consequence, multi-tuned mass dampers (MTMDs) have been developed for better tuning.

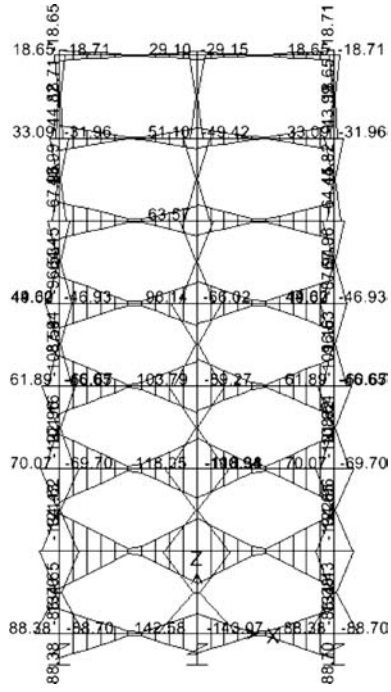

Figure 9.33 The envelope of the bending moment (kN m) diagram obtained from the time history analysis

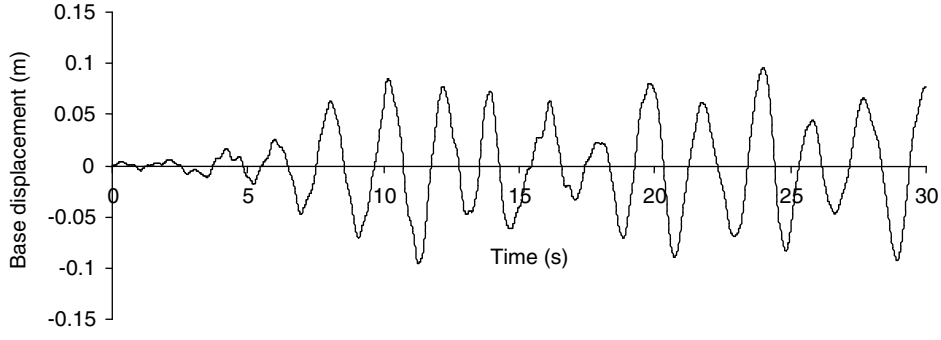

Figure 9.34 Time history of the base displacement

In order to understand how the TMD works in controlling the response of the building or any structure in which it is installed, consider a two degrees of freedom undamped system subjected to the support excitation as shown in Figure 9.36. In the absence of the second system, the amplitude of the response of the first system can easily be shown to be:

$$x_{01} = \frac{F_1}{k_1(1-\gamma^2)}; \qquad F_1 = -m_1\ddot{x}_g \tag{9.67}$$

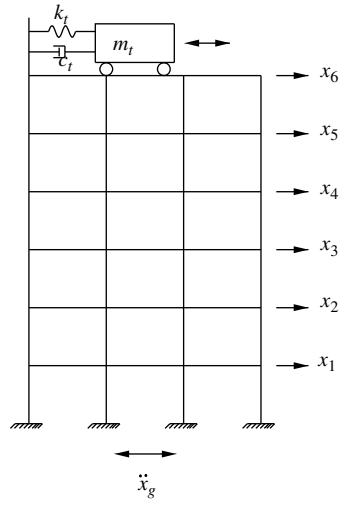

Figure 9.35 A tuned mass damper as passive control device

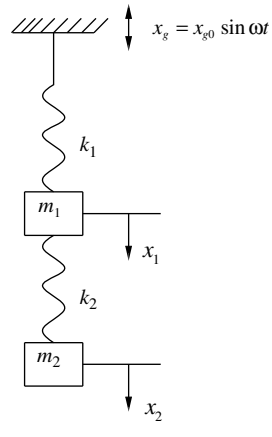

Figure 9.36 A two DOF undamped system

in which $\gamma = \omega/\omega_1$ and $\omega_1^2 = k_1/m_1$. If both systems are present, the responses x_1 and x_2 (relative to the support) will be harmonic having the same phase as that of the excitation as there is no damping. The amplitudes of responses will be given by:

$$\boldsymbol{X}_0 = \begin{Bmatrix} x_{01} \\ x_{02} \end{Bmatrix} = \boldsymbol{H}^{-1}\boldsymbol{F} \tag{9.68a}$$

in which

$$\boldsymbol{H} = \begin{bmatrix} k_1 + k_2 - m_1\omega^2 & -k_2 \\ -k_2 & k_2 - m_2\omega^2 \end{bmatrix}; \qquad \boldsymbol{F} = \begin{Bmatrix} -m_1 \\ -m_2 \end{Bmatrix} \ddot{x}_g \tag{9.68b}$$

Inverting the matrix $\boldsymbol{H}$, performing the matrix multiplication, and carrying out the required algebraic manipulations, the amplitudes of responses are given by:

$$x_{01} = \frac{-m_1\ddot{x}_g}{k_1}\frac{(1+n-\gamma_2^2)}{\left(1-\gamma_1^2-\gamma_2^2-\frac{k_2}{k_1}\gamma_2^2+\gamma_1^2\gamma_2^2\right)} \tag{9.69a}$$

$$x_{02} = \frac{-m_1\ddot{x}_{g0}}{k_1}\frac{(1+n)+\left(\frac{k_1}{k_2}-\frac{1}{n}\gamma_2^2\right)n}{\left(1-\gamma_1^2-\gamma_2^2-\frac{k_2}{k_1}\gamma_2^2+\gamma_1^2\gamma_2^2\right)} \tag{9.69b}$$

in which n is the mass ratio, that is, m_2/m_1; $\gamma_2 = \omega/\omega_2$; $\gamma_1 = \omega/\omega_1$; $\omega_1 = \sqrt{k_1/m_1}$; and $\omega_2 = \sqrt{k_2/m_2}$. If it is assumed that the two systems are perfectly tuned, that is, $k_1/m_1 = k_2/m_2$ or $\omega_1^2 = \omega_2^2$, then $k_2/k_1 = m_2/m_1 = n$ and $\gamma_1 = \gamma_2 = \gamma = \omega/\omega_1$. Thus, for perfect tuning, Equations 9.69a and 9.69b may be written as:

$$x_{01} = -\frac{\ddot{x}_{g0}}{\omega_1^2}\frac{(1+n-\gamma^2)}{[1-\gamma^2(2+n)+\gamma^4]} \tag{9.70a}$$

$$x_{02} = -\frac{\ddot{x}_{g0}}{\omega_1^2}\frac{(2+n-\gamma^2)}{[1-\gamma^2(2+n)+\gamma^4]} \tag{9.70b}$$

From Equations 9.70a and 9.70b, the ratio between the absolute values of the amplitudes of the two systems is given as:

$$\left|\frac{x_{01}}{x_{02}}\right| = \left|\frac{(1+n-\gamma^2)}{(2+n-\gamma^2)}\right| \tag{9.71a}$$

For $\gamma = 1$, that is, the condition of resonance under perfect tuning, the ratio becomes

$$\left|\frac{x_{01}}{x_{02}}\right| = \frac{n}{1+n} \quad n > 0 \tag{9.71b}$$

For $n = 0$, an SDOF system is realized with the response given by Equation 9.67. Under the condition of resonance, the amplitude of the response of the SDOF system tends to infinity. When a second system is attached and tuned to this SDOF system (the first system), the response of the first system becomes finite. Its amplitude of response becomes a fraction of that of the second system if $n < 1$ (Equation 9.71b). This means that there is a transfer of energy from the first system to the second one. A TMD operates based on the above principle. During the oscillation of a building or any other structure fitted with a TMD, there is a significant transfer of the energy of the near resonating components of ground excitation from the main system to the TMD. Thus, there is a reduction in response of the main structure due to the presence of the TMD.

Figure 9.37(a and b) shows the plot of the variation of the response ratio with the frequency ratio γ for different values of the mass ratio (n). It is seen from the figure that for near resonating conditions, that is, $\gamma = 1-1.1$, the response ratios for different values of n become minimum. Figures 9.38 and 9.39 show the plots of the absolute normalized amplitudes

$$\overline{x}_{01} = \left|\frac{x_{01}\omega_1^2}{\ddot{x}_{g0}}\right| \text{ and } \overline{x}_{02} = \left|\frac{x_{02}\omega_1^2}{\ddot{x}_{g0}}\right|$$

of the two systems with the mass ratio (n) for different values of γ. It is seen from the figures that the normalized amplitude of the first system reaches a minimum value (almost to zero) for $\gamma = 1.05$ and $n = 0.1$. The corresponding normalized amplitude of the second system is about 10. If this amplitude of displacement for the second system is within the permissible limit, then it is possible to obtain the

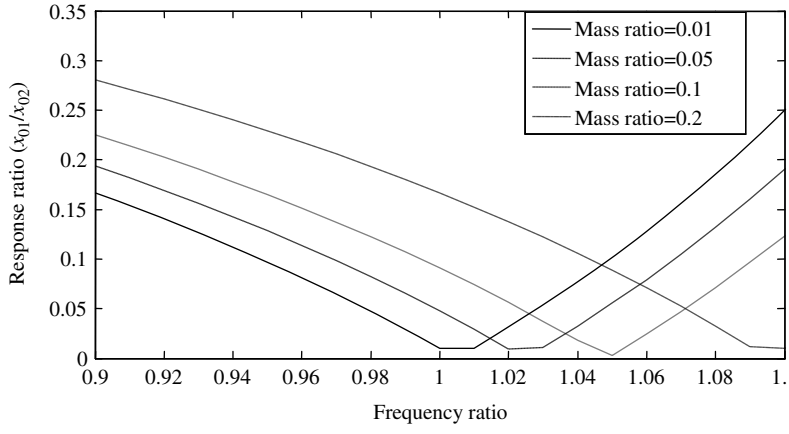

Figure 9.37 Variation of response ratio with frequency ratio for two DOFs

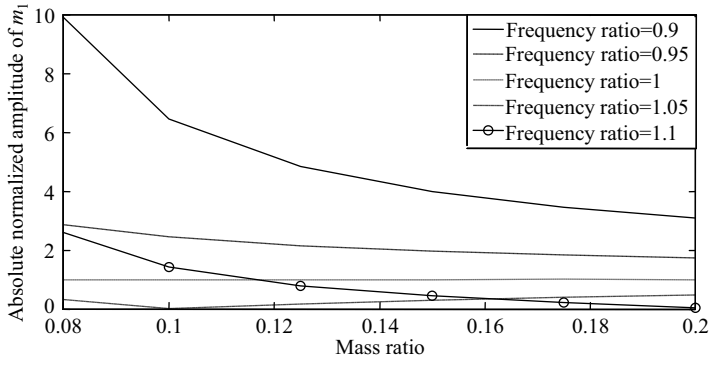

Figure 9.38 Variation of the absolute normalized amplitude of response $\overline{x}_{01}$ (m_1) with mass ratio

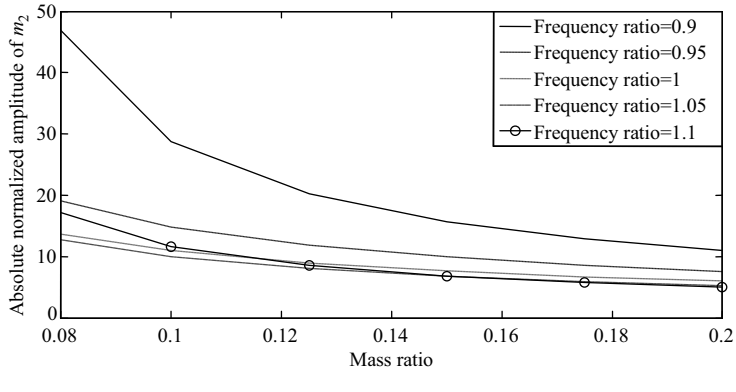

Figure 9.39 Variation of the absolute normalized amplitude of response $\overline{x}_{02}$ (m_2) with mass ratio

minimum value of the amplitude of the first system by appropriately choosing the mass ratio. Otherwise, an optimum mass ratio is selected based on the permissible limit of the displacement of the second system. In that case, the minimum response of the first system will not be achieved, but the response can be significantly reduced.

Although in practice both TMD (the second system) and the building or the main structure (represented by the first system) have damping and the earthquake excitation is irregular in nature, yet it is observed that a mass ratio exists for which optimum reduction of the response of the main structure may be achieved with the help of a TMD.

Now, consider a building frame with a TMD installed at the roof top as shown in Figure 9.35. The equation of motion takes the form

$$\boldsymbol{M}\ddot{\boldsymbol{X}} + \boldsymbol{C}\dot{\boldsymbol{X}} + \boldsymbol{K}\boldsymbol{X} = -\boldsymbol{M}\boldsymbol{I}\ddot{x}_g + \boldsymbol{G}_s \tag{9.72a}$$

in which $\boldsymbol{G}_s$ is a vector of size $n \times 1$ where all elements are zero except the last element. The last element is given by:

$$c_t(\dot{y} - \dot{x}_n) + k_t(y - x_n) \tag{9.72b}$$

The equation of motion for the TMD is given by:

$$m_t\ddot{y} + c_t(\dot{y} - \dot{x}_n) + k_t(y - x_n) = -m_t\ddot{x}_g \tag{9.73}$$

in which m_t, c_t, and k_t are the mass, damping, and stiffness of the TMD, respectively; y, $\dot{y}$, and $\ddot{y}$ are, respectively, the displacement, velocity, and acceleration of the mass of the TMD.

The solution of the equations of motion can be carried out in various ways. Three different types of solution procedure are given below.

9.6.1 Modal Coupled Analysis

If the advantage of modal decoupling of the equations of motion of the frame without TMD is used, then the equations resulting from Equation 9.72a are:

$$\ddot{z}_i + 2\xi\omega_i\dot{z}_i + \omega_i^2 z_i = -\lambda_i\ddot{x}_g + \boldsymbol{\phi}_i^T G_s \quad (i = 1 \ldots m) \tag{9.74}$$

in which ϕ_t and ω_i are the ith natural mode and frequency of frame, respectively; λ_i is the ith mode participation factor.

Using Equations 9.74 and 9.73, reduced order coupled equations of motion involving the generalized coordinates $\boldsymbol{z}_i (i = 1 \ldots m)$ and TMD displacement $\boldsymbol{y}$ are obtained. For say $m = 3$, the equations of motion take the following form

$$\overline{\boldsymbol{M}}\ddot{\boldsymbol{q}} + \overline{\boldsymbol{C}}\dot{\boldsymbol{q}} + \overline{\boldsymbol{K}}\boldsymbol{q} = -\boldsymbol{P}\ddot{x}_g \tag{9.75a}$$

in which

$$\boldsymbol{q}^T = [z_1\ z_2\ z_3\ y]; \quad \boldsymbol{P}^T = [\lambda_1\ \lambda_2\ \lambda_3\ m_t]; \quad \overline{\boldsymbol{M}} = \mathrm{diag}[1\ 1\ 1\ m_t] \tag{9.75b}$$

$$\overline{\boldsymbol{C}} = \begin{bmatrix} 2\xi\omega_1 + c_t\varphi_{n1}^2 & c_t\varphi_{n1}\varphi_{n2} & c_t\varphi_{n1}\varphi_{n3} & -c_t\varphi_{n1} \\ c_t\varphi_{n2}\varphi_{n1} & 2\xi\omega_2 + c_t\varphi_{n2}^2 & c_t\varphi_{n2}\varphi_{n3} & -c_t\varphi_{n2} \\ c_t\varphi_{n3}\varphi_{n1} & c_t\varphi_{n3}\varphi_{n2} & 2\xi\omega_3 + c_t\varphi_{n3}^2 & -c_t\varphi_{n3} \\ -c_t\varphi_{n1} & -c_t\varphi_{n2} & -c_t\varphi_{n3} & c_t \end{bmatrix} \tag{9.75c}$$

$$\overline{\boldsymbol{K}} = \begin{bmatrix} \omega_1^2 + k\varphi_{n1}^2 & k\varphi_{n1}\varphi_{n2} & k\varphi_{n1}\varphi_{n3} & -k\varphi_{n1} \\ k\varphi_{n2}\varphi_{n1} & \omega_2^2 + k\varphi_{n2}^2 & k\varphi_{n2}\varphi_{n3} & -k\varphi_{n2} \\ k\varphi_{n3}\varphi_{n1} & k\varphi_{n3}\varphi_{n2} & \omega_3^2 + k\varphi_{n3}^2 & -k\varphi_{n3} \\ -k\varphi_{n1} & -k\varphi_{n2} & -k\varphi_{n3} & k_t \end{bmatrix} \tag{9.75d}$$

φ_{ni} is the mode shape coefficient of the nth floor in the ith mode. Solution of Equation 9.75a provides the generalized co-ordinates z_1, z_2, z_3 and the TMD displacement y. The storey displacements of the frame are determined from the generalized co-ordinates using normal mode transformation.

9.6.2 Direct Analysis

Equations 9.72a and 9.73 can be combined to obtain the following equation of motion:

$$\overline{\boldsymbol{M}}\ddot{\overline{\boldsymbol{X}}}+\overline{\boldsymbol{C}}\dot{\overline{\boldsymbol{X}}}+\overline{\boldsymbol{K}}\overline{\boldsymbol{X}}=-\overline{\boldsymbol{M}}\boldsymbol{I}\ddot{x}_g \tag{9.76a}$$

in which

$$\overline{\boldsymbol{X}}=[x_1\ldots x_n,y]^T;\quad \boldsymbol{I}=[1\ldots 1]^T;\quad \overline{\boldsymbol{M}}=\text{diag}(m_1\ldots m_n,m_t) \tag{9.76b}$$

$$\overline{\boldsymbol{C}}=\begin{bmatrix} c_1 & \cdots\cdots & \vdots & \vdots \\ \vdots & & \vdots & \vdots \\ \vdots & \cdots & c_n+c_t & -c_t \\ \cdots & \cdots & -c_t & c_t \end{bmatrix};\qquad \overline{\boldsymbol{K}}=\begin{bmatrix} k_1 & \cdots\cdots & \vdots & \vdots \\ \vdots & & \vdots & \vdots \\ \vdots & \cdots & k_n+k_t & -k_t \\ \cdots & \cdots & -k_t & k_t \end{bmatrix} \tag{9.76c}$$

The $\overline{\boldsymbol{C}}$ matrix is obtained by combining the $\boldsymbol{C}$ matrix with the damping elements introduced due to TMD as shown in Equation 9.76c. The $\boldsymbol{C}$ matrix is obtained by assuming Rayleigh damping for the bare frame. Note that except for the non-zero elements shown for the last rows and last columns of $\overline{\boldsymbol{K}}$ and $\overline{\boldsymbol{C}}$ matrices, the other elements of those rows and columns are zero. Solution of Equation 9.76a provides the responses of both the TMD and the frame.

9.6.3 State-Space Analysis

In the state space, the governing equation of motion can be written as:

$$\dot{\boldsymbol{v}}=\boldsymbol{A}\boldsymbol{v}+\boldsymbol{E} \tag{9.77a}$$

in which $\boldsymbol{v}=[\boldsymbol{X},\dot{\boldsymbol{X}},y,\dot{y}]^T$ is a $2(n+1)$ state vector; $\boldsymbol{A}$ is a $2(n+1)\times 2(n+1)$ system matrix; $\boldsymbol{E}$ is a $2(n+1)$ excitation vector. Matrices $\boldsymbol{A}$ and $\boldsymbol{E}$ are given as:

$$\boldsymbol{A}=\begin{bmatrix} \boldsymbol{0} & \boldsymbol{I} \\ -\overline{\boldsymbol{M}}^{-1}\overline{\boldsymbol{K}} & -\overline{\boldsymbol{M}}^{-1}\overline{\boldsymbol{C}} \end{bmatrix}\qquad \boldsymbol{E}=\begin{bmatrix} 0 \\ -\overline{\boldsymbol{M}}\boldsymbol{I} \end{bmatrix} \tag{9.77b}$$

The state-space equation may be solved using the methods, such as SIMULINK diagrams, described in Chapter 3.

Further, a modal analysis in the complex frequency domain may also be carried out to obtain the response by using FFT of the ground motion (described in Chapter 3).

Example 9.5

The building frame shown in Figure 9.40 is provided with a tuned mass damper (TMD) to control its response. Using the direct method of analysis, compare between the controlled and uncontrolled responses for the El Centro earthquake. Mass of the TMD is $m_t = 5\%$ of the total mass of the structure.

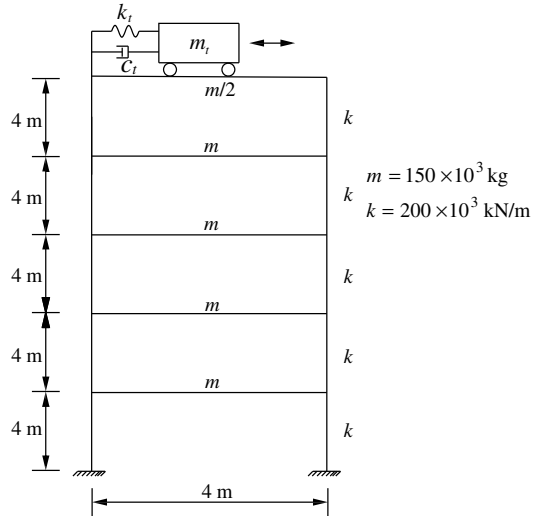

Figure 9.40 Frame with TMD at the top floor

Solution: The fundamental frequency of the bare frame is 11.42 rad s^{-1}. For perfect tuning,

$$\frac{k_t}{m_t} = (11.42)^2 = 130.4; \qquad m_t = 0.05 \times 675 \times 10^3 = 33.75 \times 10^3$$

$k_t = 130.4 \times 33.75 = 4.42 \times 10^3$ kN m^{-1}; $c_t = 2 \times 0.02 \times 33.75 \times 11.42 \times 10^3 = 15.42 \times 10^3$ N s m^{-1}

The mass, stiffness, and damping matrices of the frame-TMD system are:

$$\boldsymbol{K} = \begin{bmatrix} 400 & -200 & 0 & 0 & 0 & 0 \\ -200 & 400 & -200 & 0 & 0 & 0 \\ 0 & -200 & 400 & -200 & 0 & 0 \\ 0 & 0 & -200 & 400 & -200 & 0 \\ 0 & 0 & 0 & -200 & 204.4 & -4.4 \\ 0 & 0 & 0 & 0 & -4.4 & 4.4 \end{bmatrix} \times 10^6 \text{ N m}^{-1}$$

$$\boldsymbol{M} = \begin{bmatrix} 150 & 0 & 0 & 0 & 0 & 0 \\ 0 & 150 & 0 & 0 & 0 & 0 \\ 0 & 0 & 150 & 0 & 0 & 0 \\ 0 & 0 & 0 & 150 & 0 & 0 \\ 0 & 0 & 0 & 0 & 75 & 0 \\ 0 & 0 & 0 & 0 & 0 & 33.8 \end{bmatrix} \times 10^3 \text{ kg}$$

$$\boldsymbol{C} = \begin{bmatrix} 1024.7 & -448.6 & 0 & 0 & 0 & 0 \\ -448.6 & 1024.7 & -448.6 & 0 & 0 & 0 \\ 0 & -448.6 & 1024.7 & -448.6 & 0 & 0 \\ 0 & 0 & -448.6 & 1024.7 & -448.6 & 0 \\ 0 & 0 & 0 & -448.6 & 512.3 & 0 \\ 0 & 0 & 0 & 0 & 0 & 15.4 \end{bmatrix} \times 10^3 \text{ N s m}^{-1}$$

The $\boldsymbol{C}$ matrix for the bare frame is determined by assuming Rayleigh damping for the structure, obtained with the help of the first two natural frequencies ω_1 and ω_2. The responses of the system are obtained by solving the state-space equation, Equation 9.77a using SIMULINK of MATLAB®. The matrix $\boldsymbol{A}$ is given by:

$$\boldsymbol{A} = \begin{bmatrix}
0 & 0 & 0 & 0 & 0 & 0 & 1 & 0 & 0 & 0 & 0 & 0 \\
0 & 0 & 0 & 0 & 0 & 0 & 0 & 1 & 0 & 0 & 0 & 0 \\
0 & 0 & 0 & 0 & 0 & 0 & 0 & 0 & 1 & 0 & 0 & 0 \\
0 & 0 & 0 & 0 & 0 & 0 & 0 & 0 & 0 & 1 & 0 & 0 \\
0 & 0 & 0 & 0 & 0 & 0 & 0 & 0 & 0 & 0 & 1 & 0 \\
0 & 0 & 0 & 0 & 0 & 0 & 0 & 0 & 0 & 0 & 0 & 1 \\
-2666.71 & 1333.31 & 0 & 0 & 0 & 0 & -6.83 & 2.99 & 0 & 0 & 0 & 0 \\
1333.32 & -2666.72 & 1333.32 & 0 & 0 & 0 & 2.99 & -6.83 & 2.99 & 0 & 0 & 0 \\
0 & 1333.32 & -2666.71 & 1333.32 & 0 & 0 & 0 & 2.99 & -6.83 & 2.99 & 0 & 0 \\
0 & 0 & 1333.32 & -2666.71 & 1333.32 & 0 & 0 & 0 & 2.99 & -6.83 & 2.99 & 0 \\
0 & 0 & 0 & 2666.71 & -2725.43 & 58.73 & 0 & 0 & 0 & 5.98 & -6.83 & 0 \\
0 & 0 & 0 & 0 & 130.52 & -130.52 & 0 & 0 & 0 & 0 & 0 & -1.14
\end{bmatrix}$$

The controlled and uncontrolled responses are compared in Figures 9.41 and 9.42. It is seen from the figure that the peak displacement of the top floor of the frame is controlled by about 30%. The

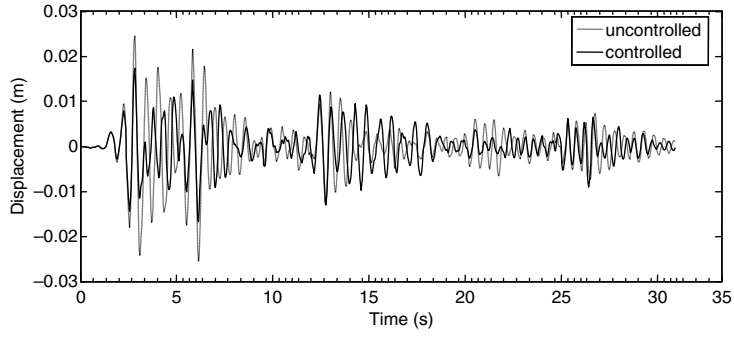

Figure 9.41 Controlled and uncontrolled displacements of first floor

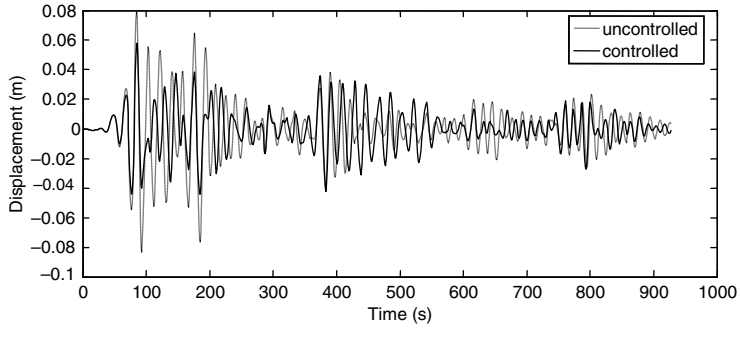

Figure 9.42 Controlled and uncontrolled displacements of fifth floor

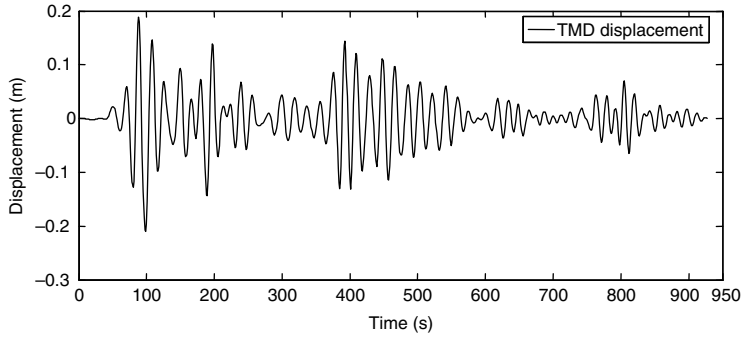

Figure 9.43 Time history of the excursion of the mass of TMD

corresponding control of the first floor is also about 30%, and hence the base shear is also controlled by the same amount. Figure 9.43 shows the time history of the excursion of the TMD mass. The maximum displacement of the TMD mass is 0.21 m, 3.62 times the controlled peak displacement of the frame.

9.7 Viscoelastic Dampers

Viscoelastic dampers (VEDs) are passive control devices that can be incorporated in building frames with relative ease compared with other passive control devices. VEDs are good alternatives to base isolation in retrofitting damaged or old buildings. They are especially attractive for buildings made of steel frames. A number of studies have been carried out to investigate the performance of VEDs in controlling the seismic response of buildings [5–7]. These studies dealt with: (i) the mechanical behavior of dampers; (ii) analysis, both exact and approximate, of framed structures fitted with VEDs; and (iii) optimal placement of VEDs is building frames. In this section, the seismic response analysis of building frames fitted with VEDs is discussed. As introduction of VEDs in the frames makes the systems non-classically damped, many approximate methods have been proposed to carry out the seismic analysis of such frames. A few of them, both in the frequency and the time domain, are presented here.

9.7.1 Modeling of Viscoelastic Dampers

There are various types of viscoelastic dampers (VEDs) reported in the literature, such as hydraulic dampers, friction dampers, Teflon coated friction dampers, and so on. A model of a Teflon coated VED is shown in Figure 9.44. Various types of mathematical models have been proposed to explain the mechanical behavior of VEDs. Of these, three linear models are described in the following sections.

9.7.1.1 Linear Models for Viscoelastic Damper

The linear model uses a linear spring that models the potential energy, quadratic in deformation, and linear dashpot, which models a dissipative force, proportional to deformation rate. Viscoelastic damper elements are modeled as parallel and series combinations of these linear springs and dashpots. The rate dependence is introduced by using the time derivative of the deformation and/or force.

In general, series and parallel combinations of linear springs and dashpots provide a force–deformation relation of the form [5]

$$C[f(t)] = D[\delta(t)] \tag{9.78}$$

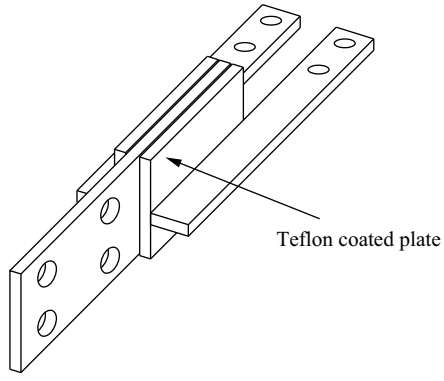

Figure 9.44 A model of Teflon coated viscoelastic damper

where $C[.]$ and $D[.]$ are linear differential operators with constant coefficients. Using a Laplace transformation, Equation 9.78 provides a transfer function $H(s)$ in the form of

$$F(s) = \frac{D(s)}{C(s)}\delta(s) = H(s)\delta(s) \tag{9.79}$$

which relates force $F(s)$ to the deformation $\delta(s)$.

The frequency response function of the viscoelastic element is then obtained by substituting $s = j\omega$ into Equation 9.79, where $j = \sqrt{-1}$ to yield

$$H(j\omega) = E_s(\omega) + jE_l(\omega) \tag{9.80}$$

in which $E_s(\omega)$ is referred to as the storage modulus; and $E_l(\omega)$ is called the loss modulus (Figure 9.45).

These moduli provide a physical understanding of the element resistance as composed of a frequency-dependent spring $K_d(\omega)$ and a frequency-dependent dashpot $C_d(\omega)$ given by:

$$K_d(\omega) = E_s(\omega); \qquad C_d(\omega) = \frac{E_l(\omega)}{\omega} \tag{9.81}$$

where $E_s(\omega)$ is an even function of frequency, while $E_l(\omega)$ is an odd function of frequency. The dynamic characteristics of the three different models of VEDs used in the study are given next.

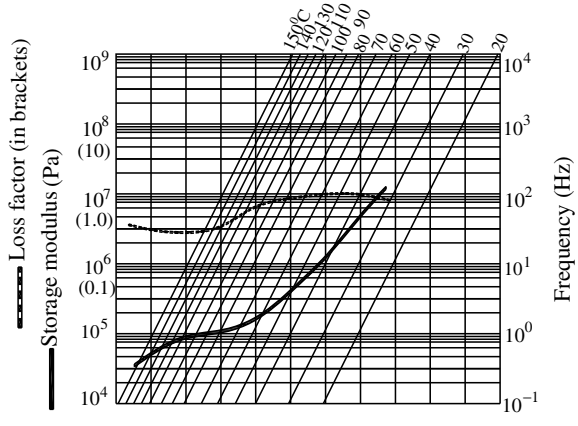

Figure 9.45 Storage and loss moduli of viscoelastic damper

9.7.1.2 Kelvin Element

The Kelvin model of VED (element) consists of a linear spring in parallel with a viscous damper. The force in the element satisfies [5]

$$\boldsymbol{f}(t) = k_d\delta(t) + c_d\dot{\delta}(t) \tag{9.82}$$

In the frequency domain, Equation 9.82 can be written as:

$$\boldsymbol{F}(j\omega) = (k_d + jc_d\omega)\delta(j\omega) \tag{9.83}$$

The dissipation of energy per cycle in harmonic deformation is linearly proportional to the deformation frequency:

$$W_{\text{cycle}} = \delta_{\max}^2 c_d \pi\omega \tag{9.84}$$

The main disadvantage of this model in modeling the viscoelastic material is that it defines a loss modulus linearly dependent on the frequency and a storage modulus independent of frequency that is not an accurate representation for most materials and, in particular, for polymers or rubbers.

9.7.1.3 Linear Hysteretic Element

In this model, the force satisfies the following equation in the frequency domain [5]

$$F(j\omega) = k_d(1 + j\xi\text{sgn}(\omega))\delta(j\omega) \tag{9.85}$$

The loss factor ξ (ratio of the loss and the storage moduli of the element) is frequency independent for this element. This model has the property of frequency independence of the dissipated energy in a deformation cycle

$$W_{\text{cycle}} = \delta_{\max}^2 \xi\pi k_d \tag{9.86}$$

Thus, the linear hysteretic element model is more versatile than the Kelvin model as many materials exhibit energy dissipation, independent of the frequency of the deformation. The fact that frequency-domain techniques may have to be used for many situations constitutes its most significant limitation.

9.7.1.4 Maxwell Element

A Maxwell element consists of a linear spring with constant β in series with a linear viscous dashpot with constant $\tau\beta$. This model satisfies the following differential equation [5]

$$\dot{f}(t) + \frac{1}{\tau}f(t) = \beta\dot{\delta}(t) \tag{9.87}$$

In the frequency domain, it may be represented as:

$$F(j\omega) = \frac{\beta\omega j}{j\omega + 1/\tau}\delta(j\omega) \tag{9.88}$$

From Equation 9.88, the storage modulus and the loss modulus for the Maxwell model may easily be obtained. Using a Maxwell model, the mechanical behavior of the viscoelastic damper can be modeled with much more accuracy as both storage modulus and loss modulus are fully dependent on the excitation frequency. The main mechanical characteristic of a Maxwell model is its relaxation time τ. The energy dissipation in one cycle is given by:

$$W_{\text{cycle}} = \delta_{\max}\beta\pi\frac{\omega\tau}{1 + (\omega\tau)^2} \tag{9.89}$$

Equation 9.89 shows that the energy dissipated in a cycle in this model increases with frequency for frequencies less than $1/\tau$ and monotonically decreases with frequency for frequencies greater than $1/\tau$.

9.7.2 MDOF System with Viscoelastic Damper

Consider a linear, damped multi-degrees of freedom structure containing linear energy dissipation devices as shown in Figure 9.46. The system can be described by the following differential equations:

$$\boldsymbol{M}\ddot{\boldsymbol{y}} + \boldsymbol{C}\dot{\boldsymbol{y}} + \boldsymbol{K}\boldsymbol{y} + \boldsymbol{B}^T\boldsymbol{f} = -\boldsymbol{M}\boldsymbol{I}_0\ddot{x}_g(t) \tag{9.90}$$

where

$\boldsymbol{y}$ is a vector of displacement
$\boldsymbol{M}$, $\boldsymbol{K}$, and $\boldsymbol{C}$ represent the mass, the stiffness, and the damping matrices, respectively
$\ddot{\boldsymbol{x}}_g$ represents the ground acceleration
$\boldsymbol{I}_0$ is the influence coefficient vector
$\boldsymbol{f}$ is the vector of forces in the energy dissipation devices
$\boldsymbol{B}$ is the location coefficient matrix of size $n_e \times n$
n is the degree of freedom
n_e is the number of energy dissipation devices.

The element forces in the energy dissipation devices are related to the deformations of the devices by one of the models of the linear constitutive relations described previously.

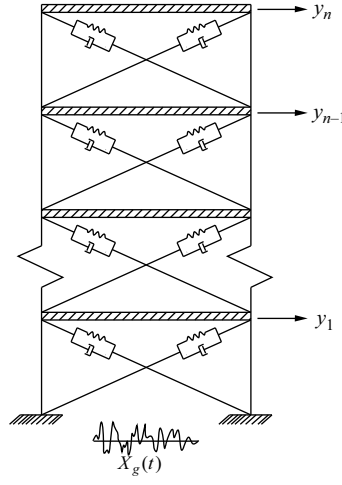

Figure 9.46 Idealized building frame with viscoelastic dampers

In the frequency domain, Equation 9.90 may be written as:

$$[-\omega^2\boldsymbol{M} + (j\omega)\boldsymbol{C} + \boldsymbol{K}]\boldsymbol{Y}(j\omega) + \boldsymbol{B}^T\boldsymbol{F}(j\omega) = -\boldsymbol{M}\boldsymbol{I}_0\ddot{x}_g(j\omega) \tag{9.91}$$

in which $\boldsymbol{Y}(j\omega)$, $\boldsymbol{F}(j\omega)$, and $\ddot{x}_g(j\omega)$ are the Fourier transforms of $\boldsymbol{y}$, $\boldsymbol{f}$, and $\ddot{x}_g$, respectively. Writing $F_i(j\omega)$ in terms of storage and loss moduli (Equation 9.80) as:

$$F_i(j\omega) = H_i(j\omega)\delta_i(j\omega) \tag{9.92a}$$

and relating $\delta(j\omega)$ to $\boldsymbol{Y}(j\omega)$ by:

$$\delta(j\omega) = \boldsymbol{B}\boldsymbol{Y}(j\omega) \tag{9.92b}$$

Equation 9.91 may be written in the form

$$\boldsymbol{S}(j\omega)\boldsymbol{Y}(j\omega) = -\boldsymbol{M}\boldsymbol{I}_0\ddot{x}_g(j\omega) \tag{9.92c}$$

in which

$$\boldsymbol{S}(j\omega) = -\omega^2\boldsymbol{M} + j\omega\boldsymbol{C} + \boldsymbol{K} + \boldsymbol{B}^T\boldsymbol{E}_s(\omega)\boldsymbol{B} + j\boldsymbol{B}^T\boldsymbol{E}_l(\omega)\boldsymbol{B} \tag{9.92d}$$

$\boldsymbol{E}_s(\omega)$ and $\boldsymbol{E}_l(\omega)$ are the diagonal matrices containing the storage and loss moduli of all dampers and depend upon the modeling of the dampers. Equations 9.92c and 9.22d may be solved in direct frequency domain using FFT to obtain $\boldsymbol{Y}(j\omega)$. IFFT of $\boldsymbol{Y}(j\omega)$ provides $\boldsymbol{y}(t)$.

If modal analysis is used, then $\boldsymbol{Y}(j\omega)$ may be written in terms of modal co-ordinates as:

$$\boldsymbol{Y}(j\omega) = \Phi\boldsymbol{q}(j\omega) \tag{9.93}$$

where Φ is the mode shape matrix of size $N \times m$ and $\boldsymbol{q}(j\omega)$ is the Fourier transform of the modal coordinates q_l, $l = 1, 2, \ldots, m$. Using the modal transformation, and pre-multiplying Equation 9.92a by Φ^T the following equation is obtained,

$$\Gamma(j\omega)\boldsymbol{q}(j\omega) = -\Phi^T\boldsymbol{M}\boldsymbol{I}_0\ddot{x}_g(j\omega) \tag{9.94a}$$

where

$$\Gamma(j\omega) = \Phi^T(-\omega^2\boldsymbol{M} + j\omega\boldsymbol{C} + \boldsymbol{K} + \boldsymbol{B}^T\boldsymbol{E}_s(\omega)\boldsymbol{B} + \boldsymbol{B}^T\boldsymbol{E}_l(\omega)\boldsymbol{B})\Phi \tag{9.94b}$$

9.7.2.1 Conditions for Modal Decoupling and Coupling

$\Gamma(j\omega)$ will not be diagonal for any modal matrix Φ, unless $\boldsymbol{C}$, $\boldsymbol{B}^T\boldsymbol{E}_s(\omega)\boldsymbol{B}$, and $\boldsymbol{B}^T\boldsymbol{E}_l(\omega)\boldsymbol{B}$ are classical for all ω. When these terms are classical, $\Gamma(j\omega)$ would be diagonal and the following equations could be written in modal co-ordinates:

$$\boldsymbol{q}_l(j\omega) = \frac{-\boldsymbol{\phi}_l^T\boldsymbol{M}\boldsymbol{I}_0\ddot{x}_g(j\omega)}{\boldsymbol{\phi}_l^T\boldsymbol{S}(j\omega)\boldsymbol{\phi}_l} = \frac{-\boldsymbol{\phi}_l^T\boldsymbol{M}\boldsymbol{I}_0\ddot{x}_g(j\omega)}{\Gamma_{ll}(j\omega)}; \quad l = 1, 2, \ldots, m \tag{9.95}$$

$$\Gamma_{ll}(j\omega) = \boldsymbol{\phi}_l^T(-\omega^2\boldsymbol{M} + j\omega\boldsymbol{C} + \boldsymbol{K} + \boldsymbol{B}^T\boldsymbol{E}_s(\omega)\boldsymbol{B} + \boldsymbol{B}^T\boldsymbol{E}_l(\omega)\boldsymbol{B})\boldsymbol{\phi}_l \tag{9.96}$$

The solution of Equations 9.92c and 9.92d can then be obtained by solving m independent modal equations in the frequency domain. Using FFT techniques and modal combination, the time histories of responses can be obtained. The conditions under which the modal equations can be decoupled is illustrated by the following example.

Consider a two-storey building frame fitted with VEDs as shown in Figure 9.47. The dampers have the same relaxation time τ. The stiffness matrix is characterized by the parameters k_1 and k_2. Location of two viscoelastic dampers modeled by Maxwell elements provide

$$\boldsymbol{B}^T = \begin{bmatrix} \cos\alpha & \cos\alpha & -\cos\alpha & -\cos\alpha \\ 0 & 0 & \cos\alpha & \cos\alpha \end{bmatrix}; \quad E_{si} = \frac{\beta_i\omega^2}{\omega^2 + \left(\frac{1}{\tau}\right)^2}; \quad E_{li} = \frac{\beta_i\frac{\omega}{\tau}}{\omega^2 + \left(\frac{1}{\tau}\right)^2} \tag{9.97}$$

Defining

$$g_1(\omega) = \frac{2\omega^2}{\omega^2 + (1/\tau)^2}\cos^2\alpha \text{ and } g_2(\omega) = \frac{2\omega/\tau}{\omega^2 + (1/\tau)^2}\cos^2\alpha$$

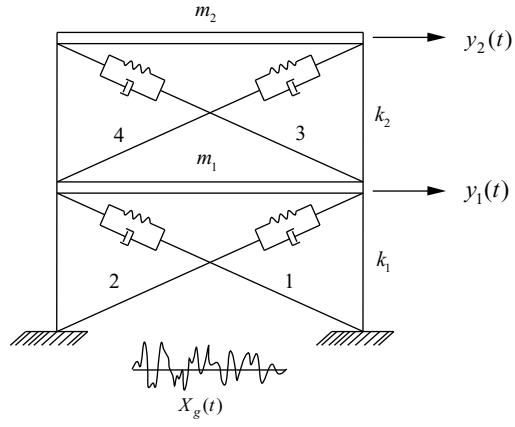

Figure 9.47 Model of a two DOF structure with viscoelastic damper

the following equation in the frequency domain may be written:

$$\left[(j\omega)^2\boldsymbol{M}+(j\omega)\boldsymbol{C}+\boldsymbol{K}+\begin{bmatrix}\beta_1+\beta_2 & -\beta_2\\ -\beta_2 & \beta_2\end{bmatrix}g_1(\omega)+j\begin{bmatrix}\beta_1+\beta_2 & -\beta_2\\ -\beta_2 & \beta_2\end{bmatrix}g_2(\omega)\right]\boldsymbol{Y}(j\omega) = -\boldsymbol{M}\boldsymbol{I_0}\ddot{x}_g(j\omega) \tag{9.98}$$

in which

$$\boldsymbol{M}=\begin{bmatrix}m_1 & 0\\ 0 & m_2\end{bmatrix};\quad \boldsymbol{C}=\begin{bmatrix}c_1+c_2 & -c_2\\ -c_2 & c_2\end{bmatrix};\quad \boldsymbol{K}=\begin{bmatrix}k_1+k_2 & -k_2\\ -k_2 & k_2\end{bmatrix};\quad \boldsymbol{I_0}=\begin{bmatrix}1\\ 1\end{bmatrix} \tag{9.99}$$

If $\beta_2/\beta_1 = k_2/k_1$ and $\boldsymbol{C}$ is mass and stiffness proportional, the system can be uncoupled into two modal equations. Let ϕ_1 and ϕ_2 be normalized with respect to the mass matrix, then for $\beta_2/\beta_1 = k_2/k_1$ the following equations hold:

$$q_i(j\omega)=\frac{\boldsymbol{\phi}_i^T\boldsymbol{M}\boldsymbol{I}}{\Gamma_{ii}(j\omega)}\ddot{x}_g(j\omega)\quad i=1,2 \tag{9.100}$$

$$\Gamma_{ii}(j\omega)=-\omega^2+\omega_i^2+\omega_i^2\frac{\beta_1}{k_1}g_1(\omega)+j\omega_i^2\omega_i^2\frac{\beta_1}{k_1}g_2(\omega)\quad i=1,2 \tag{9.101}$$

When the damping matrix or the resistance scheme of the viscoelastic elements of the structure is non-classical, $\Gamma(j\omega)$ is not diagonal and the $m \times m$ coupled equation (Equation 9.94a) can be solved to directly obtain the responses $\boldsymbol{y}$ by some approximate methods. There are various approximate methods [8–10] to solve the coupled equations of motion as given by Equation 9.94a. The simplest solution for Equation 9.94a can be obtained by ignoring the off-diagonal terms of the coupled equations of motion and solving a set of uncoupled equations, equal to the number modes considered in the analysis. The accuracy of the response thus obtained depends upon the relative magnitude of the off-diagonal terms in the coupled equations of the motion. Here, two approximate methods, namely, the iterative pseudo-force method and modal strain energy method, which are supposed to provide a good estimate of responses are presented. The reason for choosing these two methods is that both use undamped mode shapes and frequencies and solve a set of uncoupled set of equations equal to the number of modes.

9.7.3 Iterative Pseudo-Force (P-F) Method

In this method of solution, the modal coupling introduced by the off-diagonal terms are treated as pseudo-force and are transferred to the right-hand side of Equation 9.94a. The equations of motion are solved iteratively, each time solving a set of uncoupled equations of motion. At the nth iteration, the following equations of motion are solved:

$$\boldsymbol{q}^{(n)}(j\omega) = \boldsymbol{q}^{(0)}(j\omega) + \boldsymbol{A}(j\omega)\boldsymbol{q}^{(n-1)}(j\omega) \quad n = 1, 2, 3, \ldots \tag{9.102}$$

where

$$\boldsymbol{q}^{(n)^T}(j\omega) = \left[q_1^{(n)}(j\omega) \quad q_2^{(n)}(j\omega) \quad \cdots \quad q_m^{(n)}(j\omega) \right]^T \tag{9.103}$$

The elements of the matrix $\boldsymbol{A}(j\omega)$ are:

$$A_{ij} = \frac{\Gamma_{ij}(j\omega)}{\Gamma_{ii}(j\omega)} \text{ if } i \neq j \tag{9.104}$$

$$A_{ij} = 0 \text{ if } i = j \tag{9.105}$$

and $q_i^{(0)}(j\omega)$ is given by:

$$q_i^{(0)} = \frac{-\boldsymbol{M}\boldsymbol{\phi}_i^T \boldsymbol{I}_0}{\Gamma_{ii}(j\omega)} \ddot{x}_g(j\omega) \quad i = 1, 2, \ldots, m \tag{9.106}$$

It can be shown that the necessary and sufficient condition for the algorithm to converge to the exact solution for any excitation $\ddot{x}_g(t)$ is that the eigen values of $\boldsymbol{A}(j\omega)$ be in the unit circle for $(-\infty < \omega < \infty)$ [8]. A sufficient condition for the convergence of the algorithm is given by [10]:

$$\sum_{i=1}^{m} |\boldsymbol{A}_{li}(j\omega)| < 1 \quad l = 1, 2, \ldots, m \tag{9.107}$$

Furthermore, this condition can be stated in terms of the matrix $\Gamma(j\omega)$, because from Equation 9.104 it is clear that the condition given by Equation 9.107 holds if, and only if, the matrix $\Gamma(j\omega)$ is diagonal dominant, that is if

$$\left|\boldsymbol{\phi}_i^T \boldsymbol{S}(j\omega)\boldsymbol{\phi}_i\right| > \sum_{l=1, l\neq i}^{m} \left|\boldsymbol{\phi}_i^T \boldsymbol{S}(j\omega)\boldsymbol{\phi}_l\right|; \quad i = 1, 2, \ldots, m; \quad -\infty < \omega < \infty \tag{9.108}$$

The above method can be used for solving any other non-classically damped system using the mode superposition technique.

9.7.4 Modal Strain Energy Method

Modal strain energy method is a procedure to determine a set of real-valued mode shapes, natural frequencies, and damping ratios for linear structures with frequency-dependent stiffness and damping matrices to approximate the dynamics of those structures. In this approach, the mode shapes and natural frequencies of the approximate system are obtained by solving an eigen value problem that neglects the loss modulus (Equation 9.80) of the viscoelastic elements of the structure. Once a set of mode shapes and natural frequencies are obtained, the modal damping ratios of the approximate system are computed, equating the loss modulus of the viscoelastic elements of the structure at the natural frequencies of the modes to that of the modal equations. As a consequence, the modal strain energy method seeks a set of uncoupled modal equations to approximate the response of the system described by Equation 9.92a.

Consider the vector $\widehat{\boldsymbol{\phi}}_l$ and natural frequency, $\widehat{\omega}_l$ that solve the following eigen value problem:

$$\widehat{\omega}_l^2 \boldsymbol{M}\widehat{\boldsymbol{\phi}}_l = (\boldsymbol{K} + \boldsymbol{B}^T \boldsymbol{E}_s(\widehat{\omega}_l)\boldsymbol{B})\widehat{\boldsymbol{\phi}}_l \quad l = 1, 2, \ldots, m \tag{9.109}$$

Here, the values of $\boldsymbol{E}_s(\widehat{\omega}_l)$ are necessarily non-negative, non-decreasing, and bounded as in the case of viscoelastic materials.

Let $\widehat{\boldsymbol{\phi}} = [\widehat{\phi}_1 \ldots \widehat{\phi}_m]$. With these $\widehat{\boldsymbol{\phi}}$, the modal transformation of Equation 9.92c will be the same as that given by Equations 9.94a and 9.94b except that Φ is replaced by $\widehat{\boldsymbol{\phi}}$. By neglecting the off-diagonal terms of the transformed equation, taking $\omega = \widehat{\omega}_l$ in $\boldsymbol{E}_{si}(\omega)$ in the lth equation, and dividing the lth equation of Equation 9.94a by $\widehat{\boldsymbol{\phi}}_l^T \boldsymbol{M}\widehat{\boldsymbol{\phi}}_l$, the following equation is obtained:

$$\left\{-\omega^2 + j\omega \frac{1}{\widehat{\boldsymbol{\phi}}_l^T \boldsymbol{M}\widehat{\boldsymbol{\phi}}_l} \widehat{\boldsymbol{\phi}}_l^T \left[\boldsymbol{C} + \boldsymbol{B}^T \frac{\boldsymbol{E}_l(\omega)}{\omega} \boldsymbol{B}\right]\widehat{\boldsymbol{\phi}}_l + \widehat{\omega}_l^2\right\} \widehat{q}_l(j\omega) = -\frac{\widehat{\boldsymbol{\phi}}_l^T \boldsymbol{M}\boldsymbol{I}_0 \ddot{x}_g(j\omega)}{\widehat{\boldsymbol{\phi}}_l^T \boldsymbol{M}\widehat{\boldsymbol{\phi}}_l} \quad l = 1, 2, \ldots, m \tag{9.110}$$

By taking $\omega = \widehat{\omega}_l$ in the term $\boldsymbol{E}_l(\omega)/\omega$ of Equation 9.110, the lth modal equation can then be transformed back into the time domain in the form of a second-order differential equation to yield

$$\ddot{q}_l(t) + 2\widehat{\omega}_l \widehat{\xi}_l \dot{q}_l(t) + \widehat{\omega}_l^2 q_1(t) = -\frac{\widehat{\boldsymbol{\phi}}_l^T \boldsymbol{M}\boldsymbol{I}_0 \ddot{x}_g(t)}{\widehat{\boldsymbol{\phi}}_l^T \boldsymbol{M}\widehat{\boldsymbol{\phi}}_l} \quad l = 1, 2, \ldots, m \tag{9.111}$$

where the modal frequency $\widehat{\omega}_l$ and damping ratio $\widehat{\xi}_l$ can be expressed as:

$$\widehat{\omega}_l^2 = \frac{\widehat{\boldsymbol{\phi}}_l^T (\boldsymbol{K} + \boldsymbol{B}^T \boldsymbol{E}_s(\widehat{\omega}_l)\boldsymbol{B})\widehat{\boldsymbol{\phi}}_l}{\widehat{\boldsymbol{\phi}}_l^T \boldsymbol{M}\widehat{\boldsymbol{\phi}}_l} \qquad \widehat{\xi}_l = \frac{\widehat{\boldsymbol{\phi}}_l^T (\widehat{\omega}_l \boldsymbol{C} + \boldsymbol{B}^T \boldsymbol{E}_l(\widehat{\omega}_l)\boldsymbol{B})\widehat{\boldsymbol{\phi}}_l}{2\widehat{\boldsymbol{\phi}}_l^T [\boldsymbol{M}(\boldsymbol{K} + \boldsymbol{B}^T \boldsymbol{E}_s(\widehat{\omega}_l)\boldsymbol{B})]^{1/2}\widehat{\boldsymbol{\phi}}_l} \tag{9.112}$$

Once $q_1(t)$ is obtained, the response $y(t)$ may be determined as before by modal superposition. Note that the eigen value problem given by Equation 9.109 has to be solved using the iteration technique.

9.7.5 State-Space Solution

If VEDs are modeled as Maxwell elements, then a direct solution of the problem is possible in the time domain through state-space representation of the equation of motion.

Equation 9.90 together with Equation 9.87 to represent the behavior of the VED, may be written in state space as:

$$\dot{\boldsymbol{Z}} = \boldsymbol{A}\boldsymbol{Z} + \boldsymbol{E} \tag{9.113}$$

where $\boldsymbol{Z}$ is a $(2n + n_e)$ state vector, $\boldsymbol{A}$ is a $(2n + n_e, 2n + n_e)$ system matrix and $\boldsymbol{E}$ is a $(2n + n_e)$ excitation vector, respectively, given by:

$$\boldsymbol{Z} = \begin{bmatrix} \boldsymbol{y} \\ \dot{\boldsymbol{y}} \\ \boldsymbol{f} \end{bmatrix}; \quad \boldsymbol{E} = \begin{bmatrix} 0_n \\ \boldsymbol{I}_n \\ 0_m \end{bmatrix} \ddot{x}_g; \tag{9.114a}$$

$$\boldsymbol{A} = \begin{bmatrix} \boldsymbol{0} & \boldsymbol{I} & \boldsymbol{0} \\ -\boldsymbol{M}^{-1}\boldsymbol{K} & -\boldsymbol{M}^{-1}\boldsymbol{C} & -\boldsymbol{M}^{-1}\boldsymbol{B}^T \\ \boldsymbol{0} & \boldsymbol{P}\boldsymbol{B} & -\dfrac{\boldsymbol{I}}{\boldsymbol{\tau}} \end{bmatrix} \tag{9.114b}$$

in which $\boldsymbol{f}$ is the vector damper forces ($i = 1, \ldots n_e$); P is the diagonal matrix with diagonal terms as β_i. The state-space equation may be solved using direct or modal methods of analysis as described in Chapter 3. Note that the solution provides not only the responses of the structures but also the forces in each damper.

Example 9.6

The same bare building frame except the top storey mass taken as m, shown in Figure 9.40, is fitted with VEDs in all floors in the form of X bracings. Properties of the VEDs are given as $\tau = 0.2$, and $\beta/m = 1000$. Using the Maxwell model for the VEDs, find the responses of the frame under the El Centro earthquake using state-space analysis and compare them with uncontrolled responses.

Solution: $\boldsymbol{M}$, $\boldsymbol{K}$, and $\boldsymbol{C}$ matrices of the bare frame are taken from the Example 9.4 by considering the first 5×5 portion of the corresponding matrices of the same problem with appropriate change of the mass. Note that the last diagonal term of the $\boldsymbol{K}$ matrix will be 200 (in place of 204.4). Referring to Equations 9.113 and 9.114

$$\boldsymbol{B}^T = \begin{bmatrix} 0.707 & 0.707 & -0.707 & -0.707 & 0 & 0 & 0 & 0 & 0 & 0 \\ 0 & 0 & 0.707 & 0.707 & -0.707 & -0.707 & 0 & 0 & 0 & 0 \\ 0 & 0 & 0 & 0 & 0.707 & 0.707 & -0.707 & -0.707 & 0 & 0 \\ 0 & 0 & 0 & 0 & 0 & 0 & 0.707 & 0.707 & -0.707 & -0.707 \\ 0 & 0 & 0 & 0 & 0 & 0 & 0 & 0 & 0.707 & 0.707 \end{bmatrix}$$

$$P = \text{diag}\,[15 \times 10^7]_{10\times 10}; \qquad \frac{I}{\tau} = \text{diag}\,[5]_{10\times 10}$$

With the above values of the matrices, matrix $\boldsymbol{A}$ is given by:

$$\boldsymbol{A} = \begin{bmatrix} \boldsymbol{A}_1 & \boldsymbol{A}_2 \\ \boldsymbol{A}_3 & \boldsymbol{A}_4 \end{bmatrix}$$

where

$$\boldsymbol{A}_1 = \begin{bmatrix} 0 & 0 & 0 & 0 & 0 & 1 & 0 & 0 & 0 & 0 \\ 0 & 0 & 0 & 0 & 0 & 0 & 1 & 0 & 0 & 0 \\ 0 & 0 & 0 & 0 & 0 & 0 & 0 & 1 & 0 & 0 \\ 0 & 0 & 0 & 0 & 0 & 0 & 0 & 0 & 1 & 0 \\ 0 & 0 & 0 & 0 & 0 & 0 & 0 & 0 & 0 & 1 \\ -2666.71 & 1333.32 & 0 & 0 & 0 & -7.32 & 3.27 & 0 & 0 & 0 \\ 1333.32 & -2666.71 & 1333.32 & 0 & 0 & 3.27 & -7.32 & 3.27 & 0 & 0 \\ 0 & 1333.32 & -2666.71 & 1333.32 & 0 & 0 & 3.27 & -7.32 & 3.27 & 0 \\ 0 & 0 & 1333.32 & -2666.71 & 1333.32 & 0 & 0 & 3.27 & -7.32 & 3.27 \\ 0 & 0 & 0 & 1333.32 & -1333.32 & 0 & 0 & 0 & 3.27 & -4.05 \end{bmatrix}$$

$$A_2 = \begin{bmatrix} 0 & 0 & 0 & 0 & 0 & 0 & 0 & 0 & 0 & 0 \\ 0 & 0 & 0 & 0 & 0 & 0 & 0 & 0 & 0 & 0 \\ 0 & 0 & 0 & 0 & 0 & 0 & 0 & 0 & 0 & 0 \\ 0 & 0 & 0 & 0 & 0 & 0 & 0 & 0 & 0 & 0 \\ 0 & 0 & 0 & 0 & 0 & 0 & 0 & 0 & 0 & 0 \\ -4.714 & -4.714 & 4.714 & 4.714 & 0 & 0 & 0 & 0 & 0 & 0 \\ 0 & 0 & -4.714 & -4.714 & 4.714 & 4.714 & 0 & 0 & 0 & 0 \\ 0 & 0 & 0 & 0 & -4.714 & -4.714 & 4.714 & 4.714 & 0 & 0 \\ 0 & 0 & 0 & 0 & 0 & 0 & -4.714 & -4.714 & 4.714 & 4.714 \\ 0 & 0 & 0 & 0 & 0 & 0 & 0 & 0 & -4.714 & -4.714 \end{bmatrix} \times 10^{-6}$$

$$A_3 = \begin{bmatrix} 0 & 0 & 0 & 0 & 0 & 1.0607 & 0 & 0 & 0 & 0 \\ 0 & 0 & 0 & 0 & 0 & 1.0607 & 0 & 0 & 0 & 0 \\ 0 & 0 & 0 & 0 & 0 & -1.0607 & 1.0607 & 0 & 0 & 0 \\ 0 & 0 & 0 & 0 & 0 & -1.0607 & 1.0607 & 0 & 0 & 0 \\ 0 & 0 & 0 & 0 & 0 & 0 & -1.0607 & 1.0607 & 0 & 0 \\ 0 & 0 & 0 & 0 & 0 & 0 & -1.0607 & 1.0607 & 0 & 0 \\ 0 & 0 & 0 & 0 & 0 & 0 & 0 & -1.0607 & 1.0607 & 0 \\ 0 & 0 & 0 & 0 & 0 & 0 & 0 & -1.0607 & 1.0607 & 0 \\ 0 & 0 & 0 & 0 & 0 & 0 & 0 & 0 & -1.0607 & 1.0607 \\ 0 & 0 & 0 & 0 & 0 & 0 & 0 & 0 & -1.0607 & 1.0607 \end{bmatrix} \times 10^{8}$$

$$A_4 = \text{diag}\,[-5]_{10\times 10}$$

Using SIMULINK of MATLAB, the responses are obtained for the El Centro earthquake. The block diagram for the state-space solution using SIMULINK is shown in Chapter 3.

The results are shown in Figures 9.48–9.51. It is seen from Figure 9.48 that the peak value of the fifth-floor displacement is controlled by about 48%. The corresponding control for the first-floor displacement is about 50%. The maximum control force developed in the fifth-floor VEDs is 3.834×10^5 N, while that for the first floor is 1.28×10^6 N. Thus, it is observed that the control of the displacement response is

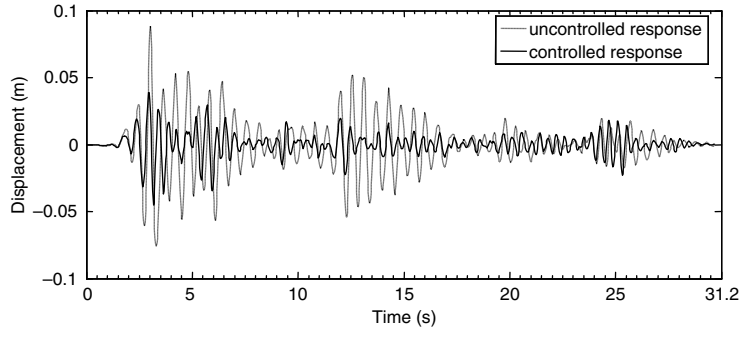

Figure 9.48 Controlled and uncontrolled displacements of fifth-floor

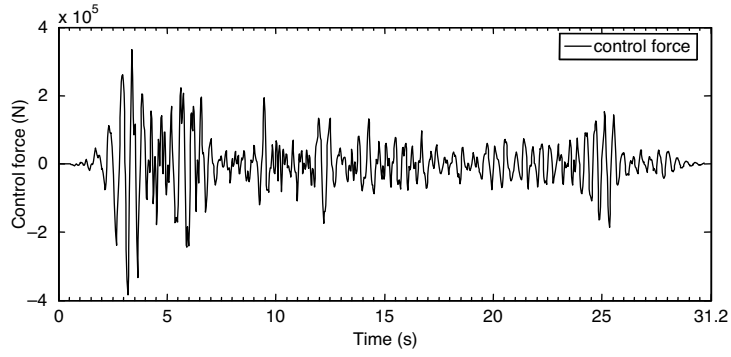

Figure 9.49 Time history of control force in the fifth-floor VEDs

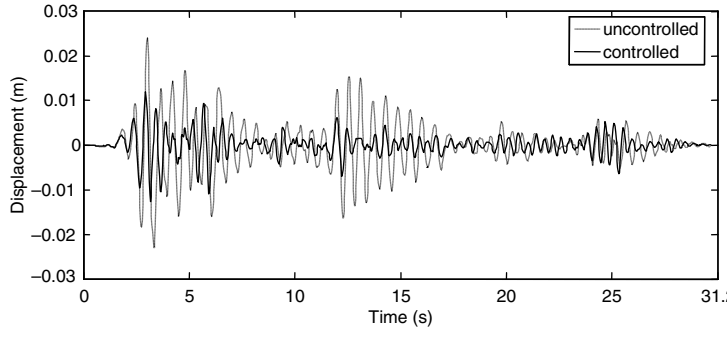

Figure 9.50 Controlled and uncontrolled displacements of first-floor

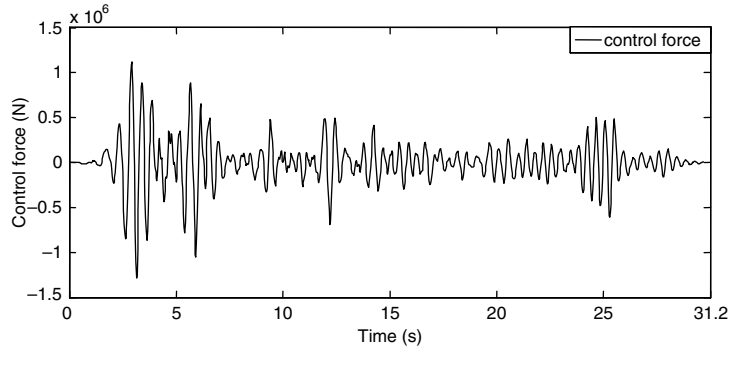

Figure 9.51 Time history of control force in the first-floor VEDs

nearly the same for all floors. However, the maximum control forces developed in the VEDs installed in different floors are different.

9.7.6 Response Spectrum Method of Analysis

In order to obtain the response spectrum method of analysis, both damping and stiffness of the system should be frequency independent. Thus, in order to implement the response spectrum method, the modal equation of motion, Equation 9.111, derived by the modal strain energy method can be used. However, because of the approximations involved in the modal strain energy method, the responses obtained by the response spectrum method using Equation 9.111 are approximate. Using $\widehat{\omega}$ and $\widehat{\xi}$ of Equation 9.112, the response spectrum method of analysis can be performed as described in Chapter 5. The equivalent lateral load for a frame fitted with VED is given by:

$$Q_i^r = \lambda_i \, \widehat{\phi}_i^{\,r} \, W^r \frac{S_{a_i}}{g} \tag{9.115a}$$

$$\lambda_i = \frac{\sum_{r=1}^{N} \widehat{\phi}_i^{\,r} \, W^r}{\sum_{r=1}^{N} W^r (\widehat{\phi}_i^{\,r})^2} \tag{9.115b}$$

where

λ_i is the mode participation factor for the ith mode
W^r is the weight of the rth floor including appropriate live load
S_{a_i}/g is the normalized spectral acceleration in the ith mode
$\widehat{\phi}_i^{\,r}$ is the mode shape coefficient for the rth floor in the ith mode.

The mode shape coefficients are obtained from Equation 9.109 and S_{a_i}/g is the normalized spectral acceleration for the time period $T_i = 2\pi/\widehat{\omega}_i$ and damping ratio $\widehat{\xi}_i$.

9.8 Active Structural Control

As mentioned in the introduction, active control of structures requires an external power source to activate and actuate the active control system. The signal that drives the actuator of the control system is generated by the computer according to a control algorithm. The control algorithm requires, apart from other structural data, online measured responses of the structure as feedback. A typical schematic diagram of the active control of structures for seismic forces is shown in Figure 9.52. It is seen from the figure that the active control of structures has three distinct components, namely: measurements, computation, and actuation. Measurements are accomplished by sensors that measure (generally) the acceleration response of the structure and the ground acceleration (if needed). Computation is performed by a computer that computes the control force signal to be applied at every instant of time to the actuator according to a desired control algorithm. Measured responses of the structure and ground acceleration (if needed) are fed into the control algorithm as one set of inputs. If only structural responses are measured and used as feedback information to the control algorithm, then it is called a closed loop control (that is, only the right loop of Figure 9.52 operates). On the other hand, if only measured excitations are used as information to the control algorithm, then it is called an open loop control (that is, only left loop operates). If both loops are operative, then it is called closed–open loop control.

There are many control algorithms that have been developed for the active control of structures. Most of them use the closed loop control strategy. Some of the popularly used algorithms are: linear quadratic

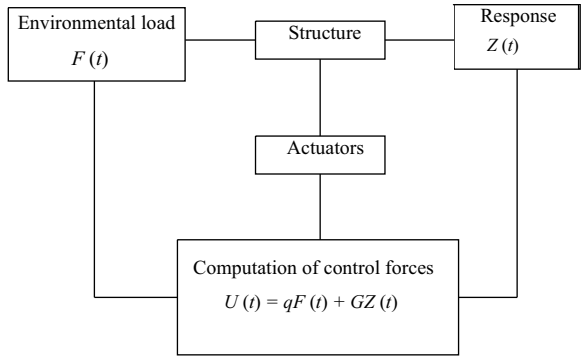

Figure 9.52 Schematic diagram of active control of structures for seismic forces

regulator (LQR) control, pole placement technique, instantaneous optimal control, discrete time control, sliding mode control, independent modal space control, bounded state control, predictive control, H_α control, and so on [11,12]. The control mechanisms, which have been developed and used in experiments and in practice, include actuated mass damper (AMD), actuated tuned mass damper (ATMD), active tendon system (AT), and so on (Figure 9.53).

Active control algorithms generate the required control signal that drives the actuators of the control device. Before describing the control algorithms, it is desirable to understand the effect of control forces on the response of a structure under ideal conditions. Consider the equation of motion of a multi-degrees of freedom system under a set of control forces $\boldsymbol{u}$:

$$\boldsymbol{M}\ddot{\boldsymbol{x}} + \boldsymbol{C}\dot{\boldsymbol{x}} + \boldsymbol{K}\boldsymbol{x} = \boldsymbol{D}\boldsymbol{u} - \boldsymbol{M}\boldsymbol{I}\ddot{\boldsymbol{x}}_g \tag{9.116}$$

where

$\boldsymbol{M}$, $\boldsymbol{C}$, and $\boldsymbol{K}$ are $n \times n$ mass, damping, and stiffness matrices, respectively
$\boldsymbol{x}$ is the n dimensional displacement vector
$\ddot{\boldsymbol{x}}_g$ is the vector ground accelerations of size r
$\boldsymbol{I}$ is the influence coefficient matrix of size $n \times r$
$\boldsymbol{D}$ is the location matrix of size $n \times m$
$\boldsymbol{u}$ is a vector of control force of size m.

It is assumed that the control force vector $\boldsymbol{u}$ is linearly proportional to the responses $\boldsymbol{x}$ and $\dot{\boldsymbol{x}}$ and the excitations $\ddot{\boldsymbol{x}}_g$. Then, $\boldsymbol{u}$ may be written as:

$$\boldsymbol{u} = \boldsymbol{K}_1\boldsymbol{x} + \boldsymbol{C}_1\dot{\boldsymbol{x}} + \boldsymbol{E}\ddot{\boldsymbol{x}}_g \tag{9.117}$$

in which $\boldsymbol{K}_1$, $\boldsymbol{C}_1$, and $\boldsymbol{E}$ are time independent matrices of size $m \times n$ and $m \times r$, respectively. Substituting Equation 9.116 into Equation 9.117 results in

$$\boldsymbol{M}\ddot{\boldsymbol{x}} + (\boldsymbol{C} - \boldsymbol{D}\boldsymbol{C}_1)\dot{\boldsymbol{x}} + (\boldsymbol{K} - \boldsymbol{D}\boldsymbol{K}_1)\boldsymbol{x} = (\boldsymbol{D}\boldsymbol{E} - \boldsymbol{M}\boldsymbol{I})\ddot{\boldsymbol{x}}_g \tag{9.118}$$

Equation 9.118 shows that the active control in a way modifies the stiffness and damping properties of the system and excitations, such that the responses of the system are reduced. The degree of reduction depends upon how $\boldsymbol{K}_1$, $\boldsymbol{C}_1$, and $\boldsymbol{E}$ are obtained. The objective of a control algorithm is to find these quantities so that the response of the system satisfies the desired criterion. In practice, closed loop control can be more readily implemented, and, therefore $\boldsymbol{K}_1$, $\boldsymbol{C}_1$ matrices are generated by the control algorithm for obtaining the control force. Furthermore, it is observed from Equation 9.116 that complete control of

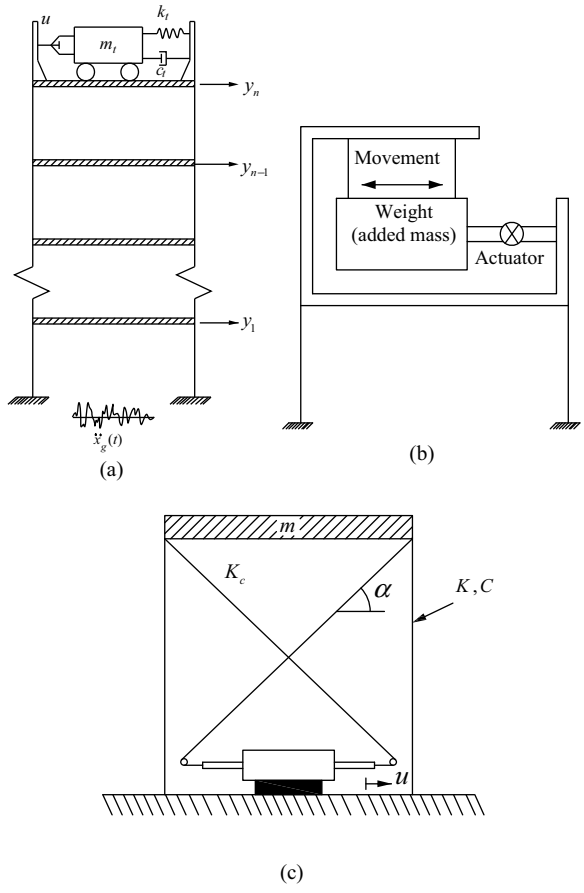

Figure 9.53 Active control devices: (a) active tuned mass damper; (b) actuated mass damper; and (c) active tendon

response of the system may be achieved theoretically by generating control force at each instant of time t that is equal and opposite to the earthquake force. However, in reality it is not realizable for several reasons, which will be discussed in the limitations of the active control scheme. Therefore, control of the response is achieved with respect to a certain norm. The choice of the norm dictates the control algorithm. As the control of the response is achieved by applying the control force that depends upon the state of the system (that is, $\boldsymbol{x}$ and $\dot{\boldsymbol{x}}$), three factors are extremely important in relation to the design of the controlled system. They are stability, controllability, and observability, that is, the system should be stable, controllable, and state observable. These three attributes are elaborated further in the following sections.

To examine these factors, the controlled equations of motion, Equation 9.116, is written in state-space as:

$$\dot{\boldsymbol{X}} = \boldsymbol{A}\boldsymbol{X} + \boldsymbol{B}\boldsymbol{u} + \boldsymbol{H}\ddot{x}_g \tag{9.119}$$

in which

$$\boldsymbol{A} = \begin{bmatrix} \boldsymbol{0} & \boldsymbol{I} \\ -\boldsymbol{M}^{-1}\boldsymbol{K} & -\boldsymbol{M}^{-1}\boldsymbol{C} \end{bmatrix}; \qquad \boldsymbol{B} = \begin{bmatrix} \boldsymbol{0} \\ \boldsymbol{M}^{-1}\boldsymbol{D} \end{bmatrix}; \qquad \boldsymbol{H} = \begin{bmatrix} \boldsymbol{0} \\ -\boldsymbol{I} \end{bmatrix} \tag{9.120}$$

where $\boldsymbol{I}$ is an identity matrix of appropriate size; the other matrices have already been defined.

9.8.1 Stability

The controlled equation, Equation 9.119, in state space can also be written in the following form if $\boldsymbol{u}$ is assumed to be of the form of Equation 9.117,

$$\dot{\boldsymbol{X}} = \overline{\boldsymbol{A}}\boldsymbol{X} + \boldsymbol{H}\ddot{\boldsymbol{x}}_g \tag{9.121}$$

in which

$$\overline{\boldsymbol{A}} = \boldsymbol{A} + [\boldsymbol{B}\boldsymbol{K}_1 + \boldsymbol{B}\boldsymbol{C}_1]; \qquad \overline{\boldsymbol{H}} = \boldsymbol{B}\boldsymbol{E} + \boldsymbol{H} \tag{9.122}$$

Stability of a dynamic system may be loosely stated as the boundedness of the state of the system in time. The stability of the system is examined by studying its intrinsic dynamic properties (and irrespective of the excitation). Therefore, it is adequate to consider the state equation:

$$\dot{\boldsymbol{X}} = \overline{\boldsymbol{A}}\boldsymbol{X} \quad \boldsymbol{X}(\boldsymbol{t}_0) = \boldsymbol{X}_0 \tag{9.123}$$

The equilibrium state of the system is described by:

$$\overline{\boldsymbol{A}}\boldsymbol{X}_e = 0 \tag{9.124}$$

that is, $\boldsymbol{X}_e = 0$ is its unique equilibrium state if $\boldsymbol{A}$ is non-singular.

An equilibrium state is said to be stable in the sense of Lyapunov if, for any t_0 and any small value $\varepsilon > 0$, there exists a real number $\delta > 0$ such that

$$\left|\left|\boldsymbol{X}_0 - \boldsymbol{X}_e\right|\right| \leq \delta \tag{9.125}$$

which implies $\left|\left|\boldsymbol{X}(t) - \boldsymbol{X}_e\right|\right| \leq \varepsilon$ for $t \geq t_0$; $\left|\left|\ \right|\right|$ indicates Euclidean norm.

Thus, the Lyapunov stability guarantees that the system state remains close to the equilibrium state for any time t by selecting the initial state close to the equilibrium state [13].

An equilibrium state is said to be asymptotically stable if it is stable and if for any t_0, there is $\delta > 0$ such that

$$\left|\left|\boldsymbol{X}_0 - \boldsymbol{X}_e\right|\right| \leq \delta \tag{9.126}$$

which implies that $\left|\left|\boldsymbol{X}(t) - \boldsymbol{X}_e\right|\right| \to 0$ as $t \to \infty$.

Thus, in addition to being stable, the state asymptotically converges to X_e when the initial condition is chosen close enough to the equilibrium state [13]. Also, it can be easily shown that the stability of the equilibrium state implies stability in any solution.

The requirements for the first stability condition are: (i) all eigen values of $\overline{\boldsymbol{A}}$ have non-positive real parts; and (ii) for any eigen value of zero real part with multiplicity k, there exist exactly k linearly independent eigen vectors [11]. The second stability condition requires that all eigen values of $\overline{\boldsymbol{A}}$ have strictly negative real parts.

9.8.2 Controllability and Observability

A system is said to be controllable at time t_0, if it is possible by means of an unconstrained control vector to transfer the system from any initial state $\boldsymbol{x}(t_0)$ to any other state in a finite interval of time.

A system is said to be observable at time t_0, if with the system in state $\boldsymbol{x}(t_0)$, it is possible to determine this state from the observation of the output over a finite time interval.

The concepts of controllability and observability were introduced by Kalman *et al.* [14]. The solution of the control design problem may not exist at all if the system is not controllable. While most physical problems are controllable and observable, the corresponding mathematical models may not always preserve the property of controllability and observability. Thus, it is necessary to know the mathematical conditions under which a mathematical model is controllable and observable.

Consider the system represented by:

$$\dot{\boldsymbol{X}} = \boldsymbol{AX} + \boldsymbol{Bu} \tag{9.127}$$

Note that Equation 9.127 is without any excitation but the unconstrained control forces are applied to change the state of the system. If the system is controllable, then it can be shown that the controllability matrix given by [13]:

$$[\boldsymbol{B}\vdots\boldsymbol{AB}\vdots\cdots\cdots\vdots\boldsymbol{A}^{n-1}\boldsymbol{B}]_{n\times nr} \tag{9.128}$$

is of rank n; in which n is the size of the $\boldsymbol{A}$ matrix and r is the size of the vector of control force $\boldsymbol{u}$. Alternatively, the matrix contains n linearly independent column vectors.

Alternative forms of the condition for complete state controllability exist, for example, if the eigen values of $\boldsymbol{A}$ are distinct, and therefore eigen vectors are also distinct, then it is possible to find a transformation matrix $\boldsymbol{P}$ such that

$$\boldsymbol{P}^{-1}\boldsymbol{AP} = \boldsymbol{D} = \boldsymbol{diag}\ \lambda \tag{9.129}$$

in which $\boldsymbol{diag}\ \lambda$ is a diagonal matrix of eigen values. With this transformation matrix, a new set of variables may be defined as:

$$\boldsymbol{Z} = \boldsymbol{PX} \tag{9.130}$$

and a new set of equations in the transformed variable may be obtained as:

$$\dot{\boldsymbol{Z}} = \boldsymbol{DZ} + \boldsymbol{Fu} \tag{9.131}$$

$$\boldsymbol{F} = \boldsymbol{P}^{-1}\boldsymbol{B} \tag{9.132}$$

The system is state controllable only if the matrix $\boldsymbol{F}$ does not possess a row that has all zero elements. Proofs of the above conditions are available in reference [13].

In the practical design of a control system, the control of the output is rather more important than the control of the state. Consider the system described by:

$$\dot{\boldsymbol{X}} = \boldsymbol{AX} + \boldsymbol{Bu} \tag{9.133}$$

$$\boldsymbol{Y} = \boldsymbol{CX} + \boldsymbol{Du} \tag{9.134}$$

in which $\boldsymbol{Y}$ is a vector of size m. Accordingly, sizes of other matrices are determined. The system described by Equations 9.133 and 9.134 is said to be completely output controllable, if it is possible to construct an unconstrained control vector $\boldsymbol{u}$ that will transfer any given initial output $\boldsymbol{Y}(t_0)$ to any final output $\boldsymbol{Y}(t_1)$ in a finite time interval $t_0 \leq t \leq t_1$. The mathematical condition for the controllability requires that the controllability matrix

$$[\boldsymbol{CB}\vdots\boldsymbol{CAB}\vdots\boldsymbol{CA}^{n}\boldsymbol{B}\vdots\cdots\cdots\vdots\boldsymbol{CA}^{n-1}\boldsymbol{B}\vdots\boldsymbol{D}]_{n\times(n+1)r} \tag{9.135}$$

is of rank m.

To study the observability, the equation of motion for the unforced system is sufficient to examine. Therefore, consider the equations

$$\dot{\boldsymbol{X}} = \boldsymbol{AX} \tag{9.136a}$$

$$\boldsymbol{Y} = \boldsymbol{CX} \tag{9.136b}$$

The system is said to be completely observable, if every state $\boldsymbol{X}(t)$ can be determined from the observation of $\boldsymbol{Y}(t)$ over a finite interval $t_0 \leq t \leq t_1$. The concept of observability is important, because in practice only a limited number of measurements are possible (of size m) and a complete state of the system may be required to generate the control signal by means of the control algorithm.

It can be shown that the system presented by Equations 9.136a and 9.136b is completely observable, if and only if, the $n \times nm$ matrix

$$[\boldsymbol{C}^* \vdots \boldsymbol{A}^*\boldsymbol{C}^* \vdots \cdots \vdots (\boldsymbol{A}^*)^{n-1}\boldsymbol{C}^*] \tag{9.137}$$

is of rank n or has n linearly independent column vectors.

9.8.3 State Observer

A state observer estimates the non-measurable state variables from the measured variables. If the state observer observes all state variables regardless of whether some state variables are available for direct measurement, it is called a full-order state observer. Generally, a full order observer is not required as the output variables are available for measurement. When the number of state variables to be estimated is less than the size of the full state, the observer is called a reduced-order state observer. A state observer can be designed only if the observability condition is satisfied.

Consider the state-space equation given by:

$$\dot{\boldsymbol{X}} = \boldsymbol{A}\boldsymbol{X} + \boldsymbol{B}\boldsymbol{u} \tag{9.138}$$

$$\boldsymbol{Y} = \boldsymbol{C}\boldsymbol{X} \tag{9.139}$$

in which $\boldsymbol{Y}$ is the output vector, which is measured. In order to design the observer, $\overline{X}$ is introduced as the estimated state by the observer. The mathematical model of the observer is

$$\dot{\overline{\boldsymbol{X}}} = \boldsymbol{A}\overline{\boldsymbol{X}} + \boldsymbol{B}\boldsymbol{u} + \boldsymbol{K}_e(\boldsymbol{Y} - \boldsymbol{C}\overline{\boldsymbol{X}}) \tag{9.140}$$

$$= [\boldsymbol{A} - \boldsymbol{K}_e\boldsymbol{C}]\overline{\boldsymbol{X}} + \boldsymbol{B}\boldsymbol{u} + \boldsymbol{K}_e\boldsymbol{Y} \tag{9.141}$$

in which $\boldsymbol{C}\overline{\boldsymbol{X}}$ is the estimated output; $\boldsymbol{K}_e$ is the observer gain matrix. The inputs to the observer are the output $\boldsymbol{Y}$ and the control force $\boldsymbol{u}$. $\boldsymbol{K}_e$ is a weighting matrix designed in such a way that the correction term $(\boldsymbol{Y} - \boldsymbol{C}\overline{\boldsymbol{X}})$ continuously corrects the output of the observer.

To design a full-order observer, an error equation can be written by subtracting Equation 9.140 from Equation 9.138 and making use of Equation 9.139, as:

$$\dot{\boldsymbol{X}} - \dot{\overline{\boldsymbol{X}}} = \boldsymbol{A}\boldsymbol{X} - \boldsymbol{A}\overline{\boldsymbol{X}} - \boldsymbol{K}_e(\boldsymbol{C}\boldsymbol{X} - \boldsymbol{C}\overline{\boldsymbol{X}}) \tag{9.142}$$

$$\dot{\boldsymbol{X}} - \dot{\overline{\boldsymbol{X}}} = [\boldsymbol{A} - \boldsymbol{K}_e\boldsymbol{C}](\boldsymbol{X} - \overline{\boldsymbol{X}}) \tag{9.143}$$

The above equation can be put in the form

$$\dot{\boldsymbol{e}} = [\boldsymbol{A} - \boldsymbol{K}_e\boldsymbol{C}]\boldsymbol{e} \tag{9.144}$$

in which $\boldsymbol{e} = \boldsymbol{X} - \overline{\boldsymbol{X}}$. Equation 9.144 is similar to Equation 9.136a. For complete state controllability, that is, $[\boldsymbol{A} - \boldsymbol{K}_e\boldsymbol{C}]$ to be a state matrix, $[\boldsymbol{A} - \boldsymbol{K}_e\boldsymbol{C}]$ has arbitrarily desired eigen values. Thus, $\boldsymbol{K}_e$ can be designed to yield the desired eigen values. The problem is similar to finding the gain matrix $\boldsymbol{G}$ for the pole placement technique (discussed later) and can be solved by Ackerman's formula [13]. Using Ackerman's formula, the gain matrix $\boldsymbol{K}_e$ can be obtained as:

$$\boldsymbol{K}_e = \varphi(\boldsymbol{A}) \begin{Bmatrix} \boldsymbol{C} \\ \boldsymbol{C}\boldsymbol{A} \\ \vdots \\ \vdots \\ \boldsymbol{C}\boldsymbol{A}^{n-2} \\ \boldsymbol{C}\boldsymbol{A}^{n-1} \end{Bmatrix}^{-1} \begin{Bmatrix} 0 \\ 0 \\ \vdots \\ \vdots \\ 0 \\ 1 \end{Bmatrix} \tag{9.145a}$$

in which $\varphi(\boldsymbol{A})$ is given by Equation 9.153b (pole placement technique). Note that the gain matrix for the pole placement technique is a row matrix, while $\boldsymbol{K}_e$ is a vector. However, in most control problems, the state feedback to generate the desired control vector uses the observed state vector $\overline{\boldsymbol{X}}$ (not $\boldsymbol{X}$).

If a minimum order (reduced order) observer is used, then the reduced order observer becomes $n-m$, where n is the size of the state vector and m is the size of measurable output vector. Thus,

$$\begin{Bmatrix} \dot{\boldsymbol{x}}_a \\ \dot{\boldsymbol{x}}_b \end{Bmatrix} = \begin{bmatrix} A_{aa} & A_{ab} \\ A_{ba} & A_{bb} \end{bmatrix} \begin{Bmatrix} x_a \\ x_b \end{Bmatrix} + \begin{bmatrix} B_a \\ \overline{B_b} \end{bmatrix} \boldsymbol{u} \tag{9.145b}$$

$$Y = \begin{bmatrix} 1 & 0 \end{bmatrix} \begin{Bmatrix} x_a \\ x_b \end{Bmatrix} \tag{9.145c}$$

in which x_a refers to the measurable state vector, and x_b refers to un-measurable state vector. The equation for the measured portion of the state becomes

$$\dot{\boldsymbol{x}}_a = \boldsymbol{A}_{aa}\boldsymbol{x}_a + \boldsymbol{A}_{ab}\boldsymbol{x}_b + \boldsymbol{B}_a\boldsymbol{u} \tag{9.146a}$$

or

$$\boldsymbol{A}_{ab}\boldsymbol{x}_b = \dot{\boldsymbol{x}}_a - \boldsymbol{A}_{aa}\boldsymbol{x}_a - B_a\boldsymbol{u} \tag{9.146b}$$

From Equation 1.146b, $\boldsymbol{x}_b$ can be obtained as $\boldsymbol{x}_a$ and $\dot{\boldsymbol{x}}_a$ are measured and therefore, Equation 1.146b is used as the output equation for the un-measured portion of the state given by:

$$\dot{\boldsymbol{x}}_b = \boldsymbol{A}_{ba}\boldsymbol{x}_a + \boldsymbol{A}_{bb}\boldsymbol{x}_b + \boldsymbol{B}_b\boldsymbol{u} \tag{9.147}$$

Thus, for the reduced order observer, the state equation and the output equations are given by Equations 1.146b and 1.147, respectively. Proceeding in the same way as for the case of the full order observer, the error equation may be written in the following form

$$\dot{\boldsymbol{e}} = (\boldsymbol{A}_{bb} - \boldsymbol{K}_e\boldsymbol{A}_{ab})\boldsymbol{e} \tag{9.148a}$$

in which $\boldsymbol{e} = \boldsymbol{x}_b - \overline{\boldsymbol{x}}_b$; $\overline{\boldsymbol{x}}_b$ is the estimated state of the un-measured variables. $\boldsymbol{K}_e$ as before can be obtained using Ackerman's formula and is given by [13]:

$$\boldsymbol{K}_e = \varphi(\boldsymbol{A}_{bb}) \begin{Bmatrix} \boldsymbol{A}_{ab} \\ \boldsymbol{A}_{ab}\boldsymbol{A}_{bb} \\ \vdots \\ \vdots \\ \boldsymbol{A}_{ab}\boldsymbol{A}_{bb}^{n-3} \\ \boldsymbol{A}_{ab}\boldsymbol{A}_{bb}^{n-2} \end{Bmatrix}^{-1} \begin{Bmatrix} 0 \\ 0 \\ \vdots \\ \vdots \\ 0 \\ 1 \end{Bmatrix} \tag{9.148b}$$

MATLAB computation to find the $\boldsymbol{K}_e$ is explained with the following example.

Example 9.7

For a control system, represented by Equations 9.138 and 9.139, find the reduced order and full order state observer using MATLAB:

$$\boldsymbol{A} = \begin{bmatrix} 0 & 1 & 0 \\ 0 & 0 & 1 \\ -6 & -11 & -6 \end{bmatrix} \quad \boldsymbol{B} = \begin{Bmatrix} 0 \\ 0 \\ 1 \end{Bmatrix} \quad \boldsymbol{C} = \begin{bmatrix} 1 & 0 & 0 \end{bmatrix}$$

Eigen values of the matrix $\boldsymbol{A}$ are:

$$\lambda_1 = -1; \qquad \lambda_2 = -2; \qquad \lambda_3 = -3$$

The desired observer poles are at $S_1 = -2 + i2\sqrt{3}$; $S_2 = -2 - i2\sqrt{3}$; $S_3 = -5$ for the full order observer and $S_2 = -10$; $S_3 = -10$ for the reduced order observer.

Solution: MATLAB program (for the full order observer)–

$$\boldsymbol{A} = [0 \quad 1 \quad 0; 0 \quad 0 \quad 1; -6 \quad -11 \quad -6\ ];$$

$$\boldsymbol{B} = [0; \quad 0; \quad 1\,];$$

$$\boldsymbol{L} = [-2 + i * 2 * sqrt(3) \qquad -2 - i * 2 * sqrt(3) \qquad -5\,];$$

$$\boldsymbol{K_e} = \text{acker}(\,\boldsymbol{A}', \quad \boldsymbol{C}', \quad \boldsymbol{L}\,)';$$

$$\boldsymbol{K_e} = \begin{Bmatrix} 3 \\ 7 \\ -1 \end{Bmatrix}$$

For the reduced order observer–

$$\boldsymbol{A} = \begin{bmatrix} 0 & 1 & 0 \\ 0 & 0 & 1 \\ -6 & -11 & -6 \end{bmatrix}; \qquad \boldsymbol{B} = \begin{bmatrix} 0 \\ 0 \\ 1 \end{bmatrix}$$

Hence

$$\boldsymbol{Abb} = [0 \quad 1; \quad -11 \quad -6\,];$$

$$\boldsymbol{Aab} = [1 \quad 0\,];$$

$$\boldsymbol{L} = [-10 \quad -10\,];$$

$$\boldsymbol{K}_e = \text{acker}\,(\,\boldsymbol{Abb}' \quad \boldsymbol{Aab}' \quad \boldsymbol{L}\,)'$$

$$\boldsymbol{K_e} = \begin{Bmatrix} 14 \\ 5 \end{Bmatrix}$$

9.9 Active Control Algorithms

There are a number of algorithms developed for finding the control force $\boldsymbol{u}(t)$. Most of the algorithms derive the control force by minimizing the norm of some responses or some appropriate performance index, and therefore are termed as optimal control algorithms. The derived control force is obtained as a linear function of the state vector, and hence they are also called linear optimal control algorithms. There are other control algorithms that are not based on any optimal criterion, but are based on a stability criterion or some other different considerations. Also, there are control algorithms that have control forces defined in terms of non-linear functions of the state vector. Here, three simple control algorithms are presented in order to demonstrate how they are developed. These control algorithms are formulated in the time domain and have been implemented for many control problems.

9.9.1 Pole Placement Technique

Consider the state-space equation for the controlled system

$$\dot{\boldsymbol{X}} = \boldsymbol{AX} + \boldsymbol{Bu} + \boldsymbol{H}\ddot{x}_g \tag{9.149}$$

Eigen values of $\boldsymbol{A}$ are called the poles of the original system. Similarly, if $\boldsymbol{u}$ is written as a function of state vector with the help of a gain matrix $\boldsymbol{G}$, that is, $\boldsymbol{u} = \boldsymbol{GX}$, then the state-space equation takes the form

$$\dot{\boldsymbol{X}} = \overline{\boldsymbol{A}}\boldsymbol{X} + \boldsymbol{H}\ddot{x}_g \tag{9.150}$$

in which $\overline{\boldsymbol{A}} = \boldsymbol{A} + \boldsymbol{BG}$. The eigen values of the matrix $\overline{\boldsymbol{A}}$ are called the poles of the controlled system. The poles of the system can be written as:

$$S = \lambda = -\xi\omega_n \pm i\omega_d \qquad \omega_{\boldsymbol{d}} = \omega_{\boldsymbol{n}}\sqrt{1-\xi^2} \tag{9.151}$$

in which ξ is the damping ratio, and ω_n is the undamped natural frequency. The problem of absolute stability can be solved by choosing the poles of the closed loop system to lie on the left-hand side of the S-plane as shown in Figure 9.54. The further away the dominant poles are from the imaginary axis, the faster is the decay of the transient response of the system.

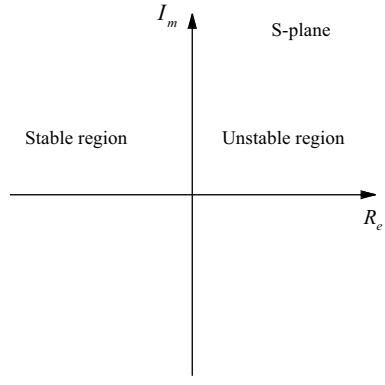

Figure 9.54 Stable and unstable regions for the poles of the system

Accordingly, poles of the closed system are selected and the gain matrix $\boldsymbol{G}$ is obtained to generate the control force. There are different methods to obtain the gain matrix $\boldsymbol{G}$, given the desired values of the poles of the closed loop system. Note that the desired values of the poles are chosen after obtaining the poles of the uncontrolled system, that is, by finding the eigen values of the matrix $\boldsymbol{A}$. The choice of the desired poles of the controlled systems consists in shifting the poles of the uncontrolled system to the farthest points on the left-hand side of the S-plane. Thus, the gain matrix $\boldsymbol{G}$ that is generated from the desired poles is not unique. Different $\boldsymbol{G}$ matrices can be generated by placing the poles at various locations and each of them provides a different control of the responses and different peak values of the control force. A tradeoff between the percentage control of the response and the peak control force is, therefore, an important consideration in the control procedure. There are different methods for generating the gain matrix $\boldsymbol{G}$. Here determination of the $\boldsymbol{G}$ matrix by using Ackermann's formula is described as MATLAB has a standard program for this. Consider the system

$$\dot{\boldsymbol{X}} = \boldsymbol{AX} + \boldsymbol{Bu} \tag{9.152}$$

The controllability matrix for the system given by Equation 9.152 is obtained and its rank or linear independency of column vectors is checked for the sufficient condition of controllability. Once the sufficient condition for controllability is ensured, the characteristic equation of the uncontrolled system is determined as:

$$|\boldsymbol{SI} - \boldsymbol{A}| = 0 \tag{9.153a}$$

which leads to the equation

$$S^n + a_1 S^{n-1} + a_2 S^{n-2} + \cdots + a_n = 0 \tag{9.153b}$$

Solution of the characteristic equation or eigen values of the matrix $\boldsymbol{A}$ will provide the poles of the original system. Knowing the poles of the original system, the desired poles of the closed loop system are assumed. Let the desired poles be denoted by $\mu_1 \ldots \mu_n$. Then,

$$(S-\mu_1)(S-\mu_2)(S-\mu_3)\cdots(S-\mu_n) = 0 \tag{9.154}$$

will provide the characteristic equation for the closed loop system as

$$S^n + \alpha_1 S^{n-1} + \alpha_2 S^{n-2} + \cdots + \alpha_n = 0 \tag{9.155}$$

The feedback gain matrix $\boldsymbol{G}$ is then given by [13]:

$$\boldsymbol{G} = [00\cdots 1][\boldsymbol{B}\vdots\boldsymbol{AB}\vdots\cdots\vdots\boldsymbol{A}^{n-1}\boldsymbol{B}]^{-1}\boldsymbol{\phi}(\boldsymbol{A}) \tag{9.156a}$$

$$\text{in which} \quad \boldsymbol{\phi}(\boldsymbol{A}) = \boldsymbol{A}^n + \alpha_1 \boldsymbol{A}^{n-1} + \alpha_2 \boldsymbol{A}^{n-2} + \cdots \alpha_n \boldsymbol{I} \tag{9.156b}$$

In MATLAB, two commands are used, namely, acker and place for the computation of feedback gain matrix. The acker command is used for $\boldsymbol{u}(t)$ as scalar (that is, single input). The place command can handle multiple input, that is, $\boldsymbol{u}(t)$ as a vector. For single input, both acker and place give the same results. However, place in certain cases is preferable over acker, such as when the system is marginally controllable. In addition to $\boldsymbol{A}$ and $\boldsymbol{B}$ matrices, the program requires the $\boldsymbol{J}$ matrix given as:

$$\boldsymbol{J} = [\mu_1 \ldots \mu_n] \tag{9.157}$$

Example 9.8A

For a control system described by Equation 9.149, obtain the $\boldsymbol{G}$ matrix using MATLAB for the following values of $\boldsymbol{A}$, $\boldsymbol{B}$, and $\boldsymbol{J}$ [13]. Note that the output matrix, that is, $\boldsymbol{K}$ of MATLAB is the $\boldsymbol{G}$ matrix. As a result, both $\boldsymbol{K}$ and $\boldsymbol{G}$ are used to denote the same gain matrix.

$$\boldsymbol{A} = \begin{bmatrix} 0 & 1 & 0 \\ 0 & 0 & 1 \\ -1 & -5 & -6 \end{bmatrix} \quad \boldsymbol{B} = \begin{bmatrix} 0 \\ 0 \\ 1 \end{bmatrix}$$

$$\boldsymbol{J} = [\,-2+j*4 \qquad -2-j*4 \qquad -10\,]$$

Solution: MATLAB program, acker–

$$\boldsymbol{A} = [\,0 \quad 1 \quad 0;\ \ 0 \quad 0 \quad 1;\ \ -1 \quad -5 \quad -6\ \ ]$$

$$\boldsymbol{B} = [0;\ \ 0;\ \ 1]$$

$$\boldsymbol{J} = [\,-2+j*4 \quad -2-j*4 \quad -10\,]$$

$$\boldsymbol{K} = \text{acker}\,(\boldsymbol{A},\ \boldsymbol{B},\ \boldsymbol{J})$$

$$\boldsymbol{K} = \{\,199 \quad 55 \quad 8\,\}$$

MATLAB program, place–

$$\boldsymbol{A} = [0 \quad 1 \quad 0;\ 0 \quad 0 \quad 1;\ -1 \quad -5 \quad -6\ ]$$

$$\boldsymbol{B} = [0;\ \ 0;\ \ 1]$$

$$\boldsymbol{J} = [\,-2 + i * 4 \quad -2 - i * 4 \quad -10\,]$$

$$\boldsymbol{K} = \text{place}\ (\boldsymbol{A},\ \boldsymbol{B},\ \boldsymbol{J})$$

place: n digits = 15

$$\boldsymbol{K} = [\,199.0 \quad 55.0 \quad 8.0\,]$$

Example 9.8B

The bare frame of Figure 9.40 is controlled by an actuator applied at the top-storey level. Find the time histories of the controlled displacements of the top storey and the first storey by the pole placement technique for the El Centro earthquake.

Solution: Using the mass, damping and stiffness matrices of the frame described in the Example 9.6, $\boldsymbol{A}$ and $\boldsymbol{B}$ matrices for the state-space Equation 9.149 are given as:

$$\boldsymbol{A} = \begin{bmatrix} 0 & 0 & 0 & 0 & 0 & 0 & 1 & 0 & 0 & 0 \\ 0 & 0 & 0 & 0 & 0 & 0 & 0 & 1 & 0 & 0 \\ 0 & 0 & 0 & 0 & 0 & 0 & 0 & 0 & 1 & 0 \\ 0 & 0 & 0 & 0 & 0 & 0 & 0 & 0 & 0 & 1 \\ 0 & 0 & 0 & 0 & 0 & 0 & 0 & 0 & 0 & 0 \\ 0 & 0 & 0 & 0 & 0 & 0 & 0 & 0 & 0 & 0 \\ -2666.71 & 1333.32 & 0 & 0 & 0 & 0 & -6.83 & 2.99 & 0 & 0 \\ 1333.32 & -2666.71 & 1333.32 & 0 & 0 & 0 & 2.99 & -6.83 & 2.99 & 0 \\ 0 & 1333.32 & -2666.71 & 1333.32 & 0 & 0 & 0 & 2.99 & -6.83 & 2.99 \\ 0 & & 1333.32 & -2666.71 & 1333.32 & 0 & 0 & & 2.99 & -6.83 \end{bmatrix}$$

$$\boldsymbol{B}^T = \begin{bmatrix} 0 & 0 & 0 & 0 & 0 & 0 & 0 & 0 & 0 & 0 & -\dfrac{10^{-3}}{75} \end{bmatrix}$$

The original poles of the system are obtained as:

$$-6.2603 + 71.8581i,\ -6.2603 - 71.8581i,\ -5.1738 + 64.8642i,\ -5.1738 - 64.8642i,$$

$$-3.4158 + 51.5271i,\ -3.4158 - 51.5271i,\ -1.6577 + 33.1131i,\ -1.6577 - 33.1131i,\ -0.5712 + 11.4112i,\ -0.57122 - 11.4112i$$

The control force is designed such that the desired poles of the system are shifted as

$$J = -10 + 71i,\ -10 - 71i,\ -10 + 70i,\ -10 - 70i,\ -10 + 30i,\ -10 - 30i,\ -10 + 12i,\ -10 - 12i,\ -22,\ -22$$

The corresponding gain matrix $\boldsymbol{K}$ is obtained using MATLAB function *place*(A, B, J). Thus, the $\boldsymbol{K}$ matrix is obtained as:

$$\boldsymbol{K} = [4.8271e + 008,\ -5.0206e + 008,\ -1.5987e + 008,\ 4.2424e + 008,\ -1.1362e + 008,$$

$$-1.5581e + 007,\ -6.7431e + 005,\ 1.4914e + 007,\ -1.6061e + 006,\ -6.7382e + 006]$$

The controlled responses are obtained by solving the following state-space equation using SIMULINK

$$\dot{\boldsymbol{X}} = (\boldsymbol{A} + \boldsymbol{BK})\boldsymbol{X} + \boldsymbol{H}\ddot{x}_g \quad \text{or} \quad \dot{\boldsymbol{X}} = (\boldsymbol{A} + \boldsymbol{BG})\boldsymbol{X} + \boldsymbol{H}\ddot{x}_g \tag{9.158}$$

The time histories of the controlled and uncontrolled displacements are shown in Figures 9.55 and 9.56. It is seen that the reductions of peak displacements of the first and the top storeys are about 68%. The time history of control force is shown in Figure 9.57. The peak control force is 1×10^6 N (about 15% of the weight of the frame). By adjusting the poles of the system, a better result may be obtained, that is, better control with less control force.

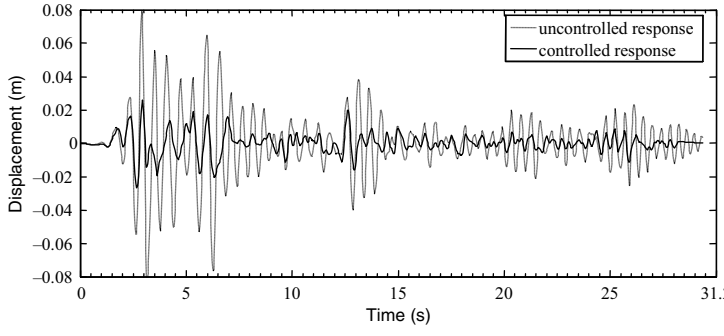

Figure 9.55 Controlled and uncontrolled displacements of fifth floor using pole placement technique

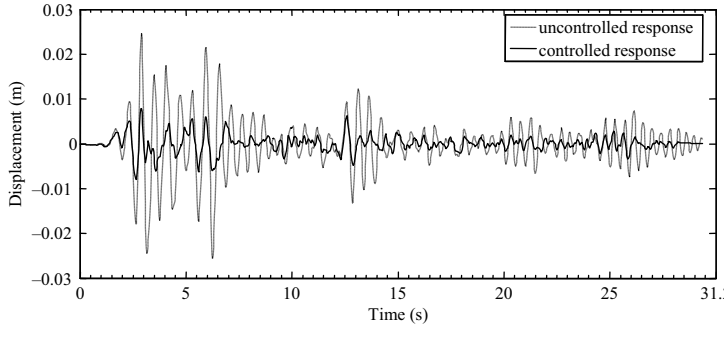

Figure 9.56 Controlled and uncontrolled displacements of first floor using pole placement technique

9.9.2 *Classical Linear Optimal Control*

In classical linear optimal control, the control force is assumed to be a linear function of the state vector and the control of the responses is obtained by minimizing a quadratic performance function. Therefore, it is popularly known as linear quadratic regulator (LQR) control. Assuming the state vector to be zero at time $t = 0$, the performance index is defined as:

$$J = \int_0^{t_f} [\boldsymbol{x}^T \boldsymbol{Q}\boldsymbol{x} + \boldsymbol{u}^T \boldsymbol{R}\boldsymbol{u}]\, \mathrm{d}t \tag{9.159}$$

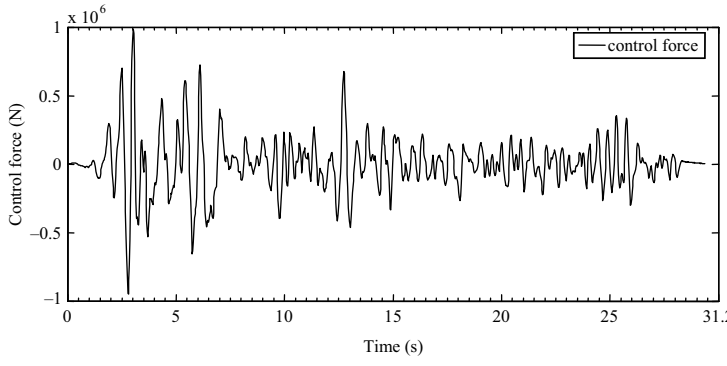

Figure 9.57 Time history of the control force using pole placement technique

in which t_f is the duration of the earthquake excitation; $\boldsymbol{Q}$ is a $2n \times 2n$ semi-definite matrix, and $\boldsymbol{R}$ is an $n \times m$ positive definite matrices. The matrices $\boldsymbol{Q}$ and $\boldsymbol{R}$ are termed weighting matrices. The relative values of the elements of the matrices are selected according to the importance attached to the different parameters of control. For example, large values of the elements of $\boldsymbol{Q}$ compared with those of $\boldsymbol{R}$ denote that response reduction is given more weightage at the cost of control force. The opposite is indicated when the elements of $\boldsymbol{R}$ are relatively large. Similarly, in the $\boldsymbol{Q}$ matrix, relatively large values of the diagonal elements corresponding to displacement response denote that the velocity response is penalized in the minimization procedure.

From Equation 9.159, it is clear that the time histories of controlled response and the control force are such that they provide a minimum value for the performance index J. Furthermore, Equation 9.159 shows that the performance index J is in a way equivalent to the total energy of the system, including that of the external force over the entire duration of the excitation. Thus, the control algorithm in some sense obtains the control force by minimizing the total energy of the system over the duration of the excitation. This algorithm is also known as linear quadratic regulator (LQR) algorithm as the control force is a linear function of the state vector and the performance function is a quadratic function of the state variable and the control force.

Many of the control laws are obtained independent of the excitation because future earthquakes are not known. Also, the development of the control algorithm becomes simpler by setting the excitation as zero. Thus, J in Equation 9.159 is minimized subject to the constraint

$$\dot{\boldsymbol{X}} = \boldsymbol{AX} + \boldsymbol{Bu} \tag{9.160}$$

The constrained minimization problem is firstly converted into an unconstrained minimization problem using a lagrangian multiplier λ and the lagrangian L is defined as:

$$L = \int_0^{t_f} \{\boldsymbol{X}^T \boldsymbol{Q} \boldsymbol{X} + \boldsymbol{u}^T \lambda^T [\boldsymbol{AX} + \boldsymbol{Bu} - \dot{\boldsymbol{X}}]\} \, \mathrm{d}t \tag{9.161}$$

The necessary conditions for optimal solution are given by $\delta L = 0$, that is,

$$\delta L = -\lambda^T(t_f)\delta \boldsymbol{X}(t_f) + \lambda^T \delta \boldsymbol{X}(0) + \int_0^{t_f} \left(\dot{\lambda}^T + \frac{\delta \boldsymbol{H}}{\delta \boldsymbol{X}} \delta \boldsymbol{X} + \frac{\delta \boldsymbol{H}}{\delta \boldsymbol{u}} \delta \boldsymbol{u} \right) \mathrm{d}t = 0 \tag{9.162}$$

in which $\boldsymbol{H}$ is the integrand of Equation 9.161.

As $\boldsymbol{X}(0)$ is specified, $\delta\boldsymbol{X}(0) = 0$. Thus, for $\delta L = 0$,

$$\frac{\delta \boldsymbol{H}}{\delta \boldsymbol{u}} = 0 \qquad 0 \le t \le t_f \tag{9.163a}$$

$$\dot{\lambda}^T + \frac{\delta \boldsymbol{H}}{\delta \boldsymbol{X}} = 0 \tag{9.163b}$$

with the boundary condition $\lambda^T(t_f) = 0$.

By carrying out the necessary partial derivatives of $\boldsymbol{H}$ with respect to $\boldsymbol{X}$ and $\boldsymbol{u}$, and algebraic manipulations, the following pair of equations are obtained:

$$\dot{\lambda} = -\boldsymbol{A}^T\lambda - 2\boldsymbol{Q}\boldsymbol{X} \qquad \lambda(t_f) = 0 \tag{9.164}$$

$$\boldsymbol{u} = -\frac{1}{2}\boldsymbol{R}^{-1}\boldsymbol{B}^T\lambda \tag{9.165}$$

The three sets of unknowns, that is, $\boldsymbol{X}$, $\boldsymbol{u}$, and λ are determined by making use of Equations 9.164 and 9.165.

Set the lagrangian multiplier λ as a function of the state vector, that is,

$$\lambda(t) = \boldsymbol{P}(t)\boldsymbol{X}(t) \tag{9.166}$$

in which $\boldsymbol{P}(t)$ is an unknown matrix to be determined. Equation 9.164 yields an equation of the form

$$\left[\dot{\boldsymbol{P}} + \boldsymbol{P}\boldsymbol{A} - \frac{1}{2}\boldsymbol{P}\boldsymbol{B}\boldsymbol{R}^{-1}\boldsymbol{B}^T\boldsymbol{P} + \boldsymbol{A}^T\boldsymbol{P} + 2\boldsymbol{Q}\right]\boldsymbol{X}(t) = 0 \tag{9.167}$$

with

$$\boldsymbol{P}(t_f) = 0 \tag{9.168}$$

Equation 9.167 provides the well known matrix Riccati equation

$$\dot{\boldsymbol{P}} + \boldsymbol{P}\boldsymbol{A} - \frac{1}{2}\boldsymbol{P}\boldsymbol{B}\boldsymbol{R}^{-1}\boldsymbol{B}^T\boldsymbol{P} + \boldsymbol{A}^T\boldsymbol{P} + 2\boldsymbol{Q} = 0 \tag{9.169}$$

For most structural engineering problems, it is observed that $\boldsymbol{P}$ remains fairly constant over the duration of excitation t_f. Thus, $\boldsymbol{P}(t)$ can be approximated by time invariant matrix $\boldsymbol{P}$ and Equation 9.169 becomes

$$\boldsymbol{P}\boldsymbol{A} - \frac{1}{2}\boldsymbol{P}\boldsymbol{B}\boldsymbol{R}^{-1}\boldsymbol{B}^T\boldsymbol{P} + \boldsymbol{A}^T\boldsymbol{P} + 2\boldsymbol{Q} = 0 \tag{9.170}$$

Solution of the Riccati matrix equation gives the solution for $\boldsymbol{P}$. The control force is then given by:

$$\boldsymbol{u} = -\frac{1}{2}\boldsymbol{R}^{-1}\boldsymbol{B}^T\lambda = -\frac{1}{2}\boldsymbol{R}^{-1}\boldsymbol{B}^T\boldsymbol{P}\boldsymbol{X} = -\boldsymbol{K}\boldsymbol{X} \tag{9.171}$$

in which $\boldsymbol{K} = \frac{1}{2}\boldsymbol{R}^{-1}\boldsymbol{B}^T\boldsymbol{P}$ is called the control gain matrix.

By substituting Equation 9.171 in Equation 9.149, the controlled response is obtained by solving the following equation

$$\dot{\boldsymbol{X}} = [\boldsymbol{A} - \boldsymbol{B}\boldsymbol{K}]\boldsymbol{X} + \boldsymbol{H}\ddot{x}_g \tag{9.172}$$

Example 9.9

Consider the system given by

$$\dot{\boldsymbol{X}} = \boldsymbol{A}\boldsymbol{X} + \boldsymbol{B}u$$

Using MATLAB, obtain the positive definite solution matrix $\boldsymbol{P}$ of the Riccati equation, the optimal feedback gain matrix $\boldsymbol{K}$ and the eigen values of the matrix $\boldsymbol{A}-\boldsymbol{BK}$ for the following values of the matrices:

$$\boldsymbol{A}=\begin{bmatrix}0 & 1 & 0\\ 0 & 0 & 1\\ -35 & -27 & -9\end{bmatrix} \qquad \boldsymbol{B}=\begin{Bmatrix}0\\ 0\\ 1\end{Bmatrix}$$

$$\boldsymbol{Q}=\begin{bmatrix}1 & 0 & 0\\ 0 & 1 & 0\\ 0 & 0 & 1\end{bmatrix} \qquad \boldsymbol{R}=[1]$$

Solution: MATLAB program (design of quadratic optimal regulator system)–

$$\boldsymbol{A}=[0 \quad 1 \quad 0;\ 0 \quad 0 \quad 1;\ -35 \quad -27 \quad -9\ ];$$

$$\boldsymbol{B}=[0;\quad 0;\quad 1\,];$$

$$\boldsymbol{Q}=[1 \quad 0 \quad 0;\ 0 \quad 1 \quad 0;\ 0 \quad 0 \quad 1\ ]$$

$$\boldsymbol{R}=[1] \quad [\boldsymbol{K},\ \boldsymbol{P},\ \boldsymbol{E}]=lqr(\boldsymbol{A},\ \boldsymbol{B},\ \boldsymbol{Q},\ \boldsymbol{R})$$

$$\boldsymbol{K}=[0.0149 \quad 0.1107 \quad 0.0676] \quad \text{(Gain matrix)}$$

$$\boldsymbol{P}=\begin{bmatrix}4.2625 & 2.4957 & 0.0143\\ 2.4957 & 2.8150 & 0.1107\\ 0.0143 & 0.1107 & 0.0676\end{bmatrix}$$

$$\boldsymbol{E}=\begin{bmatrix}-5.0958\\ -1.9859+1.7110i\\ -1.9859-1.7110i\end{bmatrix} \quad \text{(Eigen values)}$$

Example 9.10

Solve example problem 9.8B by using LQR control.

Solution: $\boldsymbol{Q}$ matrix and $\boldsymbol{R}$ are selected as:

$$\boldsymbol{Q}=\begin{bmatrix}\boldsymbol{Q}_1 & \boldsymbol{Q}_2\\ \boldsymbol{Q}_3 & \boldsymbol{Q}_4\end{bmatrix}; \quad \boldsymbol{Q}_1=1.8\times 10^{14}\boldsymbol{I}_{5\times 5}; \quad \boldsymbol{Q}_2=\boldsymbol{Q}_3=\boldsymbol{Q}_4=\boldsymbol{0}_{5\times 5}; \quad \boldsymbol{R}=1$$

Using $lqr(\boldsymbol{A},\ \boldsymbol{B},\ \boldsymbol{Q},\ \boldsymbol{R})$ of MATLAB, the gain matrix K is obtained as:

$$\boldsymbol{K}=-10^5\,[3.21 \quad 7.61 \quad 1.39 \quad 2.43 \quad 1.52 \quad 1.52 \quad 3.11 \quad 4.78 \quad 6.85 \quad 3.72]$$

The controlled state space Equation 9.172 is solved using SIMULINK. The time histories of responses are shown in Figures 9.58–9.60. The reductions in the peak displacements of the top and the first storey are 56 and 50%, respectively. The reduction in peak absolute acceleration of the top floor is 46%.

The time history of the control force is shown in Figure 9.61. It is seen from the figure that the peak control force is 8.26×10^5 N, which is about 12% of the weight of the frame. More response reduction may be achieved (which may or may not be at the expense of more control forces) by choosing different values of $\boldsymbol{Q}$ and $\boldsymbol{R}$.

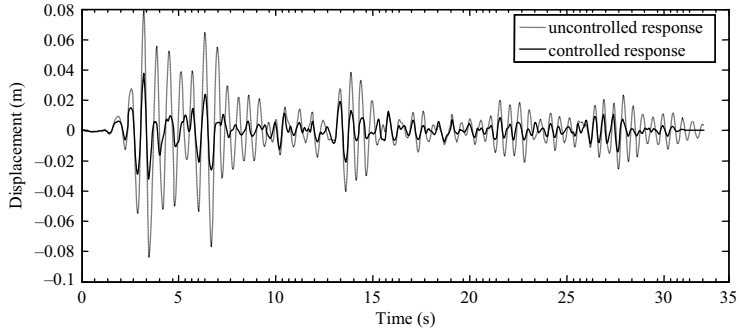

Figure 9.58 Controlled and uncontrolled displacements of fifth floor using LQR control

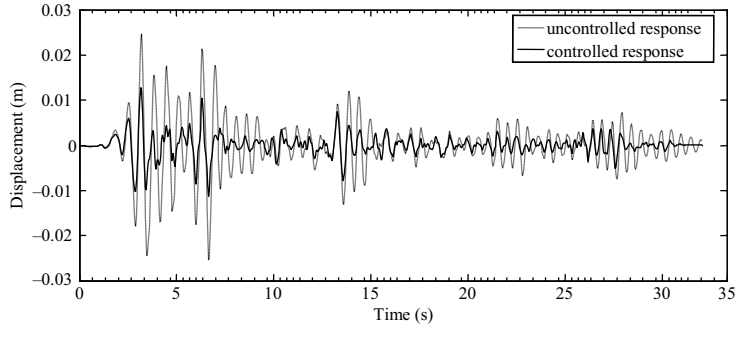

Figure 9.59 Controlled and uncontrolled displacements of first floor using LQR control

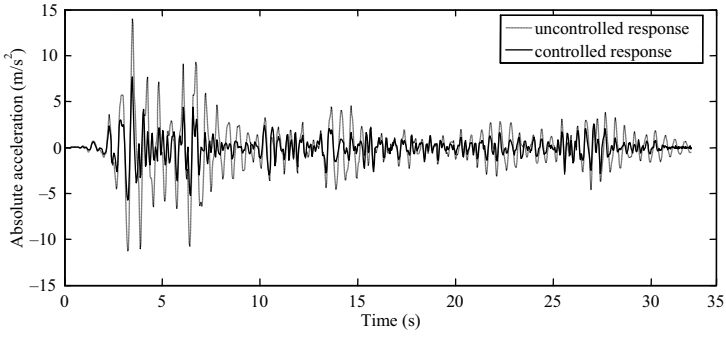

Figure 9.60 Controlled and uncontrolled absolute accelerations of the fifth floor using LQR control

9.9.3 Instantaneous Optimal Control

The classical optimal control does not take into account the excitation in obtaining the control force as it is not known a priori. However, it is possible to utilize the measured excitation up to time t in order to arrive at an improved control algorithm [11]. Such an improved algorithm may be developed by defining a time

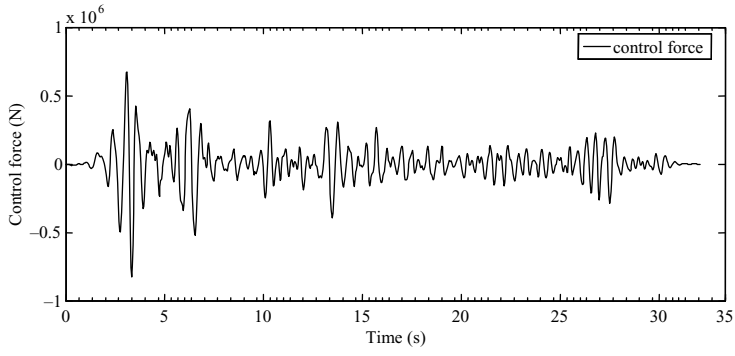

Figure 9.61 Time history of the control force using LQR control

dependent performance index $J(t)$ as:

$$J(t) = \boldsymbol{X}^T(t)\boldsymbol{Q}\boldsymbol{X}(t) + \boldsymbol{u}^T(t)\boldsymbol{R}\boldsymbol{u}(t) \tag{9.173}$$

The optimal control law is derived by minimizing $J(t)$ at every instant of time t over the entire duration of excitation. For this purpose, a modal transformation of the state space Equation 9.160 is accomplished by defining

$$\boldsymbol{X}(t) = \boldsymbol{\phi}\boldsymbol{z}(t) \tag{9.174}$$

in which $\boldsymbol{\phi}$ is $2n \times 2n$ modal matrix. The decoupled state-space equation is written as:

$$\dot{\boldsymbol{z}}(t) = \overline{\boldsymbol{A}}\boldsymbol{z}(t) + \boldsymbol{q}(t), \qquad \boldsymbol{z}(0) = 0 \tag{9.175}$$

in which $\overline{\boldsymbol{A}}$ is a $2n \times 2n$ diagonal matrix with diagonal elements as the complex eigen values $s_j (j = 1 \ldots 2n)$ of matrix $\boldsymbol{A}$ and $\boldsymbol{q}(t)$ is given by:

$$\boldsymbol{q}(t) = \boldsymbol{\phi}^{-1}[\boldsymbol{B}\boldsymbol{u}(t) - \boldsymbol{M}\boldsymbol{I}\ddot{\boldsymbol{x}}_g] \tag{9.176}$$

Over a time interval Δt, solution of Equation 9.175 provides

$$\boldsymbol{z}(t) = \int_0^{t-\Delta t} \exp\left[\overline{\boldsymbol{A}}(t-\tau)\right]\boldsymbol{q}(\tau)\,\mathrm{d}\tau + \int_{t-\Delta t}^{t} \exp\left[\overline{\boldsymbol{A}}(t-\tau)\right]\boldsymbol{q}(\tau)\,\mathrm{d}\tau \tag{9.177}$$

$$\approx \exp(\overline{\boldsymbol{A}}\Delta t)\boldsymbol{z}(t-\Delta t) + \frac{\Delta t}{2}\left[\exp\left(\overline{\boldsymbol{A}}\Delta t\right)\boldsymbol{q}(t-\Delta t) + \boldsymbol{q}(\tau)\right] \tag{9.178}$$

From the modal response, the state vector $\boldsymbol{X}(t)$ for the time interval Δt is obtained as:

$$\boldsymbol{X}(t) = \boldsymbol{\phi}\boldsymbol{E}(t-\Delta t) + \frac{\Delta t}{2}\left[\boldsymbol{B}\boldsymbol{u}(t) - \boldsymbol{M}\boldsymbol{I}\ddot{\boldsymbol{x}}_g\right] \tag{9.179}$$

in which

$$\boldsymbol{E}(t-\Delta t) = \exp\left(\overline{\boldsymbol{A}}\Delta t\right)\boldsymbol{\phi}^{-1}\left\{\boldsymbol{X}(t-\Delta t) + \frac{\Delta t}{2}\left[\boldsymbol{B}\boldsymbol{u}(t-\Delta t) - \boldsymbol{M}\boldsymbol{I}\ddot{\boldsymbol{x}}_g(t-\Delta t)\right]\right\} \tag{9.180}$$

Note that $\boldsymbol{E}(t-\Delta t)$ contains quantities at the previous time station in the time marching algorithm.

Minimization of the performance index is carried out subject to the constraint given by Equation 9.179. Introducing the lagrangian multiplier λ, Hamiltonian $\boldsymbol{H}$ is obtained as

$$\begin{aligned}\boldsymbol{H} &= \boldsymbol{X}^T(t)\boldsymbol{Q}\boldsymbol{X}(t) + \boldsymbol{u}^T(t)\boldsymbol{R}\boldsymbol{u}(t) \\ &+ \lambda^T(t)\left[\boldsymbol{X}(t) - \boldsymbol{\phi}\boldsymbol{E}(t-\Delta t) - \frac{\Delta t}{2}\left[\boldsymbol{B}\boldsymbol{u}(t) - \boldsymbol{M}\boldsymbol{I}\ddot{x}_g\right]\right]\end{aligned} \tag{9.181}$$

Minimizing the Hamiltonian with respect to the variables, that is,

$$\frac{\delta \boldsymbol{H}}{\delta \boldsymbol{X}} = 0; \qquad \frac{\delta \boldsymbol{H}}{\delta \boldsymbol{u}} = 0; \qquad \frac{\delta \boldsymbol{H}}{\delta \lambda} = 0 \tag{9.182}$$

provides,

$$2\boldsymbol{Q}\boldsymbol{X}(t) + \lambda(t) = 0 \tag{9.183}$$

$$2\boldsymbol{R}\boldsymbol{u}(t) - \frac{\Delta t}{2}\boldsymbol{B}^T\lambda(t) = 0 \tag{9.184}$$

$$\boldsymbol{X}(t) = \boldsymbol{\phi}\boldsymbol{E}(t-\Delta t) + \frac{\Delta t}{2}\left[\boldsymbol{B}\boldsymbol{u}(t) - \boldsymbol{M}\boldsymbol{I}\ddot{x}_g\right] \tag{9.185}$$

For closed loop control, the control force vector is regulated by the state vector as before, that is, by Equation 9.171. Comparing Equations 9.183 and 9.166, it follows that

$$\boldsymbol{P}(t) = -2\boldsymbol{Q} \tag{9.186}$$

Equation 9.184, thus, provides

$$\boldsymbol{u}(t) = -\frac{\Delta t}{2}\boldsymbol{R}^{-1}\boldsymbol{B}^T\boldsymbol{Q}\boldsymbol{X}(t) \tag{9.187}$$

and the response $\boldsymbol{X}(t)$ is obtained by using Equation 9.185 as:

$$\boldsymbol{X}(t) = \left[\boldsymbol{I} + \frac{\Delta t^2}{2}\boldsymbol{B}\boldsymbol{R}^{-1}\boldsymbol{B}^T\boldsymbol{Q}\right]\left[\boldsymbol{\phi}\boldsymbol{E}(t-\Delta t) - \frac{\Delta t}{2}\boldsymbol{M}\boldsymbol{I}\ddot{x}_g\right] \tag{9.188}$$

9.9.4 Practical Limitations

There are many practical problems related to the implementation of the control laws for actual control of structural responses produced by an earthquake. Some of the important ones include modeling errors, spillover effects, limited number of response measurements, and time delay effect. Each one of them deteriorates the efficiency of the control system and may even make the response of the structure unstable. Therefore, appropriate compensation for each one of these effects should be accounted for in the control algorithm leading to a modified algorithm. Details of the modifications for different effects are available in the control literature [11]. Here, compensation for two effects will be discussed namely, time delay effect and the effect due to limited measurements of responses.

The effect due to limited measurements of responses may be incorporated using the concept of state observer presented in Section 9.8.3. From the limited responses that are measured, the full state of the system is estimated with the help of the state observer and used in the control algorithm. Thus, the effect of limited measurements of responses is compensated in the control problems.

9.9.4.1 Time Delay Effect

The feedback algorithms developed assumed that all operations in the control loop can be performed instantaneously. In reality, there is a time difference between the measurement of responses and the

application of the control force on the structure. This time difference is due to the time required for processing the measured information, performing online computation, and in executing the control force on the structure according to the control signal produced by the algorithm. The time difference or the time delay not only reduces the effectiveness of the control system but also may cause dynamic instability.

The expected time delay may be incorporated in the control algorithm. The technique is called time delay compensation. There are many methods to incorporate the time delay effect into the control algorithm. A simple method based on a Taylor series expansion is described here. Consider the state-space equation for the structural control with a time delay as given below:

$$\dot{\boldsymbol{X}}(t) = \boldsymbol{A}\boldsymbol{X}(t-\tau) + \boldsymbol{B}\boldsymbol{u}(t-\tau) - \boldsymbol{M}\boldsymbol{I}\ddot{\boldsymbol{x}}_g \tag{9.189}$$

If $X_i(t-\tau)$ is one of the state variables, its Taylor series expansion about t is given by:

$$X_i(t) = X_i(t-\tau) + \tau\dot{X}_i(t-\tau) + \frac{\tau}{2}\ddot{X}_i(t-\tau) \tag{9.190}$$

Similarly, $\boldsymbol{u}(t-\tau)$ may be expanded in Taylor series.

In order to control the response at time t, say the control force at time $t-\tau$, that is, $\boldsymbol{u}(t-\tau)$ is used. As a result of application of this control force, the controlled responses are $\boldsymbol{X}(t)$, $\dot{\boldsymbol{X}}(t)$, and $\ddot{\boldsymbol{X}}_g(t)$, which are measured. Accordingly, control force $\boldsymbol{u}(t)$ at time t is calculated and is applied to control the response at time $(t+\tau)$. The equation of motion in state space can be written as:

$$\dot{\boldsymbol{X}}(t) = \boldsymbol{A}\boldsymbol{X}(t) + \boldsymbol{B}\boldsymbol{u}(t-\tau) - \boldsymbol{M}\boldsymbol{I}\ddot{\boldsymbol{x}}_g \tag{9.191}$$

Expanding $\boldsymbol{u}(t)$ by Taylor series

$$\boldsymbol{u}(t) = \boldsymbol{u}(t-\tau) + \tau\dot{\boldsymbol{u}}(t-\tau) + \frac{\tau^2}{2}\ddot{\boldsymbol{u}}(t-\tau) \tag{9.192}$$

$\boldsymbol{u}(t-\tau)$ can be expressed as a function of $\boldsymbol{u}(t)$, $\dot{\boldsymbol{u}}(t-\tau)$, that is,

$$\boldsymbol{u}(t-\tau) = \boldsymbol{u}(t) - \tau\dot{\boldsymbol{u}}(t-\tau) - \frac{\tau^2}{2}\ddot{\boldsymbol{u}}(t-\tau) \tag{9.193}$$

Substituting for $\boldsymbol{u}(t-\tau)$ in Equation 9.191 and defining a new state variable

$$\boldsymbol{Z}(t) = \begin{Bmatrix} \boldsymbol{X}(t) \\ \overline{\boldsymbol{u}}(t-\tau) \end{Bmatrix} \tag{9.194}$$

in which $\overline{\boldsymbol{u}}(t-\tau) = [\boldsymbol{u}(t-\tau) \quad \dot{\boldsymbol{u}}(t-\tau)]^T$, a new state space equation may be formed as:

$$\dot{\boldsymbol{Z}}(t) = \overline{\boldsymbol{A}}\boldsymbol{Z}(t) + \overline{\boldsymbol{B}}\boldsymbol{u}(t) + \boldsymbol{H}\ddot{x}_g \tag{9.195}$$

in which

$$\overline{\boldsymbol{A}} = \begin{bmatrix} 0 & \boldsymbol{I} & 0 & 0 \\ -\boldsymbol{K}\boldsymbol{M}^{-1} & -\boldsymbol{C}\boldsymbol{M}^{-1} & \boldsymbol{M}^{-1} & 0 \\ 0 & 0 & 0 & \boldsymbol{I} \\ 0 & 0 & -\dfrac{2}{\tau^2} & -\dfrac{2}{\tau} \end{bmatrix} \tag{9.196}$$

$$\overline{\boldsymbol{B}}^{\boldsymbol{T}} = \begin{bmatrix} 0 & 0 & 0 & -\dfrac{2}{\tau^2} \end{bmatrix} \qquad \boldsymbol{H}^{\boldsymbol{T}} = [0 \quad -\boldsymbol{I} \quad 0 \quad 0] \tag{9.197}$$

Equation 9.195 is a state-space equation for a control system for which the control force can be obtained using an LQR algorithm as:

$$\boldsymbol{u}(t) = \boldsymbol{K}\boldsymbol{Z} \tag{9.198}$$

where $\boldsymbol{K}$ is the gain matrix. Equations 9.197 and 9.194 show that control force $\boldsymbol{u}(t)$ is a function of measured responses at time t, $\boldsymbol{u}(t-\tau)$, and $\dot{\boldsymbol{u}}(t-\tau)$ (which are known). By substituting Equation 9.198 into Equation 9.195, the state of the system $\boldsymbol{X}(t)$ can be obtained as previously.

9.10 Semi-Active Control

This originates from the passive control system, modified to allow for the adjustment of mechanical properties based on feedback from the excitation or the measured response. As an active control system, it monitors the feedback measurement, and generates an appropriate command signal. As a passive control system, control forces are developed as a result of the motion of the structure. Control forces primarily act to oppose the motion, and are developed through appropriate control algorithms. Semi-active control generally requires a small amount of external power for the operation (of the order of few watts in comparison to tens of kilowatts).

9.10.1 Semi-Active Control Devices

Different types of semi-active control devices include:

a. **Stiffness Control Devices:** These devices are utilized to modify the stiffness, and hence, natural frequency of the system. This establishes a new resonant condition during an earthquake. The devices includes additional stiffness bracings, which are engaged or released so as to include or not to include the additional stiffness in the system, and operate generally through fluid control within tubes by valves [15–17].
b. **Electro-Rheological Dampers/Magneto-Rheological Dampers:** They consist of a hydraulic cylinder containing micron-size dielectric particles suspended within a fluid. In the presence of current, particles polarize and offer an increased resistance to flow (a change from a viscous fluid to a yielding solid within milliseconds). The magneto-rheological dampers are magnetic analogues of electro-rheological dampers, and have electro-magnets located within the piston head, which generates the magnetic field [18–22].
c. **Friction Control Devices:** They are energy dissipaters within the lateral bracing of a structure, or are as components within the sliding isolation system. The coefficient of friction of sliding is controlled by the modulation of fluid pressure in a pneumatic valve [23,24].
d. **Fluid Viscous Devices:** They consist of a hydraulic cylinder, with a piston dividing it into two sides. The cycling piston forces oil through an orifice, creating the output force. The output force is modulated by an external control valve, which connects two sides of the cylinder [25,26].
e. **TMDs and TLDs** The dynamic characteristics of the TMDs are controlled by the external current. In the TLDs, the length of the hydraulic tank is modified by adjusting the rotation of the rotatable baffles in the tank, and thus, the sloshing frequencies of the fluid are changed [27].

In general, the equation of motion for the semi-active control of structure takes the form

$$\boldsymbol{M}\ddot{\boldsymbol{X}} + (\boldsymbol{C} + \boldsymbol{C}_v)\dot{\boldsymbol{X}} + (\boldsymbol{K} + \boldsymbol{K}_v)\boldsymbol{X} = -\boldsymbol{M}\boldsymbol{I}\ddot{x}_g \tag{9.199}$$

in which $\boldsymbol{C}_v$ and $\boldsymbol{K}_v$ are variables. These can take positive discrete values (within specified bounds), and depend on the state. Most of the algorithms for semi-active control are studied for the variable damping. Different control algorithms developed for the variable dampers include: (i) Lyapunov stability approach, (ii) decentralized bang-bang control, (iii) clipped optimal control, and (iv) modulated homogenous friction control. Recently Ni *et al.* [28] developed semi-active vibration control by using neural networks. Fuzzy control has also been used for the semi-active variable devices [29]. The semi-active control of structures includes applications on building frames and bridges. An excellent state-of-the-art review on semi-active control system has been given in reference [30].

9.10.2 Control Algorithms

Except for the Lyapunov stability approach, other control algorithms are mostly Riccati based, that is, use of Riccati matrix solution is made to obtain an optimal control force. However, application of the algorithms varies with the control devices being used. For example, clipped optimal control or bang-bang control are applied in a different way for MR dampers than for hydraulic dampers. In this section, a simple control algorithm is presented for the semi-active control of building frames using hydraulic dampers [31]. For the semi active control of building frames using MR dampers, development of different control algorithms may be found in a number of publications [19–22].

Consider the building frame fitted with semi active hydraulic damper (SHD) as shown in Figure 9.62a. The SHD is a damping device in which the variable damping force proportional to the velocity of the movement of the piston may be generated by controlling the opening of a valve. According to the opening of the valve, the damping coefficient $c(t)$ of the damper at each instant of time t can be changed. The opening of the valve requires a very small power of the order of 70 W. The damping force $f(t)$ is given by $c(t)v(t)$, in which $v(t)$ is the piston velocity. The SHDs are designed for values of $f_{\max}$ and $c_{\max}$.

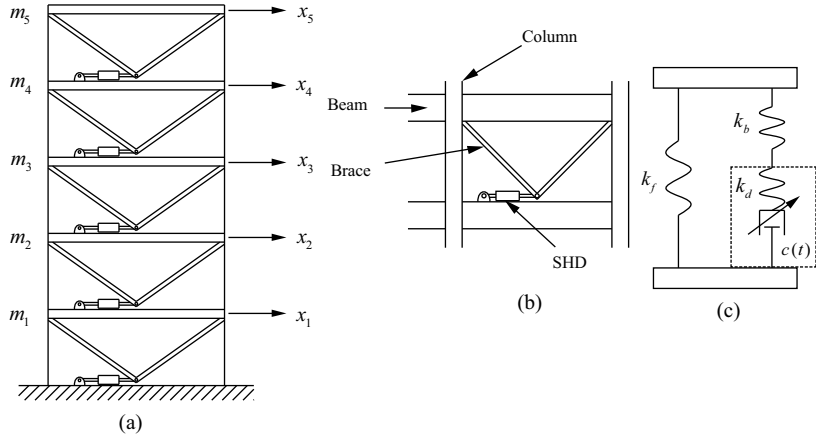

Figure 9.62 Semi-active control with SHD: (a) frame fitted with SHDs; (b) SHD in a floor; and (c) modeling of SHD

9.10.2.1 Simple LQR Control

The state-space equation for the frame fitted with SHD (Figure 9.62a) is written as:

$$\dot{\boldsymbol{X}} = \boldsymbol{AX} + \boldsymbol{Bu} + \boldsymbol{Df} \tag{9.200}$$

in which $\boldsymbol{X}$ is the vector of the state of the system; $\boldsymbol{u}$ is the control force vector; $\boldsymbol{B}$ is the location matrix, and $\boldsymbol{D}$ is the coefficient vector or matrix of the excitation force. Using the method of classical optimal control given in Section 9.9.2, the control force vector may be written as (Equation 9.171):

$$\boldsymbol{u} = -\boldsymbol{KX} \tag{9.201a}$$

$$\boldsymbol{K} = \frac{1}{2}\boldsymbol{R}^{-1}\boldsymbol{B}^{T}\boldsymbol{P} \tag{9.201b}$$

The weighting matrices $\boldsymbol{Q}$ and $\boldsymbol{R}$ in Equation 9.170 may be selected as:

$$\boldsymbol{Q} = \begin{bmatrix} \boldsymbol{Q}_d & 0 \\ 0 & \boldsymbol{Q}_v \end{bmatrix} \qquad \boldsymbol{Q}_v = \text{diag}(1) \qquad \boldsymbol{Q}_d = 0 \tag{9.202a}$$

$$\boldsymbol{R} = \text{diag}(\boldsymbol{r}) \tag{9.202b}$$

Various values of $\boldsymbol{r}$ may be selected to obtain the optimal control.

Substituting Equation 9.201 a into Equation 9.200, the controlled equation of motion may be written as:

$$\dot{\boldsymbol{X}} = (\boldsymbol{A} - \boldsymbol{B}\boldsymbol{K})\boldsymbol{X} + \boldsymbol{D}\boldsymbol{f} \tag{9.203}$$

The above controlled equation of motion is no different than the active control of the frame with actuating forces (vector $\boldsymbol{u}$) applied at different floor levels using various control devices that are operated by an external source of energy. The difference between the semi-active control and the active control consists in the actuation of the SHD and controlling of its damping coefficient to regulate the damping force developed in the damper. They are described below.

The modeling of the SHD, bracing, and the frame stiffness is shown in Figure 9.62(b and c). As shown in the figure, the bracing stiffness, damping stiffness, and the damping coefficient are in series. This bracing stiffness is made so high compared with the frame stiffness at floor levels that the horizontal piston velocity can be assumed to be equal to the relative horizontal velocities between the two floors connected by the bracing. Thus, the piston of the SHD is activated by the relative horizontal movement between any two floors. Furthermore, it is assumed that the damping elements of the damper predominantly control the response of the structure (that is, damper stiffness is neglected for the computation of the control force).

The control force is obtained from Equation 9.201a and the value of c_i is determined from Equation 9.204. The damping coefficient to be generated in the SHD is regulated by a control command. Let f_{di} be the damping force in the ith SHD. Then f_{di} is controlled by the following command:

$$f_{di} = \begin{cases} f_{\max}\text{sgn}(v_i) & u_i v_i > 0,\ |u_i| > f_{\max} \\ c_{\max} v_i & u_i v_i > 0,\ \left|\dfrac{u_i}{v_i}\right| > c_{\max},\ |u_i| \le f_{\max} \\ c_i v_i & u_i v_i > 0,\ \left|\dfrac{u_i}{v_i}\right| \le c_{\max},\ |u_i| \le f_{\max} \\ 0 & u_i v_i < 0 \end{cases} \tag{9.204}$$

where

u_i is the control force obtained from the LQR control algorithm
v_i is the damper velocity obtained from the measured floor velocity feedback (for the theoretical analysis, the feedback velocity from the state-space solution is used)
$f_{\max}$ and $c_{\max}$ are the upper limits for the damper force and damper coefficients, respectively.

The damper coefficient is changed by regulating the valve of the manifold of the damper.

The above control command is one of the simplest commands developed for semi-active control of the building frames using SHD. Many other control force commands can be developed, such as those given in clipped optimal control, bang-bang control, fuzzy control, and so on [29,30].

Example 9.11

The frame shown in Figure 9.62a is controlled by four SHDs (no SHD is used on the top floor). The frame is subjected to the El Centro earthquake, scaled to have a peak velocity of $10\,\text{cm}\,\text{s}^{-1}$. Find the time histories of controlled acceleration and displacement of the top floor. Also, obtain the peak

control force generated in the SHD for the first storey. The following dynamic characteristics of the frame are given.

$$\boldsymbol{K}\,(\text{Equation } 9.201\text{b}) = 10^6 \times \begin{bmatrix} 260 & -113 & 0 & 0 & 0 \\ -113 & 212 & -99 & 0 & 0 \\ 0 & -99 & 188 & -89 & 0 \\ 0 & 0 & -89 & 173 & -84 \\ 0 & 0 & 0 & -84 & 84 \end{bmatrix} \text{N m}^{-1}$$

$$\boldsymbol{M} = 10^2 \times \begin{bmatrix} 2152 & 0 & 0 & 0 & 0 \\ 0 & 2092 & 0 & 0 & 0 \\ 0 & 0 & 2070 & 0 & 0 \\ 0 & 0 & 0 & 2048 & 0 \\ 0 & 0 & 0 & 0 & 2661 \end{bmatrix} \text{kg}$$

$$\boldsymbol{C} = 1.843 \times 10^2 \times \begin{bmatrix} 545.2 & 0 & 0 & 0 & 0 \\ 0 & 530.0 & 0 & 0 & 0 \\ 0 & 0 & 524.4 & 0 & 0 \\ 0 & 0 & 0 & 518.9 & 0 \\ 0 & 0 & 0 & 0 & 674.2 \end{bmatrix} \text{N sm}^{-1}$$

The bracing may be assumed to be almost rigid such that the piston velocity of the damper is equal to the relative velocity between the two floors. The damper capacity is set at $f_{\max} = 900$ kN and the maximum damping coefficient is set at $c_{\max} = 200\,\text{kN s m}^{-1}$.

Solution: Using linear quadratic control with $\boldsymbol{Q}$ and $\boldsymbol{R}$ matrices taken as:

$$\boldsymbol{Q} = \begin{bmatrix} 1 & 0 & 0 & 0 & 0 & 0 & 0 & 0 & 0 & 0 \\ 0 & 1 & 0 & 0 & 0 & 0 & 0 & 0 & 0 & 0 \\ 0 & 0 & 1 & 0 & 0 & 0 & 0 & 0 & 0 & 0 \\ 0 & 0 & 0 & 1 & 0 & 0 & 0 & 0 & 0 & 0 \\ 0 & 0 & 0 & 0 & 1 & 0 & 0 & 0 & 0 & 0 \\ 0 & 0 & 0 & 0 & 0 & 0 & 0 & 0 & 0 & 0 \\ 0 & 0 & 0 & 0 & 0 & 0 & 0 & 0 & 0 & 0 \\ 0 & 0 & 0 & 0 & 0 & 0 & 0 & 0 & 0 & 0 \\ 0 & 0 & 0 & 0 & 0 & 0 & 0 & 0 & 0 & 0 \\ 0 & 0 & 0 & 0 & 0 & 0 & 0 & 0 & 0 & 0 \end{bmatrix}$$

$$\boldsymbol{R} = 10^{-14} \times \begin{bmatrix} 1 & 0 & 0 & 0 & 0 \\ 0 & 1 & 0 & 0 & 0 \\ 0 & 0 & 1 & 0 & 0 \\ 0 & 0 & 0 & 1 & 0 \\ 0 & 0 & 0 & 0 & 1 \end{bmatrix}$$

the gain matrix $\boldsymbol{K}$ (Equation 9.201b) is obtained as:

$$\boldsymbol{K} = 10^5 \times \begin{bmatrix} 3.2517 & 3.2217 & 2.3981 & 3.4018 & 4.4409 & 2.8591 & 2.7456 & 2.4769 & 2.3412 & 3.0935 \\ -0.1889 & 4.2173 & 4.1709 & 3.0864 & 5.8678 & -0.0347 & 3.3874 & 3.3519 & 3.1578 & 3.9810 \\ -0.2337 & -0.2218 & 5.6832 & 3.7692 & 5.3781 & -0.2493 & -0.2422 & 3.8252 & 3.8007 & 4.5753 \\ -1.5895 & -1.2469 & 0.7352 & 7.6013 & 3.4396 & -0.1150 & -0.2736 & -0.2544 & 4.1805 & 5.4089 \\ 0 & 0 & 0 & 0 & 0 & 0 & 0 & 0 & 0 & 0 \end{bmatrix}$$

The solution of the controlled state-space equation using SIMULINK provides the state of the system. The controlled command for SHD, given by Equation 9.204, is used to obtain the appropriate values of c_i and generate control forces in the feed back loop.

The time histories of controlled and uncontrolled responses are shown in Figures 9.63 and 9.64. It is seen from Figure 9.63 that the peak displacement of the top floor is reduced by 58%. The corresponding reduction in absolute acceleration is about 47%. The time histories of the displacements of the first floor are shown in Figure 9.65. It is seen that the reduction in the peak displacement of the first floor is 56%, and hence the base shear is also controlled by the same amount. The time history of the control force generated in the SHD for the first floor is shown in Figure 9.66. It is seen from the figure that the peak control force is about 175 kN, much less than the maximum capacity of the damper. Better control may be achieved by using different trial values of $c_{i\max}$, $f_{i\max}$, $\boldsymbol{Q}$, and R.

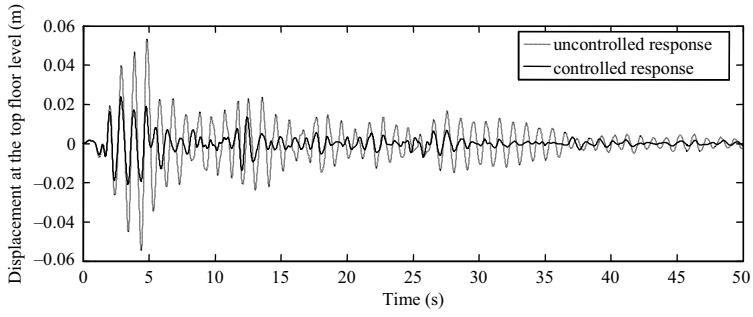

Figure 9.63 Time histories of controlled and uncontrolled displacements of the top floor using semi-active control

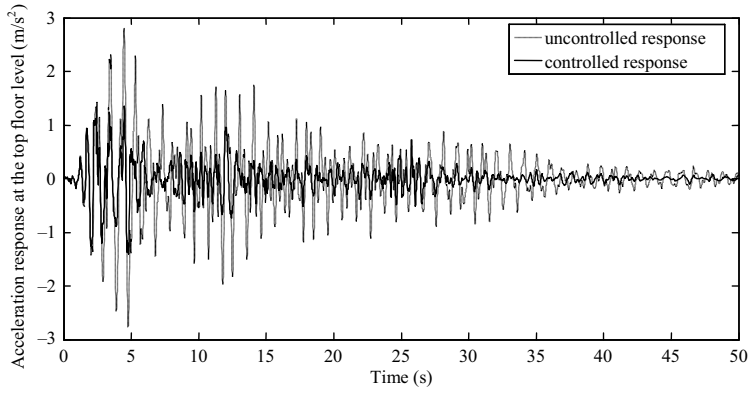

Figure 9.64 Time histories of controlled and uncontrolled absolute accelerations of the top floor using semi-active control

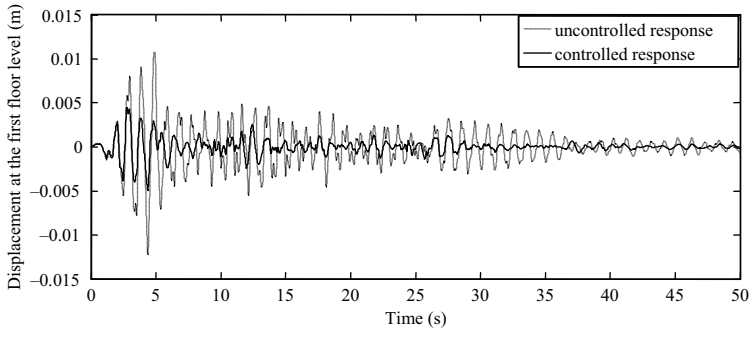

Figure 9.65 Time histories of controlled and uncontrolled displacements of the first floor using semi-active control

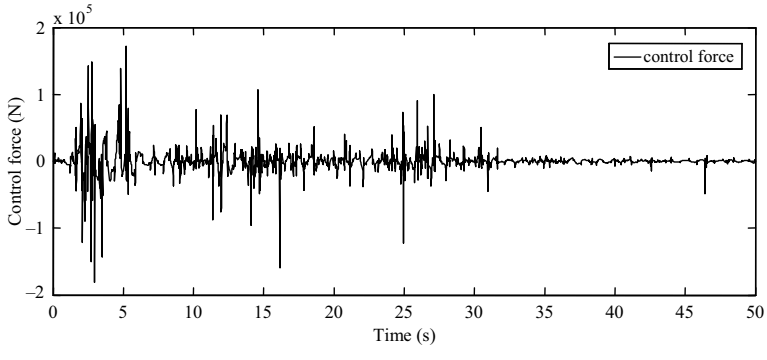

Figure 9.66 Time history of the control force generated in the first floor SHD

Exercise Problems

(Use standard programs like MATLAB, SAP2000 and ABAQUAS to solve the problems; you may also use your own program developed using the methods presented in the chapter.)

9.12 For the five-storey building frame, as shown in Figure 9.67, design: (i) the New Zealand rubber bearing; and (ii) friction pendulum isolation systems satisfying the required criteria for practical implementation for a PGA of 0.36g.

9.13 The same building frame, as shown in Figure 9.67, is subjected to the El Centro earthquake. The columns of the frame are connected to the base slab as shown in the figure. The backbone curve of the isolator which is used to isolate the building is given in Figure 9.16. Obtain the time histories of: (i) the top-floor displacement; (ii) the displacement of the base slab; and (iii) the base shear.

9.14 The same building frame, as shown in Figure 9.67, is to be base isolated using New Zealand isolators at the bases of the columns. Analyze the base isolated system starting from the preliminary design to non-linear analysis. Use the response spectrum given in Figure 9.10 and damping modification coefficient given in the Example 9.4.Take the damping of the structure as 5% and PGA as 0.36g.

9.15 The response of the building frame shown in Figure 9.68 is controlled by a TMD placed at the top of the frame for the El Centro earthquake. m_t is taken as 6% of the total mass of the frame and c_t is taken as being equivalent to a damping ratio of 4%. The TMD is tuned to the fundamental frequency of the bare frame. Obtain the time histories of controlled: (i) the top-floor displacement; (ii) the top-floor absolute acceleration; and (iii) first-storey drift by both modal and state-space analyses.

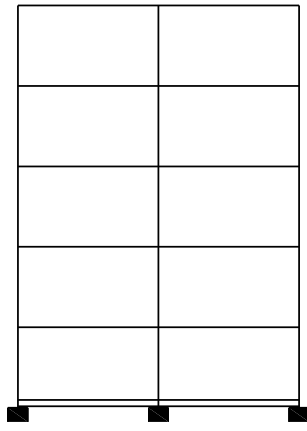

Figure 9.67 Properties of the frame to be base isolated

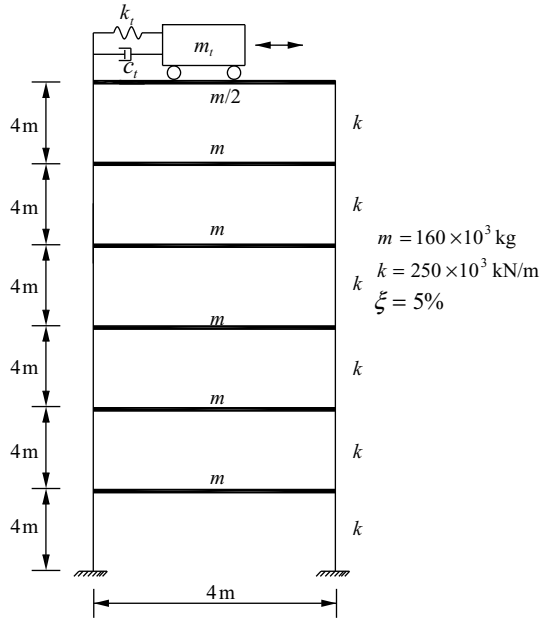

Figure 9.68 Details of the frame-TMD system

9.16 The building frame shown in Figure 9.68 is fitted with VEDs in the first four floors from the bottom. Using the Maxwell model for the VEDs, find the response of the frame for the El Centro earthquake given $\beta/m = 1200$; $\tau = 0.1$ by both frequency and time domain analyses.

9.17 The same frame shown in Figure 9.68 is actively controlled by an actuator placed at the first storey. The frame is subjected to the El Centro earthquake. Find the controlled displacements of the top

storey and the first storey using the pole placement technique with a full order observer and a reduced order observer corresponding to the responses of the first three floors. Assume the desired close loop poles such that at least 35% reduction in displacement of the first floor is achieved. Also, obtain the peak control force.

9.18 If the same frame as above is actively controlled by an actuator at the top storey, then obtain the time histories of controlled: (i) top floor displacement and acceleration; (ii) base shear; and (iii) of control force using LQR algorithm, and compare them with those obtained by the pole placement technique.

9.19 If two semi-active hydraulic dampers (SHDs) are employed at the first and the second floors of the same frame as above using the bracings as shown in Figure 9.62a, then obtain the time histories of controlled: (i) first floor displacement and absolute acceleration; (ii) top floor absolute acceleration; and (iii) of control forces in the two dampers. The specifications of the SHDs are $f_{\max} = 900$ kN; $c_{\max} = 150$ kN s m^{-1}. Assume the bracings to be rigid so that the relative velocity between the two floors can be taken as equal to the damper velocity.

References

1. Jangid, R.S. and Datta, T.K. (1995) Seismic behavior of base isolated building- a state of art review. *Journal of Structures and Buildings, Proceedings of Institute of Civil Engineers (London)*, **110**, 186–203.
2. Higashino, M. and Okamoto, S. (2006) *Response Control and Seismic Isolation of Building*, 1st edn, Taylor and Francis, London.
3. Jangid, R.S. and Datta, T.K. (1994) Non-linear response of torsionally coupled base isolated structure. *Journal of Structural Engineering, ASCE*, **120**(1), 1–22.
4. Saeid, P. and Datta, T.K. (2005) Semiactive fuzzy logic control of suspension bridge flutter. *Journal of Structural Engineering, ASCE*, **131**(6), 900–912.
5. Shukla, A.K. and Datta, T.K. (1999) Optimal use of viscoplastic dampers in building frames for seismic forces. *Journal of Structural Engineering, ASCE*, **125**(4), 401–409.
6. Inaudi, J.A., Zambrano, A., and Kelly, J.M. (1993) On the Analysis of Structure with Viscoelastic Damper. Technical Report UCB/EERC-93/06, Earthquake Engineering Research Centre, University of California, Berkeley, California.
7. Zhang, R.H., Soong, T.T., and Mahmoodi, P. (1989) Seismic response of steel frame structures with added viscoelastic dampers. *Earthquake Engineering and Structural Dynamics*, **18**(3), 389–396.
8. Claret, A.M. and Venancio-Filho, F. (1991) A modal superposition pseudo-force method for dynamic analysis of structural systems with non-proportional damping. *Earthquake Engineering and Structural Dynamics*, **20**, 303–315.
9. Chang, K.C., Chen, S.J., and Lai, M.L. (1993) Inelastic behavior of steel frames with added viscoelastic dampers. *Journal of Structural Engineering, ASCE*, **122**(10), 1178–1186.
10. Igusa, T., Kiureghian, A.D., and Sackma, J.L. (1984) Modal decomposition method for response of non-classically damped systems. *Earthquake Engineering and Structural Dynamics*, **12**, 121–136.
11. Soong, T.T. (1988) State-of-the-art review: active structure control in civil engineering. *Journal of Engineering Structures*, **10**(2), 73–84.
12. Housner, G.W., Bergman, L.A., Caughey, T.K. *et al.* (1997) Structural control: past, present and future. *Journal of Engineering Mechanics*, **123**(9), 897–971.
13. Ogata, K. (2001) *Modern Control Engineering*, 4th edn, Pearson Education Inc., Upper Saddle River, NJ.
14. Kalman, R.E., Ho, Y.C., and Narendra, K.S. (1962) Controllability of linear dynamic system, in *Contribution to Differential Equations, vol.* **II**, Wiley Interscience Inc., New York.
15. Yang, J.N., Agarwal, A.K., and Chen, S. (1996) Optimal polynomial control of seismically excited nonlinear and hysteric structures. *Earthquake Engineering and Structural Dynamics*, **25**(11), 1211–1230.
16. Nagarajaiah, S. (1997) Semi-active control of structures. Proceedings of Structures Congress XV, ASCE, Portland, OR, pp. 1574–1578.
17. He, W.L., Agrawal, A.K., and Mahmoud, K. (2001) Control of seismically excited cable-stayed bridge using resetting semiactive stiffness dampers. *Journal of Bridge Engineering, ASCE*, **6**(6), 376–384.
18. Ehrgott, R.C. and Masri, S.F. (1992) Modeling the oscillatory dynamic behaviour of electro-rheological materials in shear. *Smart Materials and Structures*, **1**(4), 275–285.
19. Ehrgott, R.C. and Masri, S.F. (1993) Structural control applications of an electro-rheological device. Proceedings of International Workshop on Structural Control, Honolulu, HI, pp. 115–129.
20. Spencer, B.F., Dyke, S.J., Sain, M.K., and Carlson, J.D. (1996) Dynamic model of a magneto-rheological damper. Proceedings of Structural Congress XIV, ASCE, Chicago, pp. 361–370.

21. Dyke, S.J., Spencer, B.F Jr., Sain, M.K., and Carlson, J.D. (1996) Experimental verification of semi-active control strategies using acceleration feedback. Proceedings of Third International Conference on Motion and Vibration Control. III, Chiba, Japan, pp. 291–296.
22. Dyke, S.J., Spencer, B.F. Jr., Sain, M.K., and Carlson, J.D. (1997) An experimental study og magneto-rheological dampers for seismic hazard mitigation. Proceedings of Structures Congress XV, Portland, OR, pp. 58–62.
23. Akbay, Z. and Aktan, H.M. (1991) Actively regulated friction slip braces. Proceedings of Sixth Canadian Conference on Earthquake Engineering, Toronto, Canada, pp. 367–374.
24. Feng, M.Q. (1993) Application of hybrid sliding isolation system to building. *Journal of Engineering Mechanics*, **119**(10), 90–108.
25. Sack, R.L., Kuo, C., Wu, H.C. *et al.* (1994) Seismic motion control via semi-active hydraulic actuators. Proceedings of fifth U.S. National Conference on Earthquake Engineering, Chicago, vol. 2, pp. 11–20.
26. Symans, M.D. and Constantinou, M.C. (1997) Seismic testing of a building structure with a semi-active fluid damper control system. *Earthquake Engineering and Structural Dynamics*, **26**(7), 759–777.
27. Yalla, S.K., Kareem, A., and Kantor, J.C. (2001) Semi-active tuned liquid column dampers for vibration control of structures. *Engineering Structures*, **23**, 1469–1479.
28. Ni, Y.Q., Chen, Y., Ko, J.M., and Cao, D.Q. (2002) Neuro control of cable vibration using semiactive magneto-rheological dampers. *Engineering Structures*, **24**, 295–307.
29. Sun, L. and Goto, Y. (1994) Application of fuzzy theory to variable dampers for bridge vibration control. Proceedings of 1st World Conference on Structural Control, International Association for Structural Control, Los Angeles, pp. 31–40.
30. Symans, M.D. and Constartinon, M.C. (1999) Semiactive control systems for seismic protection of structures: a state of the art review. *Engineering Structure*, **21**, 469–487.
31. Kurata, N., Kobori, T., Takahashi, M. *et al.* (1999) Actual seismic response controlled building with semi-active damper system. *Earthquake Engineering and Structural Dynamics*, **28**, 1427–1447.

Index